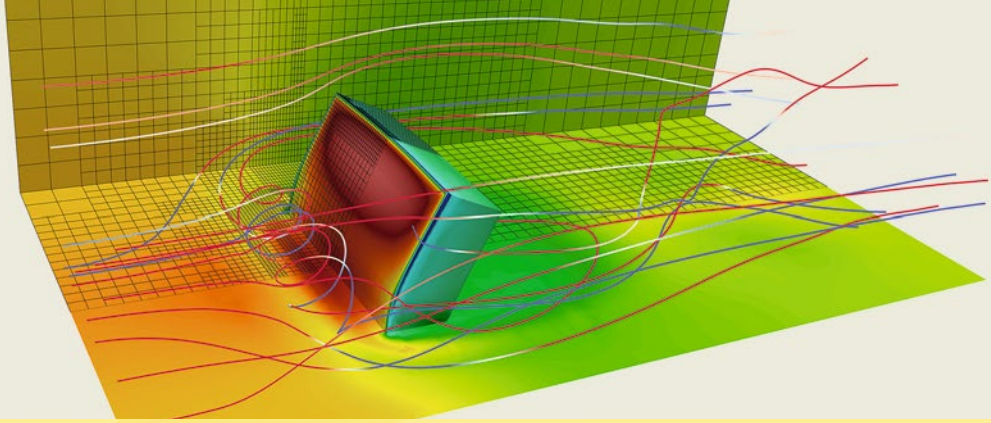

LECTURE NOTES IN COMPUTATIONAL SCIENCE AND ENGINEERING 118

Thomas Richter

Fluid-structure Interactions

Models, Analysis and Finite Elements

Springer

Lecture Notes in Computational Science and Engineering 118

Editors:

More information about this series at http://www.springer.com/series/3527

Thomas Richter

Fluid-structure Interactions

Models, Analysis and Finite Elements

Springer

Thomas Richter
Institut für Analysis und Numerik
Universität Magdeburg
Magdeburg, Germany

ISSN 1439-7358 ISSN 2197-7100 (electronic)
Lecture Notes in Computational Science and Engineering
ISBN 978-3-319-63969-7 ISBN 978-3-319-63970-3 (eBook)
DOI 10.1007/978-3-319-63970-3

Library of Congress Control Number: 2017948387

Mathematics Subject Classification (2010): 74F10, 65N30, 65M60, 65N85, 65M50, 65M15, 65M12, 65F10, 65F08

Printed on acid-free paper

This Springer imprint is published by Springer Nature
The registered company is Springer International Publishing AG
The registered company address is: Gewerbestrasse 11, 6330 Cham, Switzerland

Foreword

Fluid-structure interactions are an emerging topic in applied mathematics. Although computational methods have a long history in engineering applications, there is still no comprehensive presentation from a mathematical point of view. The work on the first manuscript on fluid-structure interactions started in the summer of 2010 along with the design of a class on *numerical methods for fluid-structure interactions* at the University of Heidelberg. A revision of this class in the winter of 2012 led to the first presentable version of lecture notes on this topic. The extensive and positive response to these notes was trigger and motivation for the much greater effort to compile a complete book on *models, analysis and finite elements for fluid-structure interactions*.

Research on fluid-structure interactions proceeds at an enormous pace that exceeds the capacity for reading and writing. A fully comprehensive study on such a topical subject will surely not be possible, but we believe that this book gives a thorough background and survey as a start for further investigations.

Magdeburg, Germany — Thomas Richter
June 2017

Preface

Fluid-structure Interactions

Fluid-structure interactions (FSI) play an important role in different applications. The classical aerodynamical problem of predicting the properties of a flying airplane is a fluid-structure interaction problem, as the plane will deform under aeroelastic forces and the deformation will alter the shape and hence the aeroelastic response of the plane. The pulsating flow of blood in big vessels causes significant deformation of the surrounding tissue with an extension of the vessel itself that will then alter the flow domain and therefore the flow pattern.

These two examples are classical FSI problems with a two-way coupling between the involved physical models: fluid flow and elastic material. Each of the subproblems acts on the other. As this coupling is acting at the *interface* that is the surface between the two subproblems fluid and solid, such problems are called *surface-coupled multiphysics problems*.

Simulations involving fluid-structure interactions have a long history in technical disciplines such as aeroelasticity or ship design. Computational methods for performing such simulations are often ad hoc and based on the coupling of existing simulation tools for the two subproblems. In fact, the state-of-the-art approach for computational fluid-structure interactions in real-world applications consists in the design of efficient coupling techniques that reuse available tools for the fluid and the solid problem. A mathematical analysis of the coupled FSI-system of equations describing the full fluid-structure interaction problem is still new. As the two subproblems, which are the (incompressible) Navier-Stokes equations for the fluid and an elastic solid equation for the solid, are big mathematical challenges on their own, it is no surprise that results for the coupled problem are rarely spread.

Scope of this Book

This book aims at giving a mathematical introduction to modeling, analysis and simulation techniques for fluid-structure interactions. As the field of possible applications is huge and as different applications will bring along different challenges that ask for adequate techniques each, we will focus our attention on problems involving a very strong coupling between the two subproblems of fluid and solid. A prototypical example is the flow of blood in blood vessels. Such problems call for strongly coupled approaches for modeling and simulation.

The book is divided into three parts. In the first part, we will start by introducing the basic models of continuum mechanics and give an overview of different material laws used to describe solids and incompressible fluids. For these models and equations, we will develop the fundamental mathematical theory that will give us answers on the existence, uniqueness and regularity of solutions. Given enough understanding of the two subproblems, we will be able to tackle coupled models for fluid-structure interactions. Both problems are coupled by means of boundary conditions on the common interface.

The first part of this book will also cover an introduction to the finite element method and into method for temporal discretization of partial differential equations. We start by gathering the essentials that are necessary to handle flow and structure problem. Afterward, we turn the attention to the special needs of the coupled fluid-structure interaction problem.

In the second part of the book, we describe two specific numerical models for the realization of fluid-structure interaction problems. This part focuses on monolithic formulations, where both subproblems are strongly linked and treated as one single common set of equations. We will derive mathematical formulation that will cover the fluid problem, the solid problem, and the interface conditions in between. Two different approaches are considered: First, we describe the *Arbitrary Lagrangian-Eulerian* approach, a well-established technique to model fluid-structure interactions that allows for very accurate discretization schemes. Second, we introduce the *Fully Eulerian* formulation of fluid-structure interactions, a novel modeling approach that is able to cover a wide range of different application problems. For these two approaches, we will introduce details on the discretization in space and time. Further, we will describe advanced techniques for the solution of the resulting algebraic systems. The complex structure of the coupled fluid-structure interaction problem combines the difficulties of flow problems with those of elastic structures. The resulting systems of equations are huge, lack desirable structure (such as symmetry), and incorporate a very stiff coupling.

Finally, we will discuss some advanced topics regarding the efficient numerical treatment of complex fluid-structure interaction problems. With the help of sensitivity analysis of the coupled problems, we will be able to design goal-oriented error estimators that will help to significantly reduce the computational costs for large simulations. Further, these techniques can be applied to solve simple optimization problems with fluid-structure interactions.

In the last third part, we gather different applications involving fluid-structure interactions. These applications are not necessarily real-world problems with an engineering background, but they describe prototypical situations with special challenges and difficulties. We start with an introduction to optimization and parameter identification problems, where the state variable is subject to a fluid-structure interaction problem. In this chapter we can make use of the sensitivity analysis that has already been introduced in the concept of error estimation and adaptivity. Next, we describe mechano chemical problems, where the fluid-structure interaction problem is coupled to further chemical reaction problem. A prototypical example for such problems is found in biomedical applications: the flow of blood in vessels is a fluid-structure interaction problem, as the vessel wall is elastic. If we consider pathological damages of the vessel tissue, we must incorporate chemical reactions that will slowly cause an alteration of the mechanical system by material change or material growth. This will affect the mechanics of the system and the fluid-structure interaction problem. If we finally assume that the chemical species that cause the reaction are transported within the blood, we are dealing with a three-way coupled fluid-solid-chemistry problem. Finally, we will analyze fluid-structure interaction problems with contact: if an elastic body—let it be a ball—touches the boundary of the fluid domain, we have contact. The topology of the coupled system changes, and we will observe that established techniques for fluid-structure interaction problems will fail. In this last chapter, further insight is given to the Fully Eulerian formulation.

Magdeburg, Germany Thomas Richter

Acknowledgments

This book would not have been possible without the scientific collaboration with various researchers working in the field of computational fluid dynamics and fluid-structure interactions. First of all, I want to highlight the contributions of Thomas Wick [285–288, 342, 344–348]. Some results within this book on the discretization of fluid-structure interactions in Arbitrary Lagrangian-Eulerian and in Fully Eulerian coordinates, but in particular results regarding sensitivity techniques for adaptivity in Sect. 8.3 and optimization in Chap. 9 are a joint effort with Thomas Wick. Furthermore, better understanding and efficient realization of the Fully Eulerian formulation of fluid-structure interactions were possible only with the help of Stefan Frei [151, 153, 154, 156–158, 212, 284], who made essential contributions in the field of interface problems (Sect. 4.5) and the accurate discretization of the Fully Eulerian formulation as presented in Chap. 6. Chapter 12 of this book is a guest article of Stefan Frei. He outlines the up-to-date details for a realization of fluid-structure interaction problems that involve contact of an elastic solid with the domain's boundary. Discussion and joint work with Florian Sonner [314, 316] helped to provide a better understanding of proper variational formulations and the coupling of fluid-structure interactions. A long-running cooperation with the optimal control group of Boris Vexler together with Lukas Failer and Dominik Meidner [133, 134] is the basis for a rigorous analysis of nonstationary fluid-structure interaction problems with applications to adaptivity and efficient time-stepping schemes [239, 240, 289].

This book project would not have been started without contact to Rolf Rannacher who gave motivation for a mathematically driven analysis of fluid-structure interaction problems [41, 212, 270]. Under his supervision Thomas Dunne [126–128] first developed the Fully Eulerian formulation for fluid-structure interactions that for the first time allowed to model large deformation and contact problems in a strictly monolithic and implicit manner. All numerical experiments included in this book have been carried out with the finite element software library GASCOIGNE 3D [43] that has initially been developed by Malte Braack and Roland Becker [35, 36, 38]. Both researchers also initiated the *local projection stabilization* scheme [37, 39], one important ingredient for the efficient discretization of complex multiphysics

problems. The *dual weighted residual method* for a posteriori error estimation and mesh adaptivity goes back to Roland Becker and Rolf Rannacher [40, 41]. Without the fundamental research of the mentioned researchers (and many others), complex problems like fluid-structure interactions could not be properly handled.

We gratefully acknowledge the funding of research projects that helped to support the investigations that led to this book. In particular we give credit to the *Juniorprofessorenprogramm* of the *Baden-Württemberg Stiftung*, the *Excellence Initiative* of *Heidelberg University*, as well as the *German Federal Ministry of Education and Research* with their program *Mathematics for Innovations in Industry and Services*.

Contents

Part I
Fundamentals

In the first part of this book we will present the fundamental concepts for modeling and simulation of fluid-structure interaction problems. Chapter 2 will present fundamental models and equations of continuum mechanics. We will discuss conservation laws as well as different material laws. Special focus is on the proper handling of coordinate systems, as one of the characteristic challenges of fluid-structure interaction problems is the motion of both subdomains of fluid and solid problem and the different coordinate concepts *Eulerian versus Lagrangian* used for their description.

The following chapter will then discuss the coupling of the two subproblems. We analyze the physical conditions that are necessary to describe the coupling at the common interface. Further, we analyze different techniques to overcome the discrepancy between the different coordinate systems *Eulerian and Lagrangian* for fluid and solid.

The fourth chapter in this first part recapitulates the necessary background in discretization techniques. We will discuss discretization in time with traditional time stepping schemes. Further we introduce temporal Galerkin schemes as modern alternatives that allow for an easier analysis. Next, the spatial discretization with the finite element method is introduced. We describe the special needs of saddle-point systems that appear in all incompressible materials. Further, we gather some facts on stabilization methods for transport dominant problems. Finally, we discuss the discretization of interface problems, i.e. problems with an interior interface where the equations changes is type or parameter. Here we already prepare the discretization of fluid-structure interaction problems.

Chapter 1
Introduction

1.1 Applications for Fluid-structure Interactions

Many application problems involve the coupling of fluid-dynamics and solid-dynamics. If a large aircraft is flying, the aerodynamical forces cause a substantial bending of the wings. This deformation significantly alters the geometry of the aircraft and affects its aerodynamical properties. Airborne, the tip of the wing will be deflected upwards by up to 10 m compared to the runway position. A simulation of the dynamics of flying planes must take this coupling into account.

If we consider the hemodynamical flow of blood in large vessels like the aorta or the blood flow in the heart, the forces on the vessel walls will lead to a widening and stretching of the tissue that again changes the overall geometry. Then, on the other hand, the new geometry will call for a new flow-field.

The lubricant flow in ball-bearings takes place in a very narrow channel between the balls and the surrounding ring. This gap can be as small as 100 nm. Enormous pressures and forces act and will cause a deformation of the surrounding steel parts. Steel of course is very stiff and deformation is small, but even a widening of the channel of only 50 nm can completely change the flow channel. Under the extreme conditions in the lubrication film, the oil reacts nonlinear on the forces, such that non-Newtonian material laws must be considered.

These problems have different characteristics, leading to different dynamics of the coupled system with different demands to the describing models and to the computational approaches. First of all, aerodynamical problems are in the regime of high Reynolds numbers with turbulent flow patterns and strictly three-dimensional character. The two other problems take place in the laminar regime. Furthermore, blood can be modeled as incompressible fluids, whereas air—at high velocity—or oil—at extreme pressures—must be treated as compressible. Numerical approaches for laminar and turbulent flows strictly differ. Here and in this context, we will deal with laminar problems only.

T. Richter, *Fluid-structure Interactions*, Lecture Notes in Computational Science and Engineering 118, DOI 10.1007/978-3-319-63970-3_1

Another striking difference between these problems is the type of material in the two phases, fluid and solid. The density of air is about $\rho_{\text{air}} \approx 1\,\text{kg}\cdot\text{m}^{-3}$, the density of water, blood or oil approximately $\rho_{\text{water}} \approx 1000\,\text{kg}\cdot\text{m}^{-3}$. Aluminum, as an important material in aircraft design has a density of $2700\,\text{kg}\cdot\text{m}^{-3}$, steel a density of about $7850\,\text{kg}\cdot\text{m}^{-3}$ and biological tissue about $\rho_{\text{tissue}} \approx 1000\,\text{kg}\cdot\text{m}^{-3}$. We will see that the ratio of the masses plays an important role in the dynamics of the coupling between an elastic solid and an incompressible fluid. Approaches that may work very efficiently for coupling the flow of air interacting with steel $\rho_{\text{air}}/\rho_{\text{steal}} \approx 0.00013$, may cease work, when used to describe a coupled configuration of blood and biological tissue with $\rho_{\text{blood}}/\rho_{tissue} \approx 1$. This effect of instability is called *added-mass effect*.

1.2 Dynamics of Fluid-structure Interactions

The dynamics of fluid-structure interactions are caused by the interplay of the two different phases, fluid and structure. Physically, the coupling is usually realized by three different principles. First, as a *geometric condition*, the common domain of fluid and solid—we always call it Ω—is divided into the fluid part $\mathcal{F}$ and the solid part $\mathcal{S}$. These two domains do not overlap $\mathcal{F} \cap \mathcal{S} = \emptyset$ and they are divided by the interface $\mathcal{I} = \partial\mathcal{F} \cap \partial\mathcal{S}$, such that $\Omega = \mathcal{F} \cup \mathcal{I} \cup \mathcal{S}$. The domains can change over time $\Omega \mapsto \Omega(t)$, $\mathcal{F} \mapsto \mathcal{F}(t)$ and $\mathcal{S} \mapsto \mathcal{S}(t)$, but the *geometric condition* will always hold, e.g. $\mathcal{S}(t) \cap \mathcal{F}(t) = \emptyset$ and $\Omega(t) = \mathcal{F}(t) \cup \mathcal{I}(t) \cup \mathcal{S}(t)$, where $\mathcal{I}(t) = \partial\mathcal{F}(t) \cap \partial\mathcal{S}(t)$. Usually, no holes will appear between fluid and structure. There are of course models, e.g. cavitation, where exactly such a thing has to be considered. The second coupling condition is the *kinematic condition*: the velocity of the fluid at the interface $\mathcal{I}(t)$ is the same, as the velocity of the solid at the interface. This means that the fluid will stick to the boundary, which is the moving interface. This model is similar to the no-slip condition in viscous fluid-dynamics. The fluid will simply stick to the wall which now might move. Alternative conditions are possible. In the inviscid regime, e.g. when considering problems of aeroelasticity, the no-slip condition can be relaxed to a non-penetration condition that only prescribes the motion in normal direction: the fluid will not enter the solid (and it will not move apart to open holes). Finally, the third *dynamic condition* prescribes a balance of normal stresses at the boundary in terms of *actio et reactio*.

These three conditions together mainly determine the dynamics of the coupled problem. One of the big challenges connected to fluid-structure interactions is the motion of the underlying domains. We have to deal with equations of fluid- and solid-dynamics on moving domains. In structure mechanics, this is typical, as the motion of the solid is exactly the unknown solution. In fluid-dynamics one usually deals with fixed domains. Moving domains only play a role in certain applications, like large scale ocean or atmospheric dynamics, where the rotation of the earth, the underlying domain, has to be taken into account. Here, in addition to dealing with moving domains, we need to face the fact that the motion is not pre-described,

but unknown part of the coupled solution. Section 5.1.1 and Chap. 11 will focus on an analysis of the nonlinear and non-stationary dynamics of coupled fluid-structure interaction problems.

1.3 Mathematical Challenges

The mathematical challenges in the analysis of fluid-structure interactions are manifold. Even for the governing equations of the two sub-systems, the Navier-Stokes equations in fluid-dynamics and conservation equations for nonlinear hyper-elastic materials, many theoretical questions are still not answered. We can show existence and uniqueness of solutions only for regular data and only locally in time. Without a full understanding of these subproblems, it is obvious that we cannot give complete results for the coupled system of equations. It will show that the main mathematical problem of coupled fluid-structure interactions will come from the motion of the domains and from the realization of the coupling conditions. While the (incompressible) Navier-Stokes equations are of parabolic type, the structural equations are of hyperbolic type. We will see that the notation of the kinematic coupling condition that glues velocities of fluid and solid together, is not well-posed. Furthermore, by the motion of the fluid domain (which follows the deflection of the structural domain) it is easily possible to lose regularity and smoothness of the interface, where all the coupling takes place.

It is well beyond the scope of this book to give new results concerning the mathematical theory of existence and uniqueness of the underlying equations. Instead, we will provide the reader with an overview of topical results and research that is currently under investigation.

1.4 Partitioned Approaches

Numerical simulations of fluid-structure interaction problems have a long history. Early approaches are based on the independent experience with problems of fluid-dynamics and structure-dynamics, which are well-understood. Existing simulation tools for these two types of problems are well developed and very efficient. In industrial applications they are established and used on a daily basis. It is not astonishing that this long experience is also adapted to the coupled configuration. This leads to the concept of *partitioned approaches* for fluid-structure interactions. Existing methods for handling fluid- and structure-dynamical problems are coupled by means of an outer control. This outer coupling is to be taken literally and extends to the coupling of two completely different software-frameworks used for the two subproblems: efficient finite volume schemes for fluid-dynamics and state of the art finite element schemes in solid dynamics are connected by means of boundary

condition and traction forces. Such an ad hoc approach will guarantee quick success and allows to treat complex application problems.

The basic approach for coupling is build on temporal discretization of the two problems by simple time stepping schemes. For approaching a new time step, one has to solve both subproblems for fluid and solid and one has to take into account the coupling conditions. These three tasks are fully coupled and each one has an effect on the others: motion of the solid changes the geometry and therefore the fluid-domain (geometric condition). Motion of the interface prescribes a motion of the attached fluid (kinematic condition). Modification of the fluid-domain will alter the flow field and hence generate new forces on the interface (dynamic condition).

Most basic partitioned methods for fluid-structure interactions can be regarded as semi-implicit time stepping schemes. Instead of performing a coupled solution step for fluid, structure and interface conditions, one first solves the one problem while neglecting the other and then takes a step of the second problem. Let us assume that f^n and s^n are the states for fluid and solid at time t_n and that Ω^n, $\mathcal{F}^n$ and $\mathcal{S}^n$ is the domain partitioning. Then, a simple partitioned scheme could consist of performing a step of the solid problem, driven by the fluid's normal stresses at time t_n

$$S(f^n, s^n, \Omega^n) \mapsto s^{n+1}. \tag{1.1}$$

This new solid state s^{n+1} includes a prediction for the deformation, i.e. the shape of the domain Ω^{n+1}, at time t_{n+1}. Furthermore, by s^{n+1} and s^n we can estimate the velocity of the interface. Using this interface velocity as boundary condition for the fluid's velocity, we can perform a step of the flow problem on the predicted domain Ω^{n+1}

$$F(f^n, s^n, s^{n+1}, \Omega^{n+1}) \mapsto f^{n+1}. \tag{1.2}$$

Such weakly coupled partitioned schemes are very easy to implement, as they only require the successive solution of the two different subproblems and the possibility to modify the fluid-domain during the simulation. In particular in aeroelasticity, partitioned schemes are widely used.

These simple schemes cannot guarantee a solution of the fully coupled problem. In each of the two sub-steps, one focuses on one problem only and one takes only parts of the coupling conditions into account. There will be a splitting error in the interface condition which is at least as large as the time step size. For many applications, this simple approach is furthermore not stable and may require vanishing time step sizes to show convergence at all.

A first step towards an accurate and controllable solution of the coupled problem is to iteration the two solution steps (1.1) and (1.2) until convergence is reached. Denoting the solution of (1.1) $s^{n+1,(0)}$ and the solution of (1.2) $f^{n+1,(0)}$ we iterate for $i = 1, 2, \ldots$

$$\begin{aligned} S(f^{n+1,(i)}, s^{n+1,(i)}, \Omega^{n+1,(i)}) &\mapsto s^{n+1,(i+1)}, \Omega^{n+1,(i+1)}, \\ F(f^{n+1,(i)}, s^{n+1,(i+1)}, \Omega^{n+1,(i+1)}) &\mapsto f^{n+1,(i+1)}, \end{aligned} \qquad i = 1, 2, \ldots$$

This iteration is repeated, until convergence is reached. Strongly coupled partitioned schemes solve the fully coupled fluid-structure interaction problem. For some applications however—in particular if the *added mass effect* acts—many sub-iterations of very small time steps can be required.

There exists vast literature on the development of acceleration schemes for strongly coupled partitioned iterations and their analysis. Most real-world applications nowadays use partitioned solvers. This is partially due to the effect that partitioned schemes allow for the use of highly tuned and efficiently implemented software frameworks for the two subproblems. Partially the success of this approach must be attributed to the necessity of reusing existing tools.

1.5 Monolithic Models and Finite Element Discretizations

From a mathematical viewpoint, partitioned approaches are not satisfying. First and most important: there exists no complete description of the coupled problem that includes fluid-problem, solid-problem and the interface conditions. Instead, the coupled problem is replaced by an algorithm. Without a fully coupled formulation of the complete problem it will never be possible to design discretization schemes that are fully implicit. For reasons of stability and to be allowed to use large time steps, this however is highly desirable. Having a fully coupled—we call it *monolithic*—model for the whole problem, we can furthermore use strongly coupled solution schemes like Newton linearization, multigrid or Krylov subspace methods for the complete problem without the need to sub-iterate between fluid and solid.

The derivation of monolithic models will be the first important task of this book. The main difficulty will be the realization of the coupling conditions and in particular mastering the moving domains. Once we have derived monolithic variational formulations of the coupled problem, we will be able to use all the powerful techniques of Galerkin methods, like simple spatial and temporal discretization, a priori and a posteriori error analysis and strongly coupled solution methods for the discrete variational problems.

For deriving variational monolithic models, we must overcome the difficulty of different coordinate frames usually used to describe the two subproblems. In this book, we follow the concept of domain mappings to bring the two different systems together. The *Arbitrary Lagrangian Eulerian* coordinate framework has

been introduced in the seventies of the last century to work with flow problems on moving domains [120, 192, 202]. It consists of defining a reference configuration $\hat{\mathcal{F}}$ and a mapping $T_f(t) : \hat{\mathcal{F}} \to \mathcal{F}(t)$ that captures the motion of the fluid-domain. The reference domain $\hat{\mathcal{F}}$ is called *arbitrary*, as it does no necessarily (it usually does not) have any physical meaning. $T_f(t)$ does not describe the mapping between the Lagrangian system and the Eulerian current system. Instead, $\hat{\mathcal{F}}$ is a fixed domain that is somewhere in between the Eulerian and the Lagrangian system. As an example, one can consider the observation of a car that is driving next to the own car at same speed. Viewing through the side window, the neighboring car appears fixed. This viewpoint is neither the Eulerian, where the car would move, or the Lagrangian, where we would follow the air-particles. If such a reference domain $\hat{\mathcal{F}}$ fits to the Lagrangian reference system of the solid $\mathcal{S}$ (as it does for the car example) and if the mapping $T_f(t)$ is such that it follows the motion of the interface, the *Arbitrary Lagrangian Eulerian* (ALE) framework is a simple way to transform the coupled fluid-structure interaction problem into a system that is fixed in space and time. While $\mathcal{S}$ is—at all times—the Lagrangian framework, $\hat{\mathcal{F}}$ is without physical meaning.

By the transformation onto the reference system, all problems can be formulated on fixed domains. The interface between solid $\mathcal{S}$ and fluid $\hat{\mathcal{F}}$ in fixed reference state will not move any more. This comes at the price of a transformation of the Navier-Stokes equations. As the motion of the domain cannot simply disappear, it enters as additional nonlinearity and as additional transport terms, comparable to the Coriolis effect in large scale flows of the ocean on the rotating earth. In ocean simulations, the computational domain is fixed and the rotation of the earth enters the equation as a Coriolis term.

The ALE framework is widely used for fluid-structure interactions. Not only to derive monolithic formulations, but also as a simple way to realize the coupling conditions in partitioned approaches. The success of the ALE method strongly depends on the quality, i.e. the regularity, of the mapping $T_f(t)$. If this mapping loses its regularity, the problem of the transformed Navier-Stokes equations will not longer be valid. ALE methods often fail, if the motion of the domains (in particular of the fluid domain) gets very large or if it is very fast. This can easily be explained using an extreme yet simple case: we want to describe the interaction of an elastic (or rigid that does not matter for this discussion) ball with a surrounding fluid. The ball is supposed to be more dense, such that it falls down. Realizing this problem in ALE coordinates requires a reference system $\hat{\mathcal{F}}$ and the ALE map $T_f(t) : \hat{\mathcal{F}} \to \mathcal{F}(t)$ mapping onto the current configuration. At some point, the ball will get close to the bottom boundary of the fluid-domain and may even touch it. Then, the topology of $\hat{\mathcal{F}}$ and $\mathcal{F}(t)$ differs. While $\hat{\mathcal{F}}$ has a hole (the ball), the domain $\mathcal{F}(t)$ at contact is simply connected, as the ball is now longer a hole in the domain, if it touches the exterior boundary. Such a mapping T_f between domains of different topology cannot be differentiable, not even continuous and the ALE formulation will fail.

Hence, we will introduce a second monolithic model for fluid-structure interaction that goes the other way around: the fluid-problem will be untouched and

reside in the Eulerian current system on the moving domain $\mathcal{F}(t)$. Instead, we will introduce a mapping $T_s(t)$ that maps the Lagrangian solid reference system to the Eulerian current system $T_s(t) : \mathcal{S} \rightarrow \mathcal{S}(t)$. The conceptual difference between the ALE map T_f and the Lagrangian-Eulerian map T_s of the solid problem is its physical background: T_f maps an artificial reference domain onto the current configuration. T_s maps between the Lagrangian and the Eulerian configuration. Both of them are physical and the elastic solid problem is well-posed in both configurations. The Lagrangian framework is usually considered, as it is more convenient for carrying out computations. The real world however is Eulerian. Regardless of the deformation or motion of the solid, both frameworks will be equivalent and can be used for describing the coupled problem. Coupling of fluid and solid will now take place on the moving interface $\mathcal{I}(t) = \partial\mathcal{F}(t) \cap \partial\mathcal{S}(t)$. This concept of *Fully Eulerian Coordinates* for fluid-structure interaction sounds strikingly simple and convincing. However, there are reasons for its very late introduction by Dunne [126] in 2005, as it allows for a simple mathematical description, but brings along plenty of difficulties. Most important, it requires to deal with moving domains and with a moving interface. While the interface location is fixed in the ALE method, its location is not even a priori known—but it has to be *captured*—during the simulation. Furthermore, convergence of all approximation techniques like finite elements or finite differences worsens, if interfaces or boundaries are not correctly approximated. The possibility to describe problems with arbitrarily large motions and deformations in a variationally coupled monolithic formulation comes at a high price.

Even if the focus of this book is on monolithic models, as they allow for more rigorous analysis of discretization and solution techniques, we will frequently discuss partitioned methods. An efficient numerical solver for a monolithic model will often make use of partitioned techniques.

1.6 Outline

The book is divided into three parts. The first one, *Fundamentals* deals with the basic models of fluid- and solid-mechanics, with the theory of coupling and with basic discretization techniques. The second part, *Realizations* details two monolithic models for fluid-structure interactions, the ALE approach and the Fully Eulerian Formulation. Further, we specify discretization and solution techniques for these two formulations. In the third part *Applications* we cover advanced topics as contact problems, interaction to chemistry or optimization problems.

Chapter 2 gives an overview of the models for fluid- and structure-dynamics that are involved in coupled fluid-structure interactions. We highlight the concept of continuum mechanics in different coordinate frameworks and configurations. Where it helps the understanding, we provide proofs for the fundamental theorems. Readers familiar with these basics can directly jump to the following Chap. 3. This overview

is too short for a comprehensive analysis, we however mention the main results and note plenty of literature for further reading.

In Chap. 3 the coupling of the two subproblems is detailed. We describe the different coupling conditions and their theoretical and practical implications. Here, we also derive variational formulations for coupled fluid-structure interactions in the two different coordinate frameworks: Arbitrary Lagrangian Eulerian and Fully Eulerian.

We continue in Chap. 4 with introducing the finite element method and techniques for discretization in time. After some basics on the discretization of elliptic and parabolic problems, followed by a discussion of saddle-point problems like the incompressible Navier-Stokes equations or conservation laws of incompressible solids, we quickly proceed to the special efforts of fluid-structure interactions. Most of this chapter is generic and does not only apply to fluid-structure interactions.

In Chaps. 5 and 6, we focus on the realization of the two monolithic models considered in this book, fluid-structure interactions in Arbitrary Lagrangian Eulerian and in Fully Eulerian coordinates. For both formulations we discuss details of the numerical realization, discretization in space and time, questions of linearization and discuss the solution of the resulting problems.

Chapter 7 is devoted to techniques for the solution of the very large linear systems arising from discretization and linearization of the coupled fluid-structure interaction problems. These large and complex problems lack any desirable structure like symmetry or positivity and are very ill-conditioned. To derive efficient numerical solvers, it will be necessary to abandon the strict monolithic character and to adapt ideas from partitioned approaches.

Advanced techniques for local mesh refinement, as a mechanism for reducing the dimension of the discretized problems are described in Chap. 8. In particular three dimensional problems quickly get huge. By introducing a posteriori error estimators for construction of efficient finite element meshes, we can strongly reduce the dimension of the discrete problem thus the time to solution.

The third part comprises four chapters with different advanced techniques. We call this part *Applications*, although we do not present industrial applications but discuss relevant configurations, that go beyond the scope of standard approaches. In Chap. 9 we start with optimization problems that involve fluid-structure interactions as constraint. We describe gradient based methods that will require the assembly of sensitivity information. Next, in Chap. 10 we tackle coupled mechano-chemical fluid-structure interaction problems. Chemistry will enter as a third field. In a prototypical problem we model the growth of plaques in blood vessels. In Chap. 11 we study the nonlinear dynamics of a fluid-structure interaction problem and will discuss the special properties that arise from the coupling of the non-stationary Navier-Stokes equations with the elastic solids. Finally, Chap. 12 will provide a method for handling fluid-structure interaction problems that include contact. Here, we make full use of the Fully Eulerian formulation. This last chapter is a guest article of Stefan Frei [151], who contributed the essential analysis and derived efficient numerical techniques for an accurate discretization of fluid-structure interactions in the Fully Eulerian formulation.

Chapter 2
Models

2.1 Continuum Mechanics

In this chapter, we derive the equations that describe the dynamics of fluids and solids. Matter is composed of molecules, atoms and smaller particles that all interact with each other. A description of the dynamics of these micro-structure is possible by fundamental physical laws. Such a particle centered view-point is however not feasible, if large physical objects are considered that consist of many atoms. To describe every particle in one liter of water, more than 10^{25} molecules must be considered. A description of every single molecule–or even every atom or subatomic particle–in a large scale hydrodynamical problem like the flow of water around a ship is completely out of bounds.

Instead, we consider a *continuum approach* for the description of the large scale dynamics. By a continuum, we denote a volume $V(t) \subset \mathbb{R}^3$ of (different) particles. Instead of describing every single particle, we only observe some few averaged properties of the complete volume. These properties are all considered as local density distributions. As example, we will denote by $\mathbf{v}(x,t)$ the average velocity of whatever particle may be in position $x \in V(t)$ at a given time t. Usually we assume that all physical quantities possess some smoothness. Depending on the situation, we will ask for integrability, continuity or differentiability.

In the following we will derive fundamental equations that describe the interplay of these averaged quantities. We will distinguish between basic physical principles, the *conservation principles* and *material laws*. While the conservation principles are based on *first principles* and we think of them as exact, *material laws* are usually simplifications, idealizations and derived by observation and measurements.

T. Richter, *Fluid-structure Interactions*, Lecture Notes in Computational Science and Engineering 118, DOI 10.1007/978-3-319-63970-3_2

2.1.1 Coordinate Systems

In the following, by $V(t) \subset \mathbb{R}^3$ we denote a *material volume*. We assume that $V(t)$ is entirely occupied by some material. This material has physical properties like density $\rho : V(t) \to \mathbb{R}$, velocity $\mathbf{v} : V(t) \to \mathbb{R}^3$, which is a three dimensional vector field, temperature $T : V(t) \to \mathbb{R}$ or pressure $p : V(t) \to \mathbb{R}$. We assume that the volume is moving. By $t_0 \in \mathbb{R}$ we denote the *initial time* and we observe the volume for $t \geq t_0$. By $V_0 := V(t_0)$ we denote the *reference configuration* of the volume. Often, t_0 is set arbitrarily, but we usually think of a system that is at rest and unstressed, e.g. a container filled with resting fluid or an elastic obstacle that is not deformed and where no stresses act. At time $t \geq t_0$, we denote by $V(t)$ the *current configuration*.

The volume $V(t)$ consists of particles, and we call $\hat{V} := V_0$ the material domain. For every particle $\hat{x} \in \hat{V}$, we denote by $x(\hat{x}, t) \in V(t)$ the location of the particle at time $t \geq t_0$. We assume that the path $\{x(\hat{x}, t), t \geq t_0\} \subset \mathbb{R}^3$ is continuous and that no two different particles $\hat{x}, \hat{x}' \in \hat{V}$ have the same position at any time $t \geq t_0$:

$$x(\hat{x}, t) = x(\hat{x}', t) \quad \Leftrightarrow \quad \hat{x} = \hat{x}'.$$

The mapping $\hat{T}(\hat{x}, t) := x(\hat{x}, t)$ is therefore invertible and we define the inverse mapping as $\hat{T}^{-1}(x, t) := \hat{x}(x, t)$. By $\hat{x}(x, t)$ we denote that particle $\hat{x} \in \hat{V}$ that at time $t \geq t_0$ takes position $x \in V(t)$.

In a continuum, we assume that no particles are destroyed or created such that the moving volume $V(t)$ is given by all coordinates $x \in \mathbb{R}^3$ that are occupied by a particle $\hat{x} \in \hat{V}$:

$$V(t) = \{x(\hat{x}, t) \in \mathbb{R}^3,\ \hat{x} \in \hat{V}\}.$$

Figure 2.1 shows this fundamental configuration.

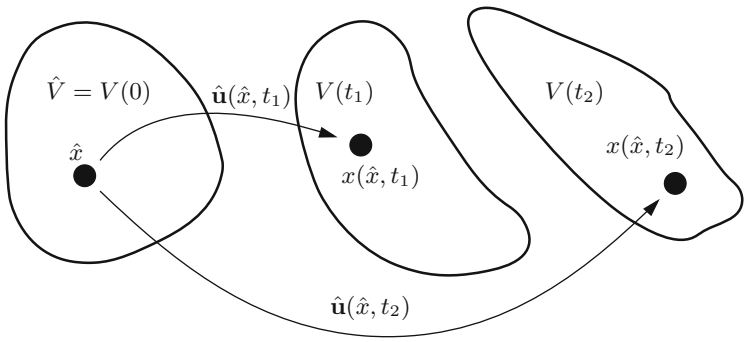

Fig. 2.1 The Lagrangian reference system. We describe the path of particles $\hat{x} \in \hat{V}$ over time. The reference volume $\hat{V}$ takes different current configurations $V(t)$ at different times. The particles within $V(t_1)$ are the same particles as in $V(t_2)$ or in $\hat{V} = V(t_0)$

We study the motion of volumes and the first fundamental property is the *deformation* of a particle $\hat{x} \in \hat{V}$. We define the *deformation* $\hat{\mathbf{u}}(\hat{x}, t)$ as

$$\hat{\mathbf{u}}(\hat{x}, t) = x(\hat{x}, t) - \hat{x}, \tag{2.1}$$

and its *material velocity* $\hat{\mathbf{v}}(\hat{x}, t)$ as

$$\hat{\mathbf{v}}(\hat{x}, t) := d_t x(\hat{x}, t) = d_t \hat{\mathbf{u}}(\hat{x}, t).$$

This particle system centered viewpoint for describing the dynamics of a continuum $V(t)$ is denoted as *Lagrangian coordinate system* or *Lagrangian framework*. In the Lagrangian system, we observe particles $\hat{x} \in \hat{V}$ and follow their paths $x(\hat{x}, t) = \hat{x} + \hat{\mathbf{u}}(\hat{x}, t)$ over time. A Lagrangian viewpoint is the natural approach for problems in solid mechanics, where the particles in the reference system are closely linked to each other and where forces are related to the relative deformation of particles to each other (think of a spring). Considering the dynamics of elastic solids, a volume comes back to the reference configuration, if the system is free of external forces

$$\begin{array}{c} \hat{V} = V_0 \\ \hat{x} = x(\hat{x}, 0) \end{array} \xrightarrow{\text{external forces act}} \begin{array}{c} V(t) \\ x(\hat{x}, t) \end{array} \xrightarrow{\text{absence of external forces}} \begin{array}{c} V(t_\infty) = \hat{V} \\ \hat{x} = x(\hat{x}, t_\infty) \end{array}$$

Deformation and velocity can also be defined in the current configuration $V(t)$. By

$$x = \hat{x} + \hat{\mathbf{u}}(\hat{x}, t) \quad \Leftrightarrow \quad \mathbf{u}(x, t) := \hat{\mathbf{u}}(\hat{x}, t) = x - \hat{x}$$

we have an expression $\mathbf{u}(x, t)$ for the deformation at the spatial location $x \in V(t)$. By $\mathbf{u}(x, t)$ we describe the deformation of a particle in location $x \in \mathbb{R}^3$ at time t, we however do not know or determine which individual particle $\hat{x}$ we have in mind. If we describe all quantities in the current configuration $V(t)$ and if we are not interested in single particles at all we do not even need the concept of a reference domain.

The difference between both approaches is the viewpoint: where $\hat{\mathbf{u}}(\hat{x}, t)$ denotes the deformation of the particle $\hat{x}$ at time t, by $\mathbf{u}(x, t)$ we denote the deformation of whatever particle $\hat{x}$ happens to be at location x at time t. If at time t it holds $x = x(\hat{x}, t)$, both concepts of deformation describe the same configuration. If we base the description of the continuum on the spatial coordinates $x \in V(t)$, we speak of the *Eulerian framework*, where the focus is set on a spatial domain $V \subset \mathbb{R}^3$ and all points $x \in V$, see Fig. 2.2. This viewpoint is natural for fluid-dynamical problems. We consider the estimation of the drag-coefficient of a car. Here, the attention is on the flow around the car and we measure forces on the surface of the car, irrespective of the actual particle that at time $t \geq 0$ interacts with the car. In fluid dynamics, we want to describe velocity and pressure at spatial points $x \in V$.

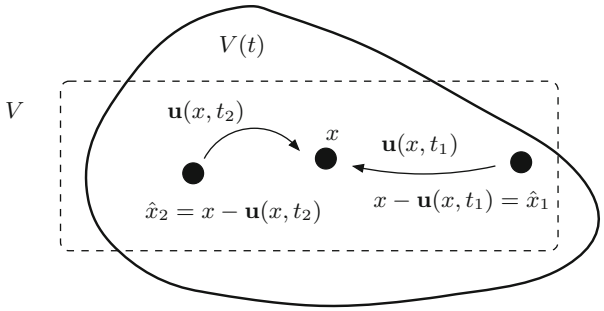

Fig. 2.2 The Eulerian reference system. We observe spatial coordinates $x \in V$, where $V \subset \mathbb{R}^3$ is a fixed view. Particles $\hat{x}$ may enter the domain V at a given time and leave it at another time. We observe properties of particles at certain times and locations, we however do not describe and follow the course of individual particles

Usually, we are not interested in what particle interacts with the car and where this particle comes from. Fluids like air or water do not have a *memory*. They behave in the same way regardless of their history. This of course is not true for all liquids. Material like polymers or rubber (which can be described as a fluid, if it is hot) actually do have a memory. Such viscoelastic fluids however are out of the scope of this book.

The Eulerian velocity $\mathbf{v}(x,t)$ is defined as the velocity in position $x \in \mathbb{R}^3$ at time t and given as

$$\mathbf{v}(x,t) = \partial_t u(x,t) = \partial_t \hat{\mathbf{u}}(\hat{x},t) = \hat{\mathbf{v}}(\hat{x},t).$$

In the Eulerian viewpoint, we do not describe, which particle $\hat{x}$ takes this position.

2.1.2 Deformation Gradient

In continuum mechanics, we study the behavior of moving and deforming continua $V(t)$ over time. In the following we describe the relative change of positions $x(\hat{x},t)$ and $x(\hat{y},t)$ of two particles $\hat{x},\hat{y} \in \hat{V}$ in a moving continuum. Relative change of location is called strain, and strain will show to be the most fundamental quantity that causes stress within the material. By stress, we denote the internal forces between the neighboring particles in a continuum.

Let $\hat{x} \in \hat{V}$ and $\hat{y} \in \hat{V}$ be two particles that are infinitesimally close to each other, i.e. $|\hat{y} - \hat{x}| \to 0$. Under deformation, these two particles have the position

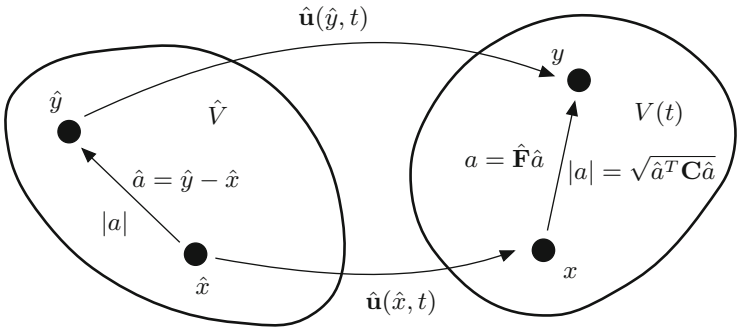

Fig. 2.3 Transformation of infinitesimal line segment $\hat{a}$ to a with $|\hat{a}| \to 0$. Deformation gradient $\hat{\mathbf{F}} = I + \hat{\nabla}\hat{\mathbf{u}}$ and squared length change $|a|^2 = \hat{a}^T\hat{\mathbf{C}}\hat{a}$ indicated by the right Cauchy-Green tensor $\hat{\mathbf{C}} = \hat{\mathbf{F}}^T\hat{\mathbf{F}}$

$x = \hat{x} + \hat{\mathbf{u}}(\hat{x}) \in V$ and $y = \hat{y} + \hat{\mathbf{u}}(\hat{y}) \in V$. We measure the change in position $y - x$ in V with respect to $\hat{y} - \hat{x}$ in $\hat{V}$, see Fig. 2.3. By first order Taylor expansion we deduce

$$\begin{aligned} y - x &= \hat{y} + \hat{\mathbf{u}}(\hat{y}) - \hat{x} - \hat{\mathbf{u}}(\hat{x}) \\ &= \hat{y} - \hat{x} + \sum_{i=1}^{d} \hat{\partial}_i \mathbf{u}(\hat{x}) \cdot (\hat{y} - \hat{x}) + O(|\hat{y} - \hat{x}|^2) \\ &= \hat{y} - \hat{x} + \hat{\nabla}\hat{\mathbf{u}}(\hat{x})(\hat{y} - \hat{x}) + O(|\hat{y} - \hat{x}|^2), \end{aligned} \tag{2.2}$$

where by $|\hat{x}| = \sqrt{\sum_{i=1}^{d} \hat{x}_i^2}$ we denote the Euclidean norm, by $\hat{x} \cdot \hat{y} = \sum_{i=1}^{d} \hat{x}_i \hat{y}_i$ the Euclidean scalar product and by $\hat{\partial}_i$ the partial derivative with respect to $\hat{x}_i$ in the Lagrangian coordinate system. Considering the relative change in position, it holds

$$\frac{y - x}{|\hat{y} - \hat{x}|} = [I + \hat{\nabla}\hat{\mathbf{u}}(\hat{x})]\frac{\hat{y} - \hat{x}}{|\hat{y} - \hat{x}|} + O(|\hat{y} - \hat{x}|). \tag{2.3}$$

We define

Definition 2.1 (Deformation Gradient) Let $\hat{\mathbf{u}}$ be a differentiable deformation field in the material volume $\hat{V}$. The *deformation gradient*

$$\hat{\mathbf{F}}(\hat{x}, t) := I + \hat{\nabla}\hat{\mathbf{u}}(\hat{x}, t),$$

denotes the local change of relative position under deformation.
The deformation gradient is the fundamental measure in structure dynamics.

Lemma 2.2 (Determinant of the Deformation Gradient) *Let $\hat{V}$ be a reference volume and $\hat{\mathbf{u}} : \hat{V} \to \mathbb{R}^d$ be a differentiable deformation field. The determinant of*

the deformation gradient $\hat{J} := \det(\hat{\mathbf{F}})$ *denotes the local change of volume:*

$$|V(t)| = \int_{\hat{V}} \hat{J} \, \mathrm{d}\, x.$$

Proof It holds by the transformation theorem

$$|V(t)| = \int_{V(t)} 1 \, \mathrm{d}\, x = \int_{\hat{V}} \det(I + \hat{\nabla}\hat{\mathbf{u}}) \, \mathrm{d}\hat{x} = \int_{\hat{V}} \hat{J} \, \mathrm{d}\hat{x}.$$

□

The deformation gradient $\hat{\mathbf{F}}$ applies to the Lagrangian viewpoint. For an Eulerian description in $V(t)$, we can define the inverse deformation gradient $\mathbf{F}$ in a similar way. For two spatial coordinates $x, y \in V$ belonging to particles $\hat{x}$ and $\hat{y}$ in $\hat{V}$ it holds

$$\frac{\hat{y} - \hat{x}}{|y - x|} = \mathbf{F}(x) \frac{y - x}{|y - x|} + O(|y - x|),$$

with the *inverse deformation gradient* $\mathbf{F}(x, t) = I - \nabla \mathbf{u}(x, t)$. It holds $\mathbf{F} = \hat{\mathbf{F}}^{-1}$.

Very often, it will be necessary to rapidly switch between different viewpoints on the same physical problem. Sometimes, it is appropriate to consider the material centered reference domain $\hat{V}$, while sometimes the Eulerian viewpoint of the current configuration $V(t)$ is better suited. Usually, we denote all entities in the material system with a hat "$\hat{\cdot}$" and use the same notation without the hat for the Eulerian notation. Every basic property like velocity and deformation has a Eulerian counterpart, e.g. $\mathbf{v}(x, t) = \hat{\mathbf{v}}(\hat{x}, t)$ and $\mathbf{u}(x, t) = \hat{\mathbf{u}}(\hat{x}, t)$, where for $\hat{x}$ and x at a given time $t \geq t_0$ it always holds $x = \hat{x} + \hat{\mathbf{u}}(\hat{x}, t)$. When referring to derivatives of these basic quantities, a simple "$\nabla \mathbf{u} = \hat{\nabla}\hat{\mathbf{u}}$" is usually wrong. Instead, we need to derive rules to map between both coordinate frames:

Lemma 2.3 (Transformation Between the Reference and the Current Configuration) *Let* $I = [0, T]$ *be a time interval,* $\hat{V}$ *be a reference domain and* $\hat{\mathbf{u}} \in C^1(I \times \hat{V})^3$. *We assume that* $T := \mathrm{id} + \hat{\mathbf{u}}$ *defines a* C^1*-diffeomorphism between* $\hat{V}$ *and*

$$V(t) = \{\hat{x} + \hat{\mathbf{u}}(\hat{x}, t), \ \hat{x} \in \hat{V}\}.$$

Let $\hat{f} \in C^1(I \times \hat{V})$ *and* $f(x, t) = f(x(\hat{x}, t), t) = \hat{f}(\hat{x}, t)$ *be its counterpart in the current configuration. It holds*

$$\hat{\nabla}\hat{f} = \hat{\mathbf{F}}^T \nabla f \tag{2.4}$$

and

$$d_t f = d_t \hat{f}, \quad \partial_t f = \partial_t \hat{f} - \hat{\mathbf{F}}^{-T} \hat{\nabla}\hat{f} \cdot \hat{\mathbf{v}}. \tag{2.5}$$

Let $\hat{\mathbf{w}} \in C^1(I \times \hat{V})^3$ *be given with counterpart* $\mathbf{w}(x,t) = \hat{\mathbf{w}}(\hat{x},t)$. *It holds*

$$\hat{\nabla}\hat{\mathbf{w}} = \nabla \mathbf{w}\hat{\mathbf{F}}. \tag{2.6}$$

Proof For the spatial derivative of $f(x,t)$ it holds with $x(\hat{x},t) = \hat{x} + \hat{\mathbf{u}}(\hat{x},t)$:

$$\hat{\partial}_i \hat{f}(\hat{x},t) = \hat{\partial}_i f(x(\hat{x},t),t) = \sum_j \partial_j f(x,t)\hat{\partial}_i x^j(\hat{x},t) = \sum_j \partial_j f(x,t)\hat{\mathbf{F}}_{ji}.$$

Hence

$$\hat{\nabla}\hat{f} = \hat{\mathbf{F}}^T \nabla f.$$

Then, for a vector field $\mathbf{w} = (\mathbf{w}_i)_i$ it follows

$$(\hat{\nabla}\hat{\mathbf{w}})_{ij} = \hat{\partial}_j \hat{\mathbf{w}}_i = \sum_k \partial_k \mathbf{w}_i \hat{\partial}_j x^k(x,t) = (\nabla \mathbf{w})_{ik}\hat{\mathbf{F}}_{kj} = (\nabla \mathbf{w}\hat{\mathbf{F}})_{ij}$$

For the total time derivative it holds with $\partial_t x(\hat{x},t) = \hat{\mathbf{v}}(\hat{x}) = \hat{\mathbf{v}}(x)$

$$d_t f(x,t) = \partial_t f + \nabla f \cdot \mathbf{v}. \tag{2.7}$$

Then, with $\hat{x} = \hat{x}(x,t) = x - \mathbf{u}(x,t)$ and using (2.4):

$$d_t \hat{f}(\hat{x},t) = d_t f(x(\hat{x},t),t) = \partial_t f + \nabla f \cdot \partial_t x(\hat{x},t) = \partial_t f + \hat{F}^{-T}\hat{\nabla}\hat{f} \cdot \hat{\mathbf{v}}.$$

Finally, the last results follows with (2.7). □

2.1.3 Strain

Strain is defined as the deformation within a body relative to a reference length. Fixed body rotations or translation undergo no strain, as the relative positions of all particles is kept constant. Strain will be the basic quantity used to describe stresses in solid mechanics. A simple model is a spring, where change of length—the strain—will be proportional to a force.

Let $\hat{a} = \hat{y} - \hat{x}$ be the vector of a line-segment between the two points $\hat{x}, \hat{y} \in \hat{V}$. Then, given a deformation field $\hat{\mathbf{u}} : \hat{V} \to \mathbb{R}^3$, let $x = \hat{x} + \hat{\mathbf{u}}(\hat{x})$ and $y = \hat{y} + \hat{\mathbf{u}}(\hat{y})$ and set $a := y - x$. It holds with (2.3) that

$$a = y - x = \hat{\mathbf{F}}(\hat{x})\hat{a} + O(|\hat{a}|^2),$$

and the length of $|a|$ is given as

$$|a| = \sqrt{(\hat{\mathbf{F}}\hat{a}, \hat{\mathbf{F}}\hat{a}) + O(|\hat{a}|^3)} = \sqrt{(\hat{a}^T, \hat{\mathbf{F}}^T\hat{\mathbf{F}}\hat{a})} + O(|\hat{a}|^2).$$

For an illustration, see Fig. 2.3. By $\hat{\mathbf{C}} = \hat{\mathbf{F}}^T\hat{\mathbf{F}}$ we denote the *right Cauchy-Green tensor* which is also denoted as the *Green deformation tensor*. This tensor is symmetric and positive definite, as

$$(\hat{\mathbf{C}}\hat{a}, \hat{a}) = (\hat{\mathbf{F}}\hat{a}, \hat{\mathbf{F}}\hat{a}) = \|\hat{\mathbf{F}}\hat{a}\|^2 > 0 \quad \forall \hat{x} \neq 0,$$

and it describes the (squared) length scaling of a line-segment in direction $\hat{a} = \hat{y} - \hat{x}$. A further commonly used strain measure is the *Green-Lagrange strain tensor* $\hat{\mathbf{E}} := \frac{1}{2}(\hat{\mathbf{C}} - I) = \frac{1}{2}(\hat{\mathbf{F}}^T\hat{\mathbf{F}} - I)$ that measures the (squared) length change of a line-segment $\hat{a} = \hat{y} - \hat{x}$ under deformation $a = y - x$:

$$\begin{aligned} \frac{1}{2}\left(|a|^2 - |\hat{a}|^2\right) &= \frac{1}{2}\left(\hat{a}^T\hat{\mathbf{C}}\hat{a} - \hat{a}^T\hat{a}\right) + O(|\hat{a}|^3) \\ &= \hat{a}^T\left(\frac{1}{2}(\hat{\mathbf{F}}^T\hat{\mathbf{F}} - I)\right)\hat{a} + O(|\hat{a}|^3). \end{aligned} \tag{2.8}$$

The tensors $\hat{\mathbf{C}} = \hat{\mathbf{F}}^T\hat{\mathbf{F}}$ and $\hat{\mathbf{E}} = \frac{1}{2}(\hat{\mathbf{C}} - I)$ are nonlinear functions in the deformation $\hat{\mathbf{u}}$:

$$\hat{\mathbf{C}} = I + \hat{\nabla}\hat{\mathbf{u}} + \hat{\nabla}\hat{\mathbf{u}}^T + \hat{\nabla}\hat{\mathbf{u}}^T\hat{\nabla}\hat{\mathbf{u}}, \quad \hat{\mathbf{E}} = \frac{1}{2}\left(\hat{\nabla}\hat{\mathbf{u}} + \hat{\nabla}\hat{\mathbf{u}}^T + \hat{\nabla}\hat{\mathbf{u}}^T\hat{\nabla}\hat{\mathbf{u}}\right).$$

Given a very small variation in deformation, i.e. $|\hat{\nabla}\hat{\mathbf{u}}| \ll 1$, one sometimes uses linearization of the strain tensors as an approximation:

$$\mathbf{c} = I + \hat{\nabla}\hat{\mathbf{u}} + \hat{\nabla}\hat{\mathbf{u}}^T, \quad \boldsymbol{\varepsilon} = \frac{1}{2}\left(\hat{\nabla}\hat{\mathbf{u}} + \hat{\nabla}\hat{\mathbf{u}}^T\right).$$

These approximations can be good approximations under certain conditions. One however has to be careful, as having a small deformation $\hat{\mathbf{u}}$ is not a sufficient condition for this linearization.

The tensors $\hat{\mathbf{F}}$, $\hat{\mathbf{C}}$, $\hat{\mathbf{E}}$ and the linearized strain tensor $\boldsymbol{\varepsilon}$ all refer to the Lagrangian material coordinate system. They are called *material strain tensors*. Sometimes, we need to express strain in the spatial coordinate system, directly on the current frame $V(t)$. Hence let $x, y \in V(t)$ be two spatial coordinates at time $t \geq t_0$, spanning the line-segment $a = y - x$. By $\hat{x}, \hat{y} \in \hat{V}$ we denote the material points corresponding to this line-segment. These span the material line-segment $\hat{a} = \hat{y} - \hat{x}$. Similar to (2.3), but using the Eulerian notation $\mathbf{u}(x, t) = \hat{\mathbf{u}}(\hat{x}, t)$ we get

$$\hat{y} - \hat{x} = y - \mathbf{u}(y) - (x - \mathbf{u}(x)) = [I - \nabla\mathbf{u}(x)](y - x) + O(|y - x|^2).$$

By $\mathbf{F}(x) = I - \nabla \mathbf{u}(x)$ we denote the *inverse deformation tensor*. It holds $\mathbf{F}(x) = \hat{\mathbf{F}}(\hat{x})^{-1}$ for $x = \hat{x} + \hat{\mathbf{u}}(\hat{x})$. $\mathbf{F}(x)$ is the deformation gradient in the current configuration and it acts on the spatial coordinate system. With help of $\mathbf{F} = I - \nabla \mathbf{u}$ we can immediately analyze length changes in the spatial system. Let $a = y - x$ and $\hat{a} = \hat{y} - \hat{x}$. It holds

$$|\hat{a}|^2 = (\mathbf{F}a, \mathbf{F}a) + O(|a|^3) = a^T \mathbf{F}^T \mathbf{F} a + O(|a|^3) = a^T \hat{\mathbf{F}}^{-T} \hat{\mathbf{F}}^{-1} a + O(|a|^3).$$

The tensor $\mathbf{b}^{-1} := \hat{\mathbf{F}}^{-T} \hat{\mathbf{F}}^{-1} = \mathbf{F}^T \mathbf{F}$ is the inverse of the *left Cauchy-Green tensor* $\mathbf{b}$

$$\mathbf{b} = \hat{\mathbf{F}} \hat{\mathbf{F}}^T.$$

As $\hat{\mathbf{C}}$, $\mathbf{b}$ is symmetric positive definite. Finally, we can define the spatial Eulerian counterpart $\mathbf{e} = \frac{1}{2}(I - \mathbf{F}^{-T}\mathbf{F}^{-1})$ to the Cauchy-Green strain tensor $\hat{\mathbf{E}}$. By (2.8), it holds

$$\frac{1}{2}\left(|a|^2 - |\hat{a}|^2\right) = \hat{a}^T \hat{\mathbf{E}} \hat{a} + O(|\hat{a}|^3),$$

and with

$$\hat{a}^T \hat{\mathbf{E}} \hat{a} = a^T \hat{\mathbf{F}}^{-1} \hat{\mathbf{E}} \hat{\mathbf{F}}^{-T} a + O(|\hat{a}|^3),$$

we introduce

$$\mathbf{e} := \frac{1}{2}\left(I - \mathbf{F}\mathbf{F}^T\right) = \frac{1}{2}\left(I - \hat{\mathbf{F}}^{-1} \hat{\mathbf{F}}^{-T}\right) = \hat{\mathbf{F}}^{-1} \hat{\mathbf{E}} \hat{\mathbf{F}}^{-T}$$

the symmetric *Euler-Almansi strain tensor* $\mathbf{e}$ that enables us to relate length changes to the Eulerian line segment a:

$$\frac{1}{2}\left(|a|^2 - |\hat{a}|^2\right) = a^T \mathbf{e} a + O(|a|^3).$$

If for a body $\hat{V}$ it holds $\hat{\mathbf{C}} = I$ it follows that $\hat{\mathbf{E}} = 0$, and no relative changes in the position of material points $\hat{x}$ and $\hat{y}$ occur. Lengths and angles are maintained. A material body that can only undergo motion with $\hat{\mathbf{E}} = 0$ is called a *rigid body*.

Remark 2.4 (Right Cauchy-Green or Green-Lagrange Strain Tensor) We have two different strain measures at hand. The right Cauchy-Green strain tensor $\hat{\mathbf{C}}$ and the Green-Lagrange strain tensor $\hat{\mathbf{E}}$. Both are firmly linked and can be used to describe strains caused by deformation. For describing material laws, we will derive models, that characterize the materials reaction on strain. Most simple models will assume a linear dependency between strain and stress: if no strain is given, no stress is induced. Here, the Green-Lagrange strain tensor $\hat{\mathbf{E}}$ is the better basis, as $\hat{\mathbf{E}} = 0$ denotes a no-strain condition and a linear function $f(\hat{\mathbf{E}})$ can be consulted to model the strain-stress relationship.

2.1.4 Rate of Deformation and Strain Rate

The strain tensor is a fundamental quantity in solid mechanics, where we assume that a finite force will cause a finite deformation. An ideal spring will linearly react on external forces by some finite extension, which directly refers to strain. In fluid-mechanics however finite forces can lead to infinite deformation. A river, which is driven by the constant gravity force causes infinite strain, although the force is bounded. Here it is not the deformation and the deformation gradient that is of interest; but it is its temporal variation that serves as key quantity to model the internal forces (stresses) of the material. We already discussed that for fluid-dynamical observations, the Eulerian viewpoint is more meaningful. Hence we will derive a measure for the rate of strain in the current system $V(t)$.

By $\hat{x}, \hat{y} \in \hat{V}$ we denote two material points spanning the line-segment $\hat{a} = \hat{y} - \hat{x}$. We follow their positions $x(t) = \hat{x} + \hat{\mathbf{u}}(\hat{x}, t) \in V(t)$, $y(t) = \hat{y} + \hat{\mathbf{u}}(\hat{y}, t) \in V(t)$ and the resulting line-segment $a(t) = y(t) - x(t)$ in the current configuration $V(t)$. With $a(t) = \hat{\mathbf{F}}(t)\hat{a}$ it holds

$$\partial_t a(t) = \partial_t \hat{\mathbf{F}}(t)\hat{a}, \tag{2.9}$$

and for the deformation gradient $\hat{\mathbf{F}}(t) = I + \hat{\nabla}\hat{\mathbf{u}}(t)$ we get

$$\partial_t \hat{\mathbf{F}} = \partial_t \hat{\nabla}\hat{\mathbf{u}} = \hat{\nabla}\hat{\mathbf{v}}.$$

where we assumed sufficient regularity to change the order of derivatives. By $\hat{\nabla}\hat{\mathbf{v}}$ we denote the *material velocity gradient*. The material velocity gradient $\hat{\nabla}\hat{\mathbf{v}}(\hat{x}, t)$ denotes the spatial change of the velocity as given in the Lagrangian material system. The *spatial velocity gradient* $\nabla\mathbf{v}(x, t)$ refers to the spatial change of the velocity of whatever particles are at location x at time t. For $\hat{\mathbf{v}}(\hat{x}) = \mathbf{v}(x)$ with $x = x(\hat{x}) = \hat{x} + \hat{\mathbf{u}}(\hat{x})$ it further holds

$$\partial_t \hat{\mathbf{F}} = \nabla\mathbf{v}\hat{\nabla}x = \nabla\mathbf{v}\hat{\mathbf{F}}.$$

Then, to continue with (2.9)

$$\partial_t a(t) = \nabla\mathbf{v}\hat{\mathbf{F}}\hat{a} = \nabla\mathbf{v}a(t),$$

and the rate of length change is given by

$$\partial_t |a(t)|^2 = (\nabla\mathbf{v}a(t), a(t)) + (a(t), \nabla\mathbf{v}a(t)) = 2\left(\frac{1}{2}(\nabla\mathbf{v} + \nabla\mathbf{v}^T)a(t), a(t)\right).$$

Definition 2.5 (Strain Rate Tensor) By

$$\dot{\boldsymbol{\varepsilon}}(x, t) = \frac{1}{2}\{\nabla\mathbf{v}(x, t) + \nabla\mathbf{v}(x, t)^T\}.$$

we denote the *strain rate* tensor or the *rate of strain* tensor. It denotes the local change of velocity in the current system.

2.1.5 Stress

Deformation, strain and strain rate are kinematic properties. They simply describe the relative motion of particles within a volume. As such, they are pure observations of the situations and do not depend on the model under consideration. We assume that a material will react on strain or the strain rate. For expanding a spring, a certain force will be necessary.

By *stress* we denote the internal force that is acting on an imaginary surface within the volume $V(t)$. The unit of stress is force per area.

In Fig. 2.4 we show a volume $V(t)$ that is cut at an inner surface $S \subset V(t)$. By $x \in S \subset V(t)$ we denote a point on this surface with normal $\mathbf{n}$. The average forces acting on a neighborhood of $x \in S$ is denoted by the *Cauchy traction vector* $\mathbf{t}$. The right sketch of the figure shows this setting in the reference system, where by $\hat{x} \in \hat{S} \subset \hat{V}$ we denote point, surface and volume in reference state. Here, the normal vector is indicated by $\hat{\mathbf{n}}$ and the resulting *first Piola-Kirchhoff traction vector* $\hat{\mathbf{t}}$:

$$\mathbf{t} = \mathbf{t}(x, t, \mathbf{n}), \quad \hat{\mathbf{t}} = \hat{\mathbf{t}}(\hat{x}, t, \hat{\mathbf{n}}).$$

By $\mathrm{d}s$ we denote an infinitesimal neighborhood of x on the surface $S \subset V(t)$ and by $\mathrm{d}\hat{s}$ the corresponding infinitesimal neighborhood of $\hat{x}$ on $\hat{S} \subset \hat{V}$. Then, it holds

$$\mathbf{t}\mathrm{d}s = \hat{\mathbf{t}}\mathrm{d}\hat{s},$$

such that both traction vectors refer to forces in the current configuration $V(t)$. While $\mathbf{t}$ is a function in variables x and $\mathbf{n}$ of the current configuration, the first Piola-

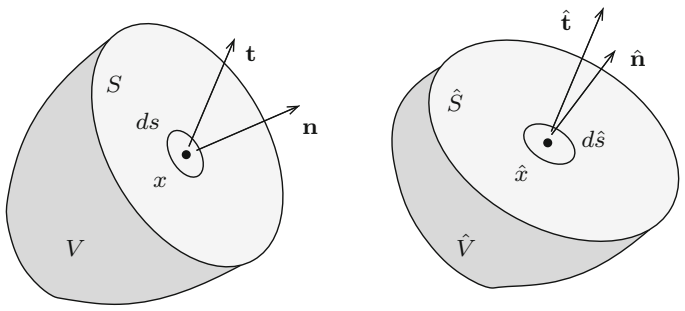

Fig. 2.4 Traction vectors on a imaginary surface in the current system (*left*) and the reference system (*right*). Cauchy's stress theorem postulates a linear dependency of the traction vectors on the normals $\mathbf{t} = \boldsymbol{\sigma}\mathbf{n}$ and $\hat{\mathbf{t}} = \hat{\mathbf{P}}\hat{\mathbf{n}}$

Kirchhoff traction vector is a function of $\hat{x}$ and $\hat{\mathbf{n}}$ in the Lagrangian reference system. Usually, it does not hold $|\mathbf{t}| = |\hat{\mathbf{t}}|$. The unit of stress is *force by area* and $\mathbf{t}$ refers to the area of a domain surface ds while $\hat{\mathbf{t}}$ refers to the area of the undeformed reference surface d$\hat{s}$.

The traction vectors describe a *surface tension*. Such surface tensions arise from friction or contact. Another example for a surface tension is the pressure in a liquid or gas that pushes the particle to each other (or apart from each other).

The surface tensions depend on the normal vector $\mathbf{n}$ of the imaginary surface. It holds

Theorem 2.6 (Cauchy's Stress Theorem) *There exist unique second order tensors $\boldsymbol{\sigma}$ and $\hat{\mathbf{P}}$, such that*

$$\mathbf{t}(x,t,\mathbf{n}) = \boldsymbol{\sigma}(x,t)\mathbf{n}, \quad \hat{\mathbf{t}}(\hat{x},t,\hat{\mathbf{n}}) = \hat{\mathbf{P}}(\hat{x},t)\hat{\mathbf{n}}.$$

The tensor $\boldsymbol{\sigma} = \boldsymbol{\sigma}^T$ is symmetric and called the Cauchy stress tensor*, the tensor field $\hat{\mathbf{P}}$ is called the* first Piola-Kirchhoff stress tensor*. $\hat{\mathbf{P}}$ is usually not symmetric.*

Proof For the proof, we refer to the literature [150]. □

One immediate consequence of Cauchy's stress theorem is that traction vectors for opposite normal vectors annihilate each other, Newton's law of *actio = reactio*

$$\mathbf{t}(x,t,-\mathbf{n}) = \boldsymbol{\sigma}(x,t)(-\mathbf{n}) = -\boldsymbol{\sigma}(x,t)\mathbf{n} = -\mathbf{t}(x,t,\mathbf{n}).$$

As the Cauchy stress tensor must be symmetric, it consists of six independent components

$$\boldsymbol{\sigma} = \begin{pmatrix} \sigma_{11} & \sigma_{12} & \sigma_{13} \\ \sigma_{12} & \sigma_{22} & \sigma_{23} \\ \sigma_{13} & \sigma_{23} & \sigma_{33} \end{pmatrix}.$$

The second order tensor $\hat{\mathbf{P}}$ is usually not symmetric and consists of nine independent entries. For the relation of $\boldsymbol{\sigma}$ and $\hat{\mathbf{P}}$ it holds

$$\boldsymbol{\sigma}\mathbf{n}\mathrm{d}s = \hat{\mathbf{P}}\hat{\mathbf{n}}\mathrm{d}\hat{s},$$

such that the two different traction vectors describe the transformation of a surface integral. We will get back to this relation in Sect. 2.1.7.

The components of the stress tensor are best understood by a decomposition of stresses into *normal stress* $\sigma \in \mathbb{R}$ and *shear stress* $\tau \in \mathbb{R}$. Let $\mathbf{t}$ be a stress vector in $x \in V(t)$ on a imaginary surface S with normal vector $\mathbf{n}$. The normal-stress σ is defined as the projection of the traction vector in normal direction

$$\sigma = \mathbf{t}^T\mathbf{n} = (\mathbf{n}, \boldsymbol{\sigma}\mathbf{n}),$$

while the shear stress is defined as the tangential part of the stress

$$\tau = \mathbf{t}^T \mathbf{t}_1 = (\mathbf{t}_1, \boldsymbol{\sigma}\mathbf{n}),$$

where $\mathbf{t}_1$ is the tangential vector that arises from projection of $\mathbf{t}$ onto the surface

$$\mathbf{t}_1 = \frac{\mathbf{t} - \boldsymbol{\sigma}\mathbf{n}}{\|\mathbf{t} - \boldsymbol{\sigma}\mathbf{n}\|}.$$

Then, the stress vector can be decomposed into the normal stress σ and shear stress τ by

$$\mathbf{t} = (\mathbf{t}, \mathbf{n})\mathbf{n} + (\mathbf{t}, \mathbf{t}_1)\mathbf{t}_1 = \sigma\mathbf{n} + \tau\mathbf{t}_1.$$

Here $\sigma, \tau \in \mathbb{R}$ are the lengths of the stress vectors in normal direction and tangential direction. Given the Cauchy stress tensor $\boldsymbol{\sigma}$, it holds

$$\sigma = (\mathbf{n}, \boldsymbol{\sigma}\mathbf{n}), \quad \tau = (\mathbf{t}, \boldsymbol{\sigma}\mathbf{n}).$$

If for the normal stress it holds $\sigma < 0$, the material undergoes a compression, while for $\sigma > 0$ an expansion is given. Further, it holds

$$|\boldsymbol{\sigma}\mathbf{n}|^2 = |\mathbf{t}|^2 = |\mathbf{n} \cdot \boldsymbol{\sigma}|^2 = \tau^2 + \sigma^2.$$

Next, let us assume that the imaginary surface has normal vector $\mathbf{n} = \mathbf{e}_i$ with $(\mathbf{e}_i)_j = \delta_{ij}$. The normal stress is given

$$\sigma = (\mathbf{e}_i, \boldsymbol{\sigma}\mathbf{e}_i) = \boldsymbol{\sigma}_{ii},$$

by the diagonal entry of the Cauchy-stress tensor, while the shear stress in $\mathbf{e}_k$ direction for $k \neq i$ gets

$$\tau = (\mathbf{e}_k, \boldsymbol{\sigma}\mathbf{e}_i) = \boldsymbol{\sigma}_{ki} = \boldsymbol{\sigma}_{ki}.$$

Hence the diagonal entries of $\boldsymbol{\sigma}$ refer to the normal stresses, while all off-diagonals refer to tangential shear stresses.

Remark 2.7 (Stress in the Reference System) Usually only static stresses act in the initial reference state of a system at reference time t_0. In case of a resting fluid, this stress can be caused by the hydrostatic pressure. Sometimes however, initial configurations cannot be considered to be stress-free. An example could be organic material like wood, where the undeformed reference system may be subject to stress caused by growth, see [209].

2.1.6 Conservation Principles

The most important physical conservation principles in the context of fluid-mechanics and structure-mechanics are conservation of mass, which says that

> mass is neither created nor destroyed,

conservation of momentum that says that

> the change in momentum is equivalent to the external forces

and conservation of angular momentum, saying that

> the change in angular momentum is equal to the torque.

Using the notation derived in the previous section, conservation of mass reads

$$d_t m(V(t)) = 0, \tag{2.10}$$

where the volume's mass $m(V(t))$ is given by

$$m(V(t)) = \int_{V(t)} \rho(x,t)\,\mathrm{d}\,x,$$

with a density ρ. Conservation of momentum gets

$$d_t I(V(t)) = K(V(t)) + K(\partial V(t)), \tag{2.11}$$

with the momentum $I(V(t))$

$$I(V(t)) = \int_{V(t)} \rho(x,t)\mathbf{v}(x,t),\mathrm{d}\,x,$$

and volume and surface forces $K(V(t))$ and $K(\partial V(t))$ given by:

$$K(V(t)) = \int_{V(t)} \rho(x,t)\mathbf{f}(x,t)\,\mathrm{d}\,x, \quad K(\partial V(t)) = \int_{\partial V(t)} \mathbf{t}\,\mathrm{d}s.$$

Here, $\mathbf{f}$ is a prescribed volume force density and $\mathbf{t}$ denotes the surface stress in direction $\mathbf{n}$. As discussed, it holds by Cauchy's Stress Theorem 2.6 that this surface force linearly depends on the normal direction such that it can be expressed with help of a stress tensor $\boldsymbol{\sigma} \in \mathbb{R}^{n\times n}$ as $\mathbf{t} = \boldsymbol{\sigma}\mathbf{n}$. The surface allows for a transformation to a volume integral via the divergence theorem

$$K(\partial V(t)) = \int_{\partial V(t)} \mathbf{n}\cdot\boldsymbol{\sigma}\,\mathrm{d}s = \int_{V(t)} \mathrm{div}\,(\boldsymbol{\sigma})\,\mathrm{d}\,x.$$

Finally, conservation of angular momentum is given by

$$d_t L(V(t)) = D(V(t)), \tag{2.12}$$

where the angular momentum $L(V(t))$ with respect to the origin is given as

$$L(V(t)) = \int_{V(t)} x \times (\rho \mathbf{v}) \, \mathrm{d}\, x,$$

and the torque $D(V(t))$ is defined by

$$D(V(t)) = \int_{V(t)} x \times (\rho \mathbf{f}) \, \mathrm{d}\, x + \int_{\partial V(t)} x \times (\mathbf{n} \cdot \boldsymbol{\sigma}) \, \mathrm{d}s.$$

Since the integration domain $V(t)$ in (2.10)–(2.12) depends on time t, evaluation of derivatives like $d_t m(V(t))$ is not straightforward and will be accomplished with help of the essential *Reynolds' Transport Theorem*

Lemma 2.8 (Reynolds' Transport Theorem) *Let $V(t) \subset \mathbb{R}^d$ be a material volume. Further, let $\Phi(x,t)$ be a differentiable scalar function defined on $V(t)$. Then, it holds*

$$d_t \int_{V(t)} \Phi(x,t) \, \mathrm{d}\, x = \int_{V(t)} \left(\partial_t \Phi(x,t) + \operatorname{div}(\Phi \mathbf{v}) \right) \mathrm{d}\, x.$$

Proof The formula can be shown by elementary calculations using the transformation of $T(t) : \hat{V} \to V(t)$ to a fixed reference domain and expressing the derivatives of the functional determinant $\det(\hat{\nabla} T(t))$ with respect to its entries $\hat{\nabla} \hat{T}_{ij}$. See also Lemma 2.60. □

Applying this theorem to the scalar value $\Phi(x,t) := \rho(x,t)$ we derive the *Law of Mass Conservation*:

$$\int_{V(t)} \partial_t \rho + \operatorname{div}(\rho \mathbf{v}) \, \mathrm{d}\, x = 0.$$

This equation is valid for every volume $V(t)$. Assuming that the expression $\partial_t \rho + \operatorname{div}(\rho \mathbf{v})$ is continuous (which is an assumption on the physical properties of the material), the equation of mass-conservation holds in a point-wise manner

$$\partial_t \rho + \operatorname{div}(\rho \mathbf{v}) = 0. \tag{2.13}$$

The second basic rule is *conservation of momentum*, derived by the scalar values $\Phi(x,t) := \rho(x,t)\mathbf{v}_i(x,t)$ for every component of the velocity field. With a column-wise representation of the stress-tensor $\boldsymbol{\sigma} = (\boldsymbol{\sigma}_1, \ldots, \boldsymbol{\sigma}_d)$ Reynolds transport theorem yields:

$$\int_{V(t)} \partial_t (\rho \mathbf{v}_i) + \operatorname{div}(\rho \mathbf{v}_i \mathbf{v}) \, \mathrm{d}\, x = \int_{V(t)} \rho \mathbf{f}_i + \operatorname{div}(\boldsymbol{\sigma}_i) \, \mathrm{d}\, x, \quad i = 1, \ldots, d.$$

Given continuity of the integrand we can again deduce a point-wise equation

$$\partial_t(\rho \mathbf{v}_i) + \operatorname{div}(\rho \mathbf{v}_i \mathbf{v}) = \rho \mathbf{f}_i + \operatorname{div}(\boldsymbol{\sigma}_i), \quad i = 1, \ldots, d.$$

By introducing the external product of two vectors

$$\mathbf{v} \otimes \mathbf{w} \in \mathbb{R}^{d \times d}, \quad (\mathbf{v} \otimes \mathbf{w})_{ij} := \mathbf{v}_i \mathbf{w}_j,$$

we can formulate the equation for the conservation of momentum in *conservative formulation*

$$\partial_t(\rho \mathbf{v}) + \operatorname{div}(\rho \mathbf{v} \otimes \mathbf{v}) = \rho \mathbf{f} + \operatorname{div}(\boldsymbol{\sigma}).$$

Combining this equation with the mass-conservation, we can further deduce the equation for conservation of momentum in the *non-conservative formulation*

$$\rho \partial_t \mathbf{v} + \rho(\mathbf{v} \cdot \nabla)\mathbf{v} = \rho \mathbf{f} + \operatorname{div}(\boldsymbol{\sigma}). \tag{2.14}$$

The equation for the *conservation of angular momentum* is given by

$$d_t \int_{V(t)} x \times (\rho \mathbf{v}) \, \mathrm{d}x = \int_{V(t)} x \times (\rho \mathbf{f}) \, \mathrm{d}x + \int_{\partial V(t)} x \times (\mathbf{n} \cdot \boldsymbol{\sigma}) \, \mathrm{d}s.$$

Applying Reynolds transport theorem we can deduce the following three equations

$$\begin{aligned} i = 1 \quad & \boldsymbol{\sigma}_{23} - \boldsymbol{\sigma}_{32} = 0 \\ i = 2 \quad & \boldsymbol{\sigma}_{13} - \boldsymbol{\sigma}_{31} = 0 \\ i = 3 \quad & \boldsymbol{\sigma}_{12} - \boldsymbol{\sigma}_{21} = 0, \end{aligned}$$

that impose the symmetry of the Cauchy stress tensor

$$\boldsymbol{\sigma} = \boldsymbol{\sigma}^T. \tag{2.15}$$

Further conservation principles are important if physical properties like entropy, energy and temperature are taken into consideration. Since we will deal with isentropic materials only, where all dynamical processes will take place without change of entropy, the three fundamental principles of mass-, momentum- and angular momentum-conservation will be sufficient to describe all desired behavior.

It remains to describe the tensor of surface-forces $\boldsymbol{\sigma}$. This tensor will heavily depend on the material under consideration, whether it is a fluid or a solid, whether the fluid is water, air or blood, the solid may be elastic or plastic or have properties of both. Here, physical modeling comes into place, exact laws for the dependence of this tensor on quantities like velocity and density usually do not exist. Since we

know that $\boldsymbol{\sigma}$ is symmetric, six additional equations are required for its description. Stress models will be discussed in Sect. 2.2.

2.1.7 Conservation Principles in Different Coordinate Systems

In this section, we discuss the transformation of the conservation equations, which have been derived in the Eulerian framework, to different coordinate frameworks. Introducing the basic concepts for solid mechanics we already argued that a Lagrangian viewpoint is more natural.

Let $V(t)$ be the moving Eulerian framework and let $\hat{V}$ be the Lagrangian reference system. Further, by $\hat{W}$ we denote an arbitrary second fixed reference system, see Fig. 2.5. While the case $\hat{W} = \hat{V}$ is possible, we will allow for arbitrary systems without physical meaning. However, we assume that $\hat{W}$ is fixed in time and that there exists an invertible mapping $\hat{T}_W(t) : \hat{W} \to V(t)$ with gradient $\hat{\mathbf{F}}_W := \hat{\nabla}\hat{T}_W$ and determinant $\hat{J}_W := \det(\hat{\mathbf{F}}_W) > 0$. If we talk about the gradient $\hat{\mathbf{F}}_W$ we request that the map $\hat{T}_W$ is differentiable with respect to the spatial variables. We further assume that $\hat{T}_W$ is differentiable with respect to the temporal variable and that the inverse of the mapping $\hat{T}_W^{-1}$ is also differentiable. In other words, $\hat{T}_W$ is assumed to be a C^1-diffeomorphism on $I \times \hat{W}$.

By introducing an arbitrary reference systems $\hat{W}$ we have to deal with three different systems: the Lagrangian particles, $\hat{x} \in \hat{V}$, their Eulerian path $x(\hat{x}, t) \in V(t)$ and further the arbitrary framework with $\hat{x}_W \in \hat{W}$ with $\hat{T}_W(\hat{x}_W, t) = x = \hat{T}(\hat{x}, t)$. Note that it does not hold $\partial_t \hat{T}_W = \hat{\mathbf{v}}$, as we have to distinguish between the physical velocity $\hat{\mathbf{v}}$ of the particles and the velocity $\partial_t \hat{T}_w$ of the arbitrary coordinate system motion.

We start by describing basic properties used to map between the two systems $\hat{W}$ and $V(t)$. First, we introduce the inverse mapping $T_W(t) : V(t) \mapsto \hat{W}$.

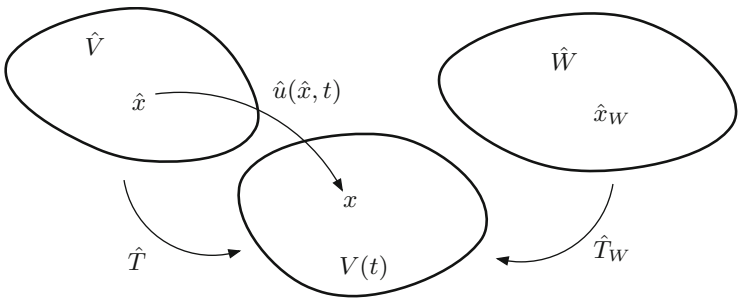

Fig. 2.5 Moving Eulerian volume $V(t)$ with Lagrangian reference $\hat{V}$ and third arbitrary reference volume $\hat{W}$

Lemma 2.9 (Inverse Mapping) *By $T_W(t) : V(t) \to \hat{W}$ we denote the* inverse mapping*, by $\mathbf{F}_W := \nabla T_W$ its gradient and by $J_W := \det(\mathbf{F}_W)$ its determinant. Given sufficient regularity, It holds*

$$\mathbf{F}_W = \hat{\mathbf{F}}_W^{-1}, \quad J_W := \hat{J}_W^{-1}, \quad \partial_t T_W = -\hat{\mathbf{F}}_W^{-1} \partial_t \hat{T}_W.$$

Proof It holds

$$T_W \circ \hat{T}_W = \widehat{\mathrm{id}} \quad \Rightarrow \quad \mathbf{F}_W \hat{\mathbf{F}}_W = I \quad \Rightarrow \quad \mathbf{F}_W = \hat{\mathbf{F}}_W^{-1}.$$

By taking the determinant of both sides, we immediately get $J_W = \hat{J}_W^{-1}$. Finally,

$$T_W \circ \hat{T}_W = \widehat{\mathrm{id}} \quad \Rightarrow \quad 0 = d_t T_W(\hat{T}_W(\hat{x}, t), t) = \partial_t T_W + \nabla T_W \partial_t \hat{T}_W.$$

Using $\nabla T_W = \mathbf{F}_W = \hat{\mathbf{F}}_W^{-1}$ we obtain the relation $\partial_t T_W = -\hat{\mathbf{F}}_W^{-1} \partial_t \hat{T}_W$. □

In Lemma 2.3 we already considered the transformation of spatial and temporal derivatives between the Eulerian and the Lagrangian coordinate system. Similarly it holds for a scalar function $f : V(t) \to \mathbb{R}$ and a vector field $\mathbf{w} : V(t) \to \mathbb{R}^d$ with counterparts $\hat{f}$ and $\hat{\mathbf{w}}$ on $\hat{W}$:

$$\nabla f = \hat{\mathbf{F}}_W^{-T} \hat{\nabla} \hat{f}, \quad \nabla \mathbf{w} = \hat{\nabla} \hat{\mathbf{w}} \hat{\mathbf{F}}_W^{-1}. \tag{2.16}$$

For temporal derivatives transformed to general coordinate systems $\hat{W}$ we must take care of two different velocities: the particle velocity $\hat{\mathbf{v}}$ and the domain velocity $\partial_t \hat{T}_W$, which do not coincide if $\hat{W} \neq \hat{V}$:

Lemma 2.10 (Transformation of Temporal Derivatives) *Let $f : V(t) \to \mathbb{R}$ with counterpart $\hat{f}(\hat{x}_W, t) = f(x, t)$. Given sufficient regularity, it holds*

$$\partial_t f = \partial_t \hat{f} - (\hat{\mathbf{F}}_W^{-1} \partial_t \hat{T}_W \cdot \hat{\nabla}) \hat{f}, \quad d_t f = \partial_t \hat{f} + (\hat{\mathbf{F}}_W^{-1} (\hat{\mathbf{v}} - \partial_t \hat{T}_W) \cdot \hat{\nabla}) \hat{f}.$$

Proof With $\hat{x}_W = T_W(x, t)$ it holds

$$\partial_t f(x, t) = d_t \hat{f}(\hat{x}_W, t) = d_t \hat{f}(T_W(x, t), t) = \partial_t \hat{f} + \hat{\nabla} \hat{f} \cdot \partial_t T_W.$$

The first result follows with help of Lemma 2.9. The relation for the material derivative is given by

$$d_t f(x, t) = \partial_t f(x, t) + \nabla f \cdot \partial_t x.$$

Here, $\partial_t x = \mathbf{v} = \hat{\mathbf{v}}$ refers to the trace of particles, where $\mathbf{v} = \hat{\mathbf{v}}$ is the velocity of the particle and not the velocity of the mapping $\hat{T}_W$. Together with (2.16) and the

transformation of the partial time derivative we get

$$d_t f = \partial_t \hat{f} - (\hat{\mathbf{F}}_W^{-1} \partial_t \hat{T}_W \cdot \hat{\nabla}) \hat{f} + \hat{\mathbf{F}}_W^{-T} \hat{\nabla} \hat{f} \cdot \hat{\mathbf{v}}.$$

□

Remark 2.11 (Transformation Between Lagrangian and Eulerian Coordinates) If $\hat{V} = \hat{W}$ it holds $\hat{T}_W = \hat{T}$ as well as $\hat{\mathbf{F}}_W = \hat{\mathbf{F}}$ and $\hat{J}_W = \hat{J}$. The statements of Lemma 2.10 simplify to

$$\hat{W} = \hat{V} \quad \Rightarrow \quad \partial_t f = \partial_t \hat{f} - (\hat{\mathbf{F}}^{-1} \hat{\mathbf{v}} \cdot \hat{\nabla}) \hat{f}, \quad d_t f = \partial_t \hat{f}.$$

This results explains, why the convective term $(\mathbf{v} \cdot \nabla)\mathbf{v}$ will not appear in Lagrangian coordinates. See also Lemma 2.3.

In the following we discuss the transformation of the conservation principles to arbitrary coordinate reference systems $\hat{W}$. This transformation will be fundamental for solid mechanics, where the natural view-point is the Lagrangian one with $\hat{W} = \hat{V}$. Further, one of the standard approaches for coupling fluid-structure interactions relies on the mapping of the fluid problem onto a fixed reference system. Since this reference system will not be the Lagrangian one, we proceed without specifying the connotation of $\hat{W}$. The equation for conservation of momentum (2.14) is given by

$$\rho \partial_t \mathbf{v} + \rho(\mathbf{v} \cdot \nabla)\mathbf{v} = \rho \mathbf{f} + \operatorname{div}(\boldsymbol{\sigma}) \text{ in } V(t),$$

with a density ρ, velocity $\mathbf{v}$, volume force $\mathbf{f}$ and the Eulerian stress-tensor $\boldsymbol{\sigma}$. The specific form of this stress-tensor will be discussed in later sections. Here, we only assume that this stress tensor is symmetric $\boldsymbol{\sigma} = \boldsymbol{\sigma}^T$. By $\hat{\mathbf{v}}(\hat{x}_W, t) = \mathbf{v}(x, t)$, $\hat{\rho}(\hat{x}_W, t) = \rho(x, t)$, $\hat{\mathbf{f}}(\hat{x}_W, t) = \mathbf{f}(x, t)$ as well as $\hat{\boldsymbol{\sigma}}(\hat{x}_W, t) = \boldsymbol{\sigma}(x, t)$ we denote the counterparts of these quantities in the reference system $\hat{W}$. By (2.16) and 2.10 it holds:

$$\partial_t \mathbf{v} = \partial_t \hat{\mathbf{v}} - (\hat{\mathbf{F}}_W^{-1} \partial_t \hat{T}_W \cdot \hat{\nabla}) \hat{\mathbf{v}},$$

$$(\mathbf{v} \cdot \nabla)\mathbf{v} = \nabla \mathbf{v} \mathbf{v} = \hat{\nabla} \hat{\mathbf{v}} \hat{\mathbf{F}}_W^{-1} \hat{\mathbf{v}} = (\hat{\mathbf{F}}_W^{-1} \hat{\mathbf{v}} \cdot \hat{\nabla}) \hat{\mathbf{v}},$$

and combined, we get:

$$\partial_t \mathbf{v} + (\mathbf{v} \cdot \nabla)\mathbf{v} = \partial_t \hat{\mathbf{v}} + (\hat{\mathbf{F}}_W^{-1} (\hat{\mathbf{v}} - \partial_t \hat{T}_W) \cdot \hat{\nabla}) \hat{\mathbf{v}}. \tag{2.17}$$

As discussed above, in the case of a mapping to the Lagrangian reference system, the mapping's temporal derivative is the velocity $\partial_t \hat{T} = \hat{\mathbf{v}}$ and the momentum terms simplify to

$$\hat{V} = \hat{W} \quad \Rightarrow \quad \partial_t \mathbf{v} + (\mathbf{v} \cdot \nabla)\mathbf{v} = \partial_t \hat{\mathbf{v}}. \tag{2.18}$$

It remains to transform the divergence of the stresses to the reference domain. Here, a simple transformation of $\operatorname{div}(\boldsymbol{\sigma})$ to the reference system is not sufficient. We need to keep the meaning of this stress-term in mind, indicating surface-forces in normal-direction. The normal vectors are transformed, if the underlying domain $\hat{V} \to V(t)$ is deformed. Therefore we must base the mapping process on the correct representation of these surface forces. We need to find a representation of the first Piola-Kirchhoff stress tensor $\hat{\mathbf{P}}$ in the reference system, such that it holds:

$$\int_{\partial \hat{W}} \hat{\mathbf{P}} \hat{\mathbf{n}} \, \mathrm{d}\hat{s} = \int_{\partial V(t)} \boldsymbol{\sigma} \mathbf{n} \, \mathrm{d}s.$$

$\hat{\mathbf{P}}$ will be called the *Piola transformation* of $\boldsymbol{\sigma}$. For the derivation of this transformation we first regard vector fields $\mathbf{w} : V(t) \to \mathbb{R}^d$ with reference counterpart $\hat{\mathbf{w}} : \hat{W} \to \mathbb{R}^d$.

Lemma 2.12 (Piola Transformation) *Let $\mathbf{w} : V(t) \to \mathbb{R}^d$ be a differentiable vector field and $\hat{\mathbf{w}}$ its representation in the reference system $\hat{W}$. The* Piola transformation *of $\mathbf{w}$ is given by*

$$\hat{J}_W \hat{\mathbf{F}}_W^{-1} \hat{\mathbf{w}}.$$

On every volume $V(t)$ with corresponding reference volume $\hat{W}$ it holds

$$\int_{\partial V(t)} \mathbf{n} \cdot \mathbf{w} \, \mathrm{d}s \int_{\partial \hat{W}} \hat{\mathbf{n}} \cdot (\hat{J}_W \hat{\mathbf{F}}_W^{-1} \hat{\mathbf{w}}) \, \mathrm{d}\hat{s},$$

$$\int_{V(t)} \operatorname{div}(\mathbf{w}) \, \mathrm{d}x = \int_{\hat{W}} \widehat{\operatorname{div}} (\hat{J}_W \hat{\mathbf{F}}_W^{-1} \hat{\mathbf{w}}) \, \mathrm{d}\hat{x}.$$

Further, in a point-wise sense it holds

$$\hat{J}_W \operatorname{div}(\mathbf{w}) = \widehat{\operatorname{div}} (\hat{J}_W \hat{\mathbf{F}}_W^{-1} \hat{\mathbf{w}}).$$

Proof We use a variational argument. Let ξ be differentiable on $V(t)$ with reference counterpart $\hat{\xi} \in \hat{W}$, such that

$$\int_{\partial V(t)} \mathbf{n} \cdot \mathbf{w} \xi \, \mathrm{d}s = \int_{V(t)} \operatorname{div}(\mathbf{w}\xi) \, \mathrm{d}x = \int_{\hat{W}} \hat{J}_W \operatorname{div}(\mathbf{w}\xi) \, \mathrm{d}\hat{x}. \tag{2.19}$$

Next, with (2.16) we get for $\hat{\xi} = \xi$:

$$\int_{\hat{W}} \hat{J}_W \operatorname{div}(\mathbf{w}\xi) \, \mathrm{d}\hat{x} = \int_{\hat{W}} \hat{J}_W \operatorname{div}(\mathbf{w}) \hat{\xi} \, \mathrm{d}\hat{x} + \int_{\hat{W}} \hat{J}_W \hat{\mathbf{w}} \cdot \hat{\mathbf{F}}_W^{-T} \hat{\nabla} \hat{\xi} \, \mathrm{d}\hat{x}. \tag{2.20}$$

With Green's formula, the second integral is transformed to

$$\begin{aligned}\int_{\hat{W}} \hat{J}_W \hat{\mathbf{w}} \cdot \hat{\mathbf{F}}_W^{-T} \hat{\nabla} \hat{\xi} \, \mathrm{d}\hat{x} &= \int_{\hat{W}} \hat{J}_W \hat{\mathbf{F}}_W^{-1} \hat{\mathbf{w}} \cdot \hat{\nabla} \hat{\xi} \, \mathrm{d}\hat{x} \\ &= -\int_{\hat{W}} \widehat{\operatorname{div}} (\hat{J}_W \hat{\mathbf{F}}_W^{-1} \hat{\mathbf{w}}) \hat{\xi} \, \mathrm{d}\hat{x} + \int_{\partial \hat{W}} \hat{\mathbf{n}} \cdot (\hat{J}_W \hat{\mathbf{F}}_W^{-1} \hat{\mathbf{w}}) \, \hat{\xi} \, \mathrm{d}\hat{s}. \end{aligned} \tag{2.21}$$

Combining (2.19)–(2.21) gives

$$\begin{aligned}\int_{\partial V(t)} n \cdot \mathbf{w} \, \xi \, \mathrm{d}s - \int_{\hat{W}} \hat{J}_W \operatorname{div} (\mathbf{w}) \hat{\xi} \, \mathrm{d}\hat{x} \\ = -\int_{\hat{W}} \widehat{\operatorname{div}} (\hat{J}_W \hat{\mathbf{F}}_W^{-1} \hat{\mathbf{w}}) \hat{\xi} \, \mathrm{d}\hat{x} + \int_{\partial \hat{W}} \hat{\mathbf{n}} \cdot (\hat{J}_W \hat{\mathbf{F}}_W^{-1} \hat{\mathbf{w}}) \hat{\xi} \, \mathrm{d}\hat{s}.\end{aligned}$$

By picking a Dirac sequence $\{\hat{\xi}_\varepsilon^y\}_{\varepsilon>0}$ where $\hat{\xi}_\varepsilon^y \in C_0^\infty(\hat{W})$ with

$$\int_{\hat{W}} \hat{\xi}_\varepsilon^y(\hat{x}) \hat{f}(\hat{x}) \, \mathrm{d}\hat{x} \xrightarrow[\varepsilon \to 0]{} \hat{f}(\hat{y}) \quad \forall \hat{f} \in C(\hat{W}),$$

we conclude for all inner points

$$\hat{J}_W \operatorname{div} (\mathbf{w}) = \widehat{\operatorname{div}} (\hat{J}_W \hat{\mathbf{F}}_W^{-1} \hat{\mathbf{w}}).$$

Hence

$$\int_{V(t)} \operatorname{div} (\mathbf{w}) \, \mathrm{d}x = \int_{\hat{W}} \hat{J}_W \operatorname{div} (\hat{\mathbf{w}}) \, \mathrm{d}\hat{x} = \int_{\hat{W}} \widehat{\operatorname{div}} (\hat{J}_W \hat{\mathbf{F}}_W^{-1} \hat{\mathbf{w}}) \, \mathrm{d}\hat{x}.$$

The relation for the surface integral follows by Gauss' divergence theorem. □

This important result is used to transform the surface forces to the reference system. Let $\boldsymbol{\sigma} = (\boldsymbol{\sigma}_i)_{i=1}^d$ be the row-vectors (or the column-vectors since $\boldsymbol{\sigma} = \boldsymbol{\sigma}^T$ by the conservation of angular momentum). It holds:

$$F_i(\partial V(t)) := \int_{\partial V(t)} \mathbf{n} \cdot \boldsymbol{\sigma}_i \, \mathrm{d}s = \int_{V(t)} \operatorname{div} (\boldsymbol{\sigma}_i) \, \mathrm{d}x$$

and with the just proven lemma we conclude

$$F_i(\partial V(t)) = \int_{\hat{W}} \widehat{\operatorname{div}} (\hat{J}_W \hat{\mathbf{F}}_W^{-1} \hat{\boldsymbol{\sigma}}_i) \, \mathrm{d}\hat{x} = \int_{\partial \hat{W}} \hat{\mathbf{n}} \cdot (\hat{J}_W \hat{\mathbf{F}}_W^{-1} \hat{\boldsymbol{\sigma}}_i) \, \mathrm{d}\hat{s}.$$

Reassembling the stress-tensor $\hat{\boldsymbol{\sigma}} = (\hat{\boldsymbol{\sigma}}_i)$ we get the reference presentation of the surface forces:

$$F(\partial V(t)) = \int_{\partial \hat{W}} (\hat{J}_W \hat{\boldsymbol{\sigma}} \hat{\mathbf{F}}_W^{-T}) \hat{\mathbf{n}} \, \mathrm{d}\hat{s} = \int_{\hat{W}} \widehat{\mathrm{div}} \, (\hat{J}_W \hat{\boldsymbol{\sigma}} \hat{\mathbf{F}}_W^{-T}) \, \mathrm{d}\hat{x}.$$

We define

Definition 2.13 (Piola Kirchhoff Stress Tensors) The *First Piola Kirchhoff stress tensor* given by

$$\hat{\mathbf{P}} := \hat{J}_W \hat{\boldsymbol{\sigma}} \hat{\mathbf{F}}_W^{-T}.$$

It relates forces in the Eulerian coordinate framework with coordinates in a reference framework $\hat{W}$. The *Second Piola Kirchhoff stress tensor* given by

$$\hat{\boldsymbol{\Sigma}} := \hat{\mathbf{F}}_W^{-1} \hat{\mathbf{P}} = \hat{J}_W \hat{\mathbf{F}}_W^{-1} \hat{\boldsymbol{\sigma}} \hat{\mathbf{F}}_W^{-T}.$$

Unlike the Eulerian stress tensor $\boldsymbol{\sigma}$, the 1st Piola Kirchhoff stress tensor $\hat{\mathbf{P}}$ is not symmetric. The 2nd Piola Kirchhoff stress tensor is symmetric but it does not have an immediate physical explanation.

Using the first Piola Kirchhoff stress tensor and Relation (2.17) the momentum equation on arbitrary reference systems $\hat{W}$ is given by:

$$\hat{J}_W \hat{\rho} \big(\partial_t \hat{\mathbf{v}} + (\hat{\mathbf{F}}_W^{-1} (\hat{\mathbf{v}} - \partial_t \hat{T}_W) \cdot \hat{\nabla}) \hat{\mathbf{v}} \big) = \hat{J}_W \hat{\rho} \hat{f} + \widehat{\mathrm{div}} \, (\hat{J}_W \hat{\boldsymbol{\sigma}} \hat{\mathbf{F}}_W^{-T}). \tag{2.22}$$

2.2 Material Laws

The basic concepts of continuum mechanics introduced in the previous section are exact in a way that they are based on fundamental physical principles. The conservation principles for mass, momentum and angular momentum constitute a systems of four partial differential equations for ten unknowns: density ρ, velocity field $\mathbf{v}$ and the six unknowns of the symmetric stress tensor $\boldsymbol{\sigma}$. This system is underdetermined. To close it, additional equations are required that connect the values of the stress tensor to computable fundamental quantities like velocity, density or deformation.

In the following sections, we will derive such *material laws* that describe the properties of the stress tensors in the different formulations like $\boldsymbol{\sigma}$, $\hat{\boldsymbol{\Sigma}}$ or $\hat{\mathbf{P}}$. We assume that these stress tensors will depend on strain or strain rate given as deformation gradient $\hat{\mathbf{F}}$, its inverse $\mathbf{F}$, or tensors like $\hat{\mathbf{C}}$, $\hat{\mathbf{E}}$, $\mathbf{b}$, $\mathbf{e}$ or $\dot{\boldsymbol{\varepsilon}}$. We denote this relation by tensor-valued functions

$$\boldsymbol{\sigma} = f(\dot{\boldsymbol{\varepsilon}}), \quad \hat{\mathbf{P}} = \hat{f}(\hat{\mathbf{F}}), \quad \hat{\boldsymbol{\Sigma}} = \hat{f}(\hat{\mathbf{E}}),$$

or by similar expressions in $\hat{\mathbf{E}}$ or $\mathbf{b}$. We assume that all materials are homogenous and do not explicitly depend on the location $x \in V(t)$.

We are not considering arbitrary material laws but postulate several assumption on the material's properties:

1. *Objectivity:* The material law is independent of the spectators viewpoint. This property will hold for every physical material.
2. *Homogeneity:* We assume that the material is homogenous, i.e. the strain-stress relation will not explicitly depend on the location $x \in V(t)$.
3. *Isentropic and isothermal processes:* We assume that entropy and temperature do not play a role. There is no conversion between heat and kinetic energy. The temperature stays constant and does not affect the material law. This assumption is a simplification, as most elastic materials and also some fluids show a strong dependency on the temperature.
4. *Isotropy:* There is no distinct direction in the material. The response to strain or strain rate is the same in all directions. This assumption rules out anisotropic materials like fiber-reinforced composites or also biological tissue, where layers are usually directed anisotropically. Most fluids however are isotropic.

These assumptions lead to a strong simplification of possible material laws. The following *Rivlin-Ericksen Theorem* shows that all such possible material laws depend on symmetric strain tensors $\mathbf{C}$, $\mathbf{E}$ or $\dot{\boldsymbol{\varepsilon}}$ only and that all material laws are quadratic polynomials in the invariants of these tensors.

Theorem 2.14 (Rivlin-Ericksen Theorem) *A stress response function $\tilde{f}(\hat{\mathbf{F}})$ is isotropic and indifferent with respect to the coordinate system, if and only if it depends on the symmetric strain tensors only*

$$\tilde{f}(\hat{\mathbf{F}}) = \hat{f}(\hat{\mathbf{F}}^T\hat{\mathbf{F}}) = \hat{f}(\hat{\mathbf{C}}).$$

Further it is given as a quadratic polynomial

$$\hat{f}(\hat{\mathbf{C}}) = \beta_0(i(\hat{\mathbf{C}}))I + \beta_1(i(\hat{\mathbf{C}}))\hat{\mathbf{C}} + \beta_2(i(\hat{\mathbf{C}}))\hat{\mathbf{C}}^2, \tag{2.23}$$

with scalar coefficients β_i that depend on the invariants (under orthogonal transformation) of the symmetric tensors $\mathbf{C}$:

$$I_1(\mathbf{C}) = \lambda_1 + \lambda_2 + \lambda_3, \quad I_2(\mathbf{C}) = \lambda_1\lambda_2 + \lambda_2\lambda_3 + \lambda_1\lambda_3, \quad I_3(\mathbf{C}) = \lambda_1\lambda_2\lambda_3,$$

where λ_1, λ_2 and λ_3 are the three eigenvalues of $\mathbf{C}$.

Proof For a proof, we refer to the original contribution by Rivlin and Ericksen [290] or to a modern presentation by Turesdell and Noll [327]. □

As a symmetric positive definite tensor, $\mathbf{C}$ has three positive eigenvalues $\lambda_1, \lambda_2, \lambda_3$ and a system of orthogonal eigenvectors. We know that eigenvalues are invariant to orthogonal transformation. To derive these invariants, we further cite the following Lemma:

Lemma 2.15 *Given a tensor* $\mathbf{A} \in \mathbb{R}^{3\times 3}$ *it holds for every* $\lambda \in \mathbb{R}$

$$\det(\mathbf{A} - \lambda I) = -\lambda^3 + I_1(\mathbf{A})\lambda^2 + I_2(\mathbf{A})\lambda + I_3(\mathbf{A}),$$

with

$$I_1(\mathbf{A}) = \operatorname{tr}(\mathbf{A}), \quad I_2(\mathbf{A}) = \frac{1}{2}\left(\operatorname{tr}(\mathbf{A})^2 - \operatorname{tr}(\mathbf{A}^2)\right), \quad I_3(\mathbf{A}) = \det(\mathbf{A}).$$

If $\mathbf{A}$ *is symmetric positive definite with eigenvalues* $\lambda_1, \lambda_2, \lambda_3$*, it further holds*

$$I_1(\mathbf{A}) = \lambda_1 + \lambda_2 + \lambda_3, \quad I_2(\mathbf{A}) = \lambda_1\lambda_2 + \lambda_2\lambda_3 + \lambda_1\lambda_3, \quad I_3(\mathbf{A}) = \lambda_1\lambda_2\lambda_3.$$

Proof See [195]. □

The Rivlin-Ericksen Theorem 2.14 strongly limits possible material laws for homogenous and isotropic materials. All material laws—including fluids and solids—considered in the context of this book will fall under this theorem.

As every matrix satisfies its own characteristic polynomial, it holds for $\hat{\mathbf{C}} \in \mathbb{R}^{3\times 3}$ that

$$\hat{\mathbf{C}}^3 = I_1(\hat{\mathbf{C}})\hat{\mathbf{C}}^2 + I_2(\hat{\mathbf{C}})\hat{\mathbf{C}} + I_3(\hat{\mathbf{C}}). \tag{2.24}$$

Using this relation, the material law (2.23) is equivalent to a second representation

$$\hat{f}(\hat{\mathbf{C}}) = \gamma_0(i(\hat{\mathbf{C}}))I + \gamma_1(i(\hat{\mathbf{C}}))\hat{\mathbf{C}} + \gamma_2(i(\hat{\mathbf{C}}))\hat{\mathbf{C}}^{-1}.$$

Remark 2.16 As the two tensors $\hat{\mathbf{E}} = \frac{1}{2}(\hat{\mathbf{C}} - I)$ are directly connected, every material law in $\hat{\mathbf{C}}$ can also be expressed in $\hat{\mathbf{E}}$, as

$$\alpha_0 I + \alpha_1\hat{\mathbf{C}} + \alpha_2\hat{\mathbf{C}}^2 = (\alpha_0 + \alpha_1 + \alpha_2)I + (2\alpha_1 + 4\alpha_2)\hat{\mathbf{E}} + 4\alpha_2\hat{\mathbf{E}}^2.$$

Further, for the eigenvalues of $\hat{\mathbf{E}}$ and $\hat{\mathbf{C}}$ there holds a linear relation

$$\lambda_i w_i = \hat{\mathbf{C}}w_i = 2\hat{\mathbf{E}}w_i + w_i \quad \Leftrightarrow \quad \frac{1}{2}(\lambda_i - 1)w_i = \hat{\mathbf{E}}w_i.$$

2.2.1 Hyperelastic Materials

A solid is called *hyperelastic* if the relation between strain and stress comes from an energy density function

$$\hat{\boldsymbol{\Sigma}} = \frac{\partial W(\hat{\mathbf{E}})}{\partial \hat{\mathbf{E}}},$$

or

$$\hat{\mathbf{P}} = \frac{\partial W(\hat{\mathbf{F}})}{\partial \hat{\mathbf{F}}}.$$

This constitutes a relation between the second Piola-Kirchhoff stress tensor and the strain or between the deformation gradient and the first Piola-Kirchhoff stress, respectively. Many of the commonly used materials like the *St. Venant Kirchhoff* model or the *Mooney-Rivlin solid* are of this type. Stress tensors for incompressible materials can be derived by energy functions of the type

$$W = W(\mathbf{F}) - p\,(\det(\mathbf{F}) - 1)$$

that penalize the change of volume $J = \det(\mathbf{F})$.

As the derivation of the models is not in the focus of this book, we just refer to the literature for more reading on this very important concept, see Holzapfel [195] for a very comprehensive exposure.

2.2.2 Linearizations

For simplicity, we sometimes consider linear models. Two different types of nonlinearities must be considered: first, the material nonlinearity which denotes a nonlinear relation between stress and strain. Second, the geometric nonlinearity, which comes from the discrepancy between reference coordinate system and current system and which is expressed by the deformation gradient $\mathbf{e} = \hat{\mathbf{F}}\hat{\mathbf{e}}$.

Regarding the Rivlin-Ericksen Theorem 2.14, linearity of a material means that only the first invariant $I_1(\mathbf{E}) = \operatorname{tr}(\mathbf{E})$ may enter the law and that no higher order terms may appear. Further, in geometrically linearized situations, the symmetric strain tensor $\hat{\mathbf{E}}$ is approximated and linearized

$$\hat{\mathbf{E}} = \frac{1}{2}(\nabla\mathbf{u} + \nabla\mathbf{u}^T + \nabla\mathbf{u}^T\nabla\mathbf{u}) \approx \frac{1}{2}(\nabla\mathbf{u} + \nabla\mathbf{u}^T) =: \hat{\boldsymbol{\varepsilon}},$$

assuming that $|\nabla\mathbf{u}| \ll 1$ is small.

Lemma 2.17 (Linear Material Law) *A stress response function $f(\cdot)$ for a linear, homogenous and isotropic material depends on the linearized strain $\hat{\boldsymbol{\varepsilon}} = \hat{\nabla}\hat{\mathbf{u}} + \hat{\nabla}\hat{\mathbf{u}}^T$ or on the strain rate tensor $\dot{\boldsymbol{\varepsilon}} = \nabla\mathbf{v} + \nabla\mathbf{v}^T$ and its first invariant only*

$$\hat{f}(\hat{\boldsymbol{\varepsilon}}) = \beta_0 \operatorname{tr}(\hat{\boldsymbol{\varepsilon}})I + \beta_1 \hat{\boldsymbol{\varepsilon}}.$$

In fluid mechanics, the Navier-Stokes equations follow such a linear material law and in structure mechanics, the Navier-Lamé problem considers these simplifications. While in fluid mechanics a fully linear material law—the Navier-Stokes model—is a very accurate model for many relevant fluids, linearization in solid mechanics is usually not feasible. Here, linear models only apply to very small deformations $|\hat{\mathbf{u}}| \ll 1$ and very small changes in deformation $|\hat{\nabla}\hat{\mathbf{u}}| \ll 1$. In particular, linearized solid models are no longer invariant with respect to fixed body rotations. In the context of fluid-structure interactions, use of linear models can significantly damp the dynamics.

2.2.3 Incompressible Materials

Some materials have an incompressible behavior which means that the volume

$$|V(t)| = \int_{V(t)} 1 \,\mathrm{d}\, x \equiv \text{“const”}$$

does not change. For an incompressible material, there is no expansion or compression. Many fluids—like water—can be considered incompressible. Incompressibility further applies to many biological structures. We can describe change of volume in the current system by Reynolds transport theorem

$$0 = d_t|V(t)| = d_t \int_{V(t)} 1 \,\mathrm{d}\, x = \int_{V(t)} \nabla \cdot \mathbf{v} \,\mathrm{d}\, x = \int_{\partial V(t)} n \cdot \mathbf{v} \,\mathrm{d}s, \tag{2.25}$$

but also in the reference configuration by transformation

$$0 = d_t|V(t)| = d_t \int_{V(t)} 1 \,\mathrm{d}\, x = \int_{\hat{V}} d_t \hat{J} \,\mathrm{d}\hat{x}. \tag{2.26}$$

For a fluid, modeled in the current configuration, (2.25) says that the flow is “divergence-free” with $\operatorname{div} \mathbf{v} = 0$ and also that the total normal flow over the volume’s boundary is zero. For a divergence free velocity field it holds

$$\operatorname{tr}(\dot{\boldsymbol{\varepsilon}}) = 0,$$

and in light of Lemma 2.17, the material law is further simplified to

$$f(\dot{\boldsymbol{\varepsilon}}) = \beta_1 \dot{\boldsymbol{\varepsilon}}.$$

To cope with isotropic expansion and compression forces, we introduce a pressure variable as part of the material law:

$$f(\dot{\boldsymbol{\varepsilon}}, p) = -pI + \beta_1 \dot{\boldsymbol{\varepsilon}}.$$

This pressure is required to enforce the incompressibility of the velocity field, see also Sect. 2.3.

Considering solid's, incompressibility in terms of (2.26) means that the determinant of the deformation gradient will be constant $d_t \hat{J} = 0$. As $\hat{\mathbf{F}} = I$ in the reference system, incompressibility simply says $\hat{J} = 1$ for all times $t \geq t_0$. Further, it then holds that

$$\det(\hat{\mathbf{C}}) = \det(\hat{\mathbf{F}})^2 = 1.$$

For the Green-Lagrange strain tensor $\hat{\mathbf{E}}$ it follows that third and second invariant fall together, see Lemma 2.15 and Remark 2.16.

2.3 The Solid Problem

As discussed, we usually describe the dynamics of elastic structures in the Lagrangian reference system. Hence considering the conservation law (2.22) we choose $\hat{W} = \hat{V}$ as reference system. In light of Remark 2.11, the momentum equation is given by

$$\hat{J}\hat{\rho}\partial_{tt}\hat{\mathbf{u}} = \hat{J}\hat{\rho}\hat{\mathbf{f}} + \widehat{\operatorname{div}}(\hat{\mathbf{F}}\hat{\boldsymbol{\Sigma}}),$$

where we eliminated the velocity using $\partial_t \hat{\mathbf{u}} = \hat{\mathbf{v}}$. Considering material laws as introduced in the previous section, stresses will depend on strain, and hence on the displacement $\hat{\mathbf{u}}$. The density is known at initial time $\rho(x, 0) = \hat{\rho}^0(\hat{x})$. For $t \geq 0$ conservation of mass yields

$$m(\hat{V}) := \int_{\hat{V}} \hat{\rho}^0(\hat{x})\, \mathrm{d}\hat{x} \overset{!}{=} \int_{V(t)} \rho(x,t)\, \mathrm{d}\, x = \int_{\hat{V}} \hat{J}\hat{\rho}(\hat{x}, t)\, \mathrm{d}\hat{x} =: m(V(t)).$$

At time $t \geq 0$, the relation

$$\hat{\rho}(\hat{x}, t) = \hat{J}^{-1}(\hat{x}, t)\hat{\rho}^0(\hat{x}) \tag{2.27}$$

describes the density in every point $\hat{x}$ of the reference system. The full problem of elastic structures formulated in the Lagrangian reference system $\hat{V}$ is given by:

$$\hat{\rho}^0 \partial_{tt} \hat{\mathbf{u}} - \widehat{\operatorname{div}}\,(\mathbf{F}\hat{\boldsymbol{\Sigma}}) = \hat{\rho}^0 \hat{\mathbf{f}} \tag{2.28}$$

It remains to complete this partial differential equation by appropriate boundary conditions and initial conditions. Let $\hat{\mathcal{S}} \subset \mathbb{R}^d$ be the solid domain in reference configuration. At time $t = 0$, we specify initial conditions for density, deformation and velocity

$$\hat{\rho}(\cdot, 0) = \hat{\rho}^0(\cdot), \quad \hat{\mathbf{u}}(\cdot, 0) = \hat{\mathbf{u}}^0(\cdot), \quad \partial_t \hat{\mathbf{u}}(\cdot, 0) = \hat{\mathbf{v}}^0(\cdot), \quad t = 0. \tag{2.29}$$

For all times $t \geq 0$, by $\hat{\mathbf{f}}(\hat{x}, t)$ we denote the acting volume force field. Note that this force field is directed in the Eulerian framework, such that for example the gravity is given by $\mathbf{f} = -9.81 e_3 \mathrm{kg} \cdot \mathrm{m} \cdot \mathrm{s}^{-2}$, with $e_3 = (0, 0, 1)^T$, independent of the reference framework. The boundary of the domain $\hat{\Gamma}_s := \partial\hat{\mathcal{S}}$ is split into a Dirichlet boundary part $\hat{\Gamma}_s^D$ and into a Neumann part $\hat{\Gamma}_s^N$. On the Dirichlet boundary, we specify boundary conditions for the deformation

$$\hat{\mathbf{u}} = \hat{\mathbf{u}}^D \text{ on } \hat{\Gamma}_s^D \times [0, T]. \tag{2.30}$$

Note that by $\hat{\mathbf{v}} = \partial_t \hat{\mathbf{u}}$ we also uniquely define the velocity on the boundary. The usual Neumann condition on Γ_s^N specifies the boundary stresses by

$$\mathbf{n} \cdot \hat{\mathbf{F}}\hat{\boldsymbol{\Sigma}} = \mathbf{n} \cdot \hat{J}\hat{\boldsymbol{\sigma}}_s \hat{\mathbf{F}}^{-T} = \hat{\mathbf{g}}_s^{(\hat{n})} \text{ on } \hat{\Gamma}_s^N \times [0, T]. \tag{2.31}$$

If the external forces $\mathbf{f}$ and the boundary data $\hat{\mathbf{g}}_s^{(\hat{n})}$ and $\hat{\mathbf{u}}^D$ do not explicitly depend on time, the solution can run into a stationary limit $\hat{\mathbf{u}}(\cdot, t) \to \hat{\mathbf{u}}(\cdot)$ that does not depend on time. In this case, it holds $\partial_t \hat{\mathbf{v}} = 0$ and hence $\partial_{tt} \hat{\mathbf{u}} = 0$. If such a stationary solution exists, we can directly consider the stationary system of equations:

$$-\widehat{\operatorname{div}}\,(\hat{\mathbf{F}}\hat{\boldsymbol{\Sigma}}) = \hat{\rho}^0 \hat{\mathbf{f}}. \tag{2.32}$$

Finally, it remains to provide material laws for specific solids. One of the most simple model is the *St. Venant Kirchhoff material* that postulates a linear dependency between strain tensor $\hat{\mathbf{E}}$ and stresses:

Definition 2.18 (St. Venant Kirchhoff Material) The St. Venant Kirchhoff material follows the material law

$$\hat{\boldsymbol{\Sigma}} = 2\mu_s \hat{\mathbf{E}} + \lambda_s \operatorname{tr}(\hat{\mathbf{E}}) I,$$

with the first λ_s and second μ_s Lamé parameters. (μ_s is also called the *shear modulus*.) These two parameters are related to the Poisson ratio ν_s that describes the compressibility and Young's modulus E_s that describes the stiffness:

$$\nu_s = \frac{\lambda_s}{2(\lambda_s + \mu_s)}, \quad E_s = \frac{\mu_s(3\lambda_s + 2\mu_s)}{\lambda_s + \mu_s}.$$

The linear relation between strain and stress is called *Hooke's Law*. The Poisson ratio ν_s describes the compressibility of the system. It holds

$$\nu_s = \frac{1}{2}\left(\frac{1}{1 + \frac{\mu_s}{\lambda_s}}\right) < \frac{1}{2}.$$

The Poisson ratio $\nu_s = \frac{1}{2}$ refers to $\lambda_s \to \infty$ hence to incompressible materials. The Poisson ratio describes the reaction of the material on directional compression, see Fig. 2.6. For a Poisson ratio $\nu_s = \frac{1}{2}$, the volume will stay constant, for $\nu_s < \frac{1}{2}$ the volume will decrease. There are some materials with negative Poisson ratio. Here, the material will react to the compression in one direction with compression in the orthogonal directions. Such materials play some role for computational means in the context of fluid-structure interactions, see Sect. 3.5.1. The St. Venant Kirchhoff model is a suitable approximation for metals at small deformations. Steel has a Poisson ratio of about $\nu_s \approx 0.3$ and a Young modulus $E_s \approx 200 \cdot 10^9\,\mathrm{kg} \cdot \mathrm{m}^{-1} \cdot \mathrm{s}^{-2}$.

Hooke's Law applied to an incompressible material leads to the incompressible Neo Hookean material law.

Definition 2.19 (Incompressible Neo-Hookean Material) The incompressible Neo-Hookean material law is given by

$$\hat{\mathbf{P}} = \hat{\mathbf{F}}\hat{\boldsymbol{\Sigma}} = -p\hat{\mathbf{F}}^{-T} + 2\mu_s\hat{\mathbf{F}}^{-T}\hat{\mathbf{E}},$$

with the shear modulus μ_s and the Poisson ratio $\nu_s = \frac{1}{2}$. By p we denote the undetermined pressure.

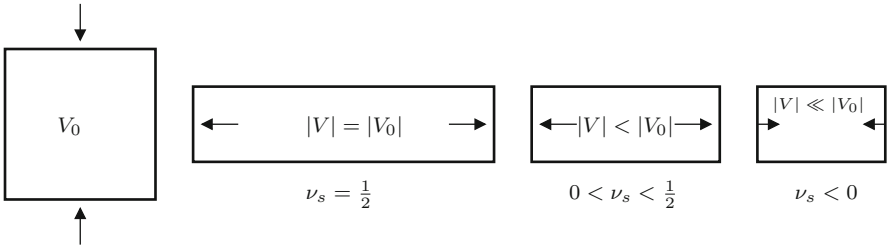

Fig. 2.6 Material behavior under compression for different Poisson ratios. *Left*: incompressible material $\nu_s = \frac{1}{2}$. *Middle*: compressible material $0 < \nu_s < \frac{1}{2}$. *Right*: auxetic material with $\nu_s < 0$

We conclude and formulate the following often used systems of equations

Problem 2.20 (Conservation Laws for a St. Venant Kirchhoff Material) *Let $\Omega \subset \mathbb{R}^d$ be a domain with boundary $\Gamma = \partial\Omega$ with $\Gamma = \Gamma^D \cup \Gamma^N$. Further, let $\hat{\rho}^0 : \Omega \to \mathbb{R}_+$ be the materials density, $\hat{\mathbf{f}} \in C(\Omega)^d$ be a given right hand side, $\hat{\mathbf{u}}^D, \hat{\mathbf{v}}^D \in C(\Gamma^D)$ be Dirichlet boundary data, $\hat{\mathbf{g}}^{(\mathbf{n})} \in C(\Gamma^N)$ be the Neumann data. With initial deformation and velocity $\hat{\mathbf{u}}^0, \hat{\mathbf{v}}^0 \in C(\Omega)^d$ find deformation and velocity*

$$\hat{\mathbf{u}}(t) \in C^2(\Omega)^d \cap C(\Omega \cup \Gamma^D)^d \cup C^1(\Omega \cup \Gamma^N)^d,$$

such that

$$\hat{\rho}^0 \partial_{tt} \hat{\mathbf{u}} - \widehat{\operatorname{div}} \left(\hat{\mathbf{F}} \hat{\boldsymbol{\Sigma}} \right) = \hat{\rho}^0 \hat{\mathbf{f}} \quad t \geq 0,$$

where

$$\hat{\boldsymbol{\Sigma}} = 2\mu_s \hat{\mathbf{E}} + \lambda_s \operatorname{tr}(\hat{\mathbf{E}}) I,$$

and

$$\hat{\mathbf{u}}(0) = \hat{\mathbf{u}}^0, \ d_t \hat{\mathbf{u}}(0) = \hat{\mathbf{v}}^0 \text{ in } \Omega,$$

with the boundary conditions

$$\hat{\mathbf{u}}(t) = \hat{\mathbf{u}}^D \text{ on } \Gamma^N, \quad \hat{\mathbf{F}} \hat{\boldsymbol{\Sigma}} \hat{\mathbf{n}} = \hat{\mathbf{g}}^{(\mathbf{n})}.$$

and, for the incompressible materials we define:

Problem 2.21 (Conservation Laws for the Incompressible Neo-Hookean Material) *Let $\Omega \subset \mathbb{R}^d$ be a domain with boundary $\Gamma = \partial\Omega$ with $\Gamma = \Gamma^D \cup \Gamma^N$. Further, let $\hat{\rho}^0 : \Omega \to \mathbb{R}_+$ be the materials density, $\hat{\mathbf{f}} \in C(\Omega)^d$ be a given right hand side, $\hat{\mathbf{u}}^D, \hat{\mathbf{v}}^D \in C(\Gamma^D)$ be Dirichlet boundary data, $\hat{\mathbf{g}}^{(\mathbf{n})} \in C(\Gamma^N)$ be the Neumann data. With initial deformation and velocity $\hat{\mathbf{u}}^0, \hat{\mathbf{v}}^0 \in C(\Omega)^d$ find deformation, velocity and pressure*

$$\hat{\mathbf{u}}(t) \in C^2(\Omega)^d \cap C(\Omega \cup \Gamma^D)^d \cap C^1(\Omega \cup \Gamma^N)^d, \quad \hat{p}(t) \in C^1(\Omega) \cap C(\Omega \cup \Gamma^N),$$

such that

$$\hat{J} = 0, \quad \hat{\rho}^0 \partial_{tt} \hat{\mathbf{u}} - \widehat{\operatorname{div}} \left(\hat{\mathbf{F}} \hat{\boldsymbol{\Sigma}} \right) = \hat{\rho}^0 \hat{\mathbf{f}} \quad t \geq 0,$$

where

$$\hat{\boldsymbol{\Sigma}} = -\hat{p} \hat{\mathbf{F}}^{-T} + 2\mu_s \hat{\mathbf{F}}^{-T} \hat{\mathbf{E}}$$

and

$$\hat{\mathbf{u}}(0) = \hat{\mathbf{u}}^0,\ d_t\hat{\mathbf{u}}(0) = \hat{\mathbf{v}}^0 \text{ in } \Omega,$$

with the boundary conditions

$$\hat{\mathbf{u}}(t) = \hat{\mathbf{u}}^D \text{ on } \Gamma^N, \quad \hat{\mathbf{F}}\hat{\boldsymbol{\Sigma}}\hat{\mathbf{n}} = \hat{\mathbf{g}}^{(\mathbf{n})}.$$

2.3.1 The Navier-Lamé Equations

The model for an elastic solid governed by one of the material laws is a system of nonlinear partial differential equations. Its analysis is difficult and theoretical results exist for small deformation only. As a nonlinear set of equations, uniqueness cannot be expected in the general case.

To get better insight into the problem, we will simplify the problem with the following assumptions:

- The deformation gradient $\hat{\mathbf{F}}$ is so small that we can approximate $\hat{\mathbf{F}} = I$ and $\hat{J} = 1$. By this simplification, the concept of Eulerian and Lagrangian coordinates fall together. We will therefore also skip all hat's that indicate reference variables.
- Further the strains are so small that we can linearize the Green-Lagrange strain tensor

$$\hat{\mathbf{E}} = \frac{1}{2}(\hat{\nabla}\mathbf{u} + \hat{\nabla}\mathbf{u}^T + \hat{\nabla}\hat{\mathbf{u}}^T\hat{\nabla}\hat{\mathbf{u}}) \approx \frac{1}{2}(\nabla\mathbf{u} + \nabla\mathbf{u}) =: \boldsymbol{\varepsilon}.$$

  This simplification not only rules out very large elastic deformations, it also penalizes rigid body rotations.
- Just for simplicity (this will not change the character of the equation) we set $\hat{\rho}^0 = 1$.

Considering the linear St. Venant Kirchhoff material (with these simplifications) the resulting set of equations are the

Problem 2.22 (Navier-Lamé Equations) *Let $\Omega \subset \mathbb{R}^3$ be a bounded domain with a boundary split into Dirichlet- and Neumann-part $\partial\Omega = \Gamma^D \cup \Gamma^N$. On the time interval $I = [0, T]$ we search for solutions $\mathbf{u} : I \times \Omega \to \mathbb{R}^3$ such that*

$$\begin{aligned} \partial_{tt}\mathbf{u} - \operatorname{div}\boldsymbol{\sigma} &= \mathbf{f} && \text{in } I \times \Omega \\ \mathbf{u} = \mathbf{u}^0, \quad d_t\mathbf{u} &= \mathbf{v}^0 && \text{for } \{0\} \times \Omega \\ \mathbf{u} &= \mathbf{u}^D && \text{on } I \times \Gamma^D \\ \boldsymbol{\sigma}\,\mathbf{n} &= \mathbf{u}^{\boldsymbol{\sigma}} && \text{on } I \times \Gamma^N, \end{aligned} \tag{2.33}$$

with the linearized material law

$$\boldsymbol{\sigma} = 2\mu\boldsymbol{\varepsilon} + \lambda \operatorname{tr}(\boldsymbol{\varepsilon}) I, \quad \boldsymbol{\varepsilon} = \frac{1}{2}\left(\nabla \mathbf{u} + \nabla \mathbf{u}^T\right).$$

As a further simplification, we also consider the stationary limit of the Navier-Lamé equations:

Problem 2.23 (Stationary Navier-Lamé Equations) *Find* $u \in C^2(\Omega)^3 \cap C(\Omega \cup \Gamma^D)^3 \cap C^1(\Omega \cup \Gamma^N)^3$ *such that*

$$\begin{aligned} -\operatorname{div} \boldsymbol{\sigma} &= \mathbf{f} && \text{in } \Omega \\ \mathbf{u} &= \mathbf{u}^D && \text{on } \Gamma^D \\ \boldsymbol{\sigma}\,\mathbf{n} &= \mathbf{u}^\sigma && \text{on } \Gamma^N, \end{aligned} \tag{2.34}$$

with the linearized material law

$$\boldsymbol{\sigma} = 2\mu\boldsymbol{\varepsilon} + \lambda \operatorname{tr}(\boldsymbol{\varepsilon}) I, \quad \boldsymbol{\varepsilon} = \frac{1}{2}\left(\nabla \mathbf{u} + \nabla \mathbf{u}^T\right).$$

As usual, analysis of classical solutions is difficult. This is partly to the fact that the solution $\mathbf{u}$ often exhibits singularities in boundary nodes at the transit between Dirichlet and Neumann parts. The well known *Theorem of Cosserat* states that classical solutions to the stationary problem, Problem 2.23, are unique if the Dirichlet boundary Γ^D contains at least three independent points and that—in the general case—they can differ by a rigid body motion only

$$\mathbf{u}_1(x) - \mathbf{u}_2(x) = \mathbf{b} + \mathbf{B}x,$$

where $\mathbf{b} \in \mathbb{R}^3$ is a translation vector and $\mathbf{B} \in \mathbb{R}^{3\times 3}$ is a skew-symmetric matrix, see e.g. [97].

For the following, we will introduce a weak formulation of the Navier-Lamé equations that will offer an easy access to show existence and uniqueness of solutions:

Lemma 2.24 (Variational Formulation) *Every classical solution to Problem 2.23 is also solution to the variational formulation*

$$\begin{aligned} &\mathbf{u} \in \bar{\mathbf{u}}^D + H_0^1(\Omega; \Gamma^D)^3 \\ &\qquad (\boldsymbol{\sigma}, \nabla\phi) = (\mathbf{f}, \phi) + \langle \mathbf{u}^\sigma, \phi \rangle_{\Gamma^N} \quad \forall \phi \in H_0^1(\Omega; \Gamma^D)^3, \end{aligned} \tag{2.35}$$

where $\bar{\mathbf{u}}^D \in H^1(\Omega)^d$ *is an extension of the Dirichlet data* $\mathbf{u}^D$ *into the domain.*

Existence and uniqueness of solutions can be shown by standard arguments of elliptic equations. The difficulty however is to show ellipticity, i.e.

$$\mu(\nabla \mathbf{u} + \nabla \mathbf{u}^T, \nabla \mathbf{u}) + \lambda\big(\operatorname{tr}(\nabla \mathbf{u} + \nabla \mathbf{u}^T)I, \nabla \mathbf{u}\big) \geq c\|\nabla \mathbf{u}\|^2,$$

as $\nabla \mathbf{u} + \nabla \mathbf{u}^T = 0$ does not necessarily impose $\nabla \mathbf{u} = 0$. This is a consequence of *Korn's inequality*:

Theorem 2.25 (1st Korn's Inequality) *Let $\Omega \subset \mathbb{R}^3$ be a domain. Then, it holds*

$$\|\nabla \mathbf{v}\| \leq c_{korn}\|\boldsymbol{\varepsilon}(\mathbf{v})\| \quad \forall \mathbf{v} \in H_0^1(\Omega)^3$$

with a constant $c_{korn} > 0$. This inequality corresponds to the case of Dirichlet boundary values on the complete boundary $\Gamma^D = \partial\Omega$.

Korn's first inequality deals with the case of homogenous Dirichlet conditions on the complete boundary $\partial\Omega$. In the context of structural mechanics, this limitation is severe, as no free boundary motion and deformation would be allowed. The case of general boundary conditions, with a Neumann part $\Gamma_N \subset \partial\Omega$ is less trivial and handled by Korn's second inequality:

Theorem 2.26 (2nd Korn's Inequality) *Let $\Omega \subset \mathbb{R}^3$ be a domain with Lipschitz-boundary. Then, it holds*

$$\|\nabla \mathbf{v}\| \leq c_{korn}\left(\|\varepsilon(\mathbf{v})\| + \|\mathbf{v}\|\right) \quad \forall \mathbf{v} \in H^1(\Omega)^3.$$

with a constant $c_{korn} > 0$.

Proof The simple proof of 1st Korn's inequality is based on integration by parts and vanishing traces of $\mathbf{v}$ on the complete boundary $\partial\Omega$. The proof of Korn's 2nd inequality is more involved and we refer to the literature, see e.g. [98, 196]. □

Continuity and ellipticity of the bilinear form allows to apply the standard theory for linear elliptic problems to the Navier-Lamé equations.

Lemma 2.27 (Existence of Unique Solutions) *Let $\mathbf{f} \in L^2(\Omega)^3$, $\bar{\mathbf{u}}^D \in H^1(\Omega)^3$ be an extension of the Dirichlet data into the domain and $\mathbf{u}^\sigma \in H^1(\partial\Omega)^3$. There exists a unique solution $\mathbf{u} \in \bar{\mathbf{u}}^D + H_0^1(\Omega; \Gamma^D)^3$ to the linear Navier-Lamé equations and it holds*

$$\|\mathbf{u}\|_{H^1(\Omega)} \leq c\left(\|\mathbf{f}\|_{L^2(\Omega)} + \|\mathbf{u}^D\|_{L^2(\Gamma^D)} + \|\mathbf{u}^\sigma\|_{H^1(\Gamma^N)}\right),$$

with a constant $c > 0$.

Proof We must show that the variational formulation is bilinear, symmetric, continuous and elliptic. Further, the right hand side is continuous, such that existence of a unique solution follows by the Theorem of Lax-Milgram, see [293]. □

Concerning the regularity of the solution, we cite the following lemma, see [97], which gives conditions that lead to classical solutions.

Lemma 2.28 (Strong Regularity of the Navier-Lamé Problem) *Let $\Omega \subset \mathbb{R}^3$ be a bounded domain of class $C^{2+\alpha}$ for $\alpha > 0$. Given that the problem data has the regularity*

$$\mathbf{f} \in C^{\alpha}(\bar{\Omega})^3, \quad \bar{\mathbf{u}}^{\sigma} \in C^{1+\alpha}(\Omega)^{3\times 3}_{sym}, \quad \bar{\mathbf{u}}^{D} \in C^{2+\alpha}(\bar{\Omega})^3,$$

the weak solution $\mathbf{u} \in H^1_0(\Omega; \Gamma^D)^3$ of (2.35) is also a classical solution

$$\mathbf{u} \in C^2(\Omega)^3 \cap C^1(\Omega \cup \Gamma^N)^3 \cap C(\Omega \cup \Gamma^D)^3.$$

A further regularity result with less strict assumption on the regularity of the domain and the problem data is given by Shi and Wright [308]:

Lemma 2.29 (Weak Regularity of the Navier-Lamé Problem) *Let $\Omega \subset \mathbb{R}^3$ be a domain with $W^{2,3}$ boundary. Further, let $\mathbf{f} \in L^2(\Omega)^d$. Then, for the solution of the stationary Navier-Lamé problem with homogenous Dirichlet data $\mathbf{u}^D = 0$ it holds*

$$\|\mathbf{u}\|_{H^2(\Omega)^3 \cap H^1_0(\Omega)^3} \leq c \|\mathbf{f}\|_{L^2(\Omega)^3}.$$

Regularity of solutions is usually restricted at points, where Neumann and Dirichlet parts of the boundary come together. Here, we usually have singularities in the gradient of the solution and the stress tensor.

2.3.1.1 The Incompressible Navier-Lamé Equations

For incompressible linear materials with $\nu = \frac{1}{2}$, the stress tensor is reduced to

$$\boldsymbol{\sigma} = \mu(\nabla \mathbf{u} + \nabla \mathbf{u}^T),$$

as $\mathrm{tr}\,(\boldsymbol{\varepsilon}) = \mathrm{div}\ \mathbf{u} = 0$. The material is no longer able to react on purely isotropic stresses. To formulate the incompressible Navier-Lamé equations, we consider a minimization problem in the space of divergence free functions

$$\mathbf{u} \in V_0 : \quad E(\mathbf{u}) \leq E(\mathbf{v}) = \frac{1}{2} a(\mathbf{v}, \mathbf{v}) - l(\mathbf{v}) \quad \forall \mathbf{v} \in V_0,$$

where $a(v, v) := (\boldsymbol{\sigma}, \nabla \mathbf{v})$, $l(\mathbf{v}) := (\mathbf{f}, \mathbf{v}) + \langle u^{\sigma}, \mathbf{v} \rangle_{\Gamma^N}$ and where V_0 is the space of weakly divergence free functions

$$V_0 = \{\phi \in H^1_0(\Omega; \Gamma^D)^3,\ (\mathrm{div}\ \phi, \xi) = 0\ \forall \xi \in L^2(\Omega)\}. \tag{2.36}$$

The Hilbert space V_0 is a closed subspace of $H^1_0(\Omega; \Gamma^D)^3$, such that the existence of a unique solution follows as shown in Lemma 2.27. To derive a variational

formulation, we use the Euler-Lagrange approach for constraint minimization problems and define the Lagrange functional

$$\mathcal{L}(\mathbf{u}, p) = \frac{1}{2}a(\mathbf{u}, \mathbf{u}) - l(\mathbf{u}) - (p, \operatorname{div} \mathbf{u}),$$

with a Lagrange multiplier $p \in L^2(\Omega)$. A possible solution is given as stationary point of $\mathcal{L}(\mathbf{u}, p)$:

$$\begin{aligned} d_{\mathbf{u}}\mathcal{L}(\mathbf{u}, p)(\phi) &= a(\mathbf{u}, \phi) - l(\phi) - (p, \operatorname{div} \phi) \stackrel{!}{=} 0 \quad \forall \phi \in H_0^1(\Omega; \Gamma^D)^3 \\ d_p\mathcal{L}(\mathbf{u}, p)(\xi) &= -(\xi, \operatorname{div} \mathbf{u}) \stackrel{!}{=} 0 \quad \forall \xi \in L^2(\Omega). \end{aligned}$$

We include the Lagrange multiplier into the stress tensor and define

$$\boldsymbol{\sigma}_I(\mathbf{u}, p) = -pI + \mu(\nabla \mathbf{u} + \nabla \mathbf{u}^T),$$

where we identify $p \in L^2(\Omega)$ with a *pressure function*. This identification is reasonable, as $-pI$ acts as isotropic stress in all directions. The problem is now to find $\{\mathbf{u}, p\} \in H_0^1(\Omega; \Gamma^D)^3 \times L^2(\Omega)$ such that

$$\left(\mu(\nabla \mathbf{u} + \nabla \mathbf{u}^T) - pI, \boldsymbol{\varepsilon}(\phi)\right) + (\operatorname{div} \mathbf{u}, \xi) = (\mathbf{f}, \phi) + \langle u^{\boldsymbol{\sigma}}, \phi \rangle_{\Gamma^N} \tag{2.37}$$

for all $\phi \in H_0^1(\Omega; \Gamma^D)^3$ and $\xi \in L^2(\Omega)$.

The incompressible Navier-Lamé equations, as a minimization problem with side condition is a *saddle-point system*. Existence and uniqueness theory cannot be based on ellipticity (in p). Instead, we split the proof for the existence of a well defined solution in two parts. We start by finding a suitable deformation field. Therefore, we restrict the space of admissible functions to those that already fulfill the divergence condition in the space V_0, see (2.36). Then, it holds

Lemma 2.30 (Incompressible Navier-Lamé—Existence of Unique Solutions (Displacement)) *Let $\mathbf{f} \in L^2(\Omega)^3$, $\bar{\mathbf{u}}^D \in H^1(\Omega)^3$ be an extension of the Dirichlet data into the domain and $\mathbf{u}^{\boldsymbol{\sigma}} \in H^1(\Gamma^N)^3$. There exists a unique solution $u \in \bar{u}^D + H_0^1(\Omega; \Gamma^D)^d$ to the variational problem*

$$(2\mu\varepsilon(\mathbf{u}), \varepsilon(\phi)) = (\mathbf{f}, \phi) + \langle \mathbf{u}^{\boldsymbol{\sigma}}, \phi \rangle_{\Gamma^N} \quad \forall \phi \in H_0^1(\Omega; \Gamma^D)^3.$$

For this solution it holds

$$\|\mathbf{u}\|_{H^1(\Omega)} \leq c \left(\|\mathbf{f}\|_{L^2(\Omega)} + \|\mathbf{u}^D\|_{L^2(\Gamma^D)} + \|\mathbf{u}^{\boldsymbol{\sigma}}\|_{H^1(\Gamma^N)} \right).$$

Finally, $\mathbf{u} \in V_0$ minimizes the energy function in the space V_0

$$E(\mathbf{u}) \leq E(\mathbf{v}) \quad \forall \mathbf{v} \in V_0.$$

Proof The subspace $V_0 \subset H_0^1(\Omega;\Gamma_D)^3$ is a Hilbert-space. The variational formulation is V_0-elliptic and the existence of a unique solution as well as the a priori estimate follow in the same way as shown in Lemma 2.27. □

Next, given a deformation field $u \in V_0$ we find a corresponding pressure by analyzing the equation

$$p \in L^2(\Omega):$$
$$-(p, \nabla\phi) = (\mathbf{f}, \phi) + \langle \mathbf{u}^\sigma, \phi\rangle_{\Gamma^N} - (2\mu\boldsymbol{\varepsilon}(\phi), \nabla\phi) \quad \forall \phi \in H_0^1(\Omega;\Gamma^D)^3.$$

Existence of solutions to this problem cannot be shown by simple variational arguments. Instead, we will define by

$$\langle \text{grad}\, p, \phi\rangle := -(p, \nabla\cdot\phi) \quad \forall \phi \in H_0^1(\Omega;\Gamma^D)^3,$$

the weak gradient operator $-\text{grad} = \text{div}^* : L^2(\Omega) \to H^{-1}(\Omega)$ and show existence by proving surjectivity of $-\text{grad}$ in appropriate function spaces. We postpone this discussion to Sect. 2.4.5, where we will come across the same pressure problem concerning the incompressible Stokes equations.

2.3.1.2 The Non-stationary Navier-Lamé Equations

The non-stationary system of Navier-Lamé equations as given in Definition 2.22 is a hyperbolic problem

$$\partial_{tt}\mathbf{u} - \text{div}\,(\boldsymbol{\sigma}) = 0, \quad \mathbf{u}(0) = \mathbf{u}^0, \quad \partial_t\mathbf{u}(0) = \mathbf{v}^0.$$

For simplicity we will consider the case of homogenous Dirichlet data only and we will further assume that $\mathbf{f} = 0$. We multiply the differential equation by $\phi = \partial_t\mathbf{u}$ and integrate over the spatial domain to get

$$0 = (\partial_{tt}\mathbf{u}, \partial_t\mathbf{u}) + (\boldsymbol{\sigma}(\mathbf{u}), \boldsymbol{\varepsilon}(\partial_t\mathbf{u})) = \frac{d}{dt}\left(\underbrace{\frac{1}{2}\|\partial_t\mathbf{u}\|^2 + \frac{1}{2}(\boldsymbol{\sigma}(\mathbf{u}), \boldsymbol{\varepsilon})}_{=:E(t)}\right),$$

where by $E(t)$ we denote the energy of the system. This energy does not change over time (remember that we consider the homogenous problem only). Integration over the temporal domain $I = [0, T]$ yields the relation

$$E(t) = E(0) \quad t \geq 0, \quad E(0) = \frac{1}{2}\|\mathbf{v}^0\|^2 + \frac{1}{2}\left(\boldsymbol{\sigma}(\mathbf{u}^0), \boldsymbol{\varepsilon}(\mathbf{u}^0)\right),$$

with the initial velocity $\mathbf{v}^0 = \partial_t \mathbf{u}^0$. Hence a solution must by unique and it is bounded by the initial data.

Conservation of energy $d_t E(t) = 0$ shows the close relation to the wave equation. Existence of solutions to this simple (linear, symmetric and positive) problem can be shown by the Fourier approach. The operator

$$\langle \mathcal{L}\mathbf{u}, \mathbf{v} \rangle := \Big(2\mu \boldsymbol{\varepsilon}(\mathbf{u}) + \lambda \operatorname{tr} \big(\boldsymbol{\varepsilon}(\mathbf{u}) \big), \boldsymbol{\varepsilon}(\mathbf{v}) \Big)$$

is symmetric, positive definite, selfadjoint and a bijection. Its inverse is bound and considered as operator $\mathcal{L}^{-1} : L^2(\Omega)^d \to L^2(\Omega)^d$ it is compact. Hence $\mathcal{L}$ has a spectrum of positive eigenvalues, with no finite accumulation point. Further, an orthonormal basis of eigenvectors exists. This allows to diagonalize the system of equations, such that it decomposes into a sequence of scalar initial values problems that have a solution that can be constructed by elementary principles. For the details on this construction, we refer to the literature [268].

A recent result on the regularity of the non-stationary Navier-Lamé problem with homogenous Dirichlet data is given by Mitrea and Monniaux [243]. They basically show that given sufficient regularity of the domain's boundary (Lipschitz), the solution of the non-stationary Navier-Lamé problem with zero initial data and zero Dirichlet data satisfies $\mathbf{u} \in H^1(I; L^2(\Omega)^3)$ for every right hand side $\mathbf{f} \in L^2(I; L^2(\Omega)^3)$.

In the upcoming chapters, we will see that the coupling of the solid equation to the fluid equations brings along further challenges for the analysis of the partial differential equations. The *kinematic coupling condition*, see Sect. 3.1 will ask for continuity of solid- and fluid-velocities on a common interface $\mathcal{I}(t) = \partial\mathcal{S}(t) \cap \partial\mathcal{F}(t)$

$$\mathbf{v}_f = \mathbf{v}_s \text{ on } \mathcal{I}(t).$$

In the case of stationary problems, this kinematic coupling condition is just a usual no-slip boundary condition $\mathbf{v}_f = 0$ for the fluid's velocity. For fully non-stationary problems, a real coupling between the two velocities is introduced. The solution of the Navier-Stokes equations is well defined for velocities with traces in

$$\mathbf{v}_f \Big|_{\partial\mathcal{F}} \in H^{\frac{1}{2}}(\partial\mathcal{F}),$$

which—as seen from the solid problem—will require

$$\mathbf{v}_f \Big|_{\mathcal{I}} = \mathbf{v}_s \Big|_{\mathcal{I}} \quad \Rightarrow \quad \mathbf{v}_s \in H^1(\mathcal{S}).$$

However, the previous analysis only gives

$$\mathbf{v}_s = \partial_t \mathbf{u}_s \in L^2(I; L^2(\Omega)^3).$$

This is not sufficient to define a $H^{1/2}$-trace on $\mathcal{I}$. This problem has two possible solutions. First—and this will be our usual procedure—we can simply assume additional a priori knowledge on the regularity of $\mathbf{u}_s$ and therefore $\mathbf{v}_s$. This can be guaranteed for small and regular problem data, if the boundaries of the coupled problem have very high regularity. Coutand and Shkoller [106] show the existence of solutions for the coupling of elastic solids with the Navier-Stokes equations, if the solid with boundary of class H^4 is completely embedded in a fluid-domain with boundary of class H^3, given sufficient regularity of the right hand side and the boundary data, see [106]. A second approach to enforce sufficient regularity it to add damping terms to the solid equation. Gazzola and Squassina show the following result, see [162].

Theorem 2.31 (Damped Wave Equation) *Let $\Omega \subset \mathbb{R}^d$ be a Lipschitz domain. The strongly damped wave equation*

$$\partial_{tt} u - \Delta u - \omega \Delta \partial_t u + \mu \partial_t u = 0 \text{ in } [0,T] \times \Omega,$$

with initial values

$$u(0,\cdot) = u_0 \in H^1(\Omega), \quad \partial_t u(0,\cdot) = u_1 \in L^2(\Omega),$$

and homogenous Dirichlet values on $\partial\Omega$ and the damping parameters

$$\omega > 0, \quad \mu > -\omega\lambda_1,$$

where λ_1 is the first eigenvalue of $-\Delta$ has a unique solution satisfying

$$u \in L^\infty([0,T], H_0^1(\Omega)) \cap W^{1,\infty}([0,T], L^2(\Omega)), \quad \partial_t u \in L^2([0,T], H_0^1(\Omega)).$$

For the proof, see Gazolla and Squassina [162].

By adding strong damping terms, we are able to assure sufficient regularity to realize the kinematic coupling condition between solid problem and fluid problem.

2.3.2 Theory of Nonlinear Hyper-Elastic Material

Tackling the existence and uniqueness problem of the full elastic structure equation (using the St. Venant Kirchhoff material law) is complicated by the nonlinearity of the problem. Here, we will not give details on the complex proofs, but will simply cite some important results. A good overview on the theory of nonlinear elastic materials is given in the textbook of Ciarlet [97].

All approaches for the nonlinear problem will at some time use a linearization of the problem and will consult the theory that has been derived for the linear Navier-Lamé problem. Further, most approaches use variational techniques, such that the starting point for every analysis is the following weak formulation of the problem:

Lemma 2.32 (Weak Formulation of the Hyper-Elastic Structures) *Let $\bar{\mathbf{u}}^D \in H^1(\hat{\mathcal{S}})^d$ be an extension of the Dirichlet data on Γ^D into the domain Ω. If the solution*

$$\hat{\mathbf{u}}_f \in \bar{\mathbf{u}}_f^D + H_0^1(\hat{\Omega}; \Gamma^D)^d$$

of the variational formulation

$$(\hat{\mathbf{F}}\hat{\mathbf{\Sigma}}_s, \hat{\nabla}\hat{\phi})_{\hat{\mathcal{S}}} = (\rho_s^0 \hat{\mathbf{f}}_s, \hat{\phi}), \quad \forall \hat{\phi} \in H_0^1(\hat{\Omega}; \Gamma^D)^d, \tag{2.38}$$

has sufficient regularity $\hat{\mathbf{u}} \in C^2(\hat{\Omega}) \cap C(\hat{\Omega} \cup \Gamma^D) \cap C^1(\hat{\Omega} \cup \Gamma^D)$, it is also a solution to the classical formulation of the elastic structure equations (2.32) with Dirichlet data on Γ_s^D.

Using the implicit function theorem, Ciarlet [97] proofs the following result for weak solutions of the elastic structure equation governed by the St. Venant Kirchhoff material:

Lemma 2.33 (Stationary St. Venant Kirchhoff Material) *Let $\Omega \subset \mathbb{R}^3$ be a domain with C^2-boundary. Then, for every $p > 3$ there exists a constant α such that for every $\mathbf{f} \in L^p(\Omega)^d$ with $\|\mathbf{f}\|_{L^p} \leq \alpha$ there exists a unique solution $\mathbf{u} \in W^{2,p}(\Omega)$ to the stationary elastic structure equation governed by the St. Venant Kirchhoff material.*

For the proof, we refer to the literature [97].

2.4 The Fluid Problem

In fluid-dynamics, we describe the flow of particles in the Eulerian framework. Looking at a fixed coordinate $x \in \mathbb{R}^d$ we observe a particle $\hat{x}(x, t)$ that at time t is in position x. The fate of a single particle is of no interest.

We will only consider incompressible fluids, i.e. a given moving volume $V(t)$ will not change its size under motion:

$$d_t|V(t)| = 0, \quad t \geq 0.$$

Applying Reynolds' Transport theorem, Lemma 2.8 to the scalar $\Phi \equiv 1$ yields:

$$d_t|V(t)| = d_t \int_{V(t)} 1 \, \mathrm{d}x = \int_{V(t)} \operatorname{div} \mathbf{v} \, \mathrm{d}x.$$

Hence as $V(t)$ can be chosen arbitrarily, we deduce the point-wise equation for the incompressibility of a fluid, see also Sect. 2.2.3:

$$\operatorname{div} \mathbf{v} = 0. \tag{2.39}$$

Using this condition, conservation of mass (2.13) reduces to a transport equation for the fluid's density:

$$\partial_t \rho_f + (\mathbf{v} \cdot \nabla)\rho_f = 0. \tag{2.40}$$

For further simplification, we will restrict all our considerations to homogenous fluids, where the density at initial time $t = 0$ is constant in the complete volume $\rho_f(x, 0) = \rho_f^0(x) \equiv \rho_f$. Given (2.40) it hereby follows that the density is homogenous at all times $t \geq 0$ and conservation of mass is reduced to the divergence condition (2.39).

To close the system of equations for incompressible fluids we must introduce material laws that model the dependency of the stress tensor $\boldsymbol{\sigma}_f$ on velocity and pressure. We are considering *Navier-Stokes* fluids only that linearly depend on the strain rate following Hooke's law

$$\boldsymbol{\sigma} = 2\mu_f \dot{\boldsymbol{\varepsilon}} + \lambda \operatorname{tr}(\dot{\boldsymbol{\varepsilon}}) I.$$

As for an incompressible fluid it holds $\operatorname{div} \mathbf{v} = \operatorname{tr}(\dot{\boldsymbol{\varepsilon}}) = 0$, the stress tensor simplifies to

$$\boldsymbol{\sigma} = -pI + \mu_f(\nabla \mathbf{v} + \nabla \mathbf{v}^T), \tag{2.41}$$

where again by p we denote the undetermined pressure that will act as Lagrange multiplier to ensure the divergence condition $\operatorname{div} \mathbf{v} = 0$. By $\mu_f = \rho_f \nu_f$ we denote the dynamic viscosity of the fluid and by ν_f its kinematic viscosity. The complete set of the Navier-Stokes equations is given by

$$\rho_f(\partial_t \mathbf{v} + (\mathbf{v} \cdot \nabla)\mathbf{v}) - \operatorname{div} \boldsymbol{\sigma} = \rho_f \mathbf{f}, \quad \operatorname{div} \mathbf{v} = 0,$$

or, using the material law for a Navier-Stokes fluid

$$\rho_f \left(\partial_t \mathbf{v} + (\mathbf{v} \cdot \nabla)\mathbf{v}\right) + \nabla p - \rho_f \nu_f \operatorname{div} (\nabla \mathbf{v} + \nabla \mathbf{v}^T) = \rho_f \mathbf{f}, \quad \operatorname{div} \mathbf{v} = 0. \tag{2.42}$$

Remark 2.34 (Symmetry of the Stress-Tensor) For an incompressible fluid, the stress-tensor allows for a further simplification. It holds:

$$\left[\operatorname{div} \left(\nabla \mathbf{v} + \nabla \mathbf{v}^T\right)\right]_i = \sum_j \partial_j \left(\partial_j \mathbf{v}_i + \partial_i \mathbf{v}_j\right) = \Delta \mathbf{v}_i + \partial_i \underbrace{\operatorname{div} \mathbf{v}}_{=0}, \quad \text{for } i = 1, 2, 3,$$

and Eq. (2.42) is equivalent to the reduced formulation

$$\rho_f \left(\partial_t \mathbf{v}_f + (\mathbf{v} \cdot \nabla)\mathbf{v}\right) - \rho_f \nu_f \Delta \mathbf{v} + \nabla p = \rho_f \mathbf{f}, \quad \text{div } \mathbf{v} = 0.$$

Usually, this simplified set of equations is considered as the Navier-Stokes equations. However, while both equations yield the same solution $(\mathbf{v}, p)$, the value of boundary stresses is altered, if the reduced tensor $\tilde{\boldsymbol{\sigma}}_f = \mu_f \nabla \mathbf{v} - pI$ would be considered:

$$\tilde{\boldsymbol{\sigma}}_f n \neq \boldsymbol{\sigma}_f n.$$

In the context of fluid-structure interactions, boundary stresses will be important to couple flow and structure problem. Out of this reason, we will always consider the full symmetric stress tensor $\boldsymbol{\sigma}_f$. One of the coupling conditions will couple normal stresses of the fluid problem and the solid problem

$$\mathbf{n} \cdot \boldsymbol{\sigma}_f = \mathbf{n} \cdot \boldsymbol{\sigma}_s,$$

where by $\boldsymbol{\sigma}_s$ we denote the Cauchy stress tensor of the solid, i.e.

$$\boldsymbol{\sigma}_s = \hat{J}^{-1} \mathbf{F} \hat{\boldsymbol{\Sigma}}_s \hat{\mathbf{F}}^T.$$

Here, it will matter, whether it holds

$$-p\mathbf{n} + \rho_f \nu_f \mathbf{n} \cdot (\nabla \mathbf{v} + \nabla \mathbf{v}^T) = \mathbf{n}\boldsymbol{\sigma}_s,$$

or

$$-p\mathbf{n} + \rho_f \nu_f \mathbf{n} \cdot \nabla \mathbf{v} = \mathbf{n}\boldsymbol{\sigma}_s,$$

as usually we have

$$\mathbf{n} \cdot \nabla \mathbf{v}^T \neq 0.$$

2.4.1 Boundary and Initial Conditions

The system of equations is completed by adequate boundary and initial conditions. Let $\mathcal{F} \subset \mathbb{R}^d$ be the fluid-domain. At time $t = 0$ we prescribe an initial condition for the velocity

$$\mathbf{v}(x, 0) = \mathbf{v}^0(x) \quad x \in \mathcal{F}.$$

As the density is constant $\rho_f(x,t) \equiv \rho_f$ for all times (and homogenous in the domain), we do not need an initial condition here, but simply consider $\rho_f \in \mathbb{R}$ as a problem parameter. The boundary $\partial\mathcal{F}$ is split into a Dirichlet part Γ_f^D and into a Neumann part Γ_f^N. On Γ_f^D we prescribe Dirichlet conditions for the velocity

$$\mathbf{v}(x,t) = \mathbf{v}^D(x,t) \quad \text{on } \Gamma_f^D \times [0,T].$$

In the case $\mathbf{v}^D = 0$, we denote this condition as the *no-slip condition*. Physical observation tells us that viscosity will cause the fluid to stick to the boundary. This condition holds for the flow of water over elastic material (at usual velocities). The importance of viscous effects is lessened at high velocities, when e.g. considering the aerodynamical flow of air around a plane. Here, one often refers to the *slip condition* that only prescribes the flow in normal direction

$$\mathbf{n} \cdot \mathbf{v}(x,t) = 0 \quad \text{on } \Gamma_f^D \times [0,T].$$

The slip boundary condition prevents the flow from entering the boundary, it however allows for tangential flow. All examples considered in this work will be in the viscous regime where no-slip condition are usually well-placed. Boundaries with non homogenous Dirichlet data are often *inflow boundaries*.

Neumann conditions model situations, where we do not know the velocity profile at the boundary, but where assumptions on the boundary stress are given:

$$\boldsymbol{\sigma}_f(x,t)n(x,t) = g^{\boldsymbol{\sigma}}(x,t) \quad \text{on } \Gamma_f^N \times [0,T].$$

The typical application of Neumann conditions are *outflow boundaries*, where the profile of the flow is not known and a Dirichlet condition cannot be prescribed. See Fig. 2.7 for a typical configuration of a flow problem with different boundary parts. We will come back to outflow boundary conditions in Sect. 2.4.2, as the exact form will depend on the material law and the Cauchy stress tensor $\boldsymbol{\sigma}_f$.

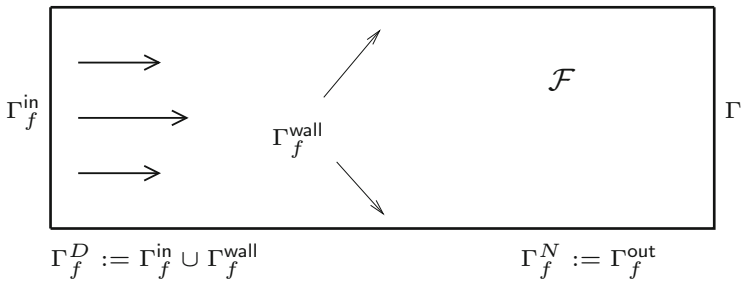

Fig. 2.7 Typical configuration of a flow problem with Dirichlet inflow boundary Γ_f^{in} and Dirichlet no-slip boundary on the walls Γ_f^{wall} as well as an outflow boundary Γ_f^{out} of Neumann type

If only no-slip and outflow boundary conditions are taken into account, the complete set of incompressible flow equations on the (fixed) domain $\mathcal{F} \subset \mathbb{R}^d$ is given by

Problem 2.35 (Incompressible Navier-Stokes Equations) *Velocity and pressure*

$$\mathbf{v}(t) \in C^2(\mathcal{F}) \cap C(\mathcal{F} \cup \Gamma_f^D) \cap C^1(\mathcal{F} \cup \Gamma_f^N), \quad p(t) \in C^1(\mathcal{F}) \cap C(\mathcal{F} \cup \Gamma_f^N),$$

are given as solution of

$$\begin{aligned} \text{div } \mathbf{v} = 0, \quad \rho_f \left(\partial_t \mathbf{v} + (\mathbf{v} \cdot \nabla)\mathbf{v}\right) &= \rho_f \mathbf{f} + \text{div } \boldsymbol{\sigma}_f && \text{on } \mathcal{F} \times [0,T], \\ \mathbf{v}(\cdot, 0) &= \mathbf{v}^0(\cdot) && \text{on } \mathcal{F}, \\ \mathbf{v} &= \mathbf{v}^D && \text{on } \Gamma_f^D \times [0,T], \\ \boldsymbol{\sigma}_f \mathbf{n} &= g^{\boldsymbol{\sigma}} && \text{on } \Gamma_f^N \times [0,T]. \end{aligned} \tag{2.43}$$

If boundary data $\mathbf{v}^D$ and g^σ as well as volume force $\mathbf{f}$ do not explicitly depend on time, the flow configurations can tend to a stationary limit, where it holds $\partial_t \mathbf{v} = 0$. Stationary in the context of fluid dynamics stands for a flow that at all times looks the same way, it does not imply that the fluid is at rest, which would mean $\mathbf{v} = 0$. If we know that the flow will reach a stationary limit, we can immediately consider the set of stationary equations, given as a boundary value problem.

Problem 2.36 (Stationary Incompressible Navier-Stokes Equations) *Velocity and pressure*

$$\mathbf{v} \in C^2(\mathcal{F}) \cap C(\mathcal{F} \cup \Gamma_f^D) \cap C^1(\mathcal{F} \cup \Gamma_f^N), \quad p \in C^1(\mathcal{F}) \cap C(\mathcal{F} \cup \Gamma_f^N),$$

are given as solution of

$$\begin{aligned} \text{div } \mathbf{v} = 0, \quad \rho_f (\mathbf{v} \cdot \nabla)\mathbf{v} &= \rho_f \mathbf{f} + \text{div } \boldsymbol{\sigma}_f && \text{on } \mathcal{F}, \\ \mathbf{v} &= \mathbf{v}^D && \text{on } \Gamma_f^D, \\ \boldsymbol{\sigma}_f \mathbf{n} &= g^{\boldsymbol{\sigma}} && \text{on } \Gamma_f^N. \end{aligned} \tag{2.44}$$

Not all autonomous flow problems have a stationary limit. This stems from the nonlinearity of the Navier-Stokes equations and whether a flow is stationary or instationary will depend on the problem data like density, viscosity, right hand side f and inflow velocity $\mathbf{v}^D$.

2.4.2 The "do-nothing" Outflow Condition

Many problem configurations feature boundaries, where the flow has mainly an outflow-character. We will call this boundary Γ_f^{out}. Here, the solution is not known a priori and cannot be specified in terms of a Dirichlet condition. Any boundary condition that is enforced, will be a model for the flow at the outflow boundary. Hence a common practice is to not describe a condition at all, but simply use the "natural" boundary condition, that arises from integration by parts. We consider the stationary Stokes equations:

$$(\boldsymbol{\sigma}_f, \nabla\phi)_{\mathcal{F}} = -(\text{div } \boldsymbol{\sigma}_f, \phi)_{\mathcal{F}} + \langle \boldsymbol{\sigma}_f \mathbf{n}, \phi \rangle_{\Gamma_f^{\text{out}}},$$

from where we can deduce the "outflow-condition"

$$\boldsymbol{\sigma}_f \mathbf{n} = 0 \text{ on } \Gamma_f^{\text{out}}.$$

In Fig. 2.8, we show a solution to a "channel-flow" problem using this natural outflow-condition. The domain is a channel with length L and height H

$$\mathcal{F} = (0, L) \times (0, H),$$

on the left boundary Γ_f^{in} we impose a Dirichlet inflow profile

$$\mathbf{v} = \mathbf{v}^D = \frac{4\bar{\mathbf{v}}}{H^2} \begin{pmatrix} y(H-y) \\ 0 \end{pmatrix} \text{ on } \Gamma_f^{\text{in}} = 0 \times (0, H), \tag{2.45}$$

where $\bar{\mathbf{v}}$ is the peak velocity. On the horizontal lines Γ_f^{wall} we impose homogenous Dirichlet conditions

$$\mathbf{v} = 0 \text{ on } \Gamma_f^{\text{wall}} = (0, L) \times 0 \cup (0, L) \times H.$$

The outflow boundary is given as

$$\Gamma_f^{\text{out}} = L \times (0, H).$$

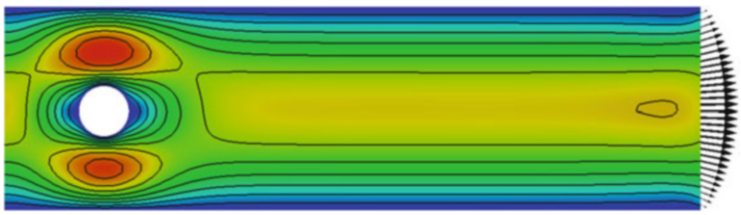

Fig. 2.8 Channel flow with natural outflow condition $\boldsymbol{\sigma}_f \mathbf{n} = 0$. The velocity field gets deflected and does not follow the Poiseuille flow

In Fig. 2.8 we see that the velocity vectors get deflected and swing out of line. Considering the outflow model $\boldsymbol{\sigma}_f \mathbf{n} = 0$, which simply states that no external stresses act, this behavior can be interpreted as a duct that ends in an open space, such that the fluid can expand in all directions.

Often, computational domains are chosen simply as a restriction of a larger domain to an area where the interesting dynamics happen. Numerically, boundary lines often must be drawn to scale the problem down to a reasonable size. In such situations, a good outflow boundary should have as little influence on the solution as possible. Regarding Fig. 2.8, the exact location of the outflow boundary should not change the flow pattern inside the domain. The natural condition does not satisfy this request.

One of the most simple analytical solutions to a channel problem is the *Poiseuille flow*. An extension of the inflow data (2.45) into the domain

$$\mathbf{v}(x, y) = \frac{4\bar{\mathbf{v}}}{H^2} \begin{pmatrix} y(H-y) \\ 0 \end{pmatrix},$$

satisfies the Navier-Stokes equations in channels (without obstacle) together with the pressure field

$$p(x, y) = \frac{8\bar{v}}{H^2} x + c,$$

for every $c \in \mathbb{R}$. In channel-like situations as shown in Fig. 2.8, an outflow condition should allow for Poiseuille flows without deterioration.

By a small modification of this outflow condition, we allow the Poiseuille flow to leave the domain without deflection. Using the reduced stress tensor introduced in Remark 2.34

$$\tilde{\boldsymbol{\sigma}}_f = \rho_f \nu_f \nabla \mathbf{v} - pI,$$

it holds for the Poiseuille flow that

$$\tilde{\boldsymbol{\sigma}}_f \mathbf{n} = (\mathbf{n} \cdot \nabla)\mathbf{v} - p\mathbf{n} = 0 \text{ on } \Gamma_f^{\text{out}}.$$

This condition is called the *do-nothing outflow condition*, as it has as little impact on the flow as possible (or as it is the natural boundary condition, that arises without doing anything, when using the reduced tensor), see [188]. In Fig. 2.9, we show the flow around a cylinder using this do-nothing condition. Here, he streamlines leave the domain in a straight way. Compare Fig. 2.8.

Remark 2.37 (Outflow Conditions) We must stress that the *do-nothing* outflow condition is not the better condition from a physical point of view. It is simply a model that allows for some standard flow situations like Poiseuille flow or Couette flow to reduce the sensitivity of the solution on the position of artificial boundaries.

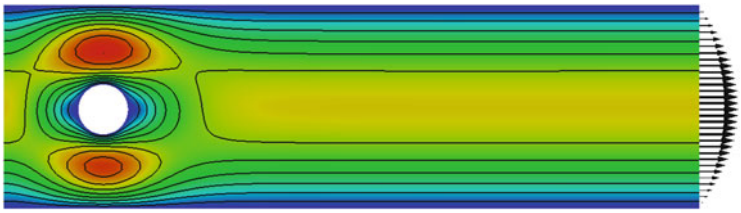

Fig. 2.9 Channel flow with the *do-nothing outflow condition* $\rho_f \nu_f \nabla \mathbf{v}\mathbf{n} - pI = 0$ on Γ_f^{out}. The streamlines are not deflected on the right outflow boundary. Compare Fig. 2.8

From a good outflow condition we expect that it has as little influence on the flow field as possible. If the outflow boundary is far away from a region of interest (e.g. from an obstacle) we expect that the flow close to the obstacle is not influenced by the position of the outflow boundary, if the outflow boundary condition does a good job. The *do-nothing* condition works excellent in several configurations. It does not only allow Poiseuille or Couette flows to leave the domain, it further allows vortices to leave the domain and has very small influence on these vortices, if the boundary is artificially cutting through them. However, many situations exist, where the analysis of outflow conditions is still not sufficiently developed: whenever the outflow boundary is not a single straight line normal to the main flow-direction, it will cause a deflection of the flow field. Further, if one considers more general material laws of non-Newtonian fluids, the *do-nothing* condition has an impact on the flow-field, see [338].

The *do-nothing* boundary condition brings along a further "hidden" boundary condition that normalizes the pressure. It can be shown [188] that on every straight outflow boundary-line segment $\Gamma_i \subset \partial\mathcal{F}$ that is enclosed by no-slip Dirichlet boundaries, it holds

$$\int_{\Gamma_i^{\text{out}}} p \, \mathrm{d}s = 0,$$

on all outflow boundaries Γ_i^{out}, such that the average outflow pressure is zero. This condition has two implications: first, whenever an outflow boundary of *do-nothing* type is given, no pressure-normalization has to be included in the trial spaces. Second, the *do-nothing* condition can be used to prescribe pressure drops on boundary segments in order to drive the flow:

$$\int_{\Gamma_i} \left\{ \rho_f \nu_f \mathbf{n} \cdot \nabla \mathbf{v} - p\mathbf{n} \right\} \mathrm{d}s = \int_{\Gamma_i} P_i \, \mathrm{d}s, \quad i = 1, \ldots, N^{\text{out}}, \quad P_i \in \mathbb{R}.$$

This gets important, if the flow is driven by pressure differences and not by means of Dirichlet conditions. A frequently considered situation arises in hemodynamical simulations in which a flow in a part of the channel-system (i.e., the cardiovascular system) is investigated. This small part of the overall problem can be coupled by

prescribing pressure values, e.g. taken from the pressure profile as measured from the heart-beat.

2.4.3 Reynolds Number

Simulations with the incompressible Navier-Stokes equations help to gain better insight into flow configurations. They can be used to replace and complement experiments. For a better comparison of similar flow-configurations that for instance arise by scaling in wind tunnel experiments, we introduce a non-dimensional form of the incompressible Navier-Stokes equations. First, let L_f be a unit length and $\bar{V}_f$ be a unit velocity. We define the non-dimensional values (without physical units)

$$x^* := \frac{1}{L_f}x, \quad \mathbf{v}^* := \frac{1}{V_f}\mathbf{v}, \quad t^* := \frac{V_f}{L_f}t, \quad p^* := \frac{1}{V_f^2\rho_f}p. \tag{2.46}$$

For these new values, it holds:

$$\frac{\partial \mathbf{v}^*}{\partial t^*} + (\mathbf{v}^* \cdot \nabla^*)v^* = \frac{L_f}{V_f^2}\left\{\frac{\partial \mathbf{v}}{\partial t} + (\mathbf{v}\cdot\nabla)\mathbf{v}\right\},$$

$$\Delta^*\mathbf{v}^* = \frac{L_f^2}{V_f}\Delta\mathbf{v}, \quad \nabla^* p^* = \frac{L_f}{V_f^2\rho_f}\nabla p,$$

and the Navier-Stokes equations in non-dimensional form (with homogenous right hand side) reads

$$\frac{\partial \mathbf{v}^*}{\partial t^*} + (\mathbf{v}^*\cdot\nabla^*)\mathbf{v}^* - \frac{\nu_f}{V_f L_f}\operatorname{div}^*\left\{\nabla^*\mathbf{v}^* + (\nabla^*\mathbf{v}^*)^T\right\} - \nabla^* p^* = 0,$$

$$\nabla^*\cdot\mathbf{v}^* = 0.$$

The quantity

$$Re := \frac{V_f L_f}{\nu_f} = \frac{V_f L_f \rho_f}{\mu_f},$$

is called the *Reynolds number*. Scaled flow configurations with the same Reynolds number are equivalent. If the flow is known in the non-dimensional unit-system, it can be scaled to every equivalent configuration via (2.46). The Reynolds number is a good measure to describe the dynamical behavior of a flow configuration. Flows at low Reynolds number tend to have a stationary solution, while flows at higher Reynolds numbers have non-stationary or even turbulent solutions. The definition of the Reynolds number is somewhat arbitrary as fixing a reference velocity V_f and

length L_f is usually not unique. The Reynolds number may therefore only by used to compare different flow situations for one configuration, e.g. the flow around a ship with length $L = 100\,\text{m}$ compared to a down-scaled model of the same ship with length 5 m.

2.4.4 The Linear Stokes Equations

In flow situations where friction effects are very large compared to acceleration terms, the Navier-Stokes equations can be simplified by neglecting the convective term $(\mathbf{v}\cdot\nabla)\mathbf{v}$. This case is given, if the Reynolds number tends to zero $Re \to 0$. If the right hand side of the equation as well as boundary data does not depend on time, the flow field will be stationary and we end up with the stationary Stokes equations

$$-\rho_f \nu_f \Delta \mathbf{v} + \nabla p = \rho_f \mathbf{f}, \quad \text{div } \mathbf{v} = 0 \text{ in } \mathcal{F},$$

with the usual Dirichlet or Neumann boundary conditions on $\partial\mathcal{F}$. By renormalizing the pressure $\bar{p} = (\rho_f \nu_f)^{-1} p$ and the volume force $\bar{\mathbf{f}} = \nu_f^{-1}\mathbf{f}$ all physical parameters can be omitted and we derive the equations in non-dimensionalized form.

Problem 2.38 (Stokes Equations) *Velocity* $\mathbf{v} \in C^2(\mathcal{F}) \cap C(\bar{\mathcal{F}})$ *and pressure* $p \in C^1(\mathcal{F})$ *are given as solution of*

$$-\Delta \mathbf{v} + \nabla \bar{p} = \bar{\mathbf{f}}, \quad \text{div } \mathbf{v} = 0 \text{ in } \mathcal{F}. \tag{2.47}$$

Compared to the full incompressible Navier-Stokes equations, this equation is rather simple looking. As a saddle-point system it however still obtains one of the most important features of incompressible flows. While the physical relevance of the Stokes equations is very limited, it serves as entry-point to the mathematical analysis and the design of finite element discretizations for flow problems.

2.4.5 Theory of Incompressible Flows

If there exists a unique solution $\{\mathbf{v}, p\}$ to the incompressible Navier-Stokes equations is still not known in all configuration. The stationary case is well understood, if we only consider Dirichlet boundary conditions. Here, a solution exists for small Reynolds numbers and it is unique, if the data is sufficiently small. When we consider general outflow conditions, we have no possibility to control the nonlinearity $(\mathbf{v}\cdot\nabla)\mathbf{v}$. In the instationary configuration there exists no proof for the existence of a unique solution under reasonable data assumptions. In three dimensions, the problem of proving the existence of a global smooth solution is considered open and one of the *Millenium Prize Problems*, see [89].

We start by deriving a weak formulation of the Navier-Stokes equations:

Lemma 2.39 (Weak Formulation of the Navier-Stokes Equations) *Let* $\bar{\mathbf{v}}^D \in H^1(\mathcal{F})^d$ *be an extension of the Dirichlet data on* Γ_f^D *into the domain* $\mathcal{F}$. *If the solution*

$$\mathbf{v} \in \bar{\mathbf{v}}^D + \mathcal{V}_f, \quad \mathcal{V}_f := H_0^1(\mathcal{F}; \Gamma_f^D)^d, \quad p \in \mathcal{L}_f, \quad \mathcal{L}_f := L^2(\mathcal{F}),$$

of the variational formulation

$$\begin{aligned}(\rho_f(\partial_t \mathbf{v} + (\mathbf{v}\cdot\nabla)\mathbf{v}), \phi)_{\mathcal{F}} + (\boldsymbol{\sigma}_f, \nabla\phi)_{\mathcal{F}} & \\ -\rho_f \nu_f \langle n \cdot \nabla \mathbf{v}^T, \phi\rangle_{\Gamma_f^{out}} = (\rho_f \mathbf{f}, \phi)_{\mathcal{F}} \qquad & \forall \phi \in \mathcal{V}_f, \\ (\text{div } \mathbf{v}, \xi)_{\mathcal{F}} = 0 \qquad & \forall \xi \in \mathcal{L}_f,\end{aligned} \tag{2.48}$$

has sufficient regularity $v_f \in C^2(\mathcal{F}) \cap C(\mathcal{F} \cup \Gamma_f^D) \cap C^1(\mathcal{F} \cup \Gamma_f^{out})$ *and* $p \in C^1(\mathcal{F})$, *it also solves the classical formulation of the Navier-Stokes equations, Problem 2.35 with Dirichlet data on* Γ_f^D *and the* do-nothing *outflow condition on* Γ_f^{out}.

Proof This follows by integration by parts and with basic variational principles. The boundary term on Γ_f^{out} is required as we use the full symmetric stress-tensor such that the solution of the variational formulation fulfills the *do-nothing* condition, see Sect. 2.4.2. □

Remark 2.40 (Uniqueness of the Pressure in Dirichlet Problem) If the configuration has Dirichlet boundaries all around the boundary $\Gamma_f^D = \partial\mathcal{F}$, a solution cannot be unique: let $\{\mathbf{v}, p\} \in \mathcal{V}_f \times \mathcal{L}_f$ be a solution. Then, it holds for $\{\mathbf{v}, p+c\}$ with $c \in \mathbb{R}$:

$$\begin{aligned}(\boldsymbol{\sigma}_f, \nabla\phi)_{\mathcal{F}} &= \rho_f \nu_f (\nabla\mathbf{v} + \nabla\mathbf{v}^T, \nabla\phi)_{\mathcal{F}} - (p_f + c, \nabla\cdot\phi)_{\mathcal{F}} \\ &= \rho_f \nu_f (\nabla\mathbf{v} + \nabla\mathbf{v}^T, \nabla\phi)_{\mathcal{F}} - (p_f, \nabla\cdot\phi)_{\mathcal{F}} + (\underbrace{\nabla c}_{=0}, \phi)_{\mathcal{F}} - \langle cn, \underbrace{\phi}_{=0}\rangle_{\partial\mathcal{F}}.\end{aligned}$$

If $\Gamma_f^D = \partial\mathcal{F}$ the pressure can only be unique up to a constant. In this case, we normalize the pressure-space

$$\mathcal{L}_f = L^2(\mathcal{F}) \setminus \mathbb{R}.$$

The Navier-Stokes equations brings along two characteristic difficulties for theoretical analysis and numerical discretization, the nonlinearity $(\mathbf{v}\cdot\nabla)\mathbf{v}$ and the side-condition of divergence freeness div $\mathbf{v} = 0$. We will first focus on this second difficulty and consider the linear Stokes equations.

2.4.5.1 Existence and Uniqueness of Solutions to the Stokes Equations

In the following, we consider the stationary Stokes equations

$$\mathbf{v}, p \in \mathcal{V}_f \times L_f, \quad \mathcal{V}_f := H_0^1(\mathcal{F}; \partial\mathcal{F})^d, \quad \mathcal{L}_f := L^2(\mathcal{F}) \setminus \mathbb{R} :$$
$$(\nabla\mathbf{v}, \nabla\phi)_\mathcal{F} - (p, \nabla\cdot\phi)_\mathcal{F} + (\nabla\cdot\mathbf{v}, \xi)_\mathcal{F} = (\mathbf{f}, \phi)_\mathcal{F} \quad \forall\{\phi, \xi\} \in \mathcal{V}_f \times \mathcal{L}_f.$$

Here, we assume homogenous Dirichlet conditions on the complete boundary $\partial\mathcal{F}$ and further we consider the non-symmetric form of the stress tensor. Every solution $\mathbf{v} \in \mathcal{V}_f$ will be weakly divergence free in the space

$$\mathbf{v} \in \mathcal{V}_0 := \{\phi \in \mathcal{V}_f,\ (\text{div}\ \phi, \xi)_\mathcal{F} = 0 \quad \forall\xi \in \mathcal{L}_f\} \subset \mathcal{V}_f.$$

By restricting the Stokes equations to this space, it remains to find

$$\mathbf{v} \in \mathcal{V}_0 : \quad (\nabla\mathbf{v}, \nabla\phi)_\mathcal{F} = (\mathbf{f}, \phi)_\mathcal{F} \quad \forall\phi \in \mathcal{V}_0. \tag{2.49}$$

Lemma 2.41 (Stokes Velocity) *For every $\mathbf{f} \in H^{-1}(\mathcal{F})^d$ there exists a unique velocity $\mathbf{v} \in \mathcal{V}_0 \subset \mathcal{V}_f$ as solution of the Stokes equations. Further, it holds*

$$\|\nabla\mathbf{v}\| \leq \|\mathbf{f}\|_{-1}.$$

Proof The space $\mathcal{V}_0 \subset \mathcal{V}_f$ is a Hilbert-space with the scalar product $(\nabla\cdot, \nabla\cdot)$. Riesz representation theorem guarantees the existence of a unique solution $\mathbf{v} \in \mathcal{V}_0$ to (2.49) and further gives the error estimate. □

2.4.5.2 Existence and Uniqueness of the Pressure

Now that we have shown the existence of a unique and divergence-free velocity field $\mathbf{v} \in \mathcal{V}_0 \subset \mathcal{V}_f$, the pressure is determined by the equation

$$p \in \mathcal{L}_f : \quad (p, \nabla\cdot\phi) = (\mathbf{f}, \phi) - (\nabla\mathbf{v}, \nabla\phi) \quad \forall\phi \in \mathcal{V}_f. \tag{2.50}$$

As this equation is not elliptic, we cannot proof existence with Riesz representation theorem or a generalization like Lax-Milgram. Instead, we reformulate this variational equation in operator notation as

$$-\operatorname{grad} p = l, \tag{2.51}$$

where $-\text{grad} : \mathcal{L}_f \to H^{-1}$ is the weak gradient

$$-\langle\operatorname{grad} p, \phi\rangle = (p, \nabla\cdot\phi) \quad \forall\phi \in \mathcal{V}_f,$$

and $l \in H^{-1}$ a linear functional defined by

$$l(\phi) = (\mathbf{f}, \phi) - (\nabla \mathbf{v}, \nabla \phi) \quad \forall \phi \in \mathcal{V}_f.$$

Whether Eqs. (2.50) or (2.51) have a solution depends on the surjectivity of the weak gradient operator. The difficulty of the analysis for this equation is the low regularity of the problem. Two important results from the literature help up to answer the questions of existence and uniqueness of solutions. It holds

Theorem 2.42 (de Rham) *Let $l \in H^{-1}$. The equation*

$$-\operatorname{grad} p = l,$$

has a unique solution $p \in \mathcal{L}_f$, if and only if

$$l \in \mathcal{V}_0^\circ,$$

where by $\mathcal{V}_0^\circ$ we denote the annihilator of $\mathcal{V}_0$ in H^{-1}

$$\mathcal{V}_0^\circ := \{f \in H^{-1},\, f(\phi) = 0 \quad \forall \phi \in \mathcal{V}_0\} \subset H^{-1}.$$

And:

Theorem 2.43 *Let $\mathcal{F}$ be a bounded domain with Lipschitz boundary and $p \in L^2(\mathcal{F})$ be such that* grad $p \in H^{-1}(\mathcal{F})$. *Then, it holds*

$$\gamma \|p\|_{L^2(\mathcal{F})\setminus\mathbb{R}} \leq \|\operatorname{grad} p\|_{-1},$$

with a constant $\gamma = \gamma(\mathcal{F})$ that depends on the domain only.

Proof For proofs of these essential theorems we refer to the literature. See Teman [321], de Rham [112] and Nečas [251]. □

We will quote yet another Theorem to show equivalence of Theorem 2.43 with further conditions that will be handy in the context of the Stokes equations; both for proofing existence and uniqueness of the pressure, as well as for numerical error analysis.

Theorem 2.44 (Nečas) *The following three properties are equivalent*

(i) The weak gradient operator $-\operatorname{grad} : \mathcal{L}_f \to \mathcal{V}_0^\circ$ *is an isomorphism.*
(ii) For every $p \in L^2(\mathcal{F})$ it holds

$$\|\operatorname{grad} p\|_{-1} \geq \gamma \|p\| \quad \forall p \in \mathcal{L}_f, \tag{2.52}$$

where $\gamma > 0$ is a constant. (This is exactly Theorem 2.43).

(ii) The inf-sup condition holds

$$\inf_{\xi \in \mathcal{L}_f} \sup_{\phi \in \mathcal{V}_f} \frac{(\xi, \nabla \cdot \phi)}{\|\xi\| \, \|\nabla \phi\|} \geq \gamma, \tag{2.53}$$

with a constant $\gamma > 0$.

Proof Again, we refer to the literature [251, 321]. □

All these preparations allow us to show the existence of a unique solution to the Stokes equations:

Lemma 2.45 (Stokes) *Let* $\mathcal{F} \subset \mathbb{R}^d$ *be a domain with Lipschitz boundary. The Stokes equation has a unique solution* $\mathbf{v} \in \mathcal{V}_f$ *and* $p \in \mathcal{L}_f$ *for every* $f \in H^{-1}$. *It holds*

$$\|\nabla \mathbf{v}\| + \gamma \|p\| \leq c \|\mathbf{f}\|_{-1},$$

where $c > 0$ *is a constant.*

Proof The existence of a unique function $\mathbf{v} \in \mathcal{V}_0$ solving the velocity equation has already been shown. The functional

$$l(\phi) = (\nabla \mathbf{v}, \nabla \phi) - (\mathbf{f}, \phi)$$

is bound in $H^{-1}(\mathcal{F})$ and further, it holds $l \in \mathcal{V}_0^\circ$. Hence existence of a unique weak pressure $p \in \mathcal{L}_f$ solving $-\operatorname{grad} p = l$ follows by Lemma 2.44.

Finally, by using the inf-sup inequality we have

$$\begin{aligned} \gamma \|p\| &\leq \sup_{\phi \in \mathcal{V}_f} \frac{(p, \nabla \cdot \phi)}{\|\nabla \phi\|} = \sup_{\phi \in \mathcal{V}_f} \frac{(\mathbf{f}, \phi) - (\nabla \mathbf{v}, \nabla \phi)}{\|\nabla \phi\|} \\ &\leq \|\mathbf{f}\|_{-1} + \|\nabla \mathbf{v}\| \leq 2 \|\mathbf{f}\|_{-1}. \end{aligned}$$

□

During the proof of this Lemma, we have used the following useful inequality for the divergence operator

$$\|\operatorname{div} \mathbf{v}\| \leq \sqrt{d} \|\nabla \mathbf{v}\| \quad \forall \mathbf{v} \in H^1(\mathcal{F})^d, \quad \|\operatorname{div} \mathbf{v}\| \leq \|\nabla \mathbf{v}\| \quad \forall \mathbf{v} \in H_0^1(\mathcal{F})^d, \tag{2.54}$$

which follows with help of Young's inequality in the general case and with help of integration by parts of the mixed terms in the case of zero trace velocity fields.

Despite the special saddle-point character of the Stokes equations it shows that we still get a unique solution that continuously depends on the right hand side $\mathbf{f}$. We only get L^2-regularity for the pressure. The most important tool in the analysis of incompressible flows is the inf-sup condition. If the right hand side $\mathbf{f}$ and the domain is sufficiently regular, we will get higher regularity of the solution. Here, the same rule of thump holds as for the Laplace equation:

Lemma 2.46 (Regularity of the Stokes Equations) *Let $\mathcal{F}$ be a convex polygonal domain and $\mathbf{f} \in L^2(\mathcal{F})^d$. Then the solution of the Stokes equations is bounded*

$$\|\nabla^2 \mathbf{v}\| + \|\nabla p\| \leq c_s \|\mathbf{f}\|,$$

with a stability constant $c_s > 0$.

If $\mathcal{F} \subset \mathbb{R}^d$ is a domain with smooth C^{k+2}-boundary for $k \geq 0$ and $\mathbf{f} \in H^k(\mathcal{F})^d$ it holds

$$\|\mathbf{v}\|_{H^{k+2}(\mathcal{F})} + \|p\|_{H^{k+1}(\mathcal{F})} \leq c \|\mathbf{f}\|_{H^k(\mathcal{F})}.$$

Proof For a proof to these results, we refer to the literature [160, 321]. □

2.4.5.3 The Stationary Navier-Stokes Equations

Next, we discuss the stationary Navier-Stokes equations including the nonlinearity

$$\{\mathbf{v}, p\} \in \mathcal{V}_f \times L_f, \quad \mathcal{V}_f := H_0^1(\mathcal{F}; \partial\mathcal{F})^d, \quad \mathcal{L}_f := L^2(\mathcal{F}) \setminus \mathbb{R} :$$
$$\frac{1}{Re}(\nabla \mathbf{v}, \nabla \phi) + (\mathbf{v} \cdot \nabla \mathbf{v}, \phi) - (p, \nabla \cdot \phi) + (\nabla \cdot \mathbf{v}, \xi) = (\mathbf{f}, \phi)$$
$$\forall \{\phi, \xi\} \in \mathcal{V}_f \times \mathcal{L}_f, \qquad (2.55)$$

again considering homogenous Dirichlet conditions $\mathbf{v} = 0$ only. Here, this restriction is essential not merely given for technical reasons, as the following Lemma shows:

Lemma 2.47 (Nonlinearity of the Navier-Stokes Equations) *For $\mathbf{v}, \mathbf{w} \in H_0^1(\mathcal{F})^d$ with* div $\mathbf{v} = 0$ *it holds:*

$$(\mathbf{v} \cdot \nabla \mathbf{w}, \mathbf{w}) = 0. \qquad (2.56)$$

In the case of an outflow boundary $\Gamma_f^{out} \subset \partial\mathcal{F}$ it holds for all $\mathbf{v}, \mathbf{w} \in H_0^1(\mathcal{F}; \Gamma_f^D)^d$ with div $\mathbf{v} = 0$

$$\Big((\mathbf{v} \cdot \nabla)\mathbf{w}, \mathbf{w}\Big) = \frac{1}{2} \int_{\Gamma_f^{out}} \mathbf{n} \cdot \mathbf{v} |\mathbf{w}|^2 \, \mathrm{d}s. \qquad (2.57)$$

Proof In the case of general boundary conditions it holds

$$\begin{aligned}\Big((\mathbf{v}\cdot\nabla)\mathbf{w},\mathbf{w}\Big)_{\mathcal{F}} &= \sum_{i,j}(\mathbf{v}_j\partial_j\mathbf{w}_i,\mathbf{w}_i)_{\mathcal{F}}\\ &= \sum_{i,j}\Big\{\int_{\partial\mathcal{F}}\mathbf{n}_j\mathbf{w}_i\mathbf{v}_j\mathbf{w}_i\,\mathrm{d}s-(\mathbf{w}_i,\partial_j\mathbf{v}_j\mathbf{w}_i)_{\mathcal{F}}-(\mathbf{w}_i,\mathbf{v}_j\partial_j\mathbf{w}_i)_{\mathcal{F}}\Big\}\\ &= -\underbrace{(\mathbf{w},(\operatorname{div}\mathbf{v})\mathbf{w})_{\mathcal{F}}}_{=0}-((\mathbf{v}\cdot\nabla)\mathbf{w},\mathbf{w})_{\mathcal{F}}+\int_{\partial\mathcal{F}}(\mathbf{n}\cdot\mathbf{v})|\mathbf{w}|^2\,\mathrm{d}s.\end{aligned}$$

This shows the two assertions. □

This special structure of the nonlinearity will be the key to theoretical analysis of the incompressible Navier-Stokes equations.

Lemma 2.48 (Stability Estimate for the Velocity) *Let* $\mathbf{v}\in\mathcal{V}_0\subset H_0^1(\mathcal{F})^d$ *be a velocity field solving the Navier-Stokes equations. It holds for* $\mathbf{f}\in L^2(\mathcal{F})^d$

$$\|\nabla\mathbf{v}\|\le\nu^{-1}\|\mathbf{f}\|_{-1}.$$

Proof This results immediately follows with Lemma 2.47. □

Remark 2.49 (Outflow Conditions and Stability Estimates) Lemma 2.47 shows that the nonlinearity of the Navier-Stokes equations is only controllable, if Dirichlet or at least no-penetration conditions

$$\mathbf{v}\cdot\mathbf{n}=0,$$

are given on all boundaries. For the *do-nothing* conditions but also for the *no-stress* condition introduced in Sect. 2.4.2 a boundary term remains. The problem of this remaining boundary term

$$\frac{1}{2}\int_{\Gamma_f^{\text{out}}}\mathbf{n}\cdot\mathbf{n}|\mathbf{w}|^2\,\mathrm{d}o,$$

is the unknown sign. If there would be only outflow, i.e. $\mathbf{n}\cdot\mathbf{v}\ge 0$, we still get stability in the sense of Lemma 2.48. In the general setting, the boundary term however can be negative or positive. Braack and Mucha [61] introduced a modification of the do-nothing condition, denoted the *directional do-nothing condition* that cancels the negative part of the boundary term and results in

$$-p\mathbf{n}+\rho_f\nu_f\mathbf{n}\cdot\nabla\mathbf{v}-\frac{1}{2}(\mathbf{v}\cdot\mathbf{n})_-\mathbf{v}=0\text{ on }\Gamma_f^{\text{out}},$$

where by $(\mathbf{v}\cdot\mathbf{n})_-$ we denote

$$(\mathbf{v}\cdot\mathbf{n})_- = \begin{cases} 0 & \mathbf{v}\cdot\mathbf{n} \geq 0, \\ \mathbf{v}\cdot\mathbf{n} & \mathbf{v}\cdot\mathbf{n} < 0. \end{cases}$$

This condition is easily realized by a modification of the variational formulation

$$(\mathbf{v}\cdot\nabla\mathbf{v},\phi) + (\rho_f \nu_f \nabla\mathbf{v},\nabla\phi) - (p,\nabla\cdot\phi) - \frac{1}{2}\int_{\Gamma_f^{\text{out}}} (\mathbf{v}\cdot\mathbf{n})_-\mathbf{v}\cdot\phi \,\mathrm{d}o = (\mathbf{f},\phi).$$

Braack and Mucha can show existence and uniqueness of solutions (for small data). Furthermore, they report better numerical stability when using this directional do-nothing condition. Finally, this modified condition still allows for Poiseuille and Couette flow as well as vortices to leave the domain with little impact. See [61] for details.

Like for the Stokes equations, proofs for existence and uniqueness are split into first finding the velocity (this is a nonlinear problem now) and second, finding an appropriate pressure. While this second part is exactly as for the linear Stokes problem, showing existence and uniqueness of a velocity requires careful treatment of the nonlinearity.

$$\nu(\nabla\mathbf{v},\nabla\phi) + ((\mathbf{v}\cdot\nabla)\mathbf{v},\phi) = (\mathbf{f},\phi) \quad \forall\phi \in \mathcal{V}_0. \tag{2.58}$$

Lemma 2.50 (Solutions for the Navier-Stokes Equations) *Let $\mathcal{F} \subset \mathbb{R}^d$ be a domain with Lipschitz boundary. Further, let $\mathbf{f} \in H^{-1}(\mathcal{F})$. There exists a solution $\{\mathbf{v},p\} \in \mathcal{V}_f \times \mathcal{L}_f$ to the Navier-Stokes equations (2.55) for every Reynolds number. It holds*

$$\|\nabla\mathbf{v}\| + \|p\| \leq c\|\mathbf{f}\|_{-1}.$$

This solution is unique, if

$$c^2\nu^{-2}\|\mathbf{f}\|_{-1} \leq 1,$$

where $c > 0$ is a constant depending on the domain $\mathcal{F}$.

Proof For the proof, we again refer to the literature [251, 321]. □

The incompressible Navier-Stokes problem with homogenous Dirichlet values has a solution $\{\mathbf{v},p\} \in \mathcal{V}_f \times \mathcal{L}_f$ for all Reynolds numbers and all right hand sides $\mathbf{f} \in H^{-1}(\mathcal{F})$. This solution is unique only if the Reynolds number is very small:

$$Re \leq \sqrt{\frac{1}{c^2\|\mathbf{f}\|_{-1}}}.$$

Most application problems however deal with high Reynolds numbers $Re \gg 1000$ and a unique solution cannot be guaranteed. As we know that flows at very high Reynolds numbers get turbulent, we cannot expect a unique result for arbitrary Reynolds numbers. The gap between theory and observation however is still very large.

Nearly no theoretical results are known for different boundary conditions, in particular for outflow conditions like the *do-nothing* condition. Here, it is even unknown, whether the homogenous problem

$$-\frac{1}{Re}\Delta \mathbf{v} + (\mathbf{v}\cdot\nabla)\mathbf{v} + \nabla p = 0, \quad \nabla\cdot\mathbf{v} = 0,$$

with homogenous boundary conditions

$$\mathbf{v} = 0 \text{ on } \Gamma_f^D, \quad \frac{1}{Re}\partial_n \mathbf{v} - p\mathbf{n} = 0 \text{ on } \Gamma_f^{\text{out}}$$

only has the trivial solution $\mathbf{v} = 0$ and $p = 0$ or if other non-trivial solutions exist.

Finally, we cite a regularity result for the stationary Navier-Stokes equations which is in agreement to the expectation:

Lemma 2.51 (Regularity of the Navier-Stokes Solution) *Let $\mathcal{F} \subset \mathbb{R}^d$ be a convex polygonal or smooth domain of class $C^{2,1}$. Further, let $\bar{\mathbf{v}}^D \in H^2(\mathcal{F})^d$ be a smooth extension of the Dirichlet data $\mathbf{v}^D$ on $\partial\mathcal{F}$ into the domain. Finally, let $\mathbf{f} \in L^2(\mathcal{F})^d$. The solution to the Navier-Stokes equations has the regularity $\mathbf{v} \in H^2(\mathcal{F}) \cap \mathcal{V}_f$ and $p \in H^1(\mathcal{F}) \cap \mathcal{L}_f$ and it holds*

$$\|\nabla^2 \mathbf{v}\| + \|\nabla p\| \le c_s\{\|\mathbf{f}\| + \|\nabla^2 \bar{\mathbf{v}}^D\|\},$$

where the stability constant is related to the Reynolds number $c_s \sim Re$.

Next, let $\mathcal{F}$ be a C^{k+2}-domain and $\mathbf{f} \in H^k(\mathcal{F})^d$. Then, every solution $\mathbf{v} \in H_0^1(\mathcal{F})^d$ and $p \in L^2(\mathcal{F})$ of the stationary Navier-Stokes equations has the regularity

$$\|\mathbf{v}\|_{H^{k+2}(\mathcal{F})} + \|p\|_{H^{k+1}(\mathcal{F})} \le c\|\mathbf{f}\|_{H^k(\mathcal{F})}.$$

Proof For a proof of this result we refer to the literature, see Girault and Raviart [165] or Sohr [312]. □

2.4.5.4 The Non-stationary Navier-Stokes Equations

Finally, we discuss the non-stationary Navier-Stokes equations

$$\begin{aligned} \mathbf{v} &= \mathbf{v}^{\text{in}} && t = 0, \\ (\partial_t \mathbf{v}, \phi) + ((\mathbf{v}\cdot\nabla)\mathbf{v}, \phi) + \nu(\nabla\mathbf{v}, \nabla\phi) - (p, \nabla\cdot\phi) &= (\mathbf{f}, \phi) && \forall \phi \in \mathcal{V}_f, \\ (\nabla\cdot\mathbf{v}, \xi) &= 0 && \forall \xi \in \mathcal{L}_f. \end{aligned}$$

Like in the stationary case, we can restrict the problem to the space of divergence free functions $\mathcal{V}_0 \subset \mathcal{V}$. Integration of the variational formulation over the time-interval $I = [0, T]$ gives

$$\int_I \{(\partial_t \mathbf{v}, \phi) + ((\mathbf{v} \cdot \nabla)\mathbf{v}, \phi) + \nu(\nabla \mathbf{v}, \nabla \phi)\} \, \mathrm{d}t = \int_I (\mathbf{f}, \phi) \, \mathrm{d}t.$$

To analyze this variational formulation, we must first specify suitable function spaces. For the velocity part, natural choices for $\mathbf{v}$ and test function ϕ are

$$\mathbf{v}, \phi \in L^2(I; \mathcal{V}_0),$$

the space of square-integrable functions in time that map into $\mathcal{V}_0$. For the time-derivative of the velocity, we further ask for

$$\partial_t \mathbf{v} \in L^2(I; H^{-1}(\mathcal{F})).$$

We denote this space by $W(0, T)$

$$W(0, T) := \{\phi \in L^2(I; \mathcal{V}_0), \ \partial_t \phi \in L^2(I; H^{-1}(\mathcal{F}))\}. \tag{2.59}$$

The spaces

$$\mathcal{V}_0 \subset H_0^1(\Omega)^d \subset L^2(\Omega)^d \cong [L^2(\Omega)^d]^* \subset H^{-1}(\Omega)$$

constitute a Gelfand triple and it holds (see [321])

$$W(0, T) \hookrightarrow C(\bar{I}; L^2(\Omega)^d).$$

Every function $\mathbf{v} \in W(0, T)$ is almost everywhere equal to a continuous function in time that maps into $L^2(\Omega)^d$. It remains to discuss the nonlinearity: does for functions $\mathbf{v}, \phi \in W(0, T)$ hold that

$$\int_I ((\mathbf{v} \cdot \nabla)\mathbf{v}, \phi) \, \mathrm{d}t < \infty?$$

An answer is given by the following result:

Lemma 2.52 *Let $\Omega \subset \mathbb{R}^d$ be an open set. For $d = 2$ it holds*

$$\|\mathbf{v}\|_{L^4(\Omega)} \leq c \|\mathbf{v}\|^{\frac{1}{2}} \|\nabla \mathbf{v}\|^{\frac{1}{2}}.$$

In the case $d = 3$ it holds

$$\|\mathbf{v}\|_{L^4(\Omega)} \leq c \|\mathbf{v}\|^{\frac{1}{2}} \|\nabla \mathbf{v}\|^{\frac{3}{2}}.$$

Proof A proof is given by Temam [321]. □

We consider the two-dimensional case. By Hölder's inequality ($1 = \frac{1}{4} + \frac{1}{2} + \frac{1}{4}$) and this Lemma we get

$$((\mathbf{v} \cdot \nabla)\mathbf{v}, \phi) \leq c\|\mathbf{v}\|_{L^4} \|\nabla \mathbf{v}\| \, \|\phi\|_{L^4} \leq c\|\mathbf{v}\|^{\frac{1}{2}} \|\nabla \mathbf{v}\|^{\frac{3}{2}} \|\phi\|^{\frac{1}{2}} \|\nabla \phi\|^{\frac{1}{2}}.$$

Using the embedding $W(0,T) \hookrightarrow C(\bar{I}; L^2(\Omega))$ it follows for the temporal integral by using Hölder's inequality (in time)

$$\begin{aligned}
&\int_I ((\mathbf{v} \cdot \nabla)\mathbf{v}, \phi) \, \mathrm{d}t \\
&\qquad \leq c\|\phi\|^{\frac{1}{2}}_{C(\bar{I};L^2(\Omega))} \|\mathbf{v}\|^{\frac{1}{2}}_{C(\bar{I};L^2(\Omega))} \int_I \|\nabla \mathbf{v}\|^{\frac{3}{2}} \|\nabla \phi\|^{\frac{1}{2}} \, \mathrm{d}t \\
&\qquad \leq c\|\phi\|^{\frac{1}{2}}_{W(0,T)} \|\mathbf{v}\|^{\frac{1}{2}}_{W(0,T)} \|\mathbf{v}\|^{\frac{3}{2}}_{W(0,T)} \|\phi\|^{\frac{1}{2}}_{W(0,T)} \\
&\qquad \leq c\|\mathbf{v}\|^2_{W(0,T)} \|\phi\|_{W(0,T)}.
\end{aligned}$$

This is exactly the desired stability result for the variational formulation. The nonlinearity is not bound in the three-dimensional case, if we ask for $\mathbf{v}, \phi \in W(0,T)$. We cite the following results that can be found in Temam [321]:

Lemma 2.53 (Instationary Navier-Stokes Equations) *Let $\mathcal{F} \subset \mathbb{R}^d$ be a Lipschitz domain and*

$$\mathbf{f} \in L^2(I; H^{-1}(\mathcal{F})), \quad \mathbf{v}^0 \in \mathcal{V}_0.$$

Then, the instationary Navier-Stokes equation has at least one solution for arbitrary Reynolds numbers. This solution is unique in the two dimensional case (for arbitrary Reynolds numbers) and it holds

$$\mathbf{v} \in L^2(I; \mathcal{V}_0), \quad \partial_t \mathbf{v} \in L^2(I; H^{-1}(\mathcal{F})).$$

In the three-dimensional case, unity is usually not given, and the solution has the reduced regularity

$$\mathbf{v} \in L^{\frac{8}{3}}(I; L^4(\Omega)), \quad \partial_t \mathbf{v} \in L^{\frac{4}{3}}(I; H^{-1}(\Omega)).$$

It is remarkable that the non-stationary solution is unique for all Reynolds numbers, if we look at the two-dimensional problem. Working with the stationary equation, uniqueness is only guaranteed for small data assumptions.

To prove existence of global solutions, uniqueness and regularity of the three dimensional problem is one of big open problems in applied mathematics, see [89].

2.5 Flow Problems on Moving Domains

In this section, we discuss models for flows on a moving domain $\mathcal{F}(t) \subset \mathbb{R}^d$. Let $I = [0, T]$ be the temporal interval. Then, the space-time domain is given as

$$\mathcal{G} = \{(t, \mathcal{F}(t)) \subset I \times \mathbb{R}^d\} \subset \mathbb{R}^{d+1}.$$

This setting is more complex then the tensor-product design of fixed domains $I \times \mathcal{F} \subset \mathbb{R}^{d+1}$. In $\mathcal{G}$ it is difficult to formulate the proper function spaces like (2.59) with a different regularity in time and space. We define

Problem 2.54 (Incompressible Navier-Stokes Equations on a Moving Domain) *Let $\mathcal{G} = \{(t, \mathcal{F}(t)),\ t \in I = [0, T]\}$ be the moving space time domain. Velocity and pressure*

$$\mathbf{v} \in L^2(I; \mathcal{V}_f(t)), \quad \partial_t \mathbf{v} \in L^2(I; \mathcal{V}_f(t)^*), \quad p \in L^2(I; L^2(\mathcal{F}(t))),$$

are determined as solution to the incompressible Navier-Stokes equations on the moving domain

$$(\partial_t \mathbf{v} + (\mathbf{v} \cdot \nabla)\mathbf{v}, \phi)_{\mathcal{F}(t)} + (\boldsymbol{\sigma}_f, \nabla\phi)_{\mathcal{F}(t)} + (\text{div } \mathbf{v}, \xi)_{\mathcal{F}(t)} = (\mathbf{f}_f, \phi)_{\mathcal{F}(t)} \quad \text{a.e. } t \in [0, T] \tag{2.60}$$

for all $\phi \in \mathcal{V}_f(t)$ and $\xi \in \mathcal{L}_f(t)$.

Mostly we will assume that the domain motion is given by a mapping from a fixed reference domain $\hat{\mathcal{F}} \subset \mathbb{R}^d$

$$\hat{T}(t) : \hat{\mathcal{F}} \mapsto \mathcal{F}(t).$$

First we assume that this mapping is given as part of the problem data, such that we can prescribe properties like invertibility, regularity. Later on, when analyzing fluid-structure interactions, this mapping will be an unknown part of the solution. This will strongly complicate the analysis, as regularity will no longer be part of the problem description but must result from the system of equations.

For here and for simplicity, we assume that $\hat{\mathcal{F}} = \mathcal{F}(0)$, i.e., the reference domain is the domain at initial time. The mapping is defined as Function from the fixed space-time domain to $\mathbb{R}^d$

$$\hat{T} : I \times \hat{\mathcal{F}} \to \mathbb{R}^d.$$

We will specify further assumptions on this mapping at a later point. The time-derivative of this mapping $\partial_t \hat{T}$ denotes a velocity. This velocity is not the physical velocity of the fluid particles, but it is the *domain velocity*. In the general case it is arbitrary and, in particular, it holds $\partial_t \hat{T} \neq \mathbf{v}$.

2.5.1 Eulerian Techniques for Flow Problems on Moving Domains

Discretization of partial differential equations is difficult if the domain is in motion. Usually, every discretization consists of first discretizing the domain $\mathcal{F} \subset \mathbb{R}^d$ by a mesh $\mathcal{F}_h$. If $\mathcal{F}(t)$ is moving the meshes $\mathcal{F}_h(t)$ also cannot be fixed.

We consider time stepping methods, where the solution determined in discrete time steps only

$$0 = t_0 < t_1 < \cdots < t_M = T.$$

By $\mathbf{v}^m := \mathbf{v}(t_m)$ and by $p^m := p(t_m)$ we denote velocity and pressure at time t_m. Then, in a discrete setting, approximations $\mathbf{v}_{kh}^m$ and $\mathbf{v}_{kh}^{m-1}$ will live on different meshes—or in the context of finite elements—in different function spaces V_{kh}^m and V_{kh}^{m-1}. Usual time-discretization schemes approximate the temporal derivative by finite differences

$$\partial_t \mathbf{v}_h(t_m) \approx \frac{\mathbf{v}_{kh}^m - \mathbf{v}_{kh}^{m-1}}{t_m - t_{m-1}}.$$

Now we assume that $\mathbf{v}_{kh}^m \in V_{kh}^m$ and $\mathbf{v}_{kh}^{m-1} \in V_{kh}^{m-1}$ are element of different finite element spaces. In this case, $\mathbf{v}_{kh}^m - \mathbf{v}_{kh}^{m-1}$ will most likely neither belong to V_{kh}^m nor to V_{kh}^{m-1}.

This problem gets even more severe, if we consider a spatial coordinate $x \in \mathcal{F}(t_m)$ that is not part of the domain at the old time step $x \notin \mathcal{F}(t_{m-1})$. Here, the expression $\mathbf{v}_{kh}^m(x) - \mathbf{v}_{kh}^{m-1}(x)$ is not well defined at all.

Eulerian schemes for moving domain problems will require non-standard discretization techniques and a non-standard analysis. We will pick up this discussion at a later point in Sect. 3.6 and Chaps. 6 and 12.

2.5.2 The Arbitrary Lagrangian Eulerian (ALE) Formulation for Moving Domain Problems

Another possibility to deal with the motion of the fluid-domain is to introduce a fixed reference domain $\hat{\mathcal{F}} \subset \mathbb{R}^d$ and the mapping

$$\hat{T}_f(t) : \hat{\mathcal{F}} \to \mathcal{F}(t).$$

We can use this mapping to transform the Navier-Stokes equations onto the reference domain $\hat{\mathcal{F}}$ and to define velocity and pressure in the reference system

$$\hat{\mathbf{v}}(\hat{x}, t) := \mathbf{v}(\hat{T}_f(\hat{x}, t), t), \quad \hat{p}(\hat{x}, t) := p(\hat{T}_f(\hat{x}, t), t) \quad \forall \hat{x} \in \hat{\mathcal{F}}. \tag{2.61}$$

The mapping $\hat{T}_f$ has to be invertible, such that at time $t \in I$, every spatial point $x \in \mathcal{F}(t)$ is uniquely given by one coordinate $\hat{x} \in \hat{\mathcal{F}}$.

If the mapping $\hat{T}_f$ is a C^1-diffeomorphism, it can be used to transform the Navier-Stokes equations onto $\hat{\mathcal{F}}$ using $\hat{\mathbf{v}}$ and $\hat{p}$ as principle variables. All relations required for this transformation have already been derived in Sect. 2.1.7. By (2.22) and with Definition 2.13 it holds by (2.61)

$$\begin{aligned}
\rho_f\big(\partial_t \mathbf{v} + (\mathbf{v}\cdot\nabla)\mathbf{v}, \phi\big)_{\mathcal{F}(t)} &= \rho_f\big(\hat{J}_f(\partial_t\hat{\mathbf{v}} + \hat{\mathbf{F}}_f^{-1}(\hat{\mathbf{v}} - \partial_t\hat{T}_f)\cdot\nabla\hat{\mathbf{v}}), \hat{\phi}\big)_{\hat{\mathcal{F}}},\\
\big(\boldsymbol{\sigma}_f, \nabla\phi\big)_{\mathcal{F}(t)} &= \big(\hat{J}_f\hat{\boldsymbol{\sigma}}_f\hat{\mathbf{F}}_f^{-T}, \hat{\nabla}\hat{\phi}\big)_{\hat{\mathcal{F}}},\\
\big(\operatorname{div}\,\mathbf{v}, \xi\big)_{\mathcal{F}(t)} &= \big(\widehat{\operatorname{div}}\,(\hat{J}_f\hat{\mathbf{F}}_f^{-1}\hat{\mathbf{v}}), \hat{\xi}\big)_{\hat{\mathcal{F}}}.
\end{aligned} \tag{2.62}$$

The Cauchy stress tensor $\hat{\boldsymbol{\sigma}}(\hat{x})$ expressed in the reference system is derived with help of (2.16)

$$\hat{\boldsymbol{\sigma}}_f := -\hat{p}I + \rho_f\nu_f(\hat{\nabla}\hat{\mathbf{v}}\hat{\mathbf{F}}_f^{-1} + \hat{\mathbf{F}}^{-T}\hat{\nabla}\hat{\mathbf{v}}^T). \tag{2.63}$$

By these transformations we formulate the system of Navier-Stokes equations in ALE coordinates.

Problem 2.55 (Incompressible Navier-Stokes Equations in ALE) *Let $\hat{\mathcal{F}}$ be a suitable reference domain, $\hat{T}_f$ a C^1-diffeomorphism on $I\times\hat{\mathcal{F}}$ with $\hat{T}_f(t) : \hat{\mathcal{F}} \mapsto \mathcal{F}(t)$. Then, velocity and pressure*

$$\hat{\mathbf{v}} \in L^2(I;\hat{\mathcal{V}}_f),\ \partial_t\hat{\mathbf{v}} \in L^2(I;\hat{\mathcal{V}}_f^*),\quad p \in L^2(I;\hat{\mathcal{L}}_f)$$

are given as solution to

$$\begin{aligned}
&\rho_f\big(\hat{J}_f(\partial_t\hat{\mathbf{v}} + \hat{\mathbf{F}}_f^{-1}(\hat{\mathbf{v}} - \partial_t\hat{T}_f)\cdot\nabla\hat{\mathbf{v}}), \hat{\phi}\big)_{\hat{\mathcal{F}}}\\
&\qquad + \big(\hat{J}_f\hat{\boldsymbol{\sigma}}_f\hat{\mathbf{F}}_f^{-T}, \hat{\nabla}\hat{\phi}\big)_{\hat{\mathcal{F}}} = (\rho_f\hat{J}_f\hat{\mathbf{f}}_f, \hat{\phi})_{\hat{\mathcal{F}}}\\
&\qquad \big(\widehat{\operatorname{div}}\,(\hat{J}_f\hat{\mathbf{F}}_f^{-1}\hat{\mathbf{v}}), \hat{\xi}\big)_{\hat{\mathcal{F}}} = 0,
\end{aligned} \tag{2.64}$$

for all $\hat{\phi} \in \mathcal{V}_f$ and $\hat{\xi} \in \mathcal{L}_f$.

The derivation of the system of equations is performed on a formal basis. We still need to argue that the solutions to Problems 2.55 and 2.54 are in a meaningful way equivalent.

Considering the strong formulation of the Navier-Stokes equations, equivalence of a notation on the moving Eulerian domain $\mathcal{F}(t)$ and the fixed reference domain $\hat{\mathcal{F}}$ can be shown by classical arguments. If we assume that $\hat{T}_W$ is a C^2-diffeomorphism the equation can be transformed to an equivalent expression. In the variational formulation, we must first discuss the question of equivalence of Sobolev spaces under a mapping of the domain.

Lemma 2.56 (Transformation of Sobolev-Spaces) *Let Ω and $\hat{\Omega}$ be two domains in $\mathbb{R}^d$ and let $\hat{T} \in C^{k,1}(\hat{\Omega})^d$ be a diffeomorphism with $\hat{T}(\hat{\Omega}) = \Omega$ and $\hat{T}^{-1}(\Omega) = \hat{\Omega}$. Then, the composition operators*

$$\phi := \hat{\phi} \circ \hat{T}^{-1} \quad \forall \hat{\phi} \in H^{k+1}(\hat{\Omega}) \text{ and } \hat{\phi} := \phi \circ \hat{T} \quad \forall \phi \in H^{k+1}(\Omega),$$

are continuous. Hence the Sobolev spaces $H^{k+1}(\Omega)$ and $H^{k+1}(\hat{\Omega})$ are equivalent

$$H^{k+1}(\hat{\Omega}) \cong H^{k+1}(\Omega),$$

such that there exist constants $c_1, c_2 > 0$ such that

$$c_1 \|\hat{v}\|_{H^{k+1}(\hat{\Omega})} \leq \|\hat{v} \circ T\|_{H^{k+1}(\Omega)} \leq c_2 \|\hat{v}\|_{H^{k+1}(\hat{\Omega})} \quad \forall \hat{v} \in H^{k+1}(\hat{\Omega}).$$

For the proof, we refer to the literature, *Satz 4.1 - Transformationssatz*, in [350].

Considering stationary problems the velocity is a H^1 function, given in $\mathbf{v} \in H^1(\mathcal{F})^d$, the pressure is a L^2 function, given in $p \in L^2(\mathcal{F})$. Hence for $H^1(\mathcal{F})$ and $H^1(\hat{\mathcal{F}})$ to be equivalent, which is a necessary assumption for equivalent solution concepts, the mapping $\hat{T}_W$ must be a $C^{0,1}$-diffeomorphism in space. Equivalence of Sobolev spaces on $\mathcal{F}$ and $\hat{\mathcal{F}}$ is important to have equivalent concepts of convergence and variational formulations. The ALE transformation is a mapping in space and time. Failer [133] showed the equivalence of the following spaces in space and time:

Lemma 2.57 (Transformation of Bochner-Spaces) *Let $\hat{\Omega}$ and $\Omega(t)$ for $t \in I = [0, T]$ be domains in $\mathbb{R}^d$ and let $\hat{T} : I \times \hat{\Omega} \to \Omega(t)$ with $\hat{T}(\hat{\Omega}) = \Omega(t)$ be a*

$$C(I; C^1(\hat{\Omega})) \cap C^1(I; C(\Omega))$$

diffeomorphism. Then, the composition operators

$$\begin{aligned} \phi &:= \hat{\phi} \circ \hat{T}^{-1} && \forall \hat{\phi} \in \{\hat{\phi} : \ \hat{\phi} \in L^2(I; H^1(\hat{\Omega})), \ \partial_t \hat{\phi} \in L^2(I; L^2(\hat{\Omega}))\} \\ \hat{\phi} &:= \phi \circ \hat{T} && \forall \phi \in \{\phi : \ \phi \in L^2(I; H^1(\Omega(t))), \ \partial_t \phi \in L^2(I; L^2(\Omega(t)))\} \end{aligned}$$

are continuous and the spaces

$$\begin{aligned} \hat{W}(I) &:= \{\hat{\phi} : \ \hat{\phi} \in L^2(I; H^1(\hat{\Omega})), \ \partial_t \hat{\phi} \in L^2(I; L^2(\hat{\Omega}))\} \\ &\cong \\ W(I) &:= \{\phi : \ \phi \in L^2(I; H^1(\Omega(t))), \ \partial_t \phi \in L^2(I; L^2(\Omega(t)))\} \end{aligned}$$

are equivalent.

Using this result, we can claim equivalence of solutions of the Navier-Stokes equations in ALE and in Eulerian coordinates, if the solution is found in $W(I)$, i.e. with $\partial_t \mathbf{v} \in L^2(I; L^2(\mathcal{F}(t)))$.

Lemma 2.58 (Navier-Stokes in ALE Coordinates) *Let $\hat{\mathcal{F}} \subset \mathbb{R}^d$ be a smooth domain and $\hat{T}_f : \hat{\mathcal{F}} \to \mathcal{F}(t)$ be a $C(I; C^1(\hat{\mathcal{F}})) \cap C^1(I; C(\hat{\mathcal{F}}))$-diffeomorphism. Then, for every solution $(\hat{\mathbf{v}}, \hat{p}) \in \hat{W}(I) \times L^2(I; L^2(\hat{\mathcal{F}}))$ of (2.64) there exists a solution $(\mathbf{v}, p) \in W(I) \times L^2(I; L^2(\mathcal{F}(t)))$ of (2.60) with $\hat{\mathbf{v}}(\hat{x}, t) = \mathbf{v}(\hat{T}_f(\hat{x}, t), t)$ and $\hat{p}(\hat{x}, t) = p(\hat{T}_f(\hat{x}, t), t)$ almost everywhere.*

The equivalence of two different representations of the Navier-Stokes equations in ALE and in Eulerian coordinates also states that both formulations allow for the same solution concept. If the Eulerian formulation of the Navier-Stokes equations has a unique solution $(\mathbf{v}(t), p(t))$, for suitable mappings $\hat{T}_f$, the ALE formulation will have a corresponding unique solution $(\hat{\mathbf{v}}, \hat{p})$ and it holds

$$c(\hat{T}_f(t))^{-1} \left\{ \|\nabla \mathbf{v}(t)\|_{\mathcal{F}(t)} + \|p(t)\|_{\mathcal{F}(t)} \right\} \leq \|\hat{\nabla} \hat{\mathbf{v}}\|_{\hat{\mathcal{F}}} + \|\hat{p}\|_{\hat{\mathcal{F}}} \leq c(\hat{T}_f(t)) \left\{ \|\nabla \mathbf{v}(t)\|_{\mathcal{F}(t)} + \|p(t)\|_{\mathcal{F}(t)} \right\}. \tag{2.65}$$

The constant $c(\hat{T}_f(t))$ will depend on the deformation and, if $\hat{T}_f$ looses its regularity, $c(\hat{T}_f(t)) \to \infty$ is possible.

The variational formulation (2.64) has the benefit, that the domain $\hat{\mathcal{F}}$ is fixed and that the function spaces $\hat{\mathcal{V}}_f$ and $\hat{\mathcal{L}}_f$ do not change in time. A standard finite element triangulation $\hat{\mathcal{F}}_h$ of $\hat{\mathcal{F}}$ can be constructed and used for defining discrete function spaces. The removal of the domain motion comes at the price of additional nonlinearities introduced in the equation. These nonlinearities all depend on the domain map $\hat{T}_f$.

The equivalence of the Eulerian and the ALE formulation of the Navier-Stokes equations strictly depends on the regularity of the mapping $\hat{T}_f$. If this mapping looses its regularity, the equivalence is also lost.

Remark 2.59 (Divergence in ALE Coordinates) On first sight, the divergence condition in ALE coordinates

$$\widehat{\operatorname{div}} \left(\hat{J} \hat{\mathbf{F}}^{-1} \hat{\mathbf{v}} \right) = 0,$$

calls for the evaluation of $\hat{\mathbf{u}}$'s second derivatives. It however turns out that all these second derivatives cancel out, if $\hat{\mathbf{u}} \in C^2(\hat{\mathcal{F}})^d$.
The following two technical lemma show this relation. First, we derive a rule for the partial derivatives of a matrices inverse and for the determinant of a matrix:

Lemma 2.60 (Partial Derivatives of Inverse and Determinant) *Let $\hat{\mathbf{F}} : \mathbb{R}^{n \times n} \to \mathbb{R}$ be differentiable and invertible, $\hat{J} = \det(\hat{\mathbf{F}})$. By $\hat{\partial}_k \hat{\mathbf{F}} = (\hat{\partial}_k \hat{\mathbf{F}}_{ij})_{ij}$ and $\hat{\partial}_k \hat{\mathbf{F}}^{-1} = (\hat{\partial}_k \hat{\mathbf{F}}^{-1}_{ij})_{ij}$ we denote matrices of partial derivatives of $\hat{\mathbf{F}}$ and its inverse. It holds*

$$\hat{\partial}_k \hat{\mathbf{F}}^{-1} = -\hat{\mathbf{F}}^{-1} \hat{\partial}_k \hat{\mathbf{F}} \hat{\mathbf{F}}^{-1}, \quad \hat{\partial}_k \hat{J} = \hat{J} \operatorname{tr}(\hat{\mathbf{F}}^{-1} \hat{\partial}_k \hat{\mathbf{F}}) \tag{2.66}$$

Proof

(i) By $\hat{\mathbf{F}}^{-1}\hat{\mathbf{F}} = I$ we get for $k = 1, \ldots, n$

$$0 = \sum_{l=1}^{n} \hat{\partial}_k \hat{\mathbf{F}}_{il}^{-1} \hat{\mathbf{F}}_{lj} + \hat{\mathbf{F}}_{il}^{-1} \hat{\partial}_k \hat{\mathbf{F}}_{lj} \quad \Rightarrow \quad \hat{\partial}_k \hat{\mathbf{F}}^{-1} \hat{\mathbf{F}} + \hat{\mathbf{F}}^{-1} \hat{\partial}_k \hat{\mathbf{F}} = 0,$$

such that the first result follows by multiplication with $\hat{\mathbf{F}}^{-1}$. Likewise, the inverse relation holds

$$\hat{\partial}_k \hat{\mathbf{F}} = -\hat{\mathbf{F}} \hat{\partial}_k \hat{\mathbf{F}}^{-1} \hat{\mathbf{F}}. \tag{2.67}$$

(ii) We denote by Δ_{ij} the cofactor of $\hat{\mathbf{F}}$

$$\Delta_{ij} := (-1)^{i+j} \det(\hat{\mathbf{F}}_{kl})_{k \neq i, l \neq j},$$

Then, the determinant j can be given as

$$\delta_{ik} \hat{J} = \sum_{l=1}^{n} \Delta_{il} \hat{\mathbf{F}}_{kl}, \quad i = 1, \ldots, n. \tag{2.68}$$

Differentiation of this formula ($k = i$) w.r.t. the entries $\hat{\mathbf{F}}_{ij}$ gives

$$\frac{\hat{\partial} \hat{J}}{\hat{\partial} \hat{\mathbf{F}}_{ij}} = \sum_{l=1}^{n} \underbrace{\frac{\hat{\partial} \Delta_{il}}{\hat{\partial} \hat{\mathbf{F}}_{ij}}}_{=0} \hat{\mathbf{F}}_{il} + \Delta_{il} \underbrace{\frac{\hat{\partial} \hat{\mathbf{F}}_{il}}{\hat{\partial} \hat{\mathbf{F}}_{ij}}}_{=\delta_{lj}} = \Delta_{ij}, \tag{2.69}$$

as Δ_{il} does not depend on $\hat{\mathbf{F}}_{ij}$. Hereby, we get with (2.67) and (2.69) and (2.68)

$$\begin{aligned} \hat{\partial}_k \hat{J} &= \sum_{ij} \frac{\hat{\partial} \hat{J}}{\hat{\mathbf{F}}_{ij}} \hat{\partial}_k \hat{\mathbf{F}}_{ij} = -\sum_{ij} \Delta_{ij} (\hat{\mathbf{F}} \hat{\partial}_k \hat{\mathbf{F}}^{-1} \hat{\mathbf{F}})_{ij} \\ &= -\sum_{jrs} \underbrace{\left(\sum_{i} \Delta_{ij} \hat{\mathbf{F}}_{ir} \right)}_{=\delta_{jr} \hat{J}} \hat{\partial}_k \hat{\mathbf{F}}_{rs}^{-1} \hat{\mathbf{F}}_{sj} = -\hat{J} \sum_{rs} \hat{\partial}_k \hat{\mathbf{F}}_{rs}^{-1} \hat{\mathbf{F}}_{sr}, \end{aligned}$$

and hence using $A : B = \operatorname{tr}(AB^T)$:

$$\hat{\partial}_k \hat{J} = -\hat{J}\hat{\partial}_k \hat{\mathbf{F}}^{-1} : \hat{\mathbf{F}}^T = \hat{J}\hat{\mathbf{F}}^{-1}\hat{\partial}_k \hat{\mathbf{F}}\hat{\mathbf{F}}^{-1} : \hat{\mathbf{F}}^T$$
$$= \hat{J} \operatorname{tr}\left(\hat{\mathbf{F}}^{-1}\hat{\partial}_k \hat{\mathbf{F}}\hat{\mathbf{F}}^{-1}\hat{\mathbf{F}}\right) = \hat{J} \operatorname{tr}\left(\hat{\mathbf{F}}^{-1}\hat{\partial}_k \hat{\mathbf{F}}\right)$$

□

With help of these differentiation rules we can reformulate the divergence in ALE coordinates

Lemma 2.61 (Divergence in ALE Coordinates) *Let* $\hat{\mathbf{u}} \in C^2(\Omega)^d$, $\hat{\mathbf{F}} = I + \hat{\nabla}\hat{\mathbf{u}}$ *be invertible and* $\hat{J} = \det(\hat{\mathbf{F}})$. *It holds*

$$\operatorname{div}\left(\hat{J}\hat{\mathbf{F}}^{-1}\mathbf{v}\right) = \sum_{kl} \hat{J}\hat{\mathbf{F}}^{-1}_{kl}\hat{\partial}_k \mathbf{v}_l = \hat{J}\hat{\mathbf{F}}^{-1} : \nabla\mathbf{v}^T = \hat{J} \operatorname{tr}(\hat{\mathbf{F}}^{-1}\nabla\mathbf{v}).$$

Proof We start by component-wise differentiation

$$\operatorname{div}\left(\hat{J}\hat{\mathbf{F}}^{-1}\mathbf{v}\right) = \sum_k \hat{\partial}_k (\hat{J}\hat{\mathbf{F}}^{-1}\mathbf{v})_k = \sum_{kl} \left\{\hat{\partial}_k \hat{J}\hat{\mathbf{F}}^{-1}_{kl}\mathbf{v}_l + \hat{J}\hat{\partial}_k \hat{\mathbf{F}}^{-1}_{kl}\mathbf{v}_l + \hat{J}\hat{\mathbf{F}}^{-1}\hat{\partial}_k \mathbf{v}_l\right\}.$$

While the third term already has the final form, we will show that the first two parts cancel out. Using the two parts of Lemma 2.60, we get

$$\operatorname{div}\left(\hat{J}\hat{\mathbf{F}}^{-1}\mathbf{v}\right)$$
$$= \hat{J}\hat{\mathbf{F}}^{-1} : \nabla\mathbf{v}^T + \hat{J}\sum_l \mathbf{v}_l \left(\sum_k \left(\operatorname{tr}(\hat{\mathbf{F}}^{-1}\hat{\partial}_k \hat{\mathbf{F}})\hat{\mathbf{F}}^{-1}_{kl} - (\hat{\mathbf{F}}^{-1}\hat{\partial}_k \hat{\mathbf{F}}\hat{\mathbf{F}}^{-1})_{kl}\right)\right)$$
$$= \hat{J}\sum_l \mathbf{v}_l \sum_{kij} \left(\hat{\mathbf{F}}^{-1}_{ij}\hat{\partial}_k \hat{\mathbf{F}}_{ji}\hat{\mathbf{F}}^{-1}_{kl} - \hat{\mathbf{F}}^{-1}_{kj}\hat{\partial}_k \hat{\mathbf{F}}_{ji}\hat{\mathbf{F}}^{-1}_{il}\right)$$

Next, we use the specific form $\hat{\mathbf{F}} = I + \hat{\nabla}\hat{\mathbf{u}}$ and the symmetry of the second derivatives $\hat{\partial}_{ij}\hat{\mathbf{u}} = \hat{\partial}_{ij}\hat{\mathbf{u}}$. Then,

$$\operatorname{div}\left(\hat{J}\hat{\mathbf{F}}^{-1}\mathbf{v}\right)$$
$$= \hat{J}\hat{\mathbf{F}}^{-1} : \nabla\mathbf{v}^T + \hat{J}\sum_l \mathbf{v}_l \sum_{kij} \left(\hat{\mathbf{F}}^{-1}_{ij}\hat{\partial}_i \hat{\mathbf{F}}_{jk}\hat{\mathbf{F}}^{-1}_{kl} - \hat{\mathbf{F}}^{-1}_{kj}\hat{\partial}_k \hat{\mathbf{F}}_{ji}\hat{\mathbf{F}}^{-1}_{il}\right)$$
$$= \hat{J}\sum_l \mathbf{v}_l \sum_{kij} \left(\hat{\mathbf{F}}^{-1}_{kj}\hat{\partial}_k \hat{\mathbf{F}}_{ji}\hat{\mathbf{F}}^{-1}_{il} - \hat{\mathbf{F}}^{-1}_{kj}\hat{\partial}_k \hat{\mathbf{F}}_{ji}\hat{\mathbf{F}}^{-1}_{il}\right) = 0,$$

where we switched the indices i and k in the first part. □

The crucial inequality for the analysis of the Navier-Stokes and Stokes equations is the inf-sup condition (2.53). We assume that on $\hat{\mathcal{F}}$ it holds:

$$\inf_{\hat{\xi}\in L^2(\hat{\mathcal{F}})} \sup_{\hat{\phi}\in H_0^1(\hat{\mathcal{F}})^d} \frac{(\widehat{\operatorname{div}}\,\hat{\phi},\hat{\xi})}{\|\hat{\nabla}\hat{\phi}\|_{\hat{\mathcal{F}}}\,\|\hat{\xi}\|_{\hat{\mathcal{F}}}} \geq \hat{\gamma} > 0.$$

For simplicity, $\hat{T}_f(t) : \hat{\mathcal{F}} \to \mathcal{F}(t)$ be a C^2-diffeomorphism with $\hat{T}_f(\hat{\mathcal{F}},0) = \hat{\mathcal{F}}$. In light of Lemma 2.56, the Sobolev-spaces on $\mathcal{F}(t)$ and $\hat{\mathcal{F}}$ are equivalent

$$H^1(\mathcal{F}(t)) \cong H^1(\hat{\mathcal{F}}), \quad L^2(\mathcal{F}(t)) \cong L^2(\hat{\mathcal{F}}).$$

On $\mathcal{F}(t)$ it holds

$$\frac{(\operatorname{div}\,\phi,\xi)_{\mathcal{F}(t)}}{\|\xi\|_{\mathcal{F}(t)}\|\nabla\phi\|_{\mathcal{F}(t)}} = \frac{(\widehat{\operatorname{div}}\,(\hat{J}_f\hat{\mathbf{F}}_f^{-1}\hat{\phi}),\hat{\xi})_{\hat{\mathcal{F}}}}{\|\hat{J}_f^{\frac{1}{2}}\hat{\xi}\|_{\hat{\mathcal{F}}}\|\hat{J}_f^{\frac{1}{2}}\hat{\nabla}\hat{\phi}\hat{\mathbf{F}}_f^{-T}\|_{\hat{\mathcal{F}}}},$$

where

$$\xi(\hat{T}_f(\hat{x},t)) = \hat{\xi}(\hat{x}), \quad \phi(\hat{T}_f(\hat{x},t)) = \hat{\phi}(\hat{x}).$$

We substitute

$$\tilde{\phi} := \hat{J}_f\hat{\mathbf{F}}_f^{-1}\hat{\phi} \quad \Rightarrow \quad \hat{\phi} = \hat{J}_f^{-1}\hat{\mathbf{F}}_f\tilde{\phi}.$$

Due to the strong regularity of $\hat{T}_f \in C^2$ it holds for every $\hat{\phi} \in H^1(\hat{\mathcal{F}})^d$

$$\|\hat{\nabla}\tilde{\phi}\|_{\hat{\mathcal{F}}} \leq \|\hat{J}_f\hat{\mathbf{F}}_f^{-1}\|_{W^{1,\infty}(\hat{\mathcal{F}})}\|\hat{\phi}\|_{H^1(\hat{\mathcal{F}})},$$

that $\tilde{\phi} \in H^1(\hat{\mathcal{F}})$. With Poincaré's inequality we get the estimate

$$\|\hat{\nabla}\hat{\phi}\|_{\hat{\mathcal{F}}} \leq \|\hat{J}_f^{-1}\hat{\mathbf{F}}_f\|_{W^{1,\infty}(\hat{\mathcal{F}})}\|\tilde{\phi}\|_{H^1(\hat{\mathcal{F}})} \leq c_P\|\hat{J}_f^{-1}\hat{\mathbf{F}}_f\|_{W^{1,\infty}(\hat{\mathcal{F}})}\|\hat{\nabla}\tilde{\phi}\|_{\hat{\mathcal{F}}}.$$

With these preparations, we can carry over the inf-sup condition from $\hat{\mathcal{F}} = \mathcal{F}(0)$ to $\mathcal{F}(t)$:

$$\inf_{\xi\in L^2(\mathcal{F}(t))} \sup_{\phi\in H^1(\mathcal{F}(t))^d} \frac{(\operatorname{div}\,\phi,\xi)_{\mathcal{F}(t)}}{\|\xi\|_{\mathcal{F}(t)}\|\nabla\phi\|_{\mathcal{F}(t)}}$$

$$= \inf_{\hat{\xi}\in L^2(\hat{\mathcal{F}})} \sup_{\hat{\phi}\in H^1(\hat{\mathcal{F}})^d} \frac{(\widehat{\operatorname{div}}\,(\hat{J}_f\hat{\mathbf{F}}_f^{-1}\hat{\phi}),\hat{\xi})_{\hat{\mathcal{F}}}}{\|\hat{J}_f^{\frac{1}{2}}\hat{\xi}\|_{\hat{\mathcal{F}}}\|\hat{J}_f^{\frac{1}{2}}\hat{\mathbf{F}}_f^{-T}\hat{\nabla}\hat{\phi}\|_{\hat{\mathcal{F}}}}$$

$$= \inf_{\hat{\xi}\in L^2(\hat{\mathcal{F}})} \sup_{\tilde{\phi}\in H^1(\hat{\mathcal{F}})^d} \frac{(\widehat{\operatorname{div}}\,\tilde{\phi},\hat{\xi})_{\mathcal{F}(t)}}{\|\hat{J}_f^{\frac{1}{2}}\hat{\xi}\|_{\hat{\mathcal{F}}}\|\hat{J}_f^{\frac{1}{2}}\hat{\mathbf{F}}_f^{-T}\hat{\nabla}(\hat{J}_f^{-1}\hat{\mathbf{F}}_f\tilde{\phi})\|_{\hat{\mathcal{F}}}}$$

$$\geq c_P^{-1}\|\hat{J}_f^{\frac{1}{2}}\|_{L^\infty}^{-1}\|\hat{J}_f^{\frac{1}{2}}\hat{\mathbf{F}}_f^{-T}\|_{L^\infty}^{-1}\|\hat{J}_f^{-1}\hat{\mathbf{F}}_f\|_{W^{1,\infty}}^{-1} \inf_{\hat{\xi}\in L^2(\hat{\mathcal{F}})} \sup_{\tilde{\phi}\in H^1(\hat{\mathcal{F}})^d} \frac{(\widehat{\operatorname{div}}\,\tilde{\phi},\hat{\xi})_{\mathcal{F}(t)}}{\|\hat{\xi}\|_{\hat{\mathcal{F}}}\|\hat{\nabla}\tilde{\phi}\|_{\hat{\mathcal{F}}}}$$

$$\geq c(\hat{T}_f(t))\hat{\gamma} =: \gamma(t) \geq \gamma_0 > 0.$$

Depending on the regularity of the transformation $\hat{T}_f$, the inf-sup constant $\gamma(t)$ can be significantly closer to zero than $\hat{\gamma}$. See [247] for a study on the stability of the Stokes problem on moving and strongly deformed domains.

2.5.3 Definition of the ALE Map

The ALE formulation of the Navier-Stokes equations carries an arbitrariness, as for a given moving domain $\mathcal{F}(t)$ different reference domains $\hat{\mathcal{F}}$ and different mappings $\hat{T}_f(t) : \hat{\mathcal{F}} \to \mathcal{F}(t)$ can be taken into account. While a straightforward choice for the reference domain is $\hat{\mathcal{F}} = \mathcal{F}(0)$, other choices are still possible. However, even for one reference domain, we can still choose between different mappings $\hat{T}_f(t) : \hat{\mathcal{F}} \to \mathcal{F}(t)$. On complex domains these ALE-maps must be constructed with help of auxiliary problems. Assuming that the motion of the boundary $\partial\mathcal{F}(t)$ is known, and that $\hat{\mathcal{F}} = \mathcal{F}(0)$, we can construct the mapping by

$$\hat{T}_f(\hat{x},t) := \hat{x} + \hat{\mathbf{u}}_f(\hat{x},t),$$

where by $\hat{\mathbf{u}}_f$ we denote a *deformation* of the fluid domain. The constraint $\partial\hat{\mathcal{F}} \to \partial\mathcal{F}(t)$ can be used as boundary values for the fluid deformation $\hat{\mathbf{u}}_f$. In the interior of $\hat{\mathcal{F}}$ the deformation $\hat{\mathbf{u}}_f$ is constructed by solving a partial differential equation. The most simple approach is to define $\hat{\mathbf{u}}_f$ as the harmonic extension of the boundary values to the fluid domain

$$-\hat{\Delta}\hat{\mathbf{u}}_f = 0 \text{ in } \hat{\mathcal{F}}, \quad \hat{\mathbf{u}}_f(t) = \hat{\mathbf{u}}_f^D(t) \text{ on } \partial\hat{\mathcal{F}}, \tag{2.70}$$

where $\hat{\mathbf{u}}_f^D(t)$ is the deformation of the boundary points. The crucial point is the regularity of this deformation $\mathbf{u}_f$ that will define the regularity of the domain mapping. We know that for strict equivalence between the ALE formulation and the Eulerian formulation of the incompressible Navier-Stokes problem, very high regularity is required. In the interior of the fluid domain $\hat{\mathcal{F}}$, qualitative regularity is given by the smoothing property of the Laplace-operator, as the right hand side is zero in (2.70). At the boundaries however, the regularity of $\mathbf{u}_f$ is limited by the regularity of $\mathbf{u}_s$ and further by the shape of the boundary. If the solid domain imposes

edges entering the fluid-domain, we must expect corner singularities. Even on convex domains, we cannot expect more than $\hat{\mathbf{u}}_f \in H^2(\hat{\mathcal{F}})$ and on concave domains we even loose H^2-regularity. Some remedy is given by choosing the biharmonic operator for extending the deformation to the fluid-domain, e.g., by the equation

$$\hat{\Delta}^2 \hat{\mathbf{u}}_f = 0 \text{ in } \hat{\mathcal{F}},$$

with the interface boundary conditions

$$\hat{\mathbf{u}}_f = \hat{\mathbf{u}}_s \text{ and } \nabla \hat{\mathbf{u}}_f = \nabla \hat{\mathbf{u}}_s \text{ on } \hat{\mathcal{I}}.$$

The biharmonic operator has better regularity properties and yields a smooth transition from fluid- to solid domain. Numerical experiments show that the case of solid domains that enter the fluid domain with sharp edges imposes strong regularity problems, if large deformation appears. To be precise, it is not a large bending of the solid domain that causes problems, but a large deformation of the fluid domain that can also be due to fixed body translation or rotation of the solid.

A drawback of the biharmonic extension is the large computational effort that is necessary to discretize fourth order equations. One either has to use finite elements with global differentiability or one has to use mixed methods that require the introduction of artificial variables, blowing up the complexity of the overall system. Yet another method for constructing the ALE map is by means of a pseudo-elasticity problem, governed by the linear Navier-Lamé problem

$$-\widehat{\operatorname{div}} \left(\mu(\hat{\nabla} \hat{\mathbf{u}}_f + \hat{\nabla} \hat{\mathbf{u}}_f^T) + \lambda_e \widehat{\operatorname{div}} \, \hat{\mathbf{u}}_f I \right) = 0 \text{ in } \hat{\mathcal{F}}, \quad \hat{\mathbf{u}}_f = \hat{\mathbf{u}}_s \text{ on } \hat{\mathcal{I}}.$$

The "material parameters" μ_e, λ_e can be chosen in such a way that a stiff mapping with little deformation is constructed close to the interface.

In Sect. 5.3.5, we will discuss the quantitative regularity properties of different extension techniques and analyze their performance on simple benchmark problems.

Chapter 3
Coupled Fluid-structure Interactions

In Fig. 3.1 we show a typical configuration of fluid-structure interactions. At time $t = 0$ the domain $\Omega \subset \mathbb{R}^2$ is split into a fluid-part $\hat{\mathcal{F}}$ and a solid-part $\hat{\mathcal{S}}$. This configuration is called the reference configuration and we assume that the system is at rest, i.e. $\mathbf{v}_f = 0$, $p_f = 0$ and $\mathbf{u}_s = 0$. The situation in Fig. 3.1 shows a case, where an elastic obstacle is attached to the bottom of a flow container at Γ_s^D. The flow is driven by an inflow boundary data on Γ_f^D and the fluid's stresses on the obstacle cause a deformation. Here we assume that the outer boundary of the computational domain does not change in time. The interface boundary between fluid- and solid-domain is denoted by $\mathcal{I}(t) = \partial\mathcal{F}(t) \cap \partial\mathcal{S}(t)$. Figure 3.2 shows a typical configuration arising in hemodynamics. Here, the fluid flow is surrounded by elastic walls (e.g. by blood vessels). The coupled dynamics may either be driven by the fluid or by active contraction of the elastic walls (or by a combination of both). Here, the fluid-structure interface $\mathcal{I}(t)$ as well as the outer structure boundary $\Gamma_s(t)$ is subject to motion. Whatever configuration is considered we assume that at all times $t \geq 0$ it holds

$$\Omega(t) = \mathcal{F}(t) \cup \mathcal{I}(t) \cup \mathcal{S}(t), \quad \mathcal{F}(t) \cap \mathcal{S}(t) = \emptyset.$$

This condition will be called the *geometric coupling condition*. The two subdomains for fluid $\mathcal{F}(t)$ and solid $\mathcal{S}(t)$ are governed by the incompressible Navier-Stokes equations and by a hyper-elastic material law. The following sections are devoted to details on the coupling of the two models. Finally, we will formulate a coupled system of equations that describes the full process, fluid, solid and interface conditions.

T. Richter, *Fluid-structure Interactions*, Lecture Notes in Computational Science and Engineering 118, DOI 10.1007/978-3-319-63970-3_3

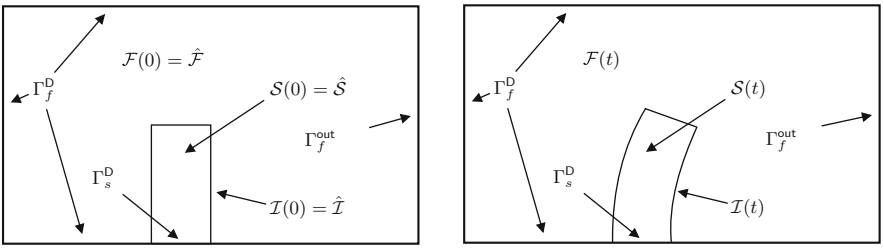

Fig. 3.1 Typical configuration of a fluid-structure interaction problem. The domain is split into fluid- and solid-domain $\Omega = \mathcal{F}(t) \cup \mathcal{I}(t) \cup \mathcal{S}(t)$, divided by the interface. Here, we assume, that the outer boundary of the domain is fixed. The *left sketch* shows the reference configuration at $t = 0$, the *right one* the configuration after some time $t > 0$

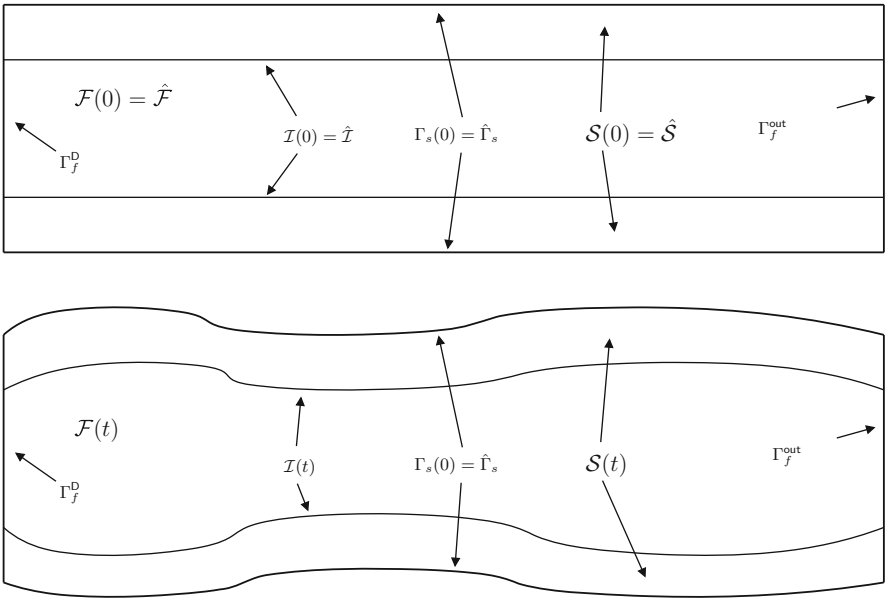

Fig. 3.2 Typical configuration for the flow of blood in a vessel. Here, the fluid is embedded in elastic structures and the outer boundary is subject to motion

3.1 Coupling Conditions

Coupling of fluid- and solid-problem is achieved by boundary conditions on the common interface $\mathcal{I}(t)$ which all stem from simple physical principles:

1. *Kinematic condition:* The velocity of the fluid and the velocity of the solid particles are continuous on the interface.
2. *Dynamic condition:* The normal stresses of fluid and solid are continuous on the interface.

3. *Geometric condition:* Fluid- and solid-domain always match, no holes appear at the interface and the domains do not overlap.

These three coupling conditions describe the interaction between the fluid-phase and the solid-problem. All of these conditions can be described as boundary conditions for the subproblems. Hence, fluid-structure interaction is called a *surface coupled multiphysics problem*, as opposed to *volume coupled multiphysics problems*, where two (or more) subproblems all live in the same domain Ω. A typical example for such volume coupled problems would be given by chemically reactive flows, where the chemical reaction interacts with a flow problem [64, 355].

In the following, we describe the three coupling conditions for fluid-structure interactions in detail.

3.1.1 The Kinematic Condition

The kinematic coupling condition stems from the observation that a viscous fluid will stick at the boundary. Continuity of the velocities on the (moving) interface is simply an extension of the typical no-slip boundary condition known in fluid-dynamics. Hence, on the interface it holds

$$\mathbf{v}_f(x,t) = \mathbf{v}_s(x,t) \text{ on } \mathcal{I}(t).$$

This simple looking boundary condition reveals the great dilemma of fluid-structure interactions, as we usually model both subsystems in different coordinate systems and as the solid's velocity is usually not available in the Eulerian configuration. We must find a way to combine fluid's velocity $\mathbf{v}_f(x_i,t)$ in an interface point $x_i \in \mathcal{I}(t)$ to the solid's velocity $\hat{\mathbf{v}}_s(\hat{x}_i,t) = d_t\hat{\mathbf{u}}_s(\hat{x}_i,t)$ in a corresponding interface material point $\hat{x}_i \in \hat{\mathcal{I}}$. The relation between these two coordinates is given by the mapping property of the solid's deformation $x_i = \hat{x}_i + \hat{\mathbf{u}}_s(\hat{x}_i,t)$ that defines a mapping between the Lagrangian and the Eulerian coordinate framework. We denote this mapping as $\hat{T}_s(\hat{x},t) := \hat{x} + \hat{\mathbf{u}}_s(\hat{x},t)$ and formulate the kinematic coupling condition in the reference system

$$\mathbf{v}_f \circ \hat{T}_s = \hat{\mathbf{v}}_s \text{ on } \hat{\mathcal{I}},$$

as well as in the current configuration

$$\mathbf{v}_f = \hat{\mathbf{v}}_s \circ \hat{T}_s^{-1} \text{ on } \mathcal{I}(t). \tag{3.1}$$

Hence, for every $\hat{x}_i \in \hat{\mathcal{I}}$, it must hold

$$\mathbf{v}_f(\hat{x}_i + \hat{\mathbf{u}}_s(\hat{x}_i,t),t) = \hat{\mathbf{v}}_s(\hat{x}_i,t).$$

This notation reveals the nonlinear character of the kinematic coupling condition. Even if we would consider the coupled dynamics of the linear Stokes equations with the linear Navier-Lamé equations coupling on moving domains introduces a nonlinearity.

If one considers the interaction between a non-viscid fluid with a solid, as appropriate for some applications in aerodynamics, instead of enforcing strong continuity at the interface, only a non-penetration condition is required

$$\mathbf{n} \cdot (\mathbf{v}_f \circ \hat{T}_s) = \mathbf{n} \cdot \hat{\mathbf{v}}_s \text{ on } \hat{\mathcal{I}}.$$

By $\mathbf{n} = J^{-1}\mathbf{F}\hat{\mathbf{n}}$ we denote the normal vector in current configuration. Continuity of the velocities in normal direction prohibits one phase entering the other, it however allows for free slipping of the fluid along the interface.

The kinematic coupling condition has the type of a Dirichlet boundary condition. Usually, one ascribes this condition to the fluid-problem as a Dirichlet condition. If the boundary of the fluid-domain is in motion, the fluid must move along.

3.1.2 The Dynamic Condition

The dynamic coupling condition relates to Newton's third law of action and reaction: the normal stresses, i.e. the forces per area acting on the interface are balanced

$$\mathbf{n}_f \cdot \boldsymbol{\sigma}_f = -\mathbf{n}_s \cdot \boldsymbol{\sigma}_s \text{ on } \mathcal{I}(t),$$

or, using either $\mathbf{n} := \mathbf{n}_f$ or $\mathbf{n} := \mathbf{n}_s$

$$\mathbf{n} \cdot \boldsymbol{\sigma}_f = \mathbf{n} \cdot \boldsymbol{\sigma}_s \text{ on } \mathcal{I}(t). \tag{3.2}$$

Here, we noted this condition in the Eulerian coordinate framework. To realize the dynamic condition, we must however consider the Lagrangian setting used to formulate the structure system. With the Piola transformation, see Definition 2.13 it holds

$$\hat{\mathbf{F}}\hat{\boldsymbol{\Sigma}}_s = \hat{\mathbf{P}} = \hat{J}\hat{\boldsymbol{\sigma}}_s\hat{\mathbf{F}}^{-T},$$

such that (3.2) may be reformulated as

$$\mathbf{n} \cdot \boldsymbol{\sigma}_f = \mathbf{n} \cdot (\hat{J}^{-1}\hat{\mathbf{F}}\hat{\boldsymbol{\Sigma}}_s\hat{\mathbf{F}}^T) = \mathbf{n} \cdot (\hat{J}^{-1}\hat{\mathbf{P}}_s\hat{\mathbf{F}}^T),$$

using the Piola-Kirchhoff stress tensors.

If the kinematic condition is assigned to the fluid problem, the dynamic condition may be added to the solid problem. The fluid's forces act as Neumann condition causing a deformation of the solid domain. Hence, we aim at reformulating the dynamic condition in the Lagrangian reference framework. As already discussed, a

Lagrangian reference system does not make sense for flow problems. Instead, we will inherit the idea of an arbitrary reference system, as introduced in Sect. 2.5.2 for the modeling of flow problems on moving domains. Hence, let $\hat{\mathcal{F}}$ be a fixed domain that shares the common interface with $\hat{\mathcal{S}}$ and let $\hat{T}_f(t) : \hat{\mathcal{F}} \to \mathcal{F}(t)$ be a C^1-diffeomorphism that satisfies

$$\hat{x}_i \in \hat{\mathcal{I}} \quad \hat{T}_f(\hat{x}_i, t) = \hat{T}_s(\hat{x}_i, t) = \hat{x}_i + \hat{\mathbf{u}}_s(\hat{x}_i, t) \in \mathcal{I}(t).$$

The mapping of the fluid domain and the mapping for the solid domain coincide on the common interface. In the inside of the fluid domain, the map $\hat{T}_f(t) : \hat{\mathcal{F}} \to \mathcal{F}(t)$ is arbitrary but sufficiently regular. Then, let

$$\hat{\mathbf{F}}_f := \hat{\nabla}\hat{T}_f, \quad \hat{J}_f := \det(\hat{\mathbf{F}}_f).$$

Following Sect. 2.5.2 we can express the stresses in the reference framework

$$\hat{\mathbf{P}}_f := \hat{J}_f \hat{\boldsymbol{\sigma}}_f \hat{\mathbf{F}}_f^{-T}$$

and base the dynamic coupling condition on the Piola-Kirchhoff traction

$$\hat{\mathbf{n}} \cdot \hat{\mathbf{F}} \hat{\boldsymbol{\Sigma}}_s = \hat{\mathbf{n}} \cdot (\hat{J}_f \hat{\boldsymbol{\sigma}}_f \hat{\mathbf{F}}_f^{-T}). \tag{3.3}$$

By $\hat{\boldsymbol{\sigma}}_f(\hat{x}, t) := \boldsymbol{\sigma}_f(x, t)$ we denote the Lagrangian representation of the fluid's Cauchy stress tensor.

The dynamic coupling condition is a Neumann boundary condition and we usually ascribe it to the solid-problem. There is no mathematical or modeling reason for assigning the conditions to one of the two problems, they have to been seen as integral part of the coupled fluid-structure interaction problem.

3.1.3 The Geometric Condition

The final coupling condition prevents the two subdomains to separate or overlap. This condition describes the domain motion along the interface. It is a consequence of the physical principle that the path of a particle $x = x(\hat{x}, t)$ and its inverse $\hat{x} = \hat{x}(x, t)$ are both continuous functions together with the condition, that the normal velocities of fluid $\mathbf{n} \cdot \mathbf{v}_f$ and solid $\mathbf{n} \cdot \mathbf{v}_s$ are continuous along the common interface.

3.1.4 Interface Regularity and Boundary Conditions

The kinematic coupling condition (3.1) reveals a regularity problem. Considering it as Dirichlet condition for the fluid's velocity on $\mathcal{I}(t)$, standard analysis asks for

Dirichlet boundary data $\mathbf{v}_f^D$ being the trace of an $H^1(\mathcal{F}(t))^3$-function, e.g.

$$\mathbf{v}_f^D \in H^{\frac{1}{2}}(\partial\mathcal{F})^3,$$

such that the trace inequality as well as the inverse inequality hold. Hence, for the solid's velocity we require the regularity

$$\hat{\mathbf{v}}_s = d_t\hat{\mathbf{u}}_s\big|_{\mathcal{I}(t)} \in H^{\frac{1}{2}}(\hat{\mathcal{I}})^3,$$

which is given for velocities

$$\hat{\mathbf{v}}_s = d_t\hat{\mathbf{u}}_s \in H^1(\hat{\mathcal{S}})^3.$$

In general, we can however only expect $\mathbf{u}_s \in H^1(\mathcal{S})^3$ and $\mathbf{v}_s \in L^2(\mathcal{S})^3$ which is not sufficient [243, 304]. If smoothing terms are added to the structure equations, sufficient regularity will be given, see Theorem 2.31. Another possibility for getting sufficient interface regularity is by means of adding stabilization terms in the structure equation. Assuming that the hyperbolic equation is split into two first order equations with help of the relation

$$\hat{\mathbf{v}}_s = d_t\hat{\mathbf{u}}_s,$$

a modification to

$$\hat{\mathbf{v}}_s - \alpha_s\hat{\Delta}\hat{\mathbf{v}}_s = d_t\hat{\mathbf{u}}_s$$

gives enough regularity. For α small enough it can even been shown that the overall accuracy does not suffer. We refer to Frei [151] for details. Finally, for theoretical analysis, the kinematic interface condition can be integrated in time, such that

$$\hat{\mathbf{v}}_f(\hat{x},t) = \hat{\mathbf{v}}_s(\hat{x},t) \Rightarrow \int_0^t \hat{\mathbf{v}}_f(\hat{x},s)\,\mathrm{d}s = \int_0^t \hat{\mathbf{v}}_s(\hat{x},s)\,\mathrm{d}s = \hat{\mathbf{u}}_s(\hat{x},t) - \hat{\mathbf{u}}_s(\hat{x},0).$$

This formulation gives a well-posed alternative for the kinematic interface condition in a weaker sense. Based on this formulation, existence and uniqueness results for a coupled system of the Stokes equations and linear elasticity can be shown [124, 125].

For the following, we will always assume that sufficient interface regularity will be given, e.g. by including strong smoothing of the solid problem, by stabilization of the velocity-deformation relation or simply by sufficient regularity of the data.

Further, the interface conditions (3.1) and (3.3) live in two different coordinate frameworks and it will be required that the two trace-spaces

$$H^{\frac{1}{2}}(\hat{\mathcal{I}}) \cong H^{\frac{1}{2}}(\mathcal{I}(t)),$$

are equivalent, which is given, if in turn

$$H^1(\hat{\mathcal{S}}) \cong H^1(\mathcal{S}(t)) \text{ and } H^1(\hat{\mathcal{F}}) \cong H^1(\mathcal{F}(t)),$$

are equivalent, see Lemma 2.56. For this equivalence to hold, the transformation $\hat{T}_s(t) : \hat{\mathcal{S}} \to \mathcal{S}(t)$ and its inverse must be Lipschitz. Usually, this high regularity (at the interface) can only be guaranteed on very regular domains, and it is usually not given for technical application problems.

3.1.5 Coupled Fluid-structure Interaction

In the following, we couple the incompressible Navier-Stokes equations (2.48) given in Lemma 2.39 and the elastic structure equation (2.38), given in Lemma 2.32 with the kinematic (3.1) and dynamic (3.3) interface condition.

Problem 3.1 (Coupled Fluid-structure Interaction) *Find fluid's velocity* $\mathbf{v}_f$ *and pressure* p_f*, as well as the solid's deformation* $\hat{\mathbf{u}}_s$ *and velocity* $\hat{\mathbf{v}}_s$*, such that*

$$\begin{aligned}
\rho_f(\partial_t \mathbf{v}_f + (\mathbf{v}_f \cdot \nabla)\mathbf{v}_f) - \operatorname{div} \boldsymbol{\sigma}_f &= \rho_f \mathbf{f}, \\
\operatorname{div} \mathbf{v}_f &= 0 \qquad \text{in } \mathcal{F}(t), \\
\hat{\rho}_s^0 \partial_t \hat{\mathbf{v}}_s - \widehat{\operatorname{div}}(\hat{\mathbf{F}}_s \hat{\boldsymbol{\sigma}}_s) &= \hat{\rho}_s^0 \hat{\mathbf{f}}_s, \\
d_t \hat{\mathbf{u}}_s &= \hat{\mathbf{v}}_s \qquad \text{in } \hat{\mathcal{S}}, \\
\mathbf{v}_f &= \hat{\mathbf{v}}_s \circ \hat{T}_s^{-1} \quad \text{on } \mathcal{I}(t), \\
\hat{\mathbf{n}} \cdot (\hat{J}_f \hat{\boldsymbol{\sigma}}_f \hat{\mathbf{F}}_f^{-T}) &= \hat{\mathbf{n}} \cdot \hat{\mathbf{F}} \hat{\boldsymbol{\Sigma}}_s \quad \text{on } \hat{\mathcal{I}}.
\end{aligned} \tag{3.4}$$

Problem 3.1 is written in a monolithic coupled formulation. However, as fluid-problem and solid-problem live in different coordinate frameworks, the interface conditions somehow stand in between both subproblems, one of them being defined in the Lagrangian framework, one in the Eulerian. Further we know that this assignment is arbitrary as we could also state the coupling conditions in the other frameworks.

This system of partial differential equations is not amenable for a standard discretization in a straightforward way, as the motion of the fluid domain and the transformation between both frameworks at the interface must be incorporated.

The coupled fluid-structure interaction problem is a nonlinear system. By coupling of the two subdomains a nonlinearity that acts non-locally is introduced, as motion of the interface will influence the complete domain and hence also the solution in parts distant to the interface. This nonlinearity is difficult to grab, as it is only hidden in the definition of the domains. Even the coupling of fully linear problems like the Stokes equations (2.47) with the linear Navier-Lamé problem (2.33) results in a nonlinear coupled interaction problem.

3.2 Existence and Uniqueness Theory for Fluid-structure Interactions

It is not surprising, that theoretical results for coupled fluid-structure interaction problems are rarely spread. The fluid problem alone is difficult as the incompressible Navier-Stokes equation does not bring along a fully developed theory that gives us general results on existence and uniqueness in two and three dimensions in the non-stationary case. Coupled fluid structure interactions bring along new difficulties. The characteristic one is the motion of the domains $\mathcal{F}(t)$ and $\mathcal{S}(t)$. This domain motion comes from the solution itself, as the interface $\mathcal{I}(t)$ will move with the solid deformation $\mathbf{u}_s$. Low regularity of $\mathbf{u}_s$ will also reduce the regularity of the domains. This in consequence will limit the regularities of the two subproblems.

To circumvent this domain regularity problem many authors study a linearized fluid-structure interaction problem, the coupled dynamics of the linear Stokes equations with the linear Navier-Lamé equations on fixed domains $\mathcal{F}$ and $\mathcal{S}$.

$$\left.\begin{aligned} \rho_f \partial_t \mathbf{v}_f - \nu \Delta \mathbf{v}_f + \nabla p_f &= \rho_f \mathbf{f}_f \\ \operatorname{div} \mathbf{v}_f &= 0 \end{aligned}\right\} \text{ in } \mathcal{F}$$

$$\left.\begin{aligned} \rho_s \partial_t \mathbf{v}_s - \mu_s \Delta \mathbf{u}_s &= \rho_s \mathbf{f}_s \\ \partial_t \mathbf{u}_s &= \mathbf{v}_s \end{aligned}\right\} \text{ in } \mathcal{S} \tag{3.5}$$

$$\left.\begin{aligned} \Big(\rho_f \nu_f \nabla \mathbf{v}_f - p_f I\Big)\mathbf{n}_f + \Big(\mu_s \nabla \mu_s\Big)\mathbf{n}_s &= 0 \\ \mathbf{v}_f &= \mathbf{v}_s \end{aligned}\right\} \text{ on } \mathcal{I}$$

Although linear and without motion of domains, this coupled problem has a similar structure as the fully nonlinear fluid-structure interaction problem. The type of the coupling condition is the same. We coupled the incompressible Stokes equations, an equation of parabolic type with the Navier-Lamé equation of hyperbolic type. And in particular the kinematic coupling condition $\mathbf{v}_f = \partial_t \mathbf{u}_s$ gives rise the regularity issues that already have been discussed.

Existence and regularity for the coupled problem has been investigated by Du et al. [124, 125], Avalos et al. [13] and Avalos and Triggiani [10–12]. We cite one of the main results from [124, 125].

Theorem 3.2 (Linear Fluid-structure Interaction) *Let the initial values* $\mathbf{u}_0, \mathbf{u}_1 \in H_0^1(\mathcal{S}; \Gamma_s^D)^d$ *and* $\mathbf{v}_0 \in H_0^1(\mathcal{F}; \Gamma_f^D)^d$ *(where* Γ_s^D *and* Γ_f^D *are the Dirichlet parts of the domains) be given such that*

$$\Delta \mathbf{u}_0 \in L^2(\mathcal{S})^d, \quad \operatorname{div} \mathbf{v}_0 \in L^2(\mathcal{F})^d, \quad \mathbf{v}_0\big|_{\mathcal{I}} = \mathbf{u}_1\big|_{\mathcal{I}},$$

and let $p_0 \in H^1(\mathcal{F})$ *be given such that*

$$\left(p_0 - \nu_0 \nabla \mathbf{v}_0^T\right)\mathbf{n}_f\Big|_{\mathcal{I}} = \left(\mu_s \nabla \mathbf{u}_0^T \mathbf{n}_s\right)\Big|_{\mathcal{I}}.$$

Further, let the right hand sides be given as

$$\mathbf{f}_f \in H^1(I; H^{-1}(\mathcal{F})), \quad \mathbf{f}_s \in H^1(I; L^2(\mathcal{S})^d).$$

Then, there exists a unique solution $\mathbf{v}_f, \mathbf{u}_s, p_f$ *with*

$$\begin{aligned}
&\mathbf{v}_f \in H^1(I; H_0^1(\mathcal{F}; \Gamma_f^D)^d) \cap W^{1,\infty}(I; L^2(\mathcal{F})^d),\\
&\mathbf{u}_s \in W^{1,\infty}(I; H_0^1(\mathcal{S}; \Gamma_s^d)^d) \cap W^{2,\infty}(I; L^2(\mathcal{S})^d),\\
&p_f \in L^2(I; L^2(\mathcal{F}))
\end{aligned}$$

satisfying the initial conditions $\mathbf{v}_f(0) = \mathbf{v}_0$, $\mathbf{u}_s(0) = \mathbf{u}_0$ *and* $\mathbf{v}_s(0) = \partial_t \mathbf{u}_s(0) = \mathbf{u}_1$ *in* L^2 *and the coupling condition*

$$\mathbf{v}_f\Big|_{\mathcal{I}} = \partial_t \mathbf{u}_s\Big|_{\mathcal{I}} \text{ in } L^2(I; H^{1/2}(\mathcal{I})^d).$$

The solution is bounded by the problem data.
The proof is given in [124, 125]. Similar results are found in [10–12]. These results can be generalized to right hand sides with lower regularity.

Based on this linear fluid-structure interaction problem Failer [133] derived and analyzed adjoint systems in the context of optimization problems.

While this linear system of differential equations is frequently studied and well understood, the full nonlinear problem (3.4) does not allow for such general results. A situation that is similar to the configuration often studied in this book, the interaction of the incompressible Navier-Stokes equations with the St. Venant material, is analyzed by Coutand and Shkoller [106, 107]. We cite the main theorem.

Theorem 3.3 (Theorem 1 of [107]) *Let* $\Omega \subset \mathbb{R}^3$ *be a bounded domain of class* H^4 *and let* $\mathcal{S} \subset \Omega$ *be an open set of class* H^4*, such that* $\bar{\mathcal{S}} \subset \Omega$ *and* $\Omega = \bar{\mathcal{S}} \cup \mathcal{F}$*. Let*

$$\mathbf{f} \in H^n(I; H^{3-n}(\Omega)), \quad n = 0, 1, 2, 3$$

with

$$f(0) \in H^4(\Omega), \quad \partial_t f(0) \in H^4(\Omega).$$

Assume, that the initial data satisfies

$$\mathbf{u}_0 = 0, \quad \mathbf{v}_0 \in H^1(\Omega) \cup H^6(\mathcal{F} \cup \mathcal{S}), \quad \text{div } \mathbf{v}_0\Big|_{\mathcal{F}} = 0.$$

In addition compatibility conditions must hold (see [106, 107] for details).

Then, there exists a $T \in I$ depending on $\mathbf{v}_0, \mathbf{f}$ and $\mathcal{F}$ such that there exists a unique velocity and pressure

$$\mathbf{v} \in L^2(\bar{I}; H_0^1(\Omega)^3), \quad p \in H^n(\bar{I}; H^{3-n}(\mathcal{F})) \quad (n = 0, 1, 2)$$

solving the nonlinear fluid-structure interaction problem on $\bar{I} = (0, \bar{T})$. It holds

$$\begin{aligned}
\mathbf{v}\big|_{\mathcal{F}} &\in H^n(\bar{I}; H^{4-n}(\mathcal{F})^3) \quad (n = 0, \dots, 4), \\
\int_0^t \mathbf{v}\big|_{\mathcal{S}} dt &\in H^n(\bar{I}; H^{4-n}(\mathcal{S})) \quad (n = 0, \dots, 4), \\
\mathbf{u} &\in C^0(\bar{I}; H^1(\Omega)) \\
\mathbf{u}\big|_{\mathcal{F}} &\in C^0(\bar{I}; H^4(\mathcal{F})) \\
\mathbf{u}\big|_{\mathcal{S}} &\in C^0(\bar{I}; H^4(\mathcal{S})),
\end{aligned}$$

where $\mathbf{u}|_{\mathcal{S}}$ is the ALE extension of the domain motion.

The theorem requests very high regularity of the initial data but in particular of the domain Ω and the interface $\mathcal{I} = \partial\mathcal{F} \cap \partial\mathcal{S}$. Only solids that are fully immersed in the fluid can reach this regularity. Extensions to more general domains are currently only available for the linear fluid-structure interaction problem. There exist however generalizations of this result to lower regular initial data [205, 214].

The results cited to this point all consider the coupling of a d-dimensional fluid with a d-dimensional elastic body. The coupling of a d-dimensional fluid to a $d-1$-dimensional solid, e.g. a plate model is investigated by Grandmont and Hillairet [167–169].

3.3 The Added Mass Effect

A proper description of the dynamics that arise in the coupled fluid-structure interaction problem (3.4) is cumbersome. In the discussion on non-dimensionalization of the Navier-Stokes equations in Sect. 2.4.3 we have identified the Reynolds number

$$Re = \frac{\rho_f L_f \bar{v}_f}{\mu_f},$$

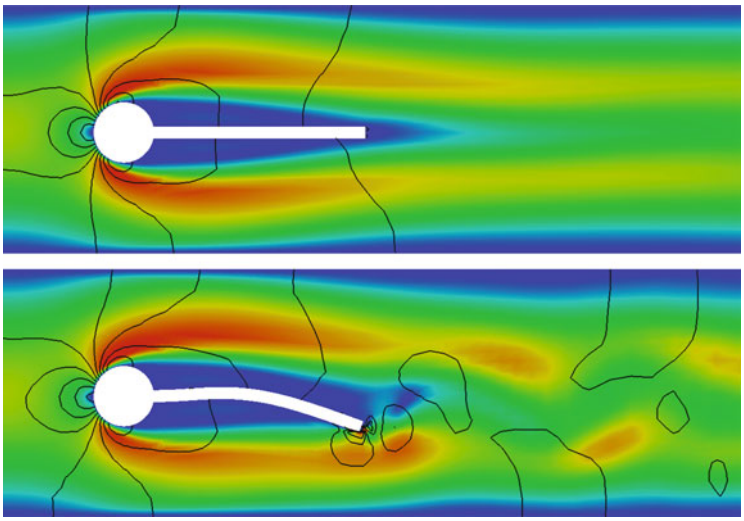

Fig. 3.3 Flow around an elastic obstacle. *Top*: rigid obstacle with stationary solution, *bottom*: elastic obstacle with non-stationary solution. Both flows are at the same Reynolds number $Re = 140$

as the key quantity to describe the property of a flow configuration. Here, by L_f we denote a characteristic length and by $\bar{v}_f$ a characteristic velocity, by $\mu_f = \rho_f \nu_f$ the dynamic viscosity. Flows at low Reynolds numbers usually have stationary solutions (if the problem data does not explicitly depend on time). In the context of fluid-structure interactions, the overall dynamic can dramatically change. In Fig. 3.3 we show the configuration of the flow around an obstacle. In the left sketch, we assume the obstacle to be rigid, where in the right sketch, the beam attached to the rigid circle is considered to be elastic. In both situations, we consider a flow at Reynolds number $Re = 140$. While the pure flow problem with a rigid fixed beam shows a stationary solution, the elastic fluid-structure interaction problem has a time-periodic non-stationary solution if the attached beam is considered to be elastic. The Reynolds number alone is not sufficient to describe the dynamics of the coupled problem, see also Sect. 5.1.1 and Chap. 11 for details on the non-stationary dynamics of coupled fluid-structure interactions.

In the following, we will analyze the interaction of the coupled system at the interface. For this analysis we closely follow the concepts given by Causin et al. [93]. For the analysis we will strongly simplify Problem 3.1 by the following assumptions:

1. The deformation is so small that fully linear models are considered. Eulerian and Lagrangian coordinates coincide "$\mathcal{S}(t) = \hat{\mathcal{S}}$" and a linear material law is taken into account, $\boldsymbol{\sigma}_s = \mu_s \nabla \mathbf{u}_s$.
2. We neglect convective terms in the fluid.

3. We neglect viscous terms in the fluid, such that $\boldsymbol{\sigma}_f = -pI$.
4. The deformation of the fluid domain is so small that it can be neglected $\mathcal{F}(t)=\hat{\mathcal{F}}$.

The remaining system of equation is given by

$$\begin{aligned} \rho_f \partial_t \mathbf{v}_f - \nabla p_f &= g_s(\mathbf{u}_s), \\ \text{div } \mathbf{v}_f &= 0 \qquad\qquad \text{in } \mathcal{F} \\ \rho_s \partial_{tt} \mathbf{u}_s - \mu \Delta \mathbf{u}_s &= g_f(\mathbf{v}_f, p_f) \quad \text{in } \mathcal{S}. \end{aligned}$$

The problem is coupled via boundary terms $g_s(\mathbf{u}_s)$ and $g_f(\mathbf{v}_f, p_f)$ coming from the other equation each. In the equilibrium it will hold $\mu_s \mathbf{n} \cdot \nabla \mathbf{u}_s = -p_f \mathbf{n}$ on the interface $\mathcal{I}$. Further, it holds $\mathbf{v}_f = \partial_t \mathbf{u}_s$ on $\mathcal{I}$. We will formulate this system of partial differential equations using an operator notation with mass $\mathcal{M}$, gradient $\mathcal{B}$, divergence $\mathcal{B}^T$ and diffusion $\mathcal{K}$:

$$\rho_f \mathcal{M} \mathbf{v}_f' + \mathcal{B} p_f = g_s, \quad \mathcal{B}^T \mathbf{v}_f = 0, \quad \rho_s \mathcal{M} \mathbf{u}_s'' + \mathcal{K} \mathbf{u}_s = g_f,$$

where by $g_s \sim \mu_s \mathbf{n} \cdot \nabla \mathbf{u}_s$ and $g_f \sim -p_f \mathbf{n}$ we denote the boundary stresses, with $g_s = g_f$ in equilibrium. Due to the various simplifications, all operators are linear and by differentiation of the divergence equation $d_t \mathcal{B}^T \mathbf{v}_f = \mathcal{B}^T \mathbf{v}_f' = 0$ we can reformulate the fluid problem as

$$\begin{pmatrix} \rho_f \mathcal{M}_{\mathcal{F}\mathcal{F}} & \rho_f \mathcal{M}_{\mathcal{F}\Gamma} & \mathcal{B}_{\mathcal{F}} \\ \rho_f \mathcal{M}_{\Gamma\mathcal{F}} & \rho_f \mathcal{M}_{\Gamma\Gamma} & \mathcal{B}_{\Gamma} \\ \mathcal{B}_{\mathcal{F}}^T & \mathcal{B}_{\Gamma}^T & 0 \end{pmatrix} \begin{pmatrix} \mathbf{v}_{\mathcal{F}}' \\ \mathbf{v}_{\Gamma}' \\ p_f \end{pmatrix} = \begin{pmatrix} 0 \\ g_s \\ 0 \end{pmatrix}.$$

Here, we have split the acceleration into inner $\mathbf{v}_{\mathcal{F}}'$ and interface acceleration $\mathbf{v}_{\Gamma}'$. Next, we simplify this equation by lumping the zeroth order mass operators $\mathcal{M} \sim \mathcal{I}|\mathcal{F}|$ such that no coupling between inner and interface acceleration appears. By $|\mathcal{F}|$ we denote a fluid element's mass:

$$\begin{pmatrix} \rho_f |\mathcal{F}| & 0 & \mathcal{B}_{\mathcal{F}} \\ 0 & \rho_f |\mathcal{F}| & \mathcal{B}_{\Gamma} \\ \mathcal{B}_{\mathcal{F}}^T & \mathcal{B}_{\Gamma}^T & 0 \end{pmatrix} \begin{pmatrix} \mathbf{v}_{\mathcal{F}}' \\ \mathbf{v}_{\Gamma}' \\ p_f \end{pmatrix} = \begin{pmatrix} 0 \\ g_s \\ 0 \end{pmatrix}. \tag{3.6}$$

In the context of finite difference discretizations, the mass will always be diagonal, in the context of spatial finite element discretization, this process is given by integration of the mass-matrix with the trapezoidal rule. The solid problem is reformulated in a similar way:

$$\rho_s |\mathcal{S}| \begin{pmatrix} \mathcal{I} & 0 \\ 0 & \mathcal{I} \end{pmatrix} \begin{pmatrix} \mathbf{u}_{\mathcal{S}}'' \\ \mathbf{u}_{\Gamma}'' \end{pmatrix} + \begin{pmatrix} \mathcal{K}_{\mathcal{S}\mathcal{S}} & \mathcal{K}_{\mathcal{S}\Gamma} \\ \mathcal{K}_{\Gamma\mathcal{S}} & \mathcal{K}_{\Gamma\Gamma} \end{pmatrix} \begin{pmatrix} \mathbf{u}_{\mathcal{S}} \\ \mathbf{u}_{\Gamma} \end{pmatrix} = \begin{pmatrix} 0 \\ g_f \end{pmatrix}. \tag{3.7}$$

For the solution of (3.6) and (3.7) we consider a partitioned approach:

1. We assume that an interface acceleration $\mathbf{v}'_\Gamma$ is given and we solve the fluid problem for $\mathbf{v}'_\mathcal{F}$ and p_f.
2. We use the resulting interface stresses $g_f(\mathbf{v}'_\Gamma, p_f)$ to solve for the new deformation $\mathbf{u}_\Gamma$ on the interface.

Given $\mathbf{v}'_\Gamma$ we can solve Eq. (3.6) for $\mathbf{v}'_\mathcal{F}$ and p_f. First, it holds

$$\mathcal{B}_\mathcal{F}^T \mathcal{B}_\mathcal{F} p_f = -\rho_f |\mathcal{F}| \mathcal{B}_\mathcal{F}^T \mathbf{v}'_\mathcal{F} = \rho_f |\mathcal{F}| \mathcal{B}_\Gamma^T \mathbf{v}'_\Gamma.$$

We assume that the operator $\mathcal{B}_\mathcal{F}^T \mathcal{B}_\mathcal{F}$ is positive. This is equivalent to the condition that the flow problem has a unique solution (see Sect. 2.4.5.1 addressing the inf-sup condition). The pressure can be computed as

$$p_f = \rho_f |\mathcal{F}| (\mathcal{B}_\mathcal{F}^T \mathcal{B}_\mathcal{F})^{-1} \mathcal{B}_\Gamma^T \mathbf{v}'_\Gamma, \tag{3.8}$$

and for the inner acceleration $\mathbf{v}'_\mathcal{F}$ we get:

$$\mathbf{v}'_\mathcal{F} = -\frac{1}{\rho_f |\mathcal{F}|} \mathcal{B}_\mathcal{F} p_f = -\mathcal{B}_\mathcal{F} (\mathcal{B}_\mathcal{F}^T \mathcal{B}_\mathcal{F})^{-1} \mathcal{B}_\Gamma^T \mathbf{v}'_\Gamma. \tag{3.9}$$

With help of relations (3.8) and (3.9) we can use the second line of (3.6) to express the interface forces g_s by:

$$\begin{aligned} g_s &= \rho_f |\mathcal{F}| \mathbf{v}'_\Gamma + \mathcal{B}_\Gamma p_f \\ &= \rho_f |\mathcal{F}| \mathbf{v}'_\Gamma + \rho_f |\mathcal{F}| \mathcal{B}_\Gamma (\mathcal{B}_\mathcal{F}^T \mathcal{B}_\mathcal{F})^{-1} \mathcal{B}_\Gamma^T \mathbf{v}'_\Gamma \\ &= \rho_f |\mathcal{F}| \underbrace{\left(\mathcal{I} + \mathcal{B}_\Gamma (\mathcal{B}_\mathcal{F}^T \mathcal{B}_\mathcal{F})^{-1} \mathcal{B}_\Gamma^T \right)}_{=:\mathcal{M}_A} \mathbf{v}'_\Gamma. \end{aligned} \tag{3.10}$$

The operator $\mathcal{M}_A$ is called the *added mass operator*. It is symmetric and positive (if the flow problem has a unique solution). It maps a given interface acceleration $\mathbf{v}'_\Gamma$ onto a force-vector g_s at the interface. The eigenvalues of $\mathcal{M}_A$ are all larger than one. The new interface stress $g_s = g_f$ goes as right hand side into the structure problem (3.7):

$$\rho_s |\mathcal{S}| \begin{pmatrix} \mathcal{I} & 0 \\ 0 & \mathcal{I} \end{pmatrix} \begin{pmatrix} \mathbf{u}''_\mathcal{S} \\ \mathbf{u}''_\Gamma \end{pmatrix} + \begin{pmatrix} \mathcal{K}_{\mathcal{S}\mathcal{S}} & \mathcal{K}_{\mathcal{S}\Gamma} \\ \mathcal{K}_{\Gamma\mathcal{S}} & \mathcal{K}_{\Gamma\Gamma} \end{pmatrix} \begin{pmatrix} \mathbf{u}_\mathcal{S} \\ \mathbf{u}_\Gamma \end{pmatrix} = \begin{pmatrix} 0 \\ \rho_f |\mathcal{F}| \mathcal{M}_A \mathbf{v}'_\Gamma \end{pmatrix}. \tag{3.11}$$

We assume little impact of diffusion such that we get a diagonal relation for the interface acceleration:

$$\rho_s |\mathcal{S}| \mathbf{u}''_\Gamma \approx \rho_f |\mathcal{F}| \mathcal{M}_A \mathbf{v}'_\Gamma = \rho_f |\mathcal{F}| \mathbf{v}'_\Gamma + \rho_f |\mathcal{F}| \mathcal{B}_\Gamma (\mathcal{B}_\mathcal{F}^T \mathcal{B}_\mathcal{F})^{-1} \mathcal{B}_\Gamma^T \mathbf{v}'_\Gamma. \tag{3.12}$$

By identifying $\mathbf{u}_\Gamma'' = \mathbf{v}_\Gamma'$ we see that the added mass operator $\mathcal{M}_A$ acts as an additional mass on the common interface. This relation is typical for incompressible flows. Due to incompressibility, the fluid has to move along with the solid. The added mass operator is responsible for the special kind of coupling between the structure equation with incompressible flows.

We proceed with the stability analysis by considering a simple time-discretization of the interface Problem (3.12). By $t_0 < \cdots < t_N$ we denote an equidistant partitioning of the time interval with $k := t_{n+1} - t_n$. The interface velocity at time t_n is denoted by $\mathbf{v}_\Gamma^n$. We approximate with backward differences

$$\mathbf{u}_\Gamma''(t_n) = \mathbf{v}_\Gamma'(t_n) \approx \frac{\mathbf{v}_\Gamma^n - \mathbf{v}_\Gamma^{n-1}}{k}. \tag{3.13}$$

We apply this difference approximation to (3.12) and assume that a predictor for the interface velocity on the right hand side is given based on the old time step $\mathbf{v}_\Gamma'(t_n)$. Then, the equation for approximating $\mathbf{v}_\Gamma'(t_{n+1})$ is given by the difference approximation

$$\frac{\rho_s|\mathcal{S}|}{k}(\mathbf{v}_\Gamma^{n+1} - \mathbf{v}_\Gamma^n) = \frac{\rho_f|\mathcal{F}|}{k}\mathcal{M}_A(\mathbf{v}_\Gamma^n - \mathbf{v}_\Gamma^{n-1}).$$

As the operator $\mathcal{M}_A$ is symmetric and positive, there exists an orthogonal system of eigenvectors ω_i and eigenvalues μ_i (larger than one) such that

$$\mathcal{M}_A\omega_i = \mu_i\omega_i, \quad \mu_i > 1, \quad i = 0, 1, \ldots.$$

We develop the unknown solution $\mathbf{v}_\Gamma^n$ in the orthonormal eigenvector basis

$$\mathbf{v}_\Gamma^n = \sum_{i\geq 0} v_i^n \omega_i, \tag{3.14}$$

with coefficients $v_i^n \in \mathbb{R}$. For each $i \geq 0$, the coefficient v_i^n satisfies a scalar difference equation:

$$(v_i^{n+1} - v_i^n) - \frac{\rho_f|\mathcal{F}|}{\rho_s|\mathcal{S}|}\mu_i(v_i^n - v_i^{n-1}) = 0, \quad i = 0, 1, \ldots \tag{3.15}$$

To analyze the stability of the recurrence equation, we solve the difference equation (3.15) using the approach $v_i^n = \lambda_i^n$ to find the fundamental solutions. We get:

$$(\lambda_i^2 - \lambda_i) - \frac{\rho_f|\mathcal{F}|}{\rho_s|\mathcal{S}|}\mu_i(\lambda_i - 1) = 0.$$

This equation has a root at $\lambda_i = 1$ and is equivalent to

$$(\lambda_i - 1)\Big(\lambda_i - \frac{\rho_f |\mathcal{F}|}{\rho_s |\mathcal{S}|}\mu_i\Big) = 0,$$

revealing a second root at

$$\lambda_i = \frac{\rho_f |\mathcal{F}|}{\rho_s |\mathcal{S}|}\mu_i.$$

Every solution to the difference equation (3.15) is given by a combination of these two roots

$$v_i^n = a_i + b_i \lambda_i^n,$$

where by a_i and b_i we denote two constants.

Stability of the solution u_Γ^n represented in the eigenvalue basis (3.14) is given, if the absolute values of all roots are bounded by one:

$$|\lambda_i| \leq 1.$$

If this second root is larger than one, the solution is not stable. The added mass analysis reveals an important stability condition for the coupling of fluid-structure interactions:

$$\frac{\rho_f |\mathcal{F}|}{\rho_s |\mathcal{S}|}\mu_i \leq 1, \quad \text{where } \mu_i \geq 1. \tag{3.16}$$

Remark 3.4 (Stability of the Solution) The simplified stability analysis of the coupled fluid-structure interaction problem is based on a partitioned iteration scheme: First we find the solution of the fluid problem; then, we use this solution to identify the new interface stresses and finally take these interface stresses to solve for the new deformation in the solid domain. Such a decoupled partitioned approach will only be stable, if condition (3.16) is fulfilled. If the density ratio condition is violated, we must use implicit solution approaches that take the full fluid-structure interaction problem as one coupled unity, without partitioning. Such an approach is called *monolithic*.

The density ratio (3.16) serves as a key quantity to describe the coupling behavior of fluid-structure interactions. In aerodynamical applications, where we usually couple the flow of air $\rho_f \approx 1\,\mathrm{kg}\cdot\mathrm{m}^{-3}$ with an elastic structure out of metal $\rho_s \approx 5000\,\mathrm{kg}\cdot\mathrm{m}^{-3}$ the density ratio is very small and partitioned approaches are well-suited for solving the coupled problem. In hemodynamics, both blood and

surrounding tissue have similar densities $\rho_f \approx \rho_s \approx 1\,\mathrm{g}\cdot\mathrm{cm}^{-3}$. Here, partitioned approaches most often fail and implicit schemes with a monolithic view of the coupled problems must be taken into consideration. For a discussion on different solution procedures see Chap. 7.

3.4 Variational Coupling Techniques

Equation (3.4) describe the coupled dynamics of the incompressible fluids in $\mathcal{F}(t)$ and the elastic structure in $\hat{\mathcal{S}}$. The coupling is realized with help of boundary conditions on the common interface $\mathcal{I}$. As preparation for the finite element discretization of the fluid-structure interaction problem, we will derive a monolithic variational formulation of the coupled problem. The variational formulations of the incompressible Navier-Stokes equation and of hyper-elastic structures are given in Lemmas 2.39 and 2.32. Here, we shortly recapitulate the two variational formulations written on the moving domain $\mathcal{F}(t)$ and the fixed structural domain $\hat{\mathcal{S}}$:

$$\begin{aligned}
&\mathbf{v}_f(t) \in \mathcal{V}_f(t), \quad p_f(t) \in \mathcal{L}_f(t) : \\
&\qquad (\rho_f(\partial_t \mathbf{v}_f + (\mathbf{v}_f \cdot \nabla)\mathbf{v}_f), \phi_f)_{\mathcal{F}(t)} + (\boldsymbol{\sigma}_f, \nabla\phi_f)_{\mathcal{F}(t)} = (\rho_f \mathbf{f}_f, \phi_f)_{\mathcal{F}(t)} \\
&\qquad\qquad (\mathrm{div}\ \mathbf{v}_f, \xi_f)_{\mathcal{F}(t)} = 0 \qquad (3.17)
\end{aligned}$$

for all $\phi_f \in \mathcal{V}_f^{\mathrm{test}}, \xi_f \in \mathcal{L}_f$, where the function spaces are defined as

$$\begin{aligned}
\mathcal{V}_f(t) &:= \{\phi \in H^1(\mathcal{F}(t))^d,\ \phi = \mathbf{v}_f^D(t) \text{ on } \Gamma_f^D\}, \\
\mathcal{V}_f(t)^{\mathrm{test}} &:= H_0^1(\mathcal{F}(t); \Gamma_f^D)^d, \\
\mathcal{L}_f(t) &:= L^2(\mathcal{F}(t)),
\end{aligned}$$

and

$$\begin{aligned}
&\hat{\mathbf{u}}_s(t) \in \widehat{\mathcal{V}}_s : \\
&\qquad (\hat{\rho}_s^0 \partial_{tt}\hat{\mathbf{u}}_s, \hat{\phi}_s)_{\hat{\mathcal{S}}} + (\hat{\mathbf{F}}_s \hat{\boldsymbol{\Sigma}}_s, \hat{\nabla}\hat{\phi}_s)_{\hat{\mathcal{S}}} = (\hat{\rho}_s^0 \hat{\mathbf{f}}_s, \hat{\phi}_s)_{\hat{\mathcal{S}}} \quad \forall \hat{\phi}_s \in \widehat{\mathcal{V}}_s^{\mathrm{test}}, \qquad (3.18)
\end{aligned}$$

where test and trial space $\widehat{\mathcal{V}}_s$ is given on the reference domain $\hat{\mathcal{S}}$:

$$\begin{aligned}
\widehat{\mathcal{V}}_s &= \{\phi \in H^1(\hat{\mathcal{S}})^d,\ \phi = \hat{\mathbf{u}}_s^D \text{ on } \Gamma_s^D\}, \\
\widehat{\mathcal{V}}_s^{\mathrm{test}} &= H_0^1(\hat{\mathcal{S}}; \Gamma_s^D)^d.
\end{aligned}$$

Both equations are given with Dirichlet values on Γ_f^D and Γ_s^D, respectively. Here, we have embedded the Dirichlet data into the trial spaces.

This approach for handling the Dirichlet data is the key for a realization of the kinematic coupling condition $\hat{\mathbf{v}}_f = \hat{\mathbf{v}}_s = d_t\hat{\mathbf{u}}_s$ on $\widehat{\mathcal{I}}$. To implement this condition, we must implicitly map between Eulerian and Lagrangian coordinates, as $\mathbf{v}_f$ is given in Eulerian and $\hat{\mathbf{v}}_s$ in the Lagrangian system. We modify the fluid's trial space to

$$\mathcal{V}_f(t, \hat{\mathbf{u}}_s(t), d_t\hat{\mathbf{u}}_s(t)) := \{\phi \in \mathcal{V}_f(t),\ \phi(\hat{x} + \hat{\mathbf{u}}_s(\hat{x}, t)) = \partial_t\hat{\mathbf{u}}_s(\hat{x}, t) \text{ on } \widehat{\mathcal{I}}\}. \tag{3.19}$$

Then, it holds for every $\mathbf{v}_f(t) \in \mathcal{V}_f(t, \hat{\mathbf{u}}_s(t), d_t\hat{\mathbf{u}}_s(t))$ that $\mathbf{v}_f = \mathbf{v}_s$ on $\mathcal{I}(t)$. We restrict possible solutions of the incompressible Navier-Stokes equations to those that already satisfy the kinematic condition.

The dynamic coupling condition can be embedded into the test space $\mathcal{V}_f^{\text{test}}(t)$ in a similar way by gluing the fluid's and solid's test functions $\phi_f \in \mathcal{V}_f^{\text{test}}$ and $\hat{\phi}_s \in \hat{\mathcal{V}}_s^{\text{test}}$:

$$\mathcal{V}_f^{\text{test}}(t, \hat{\mathbf{u}}_s(t), \hat{\phi}_s) := \{\phi_f \in \mathcal{V}_f(t),\ \phi_f(\hat{x} + \hat{\mathbf{u}}_s(\hat{x}, t)) = \hat{\phi}_s(\hat{x}) \text{ on } \widehat{\mathcal{I}}\} \tag{3.20}$$

The test spaces are not independent of each other, instead, the fluid's test space depends on both the solid's deformation (required to cope with the domain motion) and a solid's test function $\hat{\phi}_s$ to ensure continuity. By this restriction of test functions it holds on the interface that

$$\phi_f(\hat{x} + \hat{\mathbf{u}}_s(\hat{x}, t)) = \hat{\phi}_s(\hat{x}).$$

The dynamic coupling condition is recovered by variational principles using integration by parts.

Problem 3.5 (Variational Formulation of the Fluid-structure Interaction Problem) *Let*

$$\hat{\mathbf{u}}_s(t) \in \widehat{\mathcal{V}}_s, \quad \mathbf{v}_f(t) \in \mathcal{V}_f(t, \hat{\mathbf{u}}_s(t), d_t\hat{\mathbf{u}}_s(t)), \quad p_f(t) \in \mathcal{L}_f(t)$$

be the solution of

$$\begin{aligned} &(\rho_f(\partial_t\mathbf{v}_f + (\mathbf{v}_f \cdot \nabla)\mathbf{v}_f), \phi_f)_{\mathcal{F}(t)} + (\boldsymbol{\sigma}_f, \nabla\phi_f)_{\mathcal{F}(t)} \\ &+ (\hat{\rho}_s^0\partial_{tt}\hat{\mathbf{u}}_s, \hat{\phi}_s)_{\hat{\mathcal{S}}} + (\hat{\mathbf{F}}\hat{\boldsymbol{\Sigma}}_s, \hat{\nabla}\hat{\phi}_s)_{\hat{\mathcal{S}}} = (\rho_f\mathbf{f}_f, \phi_f)_{\mathcal{F}(t)} + (\hat{\rho}_s^0\hat{\mathbf{f}}_s, \hat{\phi}_s)_{\hat{\mathcal{S}}} \\ &(\text{div } \mathbf{v}_f, \xi_f)_{\mathcal{F}(t)} = 0 \end{aligned} \tag{3.21}$$

for all test functions

$$\{\phi_f, \hat{\phi}_s\} \in \mathcal{V}_f^{test}(t, \hat{\mathbf{u}}_s(t), \hat{\phi}_s) \times \hat{\mathcal{V}}_s^{test}, \quad \forall \xi_f \in \mathcal{L}_f(t).$$

Lemma 3.6 (Variational Formulation of the Fluid-structure Interaction Problem) *Given sufficient regularity* $\hat{\mathbf{u}}_s(t) \in C^2(\hat{\mathcal{S}})^d \cap C^1(\overline{\mathcal{S}})^d$, $\mathbf{v}_f(t) \in C^2(\mathcal{F}(t))^d \cap C^1(\overline{\mathcal{F}(t)})^d$ *and* $p_f(t) \in C^1(\mathcal{F}(t))^d \cap C(\overline{\mathcal{F}(t)})^d$, *the variational solution to Problem 3.5 is also a classical solution to (3.4) and fulfills the strong interface conditions.*

Proof Let $\hat{\mathbf{u}}_s(t) \in \widehat{\mathcal{V}}_s$, $\mathbf{v}_f(t) \in \mathcal{V}_f(t, \hat{\mathbf{u}}_s(t), d_t\hat{\mathbf{u}}_s(t))$ and $p_f(t) \in \mathcal{L}_f$ be solution to the variational formulation. Let $\hat{\phi}_s \in \widehat{\mathcal{V}}_s^{\text{test}}$ and $\phi_f \in \mathcal{V}_f^{\text{test}}(t, \hat{\mathbf{u}}_s(t), \hat{\phi}_s)$ be arbitrary. Given sufficient regularity we can apply integration by parts to get

$$
\begin{aligned}
&(\rho_f \mathbf{f}_f, \phi_f)_{\mathcal{F}(t)} + (\hat{\rho}_s^0 \hat{\mathbf{f}}_s, \hat{\phi}_s)_{\hat{\mathcal{S}}} \\
&\qquad = (\rho_f(\partial_t \mathbf{v}_f + (\mathbf{v}_f \cdot \nabla)\mathbf{v}_f), \phi_f)_{\mathcal{F}(t)} + (\hat{\rho}_s^0 \partial_{tt} \hat{\mathbf{u}}_s, \hat{\phi}_s)_{\hat{\mathcal{S}}} \\
&\quad - (\operatorname{div} \boldsymbol{\sigma}_f, \phi_f)_{\mathcal{F}(t)} - (\widehat{\operatorname{div}}\,(\hat{\mathbf{F}}_s \hat{\boldsymbol{\Sigma}}_s), \hat{\phi}_s)_{\hat{\mathcal{S}}} + (\operatorname{div} \mathbf{v}_f, \xi_f)_{\mathcal{F}(t)} \\
&\qquad\qquad + \int_{\mathcal{I}(t)} \mathbf{n}_f \cdot \boldsymbol{\sigma}_f \phi_f \, \mathrm{d}o + \int_{\hat{\mathcal{I}}} \hat{\mathbf{n}}_s \cdot (\hat{\mathbf{F}}_s \hat{\boldsymbol{\Sigma}}_s) \hat{\phi}_s \, \mathrm{d}\hat{o}.
\end{aligned}
$$

The classical solutions to fluid and solid problems are recovered by standard variational principles using Dirac series as test functions in the interior of $\mathcal{F}(t)$ and $\hat{\mathcal{S}}$.

Using the Piola transformation, Lemma 2.12 and recalling Definition 2.13 for the different forms of the stress tensors it holds

$$
\int_{\hat{\mathcal{I}}} \hat{\mathbf{n}}_s \cdot (\hat{\mathbf{F}}_s \hat{\boldsymbol{\Sigma}}_s) \hat{\phi}_s \, \mathrm{d}\hat{o} = \int_{\hat{\mathcal{I}}} \hat{\mathbf{n}}_s \cdot (\hat{J}_s \hat{\boldsymbol{\sigma}}_s \hat{\mathbf{F}}_s^{-T}) \hat{\phi}_s \, \mathrm{d}\hat{o} = \int_{\mathcal{I}(t)} \mathbf{n}_s \cdot \boldsymbol{\sigma}_s \phi_s \, \mathrm{d}o.
$$

On $\mathcal{I}(t)$ the two test functions ϕ_f and ϕ_s are continuous $\phi(x) := \phi_f(x) = \phi_s(x)$. Further, on $\mathcal{I}(t)$ it holds $\mathbf{n}_f = -\mathbf{n}_s$ and the dynamic coupling condition is recovered by choosing an appropriate Dirac series on the interface $\mathcal{I}(t)$. □

This variational formulation is not standard in the following sense: test and trial spaces of the velocity spaces depend on the solution itself, as a mapping of coordinates on the interface is required

$$
\mathbf{v}_f(\hat{x} + \hat{\mathbf{u}}_s(\hat{x}, t), t) = d_t \hat{\mathbf{u}}_s(\hat{x}, t), \quad \phi_f(\hat{x} + \hat{\mathbf{u}}_s(\hat{x}, t)) = \hat{\phi}_s(\hat{x}) \quad \forall \hat{x} \in \hat{\mathcal{I}}.
$$

The dependency of the function spaces on the solution has big implications: if we think of finite element discretizations, the first starting step, the creation of a finite element mesh will fail, as the domain depends on the solution itself, which in turn is to be computed on the mesh.

Remark 3.7 (Regularity of the Domain Motion) The motion of the domains must be given in such a way that $\mathcal{F}(t)$ and $\mathcal{S}(t)$ still allow for the construction of well defined Sobolev spaces like $H^1(\mathcal{S}(t))$. Figure 3.4 shows different deformations of a reference domain $\hat{\Omega}$ with C^∞ regularity (a circle) arising from three different mappings $\hat{T}_i : \hat{\Omega} \to \Omega_i$. First, we consider a mapping that is highly regular and smooth, $T_1 \in C^\infty(\hat{\Omega})^d$, second, we choose a mapping that has lower regularity but still is given in $C^{0,1}(\hat{\Omega})$. Here, the domain's boundary will loose its regularity. The cone-conditions however are still valid. Finally, we show a mapping $T_3 \notin C^{0,1}(\hat{\Omega})$. This mapping yields a domain Ω_3 that does not satisfy the cone-condition. Here, some of the important theorems for Sobolev spaces like the trace theorem do not hold any more.

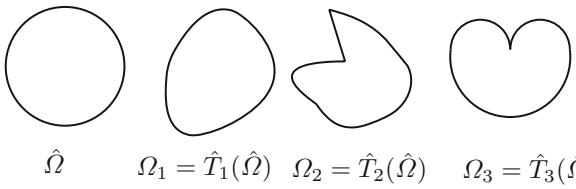

Fig. 3.4 Three different transformations of a smooth domain $\hat{\Omega}$. $T_1 \in C^\infty$, $T_2 \in C^{0,1}$ and $T_3 \notin C^{0,1}$

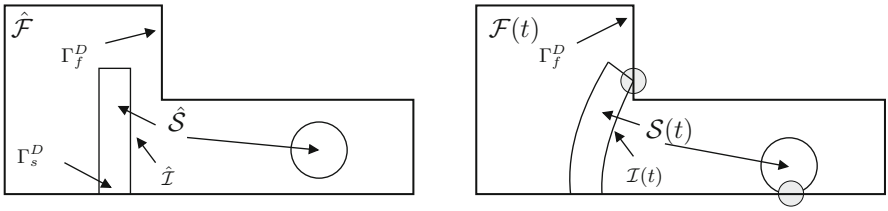

Fig. 3.5 Contact of the elastic structure with the domain's boundary. The fluid-area $\mathcal{F}(t)$ is not connected and hence no domain in the strict sense. Further, by contact the cone-condition or other regularity conditions of the domain can be violated

Remark 3.8 (Contact) Contact and topology change is part of many application problems, think of closing heart valves or of sedimenting solids. It will be important to allow such contact scenarios. However, most theoretical results will ask for strong assumptions on the domains: first as a domain it must be connected. This condition is often violated in the case of contact, see Fig. 3.5. Second, many important theorems from the theory of Sobolev spaces require all domains to fulfill the cone-condition. If a circular obstacle will touch a wall, this condition will most likely be hurt. Again, see Fig. 3.5. See also Remark 6.13 in Sect. 6.6.3 and in particular Chap. 12.

3.5 Fluid-structure Interactions in ALE Coordinates

The variational coupling technique described in the last section still faces the problem of moving domains and requires coordinate transformations between fluid- and solid-problem. While the derived formulation can serve as basis for partitioned solution algorithms that switch between the two subproblems, it cannot be used for monolithic discretization and solution schemes in a strongly coupled way. To cope with the two different coordinate systems and the domain motion, we will couple the Lagrangian solid problem to the Navier-Stokes equations in ALE coordinates, such that the ALE reference configuration $\hat{\mathcal{F}}$ will match the Lagrangian solid configuration $\hat{\mathcal{S}}$. For the following, we assume that by

$$\hat{T}_f(t) : \hat{\mathcal{F}} \to \mathcal{F}(t)$$

a map between reference configuration $\hat{\mathcal{F}}$ and the current configuration $\mathcal{F}(t)$ with sufficient regularity (in space and time) is given.

The ALE formulation of the Navier-Stokes equations has been introduced in Sect. 2.5.2, in particular, see Lemma 2.58. Coupling of test and trial spaces between the ALE formulation of the fluid problem and the Lagrangian solid problem is largely simplified compared to the Eulerian-Lagrangian coupling. Similar to (3.19) and (3.20), we modify the ALE velocity test and trial spaces to

$$\hat{\mathcal{V}}_f(\hat{d}_t\mathbf{u}_s(t)) = \{\hat{\phi} \in \hat{\mathcal{V}}_f,\ \hat{\phi} = d_t\hat{\mathbf{u}}_s \text{ on } \hat{\mathcal{I}}\},$$
$$\hat{\mathcal{V}}_f^{\text{test}}(\hat{\phi}_s) = \{\hat{\phi} \in \hat{\mathcal{V}}_f,\ \hat{\phi} = \hat{\phi}_s \text{ on } \hat{\mathcal{I}}\}.$$

Function spaces on fluid and solid side are still coupled, but this coupling does not require a coordinate system transformation any more. Here however, we must again take notice of the regularity mismatch: while we require by $\mathbf{v}_f \in H^{\frac{1}{2}}(\hat{\mathcal{I}})^d$ a regular trace on the interface, the solid's velocity $\hat{\mathbf{v}}_s = d_t\hat{\mathbf{u}}_s$ usually only has limited L^2-regularity in the domain and no $H^{\frac{1}{2}}$-trace. We will not be able to close this gap and will simply assume that every solution of the solid problem will always satisfy the additional smoothness, such that we may define $\hat{\mathbf{v}}_s \in H^1(\hat{\mathcal{S}})^d$, e.g. by applying strong damping, see Lemma 2.31.

Next, let $\hat{\mathcal{S}}$ and $\hat{\mathcal{F}}$ be such that trace inequality, and inverse trace inequality hold with respect to $\hat{\mathcal{I}}$.

Lemma 3.9 (Gluing of Function Spaces) *Let Ω be a domain of class $C^{0,1}$, split into $\Omega = \hat{\mathcal{F}} \cup \hat{\mathcal{I}} \cup \hat{\mathcal{S}}$, two domains with $C^{0,1}$-boundary and common $C^{0,1}$-interface $\hat{\mathcal{I}} = \partial\hat{\mathcal{F}} \cap \partial\hat{\mathcal{S}}$.*
1. Let $\hat{\phi} \in H_0^1(\hat{\Omega})$. For the restrictions of $\hat{\phi}$ to the subdomains it holds

$$\hat{\phi}_s := \hat{\phi}\Big|_{\hat{\mathcal{S}}} \in \mathcal{V}_s := H_0^1(\hat{\mathcal{S}}; \partial\mathcal{S} \setminus \hat{\mathcal{I}}),$$
$$\hat{\phi}_f := \hat{\phi}\Big|_{\hat{\mathcal{F}}} \in \mathcal{V}_f(\hat{\phi}_s) := \{\psi \in H_0^1(\hat{\mathcal{F}}; \partial\hat{\mathcal{F}} \setminus \hat{\mathcal{I}}),\ \psi = \hat{\phi}_s \text{ on } \hat{\mathcal{I}}\}.$$

2. For every $\hat{\phi}_s \in \mathcal{V}_s$ and $\hat{\phi}_f \in \mathcal{V}_f(\hat{\phi}_s)$ it holds for the composed function

$$\hat{\phi} := \begin{cases} \hat{\phi}_s & \text{in } \hat{\mathcal{S}}, \\ \hat{\phi}_s & \text{on } \hat{\mathcal{I}}, \\ \hat{\phi}_f & \text{in } \hat{\mathcal{F}}, \end{cases}$$

that $\phi \in H_0^1(\Omega)$.

Proof

1. directly follows from the usual results for the restriction of Sobolev spaces $W^{k,p}(\Omega)$ to subdomain $\Omega' \subset \Omega$ (see [350]) and as $\phi \in H_0^1(\hat{\Omega})$ has identical traces in $H^{\frac{1}{2}}(\hat{\mathcal{I}})$ on the interface.
2. follows, as $\hat{\phi}_f$ and $\hat{\phi}_s$ have the same trace on the common interface.

□

This Lemma allows to further simplify the coupling in ALE coordinates. Instead of searching for two velocities and using two different test functions, we simply make the global approach

$$\hat{\mathbf{v}} \in \bar{\mathbf{v}}^D + \hat{\mathcal{V}}, \quad \hat{\mathcal{V}} := H_0^1(\hat{\Omega}; \Gamma^D)^d, \quad \hat{\phi} \in \hat{\mathcal{V}},$$

where $\bar{\mathbf{v}}^D \in H^1(\hat{\Omega})^d$ is a suitable extension of the Dirichlet data. Then, trial and test functions on the two subdomains are given as restrictions

$$\hat{\mathbf{v}}_f := \hat{\mathbf{v}}\Big|_{\hat{\mathcal{F}}}, \quad \hat{\mathbf{v}}_s := \hat{\mathbf{v}}\Big|_{\hat{\mathcal{S}}}, \quad \hat{\phi}_f := \hat{\phi}\Big|_{\hat{\mathcal{F}}}, \quad \hat{\phi}_s := \hat{\phi}\Big|_{\hat{\mathcal{S}}}.$$

3.5.1 Definition of the ALE Map

Next we discuss how to define the ALE map $\hat{T}_f(t) : \hat{\mathcal{F}} \to \mathcal{F}(t)$. In the context of fluid-structure interactions, this map is not given as part of the problem data, but it depends implicitly on the solution.

The solid domain map $\hat{T}_s(t) : \hat{\mathcal{S}} \to \mathcal{S}(t)$ is defined as $\hat{T}_s(\hat{x}, t) = \hat{x} + \hat{\mathbf{u}}_s(\hat{x}, t)$ and based on the solid's deformation $\hat{\mathbf{u}}_s$. This map is physically motivated and describes the transformation between Lagrangian and Eulerian coordinates. Usually, such a map would not make sense for flow problems, as a Lagrangian reference domain most often does not properly depict the configuration. We will introduce a deformation $\hat{\mathbf{u}}_f$ of the fluid domain to define the ALE map

$$\hat{T}_f(\hat{x}, t) := \hat{x} + \hat{\mathbf{u}}_f(\hat{x}, t). \tag{3.22}$$

We note that this deformation is not a physical deformation of the material following particles. Usually, we have $d_t\hat{\mathbf{u}}_f \neq \hat{\mathbf{v}}_f$. Deformation $\hat{\mathbf{u}}_f$ and velocity $\hat{\mathbf{v}}_f$ have no immediate relation.

Defining the ALE map via (3.22) has the benefit, that mapping, deformation gradient $\hat{\mathbf{F}}_f := I + \hat{\nabla}\hat{\mathbf{u}}_f$ and its determinant $\hat{J}_f := \det(\hat{\mathbf{F}}_f)$ are described similar to the solid notation. Further, as one of the requirements of $\hat{T}_f$ is a correct mapping of interface points

$$\hat{x} \in \hat{\mathcal{I}} \quad \Rightarrow \quad \hat{T}_f(\hat{x}, t) = \hat{T}_s(\hat{x}, t) \quad \Leftrightarrow \quad \hat{x} + \hat{\mathbf{u}}_f(\hat{x}, t) = \hat{x} + \hat{\mathbf{u}}_s(\hat{x}, t),$$

we must enforce deformations that have a continuous transition to the solid's deformation $\hat{\mathbf{u}}_f = \hat{\mathbf{u}}_s$ on $\hat{\mathcal{I}}$. On the outer boundaries of the domain (that does not move) $\Gamma_f^D \cup \Gamma_f^{\text{out}} = \partial\hat{\mathcal{F}} \setminus \hat{\mathcal{I}}$, the ALE map may exhibit deformation in tangential direction, but no transformation in normal direction is allowed. Hence, $\hat{\mathbf{u}}_f$ must satisfy the boundary conditions

$$\hat{\mathbf{u}}_f = \hat{\mathbf{u}}_s \text{ on } \hat{\mathcal{I}}, \quad \hat{\mathbf{n}} \cdot \hat{\mathbf{u}}_f = 0 \text{ on } \partial\hat{\mathcal{F}} \setminus \hat{\mathcal{I}}. \tag{3.23}$$

Lemma 2.58 requires high smoothness of the ALE map, such that solutions to the ALE formulation of the Navier-Stokes equations correspond to the standard weak solution of the Navier-Stokes equations. Namely, we require that $\hat{T}_f$ is a C^1-diffeomorphism. In light of (3.22) this calls for $\hat{\mathbf{u}}_f \in C^1$ such that $\hat{x} + \hat{\mathbf{u}}_f$ is invertible, e.g. $\hat{J}_f > 0$. For $\hat{\mathbf{u}}_f \in C^1$ embedding theorems require $\hat{\mathbf{u}}_f \in H^3(\Omega)$.

We will define $\hat{\mathbf{u}}_f$ as an extension of $\hat{\mathbf{u}}_s$ from the interface $\hat{\mathcal{I}}$ into the fluid domain by using a differential operator $\mathcal{L} : \hat{\mathcal{F}} \to \mathbb{R}^d$:

$$\mathcal{L}(\hat{\mathbf{u}}_f) = 0, \quad \hat{\mathbf{u}}_f = \hat{\mathbf{u}}_s \text{ on } \hat{\mathcal{I}} \text{ and } \hat{\mathbf{n}} \cdot \hat{\mathbf{u}}_f = 0 \text{ on } \partial\hat{\mathcal{F}} \setminus \hat{\mathcal{I}}.$$

Choosing $\mathcal{L}$ as the harmonic operator, the usual smoothing property will guarantee sufficient regularity in the interior of $\hat{\mathcal{F}}$ (as the right hand side is zero). Close to the boundaries $\partial\mathcal{F}$ however, the regularity will be restricted. This restriction is one by means of the geometry, e.g. by edges of the domain, but also limited by the regularity of the boundary data $\hat{\mathbf{u}}_f = \hat{\mathbf{u}}_s$ on the interface $\hat{\mathcal{I}}$. In general, we cannot expect that the extension procedure will give a fluid deformation field with satisfactory regularity. In Sect. 5.3.5 we will see that regularity problems of this map are indeed a pitfall in implementations of the ALE method. In particular reentrant edges pose severe problems. Such edges appear, whenever the solid domain has sharp corners entering the surrounding fluid domain.

Besides regularity considerations, the extension operator $\mathcal{L}$ should be such that interior points $\hat{x} \in \hat{\mathcal{F}}$ are not mapped outside the fluid-domain $\hat{x} + \hat{\mathbf{u}}_f(\hat{x}, t) \notin \mathcal{F}(t)$. For this assumption to hold, the operator should for a start satisfy the maximum principle. In addition, the deformation $\hat{\mathbf{u}}_f$ must fulfill a certain smallness of growth. To illuminate this problem, we consider as example the one dimensional reference domain $\hat{\mathcal{F}} = (0, 2)$ and the Eulerian counterpart $\mathcal{F} = (0, 1)$. The deformation

$$\hat{\mathbf{u}}(\hat{x}) = -\frac{1}{2}\hat{x} \quad \Rightarrow \quad \hat{T}_f(\hat{x}) = \frac{1}{2}\hat{x},$$

will perfectly serve as ALE map, as $\hat{T}_f : \hat{\mathcal{F}} \to \mathcal{F}$. The map

$$\hat{\mathbf{u}}(\hat{x}) = -\frac{1}{8}\hat{x}^4 \quad \Rightarrow \quad \hat{T}_f(\hat{x}) = \hat{x} - \frac{1}{8}\hat{x}^4,$$

however satisfies $\hat{T}_f(0) = 0$ and $\hat{T}_f(2) = 1$, but $\hat{T}_f : \hat{\mathcal{F}} \not\to \mathcal{F}$, as $T_f(\frac{3}{2}) \approx 1.18 \notin \mathcal{F}$. Even if T_f has sufficient regularity, the inverse T_f^{-1} may not be well defined. The gradient of $\nabla \mathbf{u}_f$ must be bounded to prevent maps, that point out of the domain. It is difficult to guarantee this property by a priori limits, but we show in Sect. 5.3.5, that such problems frequently appear, in particular if we deal with reentrant edges.

The simplest choice for defining the extension operator $\mathcal{L}$ is a harmonic extension of the solid deformation:

$$-\hat{\Delta}\hat{\mathbf{u}}_f = 0 \text{ in } \hat{\mathcal{F}}, \quad \hat{\mathbf{u}}_f = \hat{\mathbf{u}}_s \text{ on } \hat{\mathcal{I}} \text{ and } \hat{\mathbf{u}}_f = 0 \text{ on } \hat{\partial}\mathcal{F} \setminus \hat{\mathcal{I}},$$

or, as we have noted

$$\hat{\mathbf{n}} \cdot \hat{\mathbf{u}}_f = 0 \text{ on } \hat{\partial}\mathcal{F} \setminus \hat{\mathcal{I}}.$$

The drawback of such an harmonic extension is the limited regularity of the solution. If the fluid domain has reentrant edges, e.g. a solid with sharp edges entering into the fluid domain, it will usually just hold $\hat{\mathbf{u}}_f \in H^1(\hat{\mathcal{F}})^d$, but $\hat{\mathbf{u}}_f \notin H^2(\hat{\mathcal{F}})$. Furthermore, even H^2-regularity is not sufficient for the strict C^1 assumption that is required to give equivalence of the H^1-spaces on $\mathcal{F}$ and $\hat{\mathcal{F}}$.

Another possibility for the definition of the deformation $\hat{\mathbf{u}}_f$ is by means of pseudo-elasticity problem

$$-\widehat{\operatorname{div}}\left(\mu_e(\hat{\nabla}\hat{\mathbf{u}}_f + \hat{\nabla}\hat{\mathbf{u}}_f^T) + \lambda_e \widehat{\operatorname{div}}\,\hat{\mathbf{u}}_f\right) = 0,$$

$$\hat{\mathbf{u}}_f = \hat{\mathbf{u}}_s \text{ on } \hat{\mathcal{I}} \text{ and } \hat{\mathbf{n}} \cdot \hat{\mathbf{u}}_f = 0 \text{ on } \partial\hat{\mathcal{F}} \setminus \hat{\mathcal{I}}.$$

Depending on the specific type of boundary conditions, the solution suffers from similar regularity restrictions as the harmonic extension and we might again lose $\hat{\mathbf{u}}_f \in H^2(\hat{\mathcal{F}})$, if the fluid-domain has concave corners, see [292].

A further possibility for the definition of $\hat{\mathbf{u}}_f$ is a biharmonic extension of the solid's velocity:

$$\Delta^2 \mathbf{u}_f = 0 \text{ in } \hat{\mathcal{F}},$$

that—as a fourth order operator—asks for two boundary conditions. First, for satisfying the geometric coupling condition, we choose

$$\hat{\mathbf{u}}_f = \hat{\mathbf{u}}_s \text{ on } \hat{\mathcal{I}} \text{ and } \hat{\mathbf{n}} \cdot \hat{\mathbf{u}}_f = 0 \text{ on } \partial\hat{\mathcal{F}} \setminus \hat{\mathcal{I}}.$$

Second, we can prescribe boundary conditions for the gradients or higher order derivatives of the solution. The choice

$$\hat{\mathbf{n}} \cdot \hat{\nabla}\hat{\mathbf{u}}_f = \hat{\mathbf{n}} \cdot \hat{\nabla}\hat{\mathbf{u}}_s \text{ on } \hat{\mathcal{I}} \text{ and } \hat{\Delta}\hat{\mathbf{u}}_f = 0 \text{ on } \partial\hat{\mathcal{F}} \setminus \hat{\mathcal{I}},$$

defines an extension of $\hat{\mathbf{u}}_s$ that is not only continuous but that has continuous normal derivatives. This construction will prevent rapid changes of $\hat{\mathbf{u}}_f$ close to the interface. The biharmonic extension has better regularity at edges, see e.g. [53].

In Sect. 5.3.5 we demonstrate a numerical study showing the performance of the different mesh motion models. We will see that the biharmonic extension gives us the best quality for the ALE map. Numerical approximation of this fourth order equation is however very costly, so that we usually try to avoid it.

3.5.2 Coupled ALE Formulation

By all these preparations, we can combine the variational coupling technique indicated by Lemma 3.9 with the different technique for an implicit construction of the ALE map. As fluid's and solid's deformation $\hat{\mathbf{u}}_f$ and $\hat{\mathbf{u}}_s$ both have the same H^1-regularity and as they share a common trace on $\hat{\mathcal{I}}$, coupling will also be realized with help of Lemma 3.9. Instead of separating two deformations, we search for one global field $\hat{\mathbf{u}} \in \bar{\mathbf{u}}_s^D + H_0^1(\Omega; \Gamma^D)^d$.

Problem 3.10 (Variational Formulation of the Fluid-structure Interaction Problem in ALE Coordinate) *Let $\bar{\mathbf{u}}_s^D(t) \in H_0^1(\hat{\mathcal{S}}; \hat{\mathcal{I}})^d$ and $\bar{\mathbf{v}}^D(t) \in H_0^1(\hat{\Omega}; \Gamma_f^{out})^d$ be extensions of the Dirichlet data. With*

$$\hat{\mathcal{W}} := H_0^1(\hat{\Omega})^d, \quad \hat{\mathcal{V}} := H_0^1(\hat{\Omega}; \Gamma^D)^d, \quad \hat{\mathcal{L}}_f := L^2(\hat{\mathcal{F}}),$$

we find

$$\hat{\mathbf{u}}(t) \in \bar{\mathbf{u}}_s^D + \hat{\mathcal{W}}, \quad \hat{\mathbf{v}}(t) \in \bar{\mathbf{v}}^D(t) + \hat{\mathcal{V}}, \quad \hat{p}_f(t) \in \hat{\mathcal{L}}_f,$$

as solution to the coupled problem

$$\begin{aligned}
\rho_f \big(\hat{J}_f (\partial_t \hat{\mathbf{v}} + (\hat{\mathbf{F}}_f^{-1}(\hat{\mathbf{v}} - \partial_t \hat{\mathbf{u}}) \cdot \nabla)\hat{\mathbf{v}}, \hat{\phi} \big)_{\hat{\mathcal{F}}} + (\hat{\rho}_s^0 \partial_t \hat{\mathbf{v}}, \hat{\phi})_{\hat{\mathcal{S}}} \\
+ \big(\hat{J}_f \hat{\boldsymbol{\sigma}}_f \hat{\mathbf{F}}_f^{-T}, \hat{\nabla}\hat{\phi} \big)_{\hat{\mathcal{F}}} + (\hat{\mathbf{F}}_s \hat{\boldsymbol{\Sigma}}_s, \hat{\nabla}\hat{\phi})_{\hat{\mathcal{S}}} = (\hat{J}_f \hat{\rho}_f \hat{\mathbf{f}}_f, \hat{\phi})_{\hat{\mathcal{F}}} + (\hat{\rho}_s^0 \hat{\mathbf{f}}_s, \hat{\phi})_{\hat{\mathcal{S}}} \\
\big(\widehat{\operatorname{div}} (\hat{J}_f \hat{\mathbf{F}}_f^{-1} \hat{\mathbf{v}}), \hat{\xi} \big)_{\hat{\mathcal{F}}} = 0, \\
(\partial_t \hat{\mathbf{u}} - \hat{\mathbf{v}}, \hat{\psi}_s)_{\hat{\mathcal{S}}} = 0, \\
(\hat{\nabla}\hat{\mathbf{u}}, \hat{\nabla}\hat{\psi}_f)_{\hat{\mathcal{F}}} = 0,
\end{aligned} \tag{3.24}$$

for all test functions

$$\hat{\phi} \in \hat{\mathcal{V}}, \quad \hat{\psi}_s \in \hat{\mathcal{L}}_s = L^2(\hat{\mathcal{S}})^d, \quad \hat{\xi}_f \in \hat{\mathcal{L}}_f, \quad \hat{\psi}_f \in H_0^1(\hat{\mathcal{F}}).$$

Lemma 3.11 (Variational Formulation of the Fluid-structure Interaction Problem in ALE Coordinate) *Given sufficient regularity of* $\hat{\mathbf{v}}, \hat{\mathbf{u}}, \hat{p}_f$*, the variational solution of Problem 3.10 is also a classical solution to* (3.4) *and fulfills the strong interface conditions.*

Proof Given sufficient regularity, the proof is an implication of Lemmas 2.58 and 3.6. Here, for simplicity we have considered an harmonic extension of the deformation to the fluid domain. □

Remark 3.12 (Test and Trial Spaces) The variational formulation given in Lemma 3.11 uses different trial and test spaces, as the two equations for the extension of the deformation and the relationship between solid's deformation and velocity do not interact.

It is not appropriate to combine $\hat{\psi}_f$ and $\hat{\psi}_s$ to one global function, e.g. $\hat{\phi} \in H^1(\hat{\Omega})^d$. First, H^1 is the wrong regularity to define the L^2-projection $\partial_t \hat{\mathbf{u}} \mapsto \hat{\mathbf{v}}$. Second, glueing of the test spaces would result in an additional boundary condition of the extension operator on the interface:

$$(\hat{\nabla}\hat{\mathbf{u}}, \hat{\nabla}\hat{\psi})_{\hat{\mathcal{F}}} = -(\hat{\Delta}\hat{\mathbf{u}}, \hat{\psi})_{\hat{\mathcal{F}}} + \langle \mathbf{n} \cdot \hat{\nabla}\hat{\mathbf{u}}, \hat{\psi} \rangle_{\hat{\mathcal{I}}}.$$

This second condition $\mathbf{n} \cdot \hat{\nabla}\hat{\mathbf{u}}_f = 0$, in addition to $\hat{\nabla}\hat{\mathbf{u}}_f = \hat{\nabla}\hat{\mathbf{u}}_s$ would lead to a faulty feedback on the solid's deformation. In numerical realization, it is sufficient to correct the variational formulation and use

$$A_{\text{ext}}(\hat{\mathbf{u}}, \hat{\psi}) := (\hat{\nabla}\hat{\mathbf{u}}, \hat{\nabla}\hat{\psi})_{\hat{\mathcal{F}}} - \langle \hat{\mathbf{n}}_f \cdot \hat{\nabla}\hat{\mathbf{u}}, \hat{\psi} \rangle_{\hat{\mathcal{I}}}$$

as extension operator. This modification allows to actually use one global test space.

Anyway, by defining

$$\mathcal{X} := \hat{\mathcal{W}} \times \hat{\mathcal{V}} \times \hat{\mathcal{L}}_f, \quad \mathcal{Y} := \hat{\mathcal{V}} \times \hat{\mathcal{L}}_f \times \hat{\mathcal{L}}_s \times H_0^1(\hat{\mathcal{F}}),$$

we can introduce a short notation and find $\hat{\mathbf{U}} := \{\hat{\mathbf{u}}, \hat{\mathbf{v}}, \hat{p}_f\}$ given as

$$\hat{\mathbf{U}}(t) = \bar{\mathbf{U}}^D(t) + \mathcal{X},$$

such that

$$A(\hat{\mathbf{U}}, \hat{\mathbf{\Phi}}) = 0 \quad \forall \hat{\mathbf{\Phi}} = \{\hat{\phi}, \hat{\xi}_f, \hat{\psi}_s, \hat{\psi}_f\} \in \mathcal{Y},$$

where the semilinear form $A(\cdot)(\cdot)$ is given in accordance to the variational formulation (3.24).

Further, we point out that the spaces $\mathcal{V}$ and $\mathcal{W}$ differ by boundary data only. On a fluid's outflow boundary Γ_f^{out} functions in $\mathcal{V}$ are free, where it holds $\hat{\phi} = 0$ on Γ_f^{out} for all $\hat{\phi} \in \mathcal{W}$.

A formulation of the fluid-structure interaction problem in Arbitrary Lagrangian Eulerian coordinates has the great advantage that the domain motion can be captured in the deformation field $\hat{\mathbf{u}}$. The interface between fluid and solid will be fixed at all times. Thinking of finite element discretizations it will be easy to construct meshes $\hat{\mathcal{F}}_h$ of the fluid domain $\hat{\mathcal{F}}$ and $\hat{\mathcal{S}}_h$ of the solid domain $\hat{\mathcal{S}}$ and these meshes will always resolve the interface. Such methods are called *interface-tracking techniques*. The artificial fluid domain map $\hat{T}_f$ and the fluid domain's deformation $\hat{\mathbf{u}}_f$ play the most important role. If the regularity of $\hat{x} + \hat{\mathbf{u}}_f$ is not sufficient, the ALE formulation in Lemma 3.11 will not be equivalent to the coupled formulation in physical coordinates. As the mapping $\hat{T}_f$ is not given by physical models, it will be a purely numerical task to generate mapping of high regularity.

Further, as argued in Sect. 2.5, the regularity of the ALE map will also have impact on the inf-sup constant. This enters stability estimates for the solution of the Navier-Stokes equations and it will also be an important factor for error estimates in the context of the finite element method.

Finally, the ALE method has limits, if the domain motion is such that a differentiable and invertible mapping does not exist at all. This can happen, if topology change occur due to contact of the structure with the domain's boundary or due to self-contact of the structure with other structural parts. Here, a fully monolithic ALE technique will not be suitable. In Sect. 3.6, we will introduce an alternative approach to derive a monolithic variationally coupled formulation for fluid-structure interactions. This will be able to also consider problems with large motion or contact, but it will not be of *interface-tracking* type.

The ALE method is perhaps one of the most reliable and efficient techniques, if it comes to interaction problems with such a stiff coupling that monolithic approaches must be considered. It is well suited to handle large deformations. As the domains are fixed for all times, and as the interface is always properly defined, it is possible to use standard discretization and solver techniques in approximate settings.

Finally, to better understand the limits of the ALE approach we consider a simple configuration, where a solid structure $\mathcal{S}(t)$ is moving within the fluid domain. Here, we can assume that this structure is rigid and at time $t = 0$ resting in the center of long channel, see Fig. 3.6. The fluid is falling down and getting close to the bottom. We simply assume that the rigid body motion in vertical direction is given with a constant speed $\bar{v}$ as

$$\hat{\mathbf{u}}_s(\hat{x}) = \begin{pmatrix} 0 \\ -\bar{v} \cdot t \end{pmatrix}.$$

We want to model this problem in ALE coordinates, hence we must find a deformation field $\hat{\mathbf{u}}_f$ that maps the reference state $\hat{\mathcal{F}} = \mathcal{F}(0)$ to the current configuration $\mathcal{F}(t)$. On the interface $\hat{\mathcal{I}}$ it must hold $\hat{\mathbf{u}}_f = \hat{\mathbf{u}}_s$. Further, on the bottom on top boundary, it must hold $\hat{\mathbf{u}}_f = 0$, such that in between we can approximate the

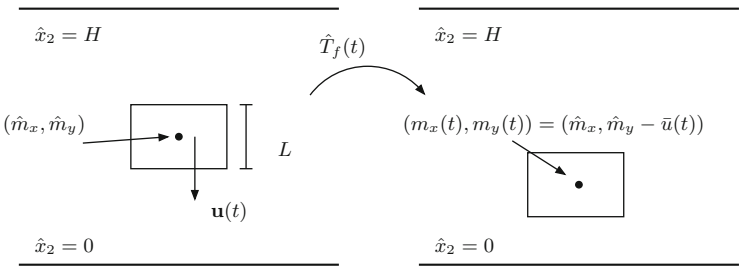

Fig. 3.6 Flow around a rigid obstacle that is falling down

ALE map $\hat{T}_f(\hat{x}, t) = \hat{x} + \hat{\mathbf{u}}_f(\hat{x}, t)$ as (considering only the lower part of the domain)

$$\hat{T}_f(\hat{x}, t) = \begin{pmatrix} \hat{x}_1 \\ \hat{x}_2 - \frac{\hat{x}_2}{\hat{m}_y - \frac{L}{2}} \bar{v} \cdot t \end{pmatrix}, \quad \hat{x}_2 \in [0, \hat{m}_y - \frac{L}{2}],$$

with gradient

$$\hat{\nabla} \hat{T}_f(\hat{x}, t) \approx \begin{pmatrix} 1 & 0 \\ 0 & 1 - \frac{1}{\hat{m}_y - L/2} \bar{v} \cdot t \end{pmatrix}, \quad \hat{x}_2 \in [0, \hat{m}_y - \frac{L}{2}],$$

with $\|\hat{\nabla} \hat{T}_f\| \to 0$ for $t \to (\hat{m}_y - L/2)/\bar{v}$. The ALE map will degenerate, if the rigid obstacle gets close to the bottom of the domain. This simple example shows that often it is the deformation of the fluid-domain that will cause a breakdown of ALE techniques and not a large deformation of the solid.

Here, relief could be given by the following approach: if for some time $t' \geq 0$ the derivatives of the mapping get too large, a new reference domain $\hat{\mathcal{F}}'$ together with a new mapping $\hat{T}_f'$ is taken as basis of the ALE formulation. The solution $\hat{v}_f(t')$ must then be mapped onto the new reference framework and the formulation can be continued from here. In the context of discretized schemes, such an approach is called *remeshing* or *reinitialization*. It is extensively discussed in literature and part of most efficient implementations of the ALE technique [80, 318].

3.6 Fully Eulerian Formulation for the Fluid-structure Interaction Problem

The success of the ALE formulation for fluid-structure interactions crucially depends on the quality of the fluid domain map $\hat{T}_f$. If this map looses its regularity or invertibility, equivalence between the variational formulation of the coupled problem in Eulerian/Lagrangian coordinate—Problem 3.5—and the variational formulation of the coupled problem in ALE/Lagrangian coordinates—Problem 3.10—

will not hold any more. Further, we have seen that bounds on $\hat{\nabla}\hat{T}_f$ and $\nabla\hat{T}_f^{-1}$ will enter basic inequalities like the trace inequality, Poincaré inequality and also the inf-sup inequality. Even if the derivatives of $\hat{T}_f$ and $\hat{T}_f^{-1}$ are bound, the constants that will finally enter stability and error estimates can get very large.

In this section, we will introduce an alternative variational formulation for the coupled fluid-structure interaction problem that takes the opposite way: Instead of mapping the moving fluid domain onto a fixed reference domain $\hat{T}_f(t) : \hat{\mathcal{F}} \to \mathcal{F}(t)$ we use an inverse map to transform the Lagrangian solid reference domain onto the Eulerian moving solid domain $\hat{T}_s(t) : \hat{\mathcal{S}} \to \mathcal{S}(t)$. Like the ALE map $\hat{T}_f$, this transformation is defined with help of the deformation $\hat{\mathbf{u}}_s$

$$\hat{T}_s(\hat{x}, t) := \hat{x} + \hat{\mathbf{u}}_s(\hat{x}, t).$$

There is one fundamental difference between $\hat{T}_s$ and $\hat{T}_f$. While the ALE map $\hat{T}_f$ is based on the arbitrary deformation field $\hat{\mathbf{u}}_f$, and $\hat{\mathcal{F}}$ does not play a physical role, the solid domain map $\hat{T}_s$ is based on $\hat{\mathbf{u}}_s$, which is the physically relevant deformation between Lagrangian and Eulerian system. Assuming that the material is continuous that it is neither infinitely extended or compressed to a point, it must hold that

1. The mapping $\hat{T}_s$ is a bijection between $\hat{\mathcal{S}}$ and $\mathcal{S}(t)$.
2. The mapping $\hat{T}_s$ and the inverse $\hat{T}_s^{-1}$ are differentiable.
3. The determinants $\hat{J}_s := \det(\hat{\nabla}\hat{T}_s)$ and $\hat{J}_s^{-1} = \det(\nabla\hat{T}_s^{-1})$ are bound away from zero and infinity.

Both formulations, Eulerian and Lagrangian are well suited for describing elastic material. The transition to the Lagrangian reference system is mainly for practical reasons, as deformation stresses can be best modeled in a particle centered viewpoint.

3.6.1 Elastic Structures in Eulerian Coordinates

In Sect. 2.1.6, we derived the basic conservation principles for moving volumes that were based on conservation of mass, momentum and angular momentum. Here, we will derive the Eulerian formulation for the structure problem in the moving solid domain $\mathcal{S}(t)$ that is given by the Lagrangian deformation of $\hat{\mathcal{S}}$:

$$\mathcal{S}(t) = \{x \in \mathbb{R}^d \,|\, x = \hat{x} + \hat{\mathbf{u}}_s(\hat{x}, t) \ \forall \hat{x} \in \hat{\mathcal{S}}\}.$$

By mass and momentum conservation, we derived the non-conservative formulation of the momentum equation (2.14)

$$\rho_s \partial_t \mathbf{v}_s + \rho_s \mathbf{v}_s \cdot \nabla \mathbf{v}_s - \nabla \cdot \boldsymbol{\sigma}_s = \rho_s \mathbf{f} \text{ in } \mathcal{S}(t), \tag{3.25}$$

where $\rho_s(x,t)$ is the Eulerian density of the solid at time t in a point $x \in \mathcal{S}(t)$, $\mathbf{v}_s(x,t)$ is the Eulerian velocity and $\boldsymbol{\sigma}_s$ the Eulerian Cauchy-Stress tensor of the solid problem. Here, it is necessary to remember that the transformation to the Lagrangian or to an arbitrary reference system only concerns the definition area of functions $\mathcal{S}(t)$ and $\hat{\mathcal{S}}$ not the image. We do not transform unit vectors, such that it holds

$$\mathbf{v}_s(x,t) = \hat{\mathbf{v}}_s(\hat{T}_s(\hat{x},t),t) = \hat{\mathbf{v}}_s(\hat{x},t)$$

for every pair x and $\hat{x}$ with $x = \hat{T}_s(\hat{x},t)$. For defining a Eulerian representation $\boldsymbol{\sigma}_s$ of the Cauchy stress tensor, we must first introduce a Eulerian counterpart $\mathbf{u}_s$ of the Lagrangian deformation $\hat{\mathbf{u}}_s$ by the relation

$$x = \hat{x} + \hat{\mathbf{u}}_s(\hat{x},t) \quad \Leftrightarrow \quad \hat{x} = x - \mathbf{u}_s(x,t),$$

such that it holds

$$\mathbf{u}_s(x,t) = \mathbf{u}_s(\hat{x} + \hat{\mathbf{u}}_s(\hat{x},t),t) = \hat{\mathbf{u}}_s(\hat{x},t). \tag{3.26}$$

By $\mathbf{u}_s(x,t)$ we can define the inverse mapping $T_s(t) : \mathcal{S}(t) \to \hat{\mathcal{S}}$:

$$T_s(x,t) := x - \mathbf{u}_s(x,t). \tag{3.27}$$

It holds

Lemma 3.13 (Inverse Mapping) *Let $\hat{\mathbf{u}}_s(\hat{x})$ be a deformation field that defines a C^1-diffeomorphism $\hat{T}_s(\hat{x}) := \hat{x} + \hat{\mathbf{u}}_s(\hat{x})$. Then, for the inverse mapping $T_s(x) := x - \mathbf{u}_s(x)$ with $\mathbf{u}_s(x) := \hat{\mathbf{u}}_s(\hat{x})$ for $x := \hat{x} + \hat{\mathbf{u}}_s(\hat{x})$ it holds*

$$T_s = \hat{T}_s^{-1}.$$

The inverse mapping is also called backward characteristics *[104, 105].*

Proof By (3.26) and (3.27), it holds

$$x = \hat{T}_s(T_s(x,t),t) = \hat{T}_s(x - \mathbf{u}_s(x,t),t) = \hat{T}_s(\hat{x},t) = \hat{x} + \hat{\mathbf{u}}_s(\hat{x},t),$$

as well as

$$T_s(\hat{T}_s(\hat{x},t),t) = T_s(\hat{x} + \hat{\mathbf{u}}_s(x,t),t) = T_s(x,t) = x - \mathbf{u}_s(x,t) = \hat{x}$$

□

Further, considering Lemma 2.9, it holds

$$T_s \circ \hat{T}_s = \mathrm{id} \quad \Rightarrow \quad \nabla T_s =: \mathbf{F}_s = \hat{\mathbf{F}}_s^{-1} = (\hat{\nabla}\hat{T}_s)^{-1} \text{and } J_s = \hat{J}_s^{-1}. \tag{3.28}$$

With $\hat{T}_s := \mathrm{id} + \hat{\mathbf{u}}_s$ and $T_s := \mathrm{id} - \mathbf{u}_s$ it finally follows that

$$[I - \nabla \mathbf{u}_s] = [I + \hat{\nabla}\hat{\mathbf{u}}_s]^{-1} \quad \Leftrightarrow \quad \nabla \mathbf{u}_s = I - [I + \hat{\nabla}\hat{\mathbf{u}}_s]^{-1} = I - \hat{\mathbf{F}}_s^{-1}.$$

By these relations, we can define the Cauchy stresses for different material laws like the St. Venant Kirchhoff model.

Lemma 3.14 (Cauchy Stress Tensor for the St. Venant Kirchhoff Material in Eulerian Coordinates) *The Eulerian Cauchy stress tensor $\boldsymbol{\sigma}_s$ of the St. Venant Kirchhoff material is given by*

$$\boldsymbol{\sigma}_s = J_s \mathbf{F}_s^{-1} \left(2\mu \mathbf{E}_s + \lambda_s \operatorname{tr}(\mathbf{E}_s) I\right) \mathbf{F}_s^{-T}, \quad E_s := \frac{1}{2}\left(\mathbf{F}_s^{-T}\mathbf{F}_s^{-1} - I\right).$$

Proof The second Piola Kirchhoff stress tensor $\hat{\boldsymbol{\Sigma}}_s$ of the St. Venant Kirchhoff material is given by (see Definition 2.18)

$$\hat{\boldsymbol{\Sigma}}_s = 2\mu_s \hat{\mathbf{E}}_s + \lambda_s \operatorname{tr}(\hat{\mathbf{E}}_s) I,$$

with the Green-Lagrangian strain tensor

$$\hat{\mathbf{E}}_s := \frac{1}{2}(\hat{\mathbf{F}}_s^T \hat{\mathbf{F}}_s - I).$$

Lemma 2.12 describes the Piola transformation as relation between the Cauchy stress tensor and the 2nd Piola Kirchhoff stresses:

$$\hat{\mathbf{F}}_s \hat{\boldsymbol{\Sigma}}_s = \hat{J}_s \hat{\boldsymbol{\sigma}}_s \hat{\mathbf{F}}^{-T} \quad \Leftrightarrow \quad \hat{\boldsymbol{\sigma}}_s = \hat{J}_s^{-1} \hat{\mathbf{F}}_s \hat{\boldsymbol{\Sigma}}_s \hat{\mathbf{F}}^T$$

This gives us a Lagrangian description of the Cauchy stresses. Finally, by (3.28), we can reformulate all quantities in the Eulerian system as

$$\boldsymbol{\sigma}_s = J_s \mathbf{F}_s^{-1} \boldsymbol{\Sigma}_s \mathbf{F}_s^{-T},$$

with the 2nd Piola Kirchhoff tensor in Eulerian coordinates

$$\boldsymbol{\Sigma}_s = 2\mu_s \mathbf{E}_s + \lambda_s \operatorname{tr}(\mathbf{E}_s) I,$$

where

$$\mathbf{E}_s := \frac{1}{2}(\mathbf{F}_s^{-T}\mathbf{F}_s^{-1} - I).$$

□

The derivation of the Cauchy stress tensor $\boldsymbol{\sigma}_s$ in Eulerian coordinates completes the description of the momentum equation (3.25). It remains to derive a relation

for the unknown Eulerian density $\rho_s(x,t)$. By defining $\rho_s(x,t) = \hat{\rho}_s(\hat{x},t)$ and by using (2.27), it holds

$$\rho_s(x,t) = J_s(x,t)\hat{\rho}_s^0,$$

where $\hat{\rho}_s^0$ is the (in many cases homogenous) density of the solid at time $t = 0$.

Finally, for splitting the second order hyperbolic equation into a system of first order equations, we must transform the relation $d_t\hat{\mathbf{u}}_s = \hat{\mathbf{v}}_s$ to the Eulerian coordinate framework. By Lemma 2.10 we have

$$d_t\hat{\mathbf{u}}_s = \partial_t\mathbf{u}_s + \mathbf{v}_s\cdot\nabla\mathbf{u}_s, \quad d_t\hat{\mathbf{v}}_s = \partial_t\mathbf{v}_s + \mathbf{v}_s\cdot\nabla\mathbf{v}_s.v$$

As outcome of the foregoing discussion it holds:

Problem 3.15 (Solid Problem in Eulerian Coordinates) *Find elastic deformation* $\mathbf{u}_s$ *and velocity* $\mathbf{v}_s$ *of a St. Venant Kirchhoff material in Eulerian coordinates as*

$$\begin{aligned} J_s\hat{\rho}_s^0(\partial_t\mathbf{v}_s + \mathbf{v}_s\cdot\nabla\mathbf{v}_s) - \nabla\cdot\boldsymbol{\sigma}_s &= J_s\hat{\rho}_s^0\mathbf{f}, \\ \partial_t\mathbf{u}_s + \mathbf{v}_s\cdot\nabla\mathbf{u}_s &= \mathbf{v}_s, \end{aligned} \quad \text{in } \mathcal{S}(t), \tag{3.29}$$

with the Eulerian formulation of the Cauchy stress tensor

$$\boldsymbol{\sigma}_s := J_s\mathbf{F}_s^{-1}(2\mu_s\mathbf{E}_s + \lambda_s\,\mathrm{tr}(\mathbf{E}_s)I)\mathbf{F}_s^{-T}, \quad \mathbf{E}_s := \frac{1}{2}\left(\mathbf{F}_s^{-T}\mathbf{F}_s^{-1} - I\right),$$

and where the domain $\mathcal{S}(t)$ *is implicitly defined as*

$$\mathcal{S}(t) := \{x\in\mathbb{R}^d \,|\, x = \hat{x} + \hat{\mathbf{u}}_s(\hat{x},t)\ \forall\hat{x}\in\hat{\mathcal{S}} = \mathcal{S}(0)\}. \tag{3.30}$$

There are several implications involved in an Eulerian formulation of elastic solids:

1. The problem is formulated on the moving domain $\mathcal{S}(t)$ that is a priori unknown and part of the solution. In (3.30) we have defined $\mathcal{S}(t)$ based on the Lagrangian version of the deformation $\hat{\mathbf{u}}_s(\hat{x},t)$. This however is not typical and available if we consider the Eulerian point of view. Instead, we need to represent the moving solid domain based on a fully Eulerian description. One possibility is to define an implicit relation

$$\mathcal{S} = \{x(t)\in\mathbb{R}^d : \quad \partial_t x(t) + (\mathbf{v}\cdot\nabla)x(t) = 0, \quad \forall x(0) = \hat{x}\in\hat{\mathcal{S}}\}, \tag{3.31}$$

   where the domain is given as solution of a transport problem. Every realization of an Eulerian formulation must keep track of the domain. We will get back to this key point in Sect. 3.6.3.
2. By transformation to Eulerian coordinates, convective terms are introduced

$$d_t\hat{\mathbf{v}} = \partial_t\mathbf{v} + (\mathbf{v}\cdot\nabla)\mathbf{v}, \quad d_t\hat{\mathbf{u}} = \partial_t\mathbf{u} + (\mathbf{v}\cdot\nabla)\mathbf{u}.$$

A discretization of this convective term can cause numerical stability problems. Numerical methods must either introduce artificial stabilization terms that will cause loss of conservation principles or be based on non-standard techniques.

A variational formulation of problem (3.29) is derived in the standard way by multiplication with test functions and integration over the (moving) domain $\mathcal{S}(t)$.

Problem 3.16 (Variational Formulation of the Solid Problem in Eulerian Coordinates) *Let $\bar{\mathbf{u}}_s^D(t), \bar{\mathbf{v}}_s^D \in H^1(\mathcal{S}(t))^d$ be extensions of the Dirichlet data. Let*

$$\mathbf{u}_s(t) \in \bar{\mathbf{u}}_s^D(t) + H_0^1(\mathcal{S}(t))^d, \quad \mathbf{v}_s(t) \in \bar{\mathbf{v}}_s^D(t) + \mathcal{V}_s(t) \in H_0^1(\mathcal{S}(t))^d$$

be the solution of the variational problem

$$\begin{aligned} \left(J_s\hat{\rho}_s^0(\partial_t\mathbf{v}_s + \mathbf{v}_s\cdot\nabla\mathbf{v}_s), \phi_s\right)_{\mathcal{S}(t)} + \left(\boldsymbol{\sigma}_s, \nabla\phi_s\right)_{\mathcal{S}(t)} &= \left(J_s\hat{\rho}_s^0\mathbf{f}, \phi\right)_{\mathcal{S}(t)}, \\ \left(\partial_t\mathbf{u}_s + \mathbf{v}_s\cdot\nabla\mathbf{u}_s - \mathbf{v}_s, \psi_s\right)_{\mathcal{S}(t)} &= 0, \end{aligned} \tag{3.32}$$

for all $\phi_s \in H_0^1(\mathcal{S}(t))^d$ and $\psi_s \in L^2(\mathcal{S}(t))^d$ and where $\boldsymbol{\sigma}$ is defined as shown in Lemma 3.15.

Given sufficient additional regularity, every solution to Problem 3.16 is also a solution of the classical Eulerian formulation given in Problem 3.15.

3.6.2 Fluid-structure Interaction in Eulerian Coordinates

Once the variational formulation of the structure problem in Eulerian coordinates is given, coupling to the flow problem is straightforward. Again, we simply glue the two velocities $\mathbf{v}_f$ and $\mathbf{v}_s$ together and use one common test function for the two momentum equations, compare Lemma 3.9.

$$\begin{aligned} (\rho_f(\partial_t\mathbf{v} + (\mathbf{v}\cdot\nabla)\mathbf{v}), \phi)_{\mathcal{F}(t)} + (J_s\hat{\rho}_s^0(\partial_t\mathbf{v} + (\mathbf{v}\cdot\nabla)\mathbf{v}), \phi)_{\mathcal{S}(t)} & \\ (\boldsymbol{\sigma}_f, \nabla\phi)_{\mathcal{F}(t)} + (\boldsymbol{\sigma}_s, \nabla\phi)_{\mathcal{S}(t)} = (\rho_f\mathbf{f}, \phi_f)_{\mathcal{F}(t)} + (J_s\hat{\rho}_s^0\mathbf{f}, \phi_s)_{\mathcal{S}(t)}. & \\ (\nabla\cdot\mathbf{v}_f, \xi_f)_{\mathcal{F}(t)} = 0, & \\ (\partial_t\mathbf{u}_s + (\mathbf{v}\cdot\nabla)\mathbf{u}_s - \mathbf{v}, \psi_s)_{\mathcal{S}(t)} = 0. & \end{aligned} \tag{3.33}$$

The kinematic condition is embedded in the test space

$$\mathbf{v}(t) \in \mathbf{v}^D(t) + H_0^1(\Omega; \Gamma_f^D)^d,$$

and the dynamic condition is realized by coupling the test functions

$$\phi \in H_0^1(\Omega; \Gamma_f^D)^d.$$

Pressure and the solid's deformation are found in

$$p_f(t) \in L^2(\mathcal{F}(t)), \quad \mathbf{u}_s(t) \in \bar{\mathbf{u}}_s^D(t) + H_0^1(\mathcal{S}(t); \Gamma_s^D)^d.$$

Test spaces for the divergence condition and the velocity deformation coupling are simply

$$\xi_f \in L^2(\mathcal{F}(t)), \quad \psi_s \in L^2(\mathcal{S}(t))^d.$$

Apparently, the Eulerian formulation of the fluid-structure interaction problem has a simpler structure than the ALE formulation. No mapping—at least no artificial mapping—between domains is necessary. Hence, there is no obvious reason, while the Eulerian formulation should show limits when treating problems with very large deformation, motion or even contact. All this is true, the simplicity of the variational formulation in (3.33) however conceals one essential vagueness: the domains $\mathcal{F}(t)$ and $\mathcal{S}(t)$ are given by the solution itself. For the solid domain, we have identified two possible definitions, given in (3.30) and (3.31). Both of them however are not well suited in a computational framework. In the following section, we will introduce a technique to close this last gap.

3.6.3 The Initial Point Set Method

For realizing a computational method based on (3.33), we must be able to determine, if a coordinate $x \in \Omega(t)$ at time $t \geq t_0$ belongs to the solid domain $x \in \mathcal{S}(t)$ or to the fluid domain $x \in \mathcal{F}(t)$. In contrast to the ALE realization, where we could deal with fixed subdomains, this partitioning will move. We must correctly capture the interface at all times. The Eulerian formulation belongs to the class of *interface-capturing* techniques. One of the most prominent *interface-capturing* methods is the *Level-Set method*, introduced and described by Sethian [307] as well as Osher and Fedkiw [257]. Here, we introduce a scalar Level-Set function $\chi^0 : \hat{\Omega} \to \mathbb{R}$ that indicates the signed distance to the interface $\hat{\mathcal{I}} = \mathcal{I}(0)$, i.e.

$$\chi^0(\hat{x}) := \begin{cases} \operatorname{dist}(\hat{x}, \hat{\mathcal{I}}) & \hat{x} \in \hat{\mathcal{S}}, \\ -\operatorname{dist}(\hat{x}, \hat{\mathcal{I}}) & \hat{x} \in \hat{\mathcal{F}}, \end{cases}.$$

It holds $\chi(\hat{x}) = 0$ for all $\hat{x} \in \hat{\mathcal{I}}$ on the interface. For a given point $\hat{x} \in \hat{\Omega}$, the sign of $\chi^0(\hat{x})$ can be used to determine the domain affiliation. Further, the normalization with the distance can be used to express normal vectors of the interface. This is a very important feature for multiphase flow problems, where the curvature has an influence on the surface tension. Then, we simply use the velocity field $\mathbf{v}$ to transport the Level-Set function over time

$$\partial_t \chi + (\mathbf{v} \cdot \nabla)\chi = 0.$$

The sign of $\chi(x,t)$ will at all times indicate whether a point x belongs to $\mathcal{S}(t)$ or $\mathcal{F}(t)$.

One immediate drawback of the Level-Set technique is the introduction of an additional unknown that will increase the complexity of the formulation. A greater challenge is the derivation of stable numerical routines to solve the transport equation. Usually, such a pure transport equation will call for stabilization techniques like upwinding or artificial diffusion that will cause unphysical smoothing of the interface. In the context of fluid-structure interactions, this could mean that points of the fluid problem will by fault be accounted to the solid domain, and vice versa. The Level-Set method is widely used and must be considered as standard method for describing interface problems. There is extensive literature on the efficient realization as well as on reinitialization techniques for maintaining the Level-Set property.

Level-Set methods have also been used to formulate fluid-structure interactions as interface problems [104, 105, 179, 222].

Here, as an alternative, we describe the *Initial Point Set method* for capturing the interface between fluid- and solid-domain. This technique was first introduced by Dunne [126].

To be precise: instead of capturing the interface location, we will capture the complete reference coordinate system. The construction of the *Initial Point Set* is based on the following observation: if we know that $x \in \Omega(t)$ at time $t \geq 0$ belongs to the solid domain, i.e. $x \in \mathcal{S}(t)$, it holds

$$T_s(x,t) = x - \mathbf{u}_s(x,t) \in \hat{\mathcal{S}}.$$

Coordinates $x \in \mathcal{S}(t)$ are deformed back to the Lagrangian system by the Eulerian deformation $\mathbf{u}_s(x,t)$. As the Lagrangian system is fixed and known, we could use the deformation $\mathbf{u}_s$ to determine, if a point $x \in \Omega(t)$ is part of the solid domain.

The flaw of this construction is the absence of fluid domain's deformation $\mathbf{u}_f$, as $\mathbf{u}_s$ is only defined in the solid domain. A computational method however can easily be derived by an implicit extension of this deformation $\mathbf{u}_f$ to the fluid domain. Hence, for the following, we assume that $\mathbf{u}_f : \mathcal{F}(t) \to \mathbb{R}^d$ is given such that

$$\mathbf{u}_f(x,t) = \mathbf{u}_s(x,t) \quad \forall x \in \mathcal{I}(t) \text{ and } x - \mathbf{u}_f(x,t) \notin \hat{\mathcal{S}} \quad \forall x \in \mathcal{F}(t).$$

The extension should map every coordinate back to a coordinate at reference time. We do not expect that

$$T_f(x,t) := x - \mathbf{u}_f(x,t)$$

defines a mapping to a reference fluid domain $T_f(t) : \mathcal{F}(t) \to \hat{\mathcal{F}}$. We are pleased, if

$$T_f(x,t) = x - \mathbf{u}_f(x,t) \notin \hat{\mathcal{S}}$$

is not part of the solid's reference domain. We will get back to this subtle (but important) difference. As $\mathbf{u}_f$ and $\mathbf{u}_s$ are continuous on the interface and by assuming

that $\mathbf{u}_f$ has sufficient regularity, we define a global deformation field $\mathbf{u}(t) : \Omega(t) \to \mathbb{R}^d$ and set

$$\mathbf{u}_s(t) := \mathbf{u}(t)\Big|_{\mathcal{S}(t)}, \quad \mathbf{u}_f(t) := \mathbf{u}(t)\Big|_{\mathcal{F}(t)}.$$

Based on this global deformation, we can finally define the *Initial Point Set* Φ_{IPS} as

$$\Phi_{\text{IPS}}(x,t) := x - \mathbf{u}(x,t),$$

and can use it to determine the domain affiliation for all coordinates $x \in \Omega(t)$:

$$x \in \Omega(t) \;\Rightarrow\; x \in \begin{cases} \mathcal{S}(t), & \Phi_{\text{IPS}}(x,t) = x - \mathbf{u}(x,t) \in \hat{\mathcal{S}}, \\ \mathcal{F}(t), & \Phi_{\text{IPS}}(x,t) = x - \mathbf{u}(x,t) \notin \hat{\mathcal{S}}. \end{cases}$$

The *Initial Point Set* allows to distinguish between the two subdomains.

We still have to provide a way to define suitable extensions $\mathbf{u}_f$ in an implicit way. In principle, we can utilize the same techniques that have been discussed in the context of constructing the ALE-map in Sect. 3.5.1. This effort however is not necessary, as the deformation $\mathbf{u}_f$ will not be used to define a mapping between $\mathcal{F}(t)$ and $\hat{\mathcal{F}}$. We only require that $T_f(x,t) = x - \mathbf{u}_f(x,t)$ points x to a coordinate outside the solid domain. We do not need any regularity of $\mathbf{u}_f$ nor do we need invertibility of the map.

Definition 3.17 (Initial Point Set) A vector field $\Phi_{\text{IPS}} : \Omega(t) \to \mathbb{R}^d$ is called *Initial Point Set*, if for $x \in \Omega$ and $t \geq 0$ it holds:

$$\begin{aligned} &\Phi_{\text{IPS}}(x,t) = x - \mathbf{u}_s(x,t) && x \in \bar{\mathcal{S}}(t) \\ &\Phi_{\text{IPS}}(x,t) \notin \hat{\mathcal{S}} && x \in \mathcal{F}(t) \end{aligned}$$

Finally, we can indicate some possibilities for the construction of $\mathbf{u}_f$. One simple option is to choose the harmonic extension of $\mathbf{u}_s$ to the fluid domain:

$$-\Delta \mathbf{u}_f = 0 \text{ in } \mathcal{F}(t), \quad \mathbf{u}_f = \mathbf{u}_s \text{ on } \mathcal{I}(t), \quad \mathbf{n} \cdot \nabla \mathbf{u}_f = 0 \text{ on } \partial\mathcal{F}(t) \setminus \mathcal{I}(t).$$

Here, we have chosen homogenous Neumann boundary conditions on the outer boundary of the fluid-domain. As $\mathbf{u}_f \neq$ on $\partial\mathcal{F}(t) \setminus \mathcal{I}(t)$, the map $T_f(x,t) := x - \mathbf{u}_f(x,t)$ will not define a mapping back to a reference domain. The Neumann condition will allow very large deformations, such that the solid domain $\mathcal{S}(t)$ can get arbitrarily close to the outer boundary. In Fig. 3.7 we show two situations of possible extensions. In the upper sketch, we have chosen homogenous Dirichlet values on the outer boundary, whereas the lower sketch is constructed with a Neumann condition. The gradient ∇T_f within the fluid domain is smaller in this case.

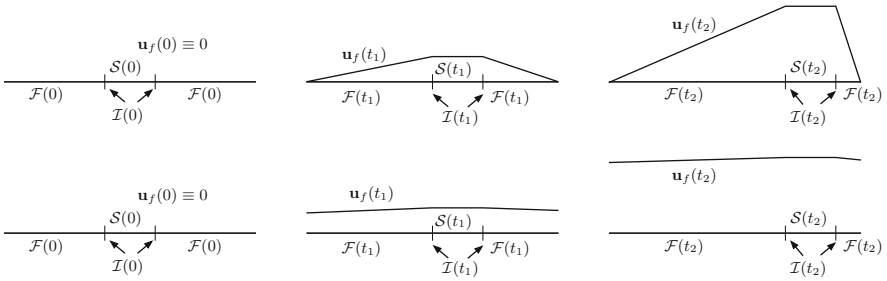

Fig. 3.7 Examples for the *Initial Point Set* using homogenous Dirichlet conditions on $\partial\mathcal{F}(t) \setminus \mathcal{I}(t)$ in the *upper* and Neumann conditions in the *lower sketch*. The *Initial Point Set* $x - \mathbf{u}_f(x,t)$ defined in the *lower sketch* does not construct an ALE map. This however is not necessary in the context of Fully Eulerian fluid-structure interactions

Finally, we can close the formulation of the coupled fluid-structure interaction problem in Eulerian coordinate:

Problem 3.18 (Initial Point Set formulation of the Eulerian Fluid-structure Interaction Problem) *Let*

$$\begin{aligned}
\mathbf{u}(t) &\in \bar{\mathbf{u}}^D(t) + H_0^1(\Omega(t); \Gamma_s^D)^d, \\
\mathbf{v}(t) &\in \bar{\mathbf{v}}^D(t) + H_0^1(\Omega(t); \Gamma^D)^d, \\
p_f(t) &\in L^2(\mathcal{F}(t))
\end{aligned}$$

be the solution of the variational problem

$$\begin{aligned}
(\rho_f(\partial_t \mathbf{v} + (\mathbf{v}\cdot\nabla)\mathbf{v}), \phi)_{\mathcal{F}(t)} + (J_s \hat{\rho}_s^0(\partial_t \mathbf{v} + (\mathbf{v}\cdot\nabla)\mathbf{v}), \phi)_{\mathcal{S}(t)} \\
+(\boldsymbol{\sigma}_f, \nabla\phi)_{\mathcal{F}(t)} + (\boldsymbol{\sigma}_s, \nabla\phi)_{\mathcal{S}(t)} = (\rho_f \mathbf{f}, \phi)_{\mathcal{F}(t)} + (J_s \hat{\rho}_s^0 \mathbf{f}, \phi)_{\mathcal{S}(t)} \\
(\nabla\cdot\mathbf{v}, \xi_f)_{\mathcal{F}(t)} = 0 \\
(\partial_t \mathbf{u} + (\mathbf{v}\cdot\nabla)\mathbf{u} - \mathbf{v}, \psi_s)_{\mathcal{S}(t)} = 0 \\
(\nabla\mathbf{u}, \nabla\psi_f)_{\mathcal{F}(t)} = 0,
\end{aligned}$$

for all test functions

$$\begin{aligned}
\phi_f &\in H_0^1(\Omega(t); \Gamma^D)^d, \\
\xi_f &\in L^2(\mathcal{F}(t)), \\
\psi_s &\in L^2(\mathcal{S}(t))^d, \\
\psi_f &\in H_0^1(\mathcal{F}(t); \mathcal{I}(t))^d.
\end{aligned}$$

Given sufficient regularity, this solution also solves the fluid-structure interaction problem in classical formulation presented in Problem 3.1.

Remark 3.19 (Similarity to Multiphase Flows) There are many similarities between the Eulerian formulation of fluid-structure interactions and multiphase flows, where two different fluids are coupled over a common (and moving) interface. To illustrate this analogy we first introduce a global notation for the stress tensors and the densities

$$\boldsymbol{\sigma}(x,t) := \begin{cases} \boldsymbol{\sigma}_f(x,t) & x \in \mathcal{F}(t), \\ \boldsymbol{\sigma}_s(x,t) & x \in \mathcal{S}(t), \end{cases} \qquad \rho(x,t) := \begin{cases} \rho_f & x \in \mathcal{F}(t), \\ J_s \hat{\rho}_s^0 & x \in \mathcal{S}(t). \end{cases}$$

With help of this notation we can shorten the formulation to

$$\begin{aligned} (\rho(\partial_t \mathbf{v} + (\mathbf{v}\cdot\nabla)\mathbf{v}), \phi) + (\boldsymbol{\sigma}, \nabla\phi) &= (\rho\mathbf{f}, \phi), \\ (\nabla\cdot\mathbf{v}, \xi_f)_{\mathcal{F}(t)} &= 0 \\ (\partial_t \mathbf{u} + (\mathbf{v}\cdot\nabla)\mathbf{u} - \mathbf{v}, \psi_s)_{\mathcal{S}(t)} &= 0 \\ (\nabla\mathbf{u}, \nabla\psi_f)_{\mathcal{F}(t)} &= 0, \end{aligned}$$

While the similarity of the Fully Eulerian formulation to multiphase flows is helpful in the design of computational algorithms, the likeness should not be overly stressed. Fluid-structure interaction is not a simple change of problem parameters along an interface, instead. Instead the complete setup of the stress tensors change, as $\boldsymbol{\sigma}_f = \boldsymbol{\sigma}_f(\mathbf{v})$ and $\boldsymbol{\sigma}_s = \boldsymbol{\sigma}_s(\mathbf{u})$ stand for a parabolic-type equation and one of hyperbolic type.

The idea of the *Initial Point Set* is alike the idea of the *backward characteristics* used to describe the Eulerian domain in the approach by Cottet et al. [105].

Chapter 4
Discretization

This chapter is devoted to discretization techniques. We start with basic methods for the discretization in time. Besides simple time stepping schemes, we will discuss Galerkin time discretization methods. They have a similar structure to the finite element discretization used in space and they are well suited for adaptivity and optimization problems. After an introduction to the fundamental schemes for parabolic equations, we put the focus on the special needs of temporal discretization methods in fluid mechanics. We continue with the introduction of the finite element methods for spatial discretization. Again, we start by presenting the fundamentals before putting spacial attention to saddle point problems and the nonlinear Navier-Stokes equations. Finally, to prepare the necessary tools for an application to fluid-structure interactions, we discuss interface problems, where the solution of exhibits limited regularity along an internal interface boundary.

4.1 Time Discretization of Partial Differential Equations

In this section we discuss the time-discretization of parabolic differential equations given in variational formulation

$$u(t) \in \mathcal{V}: \quad (\partial_t u(t), \phi) + a(u(t), \phi) = (f(t), \phi) \quad \forall \phi \in \mathcal{V} := H_0^1(\Omega) \tag{4.1}$$

almost everywhere for $t \in I := [0, T]$, where $a(\cdot, \cdot)$ is an elliptic operator and with initial data

$$u(0) = u^0 \text{ in } L^2(\Omega).$$

T. Richter, *Fluid-structure Interactions*, Lecture Notes in Computational Science and Engineering 118, DOI 10.1007/978-3-319-63970-3_4

Three different approaches for the time-discretization of parabolic problems are considered:

First space then time: This approach is called *method of lines*. By space discretization, the parabolic equations is transformed into a system of ordinary differential equations that then can be tackled with usual single or multistep-methods.

First time then space: This approach is referred to as *Rothe's method*. By discretization in time with a single-step method, the parabolic equation is resolved into a sequence of quasi-stationary elliptic partial differential equations that then can be discretized in space. The advantage of this approach is the possible use of different discretizations (adaptive meshes) in different time steps.

Simultaneously: This approach is called a *space-time discretization*. By using a simultaneous Galerkin-discretization in space and time, the equation gets accessible to strong analytical techniques. This approach allows for the easy derivation of robust error estimators and adjoint optimization techniques. The effort for solving a space-time coupled problem however is immense, as the time acts as an additional dimension. Often space-time approaches are only considered for analysis purposes and Rothe's method or the method or lines is used for solving.

It can be shown that the method of lines and Rothe's method are equivalent, if uniform discretizations are considered. Further, it is possible to design space-time Galerkin methods that—at least for linear autonomous problems—correspond to certain time stepping methods.

All time-discretizations are based on a subdivision of the time interval $I = [0, T]$ into discrete time steps

$$0 = t_0 < t_1 < \cdots < t_M = T, \quad k_m := t_m - t_{m-1}, \quad k := \max_{1 \le m \le M} \{k_m\}.$$

At every time step t_m we denote by

$$u^m = u(t_m)$$

the solution at time t_m. One of the most basic time stepping schemes used in the method of lines or Rothe's method is the one-step θ-scheme

$$\begin{aligned} m = 1, \ldots, M: \quad & (u^m, \phi) + \theta k_m a(u^m, \phi) = (u^{m-1}, \phi) \\ & - (1-\theta) k_m a(u^{m-1}, \phi) + \theta k (f^m, \phi) + (1-\theta) k (f^{m-1}, \phi) \quad \forall \phi \in \mathcal{V}. \end{aligned} \tag{4.2}$$

For $\theta = 1$, this is the implicit backward Euler method, for $\theta = 0$ the explicit forward Euler and for $\theta = \frac{1}{2}$ the Crank-Nicolson scheme. Both implicit and explicit Euler method show first order convergence, while the Crank-Nicolson method

is second order accurate. Higher order accuracy can be reached by referring to Runge-Kutta methods or linear multistep schemes like the Backward Differentiation Formulas (BDF), see [118].

By discretization with a single-step method, the parabolic equation decouples into M pseudo-stationary problems of type (4.2) that can subsequently be discretized in space by appropriate Finite Element methods. Usually, it shows that choosing only first order accurate time stepping schemes, the resulting discretization error is highly unbalanced and that very small time steps (compared to the spatial discretization parameter h)

$$k \ll h$$

are required to yield an adequate overall error accuracy. As however very high spatial approximation order is not easily obtained for complex problems like fluid-structure interactions, choosing second order accurate time stepping schemes is a good compromise between approximation property and numerical effort.

4.1.1 Numerical Stability

Numerical stability is—next to approximation accuracy—the most important quality measure for time discretization schemes. For stability analysis we consider the scalar ordinary differential equations

$$u'(t) = \lambda u(t), \quad t \geq 0, \quad u(0) = 1, \tag{4.3}$$

where $\lambda \in \mathbb{C}$ is a given complex parameter. The unique solution to this equation is

$$u(t) = \mathrm{e}^{\lambda t}$$

and it holds

$$\begin{array}{ll} |u(t)| \leq 1 & \text{for } Re(\lambda) \leq 0 \\ |u(t)| \to \infty & \text{for } Re(\lambda) > 0 \end{array} \quad (t \to \infty)$$

We define:

Definition 4.1 (Absolute Stability) A one-step method for the approximation $u^m \approx u(t_m)$ of (4.3) is *absolutely stable* for a given $\lambda \in \mathbb{C}$ and time step $k > 0$, if

$$|u^m| \leq 1, \quad m = 1, 2, \ldots.$$

A numerical scheme is usually stable for only some pairs of $\lambda \in \mathbb{C}$ and $k \in \mathbb{R}_+$. We consider the forward Euler method for approximating (4.3)

$$u^m = (1 + \lambda k)u^{m-1}$$

and we immediately get the relation:

$$|u^m| \leq |1 + \lambda k|\, |u^{m-1}| \leq \cdots \leq |1 + \lambda k|^m |u^0| = |1 + \lambda k|^m.$$

Absolute stability is given, if

$$|1 + \lambda k| \leq 1 \quad \Leftrightarrow \quad \lambda k \in \bar{B}_1(-1) := \{z \in \mathbb{C} : \ |z + 1| \leq 1\}.$$

We define:

Definition 4.2 (Region of Absolute Stability) The subset of the complex plane

$$\mathcal{R}_s = \{z = \lambda k \in \mathbb{C} : \quad \text{method is absolute stable for } \lambda \text{ and } k\},$$

is called the *region of absolute stability* of the single-step method. A method with a stability region that contains the left complex half-plane is called *A-stable*

$$\{z \in \mathbb{C} : \ Re(z) \leq 0\} \subset \mathcal{R}_s.$$

For the θ time stepping method it holds:

Lemma 4.3 (Absolute Stability of the One-Step θ-Method) *The region of stability for the implicit Euler scheme is given by*

$$\mathcal{R}_s^{IE} = \mathbb{C} \setminus B_1(1),$$

for the explicitly Euler scheme by

$$\mathcal{R}_s^{EE} = \bar{B}_1(-1),$$

and for the Crank-Nicolson scheme by

$$\mathcal{R}_s^{CN} = \{z \in \mathbb{C} |\ Re(z) \leq 0\}.$$

For all $\theta \in [\frac{1}{2}, 1]$ *it holds*

$$\mathcal{R}_s^{\theta \geq \frac{1}{2}} \supseteq \{z \in \mathbb{C} |\ Re(z) \leq 0\}.$$

and for all $\theta \in [0, \frac{1}{2})$ *it holds:*

$$\mathcal{R}_s^{\theta < \frac{1}{2}} \cap \{z \in \mathbb{C} |\ Re(z) \leq 0\} \neq \emptyset.$$

Proof The θ-scheme is written with help of the *amplification factor*:

$$u^m = R(k, \lambda, \theta)u^{m-1}, \quad R(k, \lambda, \theta) = \frac{1 + (1-\theta)k\lambda}{1 - \theta k\lambda}.$$

The region of stability is then calculated as the set of complex numbers $z = k\lambda$ that satisfy $|R(z, \theta)| \leq 1$. □

If the region of absolute stability includes the left part of the complex plane

$$\mathbb{C}_- := \{z \in \mathbb{C} |\ Re(z) \leq 0\} \subset \mathcal{R}_s,$$

the underlying method is stable for all combinations of $\lambda \in \mathbb{C}_-$ and time steps $h > 0$. There is no time step restriction.

Definition 4.4 (A-Stability) If the region of absolute stability includes the left part of the complex plane $\mathbb{C}_-$, we call the method *A-stable*.
The Crank-Nicolson scheme and the θ scheme for $\theta \geq \frac{1}{2}$ are A-stable. A-stability ensures boundedness of the numerical solution for all time steps.

Remark 4.5 (Amplification Factor) The amplification factors $R(z) = R(\lambda k)$ of single-step methods for solving the model-problem (4.3) are approximations to the complex exponential function

$$R(z) \approx \exp(z).$$

For a single-step method with truncation error $O(k^\alpha)$ it holds

$$|R(\lambda k) - \exp(\lambda k)| = O(k^{\alpha+1}).$$

The amplification factor for implicit single-step methods is always a rational approximation to the exponential function. The best rational approximations to the exponential function are called *Padé approximation*. For increasing polynomial degree of denominator r and numerator s, the Padé approximations can be given in a Padé-table:

$$\left[\begin{array}{c|cccc} s\backslash r & 1 & 2 & 3 & \cdots \\ \hline 1 & \frac{1}{1} & \frac{1+z}{1} & \frac{1+z+\frac{1}{2}z^2}{1} & \cdots \\ 2 & \frac{1}{1-z} & \frac{1+\frac{1}{2}z}{1-\frac{1}{2}z} & \frac{1+\frac{2}{3}z+\frac{1}{6}z^2}{1-\frac{1}{3}z} & \\ 3 & \frac{1}{1-z+\frac{1}{2}x^2} & \frac{1+\frac{1}{3}z}{1-\frac{2}{3}z+\frac{1}{6}z^2} & \frac{1+\frac{1}{2}z+\frac{1}{12}z^2}{1-\frac{1}{2}z+\frac{1}{12}x^2} & \ddots \\ \vdots & \vdots & & \ddots & \ddots \end{array}\right]$$

It can be shown that all diagonal Padé approximations correspond to A-stable time stepping schemes, while all sub-diagonal Padé approximations correspond to a strongly A-stable scheme [173, 289, 317].

While A-stability ensures the boundedness of the numerical approximation for all time steps

$$|u^m| \leq |R(\lambda k)|^k |u^0|,$$

higher stability requirements might be necessary, if truncation errors are considered. Assume that an additional relative error $1 + \varepsilon$ is added in every step, i.e.

$$u^m = R(\lambda k) u^{m-1}(1+\varepsilon) \;\Rightarrow\; |u^m| = |R(\lambda k)|^m |u^0|\,|1+\varepsilon|^m \geq |R(\lambda k)|^m |u^0| m\varepsilon.$$

If $R(\lambda k) \to 1$ the overall error might still be unbounded.

Definition 4.6 (Strong A-Stability) An A-stable method is called *strongly A-stable*, if it holds

$$\limsup_{Re(\lambda)\to-\infty} |R(\lambda)| \leq 1 - \delta < 1.$$

It is called *globally A-stable* , if it holds

$$\limsup_{Re(\lambda)\to-\infty} |R(\lambda h)| \leq 1 - \mathcal{O}(k).$$

Strong A-stability gives a damping property of numerical methods. Numerical errors by non-smooth boundary data, by incompletely solved linear and nonlinear systems are damped. Global A-stability is a weaker (still stronger than A-stable) concept. Usually, globally A-stable methods are sufficient to damp numerical truncation errors. They might however not be sufficient to smooth out errors in the initial data. We refer to [186, 230] for further reading.

A method lacking numerical stability usually asks for restrictive time step conditions. The forward Euler scheme requires

$$\lambda k \in B_1(-1),$$

and considering $\lambda \in \mathbb{R}$ with $\lambda < 0$ this refers to the condition:

$$0 \leq k|\lambda| \leq 2 \quad \Leftrightarrow \quad k \leq 2|\lambda|^{-1}.$$

For $|\lambda|$ large, this condition can be very restrictive. Next, we consider the heat-equation in variational formulation

$$(\partial_t u, \phi) + (\nabla u, \nabla \phi) = 0$$

written in operator notation as

$$\partial_t u + \mathcal{A} u = 0,$$

where $\mathcal{A}$ is the weak Laplace operator. We know that $\mathcal{A}$ is symmetric positive definite with an orthonormal basis of eigenvectors $\{w_i\}_{i\geq 0}$ and corresponding eigenvalues λ_i, where

$$0 < \lambda_1 \leq \lambda_2 \leq \cdots, \quad \lambda_i \to \infty \quad (i \to \infty).$$

Using the eigenvector representation

$$u(t) = \sum_{i\geq 0} u^i(t) w_i,$$

the heat-equation decomposes into a set of scalar equations

$$\partial_t u^i(t) = -\lambda_i u^i(t),$$

each of the same type as the model problem (note the reversed sign). For numerical stable time-discretization of the heat equation it has to hold for all eigenvectors that

$$-\lambda_i k \in \mathcal{R}_s \quad \forall i \geq 0.$$

If a single-step method is strongly A-stable, it is unconditionally stable for discretizing the heat-equation for all step-sizes $k > 0$. We define:

Definition 4.7 (Stiff System) A system of differential equations

$$u'(t) = f(t, u(t)), \quad t \geq 0$$

is called stiff, if the ratio

$$\frac{\max |\lambda_-(f_u)|}{\min |\lambda_-(f_u)|} \gg 1,$$

where by $\lambda_-(f_u)$ we denote the Eigenvalues of

$$f_u := \frac{d}{du} f(t, u)$$

with negative real part.
A scalar equation $u' = \lambda u$ is never called stiff, even if $Re(\lambda) \ll 0$. Stiffness describes that a small time step k is required for reasons of numerical stability, not for reasons of accuracy. A vague, however perspicuous definition of a stiff problem is that of a problem, where the implicit Euler method gives an acceptable solution, while the explicit Euler method fails to give a good solution for the same time step size.

Example 4.8 (Stiff Problem) We consider the scalar model problem

$$u'(t) = -200u(t), \quad t \geq 0, \quad u(0) = 1,$$

with a large Lipschitz-constant $L = 200$. The solution is given by $u(t) = \exp(-200t)$. We discretize this problem by the forward and backward Euler method and measure the error at time $t_n = 1$

$$\frac{\|u(t_n) - u_n\|}{\|u(t_n)\|}.$$

In Table 4.1 we gather the results using different time steps k.

Only very small time steps of $k = 2^{-11} \approx 0.0005$ give a relative error smaller than 100% in both cases—for implicit and explicit Euler scheme. This small time step is well below the time step condition $k < 2L^{-1} \approx 0.01$ of the explicit Euler scheme arising from the stability analysis, see Lemma 4.3.

The necessity for this small time step is not by stability restrictions but simply due to the large Lipschitz constant of the problems that enters all error estimates. Next, we consider a system of initial value problems:

$$u'(t) = Au(t), \quad A := \frac{1}{3}\begin{pmatrix} -202 & -398 \\ -199 & -401 \end{pmatrix} u(t), \quad u(0) = \begin{pmatrix} 11 \\ -4 \end{pmatrix} \tag{4.4}$$

The matrix A has the two eigenvalues $\lambda_1 = -200$ and $\lambda_2 = -1$. With $|\lambda_2|/|\lambda_1| = 200$ this problem can be considered stiff. It holds

$$Q := \begin{pmatrix} 1 & -2 \\ 1 & 1 \end{pmatrix}, \quad Q^{-1}AQ = D = \begin{pmatrix} -200 & 0 \\ 0 & -1 \end{pmatrix}$$

and we define the diagonalized system for $\bar{u}(t) = Q^{-1}u(t)$

$$\bar{u}'(t) = D\bar{u}(t), \quad \bar{u}(0) = Q^{-1}u_0 = \begin{pmatrix} 1 \\ -5 \end{pmatrix},$$

Table 4.1 Example 4.8. Discretization of the scalar model problem $u'(t) = -200u(t)$. Discretization with the explicit Euler (EE) and implicit Euler method (IE) for decreasing time step sizes k

k	EE	IE
2^{-6}	∞	46594
2^{-7}	0.999	2419
2^{-8}	0.996	74.76
2^{-9}	0.927	8.907
2^{-10}	0.717	2.262
2^{-11}	0.462	0.823
2^{-12}	0.265	0.354
2^{-13}	0.142	0.164

We show the relative error in $t = 1$

Table 4.2 Example 4.8 Discretization of the system of ode's (4.4). Discretization with the explicit Euler (EE) and implicit Euler method (IE) for decreasing time step sizes k

k	EE	IE
2^{-4}	∞	0.0788
2^{-5}	∞	0.1403
2^{-6}	∞	0.2016
2^{-7}	0.7781	0.1820
2^{-8}	0.2400	0.1063
2^{-9}	0.0868	0.0624
2^{-10}	0.0394	0.0333
2^{-11}	0.0188	0.0173

We show the relative error at time $t = 1$

with the solution

$$\bar{u}(t) = \begin{pmatrix} \exp(-200t) \\ -5\exp(-t) \end{pmatrix}.$$

Table 4.2 shows the results for both implicit and explicit Euler scheme used for discretization of this system of equations. Again, we measure the relative error $\|\bar{u}(t_n) - \bar{u}_n\|_\infty / \|\bar{u}(t_n)\|_\infty$ at time $t_n = 1$.

Here, the explicit Euler method gives reasonable results starting from $k = 2^{-7} \approx 0.008 < 0.01$, where the time step first enters the region of absolute stability. The implicit Euler method also gives reasonable results for larger time steps. If the time step is small enough, both methods give results of similar accuracy.

This second problem is stiff, as it is characterized by two different solution components with very different behavior. While one component quickly goes to zero, the second component governed the absolute value of the solution. Combining the solutions of the diagonalized system we can construct the original solution as

$$u(t) = Q\bar{u}(t) = \begin{pmatrix} 10\mathrm{e}^{-t} + \mathrm{e}^{-200t} \\ -5\mathrm{e}^{-t} + \mathrm{e}^{-200t} \end{pmatrix}.$$

4.1.2 Numerical Dissipation and Further Stability Concepts

Every A-stable time discretization scheme is robust for the discretization of stiff problems as solution components belonging to Eigenvalues with negative real part are quickly damped. This behavior is important for parabolic partial differential equations. Hyperbolic equations however have the property of energy conservation. We consider the following ODE as simple model for the wave equation

$$v''(t) + v(t) = 0, \quad v(0) = 1, \quad v'(0) = 0, \tag{4.5}$$

which has the solution

$$v(t) = \cos(t).$$

We introduce the notation $u_1(t) = v(t)$ and $u_2(t) = v'(t)$ to reformulate (4.5) as a system of first order equations

$$u'(t) = \begin{pmatrix} 0 & 1 \\ -1 & 0 \end{pmatrix} u(t), \quad u(0) = \begin{pmatrix} 1 \\ 0 \end{pmatrix}.$$

The matrix has two complex eigenvalues $\lambda = \pm \mathrm{i}$. And for the vector-valued solution $u : I \to \mathbb{R}^2$ it holds $|u(t)| = 1$.

In the following, we consider the model problem (4.3) with complex eigenvalues

$$u'(t) = \lambda \mathrm{i} u(t), \quad u(0) = 1,$$

with the solution

$$u(t) = \mathrm{e}^{\mathrm{i}\lambda t} = \cos(\lambda t) + \mathrm{i} \sin(\lambda t).$$

It holds $|u(t)| = 1$ for all times $t \geq 0$ and the solution $u(t)$ has the frequency π/λ. The energy of the system is optimally conserved. We define

Definition 4.9 (Numerical Dissipation) A single-step method is said to have little numerical dissipation, if

$$|R(\mathrm{i})| \approx 1.$$

For the θ-scheme, it holds:

$$R(\mathrm{i}, \theta) = \frac{1 + (1-\theta)\mathrm{i}}{1 - \theta \mathrm{i}} = 1 + \frac{\mathrm{i}}{1 - \theta \mathrm{i}}.$$

While the backward Euler method $\theta = 1$ is highly damping

$$|R(\mathrm{i}, 1)| = \frac{1}{\sqrt{2}} \ll 1,$$

the forward Euler method $\theta = 0$ is very unstable and amplifies waves:

$$|R(\mathrm{i}, 0)| = \sqrt{2} \gg 1.$$

The Crank-Nicolson method has perfect energy conservation and no numerical dissipation:

$$R\left(\mathrm{i}, \frac{1}{2}\right) = \frac{1 + \frac{1}{2}\mathrm{i}}{1 - \frac{1}{2}\mathrm{i}} = 1.$$

The good stability (it is A-stable) and the excellent dissipation properties together with second order accuracy makes the Crank-Nicolson method for a nearly optimal discretization scheme for coupled problems like fluid-structure interactions that involve both the very stiff system of flow equations and the elastic structure equation of hyperbolic type that calls for good energy conservation. It shows however that A-stability of the Crank-Nicolson method is just not enough to cope with numerical truncation errors that are accumulated over time. Further, if the initial data for the heat-equation only has minimal regularity $u^0 \in L^2(\Omega)$, which is enough to guarantee a smooth solution, the numerical schemes may fail.

It hence remains to find a time stepping scheme that is at least second order accurate, has little numerical dissipation and better stability properties.

4.1.2.1 Shifted Crank-Nicolson Methods

A popular discretization scheme with better stability properties as the Crank-Nicolson scheme is derived by an implicit shift, using

$$\theta = \frac{1}{2} + O(k).$$

The resulting scheme still is second order accurate but the stability region is slightly larger.

Lemma 4.10 (Shifted Crank-Nicolson) *The implicitly shifted Crank-Nicolson scheme is* globally A-stable*:*

$$\limsup_{Re(\lambda)\to-\infty} |\mathcal{R}_s^{\theta=\frac{1}{2}+O(k)}(\lambda, k)| = 1 - O(k)$$

Proof It holds

$$|\mathcal{R}_s| = \left|\frac{1 + \left(1 - \frac{1}{2} - O(k)\right)\lambda k}{1 - \left(\frac{1}{2} + O(k)\right)\lambda k}\right| = \left|\frac{1 + \left(\frac{1}{2} - O(k)\right)\lambda k}{1 - \left(\frac{1}{2} + O(k)\right)\lambda k}\right|$$

$$\xrightarrow[\lambda\to-\infty]{} \left|\frac{\frac{1}{2} - O(k)}{\frac{1}{2} + O(k)}\right| = 1 - O(k).$$

□

A globally A-stable scheme has stronger damping properties. When discretized with a globally A-stable scheme, we can find global discrete solutions to parabolic equations. An even stronger stability concept is given by

Lemma 4.11 (Implicitly θ-Schemes) *Given $\theta \in (\frac{1}{2}, 1]$, the θ-scheme is* strongly A-stable*:*

$$\limsup_{Re(\lambda)\to-\infty} |\mathcal{R}_s^{\theta>\frac{1}{2}}(\lambda, k)| \leq 1 - \delta < 0.$$

Proof It holds:

$$|\mathcal{R}_s| = \left|\frac{1+(1-\theta)\lambda k}{1-\theta\lambda k}\right| \xrightarrow[\lambda\to-\infty]{} \left|\frac{1-\theta}{\theta}\right| = \left|1-\frac{1}{\theta}\right| =: |1-\delta|$$

For $\theta > \frac{1}{2}$ it holds $|1-\delta| < 1$. □

Methods with strong A-stability have damping properties for all time step sizes and all eigenvalues. A time stepping method with strong A-stability applied to the heat-equation will yield the full smoothing property of parabolic equations. Even for irregular initial data $u^0 \in L^2(\Omega)$, optimal order of convergence can be obtained. See [230, 266] for details on the analysis of smoothing properties of parabolic partial differential equations.

4.1.2.2 The Fractional-Step θ-Method

For $\theta > \frac{1}{2}$ the θ-scheme is strongly A-stable, it however lacks second order accuracy. A simple idea to construct time stepping schemes with higher accuracy and with strong A-stability is to combine multiple sub-steps of the θ-scheme into one new scheme. This idea goes back to Glowinski [166]. We perform three sub steps

$$t_{m-1} \to t_{m-1+\alpha} \to t_{m-\alpha} \to t_m, \quad k_m := t_m - t_{m-1},$$

with step-sizes

$$\alpha_1 k_m, \quad \alpha_2 k_m, \quad \alpha_3 k_m,$$

where $\alpha_i \in (0,1)$ with $\alpha_1 + \alpha_2 + \alpha_3 = 1$. In each of these steps, we choose different values for $\theta_i \in [0,1]$. To reduce the number of free parameters, we choose $\alpha := \alpha_1 = \alpha_3 \in (0, 1/2)$ and $\alpha_2 = 1-2\alpha$. Further we pick $\theta := \theta_1 = \theta_3$ and $\theta_2 = 1-\theta$. This results in the three-step method

$$\begin{aligned}
(u^{m-1+\alpha},\phi) + \alpha\theta k_m a(u^{m-1+\alpha},\phi) &= (u^{m-1},\phi) - \alpha(1-\theta)k_m a(u^{m-1},\phi)\\
(u^{m-\alpha},\phi) + (1-2\alpha)(1-\theta)k_m a(u^{m-\alpha},\phi) &= (u^{m-1+\alpha},\phi) - (1-2\alpha)\theta k_m a(u^{m-1+\alpha},\phi)\\
(u^{m},\phi) + \alpha\theta k_m a(u^{m},\phi) &= (u^{m-\alpha},\phi) - \alpha(1-\theta)k_m a(u^{m-\alpha},\phi).
\end{aligned} \tag{4.6}$$

Applied to the model-problem (4.3), the amplification factor of the fractional-step θ-method is given as a combination of three θ-factors

$$R^{\text{fst}}(\theta,\alpha,z) = \frac{(1+\alpha(1-\theta)z)^2(1+(1-2\alpha)\theta z)}{(1-\alpha\theta z)^2(1-(1-2\alpha)(1-\theta)z)}$$

For small $z \in \mathbb{C}$, this amplification factor is an approximation to the exponential function and it holds:

$$|R^{\text{fst}}(\theta, \alpha, z) - \mathrm{e}^z| = (1-2\theta)\left(\alpha - \left(1 + \frac{1}{\sqrt{2}}\right)\right)\left(\alpha - \left(1 - \frac{1}{\sqrt{2}}\right)\right)|z|^2 + O(|z|^3).$$

Hence, for the choice $a = 1 - 1/\sqrt{2} \approx 0.29289$ the resulting method is second order accurate for every $\theta \in (0, 1)$. For $z = \lambda k$ it holds in the limit $\lambda \to -\infty$

$$R^{\text{fst}}(\theta, \alpha, k, \lambda) = \left|\frac{(1+\alpha(1-\theta)k\lambda)^2(1+(1-2\alpha)\theta k\lambda)}{(1-\alpha\theta k\lambda)^2(1-(1-2\alpha)(1-\theta)k\lambda)}\right| \xrightarrow[\lambda\to-\infty]{} \left|\frac{1-\theta}{\theta}\right|,$$

and strong A-stability follows for every $\theta \in (\frac{1}{2}, 1]$.

Remark 4.12 The parameter θ can be chosen to satisfy $\alpha\theta = (1-2\alpha)(1-\theta)$, such that each of the three steps has the same coefficient:

$$\alpha\theta = (1-2\alpha)(1-\theta) \quad \Leftrightarrow \quad \theta = \frac{1-2\alpha}{1-\alpha} = 2 - \sqrt{2} \approx 0.5858.$$

This choice has the advantage that application of (4.6) to a linear parabolic equation, the same system matrix

$$\mathcal{M} + \alpha\theta k\mathcal{A} \equiv \mathcal{M} + (1-2\alpha)(1-\theta)k\mathcal{A}$$

must be inverted in each of the three sub-steps. Regarding nonlinear problems with nonlinear differential operators $\mathcal{A}(u)$, this advantage is lost as a new system matrix must be assembled anyway.

Finally, it remains to analyze the dissipative character of the fractional-step θ-method. For $R(\lambda h, \theta)$, different θ values give

$$|R(\mathrm{i}, 1)| \approx 0.99687, \quad |R(\mathrm{i}, 2-\sqrt{2})| \approx 0.99970.$$

Being strongly A-stable and showing very little dissipation, the fractional step θ-scheme is one of the most-used time stepping methods for flow-problems. Second order accuracy is usually considered to be reasonable and the combination of strong A-stability with this nearly optimal dissipative character are well suited to represent the dynamics of fluid problems.

Many variants of the fractional step θ-scheme are possible, the choice of parameters $\theta \mapsto 1-\theta \mapsto \theta$ as well as $\alpha k \mapsto (1-2\alpha)k \mapsto \alpha k$ is due to symmetry reasons but not strictly required. Glowinski et al. [328] introduced a modified fractional step theta scheme that consists of only two implicit Euler like

sub-steps and one purely explicit extrapolation step:

$$t_{m-1} \xrightarrow[\alpha k]{\theta=1} t_{m-1+\alpha} \xrightarrow[(1-2\alpha)k]{\text{linear extrapolation}} t_{m-\alpha} \xrightarrow[\alpha k]{\theta=1} t_m.$$

The choice $\alpha = 1 - 1/\sqrt{2}$ again results in a second order scheme. Like the original fractional step θ-scheme, this modification is strongly A-stable and has good dissipation properties. It is slightly more damping than the original scheme, but each time step now consists of only two implicit systems and one very cheap extrapolation step. See [306] for a detailed discussion and comparison.

4.1.3 Galerkin Time Discretization Schemes

Single step methods for time stepping have the advantage of a very easy structure that makes an efficient implementation possible. Based on finite different techniques few analytical tools are available. Eriksson et al. [130, 131] as well as Thomée [323] derived Galerkin formulations of parabolic partial differential equations that are in some sense equivalent to the time stepping scheme. Having Galerkin formulations at hand, error estimates can be established by standard residual techniques known from the finite element analysis. Again, we consider a parabolic differential equation

$$\partial_t u + \mathcal{A}u = f \text{ in } I \times \Omega, \tag{4.7}$$

where $I = [0, T]$ and $\Omega \subset \mathbb{R}^d$. We have initial values for $t = 0$

$$u(0) = u^0,$$

and (homogenous) boundary data on $I \times \partial\Omega$. To derive a variational formulation in space and time, we multiply (4.7) with a function $\phi : I \times \Omega \to \mathbb{R}$ and integrate in space and time

$$\int_0^T (\partial_t u(t), \phi(t))\mathrm{d}t + \int_0^T a(u(t), \phi(t))\mathrm{d}t = \int_0^T (f(t), \phi(t))\mathrm{d}t \quad \forall \phi \in X. \tag{4.8}$$

We find the solution in the space

$$X := W(I) = \{\phi \in L^2(I; \mathcal{V}),\ \partial_t \phi \in L^2(I; V^*)\},$$

where $\mathcal{V} = H_0^1(\Omega)$, $\mathcal{V}^* = H^{-1}(\Omega)$ and with $W(I) \hookrightarrow C(I; L^2(\Omega))$, see [109, 351].

Again, we start by a splitting of $I = [0, T]$, into M discrete time steps t_i.

$$0 = t_0 < t_1 < \cdots < T_m = T, \quad k_m := t_m - t_{m-1}, \quad k := \max_{1 \le m \le M} k_m,$$

and half-open intervals $I_m := (t_{m-1}, t_m]$ to get

$$I = \{0\} \cup I_1 \cup \cdots \cup I_m.$$

Using these half-open intervals I_m, we introduce the function spaces

$$X_k^r = \{\phi_k \in C(\bar{I}; L^2(\Omega)) \mid \phi_k\big|_{I_m} \in \mathcal{P}_r(I_m; \mathcal{V}),\ m = 1, \ldots, M\},$$
$$\tilde{X}_k^r = \{\phi_k \in L^2(\bar{I}; L^2(\Omega)) \mid \phi_k\big|_{I_m} \in \mathcal{P}_r(I_m; \mathcal{V}),\ m = 1, \ldots, M,$$
$$\text{and } v_k(0) \in L^2(\Omega)\}.$$

By $\mathcal{P}_r(I; \mathcal{V})$ we denote the space of polynomials in time to degree r with values in $\mathcal{V} = H_0^1(\Omega)$. The space X_k^r consists of globally continuous (in time) functions that are piecewise polynomials. The space $\tilde{X}_k^r$ consists of globally L^2-functions that are piecewise polynomial. These functions might be discontinuous in the discrete points in time t_m. While it holds $X_k^r \subset X = W(I)$, it holds $\tilde{X}_k^r \not\subset X$. Although $\tilde{X}_k^r \not\subset X$, this space is suitable as test space for (4.8) as no temporal regularity is required. For (discontinuous) functions $u_k \in \tilde{X}_k^r$ we define

$$u_m^+ := \lim_{t \searrow t_m} u_m(t, \cdot) \in \mathcal{V},$$
$$u_m^- := \lim_{t \nearrow t_m} u_m(t, \cdot) \in \mathcal{V},$$
$$[u]_m := u_m^+ - u_m^- \in \mathcal{V}.$$

4.1.3.1 Discontinuous Galerkin Methods

A conforming discontinuous Galerkin formulation of (4.8) is given by restricting test and trial spaces to $\tilde{X}_k^r$ and finding $u_k \in \tilde{X}_k^r$ such that

$$\sum_{m=1}^{M} \int_{I_m} \Big\{(u_k'(t), \phi_k(t))_\Omega + a(u_k(t), \phi_k(t))\Big\}\, \mathrm{d}t + ([u_k]_{m-1}, \phi_{m-1}^+)_\Omega$$
$$= \sum_{m=1}^{M} \int_{I_m} (f(t), \phi_k(t))\, \mathrm{d}t \quad \forall \phi_k \in \tilde{X}_k^r.$$

The additional jump terms $([u_k]_{m-1}, \phi_{m-1}^+)$ will guarantee continuity of u in the limit $k \to 0$. Since solution $u_k \in \tilde{X}_k^r$ and test function $\phi_k \in \tilde{X}_k^r$ are discontinuous at every discrete time step t_m, the equation decouples and can be written in form of a time

stepping scheme. For $m = 1, \ldots, M$ find $u_k \in \mathcal{P}_r(I_m; \mathcal{V})$ such that

$$\int_{I_m} \left\{ (u_k'(t), \phi_k(t))_\Omega + a(u_k(t), \phi_k(t)) \right\} \mathrm{d}t + ([u_k]_{m-1}, \phi_{k,m-1}^+)_\Omega = \int_{I_m} (f(t), \phi_k(t))_\Omega \, \mathrm{d}t \quad \forall \phi_k \in \mathcal{P}_r(I_m; \mathcal{V}). \tag{4.9}$$

As example, we consider the most simple case of a dG(0)-discretization with piecewise constant trial and test functions

$$u_k\Big|_{I_m} =: u_k^m \in \mathcal{V}, \quad \phi_k\Big|_{I_m} =: \phi_k^m \in \mathcal{V},$$

where u_k and ϕ_k are piecewise constant such that it holds:

$$\phi_{k,m-1}^+ = \phi_k^m, \quad [u_k]_{m-1} = u_k^m - u_k^{m-1}.$$

The time derivative $u_k' = 0$ is zero on every interval I_m, hence the Galerkin formulation is simplified to finding $u_k^m \in \mathcal{V}$ such that for $m = 1, 2, \ldots, M$ it holds

$$(u_k^m - u_k^{m-1}, \phi_k^m)_\Omega + k_m a(u_k^m, \phi_k^m) = \int_{I_m} (f(t), \phi_k^m) \, \mathrm{d}t \quad \forall \phi_k^m \in V. \tag{4.10}$$

Apart from the integral in the right hand side this is exactly the implicit Euler scheme. By approximating the integral with the right-sided box scheme

$$\int_{I_m} (f(t), \phi_k^m)_\Omega \, \mathrm{d}t = k_m (f(t_m), \phi_k^m)_\Omega + O(k_m^2),$$

we recover the implicit Euler method.

Remark 4.13 (Equivalence Between Galerkin and Time Stepping Methods) As shown, the dG(0)-Galerkin method is equivalent to the backward Euler scheme, if the equation, namely $a(\cdot, \cdot)$, is linear, and if the problem is autonomous without explicit dependency on the time t. For nonlinear equations or with time-depending right hand side $f(t)$ (or time-depending operator $a(t)(\cdot, \cdot)$) equivalency between the Galerkin scheme and the time stepping scheme is only up to numerical quadrature error. In the case of the implicit Euler method discussed above this quadrature error has the same order as the method itself.

Remark 4.14 It can be shown that every dG(r) discretization of the model problem corresponds to a sub-diagonal $(r + 2, r + 1)$ Padé approximation of the exponential function, see [289]. Hence, we know that these approximations have optimal order:

$$|R(z) - \exp(z)| = O(k^{2r+2}).$$

This relation shows the optimal super-convergence order $2r + 1$ (in the discrete points t_m) of discontinuous Galerkin methods when applied to linear autonomous problems. See [323] for the general proof of this super-convergence property. Further, it is well known that for every sub diagonal $(r, r + 1)$ Padé approximation there exists an implicit Runge-Kutta method with the same amplification factor. This connection is guideline for a possible general procedure: The parabolic equation is solved by using an efficient time stepping scheme (e.g. a Runge-Kutta method), the error estimator is derived by using the correspondence to a Galerkin method that allows for residual based techniques. If Galerkin method and time stepping scheme differ by a numerical quadrature error, this additional error must taken into account. See Sect. 8.1.2 for details.

The effort for approximating a parabolic equation with a discontinuous Galerkin method is considerably larger than by using a single-step method. The local dG(r) solution has $r + 1$ local degrees of freedom

$$u_k(t)\Big|_{I_m} = \sum_{s=0}^{r} u_k^s t^s$$

that all couple to each other within every time step. Considering parabolic equations (and not simple initial value problems) the spatial discretization has to be taken into account. $r + 1$ degrees of freedom in time must be multiplied with $N := \operatorname{div} V_h$ degrees of freedom in space coming from the finite element (or finite difference) discretization. Where the implicit Euler or θ-scheme asks for the solution of a $N \times N$ linear system, the dG(r) method requires to solve a coupled $(r + 1)N \times (r + 1)N$ linear system of equations. This huge effort—in terms of computational time as well as memory—is usually not feasible. In [289, 317], the authors describe an approximation scheme for splitting the large linear system into a sequence of smaller N by N systems.

4.1.3.2 Continuous Galerkin Methods

Continuous Galerkin methods find the solution u_k in spaces of continuous functions:

$$X_k^r := \{\phi \in C(I; \mathcal{V}),\ \phi\big|_{I_m} \in \mathcal{P}_r(I_m; \mathcal{V})\}.$$

For $u_k \in X_k^r$ it holds $[u_k]_m = 0$. By choosing the discontinuous test space $\tilde{X}_k^{r-1}$, the discrete system decouples. Both spaces X_k^r and $\tilde{X}_k^{r-1}$ have the same dimension, as one unknown in X_k^r per interval is used to guarantee continuity. This coupled $X_k^r/\tilde{X}_k^{r-1}$ approach will be called the cG(r)-discretization.

Due to global continuity of u_k, the minimal polynomial degree is one, combined with piecewise constant test functions. On I_m, we write $u_k \in X_k^r$ and $\phi_k \in \tilde{X}_k^{r-1}$ as:

$$u_k\Big|_{I_m} = \left(\frac{t_m - t}{t_m - t_{m-1}}\right) u_k^{m-1} + \left(\frac{t - t_{m-1}}{t_m - t_{m-1}}\right) u_k^m, \quad \phi_k\Big|_{I_m} =: \phi_k^m \in \mathcal{V},$$

where $u_k^m \in \mathcal{V}$. As the trial functions are piecewise linear, the time-derivative is given by

$$\int_{I_m} (u'(t), \phi_k^m)_\Omega \, \mathrm{d}t = (u_k^m - u_k^{m-1}, \phi_k^m)_\Omega.$$

Further, it holds

$$\int_{I_m} \left(\frac{t_m - t}{t_m - t_{m-1}} \right) \mathrm{d}t = \int_{I_m} \left(\frac{t - t_{m-1}}{t_m - t_{m-1}} \right) \mathrm{d}t = \frac{t_m - t_{m-1}}{2}.$$

By these relations, the cG(1)-Version of (4.8) simplifies to solving

$$(u_k^m - u_k^{m-1}, \phi_k^m)_\Omega + \frac{k_m}{2} \left\{ a(u_k^m, \phi_k^m) + a(u_k^{m-1}, \phi_k^m) \right\} = \int_{I_m} (f(t), \phi_k^m)_\Omega \, \mathrm{d}t$$

for $m = 1, 2, \ldots M$ and for all test function $\phi_k^m \in \mathcal{V}$. If the right hand side $f(t)$ is piecewise constant, or if we approximate the integral on the right hand side by the trapezoidal rule, we recover the Crank-Nicolson method for time stepping.

Remark 4.15 The amplification factor of the Crank-Nicolson method is the diagonal $(2, 2)$-Padé approximation of the exponential function. It can be shown that every cG(r)-Galerkin formulation applied to a linear autonomous problem is equivalent to a time stepping method with amplification factor that corresponds to the $(r + 1, r + 1)$ Padé approximation. Hence, the nodal accuracy of the cG(r) formulation is $O(k^{2r})$.

It is also possible to derive Galerkin-formulation of non-standard discretization schemes, like the one-step θ method or even the fractional step θ scheme, see [239, 306]. Formally, the θ scheme can be derived by combining piecewise linear and continuous trial functions $u_k \in X_I^1$ with discontinuous θ-weighted test functions:

$$\phi_k^\theta \Big|_{I_m} = 1 + \frac{6}{k_m} (2\theta - 1) \left(t - \frac{t_{m-1} + t_m}{2} \right). \tag{4.11}$$

For $\theta = 1/2$ it holds $\phi_\theta^m \equiv 1$ and we recover the Crank-Nicolson method. For arbitrary $\theta \in [0, 1]$ it holds for $u_k \in X_k^1$:

$$\int_{I_m} u_k'(t) \cdot \phi_k^\theta(t) \, \mathrm{d}t = u_k^m - u_k^{m-1},$$

$$\int_{I_m} u_k(t) \cdot \phi_k^\theta(t) \, \mathrm{d}t = \theta k_m u_k^m + (1 - \theta) k_m u_k^{m-1}.$$

This way, the θ time stepping method can be reconstructed for linear autonomous problems. For the general non-linear case we must again rely on numerical quadrature. Here, the θ time stepping method is obtained by approximating all

integrals with the quadrature rule

$$\int_{I_m} f(t)\phi_k^\theta(t)\,\mathrm{d}t = \theta k_m f(t_m) + (1-\theta)k_m f(t_{m-1}) + O(k_m^3).$$

4.1.4 Time Discretization of the Stokes and Navier-Stokes Equations

The incompressible Stokes and Navier-Stokes equations are of saddle-point type, with a pressure variable $p \in \mathcal{L} := L^2(\Omega) \setminus \mathbb{R}$ that serves as Lagrange-multiplier to guarantee the divergence condition. Given an initial value $\mathbf{v}(0,\cdot) = \mathbf{v}^0(\cdot)$, we find $\{\mathbf{v}, p\} \in \mathcal{V} \times \mathcal{L} := H_0^1(\Omega)^d \times \{L^2(\Omega) \setminus \mathbb{R}\}$ such that

$$(\partial_t \mathbf{v}, \phi) + (\nabla \mathbf{v}, \nabla\phi) - (p, \nabla\cdot\phi) + (\nabla\cdot\mathbf{v}, \xi) = (\mathbf{f}, \phi) \quad \forall \{\phi, \xi\} \in \mathcal{V} \times \mathcal{L}.$$

Again, by $0 = t_0 < \cdots < t_M = T$ we denote the discrete time steps. We aim at deriving the Crank-Nicolson (or general θ) method for this set of equations. The first obvious choice for defining the time stepping method is to iterate:

$$\begin{aligned}(\mathbf{v}_k^m - \mathbf{v}_k^{m-1}, \phi) &+ \frac{k_m}{2}\big\{(\nabla\mathbf{v}_k^m, \nabla\phi) - (p_k^m, \nabla\cdot\phi) + (\nabla\cdot\mathbf{v}_k^m, \xi)\big\} \\ &+ \frac{k_m}{2}\big\{(\nabla\mathbf{v}_k^{m-1}, \nabla\phi) - (p_k^{m-1}, \nabla\cdot\phi) + (\nabla\cdot\mathbf{v}_k^{m-1}, \xi)\big\} \\ &= \frac{k_m}{2}(\mathbf{f}(t_{m-1}) + \mathbf{f}(t_m), \phi).\end{aligned}$$

This formulation however does not properly reflect the role of the pressure as Lagrange multiplier. As the old pressure p^{m-1} enters each time step, it will also influence the new solution. Since the continuous pressure usually comes without temporal regularity, such a relationship between old and new pressure could lead to unphysical solutions. Further, by testing with $\xi = \nabla\cdot\mathbf{v}_k^m - \nabla\cdot\mathbf{v}_k^{m-1}$ we get the relation:

$$\|\nabla\cdot\mathbf{v}_k^m\|^2 = \|\nabla\cdot\mathbf{v}_k^m\|^2.$$

If the initial solution $\mathbf{v}^0$ is not strictly divergence-free, this defect will be conserved for $m \to \infty$. Further, since we must expect truncation errors, there is no corrective that assures $\|\nabla\cdot\mathbf{v}_k^m\| \to 0$. A remedy to both problems is given by first restricting the Stokes equations into the manifold of divergence free functions

$$\mathcal{V}_0 := \{\phi \in \mathcal{V},\ \mathrm{div}(\phi) = 0\},$$

and by applying the Crank-Nicolson (or θ-scheme) on $\mathcal{V}_0$. Then, the pressure is added as Lagrange multiplier in every discrete time step:

$$(\mathbf{v}_k^m - \mathbf{v}_k^{m-1}, \phi) + \frac{k_m}{2}(\nabla \mathbf{v}_k^m, \nabla \phi) + \frac{k_m}{2}(\nabla \mathbf{v}_k^{m-1}, \nabla \phi) \\ - (p_k^m, \nabla \cdot \phi) + (\nabla \cdot \mathbf{v}_k^m, \xi) = \frac{k_m}{2}\left\{(\mathbf{f}^{m-1}, \phi) + (\mathbf{f}^m, \phi)\right\}. \tag{4.12}$$

In principle, all of the time-discretization schemes discussed in the previous section are suitable for the incompressible Navier-Stokes equations. As the equation (of nonlinear parabolic type) has a damping property [186] but also asks for the conservation of energy in terms of vortices a good method should have good stability properties while showing little dissipation. The fractional step θ-scheme or the implicitly shifted Crank-Nicolson method is a very good candidate.

It is not possible to find a Galerkin scheme that is equivalent to this time stepping method. However, we get close to this formulation by using a mixed Galerkin method with continuous piecewise linear velocities and a discontinuous, piecewise constant pressure (of course without adding jump-terms to the discrete system). This formulation will prevent the old pressure p_k^{m-1} from entering the new time step I_m, it however still does not strictly enforce divergence freeness in every interval. See [133, 134, 240] for details.

4.2 Spatial Discretization

In this section,we introduce the necessary concepts of the finite element method. We start by describing finite elements for the Laplace equation

$$u \in \mathcal{V} = H_0^1(\Omega): \quad (\nabla u, \nabla \phi)_\Omega = (f, \phi)_\Omega \quad \forall \phi \in \mathcal{V},$$

for a given right hand side $f \in L^2(\Omega)$. The domain $\Omega \subset \mathbb{R}^d$ is two or three dimensional. First, we partition this domain into a triangulation (or mesh) Ω_h, consisting of open elements $K \subset \mathbb{R}^d$. These elements are simple geometric structures like triangles, quadrilaterals or tetrahedra. The boundary of each element K has a finite number of edges $e \in K$ and nodes $x \in K$. The edges $e \in K$ are not necessarily straight, see Fig. 4.1 for different triangulations. We define

Definition 4.16 (Structural Regularity) A triangulation $\Omega_h = \{K_1, \ldots, K_N\}$ of the domain $\Omega \subset \mathbb{R}^d$ is called *structural regular*, if the elements cover the domain

$$\bar{\Omega} = \bigcup_{n=1}^{N} \bar{K}_i,$$

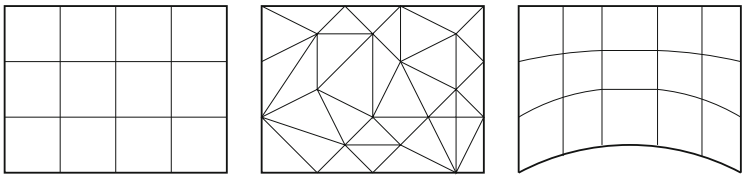

Fig. 4.1 Different triangulations Ω_h for a domain $\Omega \subset \mathbb{R}^2$. *From left to right*: structured quadrilateral mesh, unstructured triangular mesh and structured quadrilateral mesh using curved parametric elements

and if each two elements different are disjoint

$$K_i \cap K_j = \emptyset \quad \forall i \neq j,$$

and if the intersection of the closure is either a common node, or a (complete) common edge

$$\bar{K}_i \cap \bar{K}_j = \begin{cases} \emptyset & \text{or,} \\ e \in K_i \text{ and } e \in K_j & \text{or,} \\ x \in K_i \text{ and } x \in K_j. \end{cases}$$

It is obvious that a curved domain $\Omega \subset \mathbb{R}^d$ cannot be triangulated with geometric structures like triangles. Instead we must use meshes with curved elements, as shown in Fig. 4.1 (right). A common approach for curved finite element meshes is to base every element $K \in \Omega_h$ on one common reference element $\hat{K}$.

Definition 4.17 (Parametric Triangulation) Let $\hat{K} \subset \mathbb{R}^d$ be the reference element. Further, let

$$\hat{P}(\hat{K}) \subset C(\hat{K})^d$$

be a function space mapping to $\mathbb{R}^d$. A triangulation Ω_h is called *parametric*, if every element $K \in \Omega_h$ arises from the mapping of the reference element

$$\forall K \in \Omega_h \text{ there exists a } T_K \in \hat{P}(\hat{K}) \text{ such that } K = T_K(\hat{K}).$$

Usually, for the reference element $\hat{K}$ one chooses the unit triangle, the unit quad or the unit hex. If the space $\hat{P}(\hat{K})$ is the space of affine mappings, the parametric triangulation Ω_h will consist of standard elements with straight edges only. If we consider mappings $\hat{P}(\hat{K})$ of higher polynomial degree (or even rational functions), we can generate curved elements that can be used to approximate domains with curved boundaries. Next, we define conditions on the shape of each element.

Definition 4.18 (Shape Regularity of Triangular Meshes) A family of triangular meshes Ω_h, $(h > 0)$ is called *shape regular*, if there exists a constant $c > 0$, independent on $h > 0$, such that

$$\max_{K \in \Omega_h} \frac{h_K}{\rho_K} \geq c,$$

where by $h_K := \operatorname{diam}(K)$ we denote the diameter of K and by ρ_K the radius of the largest inscribed circle.
Shape regularity of a sequence of meshes describes that all triangles have approximately the same shape. It holds

Lemma 4.19 (Shape Regularity of Triangular Meshes) *For a family of triangular meshes Ω_h, $(h > 0)$ the following conditions are equivalent*

1. *The family of meshes is shape regular according to Definition 4.18.*
2. (Minimum angle condition) *There exists a constant $c > 0$ independent of $h > 0$, such that all interior angles α are bound away from zero $\alpha \geq c$.*
3. (Maximum angle condition) *There exists a constant $c > 0$ independent of $h > 0$, such that all interior angles α are bound away from π by $\alpha \leq \pi - c$.*

Proof See [96]. □

Describing suitable shape regularity conditions for other types of finite element meshes is more complicated. Already for quadrilateral meshes one must combine minimum and maximum angle conditions to prevent that quadrilaterals can degenerate to triangles. Instead we introduce a more general concept of shape regularity that can be applied to all kinds of parametric meshes.

Definition 4.20 (Shape Regularity of Parametric Meshes) A family parametric mesh Ω_h, $h > 0$ with reference element $\hat{K}$ is called shape regular, if there exists a constant $c > 0$, such that it holds

$$\|\nabla T_K\| \, \|(\nabla T_K)^{-1}\| \leq c \quad \forall K \in \Omega_h,$$

where $T_K : \hat{K} \to K$ is the reference map for element $K \in \Omega_h$ and with a constant $c > 0$ that does not depend on $h > 0$ or $K \in \Omega_h$.
This definition of shape regularity is less obvious, it however is directly usable for deriving interpolation estimates. These estimates are usually shown on fixed reference elements $\hat{K}$ and then carried over to a specific $K \in \Omega_h$ by using this reference mapping. For triangular meshes, we can show that this general definition is equivalent to those given in Lemma 4.19:

Lemma 4.21 *Let Ω_h be a triangular mesh. The condition of Definition 4.20 is equivalent to those given in Lemma 4.19.*

Proof Let $\hat{K} = \{(x, y) \in \mathbb{R}^2_+, \ 0 < x + y < 1\}$ be the reference triangle. Further, Let T_K be an element map, given as (neglecting rotation, translation and isotropic

scaling, as all these operations do not effect the shape)

$$T_K(x, y) = \begin{pmatrix} 1 & s \\ 0 & a \end{pmatrix},$$

where $1 : a$ with $a > 0$ indicates the anisotropic aspect ratio and s refers to the shearing. It holds

$$\|\nabla T_K\|_1 \, \|\nabla T_K\|_1^{-1} = \max\left\{1, |s| + |a|\right\} \max\left\{1, \frac{|s|}{|a|} + \frac{1}{|a|}\right\},$$

and for this expression to be bounded independent of $h > 0$, it must hold

$$|s|, |a| \leq c < \infty, \quad |a| \geq \frac{1}{c}.$$

By these limits, the three vertices of the reference triangle get mapped to

$$(0,0) \mapsto (0,0), \quad (0,1) \mapsto (s,a), \quad (1,0) \mapsto (1,0), \quad s \in [-c, c], \; a \in [c^{-1}, c],$$

such that the regularity conditions are fulfilled. □

Remark 4.22 (Boundary Approximation) Most commonly, one considers polynomial spaces for the element maps T_K. Such a mapping allows for higher order representation of curved boundaries, see Fig. 4.1. A more recent approach is the *Isogeometric Analysis*: the geometrical domains in application problems are usually designed with the help of CAD-programs. These programs use splines (NURBS) for representing the domain. The Isogeometric Analysis uses these splines for defining the finite element mesh and the discrete finite element spaces. By this construction, every geometrical error is eliminated, see Bazilevs et al. [31].

The quality and the resolution of the finite element mesh will determine the accuracy of the finite element approximation. Constructing a finite element mesh of a domain $\Omega \subset \mathbb{R}^d$ can be a very difficult task. In particular for complex technical structures, a mesh can consist of millions of elements just for resolving the complex geometry. Further, it is possible that this complex mesh will not have the proper resolution at the correct spots to deliver good approximative solutions. In such cases, a mesh must be *refined*. Refining a mesh is either done by *remeshing* and constructing a completely new triangulation with better resolution in certain areas or by *mesh refinement*. Here, elements of a mesh are split into smaller elements. By mesh refinement, we usually must break the structural regularity assumption. In Fig. 4.2, we show different procedures for mesh refinement. While the left sketch shows a refinement that does not satisfy the structural-regularity condition, it is simple as every triangle can be split in the same way. The right refinement type yields shape regular meshes, different types of refinement must however be used depending on the refinement topology of a triangle. If we consider quadrilateral meshes one always uses a simple refinement model, where each quad is split into

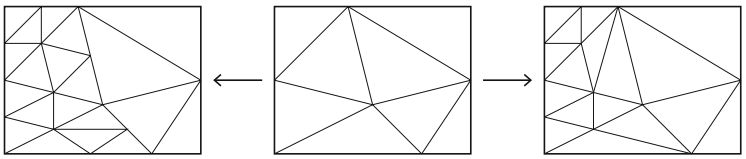

Fig. 4.2 Different types of mesh-refinement. *Left*: refinement of a triangle into three triangles using hanging nodes. *Right*: using different refinement types such that no hanging nodes appear

four smaller quads. A shape-regular refinement is only possible, if quadrilateral elements are coupled with triangular elements.

If refinement techniques are used that generate non shape regular meshes, nodes on the middle of edges appear. These nodes will be called *hanging nodes* and must be treated with special care when constructing finite element spaces. We will allow for meshes with one hanging node on an edge only. A mesh without hanging nodes and with element that all have approximately the same size is called a *uniform mesh*. A mesh with areas of mesh refinement is called a *locally refined mesh*.

Locally refined meshes are *unstructured meshes* as apposed to *structured meshes* like meshes of tensor product type with nodes

$$x_k = (x_r, y_s, z_t) = h \cdot (r, s, t) \quad 0 \leq r, s, t \leq M.$$

For unstructured meshes, there is no uniform mesh topology. Each node can be part of a different number of elements. Finite element libraries on unstructured meshes call for a dynamic memory layout. Compared to structured finite element approaches, this calls for a large computational overhead. Efficient use of modern hardware with efficient memory usage is troublesome. On the other hand, unstructured meshes allow for a more efficient distribution of the unknowns. The same approximation property can be reached with far smaller problem sizes. Often there is a narrow balance between both approaches. The concept of *mesh grading* sometimes allows for an efficient compromise between fully unstructured meshes and structured meshes. Instead of changing the number of unknowns locally, one only moves the nodal points attached to the degrees of freedom in order to reach adequate local accuracy, see [8].

If the boundaries Γ of the domain $\Omega \subset \mathbb{R}^d$ are not polygonal, a triangulation into simplices will not match the domain

$$\Omega \neq \bigcup_{K \in \Omega_h} K$$

and a geometric error will occur. For better approximation of *curved domains*, the element mapping T_K must not be affine, but is allowed to have a higher degree. Figure 4.1 (right) shows the approximation of a circular domain with a quadrilateral mesh using affine mappings and a quadrilateral mesh using a piecewise biquadratic mapping.

4.2.1 Finite Elements

Finite element spaces V_h are defined locally on the elements $K \in \Omega_h$ of the mesh Ω_h. The most basic finite element space on a triangular mesh is the space of piecewise linear functions

$$V_h = \{\phi \in C(\bar{\Omega}) \mid \phi\big|_K \in \text{span}\{1, x, y\} \ \forall K \in \Omega_h\}.$$

On every triangle $K \in \Omega_h$, the finite element space is locally constructed by three basis-functions $\phi_K^1, \phi_K^2, \phi_K^3$ such that for the three nodes x_K^1, x_K^2, x_K^3 it holds $\phi_K^j(x_K^i) = \delta_{ij}$. These basis functions are glued together with the basis functions of neighboring elements.

Such a local construction of finite element spaces is difficult on general elements like quadrilaterals that arise from the transformation of a reference element. A more general approach uses parametric finite elements, where the basis is defined on the reference element $\hat{K}$. As reference elements, we consider the reference triangle or quad in two dimensions and the reference tetrahedra or hex in three dimensions. Let

$$\begin{aligned} \hat{P}_r &:= \text{span}\,\{x^\alpha,\ 0 \le \sum_i \alpha_i \le r \text{ with } 0 \le \alpha_i \le r\}, \\ \hat{Q}_r &:= \text{span}\,\{x^\alpha,\ 0 \le \alpha_i \le r\}, \end{aligned} \tag{4.13}$$

where $\alpha \in \mathbb{N}^d$ is a multi-index. By $\{\phi_1, \ldots, \phi_n\}$ we denote a basis of these polynomial spaces. Besides the usual monomial basis functions $\phi_\alpha = x^\alpha$, we make use of nodal basis functions: let $\hat{x}_i \in \hat{K}$ be uniformly distributed piecewise distinct points in $\hat{K}$. Then, the nodal basis functions $\hat{\phi}_i \in P_r$ (or $\hat{\phi}_i \in Q_r$) are defined by the property

$$\hat{\phi}_i(\hat{x}_j) = \delta_{ij}, \quad i, j = 1, \ldots, n.$$

By this notation, we can define the nodal basis functions $\phi_i,\ i = 1, \ldots, n$ for every mesh-element $K \in \Omega_h$ by using the domain-map

$$\phi_i^K := \hat{\phi}_i \circ T_K^{-1},\ i = 1, \ldots, n.$$

If the element map $T_K : \hat{K} \to K$ is affine, the resulting basis functions are polynomials in the same space as the reference basis. For general polynomial mapping however, the nodal basis usually consists of rational functions. In the mesh-nodes $x_i^K := T_K(\hat{x}_i^K)$ it holds $\phi_i^K(x_j) = \delta_{ij}$. The global finite element space of order r is then given by

$$V_h^r := \{\phi \in C^0(\bar{\Omega}) :\ \phi\big|_K \circ T_K \in P_r \text{ (or } Q_r)\} = \text{span}\{\phi_i,\ i = 1, \ldots, N\},$$

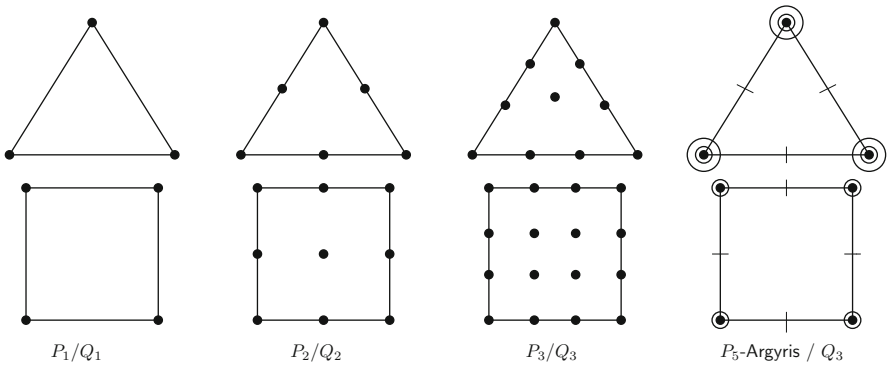

Fig. 4.3 Some finite elements. The first three columns show the degrees of freedom in the classical H^1-conforming Lagrange elements. Node-values are equally distributed in the elements. The two elements on the right are H^2-conforming. Besides the node values we indicate the first derivative $\nabla\phi$ (two values each, *small circle*), the second derivatives $\nabla^2\phi$ (three values each, *big circles*) and the normal derivatives $\partial_n\phi$ (one value each) in the edge midpoints. Altogether, we specify the $3 \cdot (1 + 2 + 3) + 3 = 21$ unknowns of the P_5 and $4 \cdot (1 + 2) + 4 = 16$ unknowns of Q_3

where the basis functions ϕ_i are given by gluing the local basis functions ϕ_i^K together. Finite element spaces with global continuity are H^1-*conforming* $V_h \subset \mathcal{V} = H^1(\Omega)$. For some applications, higher regularity is required. If $V_h \subset C^1(\Omega)$, the finite element space will be H^2-conforming, i.e. $V_h \subset H^2(\Omega)$.

In Fig. 4.3 we show typical distributions of the nodes for different reference elements and indicate the corresponding polynomial space. The first three columns show Lagrangian elements on triangles and quadrilaterals up to degree 3. The last columns shows two H^2-conforming elements, where node values and derivative values are specified.

Sometimes, we do not require H^1-conformity. Considering the Navier-Stokes equations, the pressure must only be discretized with L^2-conforming finite elements that are not necessarily continuous. Here, we introduce discontinuous finite element spaces:

$$V_h^{r,\mathrm{dc}} := \{\phi \in L^2(\Omega) \to \mathbb{R} : \ \phi\big|_K \in P_r \text{ (or } Q_r), \ \forall K \in \Omega_h\}.$$

This space is not H^1-conforming, but at least L^2-conforming. Continuous finite element spaces using the element mapping T_K are called *parametric finite elements*. If the element map is a polynomial from the same polynomial space $[P_r]^d$ or $[Q_r]^d$ as the finite element basis, the approach is called *isoparametric*.

4.2.1.1 Interpolation with Finite Elements

Interpolation operators $I_h : V \to V$ are the most important tool for finite element error analysis since due to their local construction they allow for a local analysis.

The nodal interpolant N_h of a function $u : K \to \mathbb{R}$ is constructed by a simple pointwise process on every element:

$$N_h u(x) = \sum_{i=1}^{L} u(x_i^K)\phi_i^K(x)$$

Nodal interpolants are completely local, only information on one element $K \in \Omega_h$ is required. They are however only well-defined for functions $u \in C(\bar{K})$. This is not the case for the Sobolev-space H^1. Here, single point-values must not be finite. If we require interpolants of functions with such minimal regularity, we must replace the point-evaluation $u(x_i^K)$ by some kind of averages.

Lemma 4.23 (Nodal Interpolation on $K \in \Omega_h$) *Let $K \in \Omega_h$ and $T_K : \hat{K} \to K$ and $u \in H^{r+1}(K)$. Then it holds for the nodal interpolation of polynomial degree r*

$$\|\nabla^k(u - N_h u)\|_K \leq h^{r+1-k}\|\nabla^{r+1}u\|_K, \quad 0 \leq k \leq r,$$

and, on the boundary of K it holds

$$\|u - N_h u\|_{\partial K} \leq h^{r+\frac{1}{2}}\|\nabla^{r+1}u\|_K.$$

Proof For the proof, we refer to the literature [7]. □

The nodal interpolation operator $u \mapsto N_h u$ is only well-defined, if $u \in C(\bar{\Omega})$. Point values of u must be well defined. For H^1-functions, this regularity is not necessarily given, such that a nodal interpolation can never by H^1-stable. For $u \in H^1(\Omega)$, interpolation operators must be defined in terms of averages. The most famous H^1-stable interpolation operator is the *Clement-Interpolation*:

Lemma 4.24 (Clement-Interpolation) *Let $u \in H^1(\Omega)$ and $V_h \subset H^1(\Omega)$ be a Lagrangian finite element space with basis $\phi_i(x_j) = \delta_{ij}$ on the triangulation Ω_h. Then, the Clement-Interpolation $C_h u \in V_h$ given as*

$$C_h u = \sum_{i=1}^{n} \chi_i(u)\phi_i, \quad \chi_i(u) = \frac{1}{|P_i|}\int_{P_i} u \mathrm{d}x,$$

with the patches *P_i defined as unions of all elements that touch a node x_i*

$$P_i := \bigcup_{K \in \Omega_h,\, x_i \in \bar{K}} K$$

is H^1-stable

$$\|\nabla C_h u\| \leq c\|\nabla u\| \quad \forall u \in H^1(\Omega).$$

It holds

$$\|\nabla C_h u\|_K \leq c_1 \|\nabla u\|_{P_K}, \quad P_K := \bigcup_{L \in \Omega_h,\, \bar{L} \cap \bar{K} \neq \emptyset} L.$$

Proof The proof easily follows by showing stability of the node functionals $\xi_i(\cdot)$ and using Bramble-Hilbert Lemma. See [100]. □

Remark 4.25 (Interpolation on Anisotropic Meshes) The Clement interpolation is a H^1-stable operator

$$\|\nabla C_h u\|_K \leq c \|\nabla u\|_{P_K},$$

with a constant $c > 0$ that does not depend on $h > 0$. The Clement operator however fails, if the mesh-elements $K \in \Omega_h$ are anisotropic with $h_{\min}(K) \ll h_{\max}(K)$. On such elements, it only holds

$$\|\nabla C_h u\|_K \leq c \frac{h_{\max}(K)}{h_{\min}(K)} \|\nabla u\|_{P_K}.$$

An H^1-stable alternative to the Clement operator, which is also stable on anisotropic meshes, is the Scott & Zhang operator. Here, the nodal values are also defined as averages, but averaging is only applied over edges of elements. This helps to avoid mixing of mesh-sizes in different directions. See [305] for basics on the Scott & Zhang interpolation operator, and [7] for an analysis of interpolation operators on anisotropic meshes.

4.2.2 Finite Element Analysis for Elliptic Problems

Let $\mathcal{V} = H_0^1(\Omega)$ and $V_h \subset \mathcal{V}$ be a finite element subspace. By $a(\cdot,\cdot) : \mathcal{V} \times \mathcal{V} \to \mathbb{R}$ we denote an elliptic and continuous bilinear-form, such that there exist constants $c_1, c_2 > 0$ such that

$$a(u,v) \leq c_1 \|\nabla u\|_\Omega \, \|\nabla v\|_\Omega, \quad a(u,u) \geq c_2 \|\nabla u\|^2.$$

This bilinear-form defines a the *energy norm*.

Lemma 4.26 (Energy Norm) *Let $a(\cdot,\cdot)$ be a $\mathcal{V}$-elliptic and continuous bilinear form. Then,*

$$\|u\|_a := \sqrt{a(u,u)},$$

defines a norm that is equivalent to the $\mathcal{V}$-norm.

For $f \in L^2(\Omega)$ we denote by $u \in \mathcal{V}$ and $u_h \in V_h$ solutions to

$$a(u, \phi) = (f, \phi) \quad \forall \phi \in \mathcal{V}, \quad a(u_h, \phi_h) = (f, \phi_h) \quad \forall \phi_h \in V_h. \tag{4.14}$$

It holds

Lemma 4.27 (Galerkin Orthogonality) *For the solution $u \in \mathcal{V}$ and the conforming Galerkin-solution $u_h \in V_h \subset \mathcal{V}$ it holds*

$$a(u - u_h, \phi_h) = 0 \quad \forall \phi_h \in V_h.$$

Proof This follows as $V_h \subset \mathcal{V}$ allows subtract the two equations in (4.14) and choose $\phi := \phi_h \in \mathcal{V}$. □

Using Galerkin orthogonality we can directly show the following important property:

Lemma 4.28 (Best Approximation, Cea's Lemma) *The conforming finite element approximation is best approximation in the energy norm $\|u\|_a := \sqrt{a(u,u)}$*

$$\|u - u_h\|_a \leq c_1 \min_{\phi_h \in V_h} \|u - \phi_h\|_a$$

and it holds

$$\|\nabla(u - u_h)\| \leq \frac{c_1}{c_2} \min_{\phi_h \in V_h} \|\nabla(u - \phi_h)\|.$$

Proof This follows with of Galerkin orthogonality

$$\begin{aligned} c_2 \|\nabla(u - u_h)\|^2 \leq \|u - u_h\|_a^2 &= a(u - u_h, u - u_h) \\ &= a(u - u_h, u - \phi_h) \leq c_1 \|u - u_h\|_a \, \|u - \phi_h\| \end{aligned}$$

□

Using this best-approximation property, and choosing the interpolant $\phi_h := I_h u \in V_h$ we get a first error estimate.

Lemma 4.29 (Energy Norm A Priori Estimates) *Let $u \in H^{r+1}(\Omega) \cap \mathcal{V}$ be the solution to (4.14), and $u_h \in V_h^r \subset \mathcal{V}$ be the finite element solution. It holds:*

$$\|\nabla(u - u_h)\| \leq c h^r \|\nabla^{r+1} u\|.$$

Proof This result follows by combining best approximation and interpolation estimates. □

Lemma 4.30 (L^2-Norm A Priori Error Estimate) *Let $u \in H^{r+1}(\Omega) \cap \mathcal{V}$ and $u_h \in V_h^r$ be solutions to (4.14). Then, it holds*

$$\|u - u_h\| \leq ch^{r+1} \|\nabla^{r+1} u\|.$$

Proof Let $z \in \mathcal{V}$ be the solution to the adjoint problem

$$a(\phi, z) = (f_z, \phi) \quad \forall \phi \in V, \quad f_z := \frac{u - u_h}{\|u - u_h\}}.$$

As the finite element space is conforming it holds that $f_z \in \mathcal{V} \hookrightarrow L^2(\Omega)$. Hence given sufficient solution of the domain elliptic regularity gives $z \in H^2(\Omega) \cap \mathcal{V}$ and

$$\|z\|_{H^2(\Omega)} \leq c_s \|f_z\| = c_s.$$

We choose $\phi = u - u_h$ to get by using Galerkin orthogonality:

$$\begin{aligned} \|u - u_h\| &= a(u - u_h, z) = a(u - u_h, z - I_h z) \\ &\leq c \|\nabla(u - u_h)\| \, \|\nabla(z - I_h z)\| \\ &\leq ch^r \|\nabla^{r+1} u\| \, c_I h \|\nabla^2 z\| \\ &\leq ch^{r+1} \|\nabla^{r+1} u\|. \end{aligned}$$

□

Here, we only report on the most basic a priori error estimates, namely the energy norm error and the L^2-error. Estimating the error in a pointwise sense, i.e. in the norm $\|u - u_h\|_{L^\infty(\Omega)}$ is more complex.

Lemma 4.31 (Maximum Norm Priori Estimates) *Let $u \in C^2(\bar{\Omega}) \cap \mathcal{V}$ and $u_h \in V_h^1$ be solutions to (4.14). Then, it holds*

$$\max_{\Omega} |u - u_h| \leq ch^2 \big\{ |\ln(h) + 1| \big\} \max_{\Omega} |\nabla^2 u|$$

Proofs are found in [269, 272, 301].

As $|\ln(h)| \to \infty$ for $h \to \infty$, the convergence rate is slightly less than h^2. The logarithmic term is sharp and it is possible to construct meshes, where this result is numerically validated. For higher order finite elements (starting with quadratic finite elements) one observes (and one can proof) the full order of convergence

$$m \geq 2: \quad u_h \in V_h^m \quad \max_{\Omega} |u - u_h| \leq ch^{m+1} \max_{\Omega} |\nabla^{m+1} u|.$$

4.2.3 Finite Elements on Curved Domains

The standard finite element analysis is heavily depending on the conformity of the Galerkin approach $V_h \subset \mathcal{V}$ which is essential for getting Galerkin-Orthogonality. If the domain Ω is curved and cannot be matched by the finite element mesh $\Omega_h \neq \Omega$, the finite element space will not be conforming. In this section, we shortly discuss the approximation of the Laplace problem

$$u \in H_0^1(\Omega): \quad (\nabla u, \nabla \phi)_\Omega = (f, \phi)_\Omega \quad \forall \phi \in H_0^1(\Omega), \tag{4.15}$$

on a domain $\Omega \subset \mathbb{R}^d$ that is curved and smooth, i.e., the boundary $\partial\Omega$ locally allows for a C^{r+1}-parameterization, with $r \in \mathbb{N}_+$. Finite elements on curved domains must deal with two difficulties:

1. A polygonal mesh will never exactly match the domain Ω. Hence, the discrete equation

$$u_h \in V_h: \quad (\nabla u_h, \nabla \phi_h)_{\Omega_h} = (\tilde{f}, \phi_h)_{\Omega_h} \quad \forall \phi_h \in V_h,$$

   is given on a different domain. The right hand side f must not even be defined on all of Ω_h, which is the case, if the domain Ω has concave boundary parts, where Ω_h might reach out. For this reason, we denoted a modified (extended) right hand side by $\tilde{f}$. For details, we refer to Remark 4.36.
2. The boundary conditions cannot be exactly satisfied. We consider homogenous Dirichlet conditions only. While $u \in H_0^1(\Omega)$ is zero on all of $\partial\Omega$, $u_h \in V_h$ is zero in the boundary nodes on $\partial\Omega$ but otherwise, it is zero on $\partial\Omega_h \neq \partial\Omega$.

Finite element analysis on curved domains is discussed in literature [69]. General proofs for isoparametric finite elements on curved domains, including optimal order a priori error bounds for the energy error are given in [225]. We nevertheless give details, as these techniques will be required for an analysis of interface problems as the Fully Eulerian formulation, where the interior interface $\mathcal{I}$ cannot be resolved by the mesh, see Sect. 4.5. Furthermore, we are not aware of a simple and general proof for optimal error estimates of isoparametric elements.

To cope with the two problems mentioned above, we will start by stating some definitions and lemma. Parts of the boundary can be convex or concave. We define the remainders by

$$S_h^x = \Omega \setminus \Omega_h, \quad S_h^v = \Omega_h \setminus \Omega, \quad S_h = S_h^x \cup S_h^v. \tag{4.16}$$

For a parametric triangulation Ω_h of Ω, see Definition 4.17, it holds

Lemma 4.32 (Isoparametric Triangulation of Curved Domains) *Let $\Omega \subset \mathbb{R}^d$ be a domain with smooth boundary allowing for a C^{r+1}-parameterization with $r \geq 1$. Let Ω_h be an isoparametric mesh of Ω with polynomial degree r. For the area of*

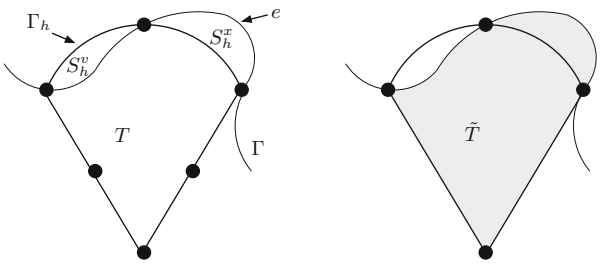

Fig. 4.4 *Left*: geometric remainders for curved boundary approximation. Definition of the mesh snippets $S_h^v = \Omega_h \setminus \Omega$ and $S_h^x = \Omega \setminus \Omega_h$. *Right*: Definition of the curved extended element $\tilde{T}$ fitting the domain Ω. Exemplarily for quadratic isoparametric elements

the mesh snippets S_h^x, S_h^v, S_h it holds

$$|S_h^x| = |S_h^v| = |S_h| = O(h^r).$$

Proof This follows by simple geometrical arguments. Let $T \in \Omega_h$ be an element at the boundary and S be that part of S_h which is connected to the element T, see Fig. 4.4. Further, let $e \in \partial T$ be the (curved) edge at the boundary Γ_h, which is a $d-1$-dimensional manifold in $\mathbb{R}^d$ with area $|e| = O(h^{d-1})$. Assume that $\psi : e \to \mathbb{R}$ is the parameterization of $\partial\Omega$ over e (see again Fig. 4.4). $\psi(s)$ has $r+1$ zero's along the edge in 2d. Hence,

$$\max_{[0,h]} |\psi| \leq ch^{r+1} \max_{[0,h]} |\psi^{r+1}|.$$

Therefore, as $|e| = O(h^{d-1})$, it holds

$$|S| = O(h^{r+d}) \quad \Rightarrow \quad |S_h| = O(h^{r+1}).$$

□

The previous lemma shows that standard finite elements will always suffer from a geometrical error. By the use of Isogeometric analysis [204] this error could be completely avoided for domains that can be described by splines.

Another technical difficulty is given by the mismatch of Ω and Ω_h. Functions $u \in H_0^1(\Omega)$ and $u_h \in V_h$ are defined on different domains, such that the expression $u - u_h$ must be discussed. The following lemma will show a way to give $u_h \in V_h$ a meaning both on Ω_h and on Ω.

Lemma 4.33 (Boundary Extension of Discrete Functions) *Under the assumptions of Lemma 4.32, let $h \leq h_0 \in \mathbb{R}$ and $T \in \Omega_h$ be an element at the boundary $\partial\Omega$ with boundary edge $e \in \partial T$. By $\tilde{T}$ we denote the curved triangle fitting the domain's boundary, see Fig. 4.4. For $u_h \in V_h$ we define by $\tilde{u}_h\big|_T$ the polynomial extension of*

$u_h\big|_T$ *to* $\tilde{T}$. *It holds*

$$c_1\|u_h\|_{H^s(T)} \leq \|\tilde{u}_h\|_{H^s(\tilde{T})} \leq c_2\|u_h\|_{H^s(T)},\ s = 0, 1, 2,$$

with two constants $c_1, c_2 > 0$ *that do not depend on* T *or* h.

Proof This follows by considering equivalence of (discrete) norms and the negligible size of the remainders.

$$|T| = |\tilde{T}| = O(h^d), \quad |(T \setminus \tilde{T}) \cup (\tilde{T} \setminus T)| = O(h^{r+d}).$$

□

In the following, we will always use the notation u_h even on $\tilde{T}$.

While $u_h \in V_h$ is well-defined on Ω_h (including S_h^v) and can be extended to Ω including S_h^x, functions $u \in H_0^1(\Omega)$ are only well-defined on Ω including S_h^x. An extension to the concave part S_h^v might fail due to limited regularity. For the analysis, we need one further—trace inequality-like—estimate:

Lemma 4.34 (Geometric Boundary Error) *Let* $u \in H_0^1(\Omega)$. *There exists a constant* $c > 0$, *such that for the convex remainder* S_h^x, *it holds*

$$\|u\|_{S_h^x} \leq ch^{\frac{r+1}{2}}\|u\|_{H^1(\Omega)}.$$

Further, let $u_h \in V_h$. *It holds*

$$\|u_h\|_{H^s(S_h)} \leq ch^{\frac{r}{2}}\|u_h\|_{H^s(\Omega)},\ s = 0, 1.$$

Proof For the proof, we refer to Fig. 4.5. Let $T \in \Omega_h$ be an element on the boundary, $e_h \in \partial T$ be the edge of the element, $\tilde{T}$ the extended element and $e \in \tilde{T}$ be the edge at the boundary $\partial\Omega$. By S we denote the remainder between T and $\tilde{T}$.

(i) Let $x \in S$ be given as $x = (s, \alpha)$, where α is the angle and s the radial coordinate, see Fig. 4.5. The local coordinate system is such, that $(0, \alpha) \in e_h \subset \Gamma_h$ is a point on the boundary of the (curved) triangle and $(s(\alpha), \alpha)$

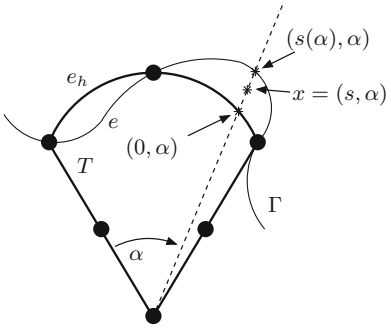

Fig. 4.5 Local coordinate system on curved elements. Sketch for the proofs of Lemmas 4.34 and 4.35. The boundary Γ with segment $e \subset \Gamma$ is given as parameterization of Γ_h with segments e_h, i.e. $s_T : e_h \to e$

is the corresponding point on the domain's boundary part $e \subset \Gamma$. It holds $|s(\alpha)| = O(h^{r+1})$, compare Lemma 4.32. Let $u \in C^1(\bar{S})$. It holds

$$u(s,\alpha) = u(0,\alpha) + \int_0^s \partial_r u(t,\alpha)\,\mathrm{d}t,$$

and hence

$$|u(s,\alpha)|^2 \leq c\left(|u(0,\alpha)|^2 + |s|\int_0^s |\partial_r u(t,\alpha)|^2\,\mathrm{d}t\right).$$

Integration over S (in s and α) and noting that $|s| \leq |s(\alpha)| \leq ch^{r+1}$ gives

$$\|u\|_S^2 \leq ch^{r+1}\|u\|_e^2 + h^{2r+1}\|\nabla u\|_S^2. \tag{4.17}$$

(ii) To proof the first estimate, we continue with (4.17) by summing over all boundary elements, using trace inequality and Poincaré and extending S_h^x to Ω

$$\|u\|_{S_h} \leq ch^{\frac{r+1}{2}}\|\nabla u\|_\Omega.$$

(iii) For the second inequality, we apply the local trace inequality and extend from S to T

$$\|u_h\|_S^2 \leq ch^{r+1}\left(h^{-1}\|u_h\|_T^2 + h\|\nabla u_h\|_T^2\right) + h^{2r+1}\|\nabla u_h\|_T^2.$$

Using the inverse inequality, we get

$$\|u_h\|_S^2 \leq ch^r\|u_h\|_T^2,$$

such that the result follows by summing over all boundary snippets. This argumentation is also valid for ∇u_h. □

Discrete functions $\phi_h \in V_h$ are not zero on $\partial\Omega$ but zero on $\partial\Omega_h$.

Lemma 4.35 (Curved Boundary Error) *Let $\phi_h \in V_h$ be arbitrary. It holds*

$$\|\phi_h\|_{\partial\Omega} \leq ch^{r+\frac{1}{2}}\|\nabla\phi_h\|_\Omega$$

Proof We again refer to Fig. 4.5. Let $T \in \Omega_h$ and $(s(\alpha),\alpha) \in e$ be a point on the boundary of $\partial\Omega$. By $(0,\alpha) \in e_h \subset \partial T$ we denote the corresponding point on the boundary of the triangle. It holds for $\phi_h \in V_h$

$$\phi_h(s(\alpha),\alpha) = \phi_h(0,\alpha) + \int_0^{s(\alpha)} \partial_r\phi_h(t,\alpha)\,\mathrm{d}t,$$

and hence by squaring and integrating over α and by noting that $|s(\alpha)| = O(h^{r+1})$ we get

$$\|\phi_h\|_e^2 \leq \|\phi_h\|_{e_h}^2 + ch^{r+1}\|\nabla\phi_h\|_S^2. \tag{4.18}$$

With Lemma 4.34 and using $\phi_h = 0$ on e_h, gives

$$\|\phi_h\|_e^2 \leq ch^{2r+1}\|\nabla\phi_h\|_\Omega^2,$$

such that the result follows by summing over all boundary parts. □

Remark 4.36 (Extension of the Right Hand Side at Concave Domain Boundaries) As discussed in the beginning of this section, problems might already arise with the definition of the right hand side $f : \Omega \to \mathbb{R}$, which is not necessarily well-defined on the discrete domain Ω_h. This issue is easily handled by defining a projection or interpolation $f_h \in V_h$ to be used as discrete right hand side:

$$(f_h, \phi_h)_\Omega = (f, \phi_h)_\Omega \quad \forall\phi_h \in V_h.$$

An additional error of type

$$(f - f_h, \phi)_\Omega \leq c\|f - f_h\|_{H^{-1}(\Omega)}\|\nabla\phi\|_\Omega,$$

will arise. By exploiting the weak norm and orthogonality of $f - f_h$ such estimates can be given with optimal order and without requiring additional regularity of $f \in H^{r-1}(\Omega)$:

$$\begin{aligned}\|f - f_h\|_{H^{-1}(\Omega)} &= \sup_{\phi\in H_0^1(\Omega)} \frac{(f - f_h, \phi)_\Omega}{\|\nabla\phi\|} \\ &= \sup_{\phi\in H_0^1(\Omega)} \frac{(f - f_h, \phi - \bar{\phi})_\Omega}{\|\nabla\phi\|} \\ &\leq ch^r\|\nabla^{r-1}f\|_\Omega.\end{aligned}$$

To shorten the proof of the following lemma we will not give details on this issue and just consider f as a well-defined right hand side function.

With these preparations, we can show the following essential theorem, that gives the a priori error estimate for the Laplace equation on smooth and curved domains:

Theorem 4.37 (A Priori Error on Curved Domains) *Let $r \in \mathbb{N}_+$. Let Ω be a domain with boundary that allows for parametrization of degree $r + 1$. Let $f \in H^{r-1}(\Omega) \cap L^2(\Omega)$. Let $u_h \in V_h$ be the isoparametric finite element solution of degree r. It holds*

$$\|u - u_h\|_{H^1(\Omega)} \leq ch^r\|f\|_{H^{r-1}(\Omega)}$$

and

$$\|u - u_h\| \leq ch^{r+1}\|f\|_{H^{r-1}(\Omega)}.$$

Proof

(i) We start with the H^1 error estimate and derive a modified Galerkin orthogonality. For $\phi_h \in V_h$ it holds (where we use the extension $\tilde{\phi}_h \cong \phi_h$ defined by Lemma 4.33 without further notice)

$$(f, \phi_h)_\Omega = (-\Delta u, \phi_h)_\Omega = (\nabla u, \nabla \phi_h)_\Omega - \langle \partial_n u, \phi_h \rangle_{\partial\Omega}.$$

The discrete problem is defined on Ω_h with $\Omega_h = \Omega \cup S_h^v \setminus S_h^x$. It holds

$$\begin{aligned}(f, \phi_h)_\Omega + (f, \phi_h)_{S_h^v} - (f, \phi_h)_{S_h^x} \\ = (\nabla u_h, \nabla \phi_h)_\Omega + (\nabla u_h, \nabla \phi_h)_{S_h^v} - (\nabla u_h, \nabla \phi_h)_{S_h^x}.\end{aligned}$$

Then, for the finite element error $e_h = u - u_h$, we get the following disturbed Galerkin orthogonality:

$$\begin{aligned}(\nabla e_h, \nabla \phi_h)_\Omega = -(f, \phi_h)_{S_h^v} + (f, \phi_h)_{S_h^x} \\ + \langle \partial_n u, \phi_h \rangle_{\partial\Omega} + (\nabla u_h, \nabla \phi_h)_{S_h^v} - (\nabla u_h, \nabla \phi_h)_{S_h^x}.\end{aligned} \tag{4.19}$$

(ii) Now, we can estimate the energy error by picking $\phi_h = I_h u - u_h$:

$$\begin{aligned}\|\nabla e_h\|_\Omega^2 \leq \|\nabla e_h\|_\Omega \|\nabla(u - I_h u)\|_\Omega + \|f\|_S \|I_h u - u_h\|_S \\ + \|\nabla u_h\|_S \|\nabla(I_h u - u_h)\|_S + \|\partial_n u\|_{\partial\Omega} \|I_h u - u_h\|_{\partial\Omega},\end{aligned} \tag{4.20}$$

where we enlarged S_h^x and S_h^v to S. The single terms can be estimates with help of Lemmas 4.34 and 4.35 and the standard interpolation estimate. Exemplarily we discuss the boundary term. With Lemma 4.35

$$\begin{aligned}\|\partial_n u\|_{\partial\Omega} \|I_h u - u_h\|_{\partial\Omega} \leq c\|u\|_{H^2(\Omega)} c h^{\frac{r+1}{2}} \|\nabla(I_h u - u_h)\|_\Omega \\ c\|u\|_{H^2(\Omega)} h^{\frac{r+1}{2}} \left(\|\nabla(u - I_h u)\|_\Omega + \|\nabla(u - u_h)\|_\Omega\right).\end{aligned}$$

The remaining terms can be handled in a similar fashion, such that combination with Young's inequality gives the final estimate.

(iii) For estimating the L^2-error, we define the adjoint problem:

$$-\Delta z = \frac{e_h}{\|e_h\|} \text{ on } \Omega \text{ with } z = 0 \text{ on } \partial\Omega,$$

such that

$$\|z\|_{H^2(\Omega)} \leq c_s.$$

Multiplication with e_h and integration over Ω yields

$$\|e_h\|_\Omega = (e_h, -\Delta z)_\Omega = (\nabla e_h, \nabla z)_\Omega + \langle u_h, \partial_n z \rangle_{\partial\Omega},$$

as $u = 0$ on $\partial\Omega$. Using (4.19) with $\phi_h = I_h z$, it follows

$$\begin{aligned}\|e_h\| \leq \|\nabla e_h\|_\Omega \|\nabla(z - I_h z)\|_\Omega + \|u_h\|_{\partial\Omega} \|\partial_n z\|_{\partial\Omega} + \|\partial_n u\|_{\partial\Omega} \|I_h z\|_{\partial\Omega} \\ + \|f\|_S \|I_h z\|_S + \|\nabla u_h\|_S \|\nabla I_h z\|_S.\end{aligned} \tag{4.21}$$

The first term can be estimated with help of the energy estimate and the interpolation estimates, followed by the stability of the adjoint solution $\|z\|_{H^2(\Omega)} \leq c_s$. For the second term, we first use (4.18) and get by introducing $\pm u$

$$\begin{aligned}\|u_h\|_{\partial\Omega} \leq ch^{\frac{r+1}{2}} \|\nabla u_h\|_s \leq ch^{\frac{r+1}{2}} \left(\|\nabla e_h\|_S + \|\nabla u\|_S\right) \\ \leq ch^{\frac{r+1}{2}} \|\nabla e_h\| + ch^{r+1} \|u\|_{H^2(\Omega)}.\end{aligned}$$

This procedure will also be used for the third term. The right hand side part in the fourth term of (4.21) is estimated with Lemma 4.34

$$\|f\|_S \leq ch^{\frac{r+1}{2}} \|f\|_{H^1(\Omega)}.$$

For the interpolation part $\|I_h z\|$ we first use the intermediate result (4.17) from the proof of Lemma 4.34 and introduce $\pm z$ on the boundary to get with interpolation estimates

$$\begin{aligned}\|I_h z\|_S \leq ch^{\frac{r+1}{2}} \|z - I_h z\|_{\partial\Omega} + ch^{\frac{r+1}{2}} \underbrace{\|z\|_{\partial\Omega}}_{=0} + ch^{r+\frac{1}{2}} \|\nabla I_h z\|_S \\ \leq ch^{2+\frac{r}{2}} \|z\|_{H^2(\Omega)} + ch^{r+\frac{1}{2}} \|z\|_{H^1(\Omega)}.\end{aligned}$$

Overall, the fourth term in (4.21) is estimated as

$$\|f\|_S \|I_h z\|_S \leq ch^{r+\frac{3}{2}} \|f\|_{H^1(\Omega)}.$$

This trick is also used in the final term of (4.21). As $(r+1)/2 \leq r + 1/2$

$$\begin{aligned}\|\nabla I_h z\|_S \leq ch^{\frac{r+1}{2}} \|\nabla I_h z\|_{\partial\Omega} + ch^{r+\frac{1}{2}} \|\nabla^2 I_h z\|_{S_h} \\ \leq ch^{\frac{r+1}{2}} \left(\|\nabla(z - I_h z)\|_{\partial\Omega} + \|\nabla^2(z - I_h z)\|_\Omega + \|z\|_{H^2(\Omega)}\right)\end{aligned}$$

The same estimate is applied to ∇u_h

$$\|\nabla u_h\|_S \leq ch^{\frac{r+1}{2}} \Big(\|\nabla(u-u_h)\|_{\partial\Omega} + \|\nabla^2(u-u_h)\|_\Omega + \|u\|_{H^2(\Omega)} \Big).$$

Together with the stability estimates of the interpolation and higher order estimates of the discrete solution (that can be shown by introducing $\pm I_h u$ and applying the inverse estimate to the discrete parts) we get

$$\|\nabla u_h\|_S \|\nabla I_h z\|_S \leq ch^{r+1} \|f\|_{L^2(\Omega)}.$$

□

Remark 4.38 (Further Estimates on Curved Boundaries) This type of estimate can directly be extended to the Stokes equations or to equations of solid-dynamics. Essential for all estimates are the lemmata given at the beginning of this section.

It is however not trivial to extend this general form of a priori estimates on curved domains to the case of non-Dirichlet type boundary conditions. If we for example consider the Stokes equations with slip boundary data,

$$\mathbf{n} \cdot \mathbf{v} = 0 \text{ on } \partial\Omega,$$

the proof cannot be extended in the same spirit. Reason for difficulties is the Lemma 4.35. For the slip-condition, we can still show that

$$\|\mathbf{n} \cdot \mathbf{v}_h\|_{\partial\Omega} \leq ch^{r+\frac{1}{2}} \|\nabla \mathbf{v}\|_\Omega + \|\mathbf{n} \cdot \mathbf{v}_h\|_{\partial\Omega_h},$$

we observe however that $\mathbf{n} \cdot \mathbf{v}_h \neq 0$ on the discrete boundary $\partial\Omega_h$ (in the case of polynomial degree $r \geq 1$). One possible loophole is to define the reference map $T_T : \hat{T} \to T$ by means of the Piola transform, such that the basis functions on T are given by

$$\phi(x) = \frac{1}{\det(\nabla T_T)} \nabla T_T \hat{\phi}(\hat{x}).$$

For a discussion, we refer to the literature [50, 271]

4.3 Finite Elements for Saddle-Point Problems

In this section, we discuss the finite element discretization for problems of saddle-point type. We have come across such problems in the case of incompressible solids and the incompressible Stokes or Navier-Stokes problem. Here, we will consider the incompressible Stokes equations exemplarily for all saddle-point problems. This saddle-point character causes various difficulties, like the need to satisfy the

inf-sup condition, Lemma 2.44. For designing numerical algorithms this saddle-point character must be taken into account. The Stokes equations on a domain $\Omega \subset \mathbb{R}^d$ are given by

$$\{\mathbf{v}, p\} \in \mathcal{V} \times \mathcal{L}: \quad (\nabla \mathbf{v}, \nabla \phi) - (p, \nabla \cdot \phi) + (\nabla \cdot \mathbf{v}, \xi) = (\mathbf{f}, \phi) \qquad \forall \{\phi, \xi\} \in \mathcal{V} \times \mathcal{L},$$

where for simplicity we consider problems with homogenous Dirichlet conditions on the boundary $\partial\Omega$ only. Let $V_h \subset \mathcal{V}$ and $L_h \subset \mathcal{L}$ be two conforming finite element spaces. Since $\mathcal{L} = L^2(\Omega)$, conformity regarding the pressure does not ask for continuity. The discretized Stokes problem is equivalent to a linear system of equations

$$\begin{pmatrix} \mathbf{A}_h & \mathbf{B}_h \\ -\mathbf{B}_h^T & 0 \end{pmatrix} \begin{pmatrix} \mathbf{v} \\ \mathbf{p} \end{pmatrix} = \begin{pmatrix} \mathbf{f} \\ 0 \end{pmatrix}, \tag{4.22}$$

where $\mathbf{v}$ and $\mathbf{p}$ are the coefficient vectors of the discrete solutions $\mathbf{v}_h \in V_h$ and $p_h \in L_h$. The matrices are given by

$$(\mathbf{A}_h)_{ij} = (\nabla \phi_j, \nabla \phi_i), \quad (\mathbf{B}_h)_{ij} = -(\xi_j, \nabla \cdot \phi_i), \quad -(\mathbf{B}_h)_{ij}^T = (\nabla \cdot \phi_j, \xi_i),$$

where $V_h = \text{span}\{\phi_i,\ i = 1, \ldots, \#V_h\}$ and $L_h = \text{span}\{\xi_i,\ i = 1 \ldots, \#L_h\}$ is a basis of the finite element space. The matrix $\mathbf{A}_h$ is symmetric and positive definite. The complete system matrix however reflects the saddle-point character of the Stokes equations. It holds

Lemma 4.39 (Stokes Solution) *Let $V_h \times L_h \subset \mathcal{V} \times \mathcal{L}$ be a conforming discretization of the incompressible Stokes equations. There exists a unique solution $\{\mathbf{v}_h, p_h\} \in V_h \times L_h$, if the discrete inf-sup condition holds*

$$\inf_{\xi_h \in L_h} \sup_{\phi_h \in V_h} \frac{(\xi_h, \nabla \cdot \phi_h)}{\|\xi_h\| \, \|\nabla \phi_h\|} \geq \gamma_h \geq \gamma > 0.$$

The solution $\{\mathbf{v}_h, p_h\}$ satisfies the a priori estimate

$$\|\nabla \mathbf{v}_h\| + \gamma_h \|p_h\| \leq c \|\mathbf{f}\|.$$

Proof

(i) First, we define the subspace $W_h \subset V_h$ of weakly divergence free functions:

$$W_h := \{\phi_h \in V_h: \quad (\nabla \cdot \phi_h, \xi_h) = 0 \quad \forall \xi_h \in L_h\}.$$

We assume that $W_h \neq \emptyset$ and find $\mathbf{v}_h \in W_h$ such that

$$(\nabla \mathbf{v}_h, \nabla \phi_h) = (\mathbf{f}, \phi_h) \quad \forall \phi_h \in W_h. \tag{4.23}$$

The existence of a unique solution $\mathbf{v}_h \in W_h$ follows by linearity and ellipticity of the scalar product $(\nabla \cdot, \nabla \cdot)$ in $W_h \subset \mathcal{V} = H_0^1(\Omega)^d$. Further, it holds with Poincaré's inequality

$$\|\nabla \mathbf{v}_h\|^2 = (\nabla \mathbf{v}_h, \nabla \mathbf{v}_h) = (\mathbf{f}, \mathbf{v}_h) \leq c_p \|\mathbf{f}\| \, \|\nabla \mathbf{v}_h\| \tag{4.24}$$

This solution $\mathbf{v}_h$ by construction fulfills the divergence condition.

(ii) Next, given $\mathbf{v}_h \in W_h \subset V_h$ we find a pressure $p_h \in L_h$ as solution to

$$(p_h, \nabla \cdot \phi_h) = (\nabla \mathbf{v}_h, \nabla \phi_h) - (\mathbf{f}, \phi_h) \quad \forall \phi_h \in V_h.$$

This finite dimensional problem is equivalent to the linear system of equations

$$\mathbf{B}_h \mathbf{p} = \mathbf{f} - \mathbf{A}_h \mathbf{v}. \tag{4.25}$$

As this problem is finite dimensional, it holds

$$\text{range}(\mathbf{B}_h) = \ker(\mathbf{B}_h^T)^{\perp}.$$

Hence, we find a solution, if the right hand side of (4.25) is orthogonal to the kernel of $\mathbf{B}_h^T$, the discrete divergence operator

$$\langle \mathbf{A}_h \mathbf{v} - \mathbf{f}, \mathbf{z} \rangle = 0 \quad \forall \mathbf{z} \in \ker(\mathbf{B}_h^T).$$

First, we characterize the kernel of $\mathbf{B}_h^T$. It holds

$$\mathbf{B}_h^T \mathbf{z} = \left(\sum_{j=1}^{\#V_h} (\xi_h^i, \nabla \cdot \phi_h^j) \mathbf{z}_j \right)_{i=1}^{\#L_h} = (\nabla \cdot z_h, \xi_h^i)_{i=1}^{\#L_h},$$

and hence, $\ker(\mathbf{B}_h^T) = W_h$. In *(i)*, we determined $\mathbf{v}_h \in W_h$ as solution of (4.23):

$$(\nabla \mathbf{v}_h, \nabla \phi_h) = (\mathbf{f}, \phi_h) \quad \forall \phi_h \in W_h \quad \Leftrightarrow \quad \langle \mathbf{b}_h - \mathbf{A}_h \mathbf{v}, \mathbf{z} \rangle = 0 \quad \forall \mathbf{z} \in \ker(\mathbf{B}_h^T).$$

At least one pressure $p_h \in L_h$ exists.

(iii) The inf-sup condition is equivalent to the formulation

$$\gamma_h \|p_h\| \leq \sup_{\phi_h} \frac{(p_h, \nabla \cdot \phi_h)}{\|\nabla \phi_h\|} \quad \forall p_h \in L_h.$$

Let p_h^1 and p_h^2 be two solutions with corresponding velocity solution $\mathbf{v}_h \in V_h$. For $q_h := p_h^1 - p_h^2 \in L_h$ it holds

$$\begin{aligned}(\nabla \mathbf{v}_h, \nabla \phi_h) - (p_h^1, \nabla \cdot \phi_h) &= (\mathbf{f}, \phi_h) \\ (\nabla \mathbf{v}_h, \nabla \phi_h) - (p_h^2, \nabla \cdot \phi_h) &= (\mathbf{f}, \phi_h)\end{aligned} \quad \Rightarrow \quad (q_h, \nabla \cdot \phi_h) = 0 \quad \forall \phi_h \in V_h.$$

Using the inf-sup condition, it holds that $q_h = 0$, as

$$\gamma_h \|q_h\| \leq \sup_{\phi_h \in V_h} \frac{(q_h, \nabla \cdot \phi_h)}{\|\nabla \phi_h\|} = 0,$$

and it follows that the pressure is unique. The a priori estimate is given by using (4.24) with help of the inf-sup condition:

$$\begin{aligned}\gamma_h \|p_h\| \leq \sup_{\phi_h \in V_h} \frac{(p_h, \nabla \cdot \phi_h)}{\|\nabla \phi_h\|} = \sup_{\phi_h \in V_h} \frac{(\mathbf{f}, \phi_h) - (\nabla \mathbf{v}_h, \nabla \phi_h)}{\|\nabla \phi_h\|} \\ \leq c_p \|\mathbf{f}\| + \|\nabla \mathbf{v}_h\| \leq c \|\mathbf{f}\|.\end{aligned}$$

□

The inf-sup condition is required to get uniqueness of the pressure. Existence is given for every pair $V_h \times L_h$. At the beginning of the proof, we assumed that the space

$$W_h = \{\phi_h \in V_h : \ (\nabla \cdot \phi_h, \xi_h) = 0 \quad \forall \xi_h \in L_h\},$$

is big enough to yield good approximation properties for $v \in \mathcal{V}$. By construction, the space W_h gets small, if L_h is large compared to V_h. For the most basic finite element pair that consists of piecewise linear velocities and a piecewise constant pressure, the space W_h empty.

4.3.1 Inf-Sup Stable Finite Element Pairs

Here, we discuss inf-sup stability for a given finite element pair $V_h \times L_h$. Proving the inf-sup condition is usually not easy and there exists not one approach that is usable for all different finite element pair. For details see the comprehensive text-books by Girault and Raviart [165] or Temam [321]. A conforming finite element space must consist of velocities that are globally continuous, where the pressure space can be discontinuous.

We denote a finite element pair by $X - Y$, where X and Y are the finite element spaces used for velocity and pressure, respectively: by $P^2 - P^1$ we denote the pair consisting of piecewise quadratic velocities and piecewise linear pressure on

triangles. This space is called the *Taylor-Hood element*. By $Q^2 - P^{1,\mathrm{dc}}$ we denote the space of piecewise quadratic velocities and discontinuous, piecewise linear pressures on quadrilaterals. Spaces with discontinues pressures have the advantage of local mass conservation. For the pair $Q^2 - P^{1,\mathrm{dc}}$ we can choose the test function $\xi_K \in L_h$ with $\xi_K \equiv 1$ on one $K \in \Omega_h$ and $\xi_K = 0$ for all $K' \neq K$. It holds:

$$(\nabla \cdot \mathbf{v}_h, \xi_K) = \int_K \nabla \cdot \mathbf{v}_h \, \mathrm{d}x = \int_{\partial K} \mathbf{n} \cdot \mathbf{v}_h \mathrm{d}s = 0.$$

Some very simple finite element pairs are not stable (Fig. 4.6). The triangular $P^1 - P^{0,\mathrm{dc}}$ element for instance is not usable, as $W_h = 0$, see [165]. Likewise, the quadrilateral $Q^1 - P^{0,\mathrm{dc}}$ cannot be used, as the inf-sup condition is not fulfilled. Solutions on regular meshes will feature the so-called *checkerboard pattern* with oscillatory pressures.

After these negative results, we cite a Lemma that gives a simple criteria for showing inf-sup stability in certain cases, see [71].

Lemma 4.40 (Fortin Criteria) *Let $V_h \times L_h \subset \mathcal{V} \times \mathcal{L}$ be a finite element pair. Given a H^1-stable projection operator $\pi_h : \mathcal{V} \to V_h$ satisfying*

$$\|\nabla \pi_h \phi\| \leq c_\pi \|\nabla \phi\| \quad \forall \phi \in \mathcal{V}, \quad (\nabla \cdot (\phi - \pi_h \phi), \xi_h) = 0 \quad \forall \xi_h \in L_h,$$

it holds

$$\inf_{\xi_h \in L_h} \sup_{\phi_h \in V_h} \frac{(\xi_h, \nabla \cdot \phi_h)}{\|\nabla \phi_h\| \, \|\xi_h\|} \geq \gamma_h := \gamma c_\pi^{-1},$$

where $\gamma > 0$ is the continuous inf-sup constant in $\mathcal{V} \times \mathcal{L}$.

Proof Let $p_h \in L_h \subset \mathcal{L}$. It holds with the continuous inf-sup condition

$$\gamma \|p_h\| \leq \sup_{\phi \in \mathcal{V}} \frac{(p_h, \nabla \cdot \phi)}{\|\nabla \phi\|} = \sup_{\phi \in \mathcal{V}} \frac{(p_h, \nabla \cdot (\phi - \pi_h \phi))}{\|\nabla \phi\|} + \sup_{\phi \in \mathcal{V}} \frac{(p_h, \nabla \cdot \pi_h \phi)}{\|\nabla \phi\|}.$$

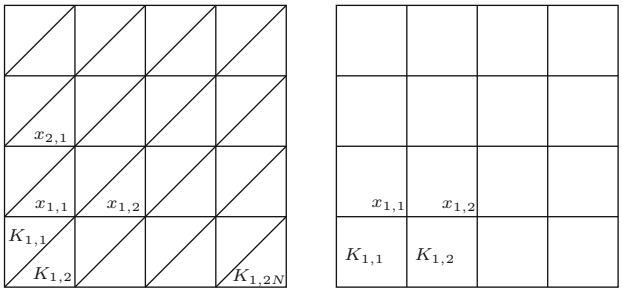

Fig. 4.6 Meshes of tensor-product type. Left triangular and right quadrilateral

As the first part is zero due to the orthogonality of the projection π_h it further follows with the stability of the projection

$$\gamma\|p_h\| \leq \sup_{\phi\in\mathcal{V}} \frac{(p_h, \nabla\cdot\pi_h\phi)}{\|\nabla\pi_h\phi\|} \sup_{\phi\in\mathcal{V}} \frac{\|\nabla\pi_h\phi\|}{\|\nabla\phi\|} \leq c_\pi \sup_{\phi_h\in V_h} \frac{(p_h, \nabla\cdot\phi_h)}{\|\nabla\phi_h\|},$$

as $\pi_h\phi \in V_h$. □

For some elements this criteria helps to show inf-sup stability:

Lemma 4.41 (Modified Taylor-Hood Elements with Discontinuous Pressure) *The $P^2 - P^{0,dc}$ and $Q^2 - P^{1,dc}$ elements are inf-sup stable.*

Proof See Fig. 4.7 for a sketch of these two element pairs. We construct a projection operator $\pi_h : \mathcal{V} \to V_h$ that has both properties, H^1-stability and the required orthogonality.

(i) The triangular element. We construct π_h as $\pi_h := C_h + E_h$, where $C_h : \mathcal{V} \to V_h^1$ is the Clement operator from Lemma 4.24 interpolating to the space of piecewise linear functions. This space has three degrees of freedom (for every velocity component) and fixes the three nodal points of a triangle. This operator C_h satisfies

$$\|\nabla C_h\mathbf{v}\|_K \leq c\|\nabla\mathbf{v}\|_{P(K)},$$

where $P(K)$ is a patch of elements around K. See Lemma 4.24 for details. It remains to fulfill the orthogonality condition. As the pressure space is discontinuous, it holds on every K choosing by $\xi_h \equiv 1$ on K and $\xi_h = 0$ elsewhere:

$$(\nabla\cdot(\mathbf{v} - \pi_h\mathbf{v}), \xi_h) = \int_K \nabla\cdot(\mathbf{v} - \pi_h\mathbf{v})\,\mathrm{d}x = \int_{\partial K} \mathbf{n}\cdot(\mathbf{v} - \pi_h\mathbf{v})\,\mathrm{d}o.$$

For $\pi_h := C_h + E_h$ one condition is imposed on every edge $e \in \partial K$:

$$\int_e \mathbf{n}\cdot E_h\mathbf{v}\,\mathrm{d}o = \int_e \mathbf{n}\cdot(\mathbf{v} - C_h\mathbf{v})\,\mathrm{d}o.$$

This is easily established by the remaining degrees of freedom (two per edge).

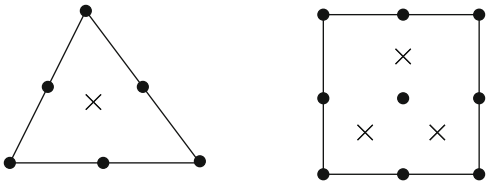

Fig. 4.7 Modified Taylor-Hood elements $P^2 - P^{0,\mathrm{dc}}$ (*left*) and $Q^2 - P^{1,\mathrm{dc}}$ (*right*). *Circles* denote (continuous) nodal values of the basis functions, crosses stand for monomial values of a discontinuous approach

(ii) The quadrilateral element. We define the projection as $\pi_h := C_h + E_h + B_h$, where C_h again is a H^1-stable Clement interpolation, E_h takes care of the edges and B_h of the additional middle degree of freedom. For the orthogonality it holds for $\xi_K \in L_h$ with $\xi_K = 0$ for all $K' \neq K$:

$$(\nabla \cdot (\mathbf{v} - \pi_h \mathbf{v}), \xi_h)_K = -(\mathbf{v} - \pi_h \mathbf{v}, \nabla \xi_h)_K + \int_{\partial K} \mathbf{n} \cdot (\mathbf{v} - \pi_h \mathbf{v}) \xi_h \, \mathrm{d}o.$$

As ξ_h is piecewise linear, $\nabla \xi_h \in \mathbb{R}^2$ is a constant vector on every element. The two inner degrees of freedom are used to define the operator B_h via

$$\int_K B_h \mathbf{v}_i \, \mathrm{d}x = \int_K \mathbf{v}_i - \pi_h \mathbf{v}_i \, \mathrm{d}x, \quad i = 1, 2.$$

Finally, $\xi_h \in L_h$ is a linear function on every edge $e \in \partial K$, and the two remaining degrees of freedom are required for satisfying

$$\int_e (\mathbf{n} \cdot E_h \mathbf{v}) \xi_h \, \mathrm{d}o = \int_e \mathbf{n} \cdot (\mathbf{v} - \pi_h \mathbf{v}) \xi_h \, \mathrm{d}o.$$

□

The $Q^2 - P^{1,dc}$ element is an excellent mixed finite element for the discretization of incompressible flows. Quadratic velocities are a good compromise between high accuracy at acceptable computational effort (as the effort is increasing in powers of the polynomial degree). Discontinuous pressures give local conservation. Finally, in the context of fluid-structure interactions, discontinuous pressures simplify the coupling to a possibly incompressible solid that also has a pressure variable (the coupling between two pressures at the interface is discontinuous). See [329, 330] for applications.

One of the most-often used finite element pairs for the discretization of the incompressible Stokes or Navier-Stokes equations is the Taylor-Hood element $P^2 - P^1$. Here, the Fortin criteria cannot be applied as easily.

Lemma 4.42 (Inf-Sup Stable Finite Element Pairs) *The finite element pairs of Taylor Hood type $Q^2 - Q^1$ and $P^2 - P^1$ as well as the generalizations $Q^k - Q^{k-1}$ and $P^k - P^{k-2}$ for $k \geq 3$ are inf-sup stable. Further, the equal order spaces using a pressure on a coarser mesh $Q_h^k - Q_{2h}^k$ are inf-sup stable.*

Proof Proofs for these and further element pairs are given in [71] and [165]. See Fig. 4.8 for some inf-sup stable finite elements. □

For inf-sup stable and conforming finite element pairs $V_h \times L_h \subset \mathcal{V} \times \mathcal{L}$, a priori error analysis is possible by standard arguments. We start by showing a best-approximation results:

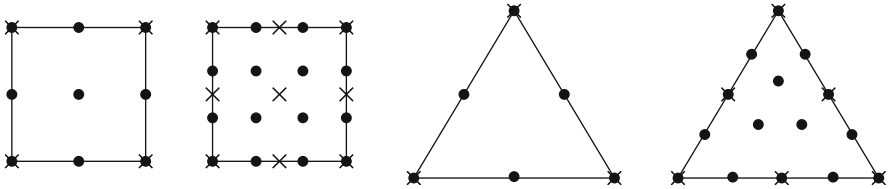

Fig. 4.8 Different inf-sup stable finite element pairs: The $Q^2 - Q^1$ Taylor Hood element, a higher order $Q^3 - Q^2$ element, the classical $P^2 - P^1$ Taylor Hood element and a higher order $P^4 - P^2$ element. Again, the *circles* denote continuous degrees of freedom and crosses the discontinuous ones

Lemma 4.43 (Stokes, Best Approximation) *Let $V_h \times L_h \subset \mathcal{V} \times \mathcal{L}$ be an inf-sup stable finite element space. It holds:*

$$\|\nabla(\mathbf{v} - \mathbf{v}_h)\| + \|p - p_h\| \leq c \left(\min_{\phi_h \in V_h} \|\nabla(\mathbf{v} - \phi_h)\| + \min_{\xi_h \in L_h} \|p - \xi_h\| \right),$$

where the constant $c > 0$ depends on the inf-sup constant γ_h. Further, on convex or smooth domains, it holds

$$\|\mathbf{v} - \mathbf{v}_h\| \leq ch \left(\min_{\phi_h \in V_h} \|\nabla(\mathbf{v} - \phi_h)\| + \min_{\xi_h \in L_h} \|p - \xi_h\| \right),$$

with constant $c = c(\gamma_h)$.

Proof We define $\mathbf{e}_v := \mathbf{v} - \mathbf{v}_h \in \mathcal{V}$ and $e_p := p - p_h \in \mathcal{L}$. It holds by Galerkin orthogonality

$$\begin{aligned} (\nabla \mathbf{e}_v, \nabla \phi_h) &= (e_p, \nabla \cdot \phi_h) \quad && \forall \phi_h \in V_h, \\ (\nabla \cdot \mathbf{e}_v, \xi_h) &= 0 && \forall \xi_h \in L_h. \end{aligned} \tag{4.26}$$

(i) First, we start with an estimate of the velocity error:

$$\|\nabla \mathbf{e}_v\|^2 = (\nabla \mathbf{e}_v, \nabla \mathbf{e}_v) - (e_p, \nabla \cdot \mathbf{e}_v) + (e_p, \nabla \cdot \mathbf{e}_v).$$

By Galerkin orthogonality, we get for arbitrary $\phi_h \in V_h$ and $\xi_h \in L_h$

$$\begin{aligned} \|\nabla \mathbf{e}_v\|^2 &= (\nabla \mathbf{e}_v, \nabla(\mathbf{v} - \phi_h)) - (e_p, \nabla \cdot (\mathbf{v} - \phi_h)) + (\nabla \cdot \mathbf{e}_v, p - \xi_h) \\ &\leq \|\nabla \mathbf{e}_v\| \, \|\nabla(\mathbf{v} - \phi_h)\| + \|e_p\| \, \|\nabla(\mathbf{v} - \phi_h)\| + \|\nabla \mathbf{e}_v\| \, \|p - \xi_h\|. \end{aligned}$$

By Young's inequality, we get for $\varepsilon > 0$:

$$\|\nabla \mathbf{e}_v\| \leq (2 + \varepsilon^{-1}) \|\nabla(\mathbf{v} - \phi_h)\| + 2\|p - \xi_h\| + \varepsilon \|e_p\|. \tag{4.27}$$

(ii) Next, we estimate the pressure error. Let $\xi_h \in L_h$ be arbitrary

$$\|p - p_h\| \le \|p - \xi_h\| + \|p_h - \xi_h\|. \tag{4.28}$$

For $p_h - \xi_h \in L_h$ we use the discrete inf-sup inequality to get

$$\begin{aligned} \gamma_h \|p_h - \xi_h\| &\le \sup_{\phi_h \in V_h} \frac{(p_h - \xi_h, \nabla \cdot \phi_h)}{\|\nabla \phi_h\|} \\ &= \sup_{\phi_h \in V_h} \frac{(p - p_h, \nabla \cdot \phi_h)}{\|\nabla \phi_h\|} + \sup_{\phi_h \in V_h} \frac{(p - \xi_h, \nabla \cdot \phi_h)}{\|\nabla \phi_h\|} \end{aligned} \tag{4.29}$$

We use (4.26) on the first part to replace the pressure error e_p by the velocity error $\mathbf{e}_v$:

$$\sup_{\phi_h \in V_h} \frac{(e_p, \nabla \cdot \phi_h)}{\|\nabla \phi_h\|} = \sup_{\phi_h \in V_h} \frac{(\nabla \mathbf{e}_v, \nabla \phi_h)}{\|\nabla \phi_h\|} \le \|\nabla \mathbf{e}_v\|.$$

Together with the second part of (4.29) we get the estimate

$$\gamma_h \|p_h - \xi_h\| \le \|\nabla \mathbf{e}_v\| + \|p - \xi_h\|,$$

and finally, with (4.28) for $\|p - p_h\|$

$$\|e_p\| \le (1 + \gamma_h^{-1}) \|p - \xi_h\| + \gamma_h^{-1} \|\nabla \mathbf{e}_v\|. \tag{4.30}$$

(iii) We insert this estimate into (4.27), using $\varepsilon = \gamma_h/2$:

$$\|\nabla \mathbf{e}_v\| \le c(\gamma_h) \left(\|\nabla(\mathbf{v} - \phi_h)\| + \|p - \xi_h\| \right).$$

Together with (4.30) we get the best-approximation property for the natural energy norm.

(iv) To derive the L^2-estimate we define the adjoint problem

$$(\nabla \phi, \nabla \mathbf{z}) - (\xi, \nabla \cdot \mathbf{z}) + (\nabla \cdot \phi, q) = \|\mathbf{e}_v\|^{-1} (\mathbf{e}_v, \phi).$$

As $\mathbf{e}_v / \|\mathbf{e}_v\| \in L^2$ it holds by Lemma 2.46 (if the domain has a convex or smooth boundary) that

$$\|\nabla^2 \mathbf{z}\| + \|\nabla q\| \le c_s \left\| \frac{\mathbf{e}_v}{\|\mathbf{e}_v\|} \right\| = c_s.$$

By diagonal testing and using Galerkin orthogonality to insert the interpolants $I_h\mathbf{z} \in V_h$ and $I_h q \in L_h$ it follows:

$$\begin{aligned}\|\mathbf{e}_v\| &= (\nabla \mathbf{e}_v, \nabla \mathbf{z}) - (e_p, \nabla \cdot \mathbf{z}) + (\nabla \cdot \phi, q) \\ &= (\nabla \mathbf{e}_v, \nabla(\mathbf{z} - \phi_h)) - (e_p, \nabla \cdot (\mathbf{z} - \phi_h)) + (\nabla \cdot \mathbf{e}_v, (q - \xi_h)) \\ &\leq \|\nabla \mathbf{e}_v\| \, \|\nabla(\mathbf{z} - I_h\mathbf{z})\| + \|\nabla e_p\| \, \|\nabla(\mathbf{z} - I_h\mathbf{z})\| + \|\nabla \mathbf{e}_v\| \, \|q - I_h q\|\end{aligned}$$

The result follows using the energy norm error estimate for $\|\nabla \mathbf{e}_v\| + \|e_p\|$ and the interpolation estimate, Lemma 4.23:

$$\begin{aligned}\|\mathbf{e}_v\| &\leq c_I h \left(\|\nabla \mathbf{e}_v\| + \|e_p\|\right) \left(\|\nabla^2 \mathbf{z}\| + \|\nabla q\|\right) \\ &\leq c(\gamma) c_S h \left(\min_{\phi_h \in V_h} \|\nabla(\mathbf{v} - \phi_h)\| + \min_{\xi_h \in L_h} \|p - \xi_h\| \right).\end{aligned}$$

□

The approximation order of the Stokes element finally depends on the polynomial degree of the finite element pair:

Lemma 4.44 (Stokes, A Priori Estimate) *Let $V_h \times L_h$ be an inf-sup stable finite element pair of order k for the velocity and l for the pressure. Further, let $\mathbf{v} \in H^{k+1}(\Omega)^d$ and $p \in H^{l+1}(\Omega)$ be the solution to the incompressible Stokes equations. It holds*

$$\|\nabla(\mathbf{v} - \mathbf{v}_h)\| + \|p - p_h\| \leq c h^{min\{k,l+1\}} \Big(\|\nabla^{k+1} \mathbf{v}\| + \|\nabla^l p\| \Big). \tag{4.31}$$

Proof First, by Lemma 4.43 it holds

$$\|\nabla(\mathbf{v} - \mathbf{v}_h)\| + \|p - p_h\| \leq c(\gamma_h^{-1}) \left(\|\nabla(\mathbf{v} - I_h\mathbf{v})\| + \|p - I_h p\| \right),$$

where $I_h\mathbf{v} \in V_h$ and $I_h p \in L_h$ are the nodal interpolations. Given sufficient regularity it holds by Lemma 4.23

$$\|\nabla(\mathbf{v} - I_h\mathbf{v})\| \leq c_I h^k \|\nabla^{k+1}\mathbf{v}\|, \quad \|p - I_h p\| \leq c_I h^{l+1} \|\nabla^{l+1} p\|.$$

This completes the estimate. □

This lemma shows that the optimal degree for velocity and pressure space differs by one. If $l = k - 1$, optimal order of convergence is given. Possible candidates for such finite element pairs are the Taylor-Hood element $P^2 - P^1$ or $Q^k - Q^{k-1}$ or the modified Taylor-Hood element with discontinuous pressure $Q^2 - P^{1,\mathrm{dc}}$. This element has the further advantage of local mass conservation.

Remark 4.45 (Optimality of the A Priori Estimates) In terms of mesh parameter $h > 0$, the estimates in Lemma 4.44 are optimal and represent the best-approximation property. They however exhibit two shortcomings which are severe under given circumstances.

First, only coupled estimates for velocity and pressure are given. Assume that the right hand side $\mathbf{f}$ is such that its divergence free part is zero with $\mathbf{f} = \nabla q$. Then, the Stokes equations have the unique solution $\mathbf{v} = 0$ and $p = q$. Equation (4.31) gives an estimate for the velocity error depending on the pressure error. And indeed, most standard approaches elements like Taylor-Hood or the Q^2-$P^{1,\mathrm{d}}$ element will show exactly this unsatisfactory behavior with very large errors. So called *gradient-robust mixed methods* are designed in such a way that the velocity approximation is independent of the pressure. See [227] for details. In most applications, the right hand side $\mathbf{f}$ itself is not critical, as it will be zero or a fixed gravity error. In large scale deformations however, Coriolis terms may have the same effect. In terms of fluid-structure interactions, the domain motion and the ALE map is a further source of such problems.

The second issue in Lemma 4.44 is the negative dependence of the error constant on the inf-sup constant. It is well known that the inf-sup constant depends on the shape of the domain and that it goes to zero for strongly anisotropic domains, see [119]. For very long channels, this would suggest large error constants. Here however, numerical reality is in favor, such that usual finite element approaches do not see this issue. The proof of Lemma 4.44 can be modified in such a way that Fortin's criteria is applied only locally, such that the bad behavior of the global inf-sup constant does impact the result. See [228, 233] for details.

4.3.2 Stabilization Techniques for the Stokes Equations

The most easy finite element pairs using equal order finite elements for both velocity and pressure do not satisfy the inf-sup condition. Hence, they cannot be used for a robust discretization of saddle point problems like the Stokes equations. The use of such equal order pairs is mainly attractive for implementation reasons. Further, equal order finite elements simplify the design of robust iterative solvers for saddle point problems. The proof of Fortin's Lemma 4.40 gives the following estimate that holds for every conforming finite element pair $V_h \times L_h \subset \mathcal{V} \times \mathcal{L}$, also for equal order finite elements that are not inf-sup stable

$$\gamma \|p_h\| \leq \sup_{\phi \in \mathcal{V}} \frac{(p_h, \nabla \cdot \phi_h)}{\|\nabla \phi\|} + \sup_{\phi \in \mathcal{V}} \frac{(p_h, \nabla \cdot (\phi - \phi_h))}{\|\nabla \phi\|} \quad \forall p_h \in L_h,\ \forall \phi_h \in V_h. \tag{4.32}$$

We choose $\phi_h := C_h \phi$ as the H^1-stable Clement interpolation $C_h : \mathcal{V} \to V_h$, see Lemma 4.24. This interpolation does not satisfy any orthogonality condition like the projection operator π_h used in Fortin's criteria. However it holds for all $p_h \in L_h$ with help of Lemma 4.24 for the two terms in (4.32)

$$\sup_{\phi \in \mathcal{V}} \frac{(p_h, \nabla \cdot C_h \phi)}{\|\nabla C_h \phi\|} \leq c \sup_{\phi_h \in V_h} \frac{(p_h, \nabla \cdot \phi_h)}{\|\nabla \phi_h\|}$$

and

$$\sup_{\phi\in\mathcal{V}} \frac{(p_h, \nabla\cdot(\phi - C_h\phi))}{\|\nabla C_h\phi\|} = \sup_{\phi\in\mathcal{V}} \frac{\sum_{K\in\Omega_h}(p_h\mathbf{n}, \phi - C_h\phi)_{\partial K} - (\nabla p_h, \phi - C_h\phi)_K}{\|\nabla C_h\phi\|}.$$

We assume that the pressure space $L_h \subset C(\Omega)$ is continuous such that the boundary integral vanishes. Then, using the error estimate for the Clement interpolation it follows that

$$\begin{aligned}\sup_{\phi\in\mathcal{V}} \frac{(p_h, \nabla\cdot(\phi - C_h\phi))}{\|\nabla C_h\phi\|} &\le c \sup_{\phi\in\mathcal{V}} \sum_{K\in\Omega_h} \frac{h_K\|\nabla p_h\|_K\,\|\nabla\phi\|_{P(K)}}{\|\nabla C_h\phi\|} \\ &\le c'\left(\sum_{K\in\Omega_h} h_K^2\|\nabla p_h\|_K^2\right)^{\frac{1}{2}} \sup_{\phi\in\mathcal{V}}\left(\sum_{K\in\Omega_h}\frac{\|\nabla\phi\|_{P(K)}^2}{\|\nabla\phi\|_P^2}\right)^{\frac{1}{2}} \\ &\le c''\left(\sum_{K\in\Omega_h} h_K^2\|\nabla p_h\|_K^2\right).\end{aligned}$$

Altogether, it holds

Lemma 4.46 (Modified Inf-Sup Condition) *Let $V_h \times L_h \subset \mathcal{V}\times\mathcal{L}$ be a finite element pair with continuous pressure $L_h \subset C(\Omega)$. Then, the modified inf-sup condition holds*

$$\gamma_h\|p_h\| \le \sup_{\phi_h\in V_h} \frac{(p_h, \nabla\cdot\phi_h)}{\|\nabla\phi_h\|} + \left(\sum_{K\in\Omega_h} h_K^2\|\nabla p_h\|_K^2\right)^{\frac{1}{2}} \quad \forall p_h \in L_h.$$

This modified inf-sup condition gives rise to an alternative discretization technique for the Stokes equations that is based on modifications of the variational formulation. It holds

Lemma 4.47 (Pressure Stabilized Stokes Elements) *Let $V_h \times L_h$ be the equal order pair of continuous, piecewise linear pressures and velocities. Let $\mathbf{f} \in L^2(\Omega)^d$. For the solution $\{\mathbf{v}_h, p_h\} \in V_h \times L_h$ of*

$$\begin{aligned}(\nabla\mathbf{v}_h, \nabla\phi_h) - (p_h, \nabla\phi_h) &= (\mathbf{f}, \phi_h) \quad \forall\phi_h \in V_h, \\ (\nabla\cdot\mathbf{v}_h, \xi_h) + \sum_{K\in\Omega_h} h_K^2(\nabla p_h, \nabla\xi_h) &= 0 \qquad \forall\xi_h \in L_h,\end{aligned}$$

it holds

$$\|\nabla(\mathbf{v}-\mathbf{v}_h)\| + \|p-p_h\| + h_k\|\nabla(p-p_h)\| \leq ch\|\mathbf{f}\|,$$

as well as the L^2-estimate

$$\|\mathbf{v}-\mathbf{v}_h\| \leq ch^2\|\mathbf{f}\|.$$

Proof The proof is a modification of Lemma 4.43, where we must use a modified Galerkin Orthogonality in the divergence equation

$$(\nabla\cdot(\mathbf{v}-\mathbf{v}_h),\xi_h) = \sum_{K\in\Omega_h} h_K^2(\nabla p_h,\nabla\xi_h)_K,$$

and finally by estimating

$$\left(\sum_{K\in\Omega_h} h_K^2\|\nabla p_h\|_K^2\right)^{\frac{1}{2}} \leq ch\|\nabla p\|_\Omega.$$

□

This first stabilized scheme for the Stokes equations has the disadvantage of a very low approximation order. Higher order finite element approaches, e.g. $P^r - P^r$ elements still suffer from the low order due to the stabilization error $h\|\nabla p\|$. Hughes et al. [203] introduced a modification of this stabilization technique that can be generalized to higher order finite elements and that will give optimal error estimates:

Lemma 4.48 (Galerkin Least Squares Stabilization (GLS)) *Let $V_h\times L_h \subset \mathcal{V}\times\mathcal{L}$ be an equal order finite element pair with velocities and pressures of degree r. Let $\alpha > 0$. The stabilized formulation*

$$\begin{aligned}(\nabla\mathbf{v}_h,\nabla\phi_h) - (p_h,\nabla\phi_h) + (\nabla\cdot\mathbf{v}_h,\xi_h)&\\ + \sum_{K\in\Omega_h}\alpha h_K^2(-\Delta\mathbf{v}_h+\nabla p_h,-\Delta\phi_h+\nabla\xi_h)_K&\\ = (\mathbf{f},\phi_h) + \sum_{K\in\Omega_h}\alpha h_K^2(\mathbf{f},-\Delta\phi_h+\nabla\xi_h)_K \qquad \forall\phi_h\in V_h,\ \xi_h\in L_h.&\end{aligned}$$

has a unique solution $\{\mathbf{v}_h,p_h\}\in V_h\times L_h$. It holds

$$\|\nabla(\mathbf{v}-\mathbf{v}_h)\| + \|p-p_h\| \leq ch^r\Big(\|\nabla^{r+1}\mathbf{v}\| + \|\nabla^r p\|\Big)$$

Proof See Hughes et al. [203]. The improvement in approximation quality is due to the consistency of the stabilization scheme. For solutions $\{\mathbf{v},p\}\in H^2(\Omega)^d\times H^1(\Omega)$

it holds

$$-\Delta \mathbf{v} + \nabla p = \mathbf{f} \quad \Rightarrow$$
$$\sum_{K\in\Omega_h} \alpha h_K^2(-\Delta \mathbf{v} + \nabla p, -\Delta \phi_h + \nabla \xi_h) - \sum_{K\in\Omega_h} \alpha h_K^2(\mathbf{f}, -\Delta \phi_h + \nabla \xi_h)_K = 0$$

for all $\phi_h \in V_h$ and $\xi_h \in L_h$. □

Applied to linear finite elements it holds $-\Delta \phi_h = 0$, such that this stabilization scheme corresponds to the simple pressure stabilization.

This method is one of the most-used discretization schemes, which is not based on inf-sup stable elements. It has the drawback of boundary layers in the pressure, introduced by the strong non-physical control of the pressure's gradient in the error estimate. Approximation properties of this stabilized scheme can even be improved by further modifications, see Droux and Hughes [123].

An alternative to the GLS formulation and related residual based schemes is the Local Projection Stabilization method (LPS) that has been introduced by Becker and Braack [37]. Here, stability is given by projection of the solution to an inf-sup stable finite element space. It holds

Lemma 4.49 (Local Projection Stabilization (LPS)) *Let $V_h \times L_h \subset \mathcal{V} \times \mathcal{L}$ be a conforming finite element space. Further, let $V_h \times \tilde{L}_h$ be an inf-sup stable finite element pair with inf-sup constant $\tilde{\gamma}_h$. By $\pi_h : L_h \to \tilde{L}_h$ we denote a projection operator and by $s(\cdot,\cdot) : L_h \times L_h \to \mathbb{R}$ a bilinear stabilization form. If it holds*

$$\|\pi_h p_h\| \le c_1 \|p_h\|, \quad \|p_h - \pi_h p_h\|^2 \le c_2 s(p_h, p_h) \quad \forall p_h \in L_h.$$

the stabilized Stokes equations

$$\begin{aligned} (\nabla \mathbf{v}_h, \nabla \phi_h) - (p_h, \nabla \cdot \phi_h) &= (\mathbf{f}, \phi_h) \qquad \forall \phi_h \in V_h, \\ (\nabla \cdot \mathbf{v}_h, \xi_h) + s(p_h, \xi_h) &= 0 \qquad \forall \xi_h \in L_h \end{aligned}$$

has a unique solution $\{\mathbf{v}_h, p_h\} \in V_h \times L_h$. Let $V_h \times L_h$ be an equal order space of polynomial degree r and $V_h \times \tilde{L}_h$ be an inf-sup stable space of degree $r-1$ in $\tilde{L}_h$. Then, given sufficient regularity of $\{\mathbf{v}, p\}$ it holds

$$\|\nabla(\mathbf{v} - \mathbf{v}_h)\| + \|p - p_h\| \le c h^r \Big(\|\mathbf{v}\|_{H^{r+1}(\Omega)} + \|p\|_{H^r(\Omega)} \Big).$$

Proof See Becker and Braack [37]. □

The Local Projection Stabilization method has the advantage of a very easy implementation. Opposed to the GLS method, no second derivatives are necessary in the variational formulations.

As a symmetric method with $s(p_h, q_h) = s(q_h, p_h)$ the discrete equations are simply structured. Many different approaches exist. Based on the Taylor-Hood elements $Q^k - Q^{k-1}$ stability for equal order pairs is given for the discrete interpolation

$$I_h^{k-1} : L_h \to \tilde{L}_h, \quad s_h(p_h, \xi_h) = \sum_{K \in \Omega_h} \alpha h_K^2 \Big(\nabla(p_h - I_h^{k-1} p_h), \nabla(\xi_h - I_h^{k-1} \xi_h) \Big)_K.$$

Another option for stable discretization is by projection to the space of equal order on a coarse mesh

$$I_{2h}^k : L_h \to \tilde{L}_h := L_{2h},$$
$$s_h(p_h, \xi_h) = \sum_{K \in \Omega_h} \alpha h_K^2 \Big(\nabla(p_h - I_{2h}^k p_h), \nabla(\xi_h - I_{2h}^k \xi_h) \Big)_K.$$

Another noteworthy stabilization scheme is the *continuous interior penalty method*, shortly denoted as *edge stabilization*, which is based on penalization of interior gradient jumps, see [85]

$$s_h(p_h, \xi_h) = \sum_{K \in \Omega_h} \sum_{e \in \partial K} \gamma h_K^\alpha \int_e [\mathbf{n} \cdot \nabla p_h] \cdot [\mathbf{n} \cdot \nabla \xi_h] \mathrm{d}s,$$

where $\gamma > 0$ is a coefficient, $\alpha \in \{1, 2\}$ an exponent and where we denote by $[\mathbf{n} \cdot \nabla p_h]$ the jumps of the normal derivative at an edge $e \in \partial K$. This technique has many similarities to the *Local Projection Stabilization* scheme. It is symmetric and can be applied to all equal order elements. By proper control of γ and α, weak consistency is achieved to guarantee optimal order error estimates. We will revisit this flexible stabilization scheme in Chap. 12 and also refer to the literature [84–86].

Research on stabilization schemes for saddle-point problems is still ongoing and improved schemes are appearing [37, 62, 67, 72, 102, 203, 253, 256, 322].

4.4 Finite Elements for the Navier-Stokes Equations

The incompressible Navier-Stokes equations

$$(\partial_t \mathbf{v} + \mathbf{v} \cdot \nabla \mathbf{v}, \phi) + \frac{1}{Re}(\nabla \mathbf{v}, \nabla \phi) - (p, \nabla \cdot \phi) = (\mathbf{f}, \phi) \quad \forall \phi \in \mathcal{V}_f,$$
$$(\nabla \cdot \mathbf{v}, \xi) = 0 \qquad \forall \xi \in \mathcal{L}_f,$$

differ from the Stokes equation by the nonlinearity only. We assume, that time-discretization is done by Rothe's method with a time stepping method, such that in every time step $t_{m-1} \to t_m$ a quasi-stationary problem must be solved

$$\begin{aligned}(\alpha \mathbf{v} + \mathbf{v} \cdot \nabla \mathbf{v}, \phi) + \frac{1}{Re}(\nabla \mathbf{v}, \nabla \phi) - (p, \nabla \cdot \phi) &= (\mathbf{g}, \phi) \quad \forall \phi \in \mathcal{V}_f, \\ (\nabla \cdot \mathbf{v}, \xi) &= 0 \qquad \forall \xi \in \mathcal{L}_f,\end{aligned}$$

where $\alpha \sim k^{-1}$. A direct discretization with an inf-sup stable finite element pair $V_h \times L_h \subset \mathcal{V}_f \times \mathcal{L}_f$ leads to a finite dimensional—but nonlinear—system of algebraic equations

$$\begin{aligned}(\alpha \mathbf{v}_h + \mathbf{v}_h \cdot \nabla \mathbf{v}_h, \phi_h) + \frac{1}{Re}(\nabla \mathbf{v}_h, \nabla \phi_h) - (p_h, \nabla \cdot \phi_h) &= (\mathbf{g}, \phi_h) \quad \forall \phi_h \in V_h, \\ (\nabla \cdot \mathbf{v}_h, \xi_h) &= 0 \qquad \forall \xi_h \in L_h,\end{aligned}$$

that can be written in operator-form as

$$\begin{pmatrix} \mathbf{A}(\mathbf{v}_h) & \mathbf{B}_h \\ -\mathbf{B}_h^T & 0 \end{pmatrix} \begin{pmatrix} \mathbf{v} \\ \mathbf{p} \end{pmatrix} = \begin{pmatrix} \mathbf{f} \\ 0 \end{pmatrix},$$

where

$$(\mathbf{A}_h(\mathbf{v}_h))_{ij} = (\alpha \phi_j, \phi_i) + \frac{1}{Re}(\nabla \phi_j, \nabla \phi_i) + (\mathbf{v}_h \cdot \nabla \phi_j, \phi_i), \quad i, j = 1, \ldots, N,$$

and where $\mathbf{B}_h$ is defined as in (4.22)

$$(\mathbf{B}_h)_{ij} = -(\xi_j, \nabla \cdot \phi_i), \quad i = 1, \ldots, N,\ j = 1, \ldots, N_p.$$

This discrete operator could further be written as a third order tensor $\mathbf{A}_h^{(3)}$ independent of the transport direction v_h

$$(\mathbf{A}_h^{(3)})_{ijk} = (\alpha \phi_j, \phi_i) + \frac{1}{Re}(\nabla \phi_j, \nabla \phi_i) + (\phi_k \cdot \nabla \phi_j, \phi_i), \quad i, j, k = 1, \ldots, N.$$

The effort for assembling this tensor would however dominate the whole procedure and storing such a third order tensor would require vast amounts of memory. Instead of discretizing the nonlinear problem one usually first treats the nonlinearity by an outer iteration. Here, we discuss two common approaches for linearization.

4.4.1 Oseen Fixed Point Linearization

We iterate $\mathbf{v}^l \to \mathbf{v} \in \mathcal{V}_f$ by linearization of the nonlinearity at the old step $\mathbf{v}^{l-1}$. Given $\mathbf{v}^{l-1} \in \mathcal{V}_f$ find $\{\mathbf{v}^l, p^l\} \in \mathcal{V}_f \times \mathcal{L}_f$ such that

$$(\alpha \mathbf{v}^l + \mathbf{v}^{l-1} \cdot \nabla \mathbf{v}^l, \phi) + \frac{1}{Re}(\nabla \mathbf{v}^l, \nabla \phi) - (p^l, \nabla \cdot \phi) = (\mathbf{g}, \phi) \quad \forall \phi \in \mathcal{V}_f,$$
$$(\nabla \cdot \mathbf{v}^l, \xi) = 0 \qquad \forall \xi \in \mathcal{L}_f.$$

In every step of this iteration a linear partial differential equation must be solved. This linear problem is called the *Oseen equation*. The same linearization is used for proving existence of a Navier-Stokes solution in Lemma 2.50. It shows that this iteration converges for small Reynolds numbers. The convergence $\mathbf{v}^l \to \mathbf{v} \in \mathcal{V}_f$ however is always only linear and the convergence rate will depend on Re. In Fig. 4.9 we show the convergence history of the Oseen fixed point iteration for different Reynolds numbers.

In a further simplification of this linearization, we treat the nonlinearity completely explicitly and iterate $\mathbf{v}^{l-1} \to \mathbf{v}^l \in \mathcal{V}$ by solving

$$(\alpha \mathbf{v}^l, \phi) + \frac{1}{Re}(\nabla \mathbf{v}^l, \nabla \phi) - (p^l, \nabla \cdot \phi) = (\mathbf{g}, \phi) - (\mathbf{v}^{l-1} \cdot \nabla \mathbf{v}^{l-1}, \phi) \quad \forall \phi \in \mathcal{V},$$
$$(\nabla \cdot \mathbf{v}^l, \xi) = 0 \qquad \forall \xi \in \mathcal{L}.$$

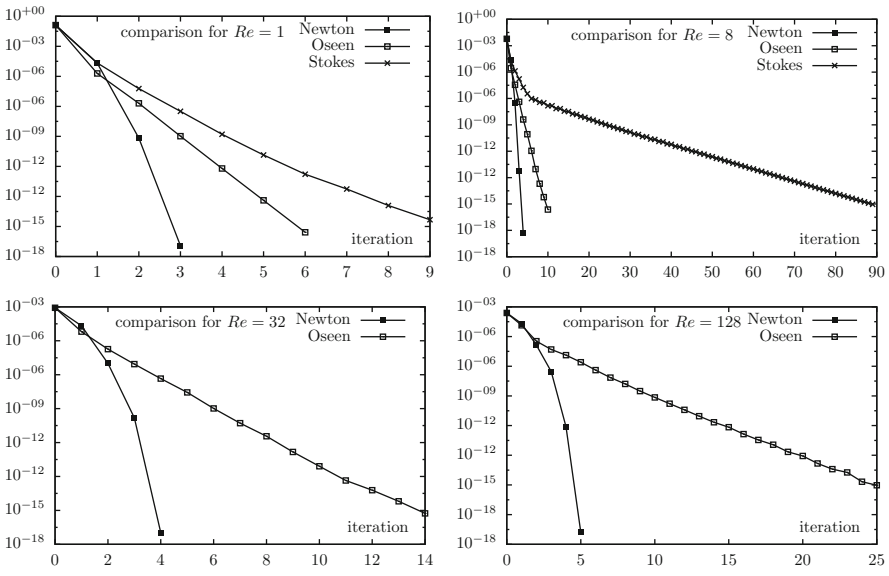

Fig. 4.9 Comparison of different linearization techniques. We show the residual over the iteration count for Reynolds numbers 1, 8, 32 and 128

Every step of this iteration consists of solving a generalized (for $\alpha > 0$) Stokes equations. This *Stokes Linearization* can only be used for very small Reynolds numbers and converges very slowly. Again, see Fig. 4.9 for the convergence behavior of this iteration compared to the Stokes linearization. Both iterations converge slowly. For Reynolds numbers $Re > 50$ both iterations can hardly be used.

4.4.2 Newton Iteration

The Newton method for solving nonlinear problems can also be defined in infinite dimensional Banach spaces. For the following, we assume, that the nonlinear partial differential equation is given in variational formulation by

$$u \in \mathcal{V}: \quad A(u)(\phi) = F(\phi) \quad \forall \phi \in \mathcal{V}, \tag{4.33}$$

where $A(\cdot)(\cdot)$ is a semi-linear form, which is linear in the second argument and sufficiently differentiable. Here, by differentiability we consider the *Gâteaux derivative* as a generalization of the directional derivative to mappings between infinite dimensional spaces. By

$$A'(u)(w,\phi) := \frac{d}{ds} A(u+sw)(\phi)\Big|_{s=0},$$

we denote the derivative of $A(\cdot)(\cdot)$ at $u \in \mathcal{V}$ in direction $w \in \mathcal{V}$. The Newton iteration for solving (4.33) starts with an initial guess $u^0 \in \mathcal{V}$ and iterates for $l = 1, \ldots$

$$\begin{aligned} w^l \in \mathcal{V}: \quad A'(u^{l-1})(w,\phi) &= F(\phi) - A(u^{l-1})(\phi) \quad \forall \phi \in \mathcal{V}, \\ u^l &:= u^{l-1} + w^l. \end{aligned} \tag{4.34}$$

In every step of the Newton method a linear partial differential equation arises that can be discretized with the finite element method. The Newton iteration is usually considered in a defect correction way like (4.34). This allows for simple damping strategies that are necessary for complicated problems if no good initial guess $u^0 \in \mathcal{V}$ is known. As this is the usual case for complex problems arising in fluid-structure interaction we shortly introduce a common damping strategy:

Definition 4.50 (Line Search) Start with $u^0 \in \mathcal{V}$ and compute $\rho^0 := \|F - A(u^0)\|$. Iterate for $l = 1, 2, \ldots$

1. Solve Newton update $w^l \in \mathcal{V}$ by

$$w^l \in \mathcal{V}: \quad A'(u^{l-1})(w,\phi) = F(\phi) - A(u^{l-1})(\phi) \quad \forall \phi \in \mathcal{V}$$

2. Set $\omega^j = 1$ and iterate $j = 1, \ldots$

   a. Update solution

   $$u^{l,j} := u^{l-1} + \omega^j w^l.$$

   b. Compute residual

   $$\rho^{l,j} := \|F - A(u^{l,j})\|.$$

   c. If $\rho^{l,j} < \rho^{l-1}$ set $u^l := u^{l,j}$ and continue with $l + 1$ at 1., otherwise set

   $$\omega^{j+1} := \gamma \omega^j,$$

   where $\gamma < 1$ and continue with $j + 1$ at 2.a.

Details on the nonlinear partial differential equations and the application of Newton's method is found in the literature [116, 117].

For applying the Newton scheme to the Navier-Stokes equations we must compute the Gatâux derivative of the variational formulation. For

$$A(\mathbf{v}, p)(\phi, \xi) := (\alpha \mathbf{v}, \phi) + (\mathbf{v} \cdot \nabla \mathbf{v}, \phi) + \frac{1}{Re}(\nabla \mathbf{v}, \nabla \phi) - (p, \nabla \cdot \phi) + (\nabla \cdot \mathbf{v}, \xi),$$

it holds for the search direction $\{\mathbf{w}, q\} \in \mathcal{V}_f \times \mathcal{L}_f$:

$$A'(\mathbf{v}, p)(\mathbf{w}, q, \phi, \xi) = (\alpha \mathbf{w}, \phi) + (\mathbf{v} \cdot \nabla \mathbf{w} + \mathbf{w} \cdot \nabla \mathbf{v}, \phi) + \frac{1}{Re}(\nabla \mathbf{w}, \nabla \phi) - (q, \nabla \cdot \phi) + (\nabla \cdot \mathbf{w}, \xi),$$

Then, in every step of the Newton iteration a linear saddle-point problem must be solved for the update $\mathbf{w}^l \in \mathcal{V}_f$ of velocity and $q^l \in \mathcal{L}_f$ of pressure:

$$\begin{aligned}
(\alpha \mathbf{w}^l, \phi) + (\mathbf{v}^{l-1} \cdot \nabla \mathbf{w}^l + \mathbf{w}^l \cdot \nabla \mathbf{v}^{l-1}, \phi) + \frac{1}{Re}(\nabla \mathbf{w}^l, \nabla \phi) &= (\mathbf{f}, \phi) \\
- (\alpha \mathbf{v}^{l-1}, \phi) - (\mathbf{v}^{l-1} \cdot \nabla \mathbf{v}^{l-1}, \phi) - \frac{1}{Re}(\nabla \mathbf{v}^{l-1}, \nabla \phi) \quad & \forall \phi \in \mathcal{V}_f \\
(\nabla \cdot \mathbf{w}^l, \xi) = -(\nabla \cdot \mathbf{v}^{l-1}, \xi) \quad & \forall \xi \in \mathcal{L}_f. \qquad (4.35)
\end{aligned}$$

Remark 4.51 (Linearization of the Navier-Stokes Equation by Newton's Method) In every step of the Newton method a linear saddle-point problem of Reaction-Diffusion-Transport type must be solved. This linear problem is difficult to solve as it is neither symmetric nor positive. The reaction part has the coefficient

$$(\alpha \mathbf{w}^l + \mathbf{w}^l \cdot \nabla \mathbf{v}^{l-1}, \phi) = ([\alpha I + \nabla \mathbf{v}^{l-1}]\mathbf{w}^l, \phi),$$

which might be—depending on $\nabla \mathbf{v}^{l-1}$—positive or negative definite or simply indefinite.

The sequence of discretization and linearization can be swapped. For a convergence analysis of the Newton iteration, one however usually treats the non-discretized set of equations and discusses the Newton method in function spaces. This approach allows to derive convergence estimates that are uniform in the mesh-size $h > 0$ and hold under mesh convergence $h \to 0$. See Deuflhard [116], or Rannacher [265, 267].

4.4.3 *Discretization of Transport Dominant Flows*

The Galerkin discretization of the Navier-Stokes equations sometimes shows spurious oscillations if the Reynolds number is large. This numerical instability arises if the convection term $\mathbf{v} \cdot \nabla \mathbf{v}$ gets dominant over the viscous term $-\nu \Delta \mathbf{v}$. In Fig. 4.10 we show the flow in a branching channel for increasing Reynolds numbers. In the top row of the figures we show the velocity profile of the fluid, in the bottom row, we plot the value of the velocity at the center-line $y = 0$ of the domain, where the fluid hits the branching. For increasing Reynolds numbers, the velocity profile oscillates and does not look physical. The simulations in Fig. 4.10 have all been carried out on a coarse mesh with mesh size $h = 2^{-3}$ (the inflow part of the domain has the width 1, consisting of 8 elements). In Fig. 4.11 we repeat these simulations for Reynolds number $Re = 2500$ on a sequence of finer and finer meshes. We observe that the oscillations disappear for $h \to 0$.

These kind of transport instabilities can be analyzed with help of a simple one-dimensional model problem

$$-\varepsilon u'' + u' = 0, \quad u(0) = 1, \quad u(1) = 0, \tag{4.36}$$

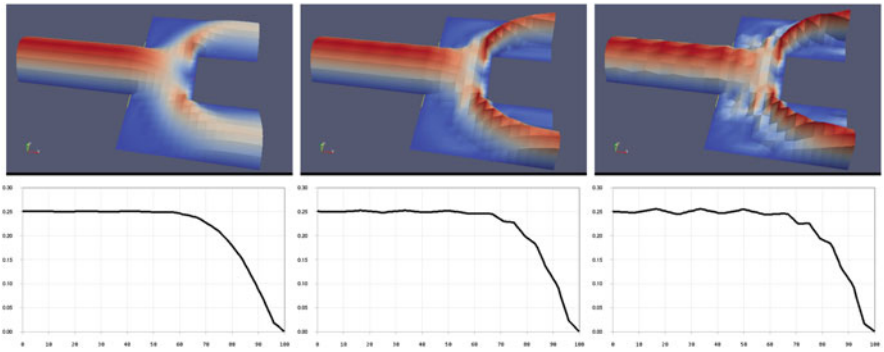

Fig. 4.10 Galerkin approximation of a branching flow for increasing Reynolds numbers $Re = 100$, $Re = 500$ and $Re = 2500$

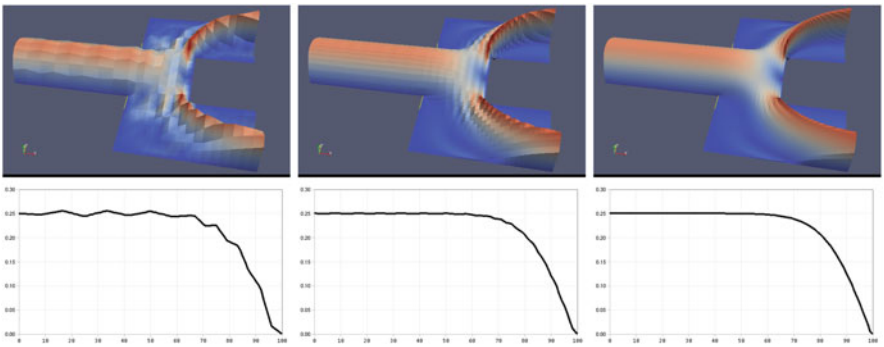

Fig. 4.11 Galerkin approximation of a branching flow Reynolds number $Re = 2500$ under mesh refinement $h = 2^{-3}$, $h = 2^{-4}$ and $h = 2^{-5}$

which has the exact solution

$$u(x) = \frac{\exp(\varepsilon^{-1}) - \exp(x\varepsilon^{-1})}{\exp(\varepsilon^{-1}) - 1},$$

and features a boundary layer of width $O(\varepsilon)$ at $x = 1$. For a Galerkin discretization of this problem with piecewise linear finite elements—that corresponds to the standard central difference discretization—one discovers that the system matrix looses its diagonal dominance if $h < 2\varepsilon$, see e.g. Johnson [207]. To tackle this problem, two different approaches are usually considered.

First, it is possible to use a Galerkin discretization with lesser smoothness properties. By a discretization with discontinuous finite elements in space using stabilizing fluxes one can avoid stability problems caused by transport. Again, see Johnson [207] or Cockburn et al. [101]. The use of discontinuous finite elements however brings along the disadvantage of a high computational effort, as the number of degrees of freedom is substantially bigger compared to a continuous finite element approach of the same order as the degrees of freedom on the element edges are doubled.

The second approach consists in adding stability by modifying the variational formulation of the problem in such a way that diffusion is added to the set of equations. This modification must be so significant that it eliminates oscillations, it however must be small enough to still give good approximation results for the original problem. In particular, we expect that the additional stabilization must vanish for $h \to 0$. The most simple approach, the *artificial diffusion method* simply adds stability by increasing the viscosity in a h-depending way. The model problem (4.36) stabilized with the artificial diffusion method gets

$$-\tilde{\varepsilon}(h)u'' + u' = 0, \quad u(0) = 1, \quad u(1) = 0, \quad \tilde{\varepsilon}(h) := \varepsilon + \frac{1}{2}h. \tag{4.37}$$

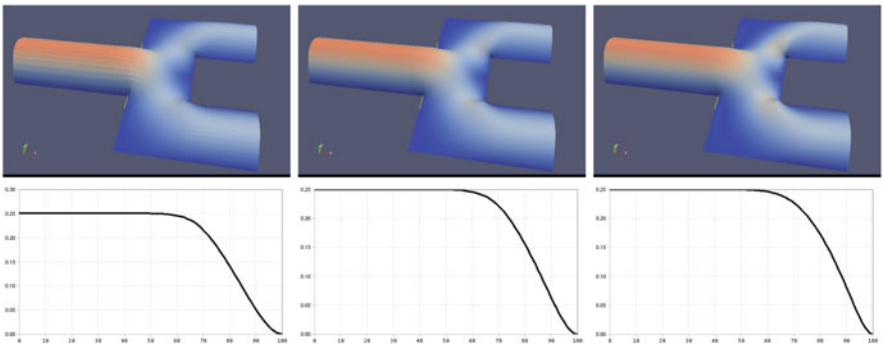

Fig. 4.12 Artificial diffusion stabilization for a branching flow at Reynolds number $Re = 2500$ under mesh refinement $h = 2^{-3}$, $h = 2^{-4}$ and $h = 2^{-5}$

As for $\tilde{\varepsilon}$ it holds $h < 2\tilde{\varepsilon}(h) = 2\varepsilon + h$ for all $h > 0$, a standard discretization of (4.37) will always by diagonally dominant and give monotone results. This simple artificial diffusion technique however limits the approximation accuracy of the resulting scheme to first order. In Fig. 4.12 we show the artificial diffusion stabilization for the branching flow example at Reynolds number $Re = 2500$. The result is stable and the velocity profile looks smooth. However, at $Re = 2500$ the solution is fully governed by the artificial viscosity, not by $\nu \sim Re^{-1}$. Comparing Figs. 4.11 (right) and 4.12 a severe discrepancy between the stabilized and the physical profile gets visible.

The *Streamline Upwind Petrov Galerkin* method (SUPG) is a stabilization scheme that adds stability by introducing a Petrov Galerkin formulation of the model problem. Modified test functions $\phi + \delta_h \phi'$ with $\delta_h \sim h$ are used to get

$$(-\varepsilon u_h'' + u_h', \phi_h + \delta_h \phi_h') = (f, \phi_h + \delta_h \phi_h') \qquad \forall \phi_h \in V_h$$

$$\Leftrightarrow$$

$$(\varepsilon u_h', \phi_h') + (u_h', \phi_h) + (\delta_h u_h', \phi_h') + (\delta_h(-\varepsilon u_h'' - f), \phi_h') = (f, \phi_h) \quad \forall \phi_h \in V_h.$$

While the term $(\delta_h u_h', \phi_h')$ adds diffusion to the equation and stabilizes the solution, the further term $(\delta_h(-\varepsilon u_h'' - f), \phi_h')$ assures consistency of the solution. It holds

Lemma 4.52 (Streamline Upwind Petrov Galerkin) *Let $u \in H^{r+1}(I)$ be the solution to the model problem (4.36) and $u_h \in V_h^r$ be the SUPG solution. It holds*

$$\|u - u_h\| + \sqrt{h}\|u' - u_h'\| \leq c h^{r+\frac{1}{2}} \|u\|_{r+1}.$$

Proof See Johnson [207]. □

The SUPG method can easily be applied to the Navier-Stokes equations. This has first been done by Brooks and Hughes [75]. We modify the test space of the

momentum equation to get

$$
\begin{aligned}
(\partial_t \mathbf{v} + \mathbf{v} \cdot \nabla \mathbf{v}, \phi) + \frac{1}{Re}(\nabla \mathbf{v}, \nabla \phi) - (p, \nabla \cdot \phi) \\
+(\partial_t \mathbf{v} - Re^{-1} \Delta \mathbf{v} + \nabla p - \mathbf{f}, \delta_h \mathbf{v} \cdot \nabla \phi) + (\mathbf{v} \cdot \nabla \mathbf{v}, \delta_h \mathbf{v} \cdot \nabla \phi) = (\mathbf{f}, \phi) \\
(\nabla \cdot \mathbf{v}, \xi) = 0.
\end{aligned}
$$

Again, stability is given by the term $(\mathbf{v} \cdot \nabla \mathbf{v}, \delta_h \mathbf{v} \cdot \nabla \phi)$, where the second additional term stands for consistency only. The drawback of this technique is the introduction of a second order coupling in the pressure $(\nabla p, \delta_h \mathbf{v} \cdot \nabla \phi)$ and a third order term regarding the velocity $(-\Delta \mathbf{v}, \delta_h \mathbf{v} \cdot \nabla \phi)$. Both terms give rise to boundary layers. Further, the SUPG technique couples the time derivative with spatial derivatives. A correct discretization of this term $(\partial_t \mathbf{v}, \delta_h \mathbf{v} \cdot \nabla \phi)$ is difficult to implement. For a discussion and analysis of the SUPG method applied to transient problems we refer to [67, 81]. The SUPG method gives accurate and stable results for all polynomial degrees and apart from the Laplacian and the time-derivative in the consistency term, an implementation is straightforward. The SUPG stabilization can easily be combined with the PSPG pressure stabilization technique as introduced in Sect. 4.3.2. This combination of stabilization techniques is one of the most common discretization approaches for the incompressible Navier-Stokes equations.

The drawback of these consistent residual based stabilization techniques is the introduction of couplings between time-derivative, velocity and pressure. These couplings are not physical. Further, the implementation of these couplings can be complex and can have a negative impact on the behavior of iterative solvers. Another stabilization technique for convective flows is based on a projection of the solution to a subspace, similar to the Local Projection Stabilization for the inf-sup condition introduced in Sect. 4.3.2. The SUPG method introduces the stabilization term

$$
s_{\text{SUPG}}(\mathbf{v}, p)(\phi) = (\partial_t \mathbf{v} - Re^{-1} \Delta \mathbf{v} + \nabla p - \mathbf{f} + \mathbf{v} \cdot \nabla \mathbf{v}, \phi).
$$

For the solution $\{\mathbf{v}, p\}$ it holds

$$
-\mathbf{v} \cdot \nabla \mathbf{v} = \partial_t \mathbf{v} - Re^{-1} \Delta \mathbf{v} + \nabla p - \mathbf{f}.
$$

Hence, we can replace the right hand side of this relation by an approximation of the left hand side, e.g. by a projection of $\mathbf{v} \cdot \nabla \mathbf{v}$ into a coarser space. This is the idea of the *Local Projection Stabilization (LPS)* for convective flows, as introduced by Becker and Braack [39] and similarly by Codina [102]

$$
s_{\text{LPS}}(\mathbf{v})(\phi) = (\mathbf{v} \cdot \nabla \mathbf{v} - \overline{\mathbf{v} \cdot \nabla \mathbf{v}}, \delta_h \mathbf{v} \cdot \nabla \phi).
$$

Different variants of the LPS method are discussed in the literature. One of the most simple variant uses a local projection to a mesh with double mesh-spacing

$\pi_{2h} : V_h \to V_{2h}$:

$$(\partial_t \mathbf{v}_h + \mathbf{v}_h \cdot \nabla \mathbf{v}_h, \phi_h) + \frac{1}{Re}(\nabla \mathbf{v}_h, \nabla \phi_h) - (p_h, \nabla \cdot \phi_h)$$
$$+\Big(\mathbf{v}_h \cdot \nabla \mathbf{v}_h - \mathbf{v}_{2h} \cdot \nabla \mathbf{v}_{2h}, \delta_h(\mathbf{v}_h \cdot \nabla \phi_h - \mathbf{v}_{2h} \cdot \nabla \phi_{2h})\Big) = (\mathbf{f}, \phi_h)$$
$$(\nabla \cdot \mathbf{v}_h, \xi) = 0,$$

where for abbreviation we used $\mathbf{v}_{2h} := \pi_{2h}\mathbf{v}_h$ and $\phi_{2h} := \pi_{2h}\phi_h$. In Fig. 4.13 we present results for the Local Projection stabilization for the branching flow problem at Reynolds number $Re = 2500$. The results have less smoothness as compared to the artificial diffusion stabilization shown in Fig. 4.12. The boundary layers are however more accurate and closer to the Galerkin discretization on fine meshes as indicated in Fig. 4.11. The LPS method has the advantage that it is diagonal in the following sense: No artificial couplings are introduced between velocity and pressure. The LPS term for stabilizing convection involves the velocity only, while the term for stabilizing the inf-sup condition requires only the pressure. This diagonal setup will be of importance when considering complex coupled problems like fluid-structure interactions.

For comparison of these stabilization techniques, for numerical analysis and different variants see the overview articles by Braack et al. [67].

Remark 4.53 Flux-Correction A completely different approach for stabilizing transport equations is the technique of *algebraic flux correction*. As the name suggests, this method does not fall into the residual based Galerkin approaches. Instead, the resulting system matrix is modified by means of algebraic transformations with the goal to ensure the discrete maximum principle. This rather new technique is very successful and provides excellent results. For an overview, we refer to [216–218] or [55] in the context of ALE schemes for moving domains.

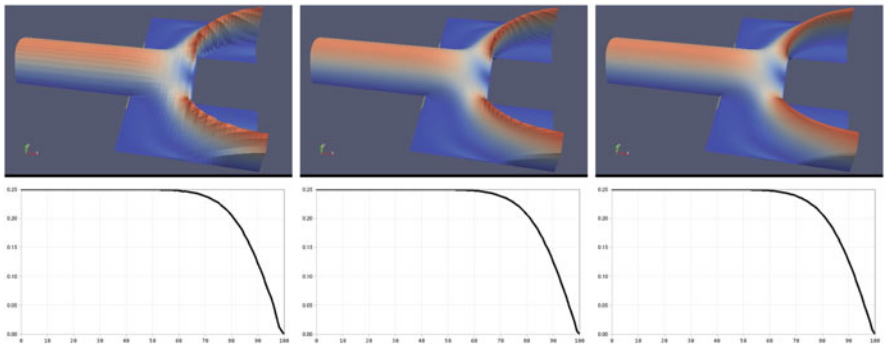

Fig. 4.13 Local Projection Stabilization for a branching flow at Reynolds number $Re = 2500$ under mesh refinement $h = 2^{-3}$, $h = 2^{-4}$ and $h = 2^{-5}$

4.5 Discretization of Interface-Problems

The Fully Eulerian formulation discussed in Sect. 3.6, Chaps. 6 and 12 is an *interface problem*, as the equation undergoes changes across an internal interface $\mathcal{I} \subset \Omega$. The interface is exactly the coupling boundary between fluid-problem and solid-problem, where the equation changes from the incompressible Navier-Stokes equations to a solid equation. Physical reasoning tells us that deformation $\mathbf{u}$ and velocity $\mathbf{v}$ (at least in normal direction) are continuous at this interface. We cannot expect differentiability. In terms of regularity, it holds $\mathbf{u}, \mathbf{v} \in [H^1(\Omega)]^d$, however $\mathbf{u}, \mathbf{v} \notin [H^2(\Omega)]^d$. In both parts $\mathcal{F}$ and $\mathcal{S}$ we can expect this higher regularity. When it comes to numerical approximation, convergence is assured by best approximation and interpolation estimates. These require high regularity, see Sect. 4.2.1. If we are able to resolve the internal interface with the finite element mesh, interface problems do not pose an additional problem, as interpolation estimates only act locally and will work, as long as no mesh-element is cut by the interface.

For the Fully Eulerian formulation however, it will in general not be possible to choose a matching finite element mesh, as

- The location of the interface is a priori not known. Instead, it is implicitly given by the solution itself.
- The interface is usually not a polygonal, such that an exact resolution will not be possible.
- The interface is moving in time—if the problem is non-stationary—and new finite element meshes would be necessary in each time step. This is in principle possible, but would be very costly.

To explain efficient concepts of discretizing interface problems, we will focus on a very simple interface problem, the Laplace equation with a coefficient that has a jump within the domain $\Omega = \Omega_1 \cup \mathcal{I} \cup \Omega_2$

$$-\nabla \cdot (\kappa_i \nabla u) = f \text{ on } \Omega_i,\ i = 1, 2, \quad [u] = 0 = [\kappa \partial_n u] = 0 \text{ on } \mathcal{I}, \tag{4.38}$$

and with $u = 0$ on the outer boundary $\partial\Omega$. $\kappa_1, \kappa_2 > 0$ are diffusion parameters. By

$$[u](x) := \lim_{s \downarrow 0} u(x + \mathbf{n}s) - \lim_{s \uparrow 0} u(x + \mathbf{n}s), \quad x \in \mathcal{I},$$

we denote the jump of u at the interface $\mathcal{I}$ with normal vector $\mathbf{n}$ on $\mathcal{I}$. The variational formulation of this interface problem is given by

$$u \in H_0^1(\Omega): \quad a(u, \phi) := \sum_{i=1}^{2} (\kappa_i \nabla u, \nabla \phi) = (f, \phi) \quad \forall \phi \in H_0^1(\Omega).$$

Existence of solutions can be shown by standard arguments. We assume that the partitioning of Ω into Ω_1 and Ω_2 is non-overlapping $\Omega_1 \cap \Omega_2 = \emptyset$ and that both

subdomains Ω_i ($i = 1, 2$) have a boundary with sufficient regularity such that for smooth right hand sides it holds for the solution of (4.38) that

$$u \in H_0^1(\Omega) \cap H^{r+1}(\Omega_1 \cup \Omega_2),$$

for a given $r \in \mathbb{N}$, with $r \geq 1$. See Babuška [14] for an early work on such an interface problem.

Interface problems are elaborately discussed in literature. If the interface $\mathcal{I}$ cannot be resolved by the mesh, the overall convergence for a standard finite element ansatz will be reduced to

$$\|\nabla(u - u_h)\|_\Omega = \mathcal{O}(h^{1/2}),$$

independent of the polynomial degree r of the finite element space. For an analysis, see Babuška [14] or MacKinnon and Carey [232]. In Fig. 4.14, we show the H^1 and L^2 errors for a simple interface problem with curved interface that is not resolved by the finite element mesh. Both linear and quadratic finite elements only give $\mathcal{O}(h^{1/2})$ accuracy in the H^1-seminorm and $\mathcal{O}(h)$ in the L^2-norm. This is due to limited regularity of the solution across the interface.

It has been shown that for interface problems with jumping coefficients causing weak discontinuities, optimal convergence can be recovered by a harmonic averaging of the diffusion constants [309, 324]. Such an averaging procedure has been applied to multiphase flows, it is however not suitable for problems, where two entirely different types of differential equations are coupled on the interface, as it is the case for fluid-structure interactions.

Given a fitted finite element configuration, the optimal order of convergence is guaranteed [14, 70, 137, 360]. If the interface is moving, curved or has small scale features, the repeated generation of fitted finite element meshes can exceed the feasible effort. Further developments are based on local modifications of the

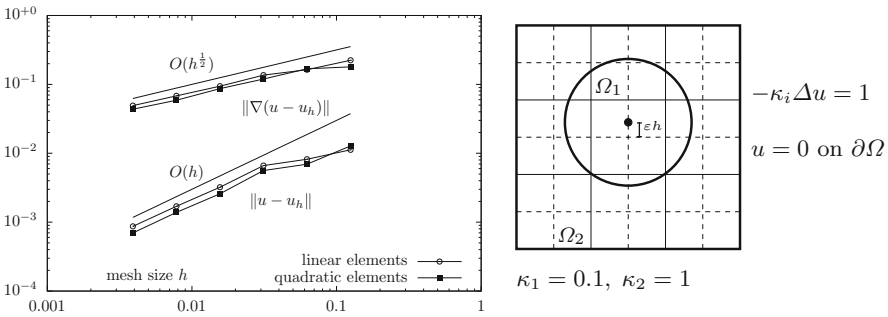

Fig. 4.14 L^2- and H^1-error for a standard finite element simulation for a diffusion problem with a discontinuity in the diffusion coefficient. Configuration of the test problem in the *right sketch*. Details on this problem are given in Sect. 4.5.3

finite element mesh that only alter mesh elements close to the interface [56, 352]. By combining local mesh modifications close to the interface with an isoparametric approximation of curved interfaces, even higher order approximation could be shown [135].

An alternative approach is based on unfitted finite elements, where the mesh is fixed and does not resolve the interface. Proper accuracy is gained by local modifications or enrichment of the finite element basis. Prominent examples for these methods are the the extended finite element method (XFEM) [246], the generalized finite element method [20] or the unfitted Nitsche method by Hansbo and Hansbo [174, 175], that casts the XFEM method into a new light. These enrichment methods are well analyzed and show the correct order of convergence. One drawback of all these methods is a complicated structure that requires local modifications in the finite element spaces leading to a variation in the connectivity of the system matrix and number of unknowns. In non-stationary computations, these methods can call for a change of the memory pattern in every time step, a potentially costly operation.

Here, we propose a finite element technique for interface problems that fits both into the context of fitted methods and modified finite element schemes. Instead of resolving the interface by a motion of mesh nodes, we locally adapt the finite element in an implicit parametric way, such that the finite element bases can reflect weak discontinuities at the interface. This scheme requires neither an enrichment of the basis nor a modification of the mesh.

The original notion of this *parametric finite element method* [153] that has been developed on quadrilateral meshes has already been adapted to triangles [161, 193].

4.5.1 Parametric Interface Finite Elements

Let Ω_h be a form and shape-regular triangulation of the domain $\Omega \subset \mathbb{R}^2$ into open quadrangles. The mesh Ω_h does not necessarily resolve the partitioning $\Omega = \Omega_1 \cup \mathcal{I} \cup \Omega_2$ and the interface $\mathcal{I}$ can cut the elements $K \in \Omega_h$. For simplicity, we assume that the outer boundary $\partial\Omega$ can be resolved by the mesh. Otherwise, the approximation of the curved boundary must be considered, see Sect. 4.2.3.

Next, we assume that the mesh Ω_h has a patch-hierarchy in such a way that each four adjacent quads arise from uniform refinement of one common father-element, see Fig. 4.15. Such a mesh-hierarchy is naturally given for finite element methods based on adaptive mesh refinement and also commonly used for error estimation methods [41] or projection based stabilization schemes [37]. The interface $\mathcal{I}$ may cut the patches in the following way:

1. Each (open) patch $P \in \Omega_h$ is either not cut $P \cap \mathcal{I} = \emptyset$ or cut in exactly two points on its boundary: $P \cap \mathcal{I} \neq \emptyset$ and $\partial P \cap \mathcal{I} = \{x_1^P, x_2^P\}$.
2. If a patch is cut, the two cut-points x_1^P and x_2^P may not be inner points of the same edge.

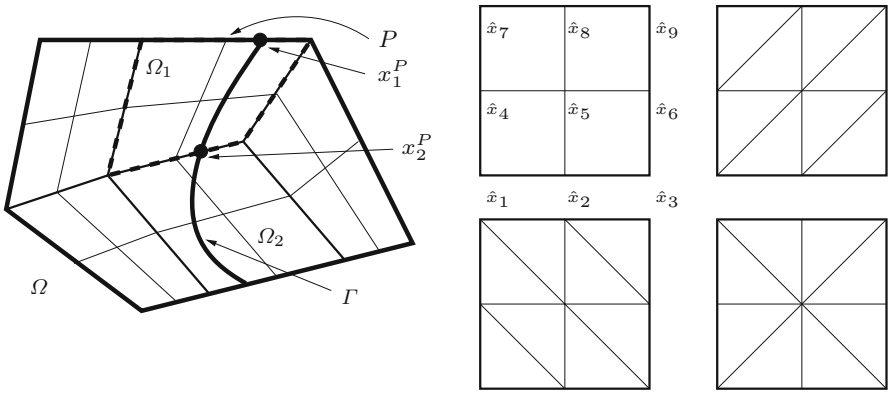

Fig. 4.15 *Left*: triangulation Ω_h of a domain Ω that split into Ω_1 and Ω_2 with interface $\mathcal{I}$. The elements in Ω_h are arranged in a patched way. Patch P is cut by $\mathcal{I}$ at x_1^P and x_2^P. *Right*: subdivision of reference patches $\hat{P}_1, \hat{P}_2, \hat{P}_3, \hat{P}_4$ (*top left to bottom right*) into eight triangles each

In principle, these assumptions only rule out two possibilities: a patch may not be cut multiple times and the interface may not enter and leave the patch at the same edge. Both situations can be avoided by refinement of the underlying mesh. If the interface is matched by an edge, the patch is not considered cut.

4.5.1.1 Modification of the Finite Element Space

We define the finite element trial space $V_h \subset H_0^1(\Omega)$ as isoparametric space on the triangulation Ω_h

$$V_h = \left\{ \phi \in C(\bar{\Omega}),\ \phi \circ T_P^{-1}\Big|_P \in \hat{Q} \text{ for all patches } P \in \Omega_h \right\},$$

where $T_P \in [\hat{Q}]^2$ is the mapping between the reference patch $\hat{P} = (0,1)^2$ and every patch $P \in \Omega_h$ such that

$$T_P(\hat{x}_i) = x_i^P, \quad i = 1, \ldots, 9$$

for the nine nodes $x_1^P, \ldots, x_9^P$ in every patch, see Fig. 4.15 (left). The reference space $\hat{Q}$ is piecewise polynomial of degree 1 that will depend on whether a patch P is cut by the interface or not. For patches $P \in \Omega_h$ that are not cut by the interface, we choose the standard space of piecewise bilinear functions:

$$\hat{Q} = \left\{ \phi \in C(\bar{P}),\ \phi\Big|_{K_i} \in \text{span}\{1, x, y, xy\},\ K_1, \ldots, K_4 \in P \right\}.$$

If a patch $P \in \Omega_h$ is cut by the interface, we divide the reference patch into eight triangles $T_1, \ldots, T_8$ and define

$$\hat{Q}_{\text{mod}} = \left\{ \phi \in C(\bar{P}),\ \phi\Big|_{T_i} \in \text{span}\{1, x, y\},\ T_1, \ldots, T_8 \in P \right\}.$$

Depending on the position of the interface $\mathcal{I}$ in the patch P, three different reference configurations are considered, see the right sketch in Fig. 4.15.

It is important to note that the functions in $\hat{Q}$ and $\hat{Q}_{\text{mod}}$ are all piecewise linear on the edges ∂P, such that mixing different element types does not affect the continuity of the global finite element space. We denote by $\{\hat{\phi}^1, \ldots, \hat{\phi}^9\}$ the standard Lagrange basis of $\hat{Q}$ or $\hat{Q}_{\text{mod}}$ with $\hat{\phi}^i(x_j) = \delta_{ij}$. The transformation T_P is given by

$$T_P(x) = \sum_{i=1}^{9} x_i^P \hat{\phi}_i(x).$$

Next, we present the subdivision of interface patches P into eight triangles each. We distinguish four different types of interface cuts, see Fig. 4.16:

Configuration A: The patch is cut at the interior of two opposite edges.
Configuration B: The patch is cut at the interior of two adjacent edges.
Configuration C: The patch is cut at the interior of one edge and in one node.
Configuration D: The patch is cut in two opposite nodes.

Configurations A and B are based on the reference patches $\hat{P}_2$ and $\hat{P}_3$, configurations C and D use the reference patch $\hat{P}_4$, see Fig. 4.15. By $e_i \in \mathbb{R}^2$, $i = 1, 2, 3, 4$ we denote the vertices on the edges, by $x_m \in \mathbb{R}^2$ the midpoint of the patch. The parameters $r, s \in (0, 1)$ describe the relative position of the intersection points with the interface on the outer edges.

If an edge is intersected by the interface we move the corresponding point e_i on this edge to the point of intersection. The position of the midpoint x_m depends on the specific configuration, see [153] for details.

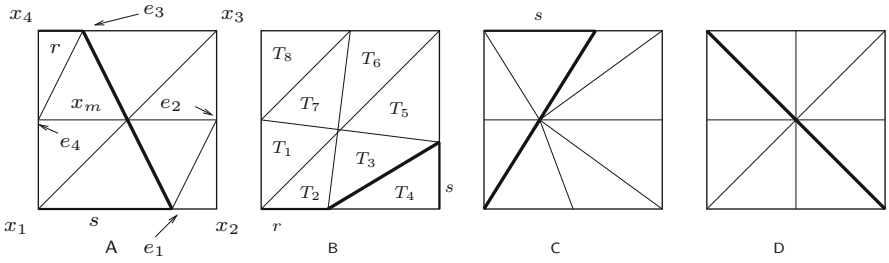

Fig. 4.16 Different types of cut patches. The subdivision can be anisotropic with $r, s \in (0, 1)$ arbitrary

As the cut of the elements can be arbitrary with $r, s \to 0$ or $r, s \to 1$, the triangle's aspect ratio can be very large, considering $h \to 0$ it is not necessarily bound. We can however guarantee that the maximum angles in all triangles will be well bound away from 180°.

Lemma 4.54 (Maximum Angle Condition) *All interior angles of the triangles shown in Fig. 4.16 are bound by* 144° *independent of* $r, s \in (0, 1)$.

Proof The proof follows by basic geometrical considerations, see [153]. □

This maximum angle conditions allows us to define robust Lagrangian interpolation operators $I_h : H^2(T) \cap C(\overline{T}) \to V_h$ with accurate error estimates

$$\|\nabla^k (u - I_h u)\|_T \leq c_i h_{T,\max}^{2-k} \|\nabla^2 u\|_T, \quad k = 0, 1, \tag{4.39}$$

where $c_i > 0$ is a constant and $h_{T,\max}$ is the maximum diameter of a triangle $T \in P$, see [7]. The interpolation error estimates are robust with respect to the maximum diameter $h_{T,\max} \approx h_P$ that is of the same order as the diameter of the patches P. We do not get (and will not depend on) an optimal interpolation result with respect to the anisotropic triangles in terms of short edges $h_{T,\min} \ll h_{T,\max}$. This simplifies the analysis compared to typical estimates for anisotropic finite elements. Again, see [7].

In order to apply such an interpolation result at the interface, i.e. on triangles $T \in \Omega_h$ that belong to patches cut by the interface, we must take care of the fact that the partitioning of the mesh $\Omega_h = \Omega_{1,h} \cup \mathcal{I}_h \cup \Omega_{2,h}$ does not conform with the partitioning of the domain $\Omega = \Omega_1 \cup \mathcal{I} \cup \Omega_2$, i.e., $\Omega_{i,h}$ does not necessarily cover the same domain as Ω_i. This is always the case, if the interface $\mathcal{I}$ is not a polygon. Then, if $T \in \Omega_{h,i}$ is an element on the interface, i.e. $\mathcal{I} \cap T \neq \emptyset$, the solution v is not smooth enough to locally apply the interpolation estimate (4.39).

The inverse trace inequality (see [350]) allows to extend $u_i \in H^2(\Omega_i)$ to $\tilde{u}_i \in H^2(\Omega)$ with

$$\|\tilde{u}_i - u_i\|_{H^2(\Omega_i)} = 0, \quad \|\tilde{u}_i\|_{H^2(\Omega)} \leq c \|u_i\|_{H^2(\Omega_i)}, \quad i = 1, 2, \tag{4.40}$$

if the interface $\mathcal{I}$ is regular enough (having a $C^{1,1}$ boundary). This construction allows to use the interpolation estimates on triangles that are cut by the interface.

Let $T \in \Omega_h$ be such an triangle and let $S \subset T$ be the small part, cut by the interface. We show the Situation in Fig. 4.17. It holds $|S| = O(h^2)$, see Lemma 4.32. Let $u \in H^1(\Omega) \cap H^2(\Omega_1 \cup \Omega_2)$ and $I_h u \in V_h$ be the interpolation. Further, let $\tilde{u} \in H^2(T)$ be the extension of $u\big|_{T \setminus S}$ to T. It holds

$$\begin{aligned} \|\nabla^k (u - I_h u)\|_T &\leq \|\nabla^k (u - \tilde{u})\|_T + \|\nabla^k (\tilde{u} - I_h u)\|_T \\ &= \|\nabla^k (u - \tilde{u})\|_S + \|\nabla^k (\tilde{u} - I_h u)\|_T. \end{aligned}$$

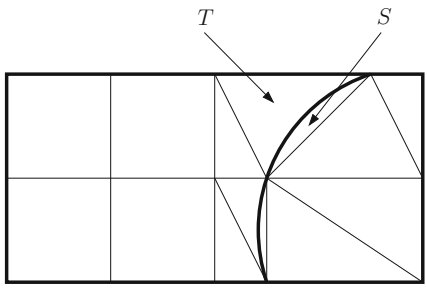

Fig. 4.17 The right patch is cut by the interface $\mathcal{I}$ and split into eight triangles. For a triangle T we denote by S the small part that enters the other domain

For the second part it holds $I_h u = I_h \tilde{u}$ such that usual interpolation estimate can be applied

$$\|\nabla(\tilde{u} - I_h u)\|_T = \|\nabla(\tilde{u} - I_h \tilde{u})\|_T \leq ch\|\nabla^2 \tilde{u}\|_T \leq ch\|\nabla^2 u\|_{T\setminus S},$$

while the first part can be estimated with Lemma 4.34:

$$\|\nabla(u - \tilde{u})\|_S \leq ch\|u\|_{H^2(T)}.$$

Altogether, the interpolation error at the interface is estimated by

$$\|\nabla(u - I_h u)\|_T \leq ch\|u\|_{H^2(T)}. \tag{4.41}$$

The parametric finite element approach is conforming, as $u_h \in V_h \subset H_0^1(\Omega)$, it is however not consistent, as the discrete solution u_h has its jump at $\mathcal{I}_h$ and not at $\mathcal{I}$.

Theorem 4.55 (A Priori Estimate) *Let $\Omega \subset \mathbb{R}^2$ be a domain with convex polygonal boundary, split into $\Omega = \Omega_1 \cup \mathcal{I} \cup \Omega_2$, where $\mathcal{I}$ is a smooth interface with C^2-parameterization. We assume that $\mathcal{I}$ divides Ω in such a way that the solution $u \in H_0^1(\Omega)$ satisfies the stability estimate*

$$u \in H_0^1(\Omega) \cap H^2(\Omega_1 \cup \Omega_2), \quad \|u\|_{H^2(\Omega_1 \cup \Omega_2)} \leq c_s \|f\|.$$

For the corresponding modified finite element solution $u_h \in V_h$ it holds

$$\|\nabla(u - u_h)\|_\Omega \leq ch\|f\|, \quad \|u - u_h\|_\Omega \leq ch^2\|f\|$$

Proof We repeat the proof from [153], as the original paper suffers from a small inaccuracy, evoked by neglecting that $\Omega_{i,h}$ is not necessarily a triangulation of Ω_i for $i = 1, 2$. This directly touches the first step *(i)* of the proof.

(i) Let $e_h = u - u_h$. It holds

$$\begin{aligned}(\kappa\nabla e_h,\nabla\phi_h)_\Omega &= \sum_{i=1}^{2}(\kappa_i\nabla e_h,\nabla\phi_h)_{\Omega_i}\\ &= \sum_{i=1}^{2}(\kappa_i\nabla u,\nabla\phi_h)_{\Omega_i} - (\kappa_i\nabla u_h,\nabla\phi_h)_{\Omega_{i,h}} + (\delta\kappa_i\nabla u_h,\nabla\phi_h)_{\Omega_i\setminus\Omega_{i,h}}\\ &= \sum_{i=1}^{2}(\delta\kappa_i\nabla u_h,\nabla\phi_h)_{\Omega_i\setminus\Omega_{i,h}},\end{aligned}$$

where

$$\delta\kappa_i = \begin{cases}\kappa_1-\kappa_2 & i=1,\\ \kappa_2-\kappa_1 & i=2.\end{cases}$$

Hence, by picking $\phi_h = I_h u - u_h$, we get the following perturbed best-approximation property:

$$\|\nabla e_h\|^2 \le c\|\nabla e_h\|\,\|\nabla(u-I_hu)\| + \sum_{i=1}^{2}\|\delta\kappa_i\nabla u_h\|_{\Omega_i\setminus\Omega_{i,h}}\|\nabla(I_hu-u_h)\|_{\Omega_i\setminus\Omega_{i,h}}$$

For estimating these additional terms close to the interface, we use Lemma 4.34. It holds

$$\begin{aligned}\|\delta\kappa_i\nabla u_h\|_{\Omega_i\setminus\Omega_{i,h}} &\le c(\kappa)h^{\frac{1}{2}}\|\nabla u_h\|_\Omega,\\ \|\nabla(I_hu-u_h)\|_{\Omega_i\setminus\Omega_{i,h}} &\le ch^{\frac{1}{2}}\|\nabla(I_hu-u_h)\|_\Omega.\end{aligned}$$

Together with the interpolation estimate (4.41), the energy estimate follows.

(ii) Let $z\in H_0^1(\Omega)\cap H^2(\Omega_1\cup\Omega_2)$ be the solution of the adjoint problem

$$z\in H_0^1(\Omega):\ (\kappa\nabla\phi,\nabla z)_\Omega = (e_h,\phi)\|e_h\|^{-1}\quad\forall\phi\in H_0^1(\Omega).$$

It holds $z\in H_0^1(\Omega)\cap H^2(\Omega_1\cup\Omega_2)$ with $\|z\|_{H^2(\Omega_1\cup\Omega_2)}\le c_s$. Using the perturbed Galerkin orthogonality, the L^2-error can be represented in the following way:

$$\|u-u_h\| = (\nabla e_h,\nabla(z-I_hz)) + \sum_{i=1}^{2}(\delta\kappa_i\nabla u_h,\nabla I_hz)_{\Omega_i\setminus\Omega_{i,h}}.$$

Here, the argumentation for estimating the interface elements is more involved. Similar to the discussion in Sect. 4.2.3, we need to insert the solutions $\pm u$ and

$\pm z$ to fully exploit the potential of Lemma 4.34. It holds

$$\begin{aligned}\|\nabla u_h\|_{\Omega_i \setminus \Omega_{i,h}} &\leq \|\nabla u\|_{\Omega_i \setminus \Omega_{i,h}} + \|\nabla(u - I_h u)\|_{\Omega_i \setminus \Omega_{i,h}} + \|\nabla(I_h u - u_h)\|_{\Omega_i \setminus \Omega_{i,h}} \\ &\leq ch\|u\|_{H^2(\Omega)} + ch^{\frac{1}{2}}\|\nabla(I_h u - u_h)\|_{\Omega}.\end{aligned}$$

By once more inserting $\pm u$, it follows that

$$\|\nabla u_h\|_{\Omega_i \setminus \Omega_{i,h}} \leq ch\|f\|_{\Omega}.$$

Similarly, it holds for the adjoint interpolation by inserting $\pm z$

$$\|\nabla I_h z\|_{\Omega_i \setminus \Omega_{i,h}} \leq \|\nabla z\|_{\Omega_i \setminus \Omega_{i,h}} + \|\nabla(z - I_h z)\|_{\Omega_i \setminus \Omega_{i,h}} \leq ch\|z\|_{H^2(\Omega)},$$

which gives second order. □

4.5.2 Condition Number Analysis

The modified finite element ansatz described above has one serious drawback. For certain anisotropies (e.g. $s, r \to 0$ in Fig. 4.16) the condition number of the stiffness matrix is not bounded. To illustrate this, we consider an interface problem where Ω_1 is a circle inside the unit square Ω (see the right sketch in Fig. 4.18). To study the sensitivity with respect to anisotropies, we move the circle in vertical direction by $\varepsilon \in [0, 1]$. We will give further details on this example in Sect. 4.5.3. In Fig. 4.18 (left sketch), we show how the condition number changes for different ε. For $\varepsilon \to 0$, the condition number increases with order $\mathcal{O}(1/\varepsilon)$.

In this section, we will present a scaled hierarchical finite element basis for the space V_h that will yield system matrices A_h that satisfy the usual bound $\text{cond}_2(A_h) = \mathcal{O}(h^{-2})$ with a constant that does not depend on the position of the interface $\mathcal{I}$ relative to the mesh elements.

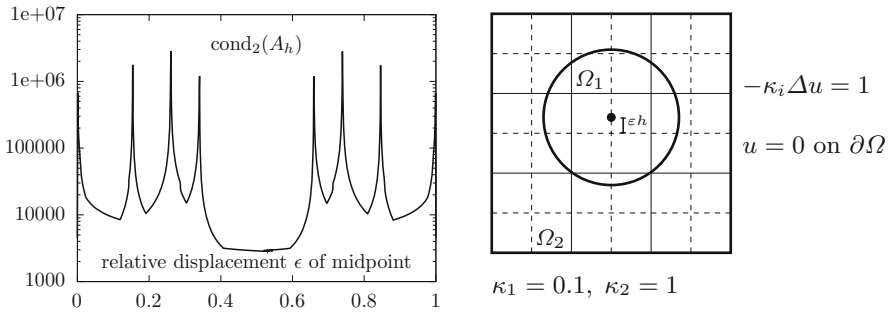

Fig. 4.18 Condition number of the system matrix $\text{cond}_2(A_h)$ depending on the displacement of the circle Ω_1

We split the finite element space V_h in a hierarchical manner

$$V_h = V_{2h} + V_b, \quad N := \dim(V_h) = \dim(V_{2h}) + \dim(V_b) =: N_{2h} + N_b.$$

The space V_{2h} is the standard space of piecewise bilinear functions in uncut patches and linear functions on cut patches (here we split the quadrilateral patch into two triangles). On the patches $P \in \Omega_h$ it is equipped with the usual nodal Lagrange basis $V_{2h} = \text{span}\{\phi_{2h}^1, \ldots, \phi_{2h}^{N_{2h}}\}$.

The space $V_b = V_h \setminus V_{2h}$ collects all functions that enrich V_{2h} to V_h. These functions are defined piecewise on $T_1, \ldots, T_8$ in the remaining five degrees of freedom, see Fig. 4.19 for an example. The basis is denoted by $V_b = \text{span}\{\phi_b^1, \ldots, \phi_b^{N_b}\}$. The finite element space V_{2h} is fully isotropic and standard analysis holds. Functions in V_{2h} do not resolve the interface, while the basis functions $\phi_b^i \in V_b$ will depend on the interface location if $\mathcal{I} \subset \text{supp}\,\{\phi_b^i\}$. For a function $v_h \in V_h$ we use the (unique) splitting

$$v_h = \sum_i \mathbf{v}_h^i \phi_h^i = \sum_{i=1}^{N_{2h}} \mathbf{v}_{2h}^i \phi_{2h}^i + \sum_{i=1}^{N_b} \mathbf{v}_b^i \phi_b^i = v_{2h} + v_b \in V_{2h} + V_b,$$

and for this splitting it holds:

Lemma 4.56 (Hierarchical Finite Element Spaces) *For every $v_h = v_{2h} + v_b \in V_h$ it holds*

$$(i) \quad \|\nabla v_h\|^2 \leq 2\|\nabla v_{2h}\|^2 + 2\|\nabla v_b\|^2,$$

and further

$$(ii) \quad \|\nabla v_{2h}\|^2 + \|\nabla v_b\|^2 \leq C\|\nabla v_h\|^2,$$

with a constant $C > 0$.

Proof See [153]. □

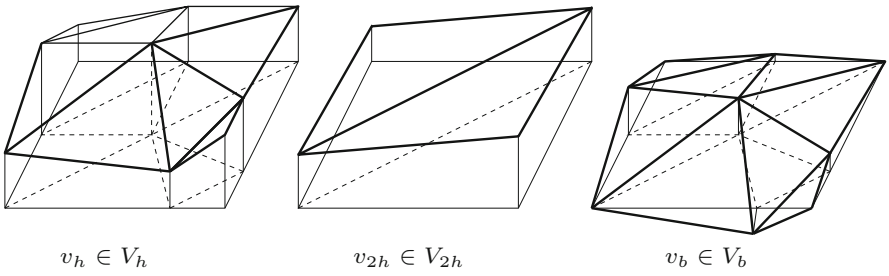

Fig. 4.19 Example for a hierarchical splitting of a function $v_h \in V_h$ into coarse mesh part $v_{2h} \in V_{2h}$ and fine mesh fluctuation $v_b \in V_b$

Using this hierarchic splitting of the finite element space together with a diagonal scaling of the system matrix, we can proof the following result:

Theorem 4.57 (Condition Number) *For the hierarchic parameterized finite element space $V_h = V_{2h} + V_b$ together with a diagonal scaling of the system matrix* $\mathbf{A}$*, it holds*

$$\text{cond}_2(\mathbf{A}) \leq Ch^{-2},$$

with a constant $C > 0$ not depending on the interface location.

Proof See [153]. □

4.5.3 Numerical Examples

In this section, design three different test cases to validate the modified finite element technique introduced in Sect. 4.5.1. We will include all different types of interface cuts (configurations A to D) with arbitrary anisotropies including $r, s \to 0$ or 1 in Fig. 4.16.

4.5.3.1 Example 1: Circular Interface

This first example has already been considered to discuss the interface approximation in Sect. 4.5.1 and the dependency of the condition number on the interface in Sect. 4.5.2. See Fig. 4.14 for a sketch of the configuration. The square $\Omega = (-1, 1)^2$ is split into a ball $\Omega_2 = B_R(x_m)$ and remainder $\Omega_1 = \Omega \setminus \bar{\Omega}_2$, where $R = 0.5$ and $x_m = (0, \varepsilon h)$ for $\varepsilon \in [0, 1]$. As diffusion parameters we choose $\kappa_1 = 0.1$ in Ω_1 and $\kappa_2 = 1$ in Ω_2. We choose the analytical solution

$$u(x) = \begin{cases} -\kappa_1 \|x - x_m\|^2 + \frac{1}{4}\kappa_1 - \frac{1}{8}\kappa_2 & x \in \Omega_1, \\ -2\kappa_2 \|x - x_m\|^4, & x \in \Omega_2, \end{cases}$$

to define both the right hand side $f_i := -\kappa_i \Delta u$ and the Dirichlet boundary data. After some steps of global refinement this simple example includes configurations A to C. In Fig. 4.20, we plot the H^1- and L^2-norm errors obtained on several levels of global mesh refinement. According to Theorem 4.55, we observe linear convergence in the H^1-norm and quadratic convergence in the L^2-norm. For comparison, Fig. 4.14 shows the corresponding results using standard non-fitted basis functions. A sketch of the solution is given in the right side of Fig. 4.20.

Next, in Fig. 4.21, we show a study of the condition number's dependency on the parameter $\varepsilon \in [0, 1]$ used to shift the midpoint of the circle $x_m = (0, \varepsilon h)$. The scaled hierarchical ansatz space shows optimal behavior $\mathcal{O}(h^{-2})$ with regard to mesh size

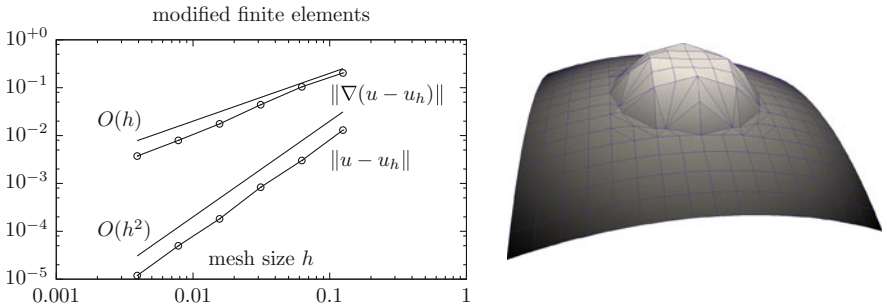

Fig. 4.20 Example 1: H^1- and L^2-Error under mesh refinement. *Right*: sketch of the solution

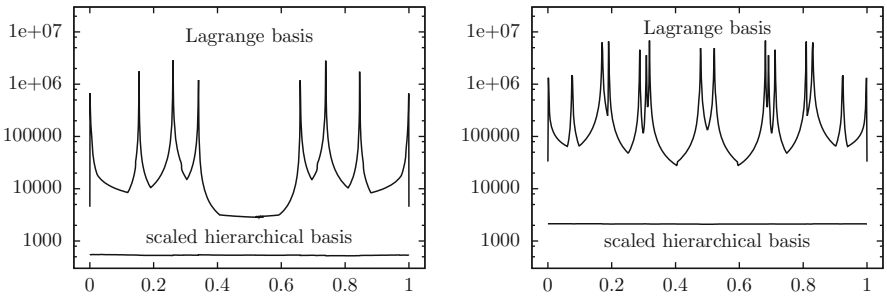

Fig. 4.21 Example 1: condition number of the system matrix depending on the displacement of the circle Ω_1 by εh for $\varepsilon \in [0,1]$. Standard Lagrange basis versus the scaled hierarchical basis introduced in Sect. 4.5.2. Left $h = 1/16$, right $h = 1/32$

h and no dependency on the shift ε, while the standard approach shows very large conditions numbers with $\mathrm{cond}_2(A_h) \to \infty$ for $\varepsilon \to 0$ and $\varepsilon \to 1$.

4.5.3.2 Example 2: Horizontal Cuts

To study the different cuts of interface patches in more detail, let us next consider a the $\Omega = (-1,1)^2$, cut horizontally into

$$\Omega_1(\varepsilon) = \{x \in \Omega \,|\, x_2 < \varepsilon h\}, \quad \Omega_2(\varepsilon) = \{x \in \Omega \,|\, x_2 > \varepsilon h\}.$$

By varying $\varepsilon \in [0,1]$ the interface patches of a Cartesian mesh will be split into rectangular with vertical edge lengths εh and $(1-\varepsilon)h$, $0 < \varepsilon < 1$. We choose right hand side $f = -\kappa_i \Delta u$ and Dirichlet data according to the solution

$$u(x) = \begin{cases} \frac{\kappa_2}{\kappa_1}(x_2-\varepsilon) - (x_2-\varepsilon)^2 & x \in \Omega_1 \\ (x_2-\varepsilon) + (x_2-\varepsilon)^2 & x \in \Omega_2. \end{cases} \tag{4.42}$$

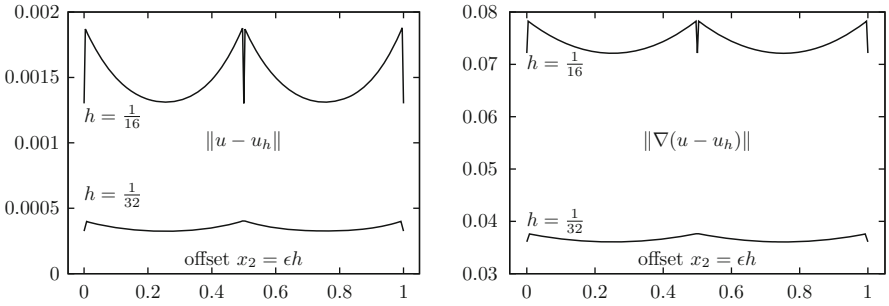

Fig. 4.22 Example 2: L^2- and H^1-norm error depending on a vertical offset $x_2 = \varepsilon h$ of the interface

In Fig. 4.22, we plot L^2-norm and H^1-norm error for $0 \leq \varepsilon \leq 1$ on meshes with patch size $h = 1/16$ and $h = 1/32$. Both errors clearly depend on the position ε of the cut. As one would expect, we get the smallest errors for $\varepsilon = 0$, $\varepsilon = \frac{1}{2}$ and $\varepsilon = 1$, where the mesh is perfectly uniform and resolves the cut. The largest error given for $\varepsilon \to 0$ and $\varepsilon \to 1$, where the anisotropy of the interface patches is maximal. Nevertheless, we see that the error remains bounded for all $\varepsilon \in [0, 1]$. The variations get smaller on the finer mesh.

These variations come from the approximation property of finite element spaces on elements with different size. If a patch is cut into equally spaces elements, the overall error is minimal. If some of the elements are larger, they will dominate the overall error. The variation is however limited but the size of the patch and the variations will get smaller with smaller mesh sizes. See [153] for an analysis that explains this variations.

4.5.3.3 Example 3: Tilted Interface Line

Next, we consider two subdomains that are separated by a straight interface line through the origin, which might be horizontal ($\alpha = 0$), vertical ($\alpha = \pi/2$) or inclined ($0 < \alpha < \pi/2$ or $\pi/2 < \alpha < \pi$). The interface $\mathcal{I}$ is defined by the relation $\cos(\alpha)x_2 = \sin(\alpha)x_1$ given the partitioning

$$\Omega_1^\alpha = \left\{x \in \Omega \;\middle|\; \cos(\alpha)x_2 < \sin(\alpha)x_1\right\},$$
$$\Omega_2^\alpha = \left\{x \in \Omega \;\middle|\; \cos(\alpha)x_2 > \sin(\alpha)x_1\right\}.$$

We choose the right hand side $f = -\kappa_i \Delta u$ and the Dirichlet data according to the given exact solution

$$u(x) = \begin{cases} \sin\left(\frac{\kappa_2}{\kappa_1}(\cos(\alpha)x_2 - \sin(\alpha)x_1)\right), & x \in \Omega_1 \\ \sin\left(\cos(\alpha)x_2 - \sin(\alpha)x_1\right) & x \in \Omega_2. \end{cases}$$

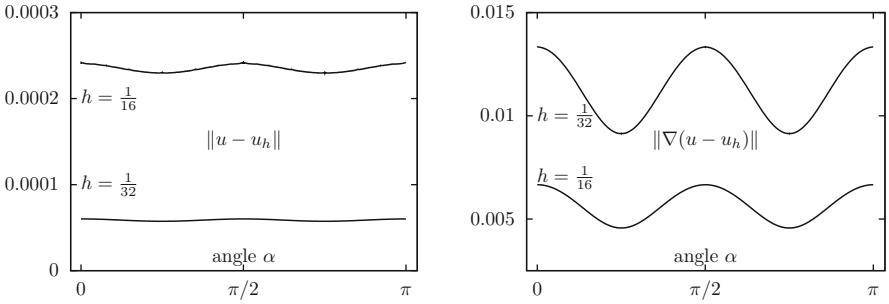

Fig. 4.23 Example 3: L^2- and H^1-norm error for a line cutting at different angles $\alpha \in [0, \pi]$

In Fig. 4.23 we plot the L^2- and H^1-norm error for angles $\alpha \in [0, \pi]$ and for two different refinement levels ($h = 1/16$ and $h = 1/32$). In the case $\alpha = \pi/2$ all the interface patches are of type D, while in the other cases types A to C appear with all kinds of anisotropies inside. Again, we observe linear convergence for the H^1-norm error and quadratic convergence in the L^2-norm. The error varies up to a factor of approximately $\sqrt{2}$ in the case of the H^1-norm and about 1.05 in the L^2-norm which can be explained similarly to the case of horizontal cuts. We emphasize that these variations are again bounded for all $\alpha \in [0, \pi]$.

4.6 Discretization of Moving Interfaces

The specific problem of fluid-structure interactions—as well as of multiphase flows—is the motion of the interface and the motion of the complete domain. Two general approaches exist for the handing of moving domains: first, the motion can be tracked by means of a mapping as the ALE formulation. Then, instead of moving domains, one has to deal with additional equations and possibly new nonlinearities. The second approach is to capture the motion and formulate all equations on moving domains. This is the approach for the Fully Eulerian model presented in Sect. 3.6 and Chaps. 6 and 12.

Moving domains add severe difficulties to the temporal discretization. The origin is similar to the spatial case. If the solution $u(x, t)$ is—across the interface—not differentiable in time, we cannot expect proper accuracy for the difference approximation

$$\partial_t u(x, t) \approx \frac{u(x, t + k) - u(x, t)}{k} \tag{4.43}$$

whenever the tuples (x, t) and $(x, t+k)$ belong to different parts of the domain. Here, we briefly comment on strategies for an accurate handling of moving interfaces. For details, we refer to [151, 154, 284].

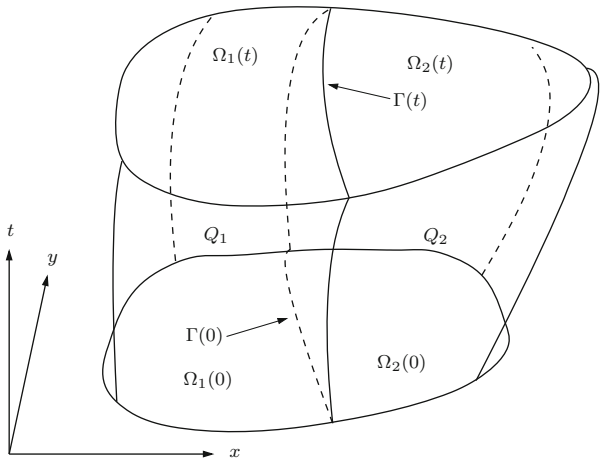

Fig. 4.24 Space-time domain with a moving interface $\mathcal{I}(t)$. Partitioning of $Q \subset \mathbb{R} \times \mathbb{R}^2$ into two space-time domains $Q_1 \cup G \cup Q_2$. At each point in time $t \in I$ it holds $\Omega(t) = \Omega_1(t) \cup \mathcal{I}(t) \cup \Omega_2(t)$. The space-time interface is given by $G := \{(t, \mathcal{I}(t)),\ t \in I\}$

We give a sketch of the situation in Fig. 4.24. Here a space-time domain $Q \subset \mathbb{R} \times \mathbb{R}^d$ ($d = 2$ in this case) is split into two space-time domains Q_1, Q_2 with interface G

$$Q = Q_1 \cup G \cup Q_2, \quad \Omega(t) = \Omega_1(t) \cup \mathcal{I}(t) \cup \Omega_2(t).$$

On such a domain partitioning we consider the parabolic problem

$$\begin{aligned} \partial_t u_i - \operatorname{div}(\kappa_i \nabla u_i) &= f_i && \text{in } Q_i,\ i = 1, 2, \\ u_1 = u_2, \quad \mathbf{n} \cdot \kappa_1 \nabla u_1 &= \mathbf{n} \cdot \kappa_2 \nabla u_2 && \text{on } \mathcal{I}(t), \\ u(\cdot, 0) &= u^0 && \text{on } \Omega(0), \\ u(\cdot, t) &= 0 && \text{on } \partial\Omega(t), \end{aligned} \tag{4.44}$$

where by $\kappa_1, \kappa_2 \in \mathbb{R}_+$ we denote two diffusion coefficients given in the two domains Q_1, Q_2. For this problem we know that a unique solution exists, if the domain has a smooth boundary and interface, if the initial solution satisfies the compatibility conditions

$$-\kappa_i \Delta u^0 - f \in H_0^1(\Omega_i(0)),\ i = 1, 2, \quad \kappa_1 \mathbf{n} \cdot \nabla u_1^0 = \kappa_2 \mathbf{n} \cdot \nabla u_2^0,$$

and if the problem data f, u^0 is sufficiently smooth, see [129]. Under these assumptions, it holds

$$\sum_{k=0}^{2} \|u\|_{k,2(2-k)} \leq c \left(\sum_{k=0}^{1} \|f\|_{k,2(1-k)} + \|u^0\|_{H^4(\Omega_1(0)\cup\Omega_2(0))} \right). \tag{4.45}$$

For the norms, we have used the short notation

$$\|u\|_{k,l} := \left(\|u\|^2_{H^k(I,H^l(\Omega_1(t)))} + \|u\|^2_{H^k(I,H^l(\Omega_2(t)))} \right)^{1/2},$$

of the Bochner spaces

$$\mathcal{H}^{k,l} := H^k(I, H^l(\Omega_1(t))) \cap H^k(I, H^l(\Omega_2(t)))$$

The aim of this section is to suggest a temporal discretization scheme that allows for second order accuracy.

Regarding the temporal discretization we must deal with two significant problems. First, as already stated above in (4.43), finite differences will fail across the interface. Another, even more fundamental problem appears, if the domain itself, i.e. the outer boundary $\partial\Omega(t)$ is moving in time. Then, considering (4.43) once more, it is possible that $x \in \Omega(t)$ but $x \notin \Omega(t+k)$ such that a difference approximation cannot even be well-defined. Considering variational formulations, which usually include terms like

$$(u_k^m - u_k^{m-1}, \phi)_\Omega,$$

reveals yet another problem. If $\Omega^m \neq \Omega^{m-1}$, as domains a moving, the functions $u_k^m \in V_k^m$ and $u_k^{m-1} \in V_k^{m-1}$ come from different function spaces, such that $u_k^m - u_k^{m-1}$ is not necessarily defined. Furthermore, what is the correct test space for ϕ and what is the domain of integration Ω? Is it Ω_{m-1} or Ω_m?

Recent advances have been made in literature for this problem. Fries and Zilian [159] presented a time stepping scheme based on the backward Euler method and a number of numerical tests that indicate first-order convergence order. A complete error analysis for this approach has been presented by Zunino [363]. For a corresponding Crank-Nicolson-like approach, Fries and Zilian found a reduced convergence order of 1.5. To the best of our knowledge, there is, however, no rigorous convergence analysis available yet. A second-order scheme based on a space-time dG(1) approach has been presented by Lehrenfeld and Reusken [223] including error analysis in space and time. Their approach can not be generalized to a continuous Galerkin scheme, however, as the spatial number of unknowns varies from time step to time step in their scheme. Numerical integration is defined in $1+d$ dimensions.

Another approach to construct accurate time stepping schemes is to apply a transformation to a fixed reference domain $\hat{Q} := I \times \{\hat{\Omega}_1 \cup \hat{\mathcal{I}} \cup \hat{\Omega}_2\}$. Let $\hat{T} : \hat{Q} \to Q$ be such a mapping. If $\hat{T}$ is a C^2-diffeomorphism, Problem (4.44) is equivalent to

$$\det(\hat{\nabla}\hat{T})\left(\partial_t \hat{u} - \partial_t \hat{T} \cdot \nabla \hat{u}\right) - \widehat{\operatorname{div}}\left(\det(\hat{\nabla}\hat{T})\hat{\kappa}\hat{\nabla}\hat{T}^{-1}\hat{\nabla}\hat{u}\hat{\nabla}\hat{T}^{-T}\right) = \det(\hat{\nabla}\hat{T})\hat{f} \text{ in } \hat{Q}. \tag{4.46}$$

This is the ALE-transform of the parabolic model problem (see e.g.[26]). Here, the domain $\hat{\Omega}$ allows a fixed partitioning $\hat{\Omega} = \hat{\Omega}_1 \cup \hat{\mathcal{I}} \cup \hat{\Omega}_2$ that does not change in time. Standard spatial and temporal discretization is possible. However, the ALE approach only works, if a mapping $\hat{T} : \hat{Q} \to Q$ with sufficient regularity can be constructed.

The approach presented here was first published in [151, 284], where a modified space-time Galerkin approach based on a cG(1) discretization is used. An application to the Fully Eulerian method will be presented in Chap. 12. Basically, the space-time domain Q is split into slices Q_j

$$I = \{0\} \cup I_1 \cup \cdots \cup I_M, \quad I_j = (t_{j-1}, t_j], \quad Q_j := \{(t, \Omega(t)),\ t \in I_j\},$$

and on every Q_j we choose linear trial and constant test functions. The trial functions however are designed in a mixed space-time way to be aligned with the interface, see Fig. 4.25.

In a second step, we define slices of reference domains $\hat{Q}^j := \hat{\Omega}^j \times I_j$ and a mapping

$$T_m : \hat{Q}^m \to Q^m,$$

see Fig. 4.26. With these notations, we can specify an equivalent (given sufficient regularity) formulation of the parabolic interface-problem (4.44). First, by multiplication with a test function and integration over the space-time domain, every solution u to (4.44) is solution to the variational formulation

$$u \in X := W(0,T) \quad B(u,\phi) = (f,\phi)_Q + (u^0, \phi(0))_{\Omega(0)} \quad \forall \phi, \tag{4.47}$$

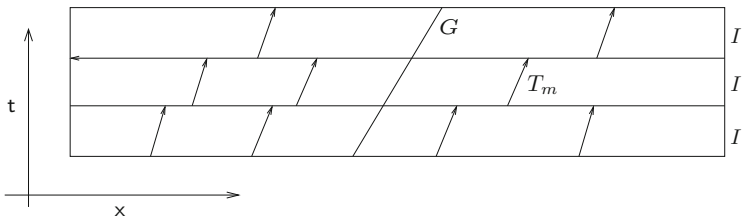

Fig. 4.25 Illustration of the modified Galerkin trial spaces X_k^0, X_k^1. The functions $v_k \in X_k^0, X_k^1$ are polynomial on trajectories that stay within each subdomain Q_i, $i = 1, 2$

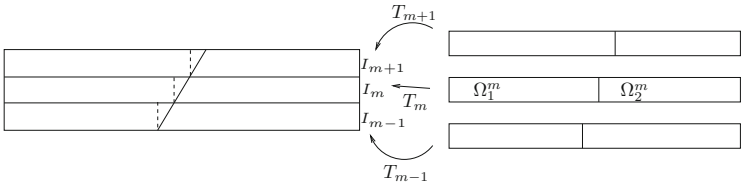

Fig. 4.26 Piecewise definition of maps T_m. The reference domain (*right sketch*) corresponds to the *new* domain Ω^m and changes in each time step

where

$$W(0,T) := \{v : Q \to \mathbb{R} : \ v \in L^2(I, H_0^1(\Omega(t))), \ \partial_t v \in L^2(I, H^{-1}(\Omega(t)))\},$$

and

$$\begin{aligned} B(u,\phi) &= (u(0),\phi(0))_{\Omega(t)} + \sum_{m=1}^{M} B^m(u,\phi), \\ B^m(u,\phi) &= (\partial_t u, \phi)_{Q^m} + (\kappa \nabla u, \nabla \phi)_{Q^m}. \end{aligned} \tag{4.48}$$

If we allow for piece-wise discontinuous (in time at t_m) test functions ϕ, formulation (4.47) decouples into a Galerkin time stepping scheme

$$B^m(u,\phi) = (f,\phi)_{Q^m} + (u(t_{m-1})^-, \phi(t_{m-1})^+)_{\Omega(t_{m-1})},$$

where by $\phi^{+/-}(t_{m-1})$ we denote the limit of ϕ at t_{m-1} from the left "-" or right "+". Formulation (4.48) is still given on slices Q^m with moving boundaries that are not necessarily adjacent to the temporal direction t, see Fig. 4.25, such that a modified basis is required. We can define such a basis by using the mapping $T_m : \hat{Q}^m \to Q^m$, as on $\hat{Q}^m$ a standard basis can be used

$$\begin{aligned} u_k \in X_k^1 = \Big\{ v \in C(\bar{I}, H_0^1(\Omega)) \ \Big| \ & (v \circ T_m)_{|I_m} \in P_1(I_m, H_0^1(\Omega)), \\ & \text{and } v(0) \in H_0^1(\Omega) \Big\} \\ \phi_k \in X_k^0 = \Big\{ v \in L^2(I, H_0^1(\Omega)) \ \Big| \ & (v \circ T_m)_{|I_m} \in P_0(I_m, H_0^1(\Omega)), \\ & \text{and } v(0) \in H_0^1(\Omega) \Big\}. \end{aligned} \tag{4.49}$$

These spaces are such that the domain partitioning at the new time step t_m serves as reference configuration, e.g. T_m is the identity $\Omega(t_m) \mapsto \Omega(t_m)$ at t_m an it maps $\Omega(t_{m-1}) \mapsto \Omega(t_m)$ at the left end of the sub interval I_m. Using this mapping, we can

derive a third equivalent formulation to (4.48) as

$$B^m(u,\phi) = \left(J_m \partial_t \hat{u} - \partial_t T_m (JF)_m^{-T} \hat{\nabla}_m \hat{u}, \hat{\phi}\right)_{\hat{Q}^m} + \left(\hat{\kappa} (JF)_m^{-T} \hat{\nabla}_m \hat{u}, F_m^{-T} \hat{\nabla}_m \hat{\phi}\right)_{\hat{Q}^m}. \tag{4.50}$$

Here, by $F_m = \hat{\nabla}_m T_m$ we denote the gradient of the mapping in I_m, where the notation $\hat{\nabla}_m$ denotes the gradient with respect to the coordinates $\hat{x}_m$ on the reference domain $\hat{\Omega}^m$. By $J_m = \det(F_m)$ we denote its determinant. On the reference domain, we define $\hat{u}, \hat{\kappa}$ and $\hat{\phi}$ as

$$\hat{\kappa}(\hat{x},t) = \kappa(x,t),\ \hat{u}(\hat{x},t) = u(x,t),\ \hat{\phi}(\hat{x},t) = \phi(x,t) \text{ where } x = T_m(\hat{x},t).$$

Galerkin formulations (4.48) and (4.50) require costly numerical integration. To avoid this effort and allow for an efficient realization, we apply numerical quadrature to (4.50) (with the midpoint rule) and define a final, approximated formulation for the discrete problem

$$\begin{aligned} B_k^m(u,\phi) &= \left(\overline{J} \partial_t \hat{u}, \hat{\phi}\right)_{\hat{Q}^m} - \left(\overline{\partial_t T}\, \overline{JF}^{-T} \hat{\nabla} \hat{u}, \hat{\phi}\right)_{\hat{Q}^m} \\ &\quad + \left(\hat{\kappa} \overline{JF}^{-T} \hat{\nabla} \hat{u}, \overline{F}^{-T} \hat{\nabla} \hat{\phi}\right)_{\hat{Q}^m}, \\ B_k(u,\phi) &= \sum_{m=1}^{M} B_k^m(u,\phi) + (u(0),\phi(0))_{\Omega(0)}. \end{aligned} \tag{4.51}$$

We use the notation

$$\overline{J}_m = \frac{1}{2}\left(J_m(t_m) + J_m(t_{m-1})\right),$$

and analogously for $\overline{JF}_m^{-T}$, $\overline{F}_m^{-T}$ and $\overline{\partial_t T}_m$. For discrete functions $u_k \in X_k^1$ and $\phi_k \in X_k^0$, this formulation corresponds to

$$\begin{aligned} B_k^m(u_k,\phi_k) &= \frac{1}{k}\left(\overline{J}\left(\hat{u}_k^m - \hat{u}_k^{m-1}\right), \hat{\phi}_k^m\right)_{\hat{Q}^m} \\ &\quad - \frac{1}{2}\left(\overline{\partial_t T}\, \overline{JF}^{-T} \hat{\nabla}\left(\hat{u}_k^m + \hat{u}_k^{m-1}\right), \hat{\phi}_k^m\right)_{\hat{Q}^m} \\ &\quad + \frac{1}{2}\left(\hat{\kappa} \overline{JF}^{-T} \hat{\nabla}\left(\hat{u}_k^m + \hat{u}_k^{m-1}\right), \overline{F}^{-T} \hat{\nabla} \hat{\phi}_k^m\right)_{\hat{Q}^m}. \end{aligned} \tag{4.52}$$

Remark 4.58 (Realization) This approximated formulation can be realized as a time stepping scheme $\hat{u}_k^{m-1} \to \hat{u}_k^m$. In the context of fluid-structure interactions,

the mapping T_m is not a priori given, but it depends on the deformation itself. The mapping is designed in such a way that it must be only applied at the old time step and to evaluate the approximations $\overline{J}_m$, $\overline{JF}_m^{-T}$. In a numerical scheme, this can be done in a semi-implicit way using extrapolations or within a Newton iteration.

An important component of the numerical algorithm is the choice of a projection of the solution at the previous time step u_k^{m-1} from the old to the new reference domain. Here, high accuracy is necessary to get optimal order of convergence. Numerical quadrature should be done exactly on an intersection of old an new mesh. Detail for a realization with the locally modified parametric finite element approach presented in Sect. 4.5.1 are given in [151, 284].

Given sufficient regularity of the right hand side, the initial data, the domain's boundary and the interface and further, given a piece-wise defined mapping T_m with sufficient regularity, we can show the following result:

Theorem 4.59 (Modified Galerkin-Time Stepping for Parabolic Interface Problems) *Let u be solution to (4.44) with regularity (4.45). Further, let the domain and the domain-motion be smooth (see [284] for details). Further, let u_k be the discrete solution to (4.52). Then, it holds*

$$\begin{aligned}\|u-u_k\|_Q + \|u(T)-u_k(T)\|_{L^2(\Omega(T))} \\ \leq ck^2 \exp(cT)\left(\|u^0\|_{H^4(\Omega_1(0)\cup\Omega_2(0))} + \|f\|_{0,2} + \|f\|_{1,0}\right). \end{aligned} \tag{4.53}$$

For a proof, we refer to [151, 284].

We conclude with a numerical example. Let $\Omega = (-1.2, 1.2)^2$ be a square domain and $\Omega_1(0)$ an ellipsoid within,

$$\Omega_1(0) = \{(x,y) \in \Omega,\ 4x^2 + 16y^2 < 1\}, \quad \Omega_2(0) = \Omega \setminus \overline{\Omega_2(t)},$$

see Fig. 4.27. We prescribe a rotational velocity field

$$\mathbf{v}(x,y) = \frac{1}{2}\begin{pmatrix} y \\ -x \end{pmatrix},$$

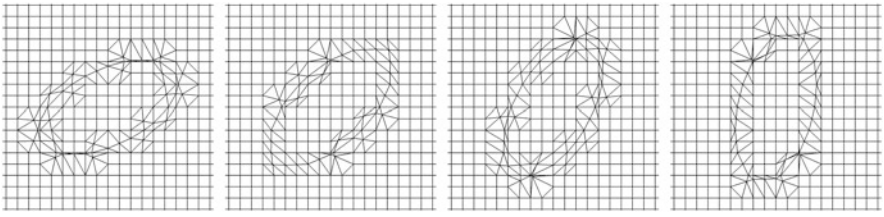

Fig. 4.27 Rotating ellipsoid at different points in time, $t = 1.5\,\mathrm{s}, 3\,\mathrm{s}, 4.5\,\mathrm{s}, 6\,\mathrm{s}$. Subset of the spatial discretization ($h = 0.075$) with the locally modified parametric finite element scheme. We do not show the mesh, but the setup of the degrees of freedom

to transport (rotate) the inner domain $\Omega_1(t)$. For transporting the domain, we choose the *Initial Point Set* as introduced in Sect. 3.6.3, i.e. we define a function Ψ as

$$\Psi(\cdot, 0) = \mathrm{id}, \quad \partial_t \Psi + \mathbf{v} \cdot \nabla \Psi = 0, \quad t > 0.$$

Then, it holds

$$\Omega_1(t) = \{(x, y) \in \Omega,\ \Psi(x, y, t) \in \Omega_1(0)\}, \quad \Omega_2(t) = \Omega \setminus \overline{\Omega_1(t)}.$$

Using the *Initial Point Set* it is straightforward to define the map T_m used in the temporal discretization, e.g. to map $\Omega_1(t_m)$ to $\Omega_1(t)$

$$T_m(t) = \Psi(t)^{-1} \circ \Phi(t_m).$$

To determine the coordinate of a point $x^{m-1} = T_m(x^m) \in \Omega(t_{m-1})$ we invert

$$\Psi(t_{m-1})(x^{m-1}) = \Psi(t_m)(x^m),$$

with help of a Newton iteration. As the outer boundary is not rotating, we extend the deformation T_m from $\Omega_1(t)$ to Ω by a linear interpolation between the interface and the outer boundary

$$T_m(t)\Big|_{\Omega_2(t)} = g(x) T_m(t) + (1 - g(x))\,\mathrm{id},$$

where $g(\cdot)$ is linear with $g = 1$ on $\mathcal{I}(t_m)$ and $g = 0$ on $\partial\Omega$.

On this domain layout we solve the parabolic interface problem (4.44) with the diffusion coefficients

$$\kappa_1 = 1, \quad \kappa_2 = 0.1,$$

and the right hand side and initial data

$$f(t) = \sqrt{1 + \cos(5t)}, \quad u^0 = 0.$$

Spatial discretization is accomplished with the locally modified finite element scheme as introduced in Sect. 4.5.1. In Fig. 4.27 we show snapshots of the modified discretization at different points in time.

In Table 4.3 we show numerical results of the newly introduced discretization scheme, combining the locally modified spatial finite element scheme with the modified Galerkin time stepping scheme. We use $k = h$ to get full second order convergence. For comparison, we also show the results for a simpler modified dG(0) scheme in time, using piece-wise constant test and trial functions. The results in the table show the expected order of convergence, linear in the case of dG(0) and

Table 4.3 L^2-norm of the solution at final time $T = 15\,\mathrm{s}$ and L^2-norm of the complete space-time domain for the rotating ellipsoid

	$\|u_k(T)\|_\Omega$		$\|u_k\|_Q$	
$k = h$	dG(0)	cG(1)	dG(0)	cG(1)
$0.15 \cdot 2^{-0}$	0.619	0.5858	2.121	2.1286
$0.15 \cdot 2^{-1}$	0.605	0.5890	2.134	2.1423
$0.15 \cdot 2^{-2}$	0.598	0.5899	2.140	2.1456
$0.15 \cdot 2^{-3}$	0.594	0.5900	2.143	2.1463
Extrap.	0.589	0.5901	2.146	2.1466
Conv.	0.87	2.01	1.11	2.08

We further show the extrapolated reference value and the numerically observed convergence order. Spatial discretization with the locally modified parametric finite element scheme and temporal discretization with the modified Galerkin time stepping scheme

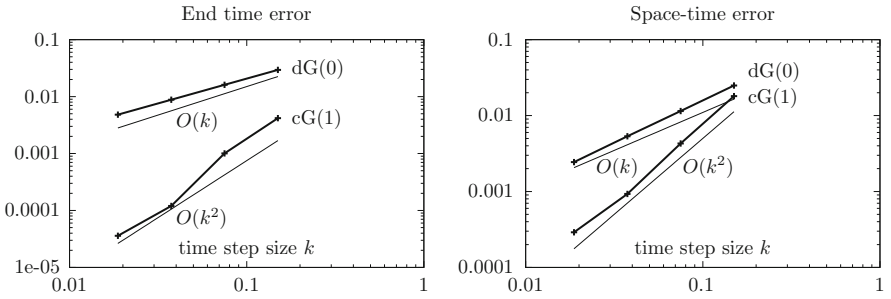

Fig. 4.28 Error at final time $T = 15\,\mathrm{s}$ and space-time error for the rotating ellipsoid test in the case of modified dG(0) and cG(1) Galerkin time stepping. Spatial discretization with the locally modified parametric finite element approach

quadratic for the interface-aligned cG(1) scheme. In Fig. 4.28 we show a graphical representation of the convergence history.

Further details and an application of this advanced time discretization method to fluid-structure interaction problems is given in Chap. 12.

Part II
Numerical Realization

The second part of this book is devoted to the practical realization of fluid-structure interaction problems. We will combine the theoretical consideration on different models and equations with the discretization techniques. In the beginning we present to alternative monolithic models for coupled fluid-structure interaction problems. In Chap. 5 we study the *Arbitrary Lagrangian Eulerian* formulation. This model must be considered as the state of the art technique for strongly coupled fluid-structure interaction problems. We give details on the construction of the ALE map and the realization of efficient numerical simulation tools. Second, the *Fully Eulerian* formulation is introduced in Chap. 6. This newer alternative approach is well-suited for problems with very large deformation or motion of the solid. It is also able to handle contact problems. Again, we present the necessary discretization and simulation tools. Chapter 7 deals with tools for the solution of the algebraic problems arising from the discretization of the ALE and Fully Eulerian formulation. In both cases, we have to deal with very large, nonlinear and stiff problems. Finally, Chap. 8 introduces the concept of adaptivity for dimension reduction of the discrete spaces. Based on *a posteriori error estimators* we study adaptive finite element schemes that will allow us to significantly reduce the complexity of the discretized systems.

Chapter 5
ALE Formulation for Fluid-structure Interactions

The following paragraphs will be devoted to the Arbitrary Lagrangian Eulerian (ALE) method for modeling fluid-structure interactions. Based on the equations derived in Sect. 3.5, we describe methods for discretization in time and space. The basic techniques have already been introduced in Chap. 4, such that we can focus on the special characteristics of the Arbitrary Lagrangian Eulerian formulation for fluid-structure interaction problems.

In this chapter, we will focus on a strict interpretation of the ALE formulation for the Navier-Stokes system

$$\left.\begin{aligned} J\rho_f\Big(\partial_t \mathbf{v} + \mathbf{F}^{-1}(\mathbf{v} - \partial_t \mathbf{u})\cdot\nabla\mathbf{v}\Big) - \operatorname{div}\Big(J\boldsymbol{\sigma}_f \mathbf{F}^{-T}\Big) &= J\rho_f \mathbf{f}, \\ \operatorname{div}\Big(J\mathbf{F}^{-1}\mathbf{v}\Big) &= 0, \end{aligned}\right\} \quad \text{in } \hat{\mathcal{F}},$$

where the set of equations is completely mapped onto the reference coordinate system in $\hat{\mathcal{F}}$, see [126, 199, 201, 285]. In literature an alternative formulation is often discussed [48, 120, 140, 147, 181, 221]. The problem is there mapped back into the Eulerian coordinate system and reads

$$\left.\begin{aligned} \rho_f\Big(\partial_t \mathbf{v} + (\mathbf{v} - \partial_t \mathbf{u})\cdot\nabla\mathbf{v}\Big) - \operatorname{div}\ \boldsymbol{\sigma}_f &= \rho_f \mathbf{f}, \\ \operatorname{div}\ \mathbf{v} &= 0. \end{aligned}\right\} \quad \text{in } \mathcal{F}(t).$$

The domain mapping only enters via the additional transport term. The benefit of this presentation is the simplicity of formulation. After every time step, the mesh must be updated. Considering time stepping schemes, where the solution and the domain motion enters at two distinct points in time at once, the derivation of accurate higher order schemes is less obvious using this second formulation. From a theoretical point of view, both formulations are equivalent. Whether one uses a fixed mesh and the reference formulation or a moving mesh and the Eulerian formulation,

T. Richter, *Fluid-structure Interactions*, Lecture Notes in Computational Science and Engineering 118, DOI 10.1007/978-3-319-63970-3_5

both problems give the same result. Considering strictly monolithically coupled schemes, the first ALE formulation is more natural, as it allows for a variational coupling of the two different sub-systems, see Sect. 3.5.

5.1 Time-Discretization for the FSI Problem in ALE-Formulation

Time discretization of fluid-structure interactions is mainly governed by two specific complexities. First, the overall stiffness of the coupled problem is by far greater than that of the two single subproblems. This is mainly due to the coupling of a parabolic type fluid equations with the solid equations of hyperbolic type. Second the ALE time derivative of the domain acts as transport direction for the fluid field. This gives rise to nonlinear couplings of temporal and spatial derivatives, which is very uncommon for most partial differential equations.

We start by repeating the coupled system of equations describing fluid-structure interactions in Arbitrary Lagrangian coordinates. Compare to Problem 3.11:

$$\begin{aligned}
\left(J(\partial_t \mathbf{v} + (\mathbf{F}^{-1}(\mathbf{v} - \partial_t \mathbf{u}) \cdot \nabla)\mathbf{v}, \phi\right)_{\mathcal{F}} + \left(J\boldsymbol{\sigma}_f \mathbf{F}^{-T}, \nabla\phi\right)_{\mathcal{F}} &= (J\rho_f \mathbf{f}, \phi)_{\mathcal{F}} \\
\left(J\mathbf{F}^{-1} : \nabla \mathbf{v}^T, \xi\right)_{\mathcal{F}} &= 0 \\
(\rho_s^0 \partial_t \mathbf{v}, \phi)_{\mathcal{S}} + (\mathbf{F}\boldsymbol{\Sigma}_s, \nabla\phi)_{\mathcal{S}} &= (\rho_s^0 \mathbf{f}, \phi)_{\mathcal{S}} \\
(\partial_t \mathbf{u} - \mathbf{v}, \psi_s)_{\mathcal{S}} &= 0 \\
(\nabla \mathbf{u}, \nabla \psi_s)_{\mathcal{F}} &= 0,
\end{aligned} \tag{5.1}$$

where we have reformulated the divergence condition in the fluid equations by means of Lemma 2.61 to ease implementation and to avoid the presence of second derivatives. For construction of the ALE map, we consider a simple harmonic extension, see Sect. 5.3.5 for variants. For simplicity of notation, we have skipped all hats that usually indicate use of Lagrangian or ALE coordinates. Apart from the strong nonlinearities, this equation has some special feature with respect to the temporal derivatives. These are not isolated but appear in coupling to spatial derivatives

$$\left(J\left(\partial_t \mathbf{v} - (\mathbf{F}^{-1}\partial_t \mathbf{u} \cdot \nabla)\mathbf{v}\right), \phi\right)_{\mathcal{F}} + \ldots \tag{5.2}$$

A detailed analysis of fluid flows on moving domains has been performed by Formaggia and Nobile [143, 144]. These studies already tackle several important aspects such as stability and order of convergence. In fluid-structure interaction, the fluid-domain movement is caused by the solid deformation. Hence, the analysis of fully coupled fluid-structure interaction is similar but must also include a discussion on the solid discretization.

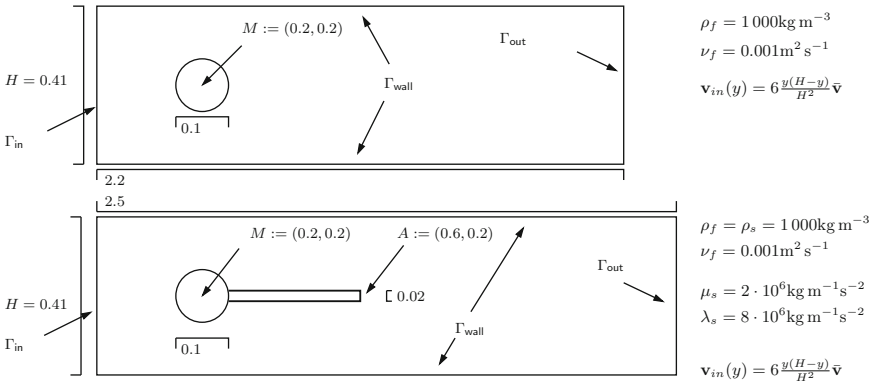

Fig. 5.1 Configuration of the two benchmark problems. The *upper figure* shows the cfd benchmark by Schäfer and Turek, the *lower figure* shows the layout of the fsi benchmark by Hron and Turek

5.1.1 Non-stationary Dynamics of Fluid-structure Interactions

We start the discussion on time-discretizations of fluid-structure interaction with a survey on results for two benchmark problems in fluid-dynamics and for fluid-structure interactions: In 1995, Schäfer and Turek [299] presented a benchmark configuration for incompressible laminar flows. In 2006, Hron and Turek [200] published results for a two dimensional fluid-structure interaction benchmark that has been constructed on top of the cfd benchmark problem. Both problems use the geometric configuration shown in Fig. 5.1. The main difference is an elastic beam that is attached to the rigid obstacle. Further, the domain of the fsi problem has been lengthened to avoid spurious feedback of the outflow boundary to the dynamics of the oscillation.

Both problems are driven by a prescribed inflow profile $\mathbf{v}^D$ on Γ_{in}. The full set of parameters for both problems is given by

$$\rho_f^{\text{cfd}} = 1\,\text{kg} \cdot \text{m}^{-3}, \quad \rho_f^{\text{fsi}} = 10^3\,\text{kg} \cdot \text{m}^{-3}$$

$$\nu_f^{\text{cfd/fsi}} = 10^{-3}\,\text{m}^2 \cdot \text{s}^{-1}, \quad \mathbf{v}^D(0, y) = 1.5\omega(t)\frac{y(H-y)}{(H/2)^2}\bar{\mathbf{v}},$$

where $\omega(t) = (1 - \cos(\pi t/2))$ for $t < 2\,\text{s}$ and $\omega(t) = 1$ for $t \geq 2\,\text{s}$ is used for regularizing the initial data. As average speed, we consider $\bar{\mathbf{v}} = 2\,\text{m} \cdot \text{s}^{-1}$. In the original cfd benchmark problem, $\bar{\mathbf{v}}^{\text{cfd}} = 1\,\text{m} \cdot \text{s}^{-1}$ was considered. With the radius of the obstacle $D = 0.1$, the Reynolds number is given by

$$Re = \frac{\bar{\mathbf{v}}D}{\nu} = 200.$$

The description of the problem is closed by providing the material parameters of the elastic solid

$$\rho_s^{\text{fsi}} = 10^3\,\text{kg}\cdot\text{m}^{-3}, \quad \mu_s = 2\cdot 10^6\,\text{kg}\cdot\text{m}^{-1}\text{s}^{-2}, \quad \lambda_s = 8\cdot 10^6\,\text{kg}\cdot\text{m}^{-1}\text{s}^{-2}.$$

As quantity of interest, we consider principal boundary stresses in x- and y-direction on the obstacle with boundary Γ_{obs}

$$\begin{aligned} J_{\text{drag}}(\mathbf{v},p) &= \frac{2}{\bar{\mathbf{v}}^2\rho_f L}\int_{\Gamma_{\text{obs}}} \boldsymbol{\sigma}_f \mathbf{n}\mathbf{e}_x \,\mathrm{d}o, \\ J_{\text{lift}}(\mathbf{v},p) &= \frac{2}{\bar{\mathbf{v}}^2\rho_f L}\int_{\Gamma_{\text{obs}}} \boldsymbol{\sigma}_f \mathbf{n}\mathbf{e}_y \,\mathrm{d}o. \end{aligned} \tag{5.3}$$

By Γ_{obs} we denote the boundary of the circle with diameter in the case of the cfd-benchmark and the circle with attached beam in the case of the fsi-benchmark problem. Efficient ways for evaluating these functionals are shown in [62, 282] as well as in Sect. 8.3.2.

Figure 5.2 shows the drag-coefficient (5.3) as function over time $I = [0, 5]$ for the two benchmark problems. Both configurations show a similar behavior with a transient initial phase leading to a periodic oscillation with dominant frequencies $f_{\text{cfd}} = 13\,\text{Hz}$ for the cfd benchmark and $f_{\text{fsi}} \approx 11\,\text{Hz}$ for the fsi problem. The first obvious difference is the longer transient phase for the fsi benchmark problem. An insight look into the subinterval $I' = [2.5, 3]$ reveals high frequent oscillations $f_{\text{high}} \approx 100\,\text{Hz}$ in the drag-coefficient with a small amplitude $a \approx 10^{-4}$ that is not visible on the large scale. These high frequent oscillations are no numerical artifacts but remain stable under temporal and spatial mesh refinement. They are only present in the coupled fsi system.

Reviewing the results published by many research groups in the two surveys on the cfd benchmark problem [299] and the fsi benchmark [199, 201] a first surprising

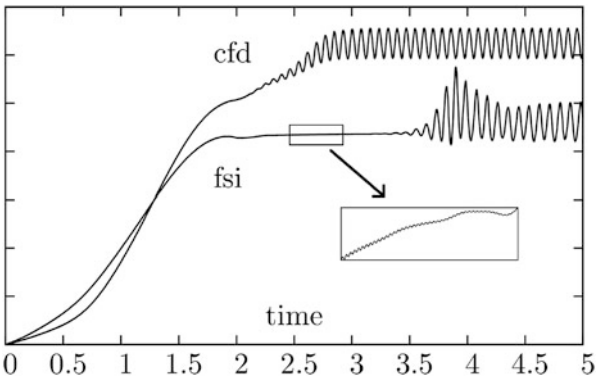

Fig. 5.2 Comparison of the two benchmark problems cfd and fsi. We plot the drag coefficient as function over time. For the fsi-problem we show a detailed view of the transient oscillations revealing high frequent modes

observation is the choice of discretization parameters that have been necessary to obtain approximations with appropriate accuracy: even though more than a decade lies between both benchmark problems, the dimension of the spatial discretization is very similar. In both cases, about 300,000 spatial degrees of freedom are sufficient to result in output values of about 1% accuracy. The increased difficulty of the fsi benchmark problem has been accounted for by a general use of higher order finite elements, where most contributors to the original cfd benchmark problem relied on lowest order finite elements. However, observing the temporal discretization, it is found that the fsi benchmark asks for significantly finer resolution in time. While less than 10 time steps per period of the oscillation were sufficient in the cfd case, accurate results to the fsi benchmark problem required up to 100 time steps per period of oscillation resulting in time steps as small as 10^{-3}. One explanation for this difference in temporal discretization can be found in the high frequent oscillations that are present with small amplitude, see Fig. 5.2.

Further insight is given by a discrete Fourier analysis of the output functional $J_{\text{drag}}(t)$ as function over time. We analyze few oscillation of the output functional with a very fine temporal resolution (down to $k \approx 10^{-5}$). Figure 5.3 reveals several dominant frequencies, at about 100 Hz (see also Fig. 5.2, 500 Hz and 800 Hz. These modes are stable under mesh refinement and further downscaling of the time step. The modes belonging to higher frequencies carry less energy. But even though the high frequent contributions take place on a much smaller scale as the dominant oscillation $f_{\text{fsi}} \approx 11\,\text{Hz}$, they must be carefully resolved to capture the overall dynamics of the coupled benchmark problem. The key question in this respect is the origin of these micro-oscillations. They are not present in pure fluid-dynamical simulations. A corresponding Fourier analysis of the fluid functions $J(\mathbf{v}, p)$ does not show any overtones. Further, they are no numerical artifact, but stable under discretization of both spatial and temporal discretization. Instead they stem from the coupling to the hyperbolic structure equations.

A further question to be investigated is the period of oscillations in coupled fluid-structure interaction systems. Figure 3.3 in Sect. 3.3 showed that the non-stationary dynamics of coupled fluid-structure systems can largely vary from pure fluid flows. Two geometrically similar problems at Reynolds number $Re = 140$ show a stationary behavior for a fixed and rigid body, whereas instationary oscillations appear for a flexible body. In laminar fluid-dynamics, the frequency of the Kármán vortex street depends on the Reynolds number of the flow, hence on the velocity. Structural systems have their own eigenmodes. Whether a coupled system is oscillating and which frequency and amplitude is obtained is not fully understood [250, 261]. We investigate this problem in Chap. 11.

5.1.2 Time Stepping Schemes for Fluid-structure Interactions

There is little theoretical background on monolithic time-discretizations of fluid-structure interactions. The main difficulty stems from the motion of the subdomains

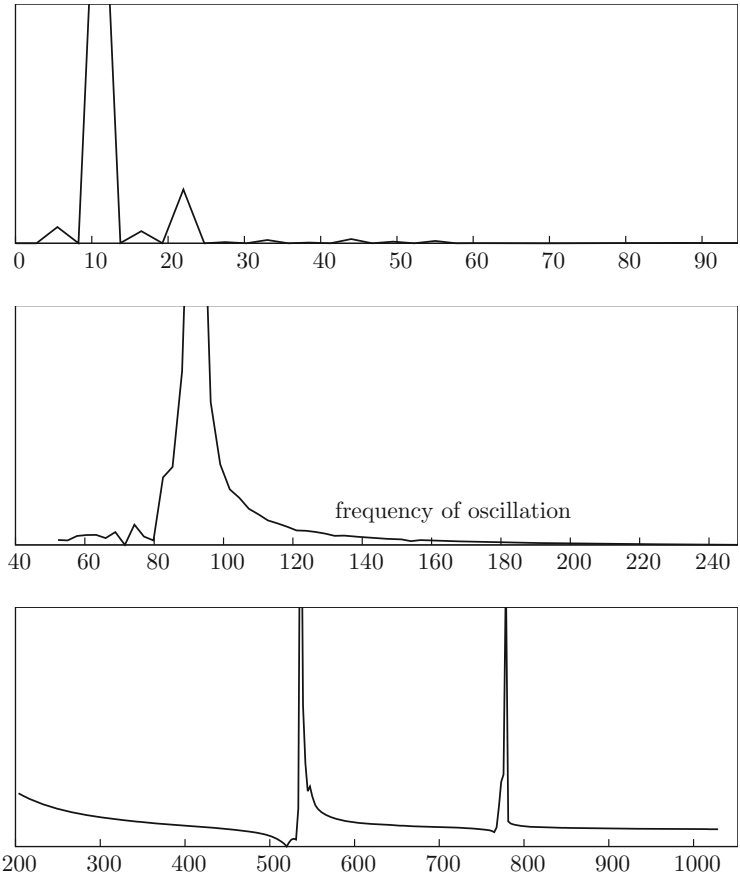

Fig. 5.3 Discrete Fourier analysis of the output functional (drag) shows the dominant frequency $f_{\text{fsi}} \approx 11\,\text{Hz}$ and further important sub-frequencies at about $f \approx 100\,\text{Hz}$ and $500\,\text{Hz}$ as well as $800\,\text{Hz}$. These modes are stable under temporal and spatial mesh refinement

that must either be modeled explicitly in partitioned approaches or that must be taken care of by implicit transformations of either the fluid-domain or the solid-domain. Concentrating first on pure fluid problems on moving domains, some crucial aspects with respect to stability and order of convergence are already identified by Formaggia and Nobile [143, 144]. In addition Fernández and Gerbeau [140] provide a stability analysis for fluid-structure interaction problems. Several studies with qualitative comparisons of different time stepping schemes and their long-time behavior have been reported in [342, 348]. In the primer study and additionally in [347] a detailed discussion on the practical realization and implementation of time stepping schemes for ALE fluid-structure interaction is given.

In the following, we put the attention on the strict variant of the ALE method that completely acts on the fixed reference domains $\mathcal{F}$ and $\mathcal{S}$, and where the complete set of equations is mapped.

Here, the domain motion is hidden in the ALE-map $T_f(x,t)$ and calls for the discretization of non-standard space-time coupled terms like, see (5.1) and (5.2):

$$(J(\mathbf{u})\nabla\mathbf{v}\mathbf{F}^{-1}(\mathbf{u})\partial_t\mathbf{u},\phi)_{\mathcal{F}}. \tag{5.4}$$

Most approaches for the temporal discretization of this term are ad hoc and based on the experience with other types of equations as Navier-Stokes of multiphase fluids, see [198].

5.1.2.1 Derivation of Second Order Time Stepping Schemes

The derivation of a second order stable time stepping scheme is not obvious. Specifically, regarding (5.4), two immediate reasonable choices for are given by the secant version

$$\left(\left[\frac{J(\mathbf{u}^{m-1})\nabla\mathbf{v}^{m-1}\mathbf{F}^{-1}(\mathbf{u}^{m-1})}{2}+\frac{J(\mathbf{u}^{m})\nabla\mathbf{v}^{m}\mathbf{F}^{-1}(\mathbf{u}^{m})}{2}\right]\frac{\mathbf{u}^m-\mathbf{u}^{m-1}}{k_m},\phi\right),$$

and the midpoint-tangent version

$$\left(\left[J(\bar{\mathbf{u}})\nabla\bar{\mathbf{v}}\mathbf{F}^{-1}(\bar{\mathbf{u}})\right]\frac{\mathbf{u}^m-\mathbf{u}^{m-1}}{k_m},\phi\right),$$

$$\bar{\mathbf{u}}:=\frac{\mathbf{u}^{m-1}+\mathbf{u}^m}{2},\quad \bar{\mathbf{v}}:=\frac{\mathbf{v}^{m-1}+\mathbf{v}^m}{2},$$

of the trapezoidal rule. This idea is explored in [343, 348].

A third version of a time stepping scheme can be derived by using a temporal $cG(1)/dG(0)$-Galerkin approach of (5.4) as described in Sect. 4.1.3. Using piecewise linear continuous trial spaces for all deformation $\mathbf{u}$ and velocity $\mathbf{v}$ in combination with piecewise constant globally discontinuous test spaces yields the time derivative term

$$\left(\left[\frac{1}{6}J(\mathbf{u}^{m-1})\nabla\mathbf{v}^{m-1}\mathbf{F}^{-1}(\mathbf{u}^{m-1})+\frac{2}{3}J(\bar{\mathbf{u}})\nabla\bar{\mathbf{v}}\mathbf{F}^{-1}(\bar{\mathbf{u}})\right.\right.$$
$$\left.\left.+\frac{1}{6}J(\mathbf{u}^{m})\nabla\mathbf{v}^{m}\mathbf{F}^{-1}(\mathbf{u}^{m})\right]\frac{\mathbf{u}^m-\mathbf{u}^{m-1}}{k_m},\phi\right),$$

where again by $\bar{\mathbf{u}}$ and $\bar{\mathbf{v}}$ we denote the average of old and new approximation. Such a Galerkin-derivation is also possible for more advanced time stepping schemes like the fractional step theta method, see [239, 240] and Sect. 4.1.2.

Simple truncation error analysis shows second order convergence for $k \to 0$ in all three cases. The leading error constants slightly differ:

$$C_1 \approx \frac{11}{8}, \quad C_2 \approx \frac{3}{8}, \quad C_3 \approx \frac{3}{4}.$$

In numerical experiments, it is found that all of these variants show very similar performance. Significant differences in temporal accuracy could not be found.

Finally, we point out that the Crank-Nicolson scheme applied to the elastic structure equation in mixed formulation is closely related to the Newmark scheme [23], which is one of the most prominent time-discretization techniques in solid mechanics.

5.1.2.2 Temporal Stability

Issues of numerical stability are of utter importance for fluid-structure interaction problems, as they consist of the coupled consideration of two different types of equations: the incompressible Navier-Stokes equations which is of parabolic type and that comes with smoothing properties and the hyper-elastic solid equation of hyperbolic type that calls for good conservation properties with very little numerical dissipation. By these considerations, the Crank-Nicolson scheme and its variants like shifted versions [230, 266] or the fractional step theta scheme [74, 328], appear to be ideal candidates. Further, both are second order accurate.

Motivated Heywood and Rannacher [187] and Formaggia and Nobile [144] it is reported in [140, 348] that the discretization of the domain-motion term (5.4) introduces further stability issues. To investigate this stability problem, we again consult the fsi benchmark problem introduced in the previous sections. Figure 5.4 shows the drag as functional over time for an unstable pair of spatial and temporal discretization parameters. Further, we also show the stable simulation using a damped version of the time stepping scheme.

In a first test, we aim at obtaining a stable solution up to $T = 10$. On a sequence of uniform meshes, we identify the largest time step k that is suited to generate a stable solution. The left part of Table 5.1 shows the results. Here, we see that on the coarsest mesh, the large step size $k = 0.02$ is sufficient, while on finer meshes $k < 0.004$ is required. We however cannot identify a direct relationship between mesh size and time step if we go to even finer spatial mesh resolutions.

In a second test case, we consider the (relatively large) step size $k = 0.005$ and $k = 0.00\bar{3}$ and determine the point in time $T_{\max}$, where the solution gets unstable. Again, we carry out this test case on different meshes. At first glance, the results in the right part of Table 5.1 for $k = 0.005$ suggest a stability relationship between time step and mesh size. The results concerning the second configuration with $k = 0.00\bar{3}$ however does not confirm this conjecture. Here, we can even reach a larger final point in time $T_{\max}$ on finer meshes. Further, the simulations on the finest mesh do

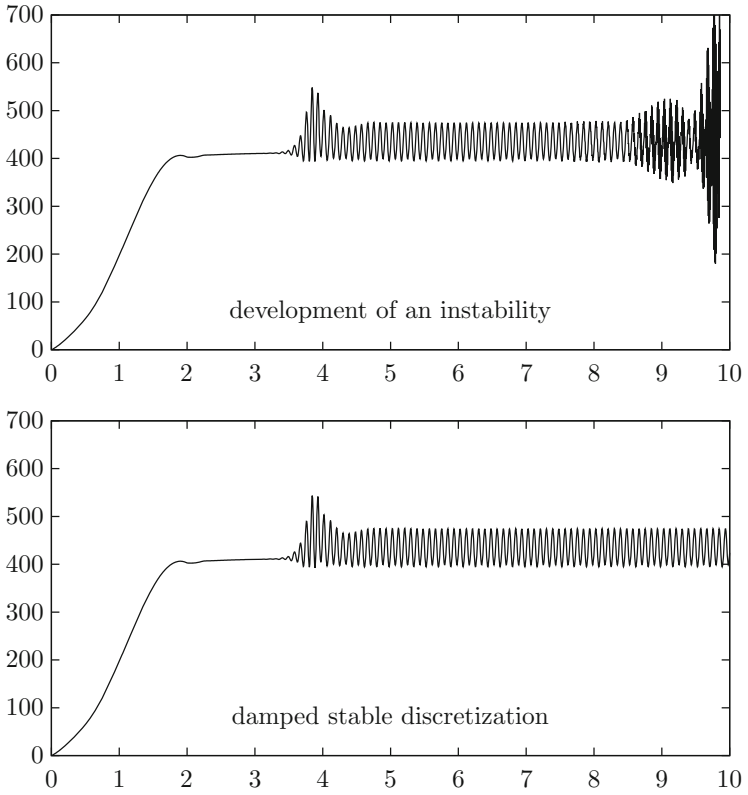

Fig. 5.4 Simulation for $k = 0.005$. *Top*: undamped Crank-Nicolson scheme develops an instability. *Bottom*: implicitly shifted scheme produces a stable solution on $I = [0, 10]$

Table 5.1 Long-term stability of the Crank-Nicolson scheme

	Time step size			
Mesh-Level	0.025	0.02	0.004	$0.00\bar{3}$
1	×	√	√	√
2	×	×	×	√
3	×	×	×	√

Mesh-Level	$k = 0.005$	$0.00\bar{3}$
1	$\gg 10$	$\gg 10$
2	8.48	10.82
3	6.04	12.54
4	3.84	3.84

Left: combination of time step k and mesh size h, such that the solution is stable in the interval $I = [0, 10]$. We cannot find a strict time step relation $k \leq h^{\alpha}$. Right: maximum interval $I = [0, T_{\max}]$, where a solution could be found for $k = 0.005$ and $k = 0.00\bar{3}$, depending on the mesh-size. Here, we also cannot identify an obvious relationship

not cease due to stability problems but due to early failure of the Newton scheme. Altogether, it is not possible to numerically certify a strict time step restriction. Instead we find a general stability problem for long-term simulations if we consider the Crank-Nicolson scheme.

5.1.2.3 Stable Time-Discretization and Damping

The analysis of the fsi benchmark problem shows that the restrictive time step condition is by stability and not by accuracy requirements. We will therefore discuss accurate time-discretization schemes with better stability properties. A possibility is to either resort to A-stable time-discretization schemes, or to apply modifications of the Crank-Nicolson schemes. Two possibilities are often discussed in literature: by a slight implicit shifting of the discretization we recover global stability, see [186, 187, 230] and also Sect. 4.1.2:

$$(u^m - u^{m-1}, \phi) + \left(\frac{1}{2} + O(k)\right) a(u^m, \phi) + \left(\frac{1}{2} - O(k)\right) a(u^{m-1}, \phi) = 0$$

This is sufficient for damping of accumulated errors by truncation, quadrature or inexact solution of the algebraic systems. If the shift depends on the time step size, the resulting scheme is still second order accurate in time. Similar results are recovered by applying some initial time steps with the A-stable backward Euler method, see [266]. If these few (usually two are sufficient) backward Euler steps are introduced after every fixed time-interval, e.g. at every $t = j$ for $j = 0, 1, \ldots$, we also recover sufficient stability for long term calculations. This scheme, also referred to as *Rannacher time-marching*, is second order accurate.

Higher stability that is also sufficient to cover non-smooth initial data is reached by applying strongly A-stable time-integration techniques. Here, the fractional-step theta method appears to be an optimal choice [74]. This time stepping scheme consists of three sub-steps that combined results in a second order, strongly A-stable scheme that further has very good dissipation properties. It is highly preferable to flow problems [328] and also frequently used in the analysis of fluid-structure interactions problems [198, 201, 287, 342].

In the following, we compare the three possibilities of a non-damped Crank-Nicolson scheme, with an implicitly shifted version using $\theta = \frac{1}{2} + k$ and the *Rannacher time-marching* algorithm with two steps of the backward Euler method at times $t = 0$, $t = 1$, $t = 2$ and so on. In Fig. 5.5 we compare these three damping strategies. We show the drag-coefficient (see Figs. 5.2 or 5.4 for a global view) in the sub-intervals $t \in [3.5, 4.2]$, $t \in [7.95, 8.15]$ and $t \in [9.3, 9.6]$. While all three versions are stable at initial time, *Rannacher time-marching* develops a first instability after two steps of backward Euler at time $t = 4$, see the upper sketch in Fig. 5.5. This instability will remain during the simulation, but it will not be further intensified, as can be seen in the middle and right sketch of the figure. The undamped version of the Crank-Nicolson scheme delivers stable solutions up to a moderate time of about $t = 5$ but develops a strong instability that will finally lead to a breakdown of the scheme, as can be seen in the middle and lower sketch. Finally, the implicitly shifted version of the Crank-Nicolson scheme gives stable and good results globally in time.

A systematic way for deriving a time stepping scheme is the detour using a Galerkin formulation. Here, we exemplarily derive the cG(1)-method that—for

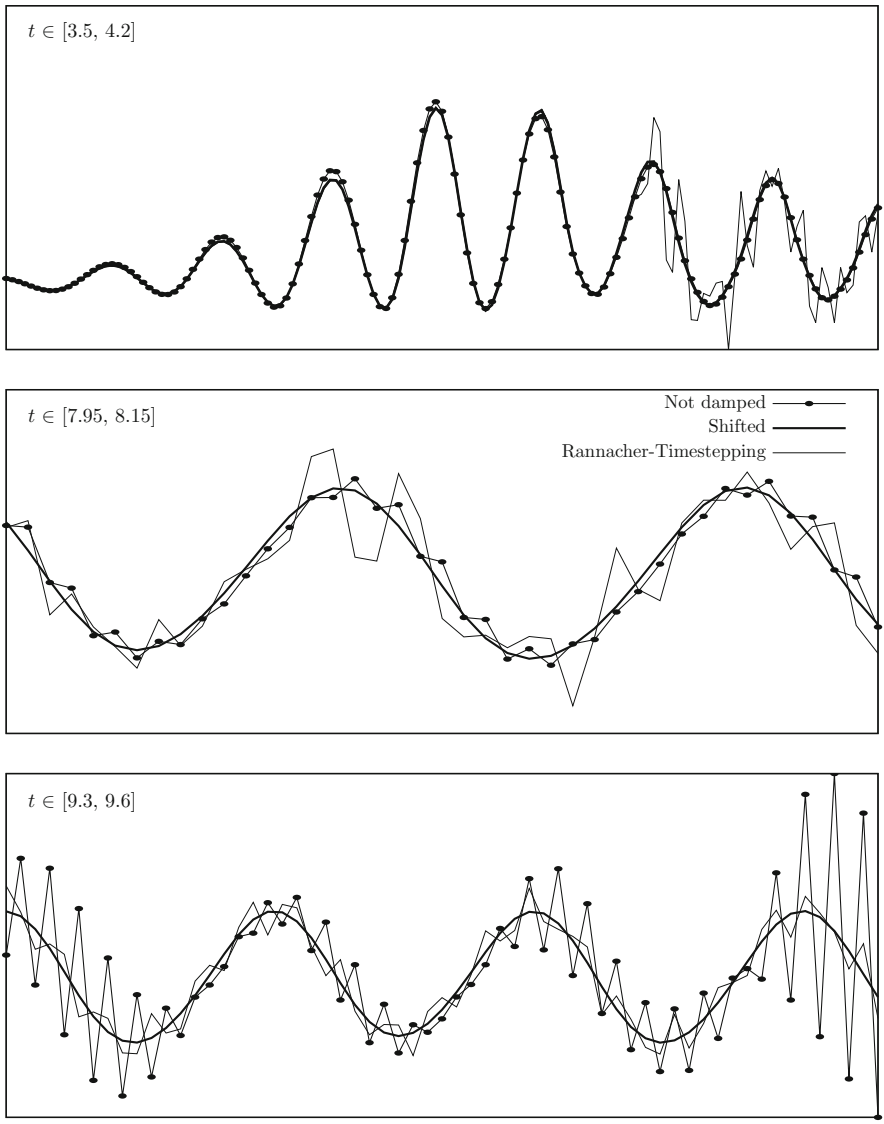

Fig. 5.5 Comparison of different damping strategies: undamped Crank-Nicolson, shifted version $\frac{1}{2} + k$ and Rannacher time-marching with two backward Euler steps at every time-unit

parabolic autonomous systems—is equivalent to the Crank-Nicolson scheme. We find $u_k, f_k, g_k \in X_I^1$ in the space of piece-wise linear, globally continuous functions and use $X_I^{0,\mathrm{dc}}$ as test space. On an interval I_m we write

$$f_k\big|_{I_m} = f_k^{m-1}\psi^{m-1} + f_k^m\psi^m, \quad g_k\big|_{I_m} = g_k^{m-1}\psi^{m-1} + g_k^m\psi^m,$$

where

$$\psi^{m-1}(t) = \frac{t_m - t}{t_m - t_{m-1}}, \quad \psi^m(t) = \frac{t - t_{m-1}}{t_m - t_{m-1}}.$$

5.2 Linearizations of Fluid-structure Interactions in the ALE Framework

Discretization in time results in a sequence of quasi-stationary systems of partial differential equations. These are highly nonlinear. Nonlinearities arise from material laws, convective terms and in the case of fluid-structure interactions due to the motion of the domain. Considering the strict ALE formulation with mapping of the complete variational system to a reference domain this domain nonlinearity is represented by the domain map T, its gradient $\mathbf{F}$ and determinant J. In the following paragraphs, we will discuss different ways to linearize these quasi-stationary systems. First of all, a straightforward way to linearize the set of equations would be the use of explicit time stepping schemes. This however is not feasible due to several reasons: first of all, the incompressibility constraint of the Navier-Stokes equations (or for incompressible solids) cannot be taken care of by explicit methods. Application of projection schemes would allow for explicit discretization of the momentum equations. We do not follow this approach, but refer to the literature [139, 262]. Another drawback of explicit discretization schemes is the limited stability that will call for very strict step-size conditions. The use of small time steps is a contrast to the benefits of monolithic schemes that allow for implicit discretizations with large time steps.

For the following we will consider implicit schemes only. Here we focus on time-discretization with the backward Euler method. Adaption to other single-step schemes is straightforward. Given velocity $\mathbf{v}^{\text{old}}$ and deformation $\mathbf{u}^{\text{old}}$ at previous time step we find (see Lemma 3.11)

$$\mathbf{v} \in \mathcal{V}, \quad \mathbf{u} \in \mathcal{W}, \quad p_f \in \mathcal{L}_f,$$

such that

$$\begin{aligned}
\left(\rho_f J \left(k^{-1}(\mathbf{v} - \mathbf{v}^{\text{old}}) + \mathbf{F}^{-1}(\mathbf{v} - k^{-1}(\mathbf{u} - \mathbf{u}^{\text{old}})) \cdot \nabla \mathbf{v}\right), \phi\right)_{\mathcal{F}} & \\
+ \left(J\boldsymbol{\sigma}_f \mathbf{F}^{-T}, \nabla\phi\right)_{\mathcal{F}} &= (J\rho_f \mathbf{f}, \phi)_{\mathcal{F}} \\
\left(J\mathbf{F}^{-1} : \nabla \mathbf{v}^T, \xi\right)_{\mathcal{F}} &= 0 \\
(\rho_s^0 k^{-1}(\mathbf{v} - \mathbf{v}^{\text{old}}), \phi)_{\mathcal{S}} + (\mathbf{F}\boldsymbol{\Sigma}_s, \nabla\phi)_{\mathcal{S}} &= (\rho_s^0 \mathbf{f}, \phi)_{\mathcal{S}} \\
(k^{-1}(\mathbf{u} - \mathbf{u}^{\text{old}}) - \mathbf{v}, \psi_s)_{\mathcal{S}} &= 0 \\
(\nabla \mathbf{u}, \nabla \psi_f)_{\mathcal{F}} &= 0,
\end{aligned} \tag{5.5}$$

for all

$$\phi \in \mathcal{V}, \quad \psi_f \in \mathcal{W}_f, \quad \psi_s \in \mathcal{L}_s, \quad \xi_f \in \mathcal{L}_f.$$

The fluid's stress tensor σ_f in ALE coordinates and the 2nd Piola Kirchhoff stress tensor of the St. Venant Kirchhoff material are given by

$$\begin{aligned} \boldsymbol{\sigma}_f &:= -pI + \rho_f \nu_f (\nabla \mathbf{v} \mathbf{F}^{-1} + \mathbf{F}^{-T} \nabla \mathbf{v}^T) \\ \boldsymbol{\Sigma}_s &:= 2\mu_s \mathbf{E}_s + \lambda_s \operatorname{tr}(\mathbf{E}_s) I, \end{aligned} \tag{5.6}$$

where the Green-Lagrangian Strain tensor is defined as

$$\mathbf{E}_s := \frac{1}{2}(\mathbf{F}^T \mathbf{F} - I).$$

Finally, we denote by $\rho_f, \rho_s^0, \nu_f, \mu_s$ and λ_s the material parameters describing density of fluid and solid, kinematic viscosity, shear modulus and Lamé coefficient.

We skipped all "hat's" denoting the use of reference coordinates. By $\mathcal{F}$ and $\mathcal{S}$ denote the fixed reference domains of fluid and solid. The function spaces $\mathcal{V}$ and $\mathcal{W}$ are basically the space $H^1(\Omega)^d$ differing only in the type of boundary values. While $\mathcal{W} = H_0^1(\Omega)^d$ has Dirichlet boundary values all around $\partial\Omega$, the velocity space $\mathcal{V} = H_0^1(\Omega; \Gamma^D)^d$ can have a Neumann outflow boundary $\Gamma_f^{\text{out}} \subset \partial\Omega$. The pressure space $\mathcal{L}_f = L^2(\mathcal{F})$ is defined on the fluid-domain only. The test space $\mathcal{W}_f = H_0^1(\mathcal{F})^d$ for the definition of the ALE-map has homogenous Dirichlet values all around the fluid-domain. The test space of the deformation-velocity relation is $\mathcal{L}_s = L^2(\mathcal{S})^d$.

5.2.1 Linearization by Fixed Point-Iterations

A simple approach to linearization of (5.5) is to apply fixed point-iterations. Starting with

$$\mathbf{v}^{(0)} = \mathbf{v}^{\text{old}}, \quad \mathbf{u}^{(0)} = \mathbf{u}^{\text{old}},$$

we search for approximations $\mathbf{v}^{(l)}$ and $\mathbf{u}^{(l)}$ that converge to $\mathbf{v}$ and $\mathbf{u}$ for $l \to \infty$. We define

$$\mathbf{F}^{(l)} := I + \nabla \mathbf{v}^{(l)}, \quad J^{(l)} := \det \mathbf{F}^{(l)}$$

and solve the sequence of linearized systems

$$\begin{aligned}
\left(\rho_f J^{(l-1)} \left(k^{-1}(\mathbf{v}^{(l)} - \mathbf{v}^{\text{old}}) + \right.\right. \\
+\mathbf{F}^{(l-1)^{-1}}(\mathbf{v}^{(l-1)} - k^{-1}(\mathbf{u}^{(l-1)} - \mathbf{u}^{\text{old}})) \cdot \nabla \mathbf{v}^{(l)}\Big), \phi\Big)_{\mathcal{F}} \\
+\left(J^{(l-1)} \boldsymbol{\sigma}_f(\mathbf{v}^{(l)}, p^{(l)}) \mathbf{F}^{(l-1)^{-T}}, \nabla\phi\right)_{\mathcal{F}} = (J^{(l-1)} \rho_f \mathbf{f}, \phi)_{\mathcal{F}} \\
\left(J^{(l-1)} \mathbf{F}^{(l-1)^{-1}} : \nabla \mathbf{v}^T, \xi\right)_{\mathcal{F}} = 0 \\
(\rho_s^0 k^{-1}(\mathbf{v}^{(l)} - \mathbf{v}^{\text{old}}), \phi)_{\mathcal{S}} + (\mathbf{F}^{(l-1)} \boldsymbol{\Sigma}_s^{(l)}, \nabla\phi)_{\mathcal{S}} = (\rho_s^0 \mathbf{f}, \phi)_{\mathcal{S}} \\
(k^{-1}(\mathbf{u}^{(l)} - \mathbf{u}^{\text{old}}) - \mathbf{v}^{(l)}, \psi_s)_{\mathcal{S}} = 0 \\
(\nabla \mathbf{u}^{(l)}, \nabla \psi_f)_{\mathcal{F}} = 0,
\end{aligned} \tag{5.7}$$

with an ad hoc linearization of the solid's stress tensor (here, given for the St. Venant Kirchhoff material)

$$\begin{aligned}
\boldsymbol{\Sigma}_s^{(l)} &:= 2\mu_s \mathbf{E}_s^{(l)} + \lambda_s \operatorname{tr}(\mathbf{E}_s^{(l)}) I, \\
\mathbf{E}_s^{(l)} &:= \frac{1}{2}\left(\nabla \mathbf{u}^{(l)} + \nabla \mathbf{u}^{(l)^T} + \nabla \mathbf{u}^{(l-1)} \nabla \mathbf{u}^{(l)^T}\right).
\end{aligned}$$

Other choices are possible. This fixed-point linearization of the fsi system is similar to the Oseen linearization of the Navier-Stokes system, see Sect. 4.4.1. A theoretical analysis on the convergence of this fixed-point iteration is difficult, but we will add numerical tests using the benchmark problem fsi-3 of Hron and Turek [199], see Sect. 5.2.3.

5.2.2 *Newton Linearization for Fluid-structure Interactions in Arbitrary Lagrangian Eulerian Formulation*

In Sect. 4.4, we have seen that general fixed-point iterations for the linearization of the Navier-Stokes system usually show very slow convergence properties, see Fig. 4.9. Only by using Newton scheme for approximation of the nonlinear systems, we could establish a robust and very fast converging scheme. This section will now describe Newton linearization for fluid-structure interactions in ALE formulation. The main difficulty will again be the handling of the domain motion, hidden in the ALE mapping T, its gradient $\mathbf{F}$ and determinant J. By consulting Sect. 4.4.2, the general Newton method for a (quasi-)stationary system of partial differential equations in variational formulation was given as (compare (4.34))

$$\mathbf{W} \in \mathcal{X}: \quad A'(\mathbf{U}^{(l-1)})(\mathbf{W}^{(l)}, \Phi) = F(\Phi) - A(\mathbf{U}^{(l-1)})(\Phi), \quad \forall \Phi \in \mathcal{Y}, \tag{5.8}$$

with

$$\mathbf{U}^{(l)} := \mathbf{U}^{(l-1)} + \omega^{(l)}\mathbf{W}^{(l)}. \tag{5.9}$$

In the context of fluid-structure interactions in ALE formulation (discretized in time with the backward Euler method) the last known approximation $\mathbf{U}^{(l-1)} \in \mathcal{X}$ is given by

$$\mathbf{U}^{(l-1)} := \{\mathbf{v}^{(l-1)}, \mathbf{u}^{(l-1)}, p_f^{(l-1)}\} \in \mathcal{X} = \mathcal{V} \times \mathcal{W} \times \mathcal{L}_f.$$

We denote the unknown update by

$$\mathbf{W}^{(l)} = \{\mathbf{z}, \mathbf{w}, q_f\} \in \mathcal{X} = \mathcal{V} \times \mathcal{W} \times \mathcal{L}_f.$$

Remark 5.1 (Initial Value) Newton convergence highly depends on a good choice of an initial approximation $\mathbf{U}^{(0)}$. In the context of non-stationary problems, a good choice is always to use the old solution at time t_{n-1}, hence $\mathbf{U}^{(0)} = \mathbf{U}(t_{n-1}) = \mathbf{U}^{\text{old}}$. This initial choice could even be enhanced by using a linear extrapolation of the two last approximations, by choosing

$$\mathbf{U}^{(0)} = \mathbf{U}(t_{n-1}) + \frac{t_n - t_{n-1}}{t_{n-1} - t_{n-2}} \left(\mathbf{U}(t_{n-1}) - \mathbf{U}(t_{n-2})\right).$$

Considering the backward Euler discretization, the semilinear form $A(\cdot)(\cdot)$ is given by (compare 5.5)

$$\begin{aligned} A(\mathbf{U})(\Phi) = &\left(\rho_f J \left(k^{-1}(\mathbf{v} - \mathbf{v}^{\text{old}}) + \nabla\mathbf{v}\mathbf{F}^{-1}\left(\mathbf{v} - k^{-1}(\mathbf{u} - \mathbf{u}^{\text{old}})\right)\right), \phi\right)_{\mathcal{F}} \\ &+ \left(J\boldsymbol{\sigma}_f\mathbf{F}^{-T}, \nabla\phi\right)_{\mathcal{F}} - (J\rho_f\mathbf{f}, \phi)_{\mathcal{F}} \\ &+ \left(J\mathbf{F}^{-1} : \nabla\mathbf{v}^T, \xi\right)_{\mathcal{F}} \\ &+ (\rho_s^0 k^{-1}\mathbf{v}, \phi)_{\mathcal{S}} + (\mathbf{F}\boldsymbol{\Sigma}_s, \nabla\phi)_{\mathcal{S}} \\ &+ (k^{-1}\mathbf{u} - \mathbf{v}, \psi_s)_{\mathcal{S}} + (\nabla\mathbf{u}, \nabla\psi_f)_{\mathcal{F}} \end{aligned} \tag{5.10}$$

and the right hand side $F(\cdot)$ by

$$F(\Phi) = (\rho_s^0\mathbf{f}, \phi)_{\mathcal{S}} + (\rho_s^0 k^{-1}\mathbf{v}^{\text{old}}, \phi)_{\mathcal{S}} + (k^{-1}\mathbf{u}^{\text{old}}\psi_s)_{\mathcal{S}}. \tag{5.11}$$

To simplify the representation of the derivatives of the convective term, we have—in (5.10)—used the relation

$$\left((\mathbf{F}^{-1}\mathbf{v}) \cdot \nabla\right)\mathbf{w} = \nabla\mathbf{v}\mathbf{F}^{-1}\mathbf{w}.$$

The data term $(J\rho_f \mathbf{f}, \phi)_{\mathcal{F}}$ must reside in the form $A(\cdot)(\cdot)$ as the deformation determinant J depends on the unknown deformation $\mathbf{u}$. The same applies to the old solution $\mathbf{v}^{\text{old}}$ appearing in the momentum equation of the fluid problem.

The derivative $A'(\mathbf{U}^{(l-1)})(\mathbf{W}^{(l)}, \Phi)$ in (5.8) is the Gâteaux derivative of the semilinear form $A(\cdot)(\cdot)$, which is the directional derivative at $\mathbf{U}^{(l-1)}$ in direction $\mathbf{W}^{(l)}$ tested with Φ. It is defined as

$$A'(\mathbf{U})(\mathbf{W}, \Phi) := \lim_{s\to 0} \frac{d}{ds} A(\mathbf{U} + s\mathbf{W})(\Phi)\Big|_{s=0}. \tag{5.12}$$

On a fixed domain, we can exchange the order of differentiation and integration, such that it holds

$$\frac{d}{ds}\left(\int_\Omega f(\mathbf{u} + s\mathbf{w})\phi \,\mathrm{d}x\right)\Big|_{s=0} = \int_\Omega \frac{d}{ds} f(\mathbf{u} + s\mathbf{w})\Big|_{s=0} \phi \,\mathrm{d}x.$$

Hence,

$$\frac{d}{ds}\left(f(\mathbf{u} + s\mathbf{w}), \phi\right)_\Omega \Big|_{s=0} = \left(f'(\mathbf{u})\mathbf{w}, \phi\right)_\Omega.$$

In the case of fluid-structure interaction, this situation is more involved, as the motion of the domain depends on the solution. Formally, variational formulations of fluid-structure interactions are defined on domains that depend on the solution. Here, differentiation and integration may not be exchanged

$$\frac{d}{ds}\left(f(\mathbf{u} + s\mathbf{w}), \phi\right)_{\Omega(\mathbf{u})} \Big|_{s=0} \neq \left(f'(\mathbf{u})\mathbf{w}, \phi\right)_{\Omega(\mathbf{u})}.$$

Instead, the derivative with respect to the domain of integration must be considered.

A straightforward and simple way for computing the derivative $A'(\cdot)(\cdot,\cdot)$ is by means of finite differences:

$$A'(\mathbf{U})(\mathbf{W}, \Phi) = \varepsilon^{-1}\left(A(\mathbf{U} + \varepsilon\mathbf{W})(\Phi) - A(\mathbf{U})(\Phi)\right) + \mathcal{O}(\varepsilon), \quad \varepsilon > 0 \tag{5.13}$$

This approach is widely used for complex simulations [170]. The main difficulty of finite difference approximations is the choice of ε. This parameter must be small enough, such that the approximation accuracy of the Jacobian (5.13) is high. On the other hand, a too small value of ε may cause cancellation effects and will give rise to a substantial truncation error. An optimal choice based on a priori information is usually not possible, see [47] where the authors investigated finite difference approximations in the context of gradient based optimization.

If the derivatives (5.12) are to be evaluated exactly, we need to manage the domain deformation. It will turn out, that our strict form of the *Arbitrary Lagrangian Eulerian* framework that works on a fixed reference system for the complete variational form, see (5.10) and (5.11), helps to avoid all difficulties, as

the computational domains are fixed. We can exchange orders of differentiation and integration. Using the alternative formulation on updated meshes, motion of the domains must be carefully included. Fernandez and Moubachir [141] use the concept of shape derivatives to include the mesh motion. They derive the exact analytical Jacobian for the fluid-structure interaction system in a very similar fashion to the present approach. Van der Zee and co workers [358, 359] describe two different approaches for differentiation of the variational formulation. The first approach [358] is very similar to our strict interpretation of the ALE method: the equations are mapped to the fixed reference domain, and all differentiation is carried out here. The second approach [359] is based on the theory of *shape calculus*, see [313, 362], where the derivative with respect to the domain motion is explicitly computed: let $T(t) : \Omega \to \Omega(t)$ be a sufficiently regular domain map. Then, the following fundamental formula holds:

$$\frac{d}{ds}\int_{\Omega(s)} f(x)\mathrm{d}x = \int_{\partial\Omega(s)} \langle \mathbf{n}\cdot\partial_s T(s)\rangle f(o)\mathrm{d}o,$$

where $\mathbf{n}$ is the outward facing unit normal at the boundary of $\Omega(s)$. We will have to get back to this approach, when dealing with the Fully Eulerian approach in Sect. 6.4. Here, we can rely on the strict variant of the ALE method, where all domains are fixed.

The following theorem gives the full Jacobian of the fluid-structure interaction problem in ALE coordinates, discretized with the backward Euler equation.

Theorem 5.2 (Jacobian for Fluid-structure Interactions in Arbitrary Lagrangian Eulerian Coordinates) *Let* $\mathbf{U} = \{\mathbf{v}, \mathbf{u}, p_f\} \in \mathcal{X}$, $\mathbf{W} = \{\mathbf{z}, \mathbf{w}, q_f\} \in \mathcal{X}$ *and* $\Phi = \{\phi, \psi_f, \psi_s, \xi_f\} \in \mathcal{Y}$. *For the directional derivative of (5.10) at* $\mathbf{U}$ *in direction of* $\mathbf{W}$, *it holds:*

$$\begin{aligned}
A'(\mathbf{U})(\mathbf{W}\,,\,\Phi) = &\left(\rho_f J\left(k^{-1}\mathbf{z} + \nabla\mathbf{z}\mathbf{F}^{-1}\left(\mathbf{v} - \frac{\mathbf{u}-\mathbf{u}^{old}}{k}\right) + \nabla\mathbf{v}\mathbf{F}^{-1}\mathbf{z}\right), \phi\right)_{\mathcal{F}} \\
&+ \left(J\frac{d\boldsymbol{\sigma}_f}{d\mathbf{v}}(\mathbf{W})\mathbf{F}^{-T}, \nabla\phi\right)_{\mathcal{F}} - \left(J\mathbf{F}^{-T}q_f, \nabla\phi\right)_{\mathcal{F}} \\
&+ \left((J\mathbf{F}^{-1} : \nabla\mathbf{z}^T, \xi\right)_{\mathcal{F}} \\
&+ \Big(\rho_f J\,\mathrm{tr}\,(\mathbf{F}^{-1}\nabla\mathbf{w})\Big(k^{-1}(\mathbf{v}-\mathbf{v}^{old}) + \\
&\quad \nabla\mathbf{v}\mathbf{F}^{-1}\left(\mathbf{v} - k^{-1}(\mathbf{u}-\mathbf{u}^{old})\right)\Big), \phi\Big)_{\mathcal{F}} \\
&- \left(\rho_f J\nabla\mathbf{v}\mathbf{F}^{-1}\nabla\mathbf{w}\mathbf{F}^{-1}\left(\mathbf{v} - k^{-1}(\mathbf{u}-\mathbf{u}^{old})\right), \phi\right)_{\mathcal{F}} \\
&- \left(\rho_f J\nabla\mathbf{v}\mathbf{F}^{-1}k^{-1}\mathbf{w}, \phi\right)_{\mathcal{F}} \\
&+ \left(J\,\mathrm{tr}\,(\mathbf{F}^{-1}\nabla\mathbf{w})\boldsymbol{\sigma}_f\mathbf{F}^{-T}, \nabla\phi\right)_{\mathcal{F}} - \left(J\boldsymbol{\sigma}_f\mathbf{F}^{-T}\nabla\mathbf{w}^T\mathbf{F}^{-T}, \nabla\phi\right)_{\mathcal{F}}
\end{aligned}$$

$$
\begin{aligned}
&+\left(J\frac{d\boldsymbol{\sigma}_f}{d\mathbf{u}}(\mathbf{W})\mathbf{F}^{-T},\nabla\phi\right)_{\mathcal{F}}\\
&+\left(J(\mathbf{F}^{-T}:\nabla\mathbf{w})(\mathbf{F}^{-1}:\nabla\mathbf{v}^T),\xi\right)_{\mathcal{F}}-\left(J\mathbf{F}^{-1}\nabla\mathbf{w}\mathbf{F}^{-1}:\nabla\mathbf{v}^T,\xi\right)_{\mathcal{F}}\\
&+\left(\rho_s^0k^{-1}\mathbf{z},\phi\right)_{\mathcal{S}}+\left(\nabla\mathbf{w}\boldsymbol{\Sigma}_s+\mathbf{F}\frac{d\boldsymbol{\Sigma}_s}{d\mathbf{u}}(\mathbf{W}),\nabla\phi\right)_{\mathcal{S}}\\
&-(\mathbf{z},\psi_s)_{\mathcal{S}}+(k^{-1}\mathbf{w},\psi_s)_{\mathcal{S}}\\
&+\left(\nabla\mathbf{w},\nabla\psi_f\right)_{\mathcal{F}},
\end{aligned}
\tag{5.14}
$$

where the directional derivatives of the Navier-Stokes stress tensor are given by

$$
\begin{aligned}
\frac{d}{d\mathbf{v}}\boldsymbol{\sigma}_f(\mathbf{U})(\mathbf{z})&=\rho_f\nu_f(\nabla\mathbf{z}_f\mathbf{F}^{-1}+\mathbf{F}^{-T}\nabla\mathbf{z}_f^T),\\
\frac{d}{d\mathbf{u}}\boldsymbol{\sigma}_f(\mathbf{U})(\mathbf{w})&=-\rho_f\nu_f\left(\nabla\mathbf{v}\mathbf{F}^{-1}\nabla\mathbf{w}\mathbf{F}^{-1}+\mathbf{F}^{-T}\nabla\mathbf{w}^T\mathbf{F}^{-T}\nabla\mathbf{v}^T\right),
\end{aligned}
$$

and where the directional derivatives of the St. Venant Kirchhoff material's tensor are given by

$$
\begin{aligned}
\frac{d\boldsymbol{\Sigma}_s}{d\mathbf{u}}(\mathbf{U})(\mathbf{w})&=2\mu_s\frac{d\mathbf{E}_s}{d\mathbf{u}}(\mathbf{W})+\lambda_s\,\mathrm{tr}\left(\frac{d\mathbf{E}_s}{d\mathbf{u}}(\mathbf{W})\right),\\
\frac{d\mathbf{E}_s}{d\mathbf{u}}(\mathbf{W})&=\frac{1}{2}(\nabla\mathbf{w}^T\mathbf{F}+\mathbf{F}^T\nabla\mathbf{w})
\end{aligned}
$$

Proof The proof is split into different part by a partitioning of the semilinear form (5.10) into subparts for Navier-Stokes momentum equation

$$
\begin{aligned}
A^{m,f}(\mathbf{U})(\Phi)=&\left(\rho_fJ\left(k^{-1}(\mathbf{v}-\mathbf{v}^{\mathrm{old}})+\mathbf{F}^{-1}(\mathbf{v}-k^{-1}(\mathbf{u}-\mathbf{u}^{\mathrm{old}}))\cdot\nabla\mathbf{v}\right),\phi\right)_{\mathcal{F}}\\
&+\left(J\boldsymbol{\sigma}_f\mathbf{F}^{-T},\nabla\phi\right)_{\mathcal{F}}-(J\rho_f\mathbf{f},\phi)_{\mathcal{F}},
\end{aligned}
\tag{5.15}
$$

the equation for divergence freeness

$$
A^{div,f}(\mathbf{U})(\Phi)=\left(J\mathbf{F}^{-1}:\nabla\mathbf{v}^T,\xi_f\right)_{\mathcal{F}},
\tag{5.16}
$$

the momentum equation of the solid problem and the velocity deformation relation

$$
\begin{aligned}
A^{m,s}(\mathbf{U})(\Phi)&=(\rho_s^0k^{-1}\mathbf{v},\phi)_{\mathcal{S}}+(\mathbf{F}\boldsymbol{\Sigma}_s,\nabla\phi)_{\mathcal{S}},\\
A^{uv,s}(\mathbf{U})(\Phi)&=(k^{-1}\mathbf{u}-\mathbf{v},\psi_s)_{\mathcal{S}},
\end{aligned}
\tag{5.17}
$$

and finally the (harmonic) extension of the deformation that defines the ALE mapping

$$A^{ale,f}(\mathbf{U})(\Phi) = (\nabla \mathbf{u}, \nabla \psi_f)_{\mathcal{F}}. \tag{5.18}$$

The full variational form $A(\mathbf{U})(\Phi)$ is given as the sum of $A^{m,f}(\mathbf{U})(\Phi) + A^{div,f}(\mathbf{U})(\Phi) + A^{m,s}(\mathbf{U})(\Phi) + A^{uv,s}(\mathbf{U})(\Phi) + A^{ale,f}(\mathbf{U})(\Phi)$.

Calculation of the different derivatives of these forms with respect to $\mathbf{v}$, $\mathbf{u}$ and p_f is done in the following lemmas. First, in Lemma 5.3 we deal with the derivatives of $A^{NS}(\cdot)(\cdot)$ and $A^{div}(\cdot)(\cdot)$ (the Navier-Stokes part). The Jacobian for the harmonic ALE extension (a linear operator) is easily available. Then, Lemma 5.5 shows the directional derivatives of the structure equation. And finally, Lemma 5.6 takes care of the derivatives of the Navier-Stokes part with respect to the artificial domain motion. This part only comes from the ALE formulation and would not be present in Eulerian formulations of the Navier-Stokes problem. □

Lemma 5.3 (Derivatives of the Navier-Stokes Equations with Respect to Velocity and Pressure) *For the directional derivatives of $A^{m,f}$ and $A^{div,f}$ in direction of velocity $\mathbf{v}$ and pressure p_f it holds*

$$\begin{aligned}
A^{m,f}_{\mathbf{v}}(\mathbf{U})(\mathbf{W}, \Phi) &= \left(\rho_f J k^{-1}\mathbf{z}, \phi\right)_{\mathcal{F}} \\
&\quad + \left(\rho_f J \left(\nabla \mathbf{z}\mathbf{F}^{-1}\left(\mathbf{v} - \frac{\mathbf{u} - \mathbf{u}^{old}}{k}\right) + \nabla \mathbf{v}\mathbf{F}^{-1}\mathbf{z}\right), \phi\right)_{\mathcal{F}} \\
&\quad + \left(J\frac{d\boldsymbol{\sigma}_f}{d\mathbf{v}}(\mathbf{W})\mathbf{F}^{-T}, \nabla\phi\right)_{\mathcal{F}}, \\
A^{m,f}_{p_f}(\mathbf{U})(\mathbf{W}, \Phi) &= -\left(J\mathbf{F}^{-T} q_f, \nabla\phi\right)_{\mathcal{F}}, \\
A^{div,f}_{\mathbf{v}}(\mathbf{U})(\mathbf{W}, \Phi) &= \left(J\mathbf{F}^{-1} : \nabla \mathbf{z}^T, \xi_f\right)_{\mathcal{F}}.
\end{aligned}$$

The derivative of the fluid's stress tensor is given by

$$\frac{d\boldsymbol{\sigma}_f}{d\mathbf{v}}(\mathbf{W}) = \rho_f \nu_f (\nabla \mathbf{z}_f \mathbf{F}^{-1} + \mathbf{F}^{T} \nabla \mathbf{z}_f^T).$$

Proof By the definition of the Gâteaux derivative (5.12), calculation of the derivatives is given by standard scalar differentiation, as the order of integration and differentiation can be exchanged. For the derivatives of the stress tensor, consult its ALE form (5.6). For basics on the linearization of the Navier-Stokes equations, see Sect. 4.4.2. □

Before proceeding with the St. Venant Kirchhoff material and the derivatives of the ALE formulation with respect to the deformation, we gather some useful relations.

Lemma 5.4 (Derivatives of the Deformation Gradient) *Let* $\mathbf{F} := I + \nabla \mathbf{u}$ *and* $J := \det \mathbf{F}$ *its gradient. It holds*

$$
\begin{aligned}
(i) \quad & \frac{d\mathbf{F}}{d\mathbf{u}}(\mathbf{w}) = \nabla \mathbf{w}, \\
(ii) \quad & \frac{d\mathbf{F}^T}{d\mathbf{u}}(\mathbf{w}) = \nabla \mathbf{w}^T, \\
(iii) \quad & \frac{d\mathbf{F}^{-1}}{d\mathbf{u}}(\mathbf{w}) = -\mathbf{F}^{-1} \nabla \mathbf{w} \mathbf{F}^{-1}, \\
(iv) \quad & \frac{d\mathbf{F}^{-T}}{d\mathbf{u}}(\mathbf{w}) = -\mathbf{F}^{-T} \nabla \mathbf{w}^T \mathbf{F}^{-T}, \\
(v) \quad & \frac{dJ}{d\mathbf{u}}(\mathbf{w}) = J\mathbf{F}^{-T} : \nabla \mathbf{w} = J \operatorname{tr}(\mathbf{F}^{-1} \nabla \mathbf{w})
\end{aligned}
$$

Proof Relations *(i)* and *(ii)* are directly available. For showing relation *(iii)* we differentiate the identity $\mathbf{F}^{-1}\mathbf{F} = I$ and use *(i)* to obtain

$$
\frac{d}{d\mathbf{u}} \left(\mathbf{F}^{-1}\mathbf{F} \right)(\mathbf{w}) = \frac{d}{d\mathbf{u}} I(\mathbf{w}) = 0 \quad \Rightarrow \quad \frac{d\mathbf{F}^{-1}}{d\mathbf{u}}(\mathbf{w})\mathbf{F} + \mathbf{F}^{-1} \frac{d\mathbf{F}}{d\mathbf{u}}(\mathbf{w}) = 0.
$$

Multiplication with $\mathbf{F}^{-1}$ gives the result:

$$
\frac{d\mathbf{F}^{-1}}{d\mathbf{u}}(\mathbf{w}) = -\mathbf{F}^{-1} \nabla \mathbf{w} \mathbf{F}^{-1}.
$$

(iv) is the transpose of *(iii)*. Relation *(v)* can be shown by component-wise calculation. □

With Lemma 5.4, we can now compute the Jacobian of the elastic structure equations with respect to velocity and deformation:

Lemma 5.5 (Derivative of the Structure Equation with Respect to Velocity and Deformation) *It holds for the derivatives of the elastic structure equation in reference coordinates with respect to velocity and deformation:*

$$
\begin{aligned}
A_{\mathbf{v}}^{m,s}(\mathbf{U})(\mathbf{W}, \Phi) &= \left(\rho_s^0 k^{-1} \mathbf{z}, \phi \right)_{\mathcal{S}} \\
A_{\mathbf{u}}^{m,s}(\mathbf{U})(\mathbf{W}, \Phi) &= \left(\nabla \mathbf{w} \boldsymbol{\Sigma}_s + \mathbf{F} \frac{d\boldsymbol{\Sigma}_s}{d\mathbf{u}}(\mathbf{W}), \nabla \phi \right)_{\mathcal{S}}, \\
A_{\mathbf{v}}^{uv,s}(\mathbf{U})(\mathbf{W}, \Phi) &= -(\mathbf{z}, \psi_s)_{\mathcal{S}}, \\
A_{\mathbf{u}}^{uv,s}(\mathbf{U})(\mathbf{W}, \Phi) &= (k^{-1}\mathbf{w}, \psi_s)_{\mathcal{S}},
\end{aligned}
$$

where the derivative of the 2nd Piola Kirchhoff stress tensor $\boldsymbol{\Sigma}_s$ (of the St. Venant Kirchhoff material) is given by

$$\frac{d\boldsymbol{\Sigma}_s}{d\mathbf{u}}(\mathbf{W}) = 2\mu_s \frac{d\mathbf{E}_s}{d\mathbf{u}}(\mathbf{W}) + \lambda_s \operatorname{tr}\left(\frac{d\mathbf{E}_s}{d\mathbf{u}}(\mathbf{W})\right),$$

and the derivative of the Green-Lagrangian strain tensor $\mathbf{E}_s$ by

$$\frac{d\mathbf{E}_s}{d\mathbf{u}}(\mathbf{W}) = \frac{1}{2}(\nabla \mathbf{w}^T \mathbf{F} + \mathbf{F}^T \nabla \mathbf{w}).$$

Proof These relations follow using *(i)* and *(ii)* of Lemma 5.4. □.

Finally, it remains to gather all derivatives with respect to the ALE domain mapping. Omitting some of the derivatives (which here correspond to the dependency of the domain motion) relates to a simplified Newton method, see Sect. 5.2.3 for a numerical study.

Lemma 5.6 (Derivative of the Navier-Stokes Equations with Respect to the Domain Motion) *It holds for the derivatives of the Navier-Stokes equations in ALE coordinates with respect to the domain motion u*

$$\begin{aligned}
A_{\mathbf{u}}^{m,f}(\mathbf{U})(\mathbf{W}, \Phi) = &\left(\rho_f \operatorname{tr}(\mathbf{F}^{-1}\nabla \mathbf{w})\left(k^{-1}(\mathbf{v} - \mathbf{v}^{old}) + \right.\right. \\
&\left.\left. \nabla \mathbf{v}\mathbf{F}^{-1}\left(\mathbf{v} - k^{-1}(\mathbf{u} - \mathbf{u}^{old})\right)\right), \phi\right)_{\mathcal{F}} \\
&- \left(\rho_f J \nabla \mathbf{v}\mathbf{F}^{-1}\nabla \mathbf{w}\mathbf{F}^{-1}\left(\mathbf{v} - k^{-1}(\mathbf{u} - \mathbf{u}^{old})\right), \phi\right)_{\mathcal{F}} \\
&- \left(\rho_f J \nabla \mathbf{v}\mathbf{F}^{-1}k^{-1}\mathbf{w}, \phi\right)_{\mathcal{F}} \\
&+ \left(\operatorname{tr}(\mathbf{F}^{-1}\nabla \mathbf{w})\boldsymbol{\sigma}_f \mathbf{F}^{-T}, \nabla \phi\right)_{\mathcal{F}} - \left(J\boldsymbol{\sigma}_f \mathbf{F}^{-T}\nabla \mathbf{w}^T \mathbf{F}^{-T}, \nabla \phi\right)_{\mathcal{F}} \\
&+ \left(J\frac{d\boldsymbol{\sigma}_f}{d\mathbf{u}}(\mathbf{W})\mathbf{F}^{-T}, \nabla \phi\right)_{\mathcal{F}}, \\
A_{\mathbf{u}}^{div,f}(\mathbf{U})(\mathbf{W}, \Phi) = &\left(\operatorname{div}\left(\operatorname{tr}(\mathbf{F}^{-1}\nabla \mathbf{w})\mathbf{F}^{-1}\mathbf{v}\right), \xi_f\right)_{\mathcal{F}} \\
&- \left(\operatorname{div}\left(J\mathbf{F}^{-1}\nabla \mathbf{w}\mathbf{F}^{-1}\right), \xi_f\right)_{\mathcal{F}}.
\end{aligned}$$

where the derivative of the stress tensor with respect to the domain motion is given by

$$\frac{d\boldsymbol{\sigma}_f}{d\mathbf{u}}(\mathbf{W}) = -\rho_f \nu_f \left(\nabla \mathbf{v}\mathbf{F}^{-1}\nabla \mathbf{w}\mathbf{F}^{-1} + \mathbf{F}^{-T}\nabla \mathbf{w}^T \mathbf{F}^{-T}\nabla \mathbf{v}^T\right)$$

Proof Again, all these derivatives can be estimated by tedious calculations and frequent use of Lemma 5.4. □

Further details on the computation of the Jacobian are given in [280], where the derivatives of the stationary fluid-structure interaction system are derived.

With the Jacobian of the fluid-structure interaction system at hand, we can formulate the linear systems of partial differential equations that define every step of the Newton approximation

$$A'(\mathbf{U}^{(l-1)})(\mathbf{W}^{(l)}, \Phi) = F(\Phi) - A(\mathbf{U}^{(l-1)})(\Phi) \quad \forall \Phi \in \mathcal{Y}. \tag{5.19}$$

The variational formulation defined by $A'(\cdot)(\cdot,\cdot)$ given in Theorem 5.2 is complex, it couples all different variables, but it is a linear problem. Finite element discretization of this problem will be subject to the following section. Later on, in Chap. 7, we will discuss the solution of the resulting (after discretization) linear systems of equations.

In every step of the Newton iteration, Eq. (5.19) is itself a coupled problem on the two domains $\mathcal{F}$ and $\mathcal{S}$. On the common interface, three coupling conditions are given. First, continuity of the velocity variation $\mathbf{z}$, second continuity of the deformation's variation $\mathbf{w}$ and finally, a Neumann condition that comes from the linearization of the dynamic coupling condition. For deriving its exact formulation, one would have to transform the Jacobian $A'(\mathbf{U})(\mathbf{W}, \Phi)$ back to the classical formulation.

A modern alternative to the analytical computation of the Jacobian is given by the idea of *automatic differentiation*, see Rall [264] and Griewank [171]. Automatic differentiation is an algorithmic approach that is based on the concept that every computer implementation, e.g. the implementation of the semilinear form $A(\cdot)(\cdot)$ will internally be split into a sequence of elementary mathematical operations (like multiplications, roots, basis functions like sine or cosine etc.). These elementary operations are then derived and set together using chain and product rule. Dunne [127] presents and implementation of a Newton method for fluid-structure interactions in ALE formulation based on automatic differentiation. In particular, if different complex models are studied, automatic differentiation will help to compute exact Jacobians in a fail-proof way. It will for instance be easy to implement complex and changing material laws. The concept of automatic differentiation is not to be confused with finite differences, where derivatives are only approximated.

Remark 5.7 (Inexact Newton Iteration) The assembly of the Jacobian is a very costly step within the Newton iteration. Considering the necessity to solve linear systems afterwards, a change of the Jacobian usually calls for additional work regarding the preparation of preconditioners in Krylov-Subspace iterations or smoothers in multigrid solvers, see Chap. 7. In the worst case, when direct solvers must be used to approximate the linear systems, a modification of the Jacobian also calls for a new decomposition of it. Hence, assembling the Jacobian must be prevented, whenever the overall efficiency does not require it. As linear systems are

usually only approximated up to a given tolerance, full quadratic convergence of the Newton method itself cannot be expected. Therefore, we only update the Jacobian, if the nonlinear convergence rate that can easily be measured as

$$\rho_n = \frac{\|F(\cdot) - A(\mathbf{U}^n)(\cdot)\|_\infty}{\|F(\cdot) - A(\mathbf{U}^{(n-1)})(\cdot)\|_\infty}, \tag{5.20}$$

is above a given threshold γ_{nt}. A good balance depends on the required tolerance and the efficiency of the linear solver. Usually, $\gamma_{nt} \approx 0.01 \sim 0.1$.

5.2.3 *Numerical Study on Linearizations*

We present a study on the linearization on the performance of different linearization techniques applied to the non-stationary benchmark problem fsi-3 introduced by Hron and Turek [200]. We have used this test case to study time discretizations in Sect. 5.1. Here we analyze the performance of the different choices for a linearization of the nonlinear problems. We investigate the time interval $I = [5, 5.5]$, where the oscillation is fully developed, such that significant deformations appear. This is important to account for the geometric nonlinearities that come from the ALE mapping, see Fig. 5.6.

All numerical studies are carried out with the implicitly shifted Crank-Nicolson scheme, see Sect. 4.1.2.1 with θ chosen as

$$\theta = \frac{1}{2} + 2k,$$

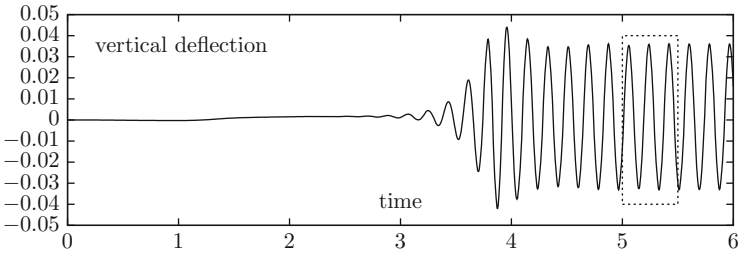

Fig. 5.6 Benchmark problem fsi-3. Vertical deflection of the tip of the beam as functional over time. We perform the numerical study on different linearization techniques in the sub-interval $I = [5, 5.5]$, where the dynamics of the flow is fully developed

where by k we denote the time step size. If not specified otherwise, we choose

$$k = 0.005,$$

such that a total of $N = 100$ steps is investigated and the effective parameter $\theta = 0.51$ is picked. For spatial discretization we choose equal-order biquadratic elements on a mesh with about 4000 unknowns.

In every time step, the nonlinear problems are approximated such that the initial residual is reduced by eight orders of magnitude

$$\|F(\cdot) - A(\mathbf{U}^n)(\cdot)\|_\infty \leq \text{tol}\|F(\cdot) - A(\mathbf{U}^0)(\cdot)\|_\infty, \quad \text{tol} = 10^{-8}.$$

The linear systems are solved by a direct method to prevent side-effects of not-sufficient accuracy.

In a first study, we compare the effects of the parameter γ_{nt} in (5.20), controlling the limiting reduction rate, where a new Jacobian is assembled. We choose the parameters

$$\gamma_{nt} \in \{0, 0.2, 0.5\},$$

where $\gamma_{nt} = 0$ corresponds to the exact Newton method with a new Jacobian in every step. Quadratic convergence should be reached.

In Fig. 5.7, we show the number of Newton steps required in every time step. Furthermore, we show the assembly-count of the Jacobian. Finally, we indicate the overall number of Jacobians and the overall computational time spend in the complete cycle $I = [5, 5.5]$.

All computations in this section are carried out on a Intel Xeon X5650 cpu using single core performance at 2.67 GHz. It can be seen that the number of Newton steps undergoes a certain periodicity. This is directly connected to the oscillation of the solution itself, see Fig. 5.6. Given a large deformation $\mathbf{u}$, the ALE-mapping has a significant nonlinear impact.

We observe that the number of required Newton steps increases, if the threshold γ_{nt} is enlarged. For the pure Newton scheme, a maximum of 7 steps is required, whereas for $\gamma_{nt} = 1$ a maximum of 15 steps is used. However, a smaller choice of γ_{nt} calls for a higher number of Jacobians to be assembled. For $\gamma_{nt} = 0$, a new Jacobian is assembled in every single step of the Newton iteration. Considering the computational time, this is a severe drawback as can be seen in the bottom plot of Fig. 5.7. Here, the cost for assembling matrix and setting up the decomposition for the direct solver is so high that the overall computational time is best for the choice $\gamma_{nt} = 0.5$. In the table below Fig. 5.7 we indicate the accumulated time for all time steps in the interval $I = [5, 5.5]$. Choosing $\gamma_{nt} = 0.2$ saves about 22% of

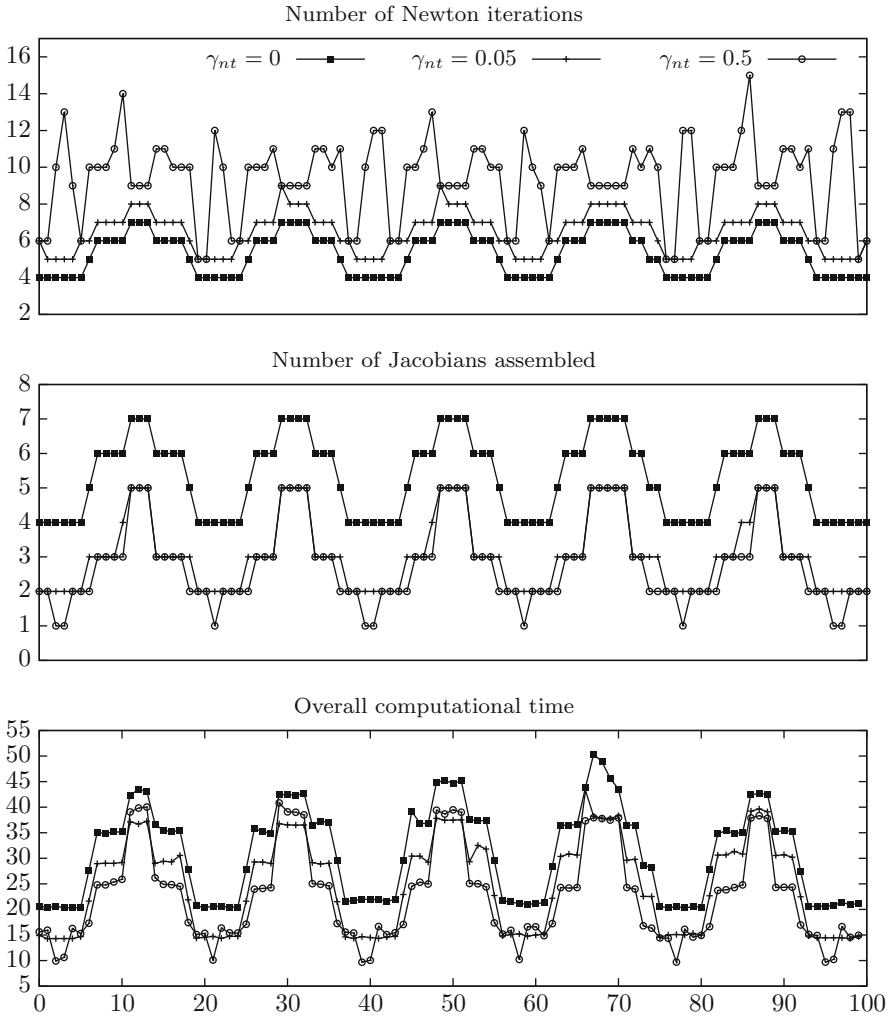

Matrix assembly tolerance γ_{nt}	0.0	0.2	0.5
Total Newton steps	532	777	938
Jacobians assembled	532	304	280
Total time (seconds)	3 099	2 388	2 250

Fig. 5.7 Comparison of the Newton iteration for different values of γ_{nt}, controlling the convergence-rate threshold, where a new Jacobian is assembled. The table shows the accumulated number of Newton steps, assemblies of the Jacobian and the total time (in seconds) for all 100 time steps

the computational time compared to $\gamma_{nt} = 0$ which corresponds to the full Newton method. The choice $\gamma_{nt} = 0.5$ increases the savings to 27%. This result however cannot be generalized, as a more efficient linear solver will have less overhead. Furthermore, increasing the effect of the nonlinearity, a too large value of γ_{nt} could severely increase the iteration count.

Next, in Fig. 5.8, we show the results for an approximation of the Jacobian by finite differences, i.e.

$$\frac{d}{ds}A(\mathbf{U} + s\mathbf{W})(\Phi)\Big|_{s=0} = \frac{A(\mathbf{U} + \varepsilon\mathbf{W})(\Phi) - A(\mathbf{U})(\Phi)}{\varepsilon} + \mathcal{O}(\varepsilon).$$

Approximation of the Jacobian by finite differences calls for multiple evaluations of the residual. First, we must compute

$$\mathcal{R}_0 = A(\mathbf{U})(\Phi),$$

then, we compute the directional derivatives with respect to the different components of velocity, deformation and pressure, i.e.

$$\mathcal{R}_{\mathbf{v}_i} = A(\mathbf{U} + \varepsilon\mathbf{z}_i)(\Phi), \quad \mathcal{R}_{\mathbf{u}_i} = A(\mathbf{U} + \varepsilon\mathbf{w}_i)(\Phi), \quad \mathcal{R}_p = A(\mathbf{U} + \varepsilon q)(\Phi),$$

for $i = 1, \ldots, d$. Altogether, 6 residual evaluations are required in 2d and 9 in 3d. By using a central difference approximation, this effort is even increased. The step size has to be chosen with care. For $\varepsilon = 10^{-6}$ we get a Newton-convergence that is comparable to the analytical evaluation of the Jacobian, see Fig. 5.8. However both for larger and smaller values of ε, the approximation quality worsens, such that a significant overhead appears. For $\varepsilon = 10^{-9}$, the approximation is governed by numerical cancellation effects. We have chosen $\gamma_{nt} = 0.2$ in all three cases. Comparing the summed values for the number of Newton steps and the number of Jacobian assemblies we see that the choice $\varepsilon = 10^{-6}$ leads to similar results compared to the table in Fig. 5.7 in the case $\gamma_{nt} = 0.2$. However, it turns out that using a finite difference approximation is more costly. Even if the Jacobian is so accurate that the Newton convergence is the same as in the case of an analytical Jacobian, the overall computational time is higher. If the finite difference parameter ε is not optimally chosen, the overall time can dramatically increase.

In Fig. 5.9 we directly compare the finite difference approximation to the analytical Jacobian. The number of Newton steps is about the same, the computational time for the difference approximation however is larger. This is due to the increased cost for the assembly of one single Jacobian. On a mesh with about 4000 unknowns, it took an average of about $t_J \approx 6.2\,\mathrm{s}$ to approximate the Jacobian with finite differences versus only $t_J \approx 1.5\,\mathrm{s}$, if the analytic derivation of the derivatives is used.

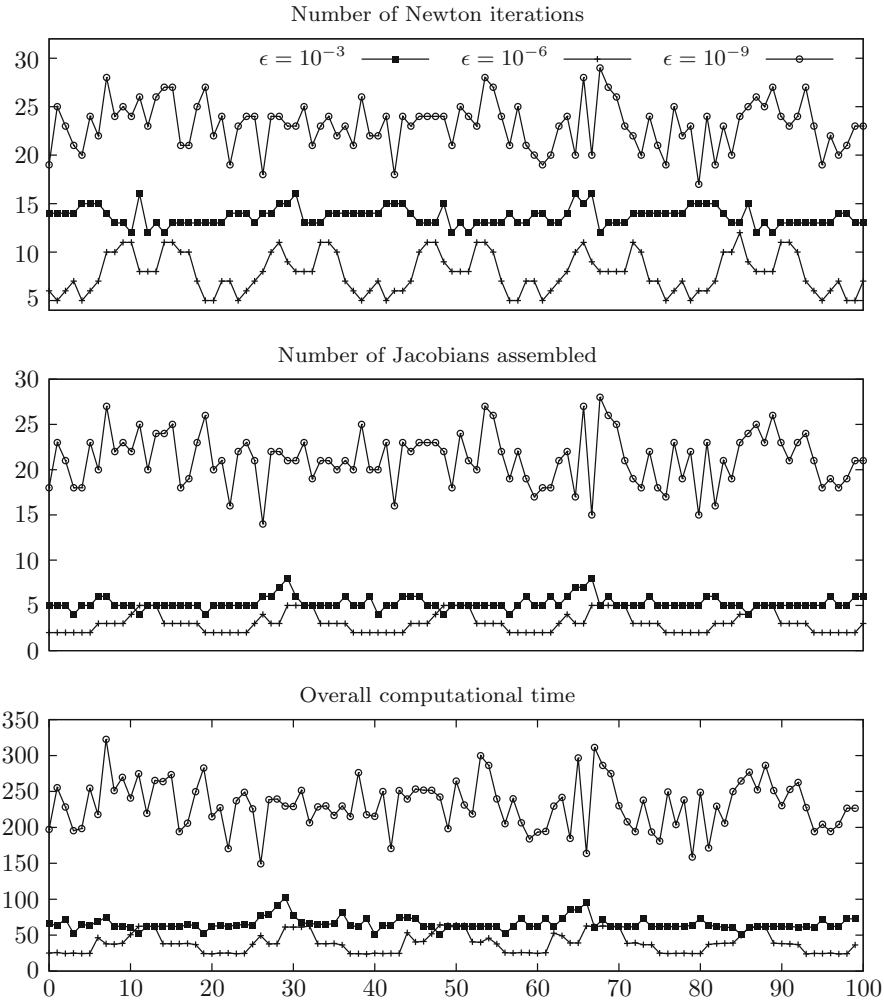

Finite difference parameter ε	10^{-3}	10^{-6}	10^{-9}
Total Newton steps	1 366	786	2 313
Jacobians assembled	525	307	2 121
Total time (seconds)	6 561	3 885	23 171

Fig. 5.8 Comparison of the Newton iteration with finite different approximation of the Jacobian $A'(\mathbf{U})(\Phi) \approx \varepsilon^{-1}(A(\mathbf{U} + \varepsilon\mathbf{W})(\Phi) - A(\mathbf{U})(\Phi))$. Different values of the step-size ε. The table shows the accumulated number of Newton steps, assemblies of the Jacobian and the total time (in seconds) for all 100 time steps

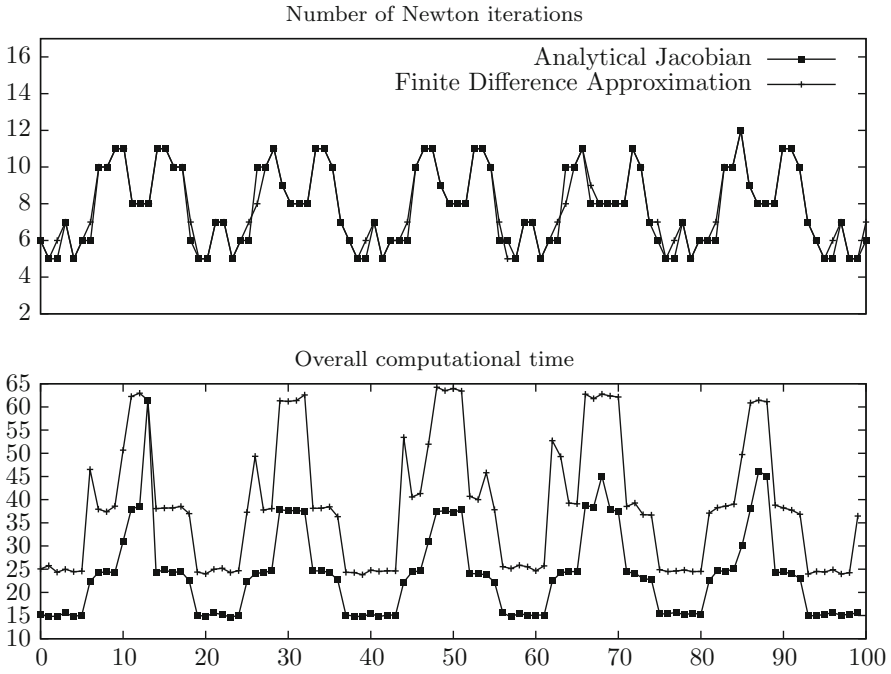

Fig. 5.9 Comparison of the Newton iteration with analytical and finite difference approximation of the Jacobian (using step-size $\varepsilon = 10^{-6}$)

We note that we used a direct solver for these calculations. On the present mesh, the time for decomposing the matrix is about 5 s in both cases, analytic evaluation and finite difference approximation.

Finally, we consider an inexact version of the Newton method, where the very costly derivatives with respect to the ALE mapping are neglected. In Fig. 5.10 we compare the Newton iteration considering a full Jacobian with the Newton iteration using the reduced Jacobian. We show the iteration count and the overall time spent in every Newton iteration. We observe that the reduced Jacobian yields a slightly larger iteration count. The overall time is reduced, as the assembly of each Jacobian takes only 1.25 s instead of 1.5 s for the full variant. Again we note that the effect would be stronger, if a more efficient linear solver is used.

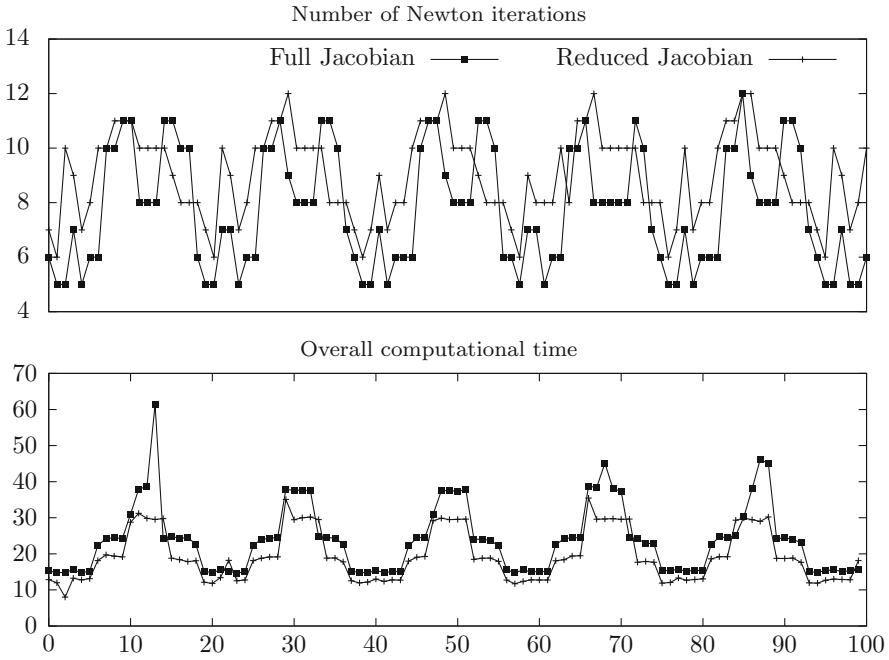

Jacobian approximation	full	approximated
Total Newton steps	777	902
Jacobians assembled	304	318
Total time (seconds)	2 388	1 937

Fig. 5.10 Comparison of the Newton iteration with full and reduced Jacobian. The table shows the accumulated number of Newton steps and Jacobian assembles as well as the computational time (in seconds) for all 100 time steps

5.3 Finite Elements for Fluid-structure Interactions in ALE Formulation

Every step of the Newton iteration requires the solution of a linear system of partial differential equations, compare (5.19)

$$\mathcal{W}^{(l)} := \{\mathbf{z}^{(l)}, \mathbf{w}^{(l)}, q_f^{(l)}\} \in \mathcal{X} := \mathcal{V} \times \mathcal{W} \times \mathcal{L}_f :$$
$$A'(\mathbf{U}^{(l-1)})(\mathbf{W}^{(l)}, \Phi) = G(\Phi)$$
$$\forall \Phi := \{\phi, \psi_f, \psi_s, \xi_f\} \in \mathcal{V} \times \mathcal{W}_f \times \mathcal{L}_s \times \mathcal{L}_f.$$

In the context of the backward Euler discretization of fluid-structure interactions on a fixed ALE domain, the bilinear-form $A'(\mathbf{U})(\cdot,\cdot)$ is given as in Theorem 5.2. The right hand side is given by

$$G(\Phi) := F(\Phi) - A(\mathbf{U}^{(l-1)})(\Phi),$$

where $\mathbf{U}^{(l-1)}$ is the last Newton approximation and $A(\mathbf{U}^{(l-1)})(\Phi)$ and $F(\Phi)$ are shown in (5.10) and (5.11). Trial spaces for velocity and deformation are defined on the whole domain

$$\mathcal{V} := H_0^1(\Omega;\Gamma^D)^d, \quad \mathcal{W} := H_0^1(\Omega;\partial\Omega)^d,$$

and differ in the choice of boundary values only. See Sect. 3.4 for a discussion.

The test function $\phi \in \mathcal{V}$ for both momentum equations is also defined on the complete domain Ω. All further test functions are defined sub-domain wise

$$\mathcal{L}_f := L^2(\mathcal{F}), \quad \mathcal{W}_f := H_0^1(\mathcal{F})^d, \quad \mathcal{L}_s := L^2(\mathcal{S})^d.$$

In the following, we will focus on the finite element discretization of these linear systems

$$\mathbf{W} \in \mathcal{X}: \quad A(\mathbf{W},\Phi) = G(\Phi) \quad \forall \Phi \in \mathcal{Y}, \tag{5.21}$$

where $A(\cdot,\cdot)$ is bilinear on $\mathcal{X}\times\mathcal{Y}$. Discretization is accomplished by restricting solution and test function to discrete spaces

$$\mathbf{W}_h \in X_h: \quad A(\mathbf{W}_h,\Phi_h) + S_h(\mathbf{W}_h,\Phi_h) = G(\Phi_h) \quad \forall \Phi \in Y_h, \tag{5.22}$$

where $S_h(\cdot,\cdot)$ defines some possible stabilization terms, see Sects. 4.3.2 and 4.4.3.

Remark 5.8 (Properties of Finite Element Spaces) For the choice of finite element spaces X_h and Y_h must consider the following properties

1. For a conforming (Petrov)-Galerkin formulation it must hold $X_h \subset \mathcal{X}$ and $Y_h \subset \mathcal{Y}$.
2. The dimension of test and trial spaces must coincide

$$\dim X_h = \dim Y_h.$$

3. The velocity- and pressure-coupling $\{\mathbf{v}_h, p_h\}$ within the fluid-domain must satisfy the inf-sup condition. Otherwise, the variational formulation has to be enriched by stabilization terms $S_h(\cdot,\cdot)$, see Sect. 4.3.2.
4. For implementation reasons, it is preferable to consider finite element spaces for velocity and deformation of the same type on $\mathcal{F}$ and $\mathcal{S}$.

5. As global velocity and deformation are continuous on the complete domain Ω, but not differentiable across the interface $\mathcal{I}$, it is preferable, if the interface is resolved by the triangulation. Otherwise, the order of convergence will be reduced, see Sect. 4.5, unless special manners are taken.

In the following we will discuss different choices of finite element triples for velocity, deformation and pressure. Besides conforming finite element spaces with continuous velocities and deformations the choice of discontinuous Galerkin methods is possible and also applied in the context of fluid-structure interactions, see Feistauer and coworkers [138].

5.3.1 *Finite Element Triangulations for Fluid-structure Interactions in ALE Formulation*

The benefit of the formulation in Arbitrary Lagrangian Eulerian coordinates is the fixation of the sub-domains $\mathcal{F}$ and $\mathcal{S}$, separated by the interface $\mathcal{I}$. We define:

Definition 5.9 (Matching Mesh) A triangulation Ω_h of the domain Ω is called a *matching mesh*, if for every element $K \in \Omega_h$ it holds

$$\Big(K \subset \mathcal{S} \ \wedge \ K \cap \mathcal{F} = \emptyset\Big) \vee \Big(K \subset \mathcal{F} \ \wedge \ K \cap \mathcal{S} = \emptyset\Big).$$

For a matching triangulation, we define the sub-triangulations

$$\Omega_{h,f} := \{K \in \Omega_h \mid K \subset \mathcal{F}\}, \quad \Omega_{h,s} := \{K \in \Omega_h \mid K \subset \mathcal{S}\}.$$

This definition implies that a matching mesh always resolves the interface $\mathcal{I}$ between fluid and solid by edges of elements, such that we can define

$$\mathcal{I}_h := \{e \in \partial K, \ K \in \Omega_h, \ e \in \mathcal{I}\},$$

and it holds

$$\bar{\mathcal{I}} = \bigcup_{e \in \mathcal{I}_h} \bar{e}.$$

This directly shows that matching meshes in this strict sense are only possible, if the interface $\mathcal{I}$ (in reference coordinates) is a polygonal, or if the interface can be described by low order polynomials, and if a parametric finite element triangulation is considered, see Definition 4.17. Here, we will always assume that all finite element meshes are matching.

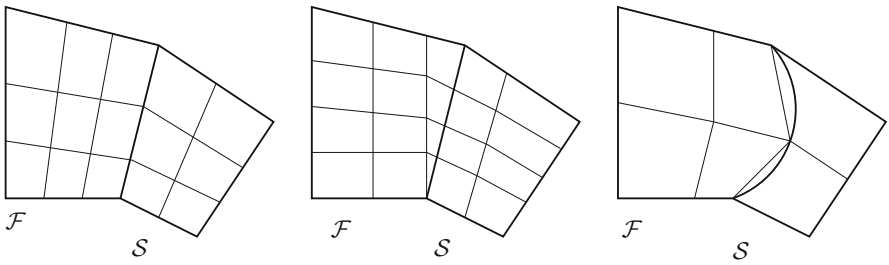

Fig. 5.11 Example of a matching mesh (*left*) and non-matching mesh (*middle*). The *right sketch* shows a generalized matching mesh at a curved interface. See Remark 5.10

Remark 5.10 (Approximation of Curved Interfaces) If the interface between fluid and solid is curved, such that it cannot be exactly resolved by the mesh, the strict definition of matching meshes is not applicable and will be relaxed: we will call a mesh matching, if all degrees of freedom used to define the parametric triangulation (see Definition 4.17) are either all part of the solid-domain $\bar{\mathcal{S}}$ or all part of the fluid-domain $\bar{\mathcal{F}}$. See Fig. 5.11 for examples of matching and non-matching triangulations.

In the finite element error analysis, the consideration of curved interfaces that cannot be resolved by the mesh (and hence not by the finite element spaces) is still an open problem.

It is not strictly required that one uses matching meshes for discretizing fluid-structure interactions. The use of matching meshes just simplifies the embedding of the coupling conditions, as we can define global function spaces V_h and W_h for velocity, deformation and the momentum equation's test function and restrict these global functions to the two sub-domains. By this approach, coupling will turn out to be as simple as in the continuous case, see Sect. 3.4.

Lemma 5.11 (Finite Elements Spaces on Matching Meshes) *Let Ω_h be a matching mesh of the domain Ω and V_h the standard space of continuous elements of degree $r \geq 1$ with Lagrangian basis $V_h = \text{span}\{\phi_h^{(i)},\ i = 1, \ldots, N\}$, e.g.*

$$\phi_h^{(i)}(x_j) = \delta_{ij},\ i, j \in \{1, \ldots, N\}.$$

See Sect. 4.2.1. The subspaces

$$V_{h,f} := \text{span}\{\phi_h^{(i)} \in V_h,\ x_i \in \bar{\mathcal{F}} \setminus \mathcal{I}\},$$
$$V_{h,s} := \text{span}\{\phi_h^{(i)} \in V_h,\ x_i \in \bar{\mathcal{S}}\},$$

define a division of V_h,

$$V_h = V_{h,f} + V_{h,s}, \quad \dim V_h = \dim V_{h,f} + \dim V_{h,s}. \tag{5.23}$$

The space $V_{h,f}$ is $H_0^1(\mathcal{F};\mathcal{I})$ conforming, the space $V_{h,s}$ is $H^1(\mathcal{S})$-conforming.

Proof For $\phi_h^{(i)}$ with $x_i \in \bar{\mathcal{F}}$, but $x_i \notin \mathcal{I}$, it holds on matching triangulations that

$$\text{supp } \phi_h^{(i)} \in \mathcal{F}.$$

Hence, $V_{h,f} \subset H_0^1(\mathcal{F};\mathcal{I})$. The relation $V_{h,s} \subset H^1(\mathcal{S})$ directly follows due to the continuity of $V_h \subset C(\bar{\Omega})$. Further, the dimension formula (5.23) follows, as the partitioning of Lagrange points $x_i \in \Omega_h$ to those on the interior of solid and fluid and those on the interface is unique. □

This lemma appears trivial, but it is essential for the following approach: if a global finite element function $\mathbf{v}_h \in V_h$ is given, we can define restrictions $\mathbf{v}_{h,f} \in V_{h,f}$ and $\mathbf{v}_{h,s} \in V_{h,s}$ in the two subspaces. This allows us to hide the coupling conditions in global trial and test spaces.

5.3.2 Inf-Sup Stable FE-Spaces for Fluid-structure Interactions in ALE Formulation

We will start by introducing some finite element triples (for velocity, deformation and pressure) that fulfill as many of the desirable properties from Remark 5.8. Let Ω_h be a matching triangulation. We will denote the velocity space by

$$\mathbf{v}_h \in V_h,$$

and the global deformation space by

$$\mathbf{u}_h \in W_h.$$

On the two sup-domains of the matching triangulation, we define the restrictions $\mathbf{v}_{h,f}, \mathbf{v}_{h,s}$ and $\mathbf{u}_{h,f}, \mathbf{u}_{h,s}$. We will denote the discrete pressure space by $L_{h,f}$.

As discussed in Sect. 4.3, the fluid's finite element pair for velocity $V_{h,f}$ and pressure $L_{h,f}$ must satisfy the inf-sup condition (in ALE coordinates):

$$\inf_{p_h \in L_{h,f}} \sup_{\mathbf{v}_h \in V_{h,f}} \frac{(p_h, \operatorname{div}(J_f \mathbf{F}_f^{-1} \mathbf{v}_h))_{\mathcal{F}}}{\|J_f^{\frac{1}{2}} p_h\|_{\mathcal{F}} \|J_f^{\frac{1}{2}} \nabla \mathbf{v}_h \mathbf{F}_f^{-T}\|_{\mathcal{F}}} \geq \hat{\gamma}_h. \tag{5.24}$$

where $\mathbf{F}_f$ and $J = \det \mathbf{F}_f$ come from the ALE-map. In terms of a computational finite element approach, the ALE-map is not a continuous, regular function, but itself defined by means of finite element functions

$$\mathbf{F}_h := I + \nabla \mathbf{u}_h, \quad J_h := \det \mathbf{F}_h.$$

In the following we will skip the index "h". The discussion of Sect. 2.5.2 has shown that the inf-sup condition in ALE formulation (5.24) is equivalent to the standard version of the inf-sup condition on the reference domains,

$$\inf_{p_h \in L_{h,f}} \sup_{\mathbf{v}_h \in V_{h,f}} \frac{(p_h, \operatorname{div} \mathbf{v}_h)_{\mathcal{F}}}{\|p_h\|_{\mathcal{F}} \|\nabla \mathbf{v}_h\|_{\mathcal{F}}} \geq \gamma, \tag{5.25}$$

if the domain mapping sufficiently regular. The two inf-sup constants however can significantly differ,

$$0 < \hat{\gamma} \ll \gamma,$$

if the deformation of the domain is large. An analysis of the inf-sup condition on transformed domains is given in [247]. By these considerations, we suggest the following choices of finite element triples for velocity, deformation and pressure. See also Fig. 5.12:

1. The generalized Taylor-Hood space

$$[Q^k]^d \times [Q^k]^d \times Q^{k-1}, \quad k \geq 2,$$

on quadrilateral meshes and

$$[P^2]^d \times [P^2]^d \times P^1, \quad [P^k]^d \times [P^k]^d \times P^{k-2}, \quad k \geq 3,$$

on triangular meshes. These spaces are inf-sup stable. Further, they have the simple property that deformation and velocity come from the same space. Finally, velocity and deformation spaces are the same on both parts of the domain.

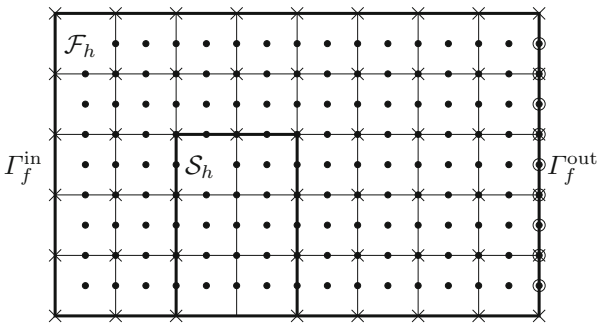

Fig. 5.12 The $Q^2-Q^2-Q^1$ finite element triple for velocity, deformation and pressure. By a *cross symbol* we denote pressure degrees of freedom and by *filled dot* degrees of freedom in velocity and deformation. By a *circled dot* we denote velocity degrees of freedom on the outflow boundary, where no deformation degree of freedom exists

2. The generalized Taylor-Hood spaces with discontinuous pressure

$$[Q^k]^d \times [Q^k]^d \times P^{k-1,dc}, \quad k \geq 2,$$

on quadrilateral meshes and the bulb-enriched space

$$[P^{2,bulb}]^d \times [P^2]^d \times P^{1,dc},$$

on triangular meshes. These two combinations have the same properties as the Taylor-Hood elements. Applications usually shows better solution quality (in particular on coarse meshes) due to local conservation properties that come from the use of discontinuous pressures.

Another advantage comes to the fore, if incompressible materials are considered, see Sect. 2.2.3. These material laws require the introduction of a second pressure variable $p_s \in L^2(\mathcal{S})$. As there is no physical reason for continuity of the two pressures p_f and p_s at the interface $\mathcal{I}$, the two discrete variables must be separated. Using continuous finite elements, this would cause technical problems, as there is only one Lagrange point on the interface. As the discontinuous space $P^{k-1,dc}$ is defined in an element-wise manner, implementation is simplified. We can define one global pressure $p_h \in L_h$ and define fluid- and solid-pressure as restrictions:

$$p_{h,f} = p_h\Big|_{\mathcal{F}}, \quad p_{h,s} = p_h\Big|_{\mathcal{S}}.$$

For the definition of the test spaces, we need to pay special attention to the interface. While velocity and deformation are defined in a global way, only the test space $\phi \in \mathcal{V}$ for the momentum equation is defined on the complete domain Ω. The test functions for extension of the deformation $\psi_f \in \mathcal{W}_f$ as well as the test space for the deformation-velocity relation $\psi_s \in \mathcal{L}_s$ must be decoupled at the interface. Based on the second (just as example) choices of finite element spaces, we define

$$\begin{aligned}
V_h &:= \text{span}\{\phi_h \in C(\Omega)^d,\ \phi_h^{(i)} \text{ piece-wise quadratic},\ \phi_h = 0 \text{ on } \Gamma^D\},\\
W_h &:= \text{span}\{\phi_h \in C(\Omega)^d,\ \phi_h^{(i)} \text{ piece-wise quadratic } \phi_h = 0 \text{ on } \partial\Omega\},\\
L_{h,f} &:= \text{span}\{\xi_h \in L^2(\mathcal{F}),\ \xi_h^{(i)} \text{ piece-wise linear}\},\\
W_{f,h} &:= \text{span}\{\phi_h \in C(\mathcal{F})^d,\ \phi_h^{(i)} \text{ piece-wise quadratic } \phi_h = 0 \text{ on } \partial\mathcal{F}\}\\
L_{s,h} &:= \text{span}\{\phi_h \in C(\mathcal{S})^d,\ \phi_h^{(i)} \text{ piece-wise quadratic}\}.
\end{aligned} \tag{5.26}$$

With this construction of finite element spaces, we can define a well-posed discrete finite element approximation of the backward-Euler discretization for fluid-structure interactions in Arbitrary Lagrangian Eulerian coordinates:

Problem 5.12 (Finite Element Discretization of the fsi-System in ALE Formulation) *Let $A(\cdot,\cdot)$ be given by (5.10), $F(\cdot)$ by (5.11). The Jacobian $A(\mathbf{U})(\cdot,\cdot)$ is given by Theorem 5.2. Given the last discrete Newton approximation $\mathbf{U}_h^{(l-1)} \in X_h$, find*

$$\mathbf{W}_h^{(l)} := \{\mathbf{v}_h, \mathbf{u}_h, p_{f,h}\} \in X_h := V_h \times W_h \times L_{h,f},$$

such that

$$A'(\mathbf{U}_h^{(l-1)})(\mathbf{W}_h^{(l)}, \Phi_h) = F(\Phi_h) - A(\mathbf{U}_h^{(l-1)})(\Phi_h) \tag{5.27}$$

for all

$$\Phi_h := \{\phi_h, \psi_{h,f}, \psi_{h,s}, \xi_{h,f}\} \in Y_h := V_h \times W_{h,f} \times L_{h,s} \times L_{h,f}.$$

The Newton update problem in step (5.27) defines a linear system of equations. Chapter 7 will be devoted to the solution of this linear problem. First we note that for our choice of finite element spaces (5.26), the system of equations is quadratic, i.e., the number of unknowns equals the number of equations.

5.3.3 Stabilized Finite Elements for Fluid-structure Interactions

In Sect. 4.3.2, we have introduced concepts for stabilizing finite element pairs that do not satisfy the inf-sup condition. Here, we want to shortly apply this concept to the discretization of fluid-structure interactions. The basic idea was to either modify the test space by a Petrov-Galerkin approach, or to modify the variational formulation by adding stabilization terms $S_h(\cdot,\cdot)$. This latter approach is more general and also covers Petrov-Galerkin discretizations. We shortly discuss the very simple case of the non-conforming pressure stabilization used in Lemma 4.47. The linearized discrete variational formulation is enriched by a pressure stabilization term

$$A_h'(\mathbf{U}_h)(\mathbf{W}_h, \Phi_h) := A(\mathbf{U}_h)(\mathbf{W}_h, \Phi_h) + S_h(\mathbf{W}_h, \Phi_h).$$

For the proper definition of pressure stabilization in Arbitrary Lagrangian Eulerian formulation, we must transfer the standard method from Eulerian coordinates to the fixed reference system. Hence, let—just for the following discussion—$\hat{\mathcal{F}}$ be the reference fluid domain and $\mathcal{F}$ be the current Eulerian fluid-domain in the current time step. Then, the pressure stabilization term in Eulerian coordinates on $\mathcal{F}$ was defined as

$$S_h(\mathbf{U}_h, \Phi_h) := (\alpha_{\text{stab}} \nabla p_h, \nabla \xi_h)_{\mathcal{F}}, \tag{5.28}$$

with an element-wise defined stabilization parameter

$$\alpha_{\text{stab}}\Big|_K = \alpha_0 \left(\frac{\nu_f}{h_K^2} + \frac{\|\mathbf{v}\|_{L^\infty(K)}}{h_K} \right),$$

see Sect. 4.3.2. The mesh-size h_K would be the mesh-size of a Eulerian mesh. The first detail that has to be analyzed in the context of Arbitrary Lagrangian formulations is the concept of the mesh-size h_K. Usually, for shape-regular triangulations (see Definition 4.18), we can define the mesh-size of the triangulation $\hat{\Omega}_h$ of the reference domain $\hat{\mathcal{F}}$ as

$$\hat{h}_K := \operatorname{diam}(K). \tag{5.29}$$

Another suitable definition is to define the mesh-size as an integral value

$$\hat{h}'_K := \left(\int_K 1 \, \mathrm{d}x \right)^{\frac{1}{d}}. \tag{5.30}$$

On shape-regular triangulations, there exists a constant $c > 0$, such that

$$c^{-1} h'_K \leq h_K \leq c h'_K \quad \forall \hat{K} \in \hat{\Omega}_h, \quad (h \to 0). \tag{5.31}$$

In the following, we will use definition (5.30) by integration. Now, let $T : \hat{K} \to K$ be the ALE map and $K := T(\hat{K})$ be the Eulerian counterpart of $\hat{K} \in \hat{\Omega}_h$. It holds

$$h_K := \left(\int_K 1 \, \mathrm{d}x \right)^{\frac{1}{d}} = \left(\int_{\hat{K}} J \, \mathrm{d}\hat{x} \right)^{\frac{1}{d}},$$

and we can estimate

$$\min_{\hat{x} \in \hat{K}} |J(\hat{x})|^{\frac{1}{d}} \hat{h}_K \leq h_k \leq \max_{\hat{K}} |J(\hat{x})|^{\frac{1}{d}} \hat{h}_K. \tag{5.32}$$

Using this relation between Eulerian and reference mesh size, the stabilization term (5.28) can be transformed in ALE coordinates

$$S_h(\hat{\mathbf{U}}_h, \hat{\Phi}_h) = (\alpha_{\text{stab}} J \mathbf{F}^{-1} \mathbf{F}^{-T} \nabla p_h, \nabla \xi_h)_{\hat{\mathcal{F}}}.$$

with a stabilization parameter α_{stab} defined on $\hat{\mathcal{F}}$ as

$$\alpha_{\text{stab}} = \alpha_0 \left(\frac{\nu_f J^{\frac{2}{d}}}{\hat{h}_K^2} + \frac{\|\hat{\mathbf{v}}\|_{L^2(\hat{K})} J^{\frac{1}{d}}}{\hat{h}_K} \right)^{-1}.$$

If the deformation of the mesh is moderate, it holds $J \approx 1$ and $\mathbf{F} \approx I$. Then we can simply take the standard setting of the stabilization term (5.28) without any mapping.

This construction is also applicable for the stabilization by means of Local Projections as discussed in Lemma 4.49

$$S_{\text{lps}}(\hat{\mathbf{U}}_h, \hat{\Phi}_h) = \left(\alpha \mathbf{F}^{-1}\mathbf{F}^{-T}\nabla(p_h - \pi_h p_h), \nabla(\xi_h - \pi_h \xi_h)\right)_{\hat{\mathcal{F}}},$$

where $\pi_h : Q_h \to \tilde{Q}_h$ is the local coarse mesh projection operator. As in the Eulerian setting, the LPS method will give optimal order of convergence, if the spaces $\tilde{Q}_h$ and Q_h are well chosen, as weak consistency holds

$$p_h \in \tilde{Q}_h \quad \Rightarrow \quad S_{\text{lps}}(p_h, \xi_h) = 0 \quad \forall \xi_h \in Q_h.$$

In the case of residual based stabilization techniques like PSPG (or SUPG), the correct application to the Arbitrary Eulerian Lagrangian formulation is more difficult. The success of these techniques is based on a consistent formulation. If $\mathbf{U} \in \mathcal{X}$ is the solution, it should hold

$$S_{\text{PSPG}}(\mathbf{U}, \Phi_h) = 0 \quad \forall \Phi_h \in X_h.$$

This is realized by testing the complete momentum equation of the fluid system (compare the Jacobian in Theorem 5.2) with the modified test function

$$\tilde{\phi}_h := \phi_h + \alpha \nabla \xi_h.$$

Such a combination gives rise to complex coupled terms including the complete strong residual. For a discussion on a practical way of applying residual based stabilization techniques to fsi-problems in Arbitrary Lagrangian Eulerian coordinates, we refer to Wall [339].

Remark 5.13 (Stabilization for Large Deformations) As long as the deformation of the domain is small and motion of the domains is slow, we can apply all stabilization techniques without any modification and just omit the ALE mapping. This does not hold true, if the deformation is very large, i.e., if $J \ll 1$ or $J \gg 1$ or if $\mathbf{F}$ significantly differs from the identity I. As long as the ALE mapping is isotropic, we only need to adjust the mesh size by means of relation (5.32). If the mapping however inhibits very strong anisotropies, the concept of stabilization must be altered. In particular, it will be necessary to separate directions. On a Eulerian, Cartesian anisotropic mesh, the simple pressure stabilization term in the case of the linear Stokes equations must be constructed as:

$$S_{h,\text{aniso}}(\mathbf{U}_h, \Phi_h) = (\alpha_0 h_x^2 \partial_x p_h, \partial_x \xi_h)_{\mathcal{F}} + (\alpha_0 h_y^2 \partial_y p_h, \partial_y \xi_h)_{\mathcal{F}}.$$

For a detailed analysis of the Local Projection stabilization on anisotropic meshes, we refer to the Literature [58, 62, 277, 278] and in particular Molnar [247] in the case of fluid-structure interactions.

Besides stabilization of the pressure-velocity coupling, we need to take care of problems with dominant convection that require stabilization of transport oscillations. Here, we can follow the same procedure: starting with a stabilization technique in Eulerian coordinate, we map the resulting stabilization terms back to the reference framework. Again, all methods work very well without modifications, if small deformations are considered. Only the case of very large deformation with substantial anisotropies is still open. See [247, 339].

Apart from the natural convection, ALE formulations include the additional transport term

$$-\left(\rho_f J\mathbf{F}^{-1}\partial_t\mathbf{u}_f\cdot\nabla\mathbf{v},\phi\right)_{\mathcal{F}},$$

coming from the ALE time derivative. This term may call for stabilization, if the domain moves rapidly. Stabilization of this part can be handled like the natural convection by simply considering a combined effective transport velocity

$$\left(\rho_f J\mathbf{F}^{-1}\left(\mathbf{v}_f-\partial_t\mathbf{u}_f\right)\cdot\nabla\mathbf{v},\phi\right)_{\mathcal{F}},$$

5.3.4 Matrix Formulation of the Linear Systems

A finite element discretization of the linearized system to be solved in every step of the Newton iteration

$$\mathbf{W}_h\in X_h\quad A'(\mathbf{U}_h)(\mathbf{W}_h,\Phi_h)=F(\Phi_h)-A(\mathbf{U}_h)(\Phi_h)\quad\forall\Phi_h\in Y_h \tag{5.33}$$

gives rise to a large linear system of equations that can be compactly written in the form

$$\mathbf{A}_h\mathbf{x}_h=\mathbf{b}_h.$$

In this section, we will give details on the derivation and resulting structure of the system matrix. The exact form of the matrix will depend on the choice of finite element spaces. For the following discussion we make further assumptions on the finite element spaces:

- First, we assume that the triangulation is matching the domain-partitioning.
- We assume that both fluid and solid problem are given with Dirichlet conditions on the outer boundaries of the domain. In this case, it holds $\mathcal{V}=\mathcal{W}$ and it will also hold (in terms of (5.26)) that $V_h=W_h$.

- We consider inf-sup stable finite elements, such that no pressure-stabilization is required.
- We choose equal-order finite element spaces for velocity $\mathcal{V}$ and deformation $\mathcal{W}$, as well as for the test function of momentum equations $\mathcal{V}$, ALE extension $\mathcal{W}_f$ and deformation-velocity relation $\mathcal{L}_s$. All these discrete spaces are based on the same set of matrix-functions.

By these assumptions, let V_h be the space of continuous finite elements on the complete domain Ω_h of degree $r \geq 2$ with strong Dirichlet-values on the complete boundary $\partial\Omega_h$. The Lagrangian nodal basis is given by

$$V_h := \text{span}\{\phi_h^{(i)},\ i = 1, \ldots, N\}.$$

Discrete velocity update and deformation update are given by

$$\mathbf{z}_h(x) = \sum_{i=1}^{N} \mathbf{z}_i \phi_h^{(i)}(x), \quad \mathbf{w}_h(x) = \sum_{i=1}^{N} \mathbf{w}_i \phi_h^{(i)}(x).$$

We define the following subsets of indices that collect all basis functions with support in the fluid, in the solid and those that touch the interface

$$\begin{aligned} I_f &:= \{i \in \{1, \ldots, N\} \mid \text{supp}(\phi_h^{(i)}) \subset \mathcal{F}\}, \quad N_f := \#I_f, \\ I_s &:= \{i \in \{1, \ldots, N\} \mid \text{supp}(\phi_h^{(i)}) \subset \mathcal{S}\}, \quad N_s := \#I_s, \\ I_i &:= \{1, \ldots, N\} \setminus (I_f \cup I_s), \quad N_i := \#I_i. \end{aligned}$$

Then, the test space of the ALE-extension is given by

$$W_{h,f} := \text{span}\{\phi_h^{(i)},\ i \in I_f\},$$

and the test space of the deformation-velocity coupling by

$$W_{h,s} := \text{span}\{\phi_h^{(i)},\ i \in I_s \cup I_i\}.$$

Finally, the pressure-space $L_{h,f}$ is given by

$$L_{h,f} = \text{span}\{\xi_h^{(i)},\ i = 1, \ldots, N_p\}.$$

By $\xi_h^{(i)}$ a basis of either a lower-degree continuous space (e.g. $r-1$ on quadrilaterals), or some discontinuous space can be given. The pressure update is given by

$$q_{h,f}(x) = \sum_{i=1}^{N_p} \mathbf{q}_i \xi_h^{(i)}(x).$$

By insertion of these basis representations in (5.33), we derive the matrix formulation of the linear system. This matrix has a block-structure on multiple levels. First, parts of the equation act on the fluid-domain, parts on the solid-domain. Second, we get a natural block-structure due to the coupled equations: momentum equation of Navier-Stokes *(NS)*, divergence condition in the Navier-Stokes equations *(div)*, equation for the extension of the ALE map *(ALE)*, momentum equation of the elastic solid *(ES)* and finally, relation between deformation and velocity *(uv)*. Each of these equations appears in the Jacobian and may appear multiple times. The momentum part of the Navier-Stokes equations *(NS)* has directional derivatives with respect to the pressure, the velocity and the deformation. We will use this terminology to denote the sub-matrices and explain this procedure based on the Navier-Stokes momentum equations including the derivatives with respect to pressure and velocity:

$$
\begin{aligned}
[F_p^{NS}]_{ij} &= -\left(J\mathbf{F}^{-T}\xi_{h,f}^{(j)}, \phi_h^{(i)}\right)_{\mathcal{F}} \\
&\qquad \forall i \in I_f \cup I_i, \quad \forall j \in \{1, \ldots, N_p\} \\
[F_{\mathbf{v}}^{NS}]_{ij} &= \left(\rho_f J\left(k^{-1}\tilde{\phi}_{h,f}^{(j)} + \nabla\tilde{\phi}_{h,f}^{(j)}\mathbf{F}^{-1}\left(\mathbf{v} - \frac{\mathbf{u} - \mathbf{u}^{\text{old}}}{k}\right)\right), \phi_h^{(i)}\right)_{\mathcal{F}} \\
&\quad + \left(\rho_f J\nabla\mathbf{v}\mathbf{F}^{-1}\tilde{\phi}_{h,f}^{(j)}, \phi_h^{(i)}\right)_{\mathcal{F}} \\
&\quad + \left(J\frac{d\boldsymbol{\sigma}_f}{d\mathbf{v}}(\mathbf{W})\mathbf{F}^{-T}, \nabla\phi\right)_{\mathcal{F}} - \left(J\mathbf{F}^{-T}q_f, \nabla\phi\right)_{\mathcal{F}} \\
&\qquad \forall i \in I_f \cup I_i, \quad \forall j \in I_f \cup I_i
\end{aligned}
$$

All the remaining parts are obtained in a similar way. Altogether, we get the following matrices for fluid- and solid-problem:

$$
\mathbf{F} = \begin{pmatrix} 0 & F_{\mathbf{v}}^{div} & F_{\mathbf{u}}^{div} \\ F_p^{NS} & F_{\mathbf{v}}^{NS} & F_{\mathbf{u}}^{NS} \\ 0 & 0 & F_{\mathbf{u}}^{ALE} \end{pmatrix}, \quad \mathbf{S} = \begin{pmatrix} S_{\mathbf{v}}^{ES} & S_{\mathbf{u}}^{ES} \\ S_{\mathbf{v}}^{uv} & S_{\mathbf{u}}^{uv} \end{pmatrix}, \tag{5.34}
$$

with

$$
\mathbf{F} \in \mathbb{R}^{(N_p+2N_f+2N_i)\times(N_p+2N_f+2N_i)}, \quad \mathbf{S} \in \mathbb{R}^{(2N_s+2N_i)\times(2N_s+2N_i)}.
$$

To assemble the coupled system matrix on the complete domain Ω, we must construct the sum of both parts. First, we define subsets of the coefficient vectors

$$
\mathbf{z} = \{\mathbf{z}_f, \mathbf{z}_i, \mathbf{z}_s\}, \quad \mathbf{w} = \{\mathbf{w}_f, \mathbf{w}_i, \mathbf{w}_s\},
$$

where $\mathbf{z}_f$, $\mathbf{z}_i$ and $\mathbf{z}_s$ denote only indices in I_f, I_i and I_s, respectively. The same splitting is applied to $\mathbf{w}$ and also to the test functions ϕ_h and ψ_h. By this definition, we can give a more detailed version of the two sub-matrices that distinguishes between degrees freedom within the domain and those on the interface

$$\mathbf{F}_h = \begin{bmatrix} \xi_{h,f} \\ \phi_{h,f} \\ \psi_{h,f} \\ \phi_{h,i} \\ \psi_{h,i} \end{bmatrix} \begin{pmatrix} 0 & F_{\mathbf{v}}^{div} & F_{\mathbf{u}}^{div} & F_{\mathbf{v}}^{div} & F_{\mathbf{u}}^{div} \\ F_p^{NS} & F_{\mathbf{v}}^{NS} & F_{\mathbf{u}}^{NS} & F_{\mathbf{v}}^{NS} & F_{\mathbf{u}}^{NS} \\ 0 & 0 & F_{\mathbf{u}}^{ALE} & 0 & F_{\mathbf{u}}^{ALE} \\ F_p^{NS} & F_{\mathbf{v}}^{NS} & F_{\mathbf{u}}^{NS} & F_{\mathbf{v}}^{NS} & F_{\mathbf{u}}^{NS} \\ 0 & 0 & 0 & 0 & 0 \end{pmatrix}$$

$$\mathbf{S}_h = \begin{bmatrix} \phi_{h,i} \\ \psi_{h,i} \\ \phi_{h,s} \\ \psi_{h,s} \end{bmatrix} \begin{pmatrix} S_{\mathbf{v}}^{ES} & S_{\mathbf{u}}^{ES} & S_{\mathbf{v}}^{ES} & S_{\mathbf{u}}^{ES} \\ S_{\mathbf{v}}^{uv} & S_{\mathbf{u}}^{uv} & S_{\mathbf{v}}^{uv} & S_{\mathbf{u}}^{uv} \\ S_{\mathbf{v}}^{ES} & S_{\mathbf{u}}^{ES} & S_{\mathbf{v}}^{ES} & S_{\mathbf{u}}^{ES} \\ S_{\mathbf{v}}^{uv} & S_{\mathbf{u}}^{uv} & S_{\mathbf{v}}^{uv} & S_{\mathbf{u}}^{uv} \end{pmatrix}$$

We note that the off-diagonal blocks that indicate couplings between interface degrees of freedom with those inside the fluid-domain are mainly zero, as only very few basis functions $\phi_{h,i}$ and $\phi_{h,f}$ have an overlapping support. The saddle-point structure of the Navier-Stokes equations is directly visible. Finally, we note that the test space for the ALE extension $W_{h,f}$ does not include test functions that live on the interface. This is the correct choice, as the ALE map is defined as an extension of the solid's deformation by using Dirichlet values. Nevertheless, this last row is included in $\mathbf{F}_h$ to yield a quadratic matrix.

Given this detailed description of the sub-matrices, we can formulation the coupled linear system of equations by the sum of the two sub-systems:

$$\mathbf{A} = \begin{pmatrix} F_p^{div} & F_{\mathbf{v}}^{div} & F_{\mathbf{u}}^{div} & F_p^{div} & F_{\mathbf{v}}^{div} & F_{\mathbf{u}}^{div} & 0 & 0 \\ F_p^{NS} & F_{\mathbf{v}}^{NS} & F_{\mathbf{u}}^{NS} & F_p^{NS} & F_{\mathbf{v}}^{NS} & F_{\mathbf{u}}^{NS} & 0 & 0 \\ 0 & 0 & F_{\mathbf{u}}^{ALE} & 0 & 0 & F_{\mathbf{u}}^{ALE} & 0 & 0 \\ F_p^{div} & F_{\mathbf{v}}^{div} & F_{\mathbf{u}}^{div} & F_p^{div} & F_{\mathbf{v}}^{div} & F_{\mathbf{u}}^{div} & 0 & 0 \\ F_p^{NS} & F_{\mathbf{v}}^{NS} & F_{\mathbf{u}}^{NS} & F_p^{NS} & F_{\mathbf{v}}^{NS} + S_{\mathbf{v}}^{ES} & F_{\mathbf{u}}^{NS} + S_{\mathbf{u}}^{ES} & S_{\mathbf{v}}^{ES} & S_{\mathbf{u}}^{ES} \\ 0 & 0 & 0 & 0 & S_{\mathbf{v}}^{uv} & S_{\mathbf{u}}^{uv} & S_{\mathbf{v}}^{uv} & S_{\mathbf{u}}^{uv} \\ 0 & 0 & 0 & 0 & S_{\mathbf{v}}^{ES} & S_{\mathbf{u}}^{ES} & S_{\mathbf{v}}^{ES} & S_{\mathbf{u}}^{ES} \\ 0 & 0 & 0 & 0 & S_{\mathbf{v}}^{uv} & S_{\mathbf{u}}^{uv} & S_{\mathbf{v}}^{uv} & S_{\mathbf{u}}^{uv} \end{pmatrix} \tag{5.35}$$

Again, we note that all the shaded matrix entries are very sparse. In every step of the Newton method we have to find the coefficient vector

$$\mathbf{x} = \left(\mathbf{q},\, \mathbf{z}_f,\, \mathbf{w}_f,\, \mathbf{z}_i,\, \mathbf{w}_i,\, \mathbf{z}_s,\, \mathbf{w}_s\right)^T \in \mathbb{R}^{N_p+2N_f+2N_i+2N_s},$$

subject to the linear system of equations

$$\mathbf{A}_h \mathbf{x} = \mathbf{b},$$

where $\mathbf{b}$ is the discrete right hand side, coming from the discretization of

$$G(\Phi) := F(\Phi) - A(\mathbf{U})(\Phi).$$

The system matrix $\mathbf{A}_h$ lacks all desirable properties like symmetry, positivity or diagonal dominance. Solution of these linear systems is a very difficult task. Application of direct solvers is problematic due to the immense dimension of the linear system. Furthermore, we will see in Chap. 7, that the condition number of the coupled matrix can be so bad that even modern direct solvers can fail.

5.3.5 *Construction of the ALE Map*

In this section, we demonstrate different ways of extending the solid deformation $\mathbf{u}_{h,s}$ from the interface to the fluid domain $\mathbf{u}_{h,f}$. Such an extension is the typical way for defining the ALE mapping by means of

$$T_{h,f}(x,t) := x + \mathbf{u}_{h,f}(x,t).$$

Here, we aim at a quantitative comparison of different mesh motion models. In Sect. 3.5.1, we have already discussed qualitative regularity restrictions that arise from different mesh motion models. Further computational overviews are given in the literature [342, 357].

We will analyze a simple numerical test case that gives rise to large rotations of an unsupported solid in a fluid domain. This rotation causes very large deformation of the fluid domain an poses severe challenges to the construction of the ALE map. We show the configuration of the geometry in Fig. 5.13a. We briefly detail the configuration. The initial domain partitioning is given as

$$\Omega = (-1,1)^2,\ \hat{\mathcal{S}} = \left(-\frac{1}{2},\frac{1}{2}\right) \times \left(-\frac{1}{8},\frac{1}{8}\right),\ \hat{\mathcal{F}} = \Omega \setminus \overline{\hat{\mathcal{S}}}.$$

The boundary $\Gamma = \partial\Omega$ consists of two inflow parts of width 0.5, Γ_1^{in} in the upper left corner and Γ_2^{in} in the lower right one. Here we prescribe a Dirichlet condition for the velocity

$$\mathbf{v}_i^{\text{in}}(x,y,t) = 4\alpha(t)(x - x_i^0)(x - x_i^1)\mathbf{n}_i \text{ on } \Gamma_i^{\text{in}},$$

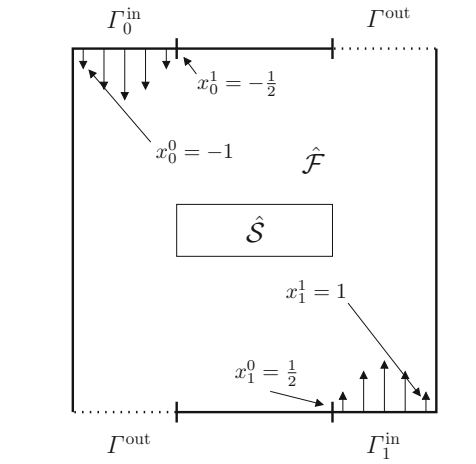

(a)

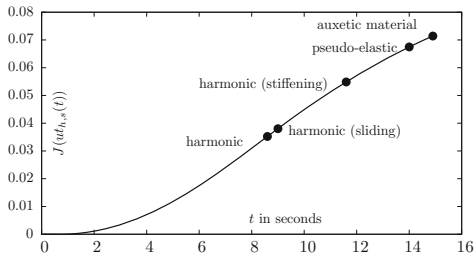

(b)

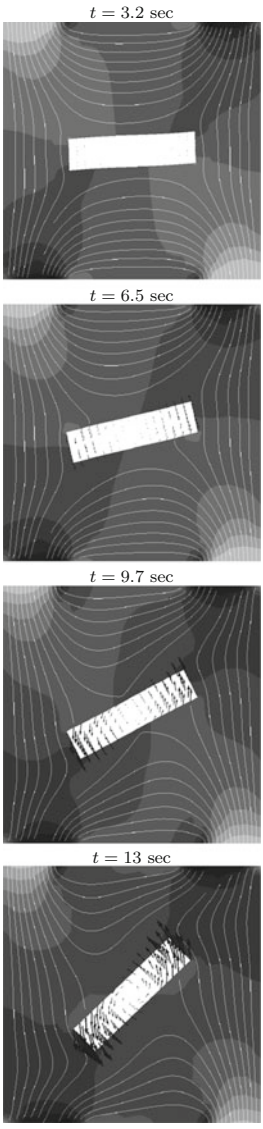

(c)

Fig. 5.13 Description of the benchmark problem for testing the influence of the ALE map definition. (**a**) Geometric configuration of the test case. The boundary consists of two inflow, two outflow parts and a rigid wall. The solid $\hat{\mathcal{S}}$ is not supported. The domain Ω is split into fluid $\hat{\mathcal{F}}$ and solid $\hat{\mathcal{S}}$ $\Omega = (-1, 1)^2$, $\hat{\mathcal{S}} = \left(-\frac{1}{2}, \frac{1}{2}\right) \times \left(-\frac{1}{8}, \frac{1}{8}\right)$, $\hat{\mathcal{F}} = \Omega \setminus \overline{\hat{\mathcal{S}}}$. On the two inflow boundary parts Γ_i^{in} $(i = 1, 2)$ we prescribe parabolic Dirichlet conditions for the velocity $\mathbf{v}_f$. (**b**) Rotation $J(\mathbf{u}_{h,s}(t))$ as function over time indicating the rigid body rotation of the solid. The *points* indicate the final time, where mesh elements start to deteriorate. (**c**) *Right*: Solution at different times with streamlines and deformation vector field. *Bright colors* indicate large pressure, *dark colors* indicate small pressures

where the x_i^j are indicated in the sketch of the configuration and where $\mathbf{n}_i$ is the outward facing normal vector at Γ_i^{in}. The function $\alpha(t)$ is added for a smooth initial transition

$$\alpha(t) = \begin{cases} \frac{1}{2}\left(1 - \cos(\pi t/2)\right) & t \leq 2\,\text{s}, \\ 1 & t \geq 2\,\text{s} \end{cases}.$$

The solid is modeled as St. Venant-Kirchhof material. All parameters are given as

$$\rho_f = 1\,\text{kg}\cdot\text{m}^{-3}, \quad \rho_s = 1000\,\text{kg}\cdot\text{m}^{-3},$$
$$\mu_s = 20\,\text{kg}\cdot\text{m}^{-1}\text{s}^{-2}, \quad \lambda_s = 80\,\text{kg}\cdot\text{m}^{-1}\text{s}^{-2}, \quad \nu_f = 1\,\text{m}^2\cdot\text{s}^{-1}.$$

In the right plot of Fig. 5.13c, we show the solution at different points in time. Bright values denote large pressures, dark colors small ones. Further, we plot streamlines of the velocity field and the vector field of the solid deformation. The symmetric flow causes a rotational movement of the solid. As quantity of interest, we measure the average rotation

$$J(\mathbf{u}_h(t)) = \frac{1}{|\hat{\mathcal{S}}|}\int_{\hat{\mathcal{S}}} \hat{x} \times \mathbf{u}_{h,s}\,\mathrm{d}\hat{x}. \tag{5.36}$$

The value of $J(\mathbf{u}_h(t))$ is shown in Fig. 5.13b. Due to very large deformation of the fluid domain and a deterioration of the ALE map, all computations will break down at some final time $t' > 0$. These points in time are indicated in Fig. 5.13b. We will see that depending on the type of extension operator, we achieve a substantial difference in the final time.

5.3.5.1 Harmonic Extension

We start by defining the extension of the solid deformation $\mathbf{u}_{h,s}$ from the interface $\hat{\mathcal{I}}$ to the fluid-domain $\mathbf{u}_{h,f} \in V_{h,f}^{\Gamma}$, by means of an harmonic extension, given as

$$(\nabla \mathbf{u}_{h,f}, \nabla \psi_{h,f})_{\mathcal{F}} = 0 \quad \forall \psi_{h,f} \in W_{h,f}^{\Gamma}, \tag{5.37}$$

where $\psi_{h,f}$ has trace zero on the complete boundary of $\mathcal{F}$, that includes the interface. Solution $\mathbf{u}_{h,f}$ and test function $\psi_{h,f}$ come from standard finite element space with the boundary constraints

$$\begin{aligned} \mathbf{u}_{h,f} \in V_{h,f}^{\Gamma} &:= \{\phi_h \in V_h(\mathcal{F}),\ \phi_h = \mathbf{u}_{h,s} \text{ on } \mathcal{I},\ \phi_h = 0 \text{ on } \partial\mathcal{F} \setminus \mathcal{I}\} \\ \psi_{h,f} \in W_{h,f}^{\Gamma} &:= \{\phi_h \in V_h(\mathcal{F}),\ \phi_h = 0 \text{ on } \mathcal{I},\ \phi_h = 0 \text{ on } \partial\mathcal{F} \setminus \mathcal{I}\}. \end{aligned} \tag{5.38}$$

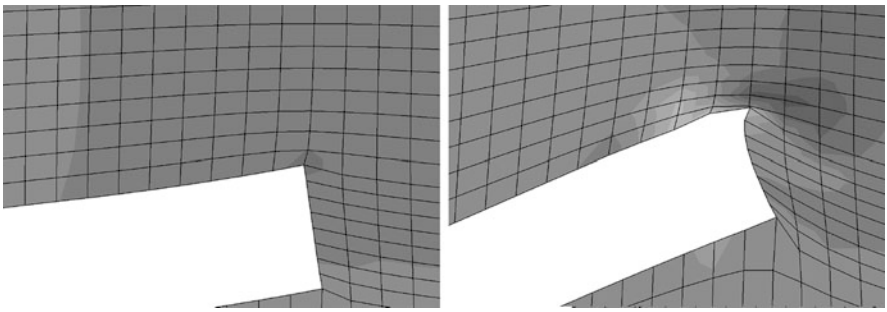

Fig. 5.14 Extension with the harmonic operator. *Left*: $t = 5$ s. *Right*: $t = 8.6$ s close to breakdown due to degeneration of map elements

We show results in Fig. 5.14 for two different points in time. While the ALE mapping yields a nicely transformed mesh at time $t = 5$ s, some elements are close to deterioration at time $t = 8.6$ s. This in particular happens at the edge of the solid. Here, we also see a very strong (and non-physical) feedback from the deformation to the elasticity problems. Bad approximation on strongly deformed meshes gives rise to artificial forces bending the solid.

This extension operator can be relaxed by varying the boundary conditions on the outer boundary

$$\Gamma_f := \partial\mathcal{F} \setminus \mathcal{I}.$$

Here, it is not strictly necessary for $\mathbf{u}_{h,f}$ to guarantee a full homogenous Dirichlet condition. If the deformation $\mathbf{u}_{h,f}$ is allowed to move freely in tangential direction, the resulting map $T_{h,f}$ will still map the reference domain to the fluid-domain. Hence, we can alter the test space $W_{h,f}$ in such a way that Dirichlet-conditions are only imposed in normal direction, similar to the free-slip condition that is known from fluid-dynamics

$$W_{h,f}^{\Gamma} := \{\phi \in C(\mathcal{F})^d, \phi_h\Big|_K \in P^r(K),\ \mathbf{n} \cdot \phi_h = 0 \text{ on } \Gamma_f,\ \phi_0 = 0 \text{ on } \mathcal{I}\},$$

where $P^r(K)$ is the local finite element space. In Fig. 5.15 we show both different choices of boundary values. Although we choose different boundary values only on the outer boundary of the domain, we see a substantial improvement of mesh quality at the interface. In particular, the solid's shape is not deteriorated at the edges. However, some mesh elements already start to lose regularity.

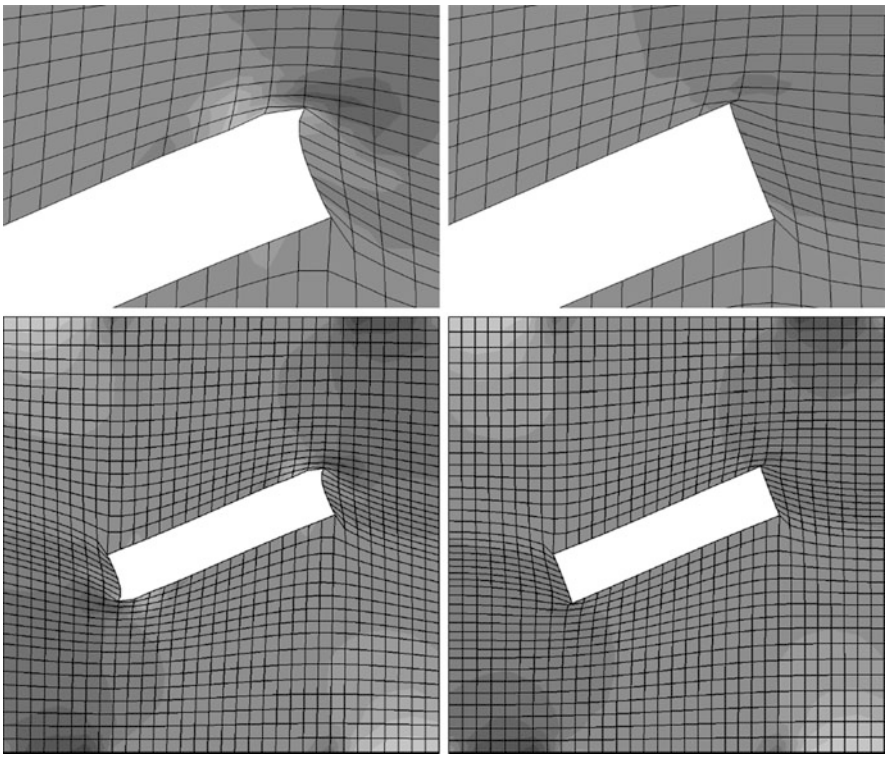

Fig. 5.15 Extension with the harmonic operator. Comparison of different boundary values at the outer boundary $\partial\mathcal{F} \setminus \mathcal{I}$. *Left*: homogenous Dirichlet $\mathbf{u}_{h,f} = 0$. *Right*: $\mathbf{n} \cdot \mathbf{u}_{h,f} = 0$. Both at times $t = 8.6\,\mathrm{s}$. In the *bottom line* we show the complete computational domain. Here, the effect of sliding boundary conditions gets obvious

5.3.5.2 Harmonic Extension with Stiffening

The examples show that we have to expect difficulties close to the solid domain, in particular close to edges. Here, stiffening of the extension can help to assure better quality of the deformed meshes. We change the extension operator by introducing a local parameter function $\alpha : \mathcal{F} \to \mathbb{R}_+$:

$$(\alpha \nabla \mathbf{u}_{h,f}, \nabla \phi_{h,f})_{\mathcal{F}} = 0 \quad \forall \psi_{h,f} \in W^{\Gamma}_{h,f}.$$

Given differentiability of $\alpha(x)$, this weak formulation belongs to a transport-diffusion problem

$$-\Delta \mathbf{u}_{h,f} - \alpha^{-1} \nabla \alpha \cdot \nabla \mathbf{u}_{h,f} = 0.$$

If we can choose $\alpha : \mathcal{F} \to \mathbb{R}_+$ in such a way that the ratio

$$\frac{|\nabla\alpha|}{|\alpha|} \gg 0 \text{ at } \mathcal{I},$$

is large close to the interface, and if the transport direction points away from the interface

$$-\nabla\alpha \sim \mathbf{n}_s \text{ at } \mathcal{I},$$

where $\mathbf{n}_s$ is the outward facing normal vector of $\mathcal{S}$, the extension mainly behaves like a simple transport-problem and the deformation $\mathbf{u}_{h,s}$ on $\mathcal{I}$ is carried into the fluid-domain with as little changes as possible. Further away from the interface, the extension should take the role of a harmonic extension. The choice of $\alpha(x)$ can be based on the distance of x to the nearest interface point

$$d_{\mathcal{I}}(x) := \min_{y\in\mathcal{I}} \|x - y\|_2.$$

A good choice of α is

$$\alpha(x) = 2.0 - \operatorname{erf}\left(5 d_{\mathcal{I}}(x)\right),$$

where erf is the Gauss error function. For this choice of α it holds

$$\frac{|\nabla\alpha(x)|}{|\alpha(x)|} > 1 \text{ if } d_{\mathcal{I}}(x) < \frac{1}{4} \text{ and } \frac{|\nabla\alpha(x)|}{|\alpha(x)|} \ll \frac{1}{100} \text{ if } d_{\mathcal{I}}(x) > \frac{1}{2}.$$

By a proper scaling of this function, the area of dominant transport can be adjusted to the specific geometry. Figure 5.16 shows the results. First, we see a significant improvement in mesh-quality. If we go on in time and rotation, we again see deterioration of mesh elements and also a non-physical deformation of the solid. We could already increase the final time, where the ALE formulation will loose its regularity by about 20%.

5.3.5.3 Extension by Pseudo-Elasticity

Another possibility for defining the extension operator is by means of the Navier-Lamé equation, see also [296]

$$\left(\mu_e(\nabla\mathbf{u}_{h,f} + \nabla\mathbf{u}_{h,f}^T) + \lambda_e \operatorname{div}\ \mathbf{u}_{h,f} I, \nabla\psi_{h,f}\right)_{\mathcal{F}} = 0 \quad \forall\psi_{h,f} \in W_{h,f}^{\Gamma}.$$

The parameters μ_e and λ_e can again be chosen in such a way that the material stiffens closer to the solid. Let $E_e(x)$ be the Young modulus, depending on the

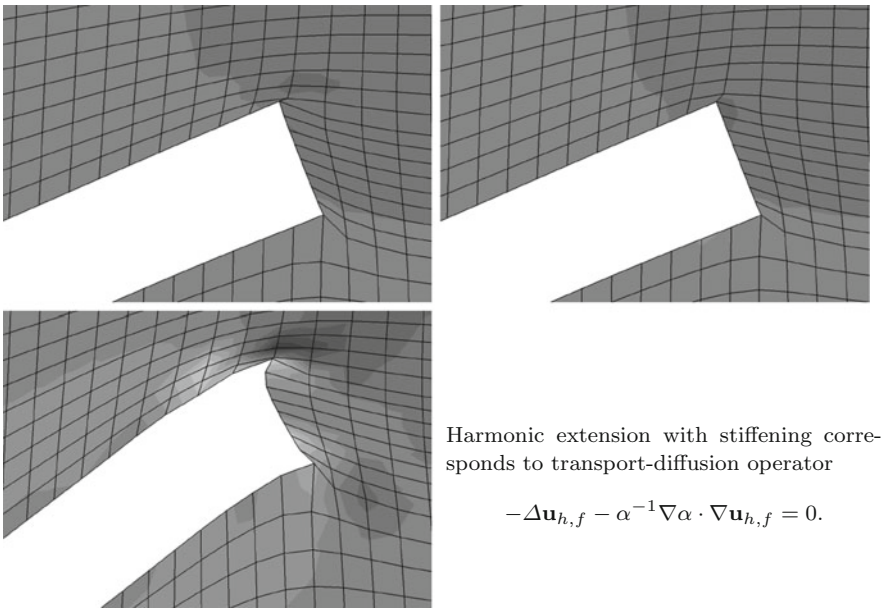

Fig. 5.16 *Upper row*: extension with the harmonic operator using sliding boundary conditions (*left*) and the harmonic operator with stiffening at the solid (*right*), both at time $t = 8.6$ s. *Lower row*: harmonic extension with stiffening at time $t = 11.6$ s

distance, and ν_e a chosen Poisson ratio. We pick the two parameters as

$$\mu_e(x) = \frac{E_e(x)}{2(1+\nu_e)}, \quad \lambda_e(x) = \frac{\nu_e E_e(x)}{(1+\nu_e)(1-2\nu_e)}.$$

The results at times $t = 11.6$ s and $t = 14$ s are shown in Fig. 5.17. At time 11.6 s we get a very good mesh quality (compared to the harmonic operator with stiffening). No artificial feedback to the solid problem is observed. The computations break down around $t = 14$ s.

Using the pseudo-elasticity model, one can improve the results by using material parameters in the *auxetic* range

$$-1 < \nu_e < 0.$$

Here, we pick $\nu_e = -0.2$. The results are shown in the lower right plot of Fig. 5.17. A significant improvement in mesh quality is not visible, but using material parameters in the auxetic range allows to reach a final time of $t = 14.9$ s.

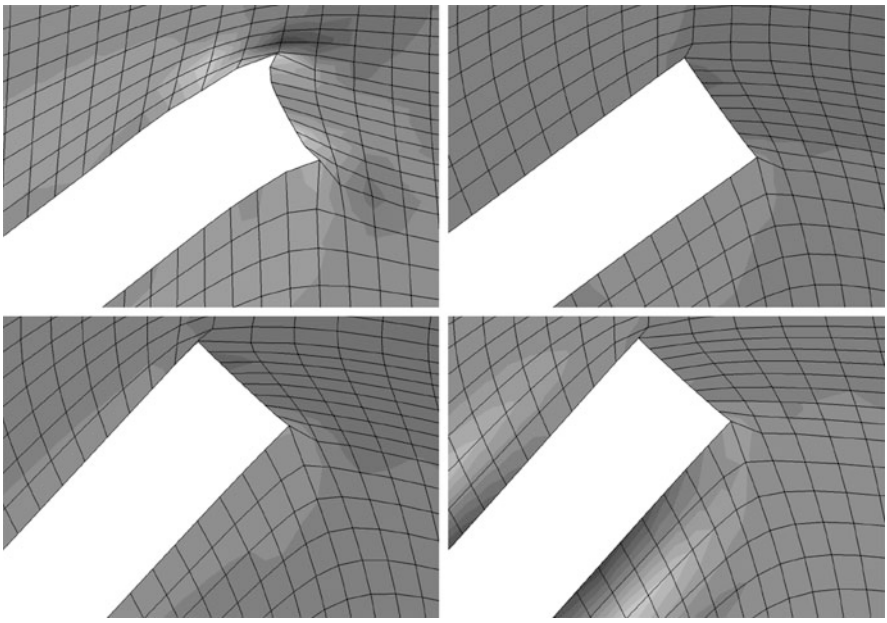

Fig. 5.17 *Upper row*: extension with the harmonic operator using stiffening (*left*) and using a pseudo-elasticity model (*right*), both at time $t = 11.6$ s. *Lower row*: pseudo-elastic extension at time $t = 14$ s (*left*) and pseudo-elasticity with an auxetic material behavior (*right*)

For a pseudo-elastic extension, it is possible to apply stiffening in a semi-automatic way, by coupling the Young modulus to the deformation gradient's determinant

$$J_e := \det(I + \nabla \mathbf{u}_h).$$

E_e is increased, if J_e gets large or close to zero:

$$E_e := E_e \left(J_e + \frac{1}{J_e} \right).$$

This technique is referred to as Jacobian-based stiffening, see [318].

5.3.5.4 Biharmonic Extension

Finally, we consider the biharmonic operator Δ^2 for defining the extension of the deformation, see also [182]. For realization, we choose a mixed formulation by

introducing a secondary variable $\mathbf{w}_f = -\Delta \mathbf{u}_f$:

$$(\nabla \mathbf{w}_{h,f}, \nabla \psi^1_{h,f})_{\mathcal{F}} + (\nabla \mathbf{u}_{h,f}, \nabla \psi^2_{h,f})_{\mathcal{F}} - (\mathbf{w}_{h,f}, \psi^2_{h,f})_{\mathcal{F}} = \langle \mathbf{n} \cdot \nabla \mathbf{u}_{h,s}, \psi^2_{h,f} \rangle_{\mathcal{I}},$$

where solution and test function come from the spaces

The biharmonic extension has the benefit that no configuration dependent parameter-tuning is necessary. Due to the fourth order character, special care has to be taken for discretization. Either, C^1-conforming finite elements, or a mixed formulation is required. For numerical benchmark problems, a very high computational effort is reported [342], with computing times up to ten times higher than for the simple harmonic extension. Hence, it is usually more advisable to spend some effort on parameter tuning and a good parameter choice for one of the previously discussed options.

5.3.5.5 Summary and Conclusion

In Table 5.2 we summarize the results from the previous section. The effect of the different methods for extending the deformation to the fluid domain and for generation of the ALE map are striking. Compared to the most simple harmonic extension, advanced techniques that are based on pseudo-elasticity can give good results for nearly twice as large deformations. Apart from the biharmonic operator all of these techniques have a comparable computational effort. Even if nonlinear models are used for stiffening, the effort for the solution of the extension problem is still negligible compared to the fluid and the solid problem.

Remark 5.14 (Alternative Approaches for Defining the ALE Map) All methods presented in this section have a similar type and based on the implicit inversion of a differential operator. This approach is natural for monolithic models, where fluid problem solid problem and mesh problem are formulated as one coupled system. Using partitioned algorithms it is easier to utilize different processed for designing the ALE map. Basting and co-workers [30] introduced the *extended ALE method* that is based on a variational mesh optimization scheme [294] that generates

Table 5.2 Final time for the breakdown of the ALE scheme for different types of ALE extension

Mesh motion model	Maximum time	Maximum rotation J
Harmonic	8.6 s	0.035
Harmonic (sliding)	9.0 s	0.038
Harmonic (stiffening)	11.6 s	0.055
Pseudo-elastic	14.0 s	0.067
Auxetic material	14.9 s	0.071

We also indicate the maximum value that has been reached for the rotation functional 5.36

distribution of the mesh nodes whenever the ALE map deteriorates. As an important feature to allow for efficient simulations the mesh connectivity is always preserved.

Schäfer et al. [300] block structure the computational mesh to allow for different mesh motion techniques in different parts depending on the distance to the elastic obstacle and the expected deformation. Among the applied techniques they also use linear interpolations to construct mesh distortions. In a monolithic setting this approach would cause global couplings in the matrix. As part of partitioned approaches this technique is very efficient.

Chapter 6
Fully Eulerian Formulation for Fluid-structure Interactions

This chapter is devoted to an alternative monolithic formulation for fluid-structure interactions. While the ALE scheme was based on a mapping of the Eulerian fluid system $\mathcal{F}(t)$ onto a fixed reference framework $\hat{\mathcal{F}}$ to be coupled with the Lagrangian solid domain, the Fully Eulerian formulation goes the other way around. Both problems, fluid as well as solid are modeled on the moving Eulerian domains $\mathcal{F}(t)$ and $\mathcal{S}(t)$ connected by the moving interface $\mathcal{I}(t)$. The general approach is comparable. Both subproblems can be variationally coupled such that we arrive at a monolithic global system. A conceptual difference is in the kind of interface treatment. While the ALE interface $\hat{\mathcal{I}}$ is temporally fixed, the Eulerian interface $\mathcal{I}(t)$ is moving in time and depends on the solution. The domain motion is not any longer hidden in the artificial deformation variable $\mathbf{u}_f$ but must be separately captured by the discretization. Here, we describe this rather new formulation that has been introduced by Dunne in 2006 [126, 127]. A very similar approach has been introduced by Cottet, Maitre and Milcent at about the same time [103–105]. Since then, similar approaches have been published [105, 179, 278, 282, 285, 345]. The underlying principle for all Eulerian formulations is to avoid the introduction of artificial coordinate systems that can cause a break down of the coupled scheme. In ALE formulations, the fluid's reference domain does not have a physical significance. As seen in Sect. 5.3.5 the construction of the ALE map is—up to certain degree—arbitrary. Picking the wrong map can result in a loss of regularity or invertibility and finally to a breakdown of the scheme. A Lagrangian-Eulerian mapping of the solid problem however is completely physical. Both formulations are equivalent, as long as material rupture or material overlapping is not allowed. However large the deformation or motion of the solid is, the Eulerian system will be well-posed.

Most of the recent progress that has been made with regard to the Fully Eulerian formulation is due to the intense work of Frei [153, 158, 284]. A good overview is found in [151, 154]. Finally, the last chapter of this book is a guest article by Stefan

T. Richter, *Fluid-structure Interactions*, Lecture Notes in Computational Science and Engineering 118, DOI 10.1007/978-3-319-63970-3_6

Frei and presents modern numerical techniques for simulations in the Fully Eulerian formulation, see Chap. 12.

6.1 Eulerian Models for Fluid-structure Interactions

The success of the ALE formulation for fluid-structure interactions crucially depends on the quality of the fluid domain map $\hat{T}_f$. If this mapping looses its regularity, equivalence between the variational ALE formulation in Lemma 3.11 and the classical formulations of the fluid-structure interaction problem in equation (3.4) will not hold any more. Further, we have seen that bounds on $\hat{\nabla}\hat{T}_f$ and $\nabla\hat{T}_f^{-1}$ will enter basic inequalities like the trace inequality, Poincaré inequality and also the inf-sup inequality. Even if the derivatives of $\hat{T}_f$ and $\hat{T}_f^{-1}$ are bound, the constants that will finally enter stability and error estimates can be very large.

Some configurations will necessarily lead to a degeneration of the ALE mapping. The most prominent example is given for contact problems, as a C^1-diffeomorphism between two domains with different topology cannot exist. In this section, we will introduce an alternative variational formulation for the coupled fluid-structure interaction problem that goes the opposite way: instead of mapping the moving fluid domain onto a fixed reference domain $\hat{T}_f(t) : \hat{\mathcal{F}} \to \mathcal{F}(t)$ we use an inverse map to transform the Lagrangian solid reference domain onto the Eulerian moving solid domain $\hat{T}_s(t) : \hat{\mathcal{S}} \to \mathcal{S}(t)$. Like the ALE map $\hat{T}_f$, this transformation is defined by the deformation $\hat{\mathbf{u}}_s$

$$\hat{T}_s(\hat{x}, t) := \hat{x} + \hat{\mathbf{u}}_s(\hat{x}, t).$$

There is one fundamental difference between $\hat{T}_s$ and $\hat{T}_f$. While the ALE map $\hat{T}_f$ is arbitrary and $\hat{\mathcal{F}}$ does not play a physical role, the solid domain map $\hat{T}_s$ is given by physical principles. It maps between Lagrangian and Eulerian coordinates. If the solid problem is well-posed, both formulations are valid and it holds that

1. the mapping $\hat{T}_s$ is a bijection between $\hat{\mathcal{S}}$ and $\mathcal{S}(t)$,
2. mapping $\hat{T}_s$ and inverse $\hat{T}_s^{-1}$ are differentiable,
3. the determinants $\hat{J}_s := \det(\hat{\nabla}\hat{T}_s)$ and $\hat{J}_s^{-1} = \det(\nabla\hat{T}_s^{-1})$ satisfy

$$0 < c_1 \leq \hat{J}_s \leq c_2 < \infty.$$

The well-posedness of an Eulerian formulation for fluid-structure interactions is obvious, since the Eulerian coordinates are the physical coordinates where the governing equations (the conservation laws) have been derived. The transition to the Lagrangian reference system was mainly for practical reasons, as deformation stresses can best be described in a particle centered framework. For structure mechanics both viewpoints, the Lagrangian and the Eulerian are physically relevant and the mapping between them is simply given by the deformation $\mathbf{u}$.

6.1.1 Elastic Structures in Eulerian Coordinates

In Sect. 2.1.6, we derived the basic conservation principles for moving volumes that where based on conservation of mass, momentum and angular momentum. Here, we will derive the Eulerian formulation for the structure problem on the moving solid domain $\mathcal{S}(t)$ that is given by the Lagrangian deformation of $\hat{\mathcal{S}}$

$$\mathcal{S}(t) = \{\hat{x} + \hat{\mathbf{u}}_s(\hat{x}, t),\ \hat{x} \in \hat{\mathcal{S}}\}.$$

By mass and momentum conservation, we derived the non-conservative formulation of the momentum equation (2.14)

$$\rho_s \partial_t \mathbf{v}_s + \rho_s \mathbf{v}_s \cdot \nabla \mathbf{v}_s - \nabla \cdot \boldsymbol{\sigma}_s = \rho_s \mathbf{f} \text{ in } \mathcal{S}(t),$$

where $\rho_s(x, t)$ is the Eulerian density of the solid at time t in point $x \in \mathcal{S}(t)$, $\mathbf{v}_s(x, t)$ is the Eulerian velocity and $\boldsymbol{\sigma}_s$ the Eulerian Cauchy-Stress tensor of the solid problem, also given in the Eulerian coordinate system. Here, it is necessary to remember that the transformation to Lagrangian or to an arbitrary reference system in ALE coordinates only touches the domain $\mathcal{S}(t)$ and $\hat{\mathcal{S}}$, not the image, e.g. it holds

$$\mathbf{v}(x, t) = \hat{\mathbf{v}}(\hat{x}, t),$$

for a pair $x = \hat{T}(\hat{x}, t)$. For defining a Eulerian representation $\boldsymbol{\sigma}_s$ of the Cauchy stress tensor, we must introduce a Eulerian counterpart $\mathbf{u}_s$ of the Lagrangian deformation $\hat{\mathbf{u}}_s$. We define

$$\mathbf{u}_s(x, t) = \hat{\mathbf{u}}_s(\hat{x}, t),$$

for a point $x = \hat{x} + \hat{\mathbf{u}}_s(\hat{x}, t)$. Then, it holds

$$\hat{x} = x - \hat{\mathbf{u}}_s(\hat{x}, t) = x - \mathbf{u}_s(x, t),$$

which defines the inverse mapping $T_s(t) : \mathcal{S}(t) \to \hat{\mathcal{S}}$

$$T_s(x, t) := x - \mathbf{u}_s(x, t), \quad T_s = \hat{T}_s^{-1}.$$

Further, considering Lemma 2.9 and (3.28), it holds

$$T_s \circ \hat{T}_s = \mathrm{id} \quad \Rightarrow \quad \nabla T_s =: \mathbf{F}_s = \hat{\mathbf{F}}_s^{-1} = (\hat{\nabla} \hat{T}_s)^{-1}, \quad J_s = \hat{J}_s^{-1}. \tag{6.1}$$

And with $\hat{T}_s := \hat{x} + \hat{\mathbf{u}}_s$ and $T_s := x - \mathbf{u}_s$ it finally follows that

$$[I - \nabla \mathbf{u}_s] = [I + \hat{\nabla} \hat{\mathbf{u}}_s]^{-1} \quad \Leftrightarrow \quad \nabla \mathbf{u}_s = I - [I + \hat{\nabla} \hat{\mathbf{u}}_s]^{-1} = I - \hat{\mathbf{F}}_s^{-1}.$$

Using these relations, we can transform the Cauchy stress tensor $\hat{\boldsymbol{\sigma}}_s$ from Lagrangian to Eulerian coordinates.

Lemma 6.1 (Cauchy Stress Tensor for the St. Venant Kirchhoff Material in Eulerian Coordinates) *The Cauchy stress tensor of the St. Venant Kirchhoff material in Eulerian coordinates is given by*

$$\boldsymbol{\sigma}_s = J_s \mathbf{F}_s^{-1} \left(2\mu \mathbf{E}_s + \lambda_s \operatorname{tr}(\mathbf{E}_s) I\right) \mathbf{F}_s^{-T}, \quad \mathbf{E}_s := \frac{1}{2}\left(\mathbf{F}_s^{-T}\mathbf{F}_s^{-1} - I\right).$$

Proof The second Piola Kirchhoff stress tensor $\hat{\boldsymbol{\Sigma}}_s$ of the St. Venant Kirchhoff material was introduced in Definition 2.18 as

$$\hat{\boldsymbol{\Sigma}}_s = 2\mu_s \hat{\mathbf{E}}_s + \lambda_s \operatorname{tr}(\hat{\mathbf{E}}_s) I$$

with the Green-Lagrangian strain tensor

$$\hat{\mathbf{E}}_s := \frac{1}{2}(\hat{\mathbf{F}}_s^T \hat{\mathbf{F}}_s - I).$$

The relation between Cauchy stress tensor and 2nd Piola Kirchhoff stress tensor is given by the Piola transformation, see Definition 2.13:

$$\hat{\boldsymbol{\sigma}}_s = \hat{J}_s^{-1} \hat{\mathbf{F}}_s \hat{\boldsymbol{\Sigma}}_s \hat{\mathbf{F}}_s^T$$

Then, by (6.1) we get the its Eulerian representation as

$$\boldsymbol{\sigma}_s = J_s \mathbf{F}_s^{-1} \boldsymbol{\Sigma}_s \mathbf{F}_s^{-T},$$

with the 2nd Piola Kirchhoff tensor expressed in Eulerian coordinates

$$\boldsymbol{\Sigma}_s = 2\mu_s \mathbf{E}_s + \lambda_s \operatorname{tr}(\mathbf{E}_s) I.$$

The Eulerian Green-Lagrangian strain tensor is given by

$$\mathbf{E}_s := \frac{1}{2}(\mathbf{F}_s^{-T}\mathbf{F}_s^{-1} - I).$$

□

The derivation of the Cauchy stress tensor $\boldsymbol{\sigma}_s$ in Eulerian coordinates completes the description of the momentum equation. It remains to add an equation for the unknown Eulerian density ρ_s. By defining

$$\rho_s(x,t) = \hat{\rho}_s(\hat{x},t),$$

and using (2.27), it holds

$$\rho_s(x,t) = J_s \hat{\rho}_s^0(\hat{x}), \tag{6.2}$$

where $\hat{\rho}_s^0$ is the density of the solid at time $t = 0$ in the corresponding reference coordinate. Usually one considers homogenous materials, such that relation (6.2) simplifies to

$$\rho_s(x,t) = J_s \hat{\rho}_s^0. \tag{6.3}$$

In the Eulerian coordinate framework, we must also transform the relation between deformation and velocity, compare Lemma 2.10:

$$d_t \hat{\mathbf{u}}_s = \partial_t \mathbf{u}_s + \mathbf{v}_s \cdot \nabla \mathbf{u}_s, \quad d_t \hat{\mathbf{v}}_s = \partial_t \mathbf{v}_s + \mathbf{v}_s \cdot \nabla \mathbf{v}_s.$$

Combining the foregoing discussion we define:

Problem 6.2 (Solid Problem in Eulerian Coordinates) *The elastic deformation of a St. Venant Kirchhoff material in Eulerian coordinates is given by*

$$J_s \hat{\rho}_s (\partial_t \mathbf{v}_s + \mathbf{v}_s \cdot \nabla \mathbf{v}_s) - \nabla \cdot \boldsymbol{\sigma}_s = J_s \hat{\rho}_s \mathbf{f}, \quad \partial_t \mathbf{u}_s + \mathbf{v}_s \cdot \nabla \mathbf{u}_s = \mathbf{v}_s,$$

with the Eulerian formulation of the Cauchy stress tensor

$$\boldsymbol{\sigma}_s := J_s \mathbf{F}_s^{-1} (2\mu_s \mathbf{E}_s + \lambda_s \operatorname{tr}(\mathbf{E}_s) I) \mathbf{F}_s^{-T}, \quad \mathbf{E}_s := \frac{1}{2} \left(\mathbf{F}_s^{-T} \mathbf{F}_s^{-1} - I \right),$$

and the Eulerian deformation gradient

$$\mathbf{F}_s = I - \nabla \mathbf{u}_s.$$

In [151, 154] a derivation of the fluid-structure interaction problem in Eulerian coordinates is given without prior introduction of the Lagrangian problems.

Apart from the complex nonlinear form of the stress tensor, the solid problem is naturally given in Eulerian coordinates. The immediate drawback of this Eulerian formulation is twofold:

- The problem is formulated on the moving domain $\mathcal{S}(t)$ that is a priori unknown and part of the solution. For defining a standard variational formulation of the solid equation in Eulerian coordinates, all difficulties already discussed in Sect. 2.5 must be tackled again.
- By transformation to Eulerian coordinate, convective terms are introduced:

$$d_t \hat{\mathbf{v}} = \partial_t \mathbf{v} + \mathbf{v} \cdot \nabla \mathbf{v}, \quad d_t \hat{\mathbf{u}} = \partial_t \mathbf{u} + \mathbf{v} \cdot \nabla \mathbf{u}.$$

A discretization of this convective term will cause numerical stability problems, as known for the transport term in the Navier-Stokes equations. Numerical methods must introduce artificial stabilization terms that will cause loss of conservation principles.

Finally, we introduce a variational formulation of the structure problem in Eulerian coordinates, derived by multiplication with suitable test functions. Find

$$\{\mathbf{v}_s, \mathbf{u}_s\} \in \mathcal{V}_s(t) \times \mathcal{W}_s(t),$$

such that

$$\begin{aligned} \left(J_s\hat{\rho}_s(\partial_t\mathbf{v}_s + \mathbf{v}_s\cdot\nabla\mathbf{v}_s), \phi_s\right)_{\mathcal{S}(t)} & \\ +\left(\boldsymbol{\sigma}_s, \nabla\phi_s\right)_{\mathcal{S}(t)} &= \left(J_s\hat{\rho}_s^0\mathbf{f}, \phi\right)_{\mathcal{S}(t)} \quad \forall\phi_s \in \mathcal{V}_s^{\text{test}} \\ \left(\partial_t\mathbf{u}_s + \mathbf{v}_s\cdot\nabla\mathbf{u}_s - \mathbf{v}_s, \psi_s\right)_{\mathcal{S}(t)} &= 0 \quad \forall\psi_s \in \mathcal{W}_s^{\text{test}}, \end{aligned} \tag{6.4}$$

While the Lagrangian velocity $\hat{\mathbf{v}}_s \in L^2(\hat{\mathcal{S}})^d$ is defined as L^2-projection the Eulerian counterpart requires some control over the derivative in direction of $\mathbf{v}_s$.

6.1.2 Fluid-structure Interaction in Eulerian Coordinates

With the variational formulation of the Eulerian structure problem shown in (6.4) it is straightforward to formulate the coupled fluid-structure interaction problem in Eulerian coordinates. We simple combine (6.4) with the incompressible Navier-Stokes equations (2.48) on the moving domain $\mathcal{F}(t)$ by adding appropriate interface conditions

$$\begin{aligned} (\rho_f(\partial_t\mathbf{v}_f + \mathbf{v}_f\cdot\nabla\mathbf{v}_f), \phi_f)_{\mathcal{F}(t)} + (\boldsymbol{\sigma}_f, \nabla\phi_f)_{\mathcal{F}(t)} &= (\rho_f\mathbf{f}, \phi_f)_{\mathcal{F}(t)} \\ (\nabla\cdot\mathbf{v}_f, \xi_f)_{\mathcal{F}(t)} &= 0 \\ (J_s\hat{\rho}_s(\partial_t\mathbf{v}_s + \mathbf{v}_s\cdot\nabla\mathbf{v}_s), \phi_s)_{\mathcal{S}(t)} + (\boldsymbol{\sigma}_s, \nabla\phi_s)_{\mathcal{S}(t)} &= (J_s\hat{\rho}_s^0\mathbf{f}, \phi)_{\mathcal{S}(t)} \\ (\partial_t\mathbf{u}_s + \mathbf{v}_s\cdot\nabla\mathbf{u}_s - \mathbf{v}_s, \psi_s)_{\mathcal{S}(t)} &= 0 \\ \mathbf{v}_f &= \mathbf{v}_s \quad \text{on } \mathcal{I}(t), \\ \boldsymbol{\sigma}_f n &= \boldsymbol{\sigma}_s\mathbf{n} \quad \text{on } \mathcal{I}(t) \end{aligned} \tag{6.5}$$

Variational coupling of these equations on $\mathcal{F}(t)$ and $\mathcal{S}(t)$ is easily possible following the guidelines introduced in Sect. 3.4. As the two domain $\mathcal{F}(t)$ and $\mathcal{S}(t)$ match and share a common interface $\mathcal{I}(t) = \partial\mathcal{F}(t) \cap \partial\mathcal{S}(t)$, we can combine the trial space to embed continuity of velocities into the variational formulation

$$\mathbf{v} \in \mathcal{V} = H_0^1(\Omega)^d, \quad \mathbf{v}_f = \mathbf{v}\big|_{\mathcal{F}(t)}, \quad \mathbf{v}_s = \mathbf{v}\big|_{\mathcal{S}(t)}.$$

For realizing the dynamic coupling condition, we combine the test spaces of the momentum equations:

$$\phi \in \mathcal{V} = H_0^1(\Omega)^d, \quad \phi_f = \phi\big|_{\mathcal{F}(t)}, \quad \phi_s = \phi\big|_{\mathcal{S}(t)}.$$

We can define the variational formulation of the Fully Eulerian fluid-structure interaction problem:

Problem 6.3 (Variational Formulation of the Eulerian Fluid-structure Interaction Problem) *Let*

$$\mathbf{v} \in \mathcal{V} = H_0^1(\Omega)^d,\ p_f \in L^2(\mathcal{F}(t)),\ \mathbf{u}_s \in H_0^1(\Omega)^d,$$

be the solution of the variational problem

$$\begin{aligned}
&(\rho_f(\partial_t \mathbf{v}_f + \mathbf{v}_f \cdot \nabla \mathbf{v}_f), \phi)_{\mathcal{F}(t)} + (\boldsymbol{\sigma}_f, \nabla\phi)_{\mathcal{F}(t)} \\
&\quad + (J_s\hat{\rho}_s(\partial_t \mathbf{v}_s + \mathbf{v}_s \cdot \nabla \mathbf{v}_s), \phi)_{\mathcal{S}(t)} + (\boldsymbol{\sigma}_s, \nabla\phi)_{\mathcal{S}(t)} = (\rho_f \mathbf{f}, \phi)_{\mathcal{F}(t)} \\
&\qquad\qquad + (J_s\hat{\rho}_s^0 \mathbf{f}, \phi)_{\mathcal{S}(t)} \qquad (6.6)\\
&(\nabla \cdot \mathbf{v}_f, \xi_f)_{\mathcal{F}(t)} = 0 \\
&(\partial_t \mathbf{u}_s + \mathbf{v}_s \cdot \nabla \mathbf{u}_s - \mathbf{v}_s, \psi_s)_{\mathcal{S}(t)} = 0,
\end{aligned}$$

for all

$$\phi \in \mathcal{V},\ \xi_f \in L^2(\mathcal{F}(t)),\ \psi_s \in L^2(\mathcal{S}(t))^d.$$

Given sufficient regularity, a transformation of $\{\mathbf{v}, p_f, \mathbf{u}_s\}$ *to Lagrangian coordinates (in the solid domain) also solves the fluid-structure interaction problem in classical formulation (3.4).*

Apparently, the Eulerian formulation of the fluid-structure interaction problem has a simpler structure than the ALE formulation. No mapping, at least no artificial mapping between domains is necessary. Hence, there is no obvious reason why the Eulerian formulation should show limits when treating problems with very large deformation, motion or even contact. All this is true, the simplicity of the variational formulation in Problem 6.3 however hides one essential vagueness. The deformation of the domains $\mathcal{F}(t)$ and $\mathcal{S}(t)$ is given by the solution, to be precise, by the deformation of the solid domain

$$\mathrm{id} + \hat{\mathbf{u}}_s : \hat{\mathcal{S}} \to \mathcal{S}(t).$$

The formulation in Eulerian coordinates is based on the inverse of this relation:

$$\mathrm{id} - \mathbf{u}_s : \mathcal{S}(t) \to \hat{\mathcal{S}},$$

the so-called *backward characteristic*. The complete derivation of the Eulerian method hides out one dilemma, that is inherent to fluid-structure interaction problems. The domains $\mathcal{F}(t)$ and $\mathcal{S}(t)$ are moving and depend on the solution. However, for assembling the Eulerian formulation (6.6), we must—for every point $x \in \Omega$—know its affiliation to the fluid-domain $x \in \mathcal{F}(t) \subset \Omega$ or solid domain $x \in \mathcal{S}(t) \subset \Omega$. This appears to be an irreconcilable barrier for implicit monolithic formulations of the Eulerian model, as the domain affiliation is prerequisite for setting up the equations, whose solution is required for defining the affiliation. The next section will describe techniques for capturing the moving interface.

6.2 Interface Capturing and the Initial Point Set Method

To work around this dilemma, we need to enrich the system of equations by variables used to capture the location of the two domains. Multi-phase methods that live on a fixed background system and where the interface between the phases in freely moving are called *interface-capturing* techniques. One of the most prominent *interface-capturing* methods is the *Level-Set method* by Osher [257] and Sethian [307].

Remark 6.4 (Level-Sets) Assume that $\mathcal{F}(0) \cup \mathcal{I}(0) \cup \mathcal{S}(0)$ is the initial partitioning of the domain. We define a level-set function $\Psi(x, 0)$ as the signed distance function belonging to this partitioning

$$\Psi(x,0) := \begin{cases} \operatorname{dist}(x, \mathcal{I}(0)) & x \in \mathcal{S}(0), \\ 0 & x \in \mathcal{I}(0), \\ -\operatorname{dist}(x, \mathcal{I}(0)) & x \in \mathcal{F}(0). \end{cases}$$

We assume that the domain-partitioning is moving with a velocity field $\mathbf{v}$. Then, the level-set function is advected with this field by

$$\frac{\partial \Psi}{\partial t} + \mathbf{v} \cdot \nabla \Psi = 0,$$

or, if motion is restricted to the normal direction by

$$\frac{\partial \Psi}{\partial t} + v_n |\nabla \Psi| = 0,$$

where $v_n = \mathbf{v} \cdot \mathbf{n}$ is the velocity in normal direction. This allows for a level set representation of the interface

$$\mathcal{I}(t) = \{x \in \mathbb{R}^d,\ \Psi(x,t) = 0\}.$$

Normal vectors and curvatures can be calculated based on the level set function. Some problems of level set formulations is the need of reinitialization if distances are to be discovered. An auxiliary equation is introduced at time t' to normalize the gradient $\nabla\Psi$ to one, e.g. by

$$\partial_\tau \Psi + \operatorname{sgn}(\Psi(t'))\,(|\nabla\Psi| - 1) = 0, \quad \tau > 0.$$

Numerical schemes for the advection of the level set function will introduce diffusion. This will cause a smearing of sharp corners, that cannot be well approximated as zero lines of level sets. Nevertheless, level sets are one of the most established methods for capturing interfaces in Eulerian based simulations, see [257, 307].

One of the disadvantages connected to the Level-Set method is a degeneration of edges. Due to numerical dissipation and due to the reinitialization procedure, edges will be smoothened. While this does not pose a major problem for multiphase flows, where the interface usually does not show edges, the conservation of sharp edges (e.g. of the solid subdomain) is crucial in fluid-structure interaction applications. He and Qiao introduced a Eulerian formulation for fluid-structure interactions, where the interface was captured with the help of three Level-Set functions [179].

Here, we describe the *Initial Point Set method* for capturing the interface between fluid- and solid-domain. To be precise: instead of capturing the interface location, we will capture the complete reference coordinate system. We know that at time $t \geq 0$, a spatial coordinate $x \in \Omega$ belongs to the solid domain $x \in \mathcal{S}(t)$, if it holds

$$T_s(x,t) = \hat{x} - \mathbf{u}_s(x,t) \in \hat{\mathcal{S}},$$

if the coordinate $x \in \Omega$ is the location of the particle $\hat{x} \in \hat{\mathcal{S}}$ at time t. This construction will be transferred to the fluid-domain. Assume that $\mathbf{u}_f(x,t)$ is a vector field, such that:

$$x - \mathbf{u}_f(x,t) \in \hat{\mathcal{F}} \quad \Leftrightarrow \quad x \in \mathcal{F}(t).$$

By $\mathbf{u}_f$ we denote the Eulerian deformation of the fluid-domain. Similar to the fluid domain map $\hat{\mathbf{u}}_f$ in the ALE formulation, this deformation $\mathbf{u}_f$ does not describe the physical motion of a particle. We use $\mathbf{u}_f$ to define the inverse fluid-map $T_f(x,t) = x - \mathbf{u}_f(x,t)$. Next, we assume that there is a continuous transition from T_f to T_s on the interface $\mathcal{I}(t)$. Then, we can define one global inverse mapping

$$T(x,t) := \begin{cases} T_s(x,t) & x \in \mathcal{S}(t) \\ T_s(x,t) = T_f(x,t) & x \in \mathcal{I}(t) \\ T_f(x,t) & x \in \mathcal{F}(t). \end{cases}$$

Based on this mapping, we can decide the domain affiliation for every spatial coordinate $x \in \Omega$

$$x \in \mathcal{S}(t) \Leftrightarrow T(x,t) \in \hat{\mathcal{S}},$$
$$x \in \mathcal{F}(t) \Leftrightarrow T(x,t) \in \hat{\mathcal{F}}.$$

This inverse map $T(x,t)$ is exactly the *backward-characteristic* $Y(x,t)$ used in the formulations of Cottet, Milcent and Maitre [105, 242].

It remains to define the Eulerian fluid-domain deformation $\mathbf{u}_f$ in an implicit way. To derive a continuous transition between T_f and T_s, the deformations $\mathbf{u}_f$ and $\mathbf{u}_s$ will need to be continuous. We can define $\mathbf{u}_f$ simply by an extension of $\mathbf{u}_s$ to $\mathcal{F}(t)$.

Remark 6.5 (Initial Point Set) This construction looks very similar to the construction of the ALE-map in the context of the Arbitrary Lagrangian Eulerian model and one could argue that the same difficulties are introduced. As we define an arbitrary extension $\mathbf{u}_f$ of the solid's deformation $\mathbf{u}_s$, numerical artifacts come into place. There are however two fundamental differences: first, the inverse map $T(x,t)$ inside the fluid domain is not used for any kind of mapping. We do not require its inverse or its derivatives. Instead, it is for look-up purposes only. Second, we do not even require that $T_f(x,t) \in \hat{\mathcal{F}}$ for $x \in FL(t)$. It is completely sufficient that $x \in \mathcal{F}(t)$ is mapped outside of the solid domain. Therefore, we can relax the definition of the extension $\mathbf{u}_f$, i.e. by requiring Dirichlet values only on the interface and by relaxing the look-up property. Instead of requiring $T(x,t) \in \hat{\mathcal{F}}$ for $x \in \mathcal{F}(t)$, we simply demand $T(x,t) \notin \hat{\mathcal{S}}$ for such fluid points.

Definition 6.6 (Initial Point Set) A vector field $\Phi_{\text{IPS}} \in C(I; C(\Omega))$ is called Initial Point Set, if for $x \in \Omega$ and $t \geq 0$ it holds

$$\Phi_{\text{IPS}}(x,t) = x - \mathbf{u}_s(x,t) \in \hat{\mathcal{S}} \quad \Rightarrow \quad x \in \mathcal{S}(t)$$
$$\Phi_{\text{IPS}}(x,t) \notin \hat{\mathcal{S}} \quad \Rightarrow \quad x \in \mathcal{F}(t)$$

Within the solid domain, the vector field Φ_{IPS} is called the *backward characteristic* [105]. Finally, we can indicate possibilities for the construction of $\mathbf{u}_f$. One simple option is to choose one more a harmonic extension of $\mathbf{u}_s$

$$-\Delta \mathbf{u}_f = 0 \text{ in } \mathcal{F}(t), \quad \mathbf{u}_f = \mathbf{u}_s \text{ on } \mathcal{I}(t), \quad \partial_n \mathbf{u}_f = 0 \text{ on } \partial\Omega_f(t) \setminus \mathcal{I}(t).$$

Here, we have chosen homogenous Neumann boundary conditions on the outer boundary of the fluid-domain. This deformation $\mathbf{u}_f$ will not define a mapping back to a reference domain, but as discussed, this property is not necessary. In Sect. 5.3.5 we have discussed techniques for defining the ALE map. Harmonic extension did not perform well, mostly due to singularities at edges entering the fluid domain. In the context of the Initial Point Set, this problem is smaller, as the extension must not be inverted. Finally, we can close the formulation of the coupled fluid-structure interaction problem in Eulerian coordinate.

Problem 6.7 (Initial Point Set Formulation of the Eulerian Fluid-structure Interaction Problem) *Let*

$$\mathbf{v} \in \mathcal{V} = H_0^1(\Omega)^d,\ p_f \in L^2(\mathcal{F}(t)),\ \mathbf{u}_s \in H_0^1(\Omega)^d,$$

be the solution of the variational problem

$$\begin{aligned}
(\rho_f(\partial_t \mathbf{v} + \mathbf{v}\cdot\nabla\mathbf{v}),\phi)_{\mathcal{F}(t)} + (\boldsymbol{\sigma}_f, \nabla\phi)_{\mathcal{F}(t)} \\
+(J_s\hat{\rho}_s(\partial_t \mathbf{v} + \mathbf{v}\cdot\nabla\mathbf{v}),\phi)_{\mathcal{S}(t)} + (\boldsymbol{\sigma}_s, \nabla\phi)_{\mathcal{S}(t)} &= (\rho_f\mathbf{f},\phi)_{\mathcal{F}(t)} + (J_s\hat{\rho}_s^0\mathbf{f},\phi)_{\mathcal{S}(t)} \\
(\nabla\cdot\mathbf{v},\xi_f)_{\mathcal{F}(t)} &= 0 \\
(\partial_t\mathbf{u} + \mathbf{v}\cdot\nabla\mathbf{u} - \mathbf{v},\psi_s)_{\mathcal{S}(t)} &= 0 \\
(\nabla\mathbf{u},\nabla\psi_f)_{\mathcal{F}(t)} &= 0
\end{aligned}$$

for all

$$\phi \in \mathcal{V},\quad \xi_f \in L^2(\mathcal{F}(t)),\quad \psi_s \in L^2(\mathcal{S}(t))^d,\quad \psi_f \in H_0^1(\mathcal{F}(t);\mathcal{I})^d.$$

Given sufficient regularity, a transformation of $\{\mathbf{v}, p_f, \mathbf{u}_s\}$ *to Lagrangian coordinates (in the solid domain) also solves the fluid-structure interaction problem in classical formulation (3.4).*

Remark 6.8 (Eulerian FSI and Multiphase-Flows) The Fully Eulerian formulation for fluid-structure interactions is closely related to Eulerian models for multiphase flows, where one conservation law is given on a domain Ω

$$\rho(\partial_t\mathbf{v} + \mathbf{v}\cdot\nabla\mathbf{v}) - \nabla\cdot\boldsymbol{\sigma} = 0,$$

and where the material parameters, such as density or viscosity depend on the location

$$\rho(x,t) = \begin{cases} \rho_1 & x \in \mathcal{F}_1(t), \\ \rho_2 & x \in \mathcal{F}_2(t) \end{cases}.$$

The fundamental difference to fluid-structure interactions however is that only one type of differential operator is defined. In fluid-structure interactions, we have a transition from a hyperbolic equation in the solid domain to a parabolic equation in the fluid domain. This brings along the already discussed regularity problems on the interface. For multiphase flows, there exist approaches, that work with a smoothing of the parameters (density and viscosity) at the interface, such that it does not need to be sharply resolved.

By introducing the characteristic functions with respect to fluid- and solid-domain χ_f and χ_s

$$\chi_s(x,t) := \begin{cases} 1 & x - \mathbf{u}(x,t) \in \hat{\mathcal{S}}, \\ 0 & x - \mathbf{u}(x,t) \notin \hat{\mathcal{S}} \end{cases}, \quad \chi_f(x,t) := 1 - \chi_s(x,t),$$

the coupled momentum equations is shortly written as

$$\begin{aligned} \Big(\rho(\partial_t \mathbf{v} + \mathbf{v}\cdot\nabla\mathbf{v}), \phi\Big) + \Big(\boldsymbol{\sigma}, \nabla\phi\Big) &= \Big(\rho\mathbf{f}, \phi\Big), \\ \rho &= \chi_f \rho_f + \chi_s J_s \hat{\rho}_s, \\ \boldsymbol{\sigma} &= \chi_f \boldsymbol{\sigma}_f + \chi_s \boldsymbol{\sigma}_s. \end{aligned} \tag{6.7}$$

The introduction of such a characteristic function simplifies the formulation. The difficulties are however only hidden in a clever formulation.

6.3 Time-Discretization of the Fully Eulerian Framework

In the spirit of Sect. 4.6, the Fully Eulerian Formulation leads to an interface problem with an interface that is moving in time. A straightforward discretization of the Eulerian momentum equation (6.7) with the backward Euler method

$$\Big(\rho(k^{-1}\mathbf{v}^n + \mathbf{v}^n\cdot\nabla\mathbf{v}^n), \phi\Big) + \Big(\boldsymbol{\sigma}(\mathbf{v}^n, p^n), \nabla\phi\Big) = \Big(\rho k^{-1}\mathbf{v}^{n-1} + \rho\mathbf{f}^n, \phi\Big),$$

would result in a reduction of the convergence order, as the solution must not be differentiable in time, i.e.

$$\frac{\mathbf{v}^n(x) - \mathbf{v}^{n-1}(x)}{k},$$

may refer to a point $x \in \Omega$, which is solid $x \in \mathcal{S}(t_{n-1})$ at the old point in time and fluid $x \in \mathcal{F}(t_n)$ at the new one.

To derive a simple first order scheme, it is sufficient, to properly evaluate the projection of the old time step to the new domain partitioning. Let

$$\Omega^n = \mathcal{F}^n \cup \mathcal{I}^n \cup \mathcal{S}^n,$$

and

$$T_n : \Omega^{n-1} \to \Omega^n,$$

be given by the deformation $\mathbf{u}^n$

$$T_n(x) := x + \mathbf{u}^n(x) - \mathbf{u}^{n-1}(x), \quad T_n^{-1}(x) = x - \mathbf{u}^n(x) + \mathbf{u}^{n-1}(x).$$

With help of this mapping, which is available by the Initial Point Set method, a function $\mathbf{v}^{n-1}$ from time step t_{n-1} can be approximated on the partitioning Ω^n via

$$F(\phi) = (\rho \mathbf{f}^n, \phi) + \big((\rho \circ T_n^{-1})(\mathbf{v}^{n-1} \circ T_n^{-1}), \phi\big).$$

As T_n and so T_n^{-1} implicitly depends on the new deformation $\mathbf{u}^n$, which is unknown in a fully coupled Eulerian fluid-structure interaction setting, the evaluation of this right hand side is an implicit part of the equation.

The theoretical analysis of high order accurate time stepping methods for moving interface problems, where the interface-motion comes from the solution itself is still open. Transferring the parabolic setting from Sect. 4.6 to the Eulerian framework for fluid-structure interactions experimentally gives the correct order, see [151].

All higher order accurate schemes will require an implicit iteration on the domain partitioning, as $\Omega^n = \mathcal{F}^n \cup \mathcal{I}^n \cup \mathcal{S}^n$ is only available, when $\mathbf{u}^n$ itself is available. In a Newton like procedure, this will call for derivatives with respect to the domain motion, see the following Sect. 6.4.

To avoid such an effort, reduced order approximation could be used. In [282], non-stationary problems in the Eulerian framework have been approximated by a fully explicit treatment of the interface location, i.e. by decoupling the geometry problem from the momentum equations. Better results can be expected by using higher order extrapolations. If problems with possible contact are considered, explicit handling of the interface motion will result in restrictive time step conditions—at least, if the interface is close to contact. Such situations can efficiently be handled by means of adaptive time step control

In [284] a second order accurate time stepping scheme for parabolic interface problems is presented. A priori estimates of optimal order are shown. This scheme has been applied to the Eulerian formulation of fluid-structure interactions as presented in [151, 154]. In Chap. 12 some details on the application of this advanced time stepping schemes are presented.

6.4 Linearizations of the Fully Eulerian Coordinates

One of the benefits of an Eulerian formulation for fluid-structure interactions is the ease of the variational setting, see Problem 6.7. The complete problem is given as

$$\begin{aligned} A(U)(\Phi) =& (\rho_f(\partial_t \mathbf{v} + \mathbf{v} \cdot \nabla \mathbf{v}), \phi)_{\mathcal{F}(t)} + (\boldsymbol{\sigma}_f, \nabla \phi)_{\mathcal{F}(t)} + (\nabla \cdot \mathbf{v}, \xi_f)_{\mathcal{F}(t)} \\ &+ (J_s \hat{\rho}_s(\partial_t \mathbf{v} + \mathbf{v} \cdot \nabla \mathbf{v}), \phi)_{\mathcal{S}(t)} + (\boldsymbol{\sigma}_s, \nabla \phi)_{\mathcal{S}(t)} \\ &+ (\partial_t \mathbf{u} + \mathbf{v} \cdot \nabla \mathbf{u} - \mathbf{v}, \psi_s)_{\mathcal{S}(t)} + (\nabla \mathbf{u}, \nabla \psi_f)_{\mathcal{F}(t)}, \end{aligned} \tag{6.8}$$

with

$$\boldsymbol{\sigma}_s = J_s \mathbf{F}_s^{-1}(2\mu \mathbf{E}_s + \lambda_s \operatorname{tr}(\mathbf{E}_s) I)\mathbf{F}_s^{-T}, \quad \mathbf{E}_s = \frac{1}{2}\left(\mathbf{F}_s^{-T}\mathbf{F}_s^{-1} - I\right).$$

Most of the terms appearing in this formulation are linear or have a quadratic nonlinearity. Only the inverse deformation gradient's determinant J_s and the solid's stresses require closer attention. The characteristic difficulty will be the dependency of the integrals on the domains $\mathcal{F}(t)$ and $\mathcal{S}(t)$, which are moving in time. Hence, geometric derivatives must be considered. For the following derivation we closely follow the approach in Sect. 5.2.2, in particular Theorem 5.2 and Lemma 5.4.

Lemma 6.9 (Derivatives of the Eulerian Deformation Gradient) *Let* $\mathbf{F} = I - \nabla \mathbf{u}$, $J := \det(\mathbf{F})$ *and* $\mathbf{E} := \frac{1}{2}(\mathbf{F}^{-T}\mathbf{F}^{-1} - I)$

$$(i) \quad \frac{d\mathbf{F}}{d\mathbf{u}}(\mathbf{w}) = -\nabla \mathbf{w},$$

$$(ii) \quad \frac{d\mathbf{F}^T}{d\mathbf{u}}(\mathbf{w}) = -\nabla \mathbf{w}^T,$$

$$(iii) \quad \frac{d\mathbf{F}^{-1}}{d\mathbf{u}}(\mathbf{w}) = \mathbf{F}^{-1}\nabla \mathbf{w}\nabla \mathbf{F}^{-1},$$

$$(iv) \quad \frac{d\mathbf{F}^{-T}}{d\mathbf{u}}(\mathbf{w}) = \mathbf{F}^{-T}\nabla \mathbf{w}^T\nabla \mathbf{F}^{-T},$$

$$(v) \quad \frac{dJ(\mathbf{u})}{d\mathbf{u}}(\mathbf{w}) = -J\mathbf{F}^{-T} : \nabla \mathbf{w} = -J \operatorname{tr}(\mathbf{F}^{-1}\nabla \mathbf{w}),$$

$$(vi) \quad \frac{d\mathbf{E}(\mathbf{u})}{d\mathbf{u}}(\mathbf{w}) = \frac{1}{2}\mathbf{F}^{-T}(\nabla \mathbf{w}^T\nabla \mathbf{F}^{-T} + \mathbf{F}^{-1}\nabla \mathbf{w})\mathbf{F}^{-1}$$

Proof We note $\mathbf{F} = \hat{\mathbf{F}}^{-1}$ and refer the reader to Lemma 5.4. □

By these derivation rules most of the terms in the Jacobian of the Eulerian formulation (6.8) can be expressed.

What remains, is the handling of the formulation's dependency on the domain motion. Here, the concept of geometric derivatives, *shape calculus* must be considered. It holds

Theorem 6.10 (Directional Shape Derivatives) *Let* $\hat{\Omega} \subset \mathbb{R}^d$ *be a domain with piece-wise* C^1 *boundary,* $\hat{T}(\hat{x}) := \hat{x} + \hat{\mathbf{u}}$ *be a smooth domain map* $\hat{T} : \hat{\Omega} \to \Omega(\mathbf{u})$, *such that* $\hat{T} \in W^{1,1}(\hat{\Omega})$. *Further, let* $f \in W^{1,1}(\Omega(\mathbf{u}))$. *It holds*

$$\frac{d}{ds}\int_{\Omega(\mathbf{u}+s\mathbf{w})} f\, dx\Big|_{s=0} = \int_{\partial\Omega(\mathbf{u})} (\mathbf{n}\cdot\mathbf{w}) f\, do, \tag{6.9}$$

where $\mathbf{n}$ *is the outward facing normal vector on* $\partial\Omega(\mathbf{u})$.

Proof Let $\mathbf{u}, \mathbf{w}$ be given with Lagrangian counter-part $\hat{\mathbf{u}}(\hat{x}, t) = \mathbf{u}(x, t)$ and $\hat{\mathbf{w}}(\hat{x}, t) = \mathbf{w}(x, t)$. It holds

$$\frac{d}{ds}\int_{\Omega(\mathbf{u}+s\mathbf{w})} f \,\mathrm{d}x = \int_{\hat{\Omega}} \frac{d}{ds}\hat{J}(\hat{\mathbf{u}} + s\hat{\mathbf{w}}) f(\hat{x} + \hat{\mathbf{u}} + s\hat{\mathbf{w}}) \,\mathrm{d}\hat{x} \tag{6.10}$$

where

$$\hat{J}(\hat{\mathbf{u}} + s\hat{\mathbf{w}}) = \det\left(I + \hat{\nabla}(\hat{\mathbf{u}} + s\hat{\mathbf{w}})\right). \tag{6.11}$$

Then, by Lemma 5.4, it holds

$$\begin{aligned}\frac{d}{ds}\hat{J}(\hat{\mathbf{u}} + s\mathbf{w}) f(\hat{x} + \hat{\mathbf{u}} + s\hat{\mathbf{w}})\Big|_{s=0} \\ = \hat{J}(\hat{\mathbf{u}}) f(\hat{x} + \hat{\mathbf{u}}) \hat{\mathbf{F}}^{-T}(\mathbf{u}) : \hat{\nabla}\hat{\mathbf{w}} + \hat{J}(\hat{\mathbf{u}}) \nabla f(\hat{x} + \hat{\mathbf{u}}) \cdot \hat{\mathbf{w}}.\end{aligned}$$

Therefore, by mapping back to $\Omega(\mathbf{u})$ and with help of integration by parts:

$$\begin{aligned}\frac{d}{d\mathbf{u}}\int_{\Omega(\mathbf{u}+s\mathbf{w})} f \,\mathrm{d}x\Big|_{s=0} &= \int_{\Omega(\mathbf{u})} fI : \nabla w \,\mathrm{d}x + \int_{\Omega(\mathbf{u})} \nabla f \cdot \mathbf{w} \,\mathrm{d}x \\ &= \int_{\partial\Omega(\mathbf{u})} (\mathbf{n} \cdot \mathbf{w}) f \,\mathrm{d}x - \int_{\Omega(\mathbf{u})} \mathrm{div}\,(fI) \cdot \mathbf{w} \,\mathrm{d}x + \int_{\Omega(\mathbf{u})} \nabla f \cdot \mathbf{w} \,\mathrm{d}x.\end{aligned} \tag{6.12}$$

□

This result is specially adapted to our requirements. For more general results and an introduction to the area of shape calculus with application to partial differential equations, we refer to Simon [311] or [114, 313].

This theorem can directly be applied to calculate the Jacobian of the variational formulations. Equation (6.9) must be considered as a simple tool for evaluation of the derivatives. This formula however requires high regularity of the function f at the boundary. For example, we consider the variational formulation of Laplace equation

$$A(\mathbf{u})(\phi) = \int_{\Omega} \nabla\mathbf{u} \cdot \nabla\phi \,\mathrm{d}x.$$

Now assume that $\Omega = \Omega(\mathbf{u})$ as stated in Theorem 6.10. The variational formulation has a double dependency on $\mathbf{u}$, appearing as trial function itself and by the domain's dependency. Formula (6.9) gives

$$A'(\mathbf{u})(\mathbf{w}, \phi) = \int_{\Omega} \nabla\mathbf{w} \cdot \nabla\phi \,\mathrm{d}x + \int_{\partial\Omega} (\mathbf{n} \cdot \mathbf{w}) \nabla\mathbf{u} \cdot \nabla\phi \,\mathrm{d}o.$$

For this expression to be well-defined, we need traces of $\nabla \mathbf{u}$ and $\nabla \phi$. For H^1-functions, this regularity is not given. The crucial step in Theorem 6.10 is hidden in (6.12) using integration by parts. While the volume-formulation of the derivative is well-defined, the boundary integral formally requires higher regularity. See [311] for a discussion.

By the combination of Theorem 6.10 and Lemma 6.9, we can derive the complete Jacobian of the Fully Eulerian fluid-structure interaction problem.

Theorem 6.11 (Jacobian of the Fully Eulerian Formulation of Fluid-structure Interactions) *For the directional derivative of formulation (6.8) in* $\mathbf{U} = \{\mathbf{v}, \mathbf{u}, p\}$ *in direction of* $\mathbf{W} = \{\mathbf{z}, \mathbf{w}, q\}$ *it holds*

$$
\begin{aligned}
A'(\mathbf{U})(\mathbf{W}, \Phi) = & \left(\rho_f(\partial_t \mathbf{z} + \mathbf{z} \cdot \nabla \mathbf{v} + \mathbf{v} \cdot \nabla \mathbf{z}), \phi\right)_{\mathcal{F}(t)} \\
& + \left(\frac{d\boldsymbol{\sigma}_f}{d\mathbf{v}}(\mathbf{z}) + \frac{d\boldsymbol{\sigma}_f}{dp_f}(q_f), \nabla \phi\right)_{\mathcal{F}(t)} \\
& + \left(\frac{dJ_s}{d\mathbf{u}}(\mathbf{w})\hat{\rho}_s(\partial_t \mathbf{v} + \mathbf{v} \cdot \nabla \mathbf{v}) + J_s(\partial_t \mathbf{z} + \mathbf{z} \cdot \nabla \mathbf{v} + \mathbf{v} \cdot \nabla \mathbf{z}), \phi\right)_{\mathcal{S}(t)} \\
& + \left(\frac{d\boldsymbol{\sigma}_s}{d\mathbf{u}}(\mathbf{w}), \nabla \phi\right)_{\mathcal{S}(t)} + (\nabla \cdot \mathbf{z}, \xi_f)_{\mathcal{F}(t)} \\
& + \left(\partial_t \mathbf{w} + \mathbf{v} \cdot \mathbf{w} + \mathbf{z} \cdot \mathbf{u} - \mathbf{z}, \psi_s\right)_{\mathcal{S}(t)} + \left(\nabla \mathbf{w}, \nabla \psi_f\right)_{\mathcal{F}(t)} \\
& + \langle \rho_f(\partial_t \mathbf{v}_f + \mathbf{v}_f \cdot \nabla \mathbf{v}_f), (\mathbf{w}_f \cdot \mathbf{n}_f)\phi \rangle_{\mathcal{I}(t)} + \langle \boldsymbol{\sigma}_f, \nabla \phi (\mathbf{w}_f \cdot \mathbf{n}_f) \rangle_{\mathcal{I}(t)} \\
& + \langle \nabla \cdot \mathbf{v}_f, \xi_f (\mathbf{w}_f \cdot \mathbf{n}_f) \rangle_{\mathcal{I}(t)} + \langle J_s \hat{\rho}_s (\partial_t \mathbf{v}_s + \mathbf{v}_s \cdot \nabla \mathbf{v}_s), \phi (\mathbf{w}_s \cdot \mathbf{n}_s) \rangle_{\mathcal{I}(t)} \\
& + \langle \boldsymbol{\sigma}_s, \nabla \phi_s (\mathbf{w}_s \cdot \mathbf{n}_s) \rangle_{\mathcal{I}(t)} + \langle \partial_t \mathbf{u}_s + \mathbf{v}_s \cdot \nabla \mathbf{u}_s - \mathbf{v}_s, \psi_s (\mathbf{w}_s \cdot \mathbf{n}_s) \rangle_{\mathcal{I}(t)} \\
& + \langle \nabla \mathbf{w}_f, \nabla \psi_f (\mathbf{w}_f \cdot \mathbf{n}_f) \rangle_{\mathcal{I}(t)},
\end{aligned}
$$

where the directional derivatives of the deformation gradient, the stresses and the strains are defined in Lemma 6.9.

For the computations of the boundary terms, it must be considered, that the gradients of $\mathbf{v}$ and $\mathbf{u}$ are not continuous across $\mathcal{I}(t)$. Therefore, we denote the correct side by adding the subscripts "f" and "s" where necessary.

Remark 6.12 Including shape derivatives in the computation of the Jacobian significantly complicates the implementation work. In [126, 127] it is noted that computational approaches for linearization and also for sensitivity based optimization work well, if these shape derivatives are neglected. At the latest when optimization problems are considered, it will be necessary to include these terms, as they will be crucial for the determination of the adjoint information transport across the interface, see also Sect. 9.

6.5 Finite Elements for the Fully Eulerian Framework

The Fully Eulerian framework for fluid-structure interactions leads to an interface problem. The interface $\mathcal{I}(t)$ must be captured and across this interface, the solution $\{\mathbf{u}, \mathbf{v}\}$ suffers from a lack of accuracy. As has been discussed in Sect. 4.5, we must expect a breakdown in convergence rates, if we do not accurately treat the are around this interface.

The parametric finite element scheme proposed in Sect. 4.5 can directly be applied to this more complex coupled problem. As velocity and deformation are globally defined as continuous functions, no special adjustments are necessary. Only the coupling between velocity and pressure must be carefully considered. In [151], Frei discusses several alternatives to stabilize the inf-sup condition on meshes resulting from the parametric interface resolution. None of the techniques however is fully satisfactory. Instead, the definition and implementation of an inf-sup stable finite element pair remains an open topic.

Away from the moving interface $\mathcal{I}(t)$, standard finite element pairs can be used for the discretization of velocity, pressure and also for the deformation. To simplify a direct variational coupling of velocities and deformations across the interface, and to avoid local changes of basis functions, the same function spaces should be used within the fluid and the solid domain. For details, we refer to Sects. 4.3 and 5.3.

For further reading, we refer to the literature [151, 154] and also to Chap. 12 of this book.

6.6 Numerical Study

For validation of the Eulerian model, we first consider two simple fluid-structure interaction benchmarks, the *csm-1* problem and the *fsi-1* problem as proposed by Hron and Turek [199]. Both benchmark problems use the configuration as shown in Fig. 6.1, where an incompressible fluid flows around a circular obstacle and an elastic beam that is attached to this rigid obstacle. In the *csm-1* benchmark configuration the fluid is initially at rest and the beam undergoes a deformation caused by a gravity force. In the *fsi-1* benchmark problem no gravity force is

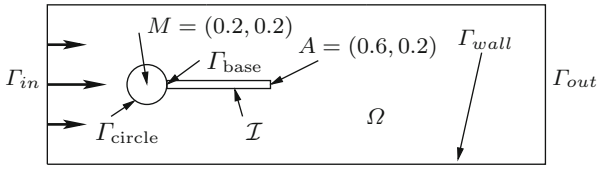

Fig. 6.1 Configuration of the *csm-1* and *fsi-1* benchmark problems as published by Hron and Turek [199]

acting, but the flow is driven by an inflow profile. Both problems have a stationary solution and highly accurate results for different functional values are available in literature [199, 201]. Finally, we describe a more challenging test case, where an elastic ball falls in an container filled with an incompressible fluid. The ball touches the bottom of the container and rebounces. Here we focus on modeling this collision of elastic structure with the domain's boundary.

6.6.1 Stationary Structure Benchmark Problem

In this first test case, a gravity force is acting on the elastic structure and causes a deflection, see Fig. 6.1. In the original benchmark configuration [199] $g_s = 2$ has been used, Wick [342] also published results for $g_s = 4$ yielding a larger deformation. To exploit the possibilities of very large deformation with the Eulerian approach, we add a further test case using $g_s = 8$. We measure the deformation $\mathbf{u}_s$ in the tip of the beam $A = (0.6, 0.2)$ in the stationary limit. In Table 6.1 we present the deflections in this measurement point on different meshes with decreasing mesh sizes under three different gravity forces. For comparison, we indicate the reference values are stated in [199, 201] and [342, 344]. The complete set of parameters used in this configuration is:

$$\begin{aligned} &\rho_f = \hat{\rho}_s = 10^3, \quad \nu_f = 10^{-3}, \quad \mu_s = 5 \cdot 10^5, \\ &\lambda_2 = 2 \cdot 10^6, \quad \mathbf{f}_s = -g_s J_s \hat{\rho}_s \chi_s. \end{aligned} \tag{6.13}$$

The Fully Eulerian method yields accurate values which are very close to the reference values cited from the literature. Further, the Eulerian framework is able to increase the gravity force up to a point ($g_s = 8$) where the beam touches the rigid bottom of the flow-channel, see Fig. 6.2. Here, no results for comparison are available in the literature.

Table 6.1 Results for the CSM-1 benchmark problem using increasing volume forces

	$g_s = 2$		$g_s = 4$		$g_s = 8$	
Mesh size	$u^x(A)$	$u^y(A)$	$u^x(A)$	$u^y(A)$	$u^x(A)$	$u^y(A)$
$h_{\min} \approx 0.008$	6.372	61.84	21.22	114.54	59.846	189.74
$h_{\min} \approx 0.004$	7.116	64.70	25.02	121.25	65.760	192.03
$h_{\min} \approx 0.002$	7.149	66.07	25.10	122.16	66.857	192.35
Hron and Turek [199]	7.187	66.10	n/a		n/a	
Wick [342, 344]	7.150	64.90	25.33	122.30	n/a	

Functional values on a sequence of meshes. Comparison to reference values taken from the literature using the ALE framework

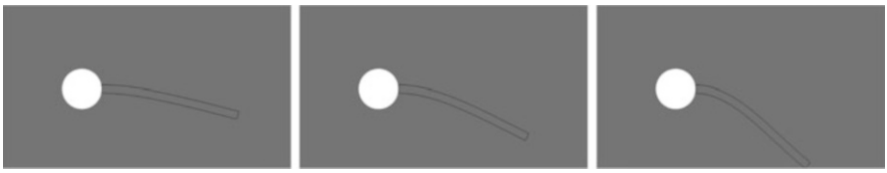

Fig. 6.2 Configuration of the *csm-1* benchmark problem and modifications with larger gravity force. *Left* $g_s = -2$, *middle* $g_s = -4$ and *right* $g_s = -8$

6.6.2 Stationary Fluid-structure Interaction Problem

As a second test case of the benchmark-suite published by Hron & Turek we refer to the *fsi-1* problem. The flow is driven by a parabolic inflow profile on the boundary Γ_{in}:

$$\mathbf{v}_{\text{in}} = \frac{y(H-y)}{4H^2} v_{\text{max}}, \quad H = 0.41, \quad \mathbf{v}_{\text{max}} = 0.3.$$

Due to a slight unbalance in the configuration (see Fig. 6.1) the elastic beam undergoes a small deflection. Apart from this modification, the material constants are taken as described in (6.13). Besides measuring the deflection of the beam, drag- and lift-values of the obstacle (rigid circle & beam) where to be estimated. Let $\Gamma_{\text{obs}} := \mathcal{I} \cup \Gamma_{\text{circle}} \setminus \Gamma_{\text{base}}$ be the complete outer boundary of the obstacle. Here, we consider the drag-value:

$$J_{\text{drag}} = \int_{\Gamma_{\text{obs}}} \mathbf{n}_f \boldsymbol{\sigma}_f \mathbf{e}_x \, \mathrm{d}s.$$

Evaluation of these integrals is accomplished by rewriting the boundary integrals over the moving interface $\mathcal{I}(t)$ into integrals over the fixed boundary around the rigid circle, followed by a reformulation into volume integrals. Finally, we can compute the drag force as a residual evaluation. We first modify the functionals by using the dynamic coupling condition and inserting zero:

$$\begin{aligned} J_{\text{drag}} &= \int_{\Gamma_{\text{circle}} \setminus \Gamma_{\text{base}}} \mathbf{n}_f \boldsymbol{\sigma}_f \mathbf{e}_x \, \mathrm{d}s + \int_{\mathcal{I}} \underbrace{\mathbf{n}_f \boldsymbol{\sigma}_f}_{=-\mathbf{n}_s \boldsymbol{\sigma}_s} \mathbf{e}_x \, \mathrm{d}s \pm \int_{\Gamma_{\text{base}}} \mathbf{n}_s \boldsymbol{\sigma}_s \mathbf{e}_x \, \mathrm{d}s \\ &= \int_{\Gamma_{\text{circle}} \setminus \Gamma_{\text{base}}} \mathbf{n}_f \boldsymbol{\sigma}_f \mathbf{e}_x \, \mathrm{d}s + \int_{\Gamma_{\text{base}}} \mathbf{n}_s \boldsymbol{\sigma}_s \mathbf{e}_x \, \mathrm{d}s - \int_{\partial \Omega_s} \mathbf{n}_s \boldsymbol{\sigma}_s \mathbf{e}_x \, \mathrm{d}s. \end{aligned}$$

In the stationary limit (and in the absence of external forces) it holds for the exact solution $\int_{\partial \Omega_s} \mathbf{n}\boldsymbol{\sigma} \, \mathrm{d}s = -\int_{\Omega_s} \operatorname{div} \boldsymbol{\sigma}_s \, \mathrm{d}x = 0$ and hence:

$$J_{\text{drag}} = \int_{\Gamma_{\text{circle}}} \mathbf{n}\boldsymbol{\sigma} e_1 \, \mathrm{d}s,$$

where by $\mathbf{n}$ we denote the outward facing normal vector (whether in Ω_f or Ω_s) and by $\boldsymbol{\sigma}$ the corresponding acting tensor. Evaluation of this boundary integral is straightforward, since the boundary Γ_{circle} is fixed, even in the Eulerian setting. The accuracy of this functional evaluation can be further enhanced by expressing it in terms of variational residuals,the *Babuška-Miller-Trick* [16, 88, 280]. In Table 6.2 we gather the drag-value obtained with the Eulerian approach. For evaluation of the functional we consider both the boundary integrals as well as the reformulation into residual terms. A good reference value $J_{\text{drag}} = 14.2940 \pm 10^{-5}$ is available in the literature [201, 280]. In Fig. 6.3 we show the error slopes of the drag approximation. Here we observe linear order of convergence (in the mesh-size h) for the boundary integral and quadratic convergence for the residual reformulation. Using piecewise linear finite elements one would expect (at least for a pure incompressible flow problem) the double order of convergence. Order reduction will take place due to the limited discretization accuracy close at the elements that are cut by the moving interface. Remedy could be found by using local mesh adaptation close to the interface or considering the extended finite element method [95] for better accuracy in the interface region. See Chap. 8 for details on adaptivity and Sect. 4.5 for techniques to discretize interface problems. Frei [151] showed results for the

Table 6.2 *fsi-1* benchmark results

Mesh-size	dof's	Boundary	Variational
0.1	53,450	15.1052	14.9004
0.05	176,790	15.2333	14.5971
0.025	640,490	14.7836	14.4062
0.0125	2,466,390	14.5118	14.3280

Drag-coefficient $J_{\text{drag}}(U_h)$ evaluates as boundary integral and reformulated as residual expression. The reference value taken from literature is given by $J_{\text{drag}} = 14.2940 \pm 10^{-5}$

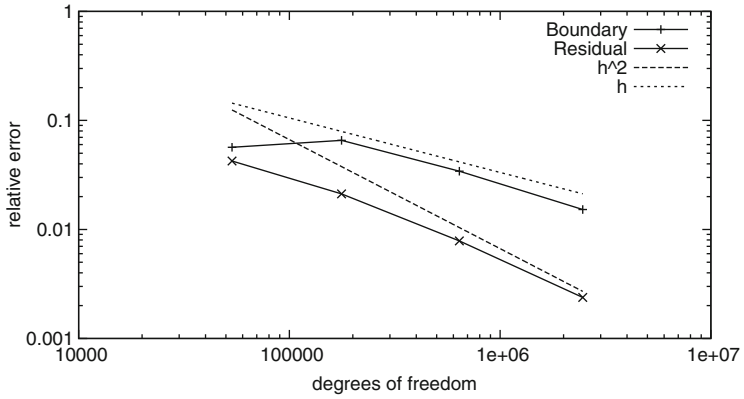

Fig. 6.3 Convergence of the drag-approximation with the Eulerian coordinate framework. Evaluated as boundary integral (linear convergence) and as residual term (quadratic convergence)

Fully Eulerian approach that do not suffer these order reductions, as accurate and efficient numerical schemes are used. Once more, we also refer to Chap. 12.

For a study of the time-dependent version fsi-3 of the benchmark problem, we refer to the results shown by Frei [151]. Given an adequate handling of the interface discretization with the locally modified scheme presented in Sect. 4.5 and accurate time stepping on moving interfaces as presented in Sect. 4.6, the Fully Eulerian model is able to reproduce the reference results from [330].

6.6.3 Contact Problem

Finally, we model the "free fall" of an elastic ball Ω_s with radius $r_{\text{ball}} = 0.4$ in a container $\Omega = (-1, 1)^2$ filled with a viscous fluid Ω_f. The container is closed at the bottom boundary $\Gamma_{\text{bot}} = \partial\Omega_{y=-1}$ but open at the top and the sides. Here, by open we refer to the "do-nothing" boundary condition

$$\nu \partial_n \mathbf{v} - p\mathbf{n} = 0,$$

which allows free in- and outflow of the fluid, see [188].

Figure 6.4 shows the configuration of this test case. At time $t = 0$, the midpoint of the ball is at $x_0 = (0, 0)$. Since gravity is the only acting force on the solid, the ball will accelerate and fall to the bottom

$$\Gamma_{\text{bot}} = \{(x, -1),\ x \in (-1, 1)\}.$$

At this rigid wall with homogenous Dirichlet condition $\mathbf{v}_f = 0$, the ball stops and due to elasticity it will bounce off again. The parameters used for this test case are given by

$$\begin{aligned} &\rho_f = 10^3, \quad \hat{\rho}_s = 10^3, \quad \nu_f = 10^{-2} \\ &\mu_s = 10^4, \quad \lambda_s = 4 \cdot 10^4, \quad \mathbf{f} = -J_s \hat{\rho}_s \chi_s. \end{aligned} \tag{6.14}$$

To get a closer look at the processes during "contact", we show in Fig. 6.5 a zoom into the are close to the lower boundary. We note that these computations have been done with a standard finite element basis, without using the parametric approach described in Sect. 4.5. Figure 6.5 shows simulation results for the time, where the structure enters the last layer of elements at the boundary, the time, where the ball gets closest to the boundary (here, a significant deformation of the structure is visible) and at a time, where the ball starts to release and finally, a snap-shot of the simulation, where the ball is completely detached. The Fully Eulerian formulation does not model real contact, as solid and boundary never touch.

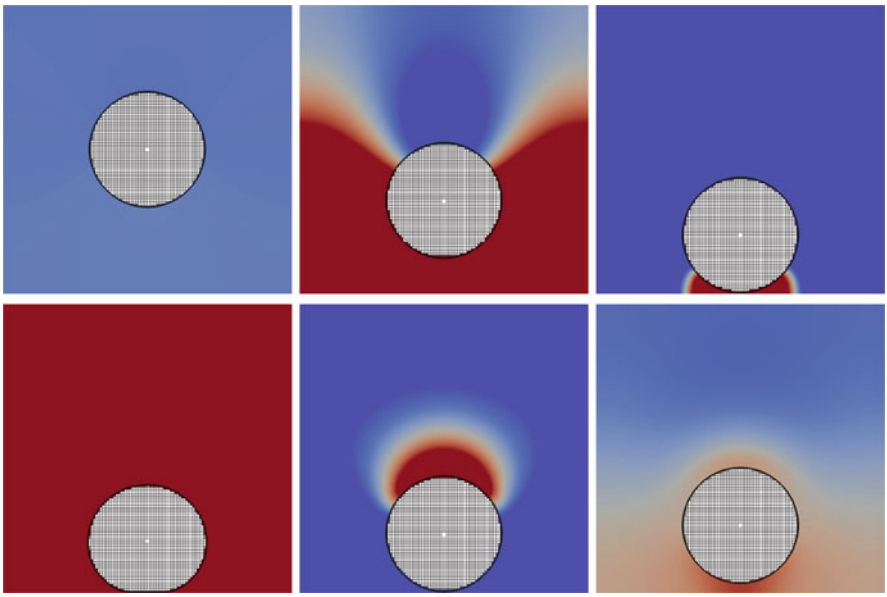

Fig. 6.4 Falling ball bouncing of the bottom wall. Snapshots of the solution at times $t = 0$, $t = 0.71$, $t = 0.96$ (first contact), $t = 1.035$ (biggest deformation), $t = 1.125$ (breaking contact) and $t = 1.38$ (highest bounce-off)

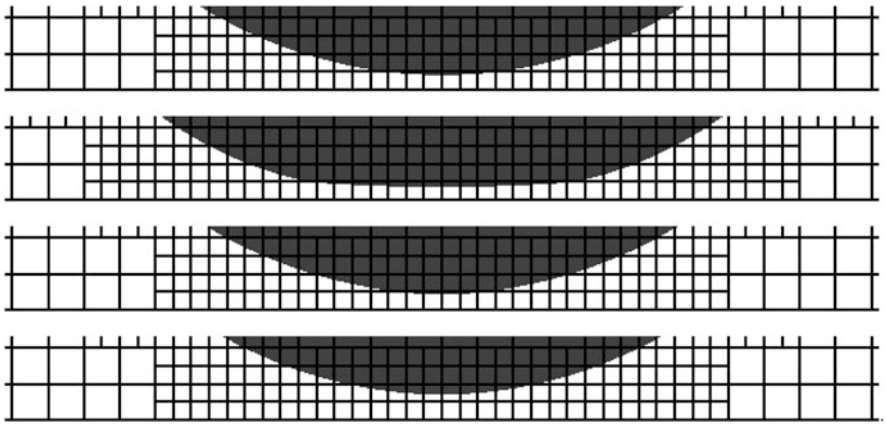

Fig. 6.5 Close ups of the contact problem. *From top to bottom*: simulation at times, where the ball first gets into the last layer of elements at the contact boundary, shortest distance to the boundary, beginning of release and full detachment

Remark 6.13 (Contact in Fluid-structure Interactions) It is a widely discussed question if contact in the case of the coupled dynamics of the incompressible Navier-Stokes equations and a solid body is possible at all. First of all, physical observation, i.e. a steel ball touching the ground, tells us that contact is established. On the other

hand, theoretical results, considering the fall of an rigid body with smooth boundary in an incompressible fluid show that contact (in the usual variational sense) will not be reached in finite time, see e.g. [115, 136, 189, 190, 241]. To the best knowledge of the author, no theoretical analysis has been done for collision problems of elastic structures in viscous fluids.

For the interaction of an elastic solid with smooth boundaries and a viscous fluid, one hypothesis is that a finite layer of fluid will always remain. In numerical simulations based on strong local adaptivity, this could however not be assured (neither disproved) so far.

From a modeling point of view, the use of the incompressible Navier-Stokes equations is questionable for such limiting applications. First of all, also water will not behave strictly incompressible, if very large forces act on a very thin film. Secondly, the continuum hypothesis must be queried in the transmission to contact.

To shed further light on the mechanism acting at "close contact", we consider the following functional outputs measuring stresses in fluid and solid: We measure the wall stress acting on the lower boundary and the elastic stress stored in the solid:

$$J_{\text{fluid}}(U) = \int_{\Gamma_{\text{bot}}} \boldsymbol{\sigma}_f \mathbf{n}_f \cdot \mathbf{n}_f \, \mathrm{d}o, \quad J_{\text{solid}}(U) = \left(\int_{\mathcal{S}(t)} \boldsymbol{\sigma}_s : \boldsymbol{\sigma}_s \, \mathrm{d}x \right)^{\frac{1}{2}}. \tag{6.15}$$

The results—together with the distance of the ball from the lower boundary—are shown in Fig. 6.6. Forces are transmitted through the remaining small liquid film and elastic energy is stored in the solid.

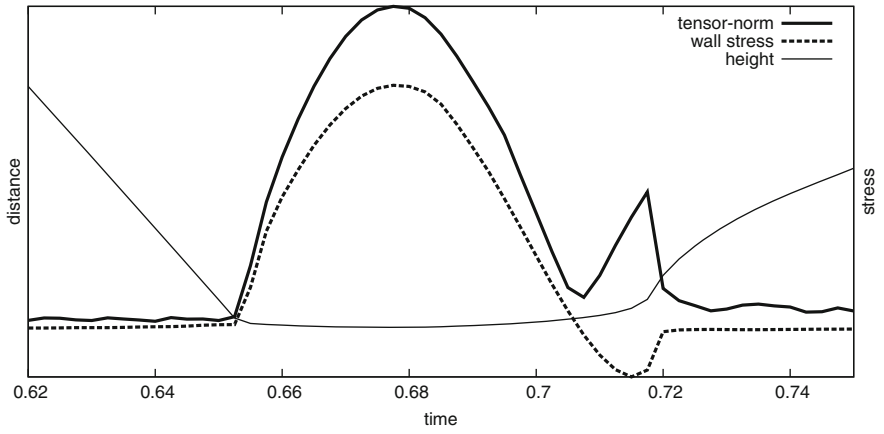

Fig. 6.6 Wall stress on the lower boundary and stresses in the solid during "contact"

Table 6.3 Error in mass conservation for the falling ball

h/k	0.0100	0.0050	0.0025
2^{-5}	$2.68 \cdot 10^{-3}$	$2.66 \cdot 10^{-3}$	$2.69 \cdot 10^{-3}$
2^{-6}	$7.82 \cdot 10^{-4}$	$6.95 \cdot 10^{-4}$	$6.72 \cdot 10^{-4}$
2^{-7}	$2.63 \cdot 10^{-4}$	$1.92 \cdot 10^{-4}$	$1.68 \cdot 10^{-4}$

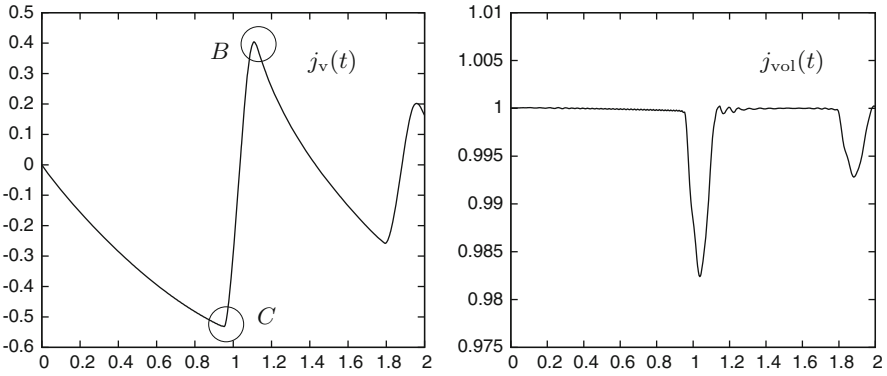

Fig. 6.7 Falling ball: functionals as plot over time. *Left*: solid's average velocity. *Right*: solid's relative volume. The two turning points of the velocity for contact (C) and maximum bounce-off (B) are indicated in the middle plot

Finally, to measure the quality of the approximation we indicate some further output functionals of the solution. First, as the Eulerian model does not have exact conservation properties, we analyze the solid's mass, measured as

$$J_{\text{mass}}(U) = \int_{\mathcal{S}(t)} J_s \hat{\rho}_s^0 \, \mathrm{d}x.$$

In Table 6.3 we show the error in mass conservation

$$\| j_{\text{mass}}(t) - \hat{\rho}_s \pi r_{\text{ball}}^2 \|_{L^2([0,2])},$$

depending on the accuracy of the spatial and temporal discretization. The time-interval $I = [0, 2]$ is so large that the ball hits the bottom boundary twice. We observe $O(h^2)$ convergence, even if we did not use the modified finite element approach described in Sect. 4.5. The time-discretization parameter k appears to be too small to have a substantial influence on the accuracy. strictly guarantee this conservation.

In Fig. 6.7 we show two further output functionals measuring the average vertical velocity of the ball and the volume of ball, both as functions over time:

$$J_{\mathbf{v}}(t) := \int_{\Omega_s(t)} \mathbf{v}_s^y(t) \, \mathrm{d}x, \quad J_{\text{vol}}(t) := \int_{\Omega_s(t)} 1 \, \mathrm{d}x. \tag{6.16}$$

Table 6.4 Left: maximum (negative) velocity reached in free fall. Right: maximum average velocity after bounce-off

h/k	0.0100	0.0050	0.0025
2^{-5}	−0.4977	−0.4990	−0.5006
2^{-6}	−0.5248	−0.5286	−0.5298
2^{-7}	−0.5402	−0.5311	−0.5315

h/k	0.0100	0.0050	0.0025
2^{-5}	0.320	0.348	0.365
2^{-6}	0.318	0.369	0.396
2^{-7}	0.357	0.388	0.404

Calculations on three different spatial and temporal meshes

Note that mass should be conserved, the volume of the elastic obstacle however is subject to change, as $\nu_s = 0.4$, compare (6.14).

Figure 6.7 shows the progress of the functionals (6.16) as function over time. The left sketch shows the average velocity. Here, acceleration by gravity and acceleration due to bounce of are clearly visible. The boundary of height is smaller (due to viscous damping). The right sketch shows the volume of the ball. Due to the compression at impact-time, the volume gets reduced during the contact. Reduction of volume is possible, since the flow-container is open on the upper, left and right boundaries.

Finally, in Table 6.4 we indicate the maximum (negative) velocity that is reached at the time of first contact $t_C \approx 0.952$, as well as the maximum velocity that is reached after the first bounce-off $t_B \approx 1.105$, see Fig. 6.7. Computations are done using three different temporal and spatial discretization parameters h and k. All meshes are uniform in space and time. While the time step has only a very small influence on the functional values we observe convergence under mesh-refinement.

The problem of an elastic ball, falling in a viscous fluid has been revisited by Frei [151]. Here, detailed studies including contact modeling are given. In particular it is found that for certain configurations, a minimal distance between ball and bottom of the flow container can be identified in numerical simulation, such that no real contact will take place at first touch-down. A numerical study with accurate interface discretization techniques is found in the guest article of Frei, Chap. 12 of this book.

Chapter 7
Linear Solvers for Fluid-structure Interactions

This chapter is devoted to different algebraic solution techniques for discretized fluid-structure interaction problems. We will consider discretizations in time and space as discussed in the previous chapters. The main focus will be put to fluid-structure interactions in Arbitrary Lagrangian Eulerian coordinates, as described in Chap. 5. Solution techniques for the alternative Eulerian approach from Chap. 6 will be mentioned, where standard approaches fail.

From finite element discretization and discretization in time, we derived nonlinear systems of algebraic equations. Find

$$\mathbf{U}_h \in X_h : \quad A_h(\mathbf{U}_h)(\Phi_h) = F(\Phi_h) \quad \forall \Phi_h \in Y_h,$$

where U_h is the unknown solution, $\Phi_h \in Y_h$ the finite element test function and $F(\cdot)$ is the right hand side that depends—in the case of non-stationary problems—on the old solution at the previous time step. In Sects. 5.2 and 6.4 we have discussed the linearization of this system by fixed-point iterations or by means of the Newton method. In any way linearization results in the necessity to solve linear systems of equations of the type

$$\mathbf{A}_h \mathbf{x} = \mathbf{b}.$$

These systems are huge, usually very ill-conditioned and without structure such as symmetry or positivity. In the following sections, we will give an overview over different solution techniques for these linear systems of equations arising from the finite element discretization of fluid-structure interactions. The main focus will be on solution techniques for fluid-structure interactions in Arbitrary Eulerian Lagrangian coordinates.

T. Richter, *Fluid-structure Interactions*, Lecture Notes in Computational Science and Engineering 118, DOI 10.1007/978-3-319-63970-3_7

7.1 Partitioned Solvers

The traditional approach for solving fluid-structure interactions is to choose a partitioning, where the problem is split into the Navier-Stokes problem on the fluid domain and into the elastic structure problem on the solid domain. Often this partitioning is considered as a Dirichlet-Neumann coupling. Given the interface deformation $\mathbf{u}_\mathcal{I}$ and velocity $\mathbf{v}_\mathcal{I}$, the fluid problem and the domain extension can be solved

$$F(\mathbf{u}_\mathcal{I}, \mathbf{v}_\mathcal{I}) \mapsto \{\mathbf{v}_f, \mathbf{u}_f, p_f\}. \tag{7.1}$$

Given the fluid's normal stresses on the interface $\boldsymbol{\sigma}_f \mathbf{n}_\mathcal{I}$ we can solve for the new solid deformation and velocity

$$S(\boldsymbol{\sigma}_f \mathbf{n}_\mathcal{I}) \mapsto \{\mathbf{u}_s, \mathbf{v}_s\}. \tag{7.2}$$

Both problems are solved separately and the coupling is realized by means of boundary conditions. The system is not only partitioned for the solution of the algebraic problems. Instead, one starts with two separated formulations. Strongly implicit discretization techniques, like a backward Euler for the coupled problem are not possible.

We assume that the interface values $\mathbf{u}_\mathcal{I}, \mathbf{v}_\mathcal{I}, \boldsymbol{\sigma}_f \mathbf{n}_\mathcal{I}$ are exactly known. Then, the solutions to (7.1) and (7.2) are the exact solutions to the coupled fluid-structure interaction problem. Of course, this idealistic assumption is usually not true. Instead, partitioned approaches employ outer loops to approximate the coupled solution by solving the two subfield problems (7.1) and (7.2). Approximations to the interface values $\mathbf{u}_\mathcal{I}, \mathbf{v}_\mathcal{I}, \boldsymbol{\sigma}_f \mathbf{n}_\mathcal{I}$ can be obtained from the approximations to the fluid problem $\mathbf{v}_f, p_f, \mathbf{u}_f$ and the solid problem $\mathbf{u}_s, \mathbf{v}_s$

$$\mathbf{u}_\mathcal{I} = \mathbf{u}_s\Big|_\mathcal{I}, \quad \mathbf{v}_\mathcal{I} = \mathbf{v}_s\Big|_\mathcal{I}, \quad \boldsymbol{\sigma}_f \mathbf{n}_\mathcal{I} = \boldsymbol{\sigma}_f(\mathbf{v}_f, \mathbf{u}_f, p_f)\mathbf{n}\Big|_\mathcal{I}.$$

Fluid and solid problem can therefore be written as

$$\{\mathbf{u}_s, \mathbf{v}_s\} \overset{F}{\mapsto} \{\mathbf{v}_f, \mathbf{u}_f, p_f\}$$

$$\{\mathbf{u}_f, \mathbf{u}_f, p_f\} \overset{S}{\mapsto} \{\mathbf{u}_s, \mathbf{v}_s\}.$$

The most basic partitioned approach is the *weakly coupled scheme*. This method can be regarded as a semi-explicit time stepping scheme. For solving the fluid and solid problem we take the interface approximations from the last time step, e.g. we perform simple subfield solutions of

$$\begin{aligned} \{\mathbf{u}_s(t_n), \mathbf{v}_s(t_n)\} &\overset{F}{\mapsto} \{\mathbf{v}_f(t_{n+1}), \mathbf{u}_f(t_{n+1}), p_f(t_{n+1})\} \\ \{\mathbf{u}_f(t_{n+1}), \mathbf{u}_f(t_{n+1}), p_f(t_{n+1})\} &\overset{S}{\mapsto} \{\mathbf{u}_s(t_{n+1}), \mathbf{v}_s(t_{n+1})\}. \end{aligned} \tag{7.3}$$

This approach introduces a splitting error that is at least of order $\mathcal{O}(\Delta t)$, where Δt is the time step size. Even if implicit and A-stable time-discretization schemes are considered for both of the subproblems, the semi-explicit character of the splitting can cause stability problem. Indeed, this is the most often observed drawback of simple weakly coupled approaches. In particular *added mass instabilities* will cause problems, see Sect. 3.3 and [148].

An improvement of partitioned approaches is by adding an outer iteration to approximate the solution of (7.3)

$$\begin{aligned} \{\mathbf{u}_s^{(i)}, \mathbf{v}_s^{(i)}\} &\overset{F}{\mapsto} \{\mathbf{v}_f^{(i+1)}, \mathbf{u}_f^{(i+1)}, p_f^{(i+1)}\} \\ \{\mathbf{u}_f^{(i+1)}, \mathbf{u}_f^{(i+1)}, p_f^{(i+1)}\} &\overset{S}{\mapsto} \{\mathbf{u}_s^{(i+1)}, \mathbf{v}_s^{(i+1)}\}, \end{aligned} \tag{7.4}$$

with

$$\mathbf{u}_s^{(0)} := \mathbf{u}_s(t_n), \quad \mathbf{v}_s^{(0)} := \mathbf{v}_s(t_n).$$

Such an iteration can be run, until the coupling conditions are fulfilled, i.e.,

$$\|\mathbf{v}_f^{(i+1)} - \mathbf{v}_s^{(i+1)}\|_{\mathcal{I}} + \|\boldsymbol{\sigma}_f^{(i+1)}\mathbf{n} - \boldsymbol{\sigma}_s^{(i+1)}\mathbf{n}\|_{\mathcal{I}} < tol,$$

or until the interface increment is small enough

$$\|\mathbf{v}_s^{(i+1)} - \mathbf{v}_s^{(i)}\|_{\mathcal{I}} + \|\mathbf{u}_s^{(i+1)} - \mathbf{u}_s^{(i)}\|_{\mathcal{I}} < tol.$$

In principle, such *strongly coupled partitioned approaches* are able to really solve the fluid-structure interaction problem. However *added mass instabilities* still give rise to problems and may require many subiterations of (7.4), see [93, 181].

For accelerating and stabilizing iterations of type (7.4) proper relaxation strategies are crucial. The interface update can be relaxed to

$$\tilde{\mathbf{u}}_s^{(n+1)}\Big|_{\mathcal{I}} = \omega \mathbf{u}_s^{(n+1)}\Big|_{\mathcal{I}} + (1-\omega)\mathbf{u}_s^{(n)}\Big|_{\mathcal{I}}.$$

A well-known strategy for controlling the relaxation parameter ω is by *Aitken's relaxation*, see [206]. The coupling iteration (7.4) can either be based on a simple relaxed Richardson iteration or by means of more advanced techniques, such as an Newton like scheme for the interface variables [113].

The major benefit of partitioned approaches is the efficiency of available tools for the two subproblems fluid and solid. Partitioned approaches can be build around these existing tools. If convergence in not too many iterations of (7.4) can be reached, partitioned approaches are very successful.

A comprehensive survey on partitioned methods is out of the scope of this book. Here, we focus on the monolithic approach, as it will allow us to design stable

methods with good accuracy and robustness. This does not mean that we will not use the idea of partitioning at all. In the following sections we will see that without splitting of the systems into the two ingredients, coupled fluid-structure problems often are too large and stiff to be solved in reasonable time.

For many applications like wind turbine simulation [32], where the added-mass effect does not act strongly, partitioned approaches can be very efficient computational tools. Recent research often aims at increasing the stability and robustness of strongly coupled partitioned approaches. For an overview on partitioned methods, we refer to [22, 77, 79, 80, 82, 83, 142, 163, 181, 183, 184, 197, 213, 215, 229, 235, 236, 263, 332] and many more. For the case of lower-dimensional structures, e.g. the description of the vessel wall as two dimensional boundary of the three dimensional fluid-domain in blood flow simulations, very efficient partitioned schemes exist. Here, by a proper decoupling and relaxation, the effect of the *added mass instability* can be dealt with.

7.2 Direct Solution of Linear Systems

Let

$$\mathbf{A}_h \mathbf{x} = \mathbf{b}, \tag{7.5}$$

be the linear system arising from the discretization of a coupled fluid-structure interaction problem. We assume that the matrix $\mathbf{A}_h \in \mathbb{R}^{n\times n}$ with $(\mathbf{A}_h)_{i,j} = a_{ij}$ is very large $n \gg 10^3 - 10^8$ but sparse, i.e. for every row $i \in \{1, \dots, n\}$ the set of non-zero entries

$$\mathcal{A}_i := \{j \in \{1, \dots, n\},\ a_{ij} \neq 0\}$$

is small, $\#\mathcal{A}_i = O(1)$. Solution of linear systems is very sensitive to error propagation from errors in the data $\mathbf{A}_h$ and $\mathbf{b}$. The following (pessimistic) bound holds for the propagation of errors

$$\frac{\|\mathbf{x} - \tilde{\mathbf{x}}\|}{\|\mathbf{x}\|} \leq \frac{\mathrm{cond}(\mathbf{A}_h)}{1 - \mathrm{cond}_2(\mathbf{A}_h)\frac{\|\delta\mathbf{A}_h\|}{\|\mathbf{A}_h\|}} \left(\frac{\|\delta\mathbf{b}\|}{\|\mathbf{b}\|} + \frac{\|\delta\mathbf{A}_h\|}{\|\mathbf{A}\|} \right),$$

if $\delta\mathbf{A}_h$ is a small perturbation of the system matrix $\mathbf{A}_h$, $\delta\mathbf{b}$ a perturbation of the right hand side. By

$$\mathrm{cond}(\mathbf{A}_h) := \|\mathbf{A}_h\|\,\|\mathbf{A}_h^{-1}\|$$

we denote the condition number of the matrix $\mathbf{A}_h$. For discretizations of partial differential equations, the condition number is usually very large. For elliptic problems, it holds

$$\text{cond}(\mathbf{A}_h) = \mathcal{O}\left(\frac{1}{h^2}\right),$$

such that we must expect a very strong error amplification. In Sect. 7.3.2, we will see that the condition numbers of coupled fluid-structure interactions in ALE coordinates is even far worse than that, of the single systems.

Without special knowledge and usage of the matrix structure, a direct solution of the linear systems is always a possibility. For general matrices $\mathbf{A}_h \in \mathbb{R}^{n\times n}$, direct solvers have a very great demand in computational time and also in memory use. The numerical effort scales by $\mathcal{O}(nm^2)$, where m is the bandwidth of the sparsity pattern of the matrix. The memory usage scales by $\mathcal{O}(nm)$. Problem on two dimensional meshes can usually be rearranged, such that $m \ll n$, making direct solvers a good option, see [210]. For three dimensional problems however, the sparsity is so excessive that the success of reordering is limited. See [110, 210, 219, 226] for an overview of powerful packages for the direct solution of linear systems. Considering three-dimensional problems, most direct solvers however lack efficiency. Finite element discretization of three dimensional problems leads to matrices with significantly more unknowns per matrix row, then their two dimensional counterparts. Here, modern and problem-adapted iterative solvers are usually preferable.

In a study using the linear solver UMFPACK [110] we have found that the very bad conditioning of coupled fluid-structure interactions can be so bad that the direct solver is not able to give satisfactory error reduction, see [283]. Instead, the direct solver had to be utilized in a defect-correction procedure with multiple steps. A very similar study by Aulisa et al. [9] using the direct solver MUMPS [5, 6] found comparable condition numbers but could not report on reduced convergence rates of the direct solver.

7.3 Analysis of Benchmark-Problems

To start the discussion, we first present two different test problems to be used throughout this article. First, we consider the non-stationary *fsi-3 benchmark* problem of Hron and Turek [199], a 2d test case featuring large deformation and stability problems caused by the *added-mass effect*. Second, we choose a three dimensional test case [280, 283] with smaller deformation. This three dimensional problem is also discussed in [9]. In the following, we describe the full configuration including all problem parameters for both test cases.

7.3.1 Configuration of the Benchmark Problems

Figure 7.1 shows a sketch of the geometry describing both benchmark problems. The two configurations are driven by an inflow condition $\mathbf{v}_f = \mathbf{v}_{\text{in}}$ for the velocity on Γ_{in}:

$$\mathbf{v}_{\text{in}}^{\text{2d}}(y) = \frac{y(H-y)}{(H/2)^2} \cdot \frac{3}{2}\bar{\mathbf{v}}_{\text{mean}}^{\text{2d}}, \quad \mathbf{v}_{\text{in}}^{\text{3d}}(y,z) = \frac{y(H-y)(H^2-z^2)}{(H/2)^2 H^2} \cdot \frac{9}{8}\bar{\mathbf{v}}_{\text{mean}}^{\text{3d}},$$

with average inflow velocities of $\bar{\mathbf{v}}_{\text{mean}}^{\text{2d}} = 2\,\text{m/s}$ and $\bar{\mathbf{v}}_{\text{mean}}^{\text{3d}} = 1\,\text{m/s}$. Both profiles are temporally smoothed to give a smooth transition from $\mathbf{v} = 0$ at $t = 0$ to the maximum velocity at time $t = 2\,\text{s}$, by multiplying with $\alpha(t) \in \mathbb{R}$ given by

$$\alpha(t) = \begin{cases} \frac{1}{2}\left(1 - \cos(\pi t/2)\right) & t < 2 \\ 1 & t \geq 2 \end{cases}.$$

On the outflow boundary Γ_{out} we prescribe the do-nothing condition

$$\rho_f \nu_f \mathbf{n} \cdot \nabla \mathbf{v}_f - p_f \mathbf{n} = 0, \tag{7.6}$$

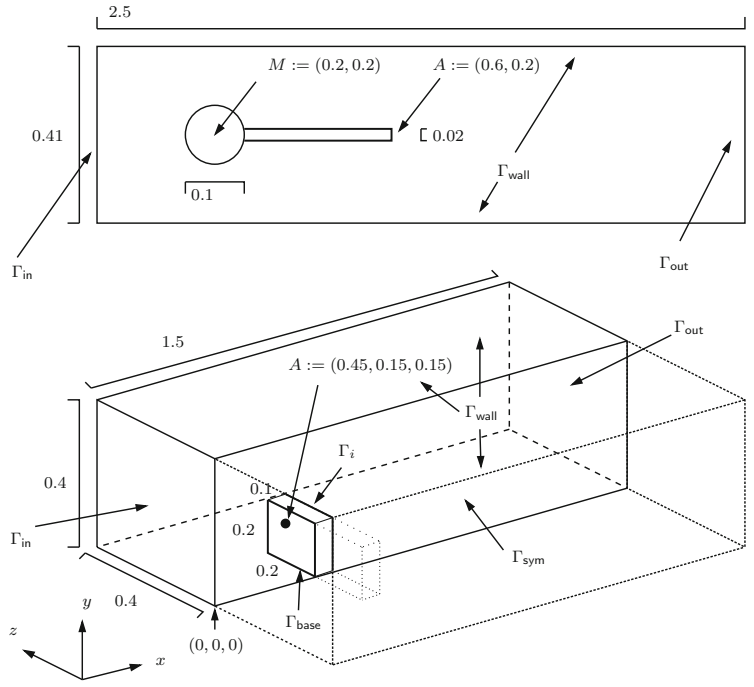

Fig. 7.1 Configuration of the two test cases

Table 7.1 Description of the two benchmark problems

Problem configuration	2D	3D
Fluid density ρ_f	$10^3\,\mathrm{kg}\cdot\mathrm{m}^{-3}$	$10^3\,\mathrm{kg}\cdot\mathrm{m}^{-3}$
Kinematic viscosity ν_f	$10^{-3}\,\mathrm{m}^2\,\mathrm{s}^{-1}$	$10^{-3}\,\mathrm{m}^2\,\mathrm{s}^{-1}$
Average inflow velocity $\bar{v}_{\mathrm{mean}}$	$2\,\mathrm{m}\,\mathrm{s}^{-1}$	$1\,\mathrm{m}\,\mathrm{s}^{-1}$
Solid density ρ_s	$10^3\,\mathrm{kg}\cdot\mathrm{m}^{-3}$	$10^3\,\mathrm{kg}\cdot\mathrm{m}^{-3}$
Shear modulus μ_s	$2\cdot 10^6\,\mathrm{kg}\cdot\mathrm{m}^{-1}\mathrm{s}^{-2}$	$5\cdot 10^5\,\mathrm{kg}\cdot\mathrm{m}^{-1}\mathrm{s}^{-2}$
Poisson ratio ν_s	0.4	0.4

Table 7.2 Number of unknowns, average convergence rates (see Remark 7.1), memory usage and average computational time for linear solution with monolithic geometric multigrid solver using a fully coupled block-wise incomplete decomposition as smoother

Mesh level (2d)	2	3	4	5	6	7
Unknowns	5260	20,640	80,960	320,640	1,276,160	5,091,840
Avg. conv. rate	0.14	0.29	>0.99	>0.99	>0.99	>0.99
Memory usage	19 MB	48 MB	–	–	–	–
Avg. time	0.12 s	0.72 s	–	–	–	–
Mesh level (3d)	2	3	4	5		
Unknowns	18,711	131,495	983,367	7,600,775		
Avg. conv. rate	0.086	0.067	0.094	0.33		
Memory usage	156 MB	1.0 GB	7.8 GB	64 GB		
Avg. time	1.23 s	10.17 s	120.15 s	2399 s		

In the 2D case, there was no convergence starting from mesh-level 4

see [188], on the walls Γ_{wall} a no-slip condition $\mathbf{v}_f = 0$. In the case of the 3d-configuration, we consider a symmetry condition at Γ_{sym}. In both cases, the solid is firmly attached to the boundary at Γ_{base} by prescribing Dirichlet conditions for velocity and deformation $\mathbf{v}_s = \mathbf{u}_s = 0$. In Table 7.2, we collect all parameters that completely describe the settings.

The 2d-case is challenging due large deformations that makes up about 50% of the fluid domain. The 3d-case is less demanding in this respect, as deformations are small. This reduces the effects of nonlinearities as well as the role of the ALE-mapping of the fluid problem. We start by collecting convergence rates of a fully monolithic multigrid solver in Table 7.1 for both problems.

Remark 7.1 (Estimation of Convergence Rate and Time, Computational Setup) As the coupled fsi problem is highly nonlinear with time-dependent dynamics, we always estimate convergence rates and computational time as averages over a sequence of time steps. Furthermore, as the number of Newton steps may vary from time step to time step, we fix the averaging by the following algorithm: in the case of the 2d-problem, we compute averages over 100 time steps and we include 5 Newton steps per time step into the averaging. Furthermore, we use an approximate Newton scheme by reusing the Jacobian: only every tenth time step, a new Jacobian is assembled. In the case of the 3d-problem we choose the same procedure, but

averaging is limited to 20 time steps. To sum up: all results belonging to the 2d test case contain averages over 500 steps of the linear solver, including 10 assemblies of the system matrix. In the 3d test cases, we average over 100 runs of the linear solver including 2 assemblies of the Jacobian (and the necessary preparation of the smoother or preconditioner).

This fixation allows for a fair comparison scaling over the mesh levels. All computations have been carried out on a Xeon E5-2690 cpu at 2.90 GHz with 256 GB of memory. Single core performance only is used for all computations.

The results in Table 7.2 present the performance of a standard geometric multigrid solver, used as preconditioner in an outer GMRES iteration. Coarse mesh problems are solved with help of a direct solver, and smoothing is done by a blockwise incomplete decomposition of the coupled system matrix. This solver is the standard technique in the software library GASCOIGNE 3D [43] and is highly efficient for problem in fluid-dynamics (compressible and incompressible), solid mechanics and various coupled multiphysics problems, see [211]. Here however, we see that the convergence rates quickly deteriorate on fine meshes. Already starting with about 81,000 unknowns, this solvers ceases to work in the (more difficult) 2d-case. In terms of material parameters and deformation, the three dimensional test case is easier. This explains the better convergence rates. Besides the computational times, we see that memory consumption is a severe issue, in particular for the three dimensional benchmark configuration. Although multigrid convergence rates are worsening for large problem sizes, the robustness of this standard solver must be highly appreciated.

A straight-ahead alternative to coupled multigrid solvers is the solution via direct solvers. In Table 7.3 we give indications of the convergence rates, memory usage and computational time for the two benchmark problems using the direct solver UMFPACK [110]. Memory consumption quickly goes beyond feasible limits. Computations on the finest meshes have not been possible. Furthermore, solution times increase in a similar fashion, such that direct solution—in particular for 3d problems—is no alternative. It is surprising that the direct solver (using double precision arithmetic) shows very bad error reduction, giving only one or two digits in every step. We will see that this behavior is due to the very bad conditioning of the coupled matrix. A similar study in [9] using the direct solver MUMPS [5, 6] did

Table 7.3 Convergence rates, memory usage and average computation time for linear solution with a monolithic direct solver

Mesh level (2d)	2	3	4	5	6	7
Avg. conv. rate	0.015	0.011	0.019	0.043	0.069	–
Memory usage	36 MB	135 MB	527 MB	2.9 GB	18.1 GB	>256 GB
Avg. time	0.042 s	0.21 s	1.18 s	8.75 s	47.74 s	–
Mesh level (3d)	2	3	4	5		
Avg. conv. rate	0.084	0.048	0.14	–		
Memory usage	307 MB	7.3 GB	132 GB	>256 GB		
Avg. time	0.92 s	36.25 s	2472 s	–		

not show this defect. MUMPS was able to solve the two dimensional problem with very good convergence rates. The setting and the finite element approach slightly differs from our techniques. Therefore it is too early to attribute these differences to the direct solver only.

7.3.2 Condition Number Analysis of the System Matrices

In this section, we will analyze the condition numbers of the Jacobian $\mathbf{A}_h$ and its different sub-parts. For this analysis, we consider the two benchmark problems introduced in Sect. 7.3. For a derivation of the system matrix, we refer to Sect. 5.3.4. Here, we shortly repeat the notation. The coupled problem consists of two matrices, $\mathbf{F}$ for the fluid-problem and $\mathbf{S}$ for the solid-problem that overlap on the interface degrees of freedom. The two sub-matrices can be written as

$$\mathbf{F} = \begin{pmatrix} F_p^{div} & F_{\mathbf{v}}^{div} & F_{\mathbf{u}}^{div} \\ F_p^{NS} & F_{\mathbf{v}}^{NS} & F_{\mathbf{u}}^{NS} \\ 0 & 0 & F_{\mathbf{u}}^{ALE} \end{pmatrix}, \quad \mathbf{S} = \begin{pmatrix} S_{\mathbf{v}}^{ES} & S_{\mathbf{u}}^{ES} \\ S_{\mathbf{v}}^{uv} & S_{\mathbf{u}}^{uv} \end{pmatrix}, \tag{7.7}$$

the coupled system matrix is given by

$$\mathbf{A}_h = \left(\begin{array}{ccc|ccc|cc} F_p^{div} & F_{\mathbf{v}}^{div} & F_{\mathbf{u}}^{div} & F_p^{div} & F_{\mathbf{v}}^{div} & F_{\mathbf{u}}^{div} & 0 & 0 \\ F_p^{NS} & F_{\mathbf{v}}^{NS} & F_{\mathbf{u}}^{NS} & F_p^{NS} & F_{\mathbf{v}}^{NS} & F_{\mathbf{u}}^{NS} & 0 & 0 \\ 0 & 0 & F_{\mathbf{u}}^{ALE} & 0 & 0 & F_{\mathbf{u}}^{ALE} & 0 & 0 \\ \hline F_p^{div} & F_{\mathbf{v}}^{div} & F_{\mathbf{u}}^{div} & F_p^{div} & F_{\mathbf{v}}^{div} & F_{\mathbf{u}}^{div} & 0 & 0 \\ F_p^{NS} & F_{\mathbf{v}}^{NS} & F_{\mathbf{u}}^{NS} & F_p^{NS} & F_{\mathbf{v}}^{NS} + S_{\mathbf{v}}^{ES} & F_{\mathbf{u}}^{NS} + S_{\mathbf{u}}^{ES} & S_{\mathbf{v}}^{ES} & S_{\mathbf{u}}^{ES} \\ 0 & 0 & 0 & 0 & S_{\mathbf{v}}^{uv} & S_{\mathbf{u}}^{uv} & S_{\mathbf{v}}^{uv} & S_{\mathbf{u}}^{uv} \\ \hline 0 & 0 & 0 & 0 & S_{\mathbf{v}}^{ES} & S_{\mathbf{u}}^{ES} & S_{\mathbf{v}}^{ES} & S_{\mathbf{u}}^{ES} \\ 0 & 0 & 0 & 0 & S_{\mathbf{v}}^{uv} & S_{\mathbf{u}}^{uv} & S_{\mathbf{v}}^{uv} & S_{\mathbf{u}}^{uv} \end{array}\right) \tag{7.8}$$

compare also (5.35). This coupled matrix is given as the prolongation of the two sub-matrices:

$$\mathbf{A}_h = \mathcal{R}_f^T \mathbf{F} \mathcal{R}_f + \mathcal{R}_s^T \mathbf{S} \mathcal{R}_s.$$

The first lines of Table 7.4 show the condition number of the coupled matrix

$$\text{cond}(\mathbf{A}_h) = \|\mathbf{A}_h\|_1 \|\mathbf{A}_h^{-1}\|_1,$$

in the 1-norm (maximum column sum). Furthermore, we indicate the condition numbers for the solid matrix $\mathbf{S}$ in (7.7), the main part of the Navier-Stokes problem

$$\mathbf{F}^{NS} = \begin{pmatrix} F_p^{div} & F_{\mathbf{v}}^{div} \\ F_p^{NS} & F_{\mathbf{v}}^{NS} \end{pmatrix},$$

Table 7.4 Condition numbers of the 2d (top) and 3d (bottom) benchmark problems for the full system matrix $\mathbf{A}$, the solid part $\mathbf{S}$, the Navier-Stokes part $\mathbf{F}^{NS}$ and the matrix of the ALE extension $F_{\mathbf{u}}^{ALE}$ (considering harmonic extension)

Mesh level (2d)	1	2	3	4	5
cond($\mathbf{A}$)	$\mathbf{3.30 \cdot 10^{12}}$	$\mathbf{9.85 \cdot 10^{12}}$	$\mathbf{4.36 \cdot 10^{13}}$	$\mathbf{1.76 \cdot 10^{14}}$	$\mathbf{7.40 \cdot 10^{14}}$
cond($\mathbf{S}$)	$4.19 \cdot 10^{7}$	$1.49 \cdot 10^{8}$	$5.54 \cdot 10^{8}$	$1.45 \cdot 10^{9}$	$5.26 \cdot 10^{9}$
cond($\mathbf{F}^{NS}$)	$3.12 \cdot 10^{8}$	$5.78 \cdot 10^{8}$	$1.15 \cdot 10^{9}$	$2.27 \cdot 10^{9}$	$4.34 \cdot 10^{9}$
cond($F_{\mathbf{u}}^{ALE}$)	$1.85 \cdot 10^{3}$	$7.67 \cdot 10^{3}$	$2.95 \cdot 10^{4}$	$1.16 \cdot 10^{5}$	$4.59 \cdot 10^{5}$
Mesh level (3d)	1	2	3		
cond($\mathbf{A}$)	$\mathbf{5.25 \cdot 10^{12}}$	$\mathbf{3.52 \cdot 10^{13}}$	$\mathbf{1.80 \cdot 10^{14}}$		
cond($\mathbf{S}$)	$3.48 \cdot 10^{5}$	$2.22 \cdot 10^{6}$	$8.36 \cdot 10^{6}$		
cond($\mathbf{F}^{NS}$)	$1.43 \cdot 10^{7}$	$3.25 \cdot 10^{7}$	$5.39 \cdot 10^{7}$		
cond($F_{\mathbf{u}}^{ALE}$)	$7.74 \cdot 10^{1}$	$2.86 \cdot 10^{2}$	$1.62 \cdot 10^{3}$		

and the ALE extension matrix $F_{\mathbf{u}}^{ALE}$. The latter two matrices implement homogenous Dirichlet values on the fluid-structure interface $\mathcal{I}$. A separate discussion of $\mathbf{F}^{NS}$ and $F_{\mathbf{u}}^{ALE}$ is reasonable, as the system naturally decouples. All condition numbers are approximated with Matlab [234]. To avoid scaling effects (from the size of mesh elements or from problem parameters), we apply diagonal scaling before computing the condition numbers. For both benchmark problems we show the resulting condition numbers on a sequence of uniform meshes.

A first glance at the numbers in Table 7.4 reveals the expected results with a proper scaling in terms of the mesh-size. This analysis however puts forward the dramatic effect of the monolithic coupling on the conditioning of the coupled system matrix $\mathbf{A}_h$ that finally causes standard coupled multigrid solvers (with coupled multigrid smoothers) to cease work, see the introduction and Table 7.2. By a decoupling, all condition numbers are within reasonable limits. This observation will guide the design of the partitioned multigrid smoother in Sect. 7.5. A similar study was performed by Aulisa et al. [9]. Here, similar values where identified by using MATLAB. In addition, conditioning of the systems was also estimated using the direct solver MUMPS [5, 6] that showed better values.

7.4 Krylov Space Solvers for Fluid-structure Interactions

Most of the versatile and efficient iterative solution methods are Krylov subspace methods like the *Conjugate Gradient* (CG) or the *Generalized Minimum Residual Method* (GMRES) or the *Biconjugate Gradient Stabilized Method* (BiCGStab). See [295] for a general overview.

The basic idea of these methods is to approximate the solution of $\mathbf{A}_h\mathbf{x} = \mathbf{b}$ rewritten as a minimization problem

$$\|\mathbf{b} - \mathbf{A}_h\mathbf{x}^{(l)}\| \to \min,$$

in the Krylov subspaces, given by

$$K^l(\mathbf{A}_h, \mathbf{r}) = \{\mathbf{r}, \mathbf{A}_h\mathbf{r}, \ldots, \mathbf{A}_h^{l-1}\mathbf{r}\}, \quad \mathbf{r} = \mathbf{b} - \mathbf{A}_h\mathbf{x}^{(0)}.$$

Krylov subspace techniques can be very efficient. The minimization problems are usually solved—or approximated—based on an orthogonalization of the Krylov spaces. The convergence rate however strongly depends on the condition number of the system matrix $\text{cond}(\mathbf{A}_h)$. For acceleration, the concept of preconditioning is applied. Instead of approximating $\mathbf{A}_h\mathbf{x} = \mathbf{b}$, one tries to solve the problem

$$\mathbf{P}_h\mathbf{A}_h\mathbf{x} = \mathbf{P}_h\mathbf{b},$$

where by $\mathbf{P}_h : \mathbb{R}^n \to \mathbb{R}^n$ we denote the *preconditioner*, an operator (most often a matrix), which should be spectrally similar to $\mathbf{A}_h^{-1}$, such that

$$\text{cond}(\mathbf{P}_h\mathbf{A}_h) \ll \text{cond}(\mathbf{A}_h).$$

There exist general purpose preconditioners like Jacobi, Gauss-Seidel or incomplete decompositions of the system matrix $\mathbf{A}_h$. All these techniques are not very successful in the context of fluid-structure interactions. Table 7.2 in Sect. 7.3 shows results for a geometric multigrid solver, smoothed by an incomplete decomposition. This approach failed on fine meshes.

Regarding fluid-structure interactions, a preconditioner should consider the structure of the problem. Assume that the general linear system of fluid-structure interactions can be written in the compact form

$$\begin{pmatrix} \mathbf{F} & \mathbf{C}_{fs} \\ \mathbf{C}_{sf} & \mathbf{S} \end{pmatrix} \begin{pmatrix} \mathbf{x}_f \\ \mathbf{x}_s \end{pmatrix} = \begin{pmatrix} \mathbf{b}_f \\ \mathbf{b}_s \end{pmatrix},$$

with a splitting into fluid-part, solid-part as well as the coupling parts. Then, be basic idea of a preconditioner would be to neglect some of the off-diagonal coupling

$$\mathbf{P} = \begin{pmatrix} \mathbf{F} & 0 \\ \mathbf{C}_{sf} & \mathbf{S} \end{pmatrix}^{-1} = \begin{pmatrix} \mathbf{F}^{-1} & 0 \\ -\mathbf{S}^{-1}\mathbf{C}_{sf}\mathbf{F}^{-1} & \mathbf{S}^{-1} \end{pmatrix}$$

Application of the preconditioner requires multiplication with the matrix $\mathbf{P}$. This itself requires the solution of linear systems coming from the solid-equation $\mathbf{S}$ and the fluid-equation $\mathbf{F}$. These again must be approximated with a suitable method. The large benefit of this approach however is that smaller systems with a well known character and better conditioning have to be approximated [148]. Furthermore, by applying the partitioning in the preconditioner, it is possible to break the very bad conditioning of the coupled system, see again Sect. 7.3.2.

Preconditioned Krylov subspace methods (usually it is GMRES) are among the most powerful solution methods for monolithic fluid-structure interactions. For increasing robustness and efficiency, a careful design of the preconditioner is

crucial. The main guideline on how to setup the matrix **P** is given in the following Sect. 7.5.2 where a similar concept is analyzed in the context of multigrid solvers. Furthermore, we refer to the extensive literature on this topic [21, 27, 79, 80, 108, 180, 181, 249, 340, 353]. In [220] an overview on state of the art precondition techniques for iterative fluid-structure interaction solvers is given.

7.5 Multigrid Solvers for the Arbitrary Lagrangian Eulerian Formulation

Another class of very efficient solvers is the multigrid method. Classic geometric multigrid methods [172, 341] are based on an approximation of the linear system on a hierarchy of levels, coming from the finite element discretization of the differential equation on a hierarchical sequence of meshes

$$\Omega_0, \Omega_1, \ldots, \Omega_L = \Omega_h,$$

with its own hierarchical sequence of finite element spaces

$$V_0 \subset V_1 \subset \cdots \subset V_L = V_h.$$

Geometric multigrid solvers are based on the observation that typical iterative methods like Jacobi or Gauss-Seidel do a very bad job in solving the problem, they however are very efficient and quick in removing all high frequent error contributions. Hence, instead of "solving" the problem on the finest mesh level $\Omega_L = \Omega_h$, only high frequent error parts are removed in very few iterations of a simple iterative algorithm. The remaining error (i.e. the residual) is then restricted to the next coarse mesh level Ω_{L-1}, where this strategy is repeated. Finally, arriving at the coarsest mesh level, the remaining problem is that small that it can efficiently be solved with help of a direct solver or a standard Krylov subspace method. So far the theory—which is the reality for simple elliptic problems. In the practical application to complex multiphysics problems, several challenges appear.

1. Very often a hierarchy of meshes is not available. It is never difficult to get finer meshes (simply by refinement), if however the only mesh at hand is already very complex, e.g. coming from a mesh generator, and no coarse mesh is available, the idea of geometric multigrid fails. There are strategies of generating coarse meshes, this however is not standard.
2. Simple iterations like Gauss-Seidel or Jacobi fail to work as smoother for problems without an elliptic character. There are robust options like iterations based on incomplete decompositions [35, 46, 211]. These however are costly and may fail for problems such as fluid-structure interactions, see Sect. 7.3. For saddle-point problems, the class of Vanka smoothers [198, 199, 275, 334, 357], based on solving local subproblems is very successful. Hron, Turek and coworkers

used Vanka-based smoothers in a geometric multigrid iteration with good success for 2d fluid-structure interactions [198, 275], considering 3d problems however, efficiency was reported to be lost (Hron, personal communication, 2014).

Very often, multigrid iterations are not directly used as solvers, instead, they serve as preconditioners in outer Krylov subspace methods. This approach is promising, as multigrid iterations—due to the hierarchical setup—allow to lessen the effect of small mesh sizes on the conditioning of the system matrix, see [172]. This is also the approach that we follow in this section. We develop a multigrid iteration for fluid-structure interactions in ALE coordinates, this iteration however will only be used as preconditioner in a Krylov subspace method as introduced in Sect. 7.4. A very similar approach has recently be presented for non-stationary fluid-structure interactions [9].

Remark 7.2 (Algebraic Multigrid) A possible solution for the first issue is the concept of *algebraic multigrid methods*, where the hierarchy of problems is generated on the algebraic level by agglomeration of matrix entries [320]. In theory, these new methods are very robust and versatile and could serve as black-box solvers. For complex applications however, specially adapted smoothers and also agglomeration techniques must be developed.

Gee et al. [163] presented a monolithic algebraic multigrid as preconditioner for Krylov subspace iterations. Here, Gauss-Seidel splitting is applied as smoother and not for preconditioning. This change of order can help to get access to the full power of linear multigrid convergency. Yang and Zulehner [353] derived a nonlinear iteration on the interface unknowns. In every step of a Newton approach decoupled linear problems in the fluid and solid domain must be solved. These are approximated with an algebraic multigrid solver.

This section will be devoted to the derivation of an efficient multigrid method for the preconditioning of the linear systems that arise from the finite element discretization of fluid-structure interaction problems in Arbitrary Lagrangian Eulerian coordinates. Here, we have the setting of Chap. 5 in mind and in particular, the linear systems of equations described in Sect. 5.3.4.

The main focus will be on the design of a robust smoother that takes the special structure of fluid-structure interactions into account.

Brummelen et al. [76] analyzed a simplified problem with potential flow and a lower dimensional solid. The authors argued that a monolithically coupled multigrid iteration with a decoupling within the multigrid smoother would serve as an optimal solver (convergence rates going to zero for increasing mesh-levels), if the two subproblems in the smoother are solved exactly. In the following we want to extend this approach.

7.5.1 GMRES Multigrid Iteration

In this section, we present the general layout of a multigrid preconditioned GMRES iteration for the coupled system

$$\mathbf{A}_h \mathbf{x} = \mathbf{b},$$

where $\mathbf{x} = (\mathbf{v}, \mathbf{u}, \mathbf{p})$ with $\mathbf{v}, \mathbf{u} \in \mathbb{R}^{2dN}$ and $\mathbf{p} \in \mathbb{R}^{N_f+N_i}$ is the vector of solution coefficients. By $\mathbf{v}_f, \mathbf{u}_f \in \mathbb{R}^{2d(N_f+N_i)}$ and $\mathbf{v}_s, \mathbf{u}_s \in \mathbb{R}^{2d(N_i+N_s)}$ we denote the overlapping (on the interface) restrictions of these vectors to the fluid- and solid degrees of freedom. $\mathbf{A}_h$ is the coupled system matrix (Sect. 7.8). The philosophy of the linear solver is to treat the coupled problem in a monolithic manner as long as possible. The analysis in Sect. 7.3.2 shows that the condition number $\text{cond}(\mathbf{A}_h)$ is very large. This large condition number not only stems from the second order character of the partial differential equations, but also from the different numerical scales acting in fluid- and solid-problem. Just to highlight one example: the viscosity of water is about 10^{-3} Pa $\cdot$ s, the Young's modulus of steel is $2 \cdot 10^{11}$ Pa. At the interface degrees of freedom, both equations are coupled in $\mathbf{A}_h$. Diagonal preconditioning does not significantly help to improve the condition number, see Sect. 7.3.2. Hence, whenever it is necessary to compute the inverse of $\mathbf{A}_h$, we will apply a splitting into fluid- and solid-part. The general outline of the solver is as follows.

1. As outer iteration to solve $\mathbf{A}_h \mathbf{x} = \mathbf{b}$ we employ a monolithic GMRES iteration, see Sect. 7.4.
2. The GMRES solver is preconditioned by a geometric monolithic multigrid solver.
3. The multigrid smoother is constructed as a domain decomposition iteration with a Dirichlet-Neumann coupling on the interface into solid-problem governed by $\mathbf{S}$ and fluid-problem governed by $\mathbf{F}$ (formulated as Dirichlet problem).
4. Each of these subproblems is smoothed with some steps of a simple iteration, e.g. Richardson or BiCGStab [295] preconditioned with solvers of Vanka type [275, 334], or of block-ILU type [46, 211].
5. The coarse-mesh problem will be treated by a direct solution of the monolithic coupled system.

The reason for applying the partitioning in the multigrid smoother and not as outer preconditioner is motivated by two arguments: first, it has been shown by Brummelen and coworkers [76] that a partitioned smoother with exact solution of the two subproblems is a perfect smoother for a certain class of fluid-structure interactions. Perfect here implies that the convergence rate will go to zero for increasing number of mesh-levels. Second, it is the simple observation that the role of the multigrid smoother is not that of finding a global solution, but its only intend is to locally smooth high frequent error contributions. Here, global coupling conditions must not be resolved.

We assume that a hierarchy of finite element meshes Ω_l and finite element spaces X_l is given. The classical multigrid iteration is given in a recursive fashion. The iteration itself is used to approximate the coarse mesh problems.

Definition 7.3 (Geometric Multigrid Algorithm) By Ω_l and X_l for $l = 1, \ldots, L$ we denote a hierarchy of multigrid meshes and finite element spaces, by $\mathbf{A}_l$ the hierarchy of system matrices. Let $\mathbf{x}^{(0)}$ be the initial guess and $\mathbf{b}$ be the right hand side. Iterate for $i = 1, 2, \ldots$

$$\mathbf{x}^{(i)} = \mathcal{MG}(L, \mathbf{x}^{(i-1)}),$$

where the multigrid iteration on level l is given by

$$\mathbf{y} = \mathcal{MG}(l, \mathbf{A}_l, \mathbf{b}_l, \mathbf{x}_l) :$$

1.	Pre-Smooth	$\mathbf{s}_l = \mathcal{S}(\mathbf{A}_l, \mathbf{b}_l, \mathbf{x}_l, \nu^1)$,
2.	Residual	$\mathbf{r}_l = \mathbf{b}_l - \mathbf{A}_l \mathbf{s}_l$,
3.	Restrict	$\mathbf{r}_{l-1} = \mathcal{R}(l, \mathbf{r}_l)$,
4.	Coarse-Mesh	$\mathbf{c}_{l-1} = \mathcal{MG}(l-1, \mathbf{A}_{l-1}, \mathbf{r}_{l-1}, 0)$
5.	Prolongate	$\mathbf{x}'_l = \mathbf{s}_l + \mathcal{P}(l, \mathbf{c}_{l-1})$
6.	Post-Smooth	$\mathbf{s}'_l = \mathcal{S}(\mathbf{A}_l, \mathbf{b}_l, \mathbf{x}', \nu^2)$,
7.	return	$\mathbf{s}'_l$

The coarse mesh problem for $l = 0$ is solved exactly

$$\mathcal{MG}(0, \mathbf{A}_0, \mathbf{b}_0, \mathbf{x}_0) := \mathbf{A}_0^{-1} \mathbf{b}_0.$$

Remark 7.4 (Multigrid Variants) The multigrid algorithm shows the so called V-cycle, where the multigrid iteration in step (4) is called only once to approximate the coarse mesh problem. Variants are the W-cycle, where two calls are applied or the F-cycle, see [172] or [341].

Further, regarding locally refined meshes, different concepts of generating the multigrid hierarchy exist. In order to obtain an algorithm with optimal linear runtime, is common to start the mesh-hierarchy in a bottom-up way: while the coarsest level Ω_0 covers the complete domain, finer mesh levels Ω_l only cover those parts, where local refinement is added. The advantage of this procedure is the reduced complexity on every mesh level. As the single mesh-levels do not cover the complete domain, it is not easily possible to treat the intermediate levels as approximations to the full problem. Furthermore, it is not trivial to realize global constraints (such as a pressure with average zero), see [35]. As an alternative, meshes can be generated in a top-down procedure, where Ω_L, the fines level is the actual finite element mesh of Ω, and where the coarser levels Ω_l are generated by coarsening. Apart from very

localized refinements, this procedure is able to give optimal runtimes. As every mesh level can be considered as an approximation to the global problem, implementation and analysis is strongly simplified [35, 211, 277].

Remark 7.5 (Mesh Transfer) The mesh prolongation and restriction operators in steps `3.` and `5.` are defined as the L^2-projections of the solution onto the next mesh level. In terms of the prolongation, this is simply the embedding and can be computed by local algebraic modifications of the coefficient vectors.

For the following, we discuss the restriction of the residual $\mathbf{r}_l \rightarrow \mathbf{r}_{l-1}$. An efficient method can be derived by using the interplay of finite element functions $r_l \in V_l$ and $r_{l-1} \in V_{l-1}$ and integrated coefficients $\mathbf{r}_l \in \mathbb{R}^{N_l}$ and $\mathbf{r}_{l-1} \in \mathbb{R}^{N_{l-1}}$. On the fine mesh, the residual vector is defined as

$$(\mathbf{r}_l)_i := (f, \phi_l^i) - a(x_l, \phi_l^i) \quad \forall \phi_l^i \in V_l. \tag{7.9}$$

The restriction is defined as L^2-projection of $r_l \in V_l$ to $r_{l-1} \in V_{l-1}$

$$(r_{l-1}, \phi_{l-1}) = (r_l, \phi_{l-1}) \quad \forall \phi_{l-1} \in V_{l-1}. \tag{7.10}$$

The restricted residual serves as right hand side to the coarse mesh problem. We do not need the finite element representation $r_{l-1} \in V_{l-1}$ but only the integrated residual vector $\mathbf{r}_{l-1}$ given as

$$(\mathbf{r}_{l-1})_i = (r_{l-1}, \phi_{l-1}^i).$$

Using the definition of the L^2-projection (7.10), the definition of the residual (7.9) and using the nested construction of the spaces $V_{l-1} \subset V_l$ we write

$$(\mathbf{r}_{l-1})_i = (r_{l-1}, \phi_{l-1}^i) = (r_l, \phi_{l-1}^i) = (f, \phi_{l-1}^i) - a(x_l, \phi_{l-1}^i). \tag{7.11}$$

As $\phi_{l-1}^i \in V_{l-1} \subset V_l$ it can be presented as linear combination of different test functions ϕ_l^j in V_l, e.g.

$$\phi_{l-1}^i = \sum_{j \in \mathcal{N}_{l-1}^i} \alpha_j \phi_l^j,$$

with given coefficients $\alpha_j \in \mathbb{R}$. Then, the residual restriction can be performed as linear combination in terms of

$$\begin{aligned}(\mathbf{r}_{l-1})_i &= (f, \phi_{l-1}^i) - a(x_l, \phi_{l-1}^i) \\ &= \sum_{j \in \mathcal{N}_{l-1}^i} \alpha_j \Big((f, \phi_{l-1}^i) - a(x_l, \phi_{l-1}^i) \Big) = \sum_{j \in \mathcal{N}_{l-1}^i} \alpha_j (\mathbf{r}_l)_j\end{aligned}$$

7.5.2 Partitioned Multigrid Smoother

Every smoothing step of the multigrid algorithm requires the approximation of the system

$$\mathbf{A}_l \mathbf{x}_l = \mathbf{b}_l.$$

For the following, we can skip the level index, as all levels cover the complete domain and can be treated in the same way. We consider a smoothing operator

$$\mathbf{x}^{(i)} = \mathscr{S}(\mathbf{x}^{(i-1)}, \mathbf{b}), \quad i = 1, \ldots, \nu,$$

which is realized as a preconditioned iteration with Gauss-Seidel coupling. This procedure is comparable to preconditioners for Krylov solvers, see [220].

Definition 7.6 (Geometric Multigrid Smoother) Given approximation $\mathbf{x}^0 := \mathbf{x}^{(n-1)}$ iterate for $i = 1, \ldots, \nu$

1.	Residual of solid	$\mathbf{r}_s^{(i)} = \mathcal{R}_s(\mathbf{b} - \mathbf{A}\mathbf{x}^{(i-1)})$
2.	Solve solid	$\mathbf{S}\mathbf{w}_s^{(i)} = \mathbf{r}_s^{(i)}$
3.	Update solid	$\mathbf{x}^{(i-\frac{1}{2})} = \mathbf{x}^{(i-1)} + \mathcal{R}_s^T \mathbf{w}_s^{(i)}$
4.	Residual of fluid	$\mathbf{r}_f^{(i)} = \mathcal{R}_f(\mathbf{b} - \mathbf{A}\mathbf{x}^{(i-\frac{1}{2})})$
5.	Solve fluid	$\bar{\mathbf{F}}\mathbf{w}_f^{(i)} = \bar{\mathbf{r}}_f^{(i)}$
6.	Update fluid	$\mathbf{x}^{(i)} = \mathbf{x}^{(i-\frac{1}{2})} + \mathcal{R}_f^T \mathbf{w}_f^{(i)}$

The two subproblems for solid and fluid are treated by a Dirichlet-Neumann coupling with homogenous Dirichlet values realized for velocity and deformation on the interface $\mathcal{I}$ in the fluid matrix $\bar{\mathbf{F}}$ and the right hand side $\bar{\mathbf{r}}_f^{(i)}$ (indicated by the bar). This corresponds to assigning the kinematic coupling condition to the fluid problem and the dynamic condition to the solid problem. An alternative would be to treat the interface in a balanced way with a Robin condition for both subproblems. Matrix entries belonging to the interface variables would be mixed, see (7.8).

We continue by describing the single fields. In a first step, we assume, that the local subproblems are solved exactly with help of a direct solver. By this intermediate construction, we will validate the smoothing property of the partitioning.

7.5.2.1 The Solid Problem

The solid part in the smoothing operation asks for an approximation of the system

$$\mathbf{S}\mathbf{w} = \mathbf{r} \quad \Leftrightarrow \quad \begin{pmatrix} S_{\mathbf{v}}^{ES} & S_{\mathbf{u}}^{ES} \\ S_{\mathbf{v}}^{uv} & S_{\mathbf{u}}^{uv} \end{pmatrix} \begin{pmatrix} \mathbf{v}_{s+i} \\ \mathbf{u}_{s+i} \end{pmatrix} = \mathbf{r}_s := \mathcal{R}_s \left(\mathbf{b} - \mathbf{A}\mathbf{x}^{\text{old}} \right), \tag{7.12}$$

where $\mathbf{x}^{\text{old}}$ is the last approximation. We start by analyzing the effect of this solid problem on the interface condition. Acting on the interface unknowns $\mathbf{v}_i$ and $\mathbf{u}_i$ only, the solid problem relates to (omitting the right hand side $\mathbf{b}$)

$$S_{\mathbf{v}}^{ES}(\underbrace{\mathbf{v}_i + \mathbf{v}_i^{\text{old}}}_{\mathbf{v}_i^{\text{new}}}) + S_{\mathbf{u}}^{ES}(\underbrace{\mathbf{u}_i + \mathbf{u}_i^{\text{old}}}_{\mathbf{u}_i^{\text{new}}}) = F_p^{NS}\mathbf{p}_i^{\text{old}} - F_{\mathbf{v}}^{NS}\mathbf{v}_i^{\text{old}} - F_{\mathbf{u}}^{NS}\mathbf{u}_i^{\text{old}}.$$

The dynamic condition constitutes itself as boundary terms in $S_{\mathbf{u}}^{ES}$, $F_{\mathbf{v}}^{NS}$ and F_p^{NS}. Hence, this iteration corresponds to the dynamic coupling condition

$$\boldsymbol{\sigma}_s(\mathbf{u}^{\text{new}})\mathbf{n}_s + \boldsymbol{\sigma}_f(\mathbf{v}^{\text{old}}, p^{\text{old}})\mathbf{n}_f = 0.$$

Alternative approaches are possible. By adding fluid-interface parts to the solid-matrix $S_{\mathbf{v}}^{ES}$, the dynamic condition would include an intermediate fluid-velocity. Gee et al. [163] shift the complete interface treatment to the fluid-subproblem. Here, we strictly decouple both problems in a Dirichlet-Neumann sense in order to separate different parameter scales.

Problem (7.12) can be decoupled, as both $S_{\mathbf{v}}^{ES}$ and $S_{\mathbf{v}}^{uv}$ correspond to the mass matrix, see Sect. 5.3.4. It holds

$$\left.\begin{aligned} a_v^{ES}(\mathbf{w}, \phi) &= k^{-1}(\rho_s^0\mathbf{w}, \phi), \\ a_v^{uv}(\mathbf{w}, \psi_s) &= -(\mathbf{w}, \psi_s) \end{aligned}\right\} \quad \Rightarrow \quad S_{\mathbf{v}}^{ES} = -\rho_s^0 k^{-1} S_{\mathbf{v}}^{uv}.$$

Hence, instead of solving (7.12) as one coupled system, we can approximate the solution in two sub-steps:

$$\begin{aligned} \left[\rho_s^0 k^{-1} S_{\mathbf{u}}^{uv} + S_{\mathbf{u}}^{ES}\right]\mathbf{u}_{s+i} &= \mathbf{r}_{s,\mathbf{v}} + \rho_s^0 k^{-1}\mathbf{r}_{s,\mathbf{u}}, \\ S_{\mathbf{v}}^{ES}\mathbf{v}_{s+i} &= \mathbf{r}_{s,\mathbf{v}} - S_{\mathbf{u}}^{ES}\mathbf{u}_{s+i}. \end{aligned} \tag{7.13}$$

In Sect. 7.5.3 we describe, how these problems can be approximated by an iterative scheme.

7.5.2.2 The Fluid Problem

The fluid problem

$$\bar{\mathbf{F}}\mathbf{w} = \mathbf{r} \quad \Leftrightarrow \quad \begin{pmatrix} F_p^{div} & \bar{F}_{\mathbf{v}}^{div} & \bar{F}_{\mathbf{u}}^{div} \\ \bar{F}_p^{NS} & \bar{F}_{\mathbf{v}}^{NS} & \bar{F}_{\mathbf{u}}^{NS} \\ 0 & 0 & \bar{F}_{\mathbf{u}}^{ALE} \end{pmatrix} \begin{pmatrix} \mathbf{p}_{f+i} \\ \mathbf{v}_{f+i} \\ \mathbf{u}_{f+i} \end{pmatrix} = \bar{\mathbf{r}}_f := \bar{\mathcal{R}}_f(\mathbf{b} - \mathbf{A}\mathbf{x}^{\text{old}}),$$

is modified to carry homogenous Dirichlet values for velocity and deformation on all interface nodes. This problem decouples into the ALE extension part

$$\bar{F}_{\mathbf{u}}^{ALE}\mathbf{u}_{f+i} = \bar{\mathbf{r}}_{f,\mathbf{u}}, \tag{7.14}$$

followed by the Navier-Stokes part

$$\begin{pmatrix} F_p^{div} & \bar{F}_{\mathbf{v}}^{div} \\ \bar{F}_p^{NS} & \bar{F}_{\mathbf{v}}^{NS} \end{pmatrix} \begin{pmatrix} \mathbf{p}_{f+i} \\ \mathbf{v}_{f+i} \end{pmatrix} = \begin{pmatrix} \mathbf{r}_{f,p} - \bar{F}_{\mathbf{u}}^{div}\mathbf{u}_{f+i} \\ \mathbf{r}_{f,\mathbf{v}} - \bar{F}_{\mathbf{u}}^{NS}\mathbf{u}_{f+i} \end{pmatrix}. \tag{7.15}$$

Again, we first assume that these two problems (7.14) and (7.15) are inverted with help of a direct solver. An approximative approach is described in Sect. 7.5.3.

7.5.2.3 Numerical Validation of the Partitioned Smoother with Exact Subproblems

Before presenting the final multigrid solver that avoids all direct matrix inversions, we show in Table 7.5 convergence rates, memory usage and computational times for the multigrid iteration with a partitioned smoother. On every mesh level we use one single smoothing step of the iteration given in Definition 7.6. The different subproblems (7.13)–(7.15), are solved with help of the direct solver UMFPACK [110]. Comparing to the results given in Table 7.3 that correspond to a monolithic direct solver for the coupled problem, we first observe that only about half of the memory is used. Further on, the average convergence rates of the linear solver are even better than those obtained with a monolithic direct solver. This is due to the very bad conditioning that causes significant loss of digits in applying direct inversion. Actually, we observe better convergence rates on finer meshes. This result is in accordance to the theoretical observations of Brummelen and coworkers [76].

In Table 7.5 we collect the results for the two benchmark problems. It is well seen that the convergence rates are stable under mesh-refinement. Furthermore, convergence is very fast, in particular compared to the rates of the monolithic

Table 7.5 Convergence rates, memory usage and average computation time for linear solution with splitting smoother and exact subproblems

Mesh level (2d)	2	3	4	5	6	7
Avg. conv. rate	0.049	0.034	0.018	0.016	0.019	0.014
Memory usage	21 MB	71 MB	292 MB	1.2 GB	5.2 GB	49 GB
Avg. time	0.07 s	0.27 s	1.18 s	5.90 s	35.93 s	345 s
Mesh level (3d)	2	3	4	5		
Avg. conv. rate	<0.01	<0.01	<0.01	–		
Memory usage	194 MB	2.1 GB	44 GB	>256 GB		
Avg. time	2.51 s	37.03 s	1217 s	–		

multigrid smoother given in Table 7.2. However we note that the separate problems within the smoother are solved with a direct solver. Nevertheless, compared to a direct solution of the monolithic problem, we could already substantially reduce the effort, as (in 3d) separate and smaller systems with three unknowns (extension) and four unknowns (Navier-Stokes and elasticity) are solved instead of one global system with seven unknowns.

7.5.3 *Approximation of the Subproblems*

The different sub-steps described in the previous section ask for the approximation (smoothing) of subproblems for the structure (7.13), the ALE extension (7.14) and the Navier-Stokes equations in ALE formulation (7.15). For all of these problems of type $\mathbf{Ax} \approx \mathbf{b}$, we choose a simple preconditioned Richardson iteration

$$\mathbf{x}^k = \mathbf{x}^{k-1} + \mathbf{P}(\mathbf{A}^{-1})(\mathbf{b} - \mathbf{A}\mathbf{x}^{k-1}), \quad k = 1, 2, \ldots, K,$$

with $\mathbf{x}^0 = 0$. Usually $K = 4$ is a good choice. As preconditioner we choose a stabilized incomplete lower-upper decomposition of the Matrix $\mathbf{A}$. This decomposition is performed in a block-wise sense. All degrees of freedom coupling in one node are strongly coupled. For the Navier-Stokes part (in three dimensions), this corresponds to small 4×4 blocks coupling pressure and the three velocities. For stabilization, we strengthen the diagonal by adding the weighted sum of all off-diagonals. This approximation is well suited as smoothing operation for various complex problems. In literature [36, 45, 46, 64, 211] descriptions of this smoother for various applications is found. It is possible to use stronger iterations for enhancing the smoothing process.

The idea of this smoother can be seen as a mixture of Vanka-smoother and ILU-smoother. It is stronger than a Vanka-smoother with Jacobi- or Gauss-Seidel coupling, as the inversion of the local blocks is embedded into an incomplete decomposition of the matrix. On the other hand, we use smaller block-sizes coupling only the degrees of freedom in single nodes (and not even those of one element). It will be worthwhile to analyze different smoothers for the subproblems, as standard Vanka-smoothers will be better suited for parallelization [275, 310].

In [9] the authors describe a smoother of domain decomposition type. This can also be regarded as generalization of the Vanka idea.

In Table 7.6, we report on the performance of the multigrid solver with split smoothing and approximate solution of the subproblems as described in Sect. 7.5.3. The first glance shows three desired effects: the convergence rates are nearly robust with respect to the mesh size, memory usage is optimal (linear) and the computational time is nearly linear. Comparing the results of Table 7.6 with those for the standard multigrid solver in Table 7.2 or those using the direct solver in Table 7.3, we see a substantial improvement in both memory consumption and computational costs.

Table 7.6 Convergence rates, memory usage and average computation time for linear solution with splitting smoother and iterative smoother in subproblems

Mesh level (2d)	2	3	4	5	6	7
Avg. conv. rate	0.078	0.042	0.043	0.040	0.048	0.054
Memory usage	17 MB	42 MB	142 MB	540 GB	2.1 GB	8.8 GB
Avg. time	0.10 s	0.43 s	1.89 s	8.47 s	38.22 s	171.92 s
Mesh Level (3d)	2	3	4	5		
Avg. conv. rate	0.049	0.052	0.059	0.068		
Memory usage	115 MB	510 MB	4.5 GB	27 GB		
Avg. time	0.48 s	4.10 s	42.90 s	401.2 s		

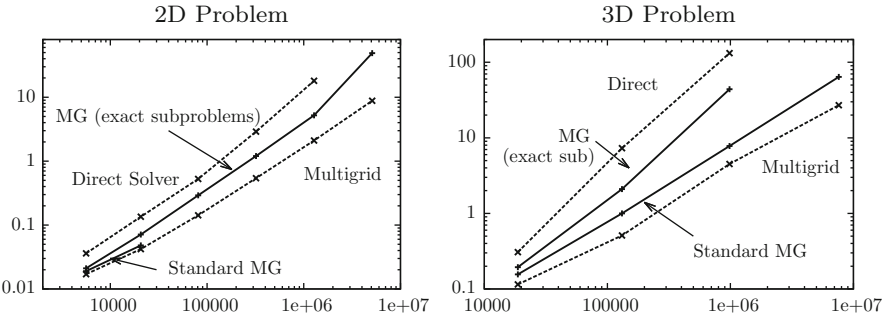

Fig. 7.2 Memory usage in Gigabyte for the different solvers. 2D problem in *left column* and 3D problem in *right one*. The final multigrid solver shows linear memory consumption of about 1.8 kB per unknown for the 2d-problem and 4 kB per unknown in the 3d-case

In Fig. 7.2 we show a comparison of the memory performance of the different approaches. Here, we observe a great benefit of the splitting approach within the smoother and the avoidance of direct solvers that always bring along fill-ins. Regarding the 3d problems, we observe a substantial improvement of the final multigrid solver with regard to the standard multigrid solver of GASCOIGNE 3D [43, 211]. This stems from the reduction of the overall matrix size: instead of one global 7×7 matrix, we only deal with smaller sub-matrices on either the fluid- or the solid-domain. The memory savings compared to direct solvers are dramatic, both for 2d and 3d problems.

Figure 7.3 shows a similar comparison regarding the average computational time required for solving the linear systems. The very similar performance of all methods in case of the 2d problem is a striking result (and a disappointment in terms of heavy implementation work attached to iterative techniques). In particular the excellent performance of the direct solver UMFPACK [110] must be appreciated. This result is even more surprising, as Fig. 7.2 does show a significant and non-optimal increase of memory usage. Regarding the 3d test case, there is a substantial discrepancy between the different solver's performance. Direct inversion of the global matrix or use of direct solvers within the smoother process immediately

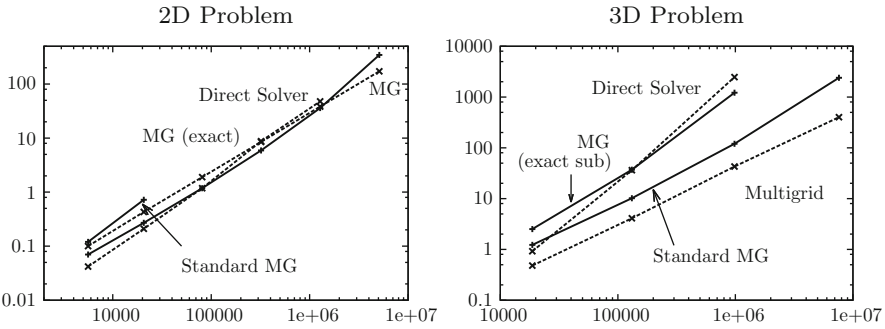

Fig. 7.3 Computational time in seconds (*lower row*) for the different solvers. 2D problem in *left column* and 3D problem in *right one*. Nearly linear run-time for the final multigrid solver in 3D. In 2d, similar performance of all solvers

ruins the performance. The standard multigrid solver of GASCOIGNE 3D [43, 211] shows a good performance, that is however sub-optimal, as the convergence rates deteriorates on fine meshes, see Table 7.2. Only the final multigrid solver based on partitioned smoothing operations shows a nearly optimal (linear) scaling.

In Fig. 7.4 we show a detailed analysis on the number of Newton- and GMRES-steps required in every time step for two different meshes. Both iteration counts do not depend on the mesh-level. In most of the iterations, exactly four Newton-steps are required. About 6 GMRES iterations are needed in every cycle of the Newton method, such that we totally use about 25 step of the linear solver in every time step.

To conclude we summerize the total finding from this study in Table 7.7. We show the relative computational time and the relative memory consumption of the geometric multigrid solver vs. the monolithic direct solver. In particular the 3d problem can be substantially accelerated by using a multigrid solver as preconditioner. Due to the linear scaling of the multigrid solver the effect gets larger on finer meshes. The memory savings are essential in 2d and in 3d.

Remark 7.7 (Numerical Studies in the Literature) The two dimensional example discussed by Gee, Küttler and Wall in Sect. 8.2 of [163] is comparable to the 2d-benchmark problem. Both configurations describe the self-excited motion of a flexible beam in a laminar flow. The authors [163] used a discretization with about 80,000 degrees of freedom, similar to mesh-level 4, see Table 7.2. On this mesh, the geometric multigrid solver with partitioned smoother requires an average of 1.89 s in every time step. An average of 5 Newton steps in every time steps results in 9.5 s per time step compared to an average of 7 s taken from [163]. In Fig. 7.4, we show the number of Newton steps and GMRES iterations required in each time step. Here, we show the results belonging to the discretization with 80,960 and the discretization with 320,640 degrees of freedom. A direct comparison is difficult, as the authors of [163] used a Newton tolerance of 10^{-4} vs. 10^{-8} in my work. Furthermore, the results in [163] have been obtained by a parallel solver on four cores, whereas the present results use single core performance only.

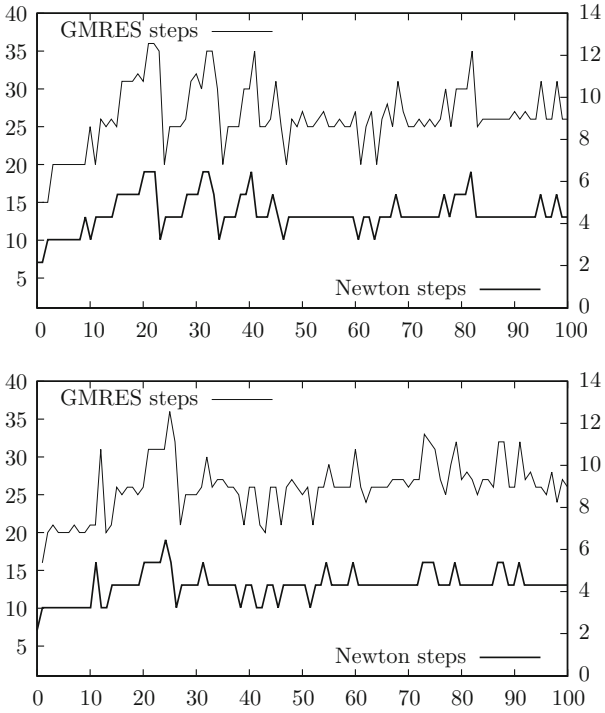

Fig. 7.4 Number of GMRES (*left*) and Newton (*right*) iterations in every time step. *Upper figure*: problem with 80,960 unknowns on mesh level 4. *Lower figure*: problem with 320,640 unknowns on mesh level 5

Table 7.7 Savings in computational time and memory consumption in relation to a monolithic direct solver

	2d benchmark			3d benchmark	
Unknowns	80,960	320,640	1,276,160	131,495	984,367
Avg. time (%)	160	97	80	11.3	1.7
Memory (%)	27	19	12	7	3.4

We indicate values on meshes, where the available memory was sufficient for both the geometric multigrid solver and the direct solver UMFPACK [110]

In [249, Sect. 4.3.1] the authors investigate a partitioned scheme as preconditioned for a monolithic GMRES iteration. Comparable to Sect. 7.5.2.3, the authors investigate the performance of their solver, if all subproblems are solved by direct inversion. They show nearly robust and good convergence rates. However, in contrast to the results shown in Table 7.5, convergence does not improve on finer meshes. This supports the assumption that a multigrid solver with a partitioned smoother (with exact solution of the subproblem) shows better robustness as preconditioner to a GMRES iteration, than a preconditioner that is based on a

partitioned iteration. Again, we refer to [76], where exactly this relation was shown for a linear model problem.

A work similar to our approach was recently published by Aulisa et al. [9]. They use a geometric multigrid solver with a domain decomposition smoother for stationary and non-stationary fluid-structure interaction problems in 2d and in 3d with incompressible fluids and solids. In their study the authors come to similar conclusions with respect to the conditioning of the systems and the need for a partitioning in the multigrid smoother. For comparison they use the direct solver MUMPS [4] which appears to have more success in dealing with the coupled fluid-structure interaction problem. In particular for 3d problems they also demonstrate substantial savings in terms of memory consumption and computational time. The approach presented by Aulisa et al. [9] is able to efficiently compute *direct-to-steady-state* solution.

7.5.4 Robustness Versus Problem Parameters

Next, we have a look at the robustness of the partitioned smoother with regard to different problem parameters. For example variations in the density ratio ρ_f/ρ_s could lead to instabilities due to the *added-mass effect* [93, 331, 332]. In Table 7.8, we modify different parameters in separate computations. All remaining settings are kept as in the standard configuration, see Table 7.1. All computations are carried out on mesh-level three with 131,495 unknowns. We indicate the average linear convergence rate over a total of 20 time steps. The results collected in Table 7.8 show good robustness of the multigrid smoother. It is able to handle large variations of the density ratio as well as variations in the fluid velocity (that will lead to variation of the Reynolds number). Further, we are able to cover nearly incompressible materials without breakdown of the smoother. This will stem from the fact that the partitioned smoother operation is based on incomplete block-wise decomposition of the matrices that initially was designed for incompressible flows, see [36, 211]. A dramatic effect on the convergence rate is only found for the very small shear

Table 7.8 Convergence rate of the multigrid solver with partitioned smoother depending on variation of different problem parameters

Fluid density ρ_f	0.001	0.01	0.1	1
Convergence rate	0.047	0.050	0.046	0.047
Average inflow velocity $\bar{v}_{\text{in}}$	1 m/s	2 m/s	4 m/s	8 m/s
Convergence rate	0.047	0.045	0.045	0.046
Shear modulus μ_s	$2 \cdot 10^5$	$2 \cdot 10^6$	$2 \cdot 10^7$	$2 \cdot 10^8$
Convergence rate	0.092	0.047	0.045	0.045
Poisson's ratio ν_s	0.1	0.2	0.4	0.49
Convergence rate	0.048	0.049	0.047	0.046

3d-benchmark problem on a mesh with 131,495 unknowns

Table 7.9 3d-benchmark problem on a mesh with 131,495 unknowns

Pre–post	0	1	2
0	–	0.047	0.048
1	0.052	0.039	0.023
2	0.050	0.022	0.031

Convergence rates of the multigrid solver depending on the number of pre- and post-smoothing steps

modulus $\mu_s = 1.4 \cdot 10^5$ that belongs to a very soft material. This choice results in very large deformation at the base Γ_{base}, where the elastic obstacle is attached to the fluid domain, see Fig. 7.1.

Finally, we show in Table 7.9 the sensitivity of the multigrid solver to different numbers of pre- and post-smoothing steps in the multigrid iteration. Here, this corresponds to the number of Gauss-Seidel iterations described in Sect. 7.5.2. The effect of increasing the number of iterations in the smoother is very little. This result corresponds to the findings of Brummelen and coworkers [76] and the results presented in Sect. 7.5.2.3, dealing with the partitioned smoother based on exact solution of the subproblems: if these are approximated with sufficient accuracy, one step of post-smoothing is sufficient to yield good and robust convergence, see Table 7.5.

Chapter 8
Error Estimation and Adaptivity

This chapter is devoted to a posteriori error estimation and adaptivity. Error estimators can help to control the quality of simulation results and serve as stopping criteria for our algorithms. In the following section we will start by gathering the basics of a posteriori error estimation in the finite element method. As we aim at the application to complex problems like fluid-structure interactions, the main target will be efficiency and ease of realization. Error estimation will be based on the *Dual Weighted Residual Method*, that has been developed by Becker and Rannacher [40, 41] as a very flexible tool to estimate errors in *goal functionals* of the solution that can be any kind of output values, such as the deformation of a solid-point, the wall stress on an elastic obstacle or the vorticity in a flow field.

We do not discuss other techniques for error estimation. They are of no lesser importance but we focus on the dual weighted residual method due to its simplicity in application to complex coupled problems.

What follows in Sect. 8.2 is an overview of methods that can used to control the quality of the spatial discretization. In the finite element method, this refers to the refinement (or the coarsening) of the underlying triangulation. Control of the temporal discretization, i.e. the choice of optimal time step sizes is the topic of Sect. 8.1.2. Finally, in Sect. 8.3, we describe the application of all these methods to coupled fluid-structure interaction problems.

8.1 A Posteriori Error Estimation

We start by discussing estimators for the discretization error $u - u_h$ of finite element solution. Such error estimators are important to guarantee that a computed solution $u_h \in X_h$ satisfies a required error bound, e.g. a relative error of 1%

$$\frac{\|u - u_h\|}{\|u\|} \leq 1\%.$$

T. Richter, *Fluid-structure Interactions*, Lecture Notes in Computational Science and Engineering 118, DOI 10.1007/978-3-319-63970-3_8

The a priori estimators derived in Sect. 4.2.2 or 4.3 have the drawback of involving constants from interpolation estimates, trace inequality or inverse inequalities. Exact values are usually not known. If an error bound of 1% is to be reached, it will make a considerable difference, if such a constant is 10 or 0.1.

The aim of a posteriori error estimates is to derive error bounds that involve as few unknown quantities as possible. Instead, a posteriori estimates make use of the already computed discrete approximation $u_h \in V_h$.

A posteriori error estimation in the context of finite elements has a long history. At the beginning, mostly the Laplace equation

$$-\Delta u = f \text{ in } \Omega,\ u = 0 \text{ on } \Gamma = \partial\Omega,$$

has been studied, which allows direct access to estimating the error in the energy norm with help of the residual

$$\|\nabla(u - u_h)\| = \sup_{\phi \in H_0^1(\Omega)} \frac{R(u_h)(\phi)}{\|\nabla\phi\|},$$

$$R(u_h)(\phi) := (f, \phi) - (\nabla u_h, \phi).$$

Using this error representation, the following simple *residual based energy norm estimator* can be derived

$$\|\nabla(u - u_h)\| \leq c_i \left(\sum_{K \in \Omega_h} h_K^2 \|f + \Delta u_h\|_K^2 + \frac{h_K}{4} \|[\mathbf{n} \cdot \nabla u_h]\|_{\partial K}^2 \right)^{\frac{1}{2}}, \tag{8.1}$$

where by h_K we denote the diameter of the element $K \in \Omega_h$ and by $[\mathbf{n} \cdot \nabla u_h]_e$ the jump of the (discontinuous) normal derivative $\mathbf{n} \cdot \nabla u_h$ across the elements edge $e \subset \partial K$. The constant $c > 0$ mainly depends on the constant of the interpolation operator and the topological layout of the finite element mesh. This estimator is proven to be *robust* which means that the estimator

$$\eta_h(u_h) := \left(\sum_{K \in \Omega_h} h_K^2 \|f + \Delta u_h\|_K^2 + \frac{h_K}{4} \|[\mathbf{n} \cdot \nabla u_h]\|_{\partial K}^2 \right)^{\frac{1}{2}},$$

really bounds the error (up to the constant c)

$$\|\nabla(u - u_h)\| \leq c\eta_h(u_h).$$

Furthermore, it is sharp up to higher order oscillations in the data

$$\eta_h(u_h) \leq c\|\nabla(u-u_h)\| + c\left(\sum_{K\in\Omega_h} h_K^2\|f-f_K\|_K^2\right)^{\frac{1}{2}},$$

$$f_K\Big|_K := \frac{1}{|K|}\int_K f(x)\,\mathrm{d}x.$$

By $f_K \in \mathbb{R}$ we denote a piece-wise constant approximation to f. This *data oscillation* term is of higher order. If $f \in H^1(\Omega)$, we can expect $\|f-f_K\|^2 \leq ch^2$. For details on residual based error estimators for elliptic problems, we refer to the literature [1, 15, 19, 336].

Estimators of residual type have been extended to different problems including transport, flow problems [2] to general conservation laws [208], to Eigenvalue problems [254], to elasto-plasticity [274] and many more.

Classical residual estimators are based on the estimation in the energy norm. By means on duality, the *Aubin Nitsche Trick*, an estimation in the L^2-norm is at hand

$$-\Delta z = \frac{u-u_h}{\|u-u_h\|} \quad \Rightarrow \quad \|u-u_h\| = R(u_h)(z),$$

where by $R(u_h)(z)$ we again denote the residual. This approach has been carried over to a more general setting by Estep [132]. Adjoint solutions, which are introduced to express the error in different functionals $j : H^1(\Omega) \to \mathbb{R}$

$$-\Delta z = j,$$

are further on estimated to achieve computable error bounds. Becker and Rannacher [40, 41] then advanced this technique to a computational method, where adjoint solutions to arbitrary functionals are not analytically estimated, but approximated by means of finite element discretizations and enter the error estimate as weights, such that the computable estimator for a functional error takes the form

$$|J(u-u_h)| \leq c\eta_h(u_h, z_h).$$

In the following, we will outline this error estimation technique, that is very versatile and has found much attention in literature [2, 42, 44, 164, 177, 231, 273, 335] and many more.

In the following, we shortly recapitulate the idea behind the *Dual Weighted Residual Method* (DWR) for error estimation. We start by discussing the linear case and quickly proceed to general nonlinear problems.

8.1.1 The Dual Weighted Residual Method

Considering linear problems, the *dual weighted residual method* (DWR) for error estimation is a direct application of the Aubin Nitsche Trick to general linear error functional on the right hand side of the adjoint problem. The nonlinear theory that gives us an error approximation for nonlinear problems and nonlinear functions is based on an optimization approach. We start with the linear case.

8.1.1.1 Linear Problems

For the beginning, we consider an elliptic diffusion-reaction-transport equation given by the variational formulation

$$u \in \mathcal{V} := H_0^1(\Omega): \quad A(u,\phi) = F(\phi) \quad \forall \phi \in \mathcal{V}, \tag{8.2}$$

where

$$A(u,\phi) = (\nabla u, \nabla \phi) + (\beta \cdot \nabla u, \phi) + (\alpha u, \phi), \quad F(\phi) = (f, \phi), \tag{8.3}$$

with a constant $\alpha \geq 0$ and a differentiable transport field $\beta \in C^1(\Omega)^d$ that satisfies

$$\| \operatorname{div} \beta \|_{L^\infty(\Omega)} \leq 2\alpha. \tag{8.4}$$

For every $f \in H^{-1}(\Omega)$ this equation has a unique solution, that satisfies $\|\nabla u\| \leq c\|f\|_{-1}$. Higher regularity of f, the domain Ω and the transport field β carries over to higher regularity in the solution. We aim at estimating the error $u - u_h$ in different functionals of the solution. Possibilities are the error in a single point of interest

$$J_a(u - u_h) = u(a) - u_h(a), \quad a \in \Omega, \tag{8.5}$$

the average error in the complete domain

$$J_\Omega(u - u_h) = \int_\Omega u(x) - u_h(x)\,\mathrm{d}x, \tag{8.6}$$

or the average over a subdomain $\Omega_1 \subset \Omega$

$$J_{\Omega_1}(u - u_h) = \int_{\Omega_1} u(x) - u_h(x)\,\mathrm{d}x, \tag{8.7}$$

or many more. Such error functionals can be very general, they should however be well-defined on the solution space $\mathcal{V} = H_0^1(\Omega)$, i.e., the functional should be an element of the dual space $J \in \mathcal{V}^* = H^{-1}(\Omega)$. In two or more spatial

dimensions, point-values are note well-defined, such that a functional like (8.5) has to be regularized

$$J_{a,\varepsilon}(u-u_h) = \frac{1}{\pi\varepsilon^2}\int_{B_\varepsilon(a)} u(x) - u_h(x)\,\mathrm{d}x, \qquad B_\varepsilon(a) = \{x \in \Omega,\ |x-a| < \varepsilon\}. \tag{8.8}$$

Remark 8.1 (Point Errors) From an analytical point of view, point functionals are not well-posed in an H^1-sense and should be regularized in terms of (8.8). In practical realizations however, the evaluation of such an integral for small $\varepsilon > 0$ is cumbersome. Hence, usual implementations simply evaluate in the single point. Given sufficient regularity of the data, e.g. $f \in H^1(\Omega)$, solutions to elliptic problems will have sufficient regularity (away from the boundary), such that point values are well defined.

Lemma 8.2 (Adjoint Problem) *Let $J \in H^{-1}(\Omega)$. The adjoint problem*

$$z \in \mathcal{V}: \quad A(\phi, z) = J(\phi) \quad \forall \phi \in \mathcal{V}, \tag{8.9}$$

where $A(\cdot,\cdot)$ is given as in (8.3), (8.4) has a unique solution $z \in \mathcal{V}$ with

$$\|\nabla z\| \le c\|J\|_{H^{-1}(\Omega)}.$$

Given sufficient regularity $z \in \mathcal{V} \cap H^2(\Omega)$ and $J \in L^2(\Omega)^*$, the adjoint solution is given by the classical formulation

$$-\Delta z - \beta \cdot \nabla z + (\alpha - \operatorname{div}\,\beta) z = j,$$

where $j \in L^2(\Omega)$ is defined as

$$(j, \phi) = J(\phi) \quad \forall \phi \in L^2(\Omega).$$

Proof As $z \in H_0^1(\Omega)$ has homogenous Dirichlet values, it holds with $\phi := z$

$$A(z,z) = \|\nabla z\|^2 + \left(\alpha - \frac{\operatorname{div}\,\beta}{2}\right)\|z\|^2 \ge c\|\nabla z\|^2,$$

where we could use the identity $(\beta\cdot\nabla z, z) = -(\beta\cdot\nabla z, z) - ((\operatorname{div}\,\beta)z, z)$ as boundary terms are zero. Together with the continuity of the form $A(\cdot,\cdot)$ we get existence of unique solutions with Lax Milgram. Integration by parts gives

$$A(\phi, z) = \big(\phi, -\Delta z - \beta\cdot\nabla z + (\alpha - \operatorname{div}\,\beta)z\big)$$

the classical formulation. □

The regularity of the adjoint solution z depends on the regularity of the domain Ω, the problem data, here α and β, and the regularity of the right hand side j, or J. We have already discussed that for the point error it holds $J_a \notin H^{-1}(\Omega)$. For the regularized point error with $\varepsilon > 0$ fixed and for the subdomain functional, we can write

$$J(\phi) = \frac{1}{\pi\varepsilon^2}\int_{B_\varepsilon(a)} \phi(x)\,\mathrm{d}x = \frac{1}{\pi\varepsilon^2}\int_\Omega \chi_{B_\varepsilon(a)}(x)\phi(x)\,\mathrm{d}x,$$

where by $j = \chi_{\Omega_1}$ we denote the characteristic function with respect to a subdomain

$$\chi_{\Omega_1}(x) = \begin{cases} 1 & x \in \Omega_1 \\ 0 & x \notin \Omega_1 \end{cases}.$$

Given sufficient regularity of Ω_1's boundary, e.g. being Lipschitz, it holds $\chi_{\Omega_1} \in L^2(\Omega)$. If $\Omega_1 \neq \Omega$ we do not have more regularity. Hence, for subdomain-type functionals, we can conclude

$$J_{\Omega_1}, J_{a,\varepsilon} \in L^2(\Omega)^*, \quad j_{\Omega_1}, j_{a,\varepsilon} \in L^2(\Omega).$$

With sufficient regularity of the domain, α and β, we can expect

$$z \in H^2(\Omega), \quad \|z\|_{H^2(\Omega)} \leq c_s \|j\|_{L^2(\Omega)}. \tag{8.10}$$

For the subdomain- or the point-functional it holds

$$\|j_{a,\varepsilon}\|_{L^2(\Omega)} = \frac{1}{\sqrt{\pi}\varepsilon}, \quad \|j_{\Omega_1}\|_{L^2(\Omega)} = \sqrt{|\Omega_1|}. \tag{8.11}$$

The global average corresponds to the adjoint right hand side $j_\Omega = 1$ with $j_\Omega \in C^\infty(\Omega)$. Given sufficient regularity of the domain Ω we get high regularity of the adjoint z

$$\|z\|_{H^{k+2}(\Omega)} \leq c_s \|j_\Omega\|_{H^k(\Omega)} = c_s\sqrt{|\Omega|}. \tag{8.12}$$

Following [40, 41] the following simple error identities for the functional error hold:

Theorem 8.3 (Dual Weighted Residual Method for Linear Problems) *Let $J \in H^{-1}(\Omega)$ be a given error functional. Let $u \in \mathcal{V}$ and $u_h \in V_h$ be solutions to*

$$A(u,\phi) = F(\phi) \quad \forall \phi \in \mathcal{V},$$
$$A(u_h,\phi_h) = F(\phi_h) \quad \forall \phi_h \in V_h,$$

and $z \in \mathcal{V}$ and $z_h \in V_h$ be the adjoint solutions

$$A(\phi, z) = J(\phi) \quad \forall \phi \in \mathcal{V},$$
$$A(\phi_h, z_h) = J(\phi_h) \quad \forall \phi_h \in V_h.$$

The following error identities hold for arbitrary $\phi_h \in V_h$:

$$\begin{aligned} J(u - u_h) &= F(z - \phi_h) - A(u_h, z - \phi_h), \\ J(u - u_h) &= J(u - \phi_h) - A(u - \phi_h, z_h). \end{aligned} \tag{8.13}$$

Proof We test (8.9) with the error $\phi := u - u_h$ to get with Galerkin orthogonality and using (8.3)

$$\begin{aligned} J(u - u_h) &= A(u - u_h, z) = A(u - u_h, z - \phi_h) \\ &= F(z - \phi_h) - A(u_h, z - \phi_h). \end{aligned}$$

The second estimate follows, by using Galerkin orthogonality of the adjoint problem:

$$\begin{aligned} A(u - u_h, z) &= A(u - u_h, z - z_h) = A(u - \phi_h, z - z_h) \\ &= J(u - \phi_h) - A(u - \phi_h, z_h). \end{aligned}$$

□

If we know analytical stability estimates of the adjoint solution, compare (8.10), (8.11) or (8.12), we can estimate the error identity

$$\begin{aligned} J(u - u_h) &= A(u - u_h, z - i_h z) \le c_A \|\nabla(u - u_h)\| \|\nabla(z - i_h z)\| \\ &\le c_A h^r \|f\|_{H^{r-1}(\Omega)} c h^k \|z\|_{H^{k+1}(\Omega)}, \end{aligned}$$

where $c_A > 0$ is the constant of the continuity estimate, r the degree of the finite element approach (assuming maximum regularity of u) and where k depends on the regularity of the adjoint solution. For the cases discussed above, we get

$$|J_{\Omega_1}(u - u_h)| \le c(\Omega_1) h^{r+1} \|f\|_{H^{r-1}(\Omega)}$$
$$|J_{\Omega}(u - u_h)| \le c h^{2r} \|f\|_{H^{r-1}(\Omega)}.$$

These estimates do not consider the local structure of the adjoint solution. In case of (regularized) point errors, the estimate would result in $|J(u - u_h)| \to \infty$ for $\varepsilon \to \infty$ (which in most cases is wrong). In other cases, where an a priori estimate of the adjoint solution is not easily possible, one can only approximate the estimator weight by computing a numerical approximation to the adjoint solution $\tilde{z}_h$.

In the following we discuss different ways for numerical approximations of the adjoint solution z and the adjoint interpolation error $z - i_h z$. Considering the error representation in Theorem 8.3, direct use of the primal finite element space $z_h \in V_h$ is no option, as orthogonality would give

$$\begin{aligned} J(u - u_h) &= F(z - \phi_h) - A(u_h, z - \phi_h) \\ &\approx F(z_h - \phi_h) - A(u_h, z_h - \phi_h) = 0. \end{aligned}$$

In literature [41, 277, 288] various approaches for the approximation of the weights $z - \phi_h$ are discussed. One straightforward and often used possibility is to compute the discrete adjoint solution in a finer finite element space, e.g.

$$\tilde{z}_h = z_h^{(2)} \in V_h^{(2)} \text{ or } \tilde{z}_h = z_{h/2} \in V_{h/2},$$

the spaces of double polynomial degree or the same-degree space on a finer mesh. In both cases the approximation $z - \phi_h \approx \tilde{z}_h - i_h \tilde{z}_h$, where i_h is the interpolation into V_h gives very satisfactory results and leads to the fully computable error approximation

$$J(u - u_h) \approx \eta_h(u_h, \tilde{z}_h) := F(\tilde{z}_h - i_h \tilde{z}_h) - A(u_h, \tilde{z}_h - i_h \tilde{z}_h).$$

The DWR method is not an error estimator, but it must be regarded as an error approximation. We cannot guarantee $|J(u - u_h)| \leq c|\eta_h|$. Furthermore—which is unusual for error estimates—the DWR method estimates the sign of the error. To measure the quality of the DWR estimator, we introduce the *effectivity index* eff_h as the ratio between error estimate and error

$$\mathrm{eff}_h(u_h, z_h) := \frac{\eta_h}{J(u - u_h)}. \tag{8.14}$$

In the limit $h \to 0$, a good error approximation should give $\mathrm{eff}_h(u_h, z_h) \to 1$. For any approximation $\tilde{z}_h$ to z, we get the estimate

$$\begin{aligned} \mathrm{eff}_h(u_h, z_h) &= \frac{\eta_h}{J(u - u_h)} = 1 + \frac{\eta_h - J(u - u_h)}{J(u - u_h)} \\ &= 1 + \frac{F(z - \tilde{z}_h) - A(u_h)(z - \tilde{z}_h)}{F(z - z_h) - A(u_h)(z - \tilde{z}_h)}, \end{aligned}$$

and the effectivity will depend on the ratio

$$\frac{\|\nabla(z - \tilde{z}_h)\|}{\|\nabla(z - z_h)\|} = O(h^\alpha).$$

If we could show convergence with an order $\alpha > 0$, the estimator would be asymptotically exact.

Example 8.4 (DWR Method for Elliptic Problems) We consider the diffusion transport equation

$$u \in H_0^1(\Omega) \quad (\nabla u, \nabla \phi) + (\beta \cdot \nabla u, \phi) = (f, \phi) \quad \forall \phi \in H_0^1(\Omega),$$

on the unit square $\Omega = (0,1)^2$ with a constant transport field

$$\beta = \begin{pmatrix} 2 \\ 1 \end{pmatrix},$$

and the right hand side $f \equiv 1$. By $V_h \subset H_0^1(\Omega)$ we denote the space of linear finite element on a uniform mesh with mesh size h and by $u_h \in V_h$ the discrete solution. As error quantity we consider the average of the solution on a subdomain $\Omega_0 \subset \Omega$

$$J(\phi) = \int_{\Omega_0} \phi \, \mathrm{d}x, \quad \Omega_0 = \left\{ (x,y) \in \Omega, \ \left|x - \frac{1}{2}\right| < \frac{1}{8}, \quad \left|y - \frac{1}{4}\right| < \frac{1}{8} \right\}$$

The adjoint problem is given by

$$z \in H_0^1(\Omega) \quad (\nabla \phi, \nabla z) + (\beta \cdot \nabla \phi, z) = J(\phi) \quad \forall \phi \in H_0^1(\Omega),$$

and it corresponds to the diffusion transport problem with opposite transport direction

$$z \in H_0^1(\Omega): \quad (\nabla z, \nabla \phi) - (\beta \cdot \nabla z, \phi) = J(\phi) \quad \forall \phi \in H_0^1(\Omega).$$

By $z_h^{(2)} \in V_h^{(2)}$ we denote the Galerkin solution of the adjoint problem with polynomials of degree two. In Fig. 8.1, we show both the solution u_h and adjoint solution $z_h^{(2)}$ of this problem. Further, we show the values of the real error $J(u - u_h)$, the estimated error $\eta_h(u_h, z_h^{(2)})$ and effectivity index $\mathrm{eff}_h(u_h, z_h)$. It can be well seen that the error estimator is highly accurate.

The estimator shows very accuracy. However, the effort for evaluation of the error estimator is higher than the effort for solving the problem itself. If one solves the adjoint problem with double polynomial degree, this high accuracy is also desirable for the primal solution u_h itself. Then however, we would need an even higher order in the adjoint problem to get good estimator accuracy.

An alternative scheme for getting higher order approximation of $z \in V$ is by solving local subproblems. Let $z_h \in V_h$ be the adjoint solution in the primal space V_h. Then, we define local subproblems on small parts of the mesh as

$$z_h^i \in V_h^*(P_i) \quad a(\phi_h^i, z_h + z_h^i) = J(\phi_h^i) \quad \forall \phi_h^i \in V_h^*(P_i),$$

where P_i is a set of some mesh elements $P_i = \{K_i^1, \ldots, K_i^m\}$ of the mesh Ω_h. One possibility for choosing these patches is to combine all elements that have one

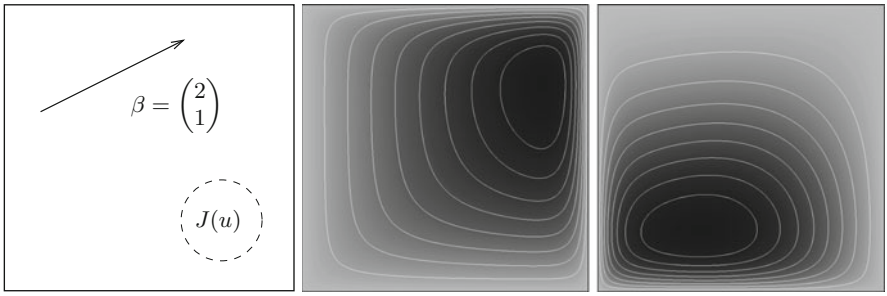

h	$J(u-u_h)$	$\eta_h(u_h, z_h)$	eff_h
2^{-1}	$-3.92 \cdot 10^{-2}$	$4.52 \cdot 10^{-2}$	-1.15
2^{-2}	$4.40 \cdot 10^{-4}$	$5.08 \cdot 10^{-3}$	11.53
2^{-3}	$4.57 \cdot 10^{-4}$	$5.47 \cdot 10^{-4}$	1.20
2^{-4}	$1.17 \cdot 10^{-4}$	$1.22 \cdot 10^{-4}$	1.04
2^{-5}	$2.94 \cdot 10^{-5}$	$2.96 \cdot 10^{-5}$	1.01
2^{-6}	$7.37 \cdot 10^{-6}$	$7.38 \cdot 10^{-6}$	1.00
2^{-7}	$1.84 \cdot 10^{-6}$	$1.84 \cdot 10^{-6}$	1.00

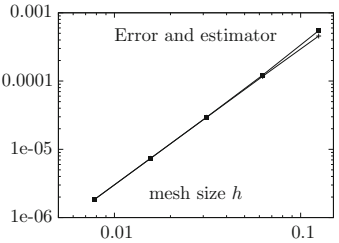

Fig. 8.1 Configuration and results for Example 8.4. *Upper row*: configuration (*left*), primal solution u_h (*middle*) and adjoint solution z_h (*right*). *Lower row*: error, estimator values and effectivity index on a sequence of meshes

common node $x_i \in \Omega_h$ in common. On the outer boundary of P_i the subproblem can be solved with either homogenous Neumann or Dirichlet boundary conditions for the enrichment z_h^i. For details, we refer to the literature [185]. One benefit of this local approach is that the small subproblems can be solved in parallel, and that high order polynomials can be considered without large additional costs. As for $\phi_h := I_h z$ the weights can be regarded as interpolation errors $z - I_h z$, which are local error quantities only, a local enrichment by small subproblems is well justified.

A third possibility for approximating $z - I_h z$ frequently used in literature [59, 280] is by a local reconstruction procedure (Fig. 8.2). First, the discrete adjoint problem is solved in the primal trial space $z_h \in V_h$. Then, mesh-elements of Ω_h are combined to larger patches, e.g. 2×2 elements $K \in \Omega_h$ form one patch $P \in \Omega_{2h}$. The discrete adjoint solution z_h is reinterpreted as a higher order solution $z_{2h}^{(2)} \in V_{2h}$ on a coarser mesh Ω_{2h}. If the mesh already features this patch-structure, see e.g. Fig. 8.3, this reconstruction is simply done by a local replacement of the basis functions

$$z_h(x) = \sum_{i=1}^{N} \mathbf{z}_i \phi_h^i(x) \quad \xrightarrow{z_{2h}^{(2)} = I_{2h}^{(2)} z_h} \quad z_{2h}^{(2)}(x) = \sum_{i=1}^{N} \mathbf{z}_i \phi_{2h}^{(2),i}(x).$$

In Fig. 8.2 we show this construction. A theoretical justification of this reconstruction process is by super-approximation only. Given a mesh with an—at least—locally uniform structure, we can expect higher order accuracy in the mesh-nodes that then can be used for reconstructing a higher order solution, see [52, 54]

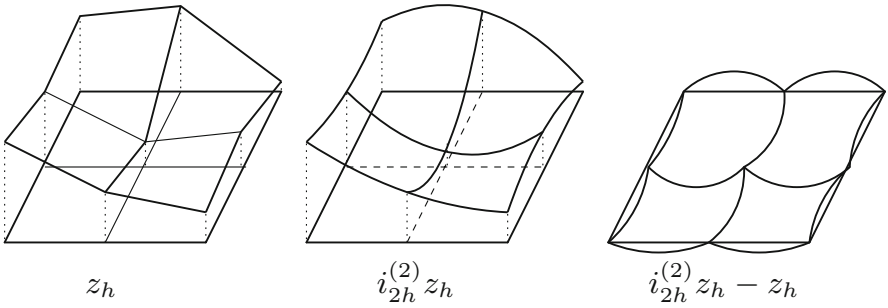

Fig. 8.2 Approximation of the weights $z - i_h z \approx \tilde{z}_h - i_h \tilde{z}_h$ by a higher order reconstruction of the adjoint solution $z_h \in V_h$ be means of interpolation into a higher-order coarse-mesh space $i_{2h}^{(2)} : V_h \to V_{2h}^{(2)}$. *From left to right*: adjoint solution, higher order reconstruction and reconstruction error

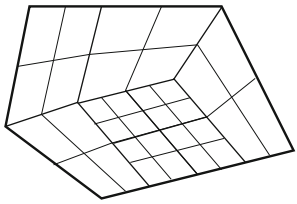

Fig. 8.3 Mesh with a patch-structure: four adjacent elements each arise from uniform refinement of one father-element

for details. Extensive studies in the literature have shown that this higher order reconstruction operator $I_{2h}^{(2)}$ is highly accurate for a large class of problems [42, 280]. Even if the mesh is completely unstructured and lacks such a patch structure, a higher order reconstruction can be undertaken, see [90].

The DWR method estimates the error in arbitrary functionals. This concepts brings along a number of possible pitfalls. First, a functional error $J(u - u_h)$ has a sign. It can hold $J(u-u_h) > 0$ or $J(u-u_h) < 0$ and very often the sign changes under mesh-refinement. When such a zero-crossing happens, the absolute error $|J(u-u_h)|$ can be very small, whereas the discretization error (measured in a norm) would still be very large. Then, going to even finer meshes, the absolute error will increase again. The table in Fig. 8.1 shows such an example. The sign of the error changes from first to second mesh. On the next two meshes, the absolute error even increases. While the estimator shows second order convergence from the beginning, the real error $J(u - u_h)$ does not depict such a monotonic character.

As the functional error can change the sign and as convergence must not be monotone, the dual weighted residual estimator is not well suited for the concept of convergent finite element schemes, where error estimation and adaptivity is combined in such a way that strict convergence of the solution (with fixed rates) can be certified [91, 121, 248, 319]. First attempts to showing efficiency for goal oriented error estimators are found in literature [3, 178].

One approach for getting a bound of the functional error is to combination of primal and adjoint energy error. Considering the error identity, we have

$$\begin{aligned} J(u-u_h) &= A(u-u_h)(z) = A(u-u_h)(z-z_h) \\ &\leq c_A \|\nabla(u-u_h)\| \, \|\nabla(z-z_h)\|. \end{aligned} \tag{8.15}$$

In [194], the authors use this bound to combine convergence results for both error contributions. In [252], the authors combine the DWR method with robust energy norm estimators to derive a *safeguarded* DWR estimator that is robust even if the effectivity index is very bad on coarse meshes.

8.1.1.2 Nonlinear Problems

The theory presented in the last section is based on a simple duality argument linking error functional to the variational formulation. Here, we will consider general nonlinear equations described by the form $A : \mathcal{V} \times \mathcal{V} \to \mathbb{R}$, which is supposed to be linear in the second argument and three times differentiable in the first. By $J : \mathcal{V} \to \mathbb{R}$ we denote the error functional, will now also can be nonlinear and which is supposed to be three times differentiable. We present the theory as introduced by Becker and Rannacher [41]. Examples for nonlinear functionals are the vorticity of a velocity field

$$J_\times(\mathbf{v}) = \int_\Omega |x \times \mathbf{v}|^2 \, \mathrm{d}x, \tag{8.16}$$

the wall stress induced by nonlinear material laws

$$J_\Sigma(\mathbf{u}) = \int_\Gamma \mathbf{F}(\mathbf{u})\boldsymbol{\Sigma}(\mathbf{u})\mathbf{n} \cdot \mathbf{e} \, \mathrm{d}x,$$

and many other quantities. In the following, the solution $u \in V$ is given by the nonlinear variational formulation

$$u \in \mathcal{V} \quad A(u)(\phi) = F(\phi) \quad \forall \phi \in \mathcal{V}, \tag{8.17}$$

where $F \in \mathcal{V}^*$ is the right hand side functional. For a finite element discretization $V_h \subset \mathcal{V}$ we define the discrete solution as

$$u_h \in V_h \quad A(u_h)(\phi_h) = F(\phi_h) \quad \forall \phi \in V_h. \tag{8.18}$$

Following the approach by Becker and Rannacher [41], we define the Lagrange functional

$$\mathcal{L}(u, z) = J(u) + F(z) - A(u)(z). \tag{8.19}$$

If $u \in \mathcal{V}$ is the solution to (8.17) and $u_h \in V_h$ solution to (8.18) it holds

$$J(u) - J(u_h) = \mathcal{L}(u, z) - \mathcal{L}(u_h, z_h)$$

for all $z \in \mathcal{V}$ and $z_h \in V_h$. Note that the functional error is given by $J(u) - J(u_h)$ and not by $J(u - u_h)$. These two expressions coincide for linear functionals only. We state the main theorem

Theorem 8.5 (Dual Weighted Residual Method for Nonlinear Problems) *Let $u \in \mathcal{V}$ and $u_h \in V_h$ be the solutions to*

$$\begin{aligned} A(u)(\phi) &= F(\phi) \quad \forall \phi \in \mathcal{V} \\ A(u_h)(\phi_h) &= F(\phi_h) \quad \forall \phi_h \in V_h \end{aligned}$$

and $z \in \mathcal{V}$ and $z_h \in V_h$ be the adjoint solutions to

$$\begin{aligned} A'(u)(\phi, z) &= J'(u)(\phi) \quad \forall \phi \in \mathcal{V}, \\ A'(u_h)(\phi_h, z_h) &= J'(u_h)(\phi_h) \quad \forall \phi_h \in V_h, \end{aligned}$$

where by $A'(\cdot)(\cdot, \cdot)$ and $J'(\cdot)(\cdot)$ we denote the Gâteaux derivatives

$$\begin{aligned} A'(u)(\phi, z) &= \frac{d}{ds} A(u + s\phi)(z)\Big|_{s=0}, \\ J'(u)(\phi) &= \frac{d}{ds} J(u + s\phi)\Big|_{s=0}. \end{aligned}$$

For the functional error it holds

$$\begin{aligned} J(u) - J(u_h) = &\frac{1}{2}\Big\{(f, z - I_h z) - A(u_h)(z - I_h z)\Big\} \\ &+ \frac{1}{2}\Big\{J'(u_h)(u - I_h u) - A'(u_h)(u - I_h u, z_h)\Big\} + \mathcal{R}^{(3)}, \end{aligned}$$

with a remainder $\mathcal{R}^{(3)}$ of third order in the error $e_h = \{u - u_h, z - z_h\}$ and where $I_h : \mathcal{V} \to V_h$ is an arbitrary interpolation operator.

Proof For simplicity, we introduce the notation $x := (u, z) \in \mathcal{V} \times \mathcal{V}$ and $x_h := (u_h, z_h) \in V_h \times V_h$. It holds:

$$J(u) - J(u_h) = \mathcal{L}(x) - \mathcal{L}(x_h) = \int_0^1 \frac{d}{ds} \mathcal{L}(x + s(x - x_h))\, \mathrm{d}s.$$

We approximate this integral be the trapezoidal rule to get

$$J(u) - J(u_h) = \frac{1}{2}\mathcal{L}'(x)(x - x_h) + \frac{1}{2}\mathcal{L}'(x_h)(x - x_h) + \mathcal{R}^{(3)},$$

where the remainder $\mathcal{R}^{(3)}$ is given by

$$\mathcal{R}^{(3)} = \int_0^1 s(1-s)\mathcal{L}'''(x + s(x - x_h))(x - x_h, x - x_h, x - x_h)\,\mathrm{d}s.$$

As our Galerkin approach is conforming, it holds $\mathcal{L}'(x)(x - x_h) = 0$. Further we introduce the interpolation error and get

$$J(u) - J(u_h) = \frac{1}{2}\mathcal{L}'(x_h)(x - I_h x) + \mathcal{R}^{(3)}.$$

The final estimate follows by using the definition of $\mathcal{L}(\cdot)(\cdot)$, see (8.19) and its derivatives

$$\begin{aligned}\mathcal{L}'_z(u,z)(\phi) &= F(\phi) - A(u)(\phi),\\ \mathcal{L}'_u(u,z)(\phi) &= J'(u)(\phi) - A'(u)(\phi, z).\end{aligned}$$

□

The DWR method is a very general concept. It can be applied to spacial finite element discretizations but also to time Galerkin discretizations as introduced in Sect. 4.1.3. The remainder $\mathcal{R}^{(3)}$ comes from the application of the trapezoidal rule. If we consider linear problems only, the estimator of Theorem 8.5 is equivalent to the estimators of Theorem 8.3. The error approximation depends on the unknown weights $z - i_h z$ and also the primal weight $u - i_h u$. For approximation of $z \in \mathcal{V}$ and $u \in \mathcal{V}$, the same procedures are in the preceding section can be utilized.

Example 8.6 (Adjoint Solution to the Navier-Stokes Equations) To discuss the linearized adjoint used for the nonlinear DWR method, we consider the Navier-Stokes equations, given by

$$\mathbf{U} \in \mathcal{X} := \mathcal{V} \times \mathcal{L} \quad A(\mathbf{U})(\Phi) = F(\Phi) \quad \forall \Phi \in \mathcal{X},$$

where $\mathcal{V} = H_0^1(\Omega)^d$, $\mathcal{L} = L^2(\Omega) \setminus \mathbb{R}$ and

$$\begin{aligned}A(\mathbf{U})(\Phi) &:= (\rho_f \mathbf{v} \cdot \nabla \mathbf{v}, \phi) + (\rho_f \nu_f \nabla \mathbf{v}, \nabla \phi) - (p, \nabla \cdot \phi) + (\operatorname{div} \mathbf{v}, \xi)\\ F(\Phi) &:= (\mathbf{f}, \phi)\end{aligned}$$

The Gâteaux derivative at $\mathbf{U} \in \mathcal{X}$ in direction $\mathbf{Z} = \{\mathbf{z}, q\} \in \mathcal{X}$ is given as

$$A'(\mathbf{U})(\mathbf{Z}, \Phi) = \Big(\rho_f(\mathbf{v} \cdot \nabla \mathbf{z} + \mathbf{z} \cdot \nabla \mathbf{v}), \phi\Big) + (\rho_f \nu_f \nabla \mathbf{z}, \nabla \phi) - (q, \operatorname{div} \phi) + (\operatorname{div} \mathbf{z}, \xi)$$

The adjoint solution is determined by the linearized adjoint form $A'(\mathbf{U})(\Phi, \mathbf{Z})$

$$A'(\mathbf{U})(\Phi, \mathbf{Z}) = \Big(\rho_f(\mathbf{v}\cdot\nabla\phi + \phi\cdot\nabla\mathbf{v}), \mathbf{z}\Big) + (\rho_f \nu_f \nabla\phi, \nabla\mathbf{z}) + (\text{div } \phi, q) - (\xi, \text{div } \mathbf{z}) \tag{8.20}$$

As functional of interest, we consider the vorticity (8.16). Its derivative is given by

$$J'(\mathbf{U})(\Phi) = 2\int_\Omega (x\times\mathbf{v})\cdot(x\times\phi)\,\mathrm{d}x.$$

This right hand side, together with the adjoint variational formulation corresponds to the classical formulation of the adjoint Navier-Stokes system

$$\rho_f\Big(\nabla\mathbf{v}^T\mathbf{z} - \mathbf{v}\cdot\nabla\mathbf{z}\Big) + \nabla q = j(\mathbf{v}), \quad \text{div } \mathbf{z} = 0.$$

The transport direction is switched and an additional reaction term appears. Furthermore, the new "pressure variable" $q \in \mathcal{L}$ appears with a positive sign. The appearance of the reaction term can lead to stability problems, as its sign cannot be controlled.

Theorem 8.5 covers the case of conforming and consistent finite element schemes. It can directly be applied to many different configurations and equations. We simply need a Galerkin structure in such a way that a solution $u \in \mathcal{X}$ is given by

$$A(u)(\phi) = F(\phi) \quad \phi \in \mathcal{X},$$

and an approximation in a subspace $X_h \subset \mathcal{X}$ that defines $u_h \in X_h$ such that

$$A(u_h)(\phi_h) = F(\phi_h) \quad \forall \phi_h \in X_h.$$

Finally, we present a modification of this theorem that can be applied to non-conforming discretizations, i.e. problems, where the discrete solution $u_h \in X_h$ is defined as

$$A_h(u_h)(\phi_h) = F_h(\phi_h),$$

where A_h and F_h are modifications of A and F, respectively.

A common situation is the use of stabilization techniques. In the context of equal order discretizations of the Navier-Stokes equations we add a term to stabilize the velocity pressure coupling

$$A_h(\mathbf{U}_h)(\Phi_h) := A(\mathbf{U}_h)(\Phi_h) + S_h(\mathbf{U}_h)(\Phi_h),$$

where $\mathbf{U}_h = \{\mathbf{v}_h, p_h\}$ and where $A(\cdot)(\cdot)$ is given as in Example 8.6. Considering the simple *pressure stabilization* as introduced in Sect. 4.3.2 and *artificial diffusion* like

discussed in Sect. 4.4.3, this stabilization term is given as

$$S_h(\mathbf{U}_h)(\Phi_h) = (\alpha \nabla p_h, \nabla \xi_h) + (\delta \nabla \mathbf{v}_h, \nabla \phi_h). \tag{8.21}$$

Theorem 8.7 (DWR Method for Non-conforming Discretizations) *Let $u \in \mathcal{V}$ and $u_h \in V_h$ be the solutions to*

$$A(u)(\phi) = F(\phi) \quad \forall \phi \in \mathcal{V}, \quad A_h(u_h)(\phi_h) = F(\phi_h) \quad \forall \phi_h \in V_h,$$

and $z \in \mathcal{V}$ and $z_h \in V_h$ be solutions to

$$\begin{aligned} A'(u)(\phi, z) &= J'(u)(\phi) \quad \forall \phi \in \mathcal{V}, \\ A_h'(u_h)(\phi_h, z_h) &= J'(u_h)(\phi_h) \quad \forall \phi_h \in V_h. \end{aligned}$$

Then, it holds

$$\begin{aligned} J(u) - J(u_h) = &\frac{1}{2}\Big\{F(z - I_h z) - A_h(u_h)(z - I_h z)\Big\} \\ &+ \frac{1}{2}\Big\{J'(u_h)(u - I_h u) - A_h'(u_h)(u - I_h u, z_h)\Big\} \\ &+ S_h(u_h)(z) + S_h'(u_h)(u - u_h, z_h) + \mathcal{R}^{(3)} \end{aligned} \tag{8.22}$$

Proof First, we define $\mathcal{L}_h(u_h, z_h) = J(u_h) + F(z_h) - A_h(u_h)(z_h)$. It holds

$$\mathcal{L}_h(u_h, z_h) = \mathcal{L}(u_h, z_h) - S_h(u_h)(z_h).$$

Using $x := (u, z)$ and $x_h := (u_h, z_h)$ the error is given as

$$J(u) - J(u_h) = \mathcal{L}(x) - \mathcal{L}_h(x_h) = \mathcal{L}(x) - \mathcal{L}(x_h) + S_h(u_h)(z_h).$$

Again, by using an integral representation and approximation with the trapezoidal rule it holds

$$J(u) - J(u_h) = \frac{1}{2}\mathcal{L}'(x)(x - x_h) + \frac{1}{2}\mathcal{L}'(x_h)(x - x_h) + S_h(u_h)(z_h) + \mathcal{R}^{(3)},$$

where, $\mathcal{L}'(x)(x - x_h) = 0$. We cannot immediately use Galerkin orthogonality in the second part. Instead,

$$\begin{aligned} J(u) - J(u_h) = &S(u_h, z_h) \\ &+ \frac{1}{2}\Big\{F(z - I_h z) - A(u_h)(z - I_h z) - S_h(u_h)(z - I_h z)\Big\} + S(u_h)(z - z_h) \end{aligned}$$

$$+\frac{1}{2}\Big\{J'(u_h)(u-I_hu)-A'(u_h)(u-I_hu,z_h)-S_h'(u_h)(u-I_hu,z_h)\Big\}$$
$$+S_h'(u_h)(u-u_h,z_h)+\mathcal{R}^{(3)}$$

□

To evaluate this error estimator we must approximate the remainders given by the stabilization term. This will depend on the specific type of stabilization scheme. As example, we consider a simple stabilization of the Stokes equations

Example 8.8 (DWR for the Stokes Equations with Pressure Stabilization) Let $\Omega = (0,1)^2$ and $\{\mathbf{v},p\} \in \mathcal{V}\times\mathcal{L} := H_0^1(\Omega)^2 \times L^2(\Omega)\setminus\mathbb{R}$ be the solution to the Stokes equations

$$\begin{aligned}(\nabla\mathbf{v},\nabla\phi)-(p,\nabla\cdot\phi)&=(\mathbf{f},\phi) &&\forall\phi\in\mathcal{V}\\ (\text{div }\mathbf{v},\xi)&=0 &&\forall\xi\in\mathcal{L}.\end{aligned}$$

The finite element solution $\{\mathbf{v}_h,p_h\}\in V_h\times Q_h$ is given using the simple pressure stabilizations scheme, see Lemma 4.47:

$$\begin{aligned}(\nabla\mathbf{v}_h,\nabla\phi_h)-(p_h,\nabla\cdot\phi_h)&=(\mathbf{f},\phi) &&\forall\phi_h\in V_h,\\ (\text{div }\mathbf{v}_h,\xi)+\sum_K h_K^2(\nabla p_h,\nabla\xi_h)&=0 &&\forall\xi_h\in L_h.\end{aligned}$$

Here, the stabilization is linear, symmetric and takes the form

$$S_h(p)(\xi)=\sum_K h_K^2(\nabla p,\nabla\xi).$$

The discrete adjoint solution $\{\mathbf{z}_h,q_h\}\in V_h\times Q_h$ is given as

$$\begin{aligned}(\nabla\mathbf{z}_h,\nabla\phi_h)+(q_h,\nabla\cdot\phi_h)&=J'_{\mathbf{v}}(\mathbf{v}_h,p_h)(\phi_h) &&\forall\phi_h\in V_h,\\ -(\text{div }\mathbf{z}_h,\xi_h)+\sum_K h_K^2(\nabla q_h,\nabla\xi_h)&=J'_p(\mathbf{v}_h,p_h)(\xi_h) &&\forall\xi_h\in L_h.\end{aligned}$$

Then, the exact form of the estimator in (8.22) gets

$$\begin{aligned}J(\mathbf{v})-J(\mathbf{v}_h)=\frac{1}{2}\Big\{&(f,\mathbf{z}-I_h\mathbf{z})-(\nabla\mathbf{v}_h,\nabla(\mathbf{z}-I_h\mathbf{z}))\\ &+(p_h,\nabla\cdot(\mathbf{z}-I_h\mathbf{z}))-(\nabla\cdot\mathbf{v}_h,q-I_hq)-S_h(p_h)(q-I_hq)\Big\}\\ +\frac{1}{2}\Big\{&J'(\mathbf{v}_h)(\mathbf{v}-I_h\mathbf{v},p-I_hp)-(\nabla\mathbf{z}_h,\nabla(\mathbf{v}-I_h\mathbf{v}))\end{aligned}$$

$$- (q_h, \nabla \cdot (\mathbf{v} - I_h \mathbf{v})) + (\nabla \cdot \mathbf{z}_h, q - I_h q) - S_h(p - I_h p)(q_h)\Big\}$$
$$- S_h(p - p_h)(q - q_h) + S_h(p)(q)$$

For evaluation, the term $S_h(p - p_h)(q - q_h)$ is of higher order and can be neglected. The second stabilization term can be approximated as

$$S_h(p)(q) \approx S(I_{2h}^{(2)} p_h, I_{2h}^{(2)} q_h),$$

using the higher order interpolation operator.

The DWR method has been applied to a large variety of equations and coupled systems of equations ranging from reactive flows [64, 66], general conservation laws [176], plasticity [273] to applications like model error analysis [59, 255] or optimization and parameter identification problems [42, 337]. We will continue with the extension of the DWR method to time-dependent problems.

8.1.2 The DWR Method for Galerkin Time Stepping Schemes

Traditional techniques for estimating the error due to time-discretization are usually based on an estimation of the truncation error. Here, we shortly want to present a technique to apply the Dual Weighted Residual method to error control in time. We loosely follow the extensive studies by Schmich, Vexler, Rannacher [51, 302, 303].

In Sect. 4.1.3, we have presented Galerkin methods for time-discretization, where the following variational formulation for the heat equation was derived

$$u \in X_I^1$$
$$\sum_{m=1}^{M} \int_{I_m} \Big\{ (u'(t), \phi(t))_\Omega + A(u(t))(\phi(t)) \Big\} \, \mathrm{d}t + ([u]_{m-1}, \phi(t_{m-1})^+)$$
$$= \sum_{m=1}^{M} \int_{I_m} (f(t), \phi(t)) \, \mathrm{d}t \quad \forall \phi \in X_I^0.$$

By X_I^1 we denote the space of piecewise linear (on $I_m = [t_{m-1}, t_m]$), globally (on $I = [0, T]$) continuous functions and by X_I^0 the space of piecewise constant functions. For linear and autonomous problems this $cG(1)$-Formulation is equivalent to the Crank-Nicolson scheme. In the general setting however, the Galerkin approach must be considered as a new time-discretization scheme that differs from the Crank-Nicolson method by an error of order $O(k^2)$, where $k = \max_m |t_m - t_{m-1}|$ is the step-size. This is exactly the same convergence order as the order of the Crank-Nicolson's

truncation error itself. We define

$$A_I(u)(\phi) = \sum_{m=1}^{M} \Big\{ \int_{I_m} (u'(t), \phi(t))_\Omega + A(u(t))(\phi(t))\,\mathrm{d}t + ([u]_{m-1}, \phi(t_{m-1})^+) \Big\}.$$

The solution $u \in W(I)$ with

$$W(I) = \{\phi \in L^2(I; H^1(\Omega)),\ \partial_t \phi \in L^2(I; H^{-1}(\Omega))\}$$

is given as

$$A_I(u)(\phi) = F(\phi) \quad \forall \phi \in W(I). \tag{8.23}$$

Given discrete trial and test spaces X_I and Y_I, the discrete solution is defined as

$$u_k \in X_I \quad A_I(u_k)(\phi_k) = F(\phi_k) \quad \forall \phi_k \in Y_I. \tag{8.24}$$

We assume that Y_I is globally discontinuous. Then, the Galerkin formulation decouples to a time stepping scheme for $m = 1, \ldots, M$

$$\int_{I_m} (\partial_t u_k, \phi_k)_\Omega + A(u_k)(\phi_k)\,\mathrm{d}t + (u_k^+(t_{m-1}), \phi_k^+(t_{m-1}))_\Omega$$
$$= (u^0, \phi_k^-(t_0)) + (u_k^-(t_{m-1}), \phi_k^+(t_{m-1}))_\Omega + \int_{I_m} (f, \phi_k)\,\mathrm{d}t,$$

where $u_k^-(t_0) = u^0$ and $\phi_k^-(t_0)$ is introduced to include the initial value. As error functional we consider values at final time T and distributed values

$$J(u) = J_T(u(T)) + \int_I J_I(t, u(t))\,\mathrm{d}t, \tag{8.25}$$

where $J_T \in H^{-1}(\Omega)$ and $J_I \in L^2(I; H^{-1}(\Omega))$.

With these preparations, we can define the adjoint non-stationary solution $z \in W(I)$ as

$$A_I'(u)(\phi, z) = J'(u)(\phi) \quad \forall \phi \in W(I), \tag{8.26}$$

and the discrete counterpart $z_k \in Y_I$ by

$$A_I'(u_k)(\phi_k, z_k) = J'(u_k)(\phi_k) \quad \forall \phi_k \in X_I, \tag{8.27}$$

where the role of trial and test spaces are switched. The adjoint solution *runs backward in time*, as switching test and trial functions with integration by parts gives

$$\int_I (\partial_t \phi, z)\,\mathrm{d}t = \int_I (\phi, -\partial_t z)\,\mathrm{d}t + \phi(T)^- z(T)^- - \phi(0)^+ z(0)^+. \tag{8.28}$$

Right hand side of the adjoint problem, as well as initial data at time $t = T$ are given by the functional (8.25). The integrated part J_I defined the adjoint right hand side, the part J_T defines the adjoint initial at time $t = T$, as combination with (8.28) gives

$$(\phi(T)^-, z(t)^-) = J_T'(u(T))(\phi(T)^-).$$

Lemma 8.9 *The discrete adjoint problem decouples to a time stepping method running backward in time.*

Proof It holds with integration by parts and reordering

$$\begin{aligned}
A_I'(u)(\phi, z) &= \sum_{i=1}^{M} \int_{I_m} \left\{ (\phi'(t), z(t)) + A'(u(t))(\phi(t), z(t)) \right\} \mathrm{d}t \\
&\quad + \sum_{i=1}^{M} (\phi(t_{m-1})^+, z(t_{m-1})^+) - \sum_{i=2}^{M} (\phi(t_{m-1})^-, z(t_{m-1})^+) \\
&= \sum_{i=1}^{M} \int_{I_m} \left\{ (-z'(t), \phi(t)) + A'(u(t))(\phi(t), z(t)) \right\} \mathrm{d}t \\
&\quad + \sum_{i=1}^{M} (z(t_m)^-, \phi(t_m)^-) - (z(t_{m-1})^+, \phi(t_{m-1})^+) \\
&\quad + \sum_{i=1}^{M} (\phi(t_{m-1})^+, z(t_{m-1})^+) - \sum_{i=2}^{M} (\phi(t_{m-1})^-, z(t_{m-1})^+) \\
&= \sum_{i=1}^{M} \int_{I_m} \left\{ (-z'(t), \phi(t)) + A'(u(t))(\phi(t), z(t)) \right\} \mathrm{d}t \\
&\quad + (z(t_M)^-, \phi(t_M)^-) + \sum_{i=1}^{M-1} (z(t_m)^- - z(t_m)^+, \phi(t_m)^-)
\end{aligned}$$

Coupling takes place via the jump-terms only. For the Crank-Nicolson scheme with a continuous and piecewise linear primal space and a piecewise constant discontinuous dual space coupling takes place by

$$z_k(t_m)^- \neq z_k(t_m)^+.$$

For the adjoint problem, the first and the last step then takes a different form. On $I_M = [t_{M-1}, t_M]$ it holds

$$(z_k(T)^-, \phi(T)^-) + \int_{I_M} (-z_k'(t), \phi_k(t)) + A_I'(u_k(t))(\phi_k(t), z_k(t))\,\mathrm{d}t$$
$$= J_T'(u(T))(\phi(T)) + \int_{I_M} J_I'(t, u(t))(\phi(t))\,\mathrm{d}t.$$

For $m = M-1, \ldots, 1$ we have

$$(z_k(t_m)^-, \phi(t_m)^-) + \int_{I_m} (-z_k'(t), \phi_k(t)) + A_I'(u_k(t))(\phi_k(t), z_k(t))\,\mathrm{d}t$$
$$= (z_k(t_m)^+, \phi(t_m)^-) + \int_{I_m} J_I'(t, u(t))(\phi(t))\,\mathrm{d}t.$$

□

Theorem 8.10 (DWR Method for Temporal Galerkin Methods) *Let $u \in W(I)$ be solution to (8.23), $u_k \in X_I \subset W(I)$ solution to (8.24). Let J be an error functional in the sense of (8.25). Let $z_k \in Y_I$ be the adjoint solution to (8.27), $z \in W(I)$ the continuous counterpart given by (8.26). Then, it holds*

$$J(u - u_k) = \frac{1}{2}\Big\{F(z - i_k^* z) - A_I(u_k)(z - i_k^* z)\Big\}$$
$$+ \frac{1}{2}\Big\{J'(u_k)(u - i_k u) - A_I'(u_k)(u - i_k u, z_k)\Big\} + \mathcal{R}^3(u - u_k, z - z_k),$$

where $\mathcal{R}^3$ is the third order remainder and $i_k : W(I) \to X_I$ and $i_k^* : W(I) \to Y_I$ are projection operators in time.

Proof The proof directly follows by applying Theorem 8.5 to the Galerkin-in-time setting. □

Remark 8.11 (Galerkin Time-Integration) There are various realizations of the Dual Weighted Residual method for error estimation in space and time based on Galerkin approximations of the time-dependent problem [51, 302]. The benefit of Galerkin time-discretization is that the non-stationary problem is cast into a variational setting that allows for the application of analytical tools known from the finite element method. The method is universal and various continuous or discontinuous trial and test spaces can be combined.

It is well known that the $dG(0)$-method corresponds to the backward Euler and the $cG(1)$-discretization (that is $cG(1)$ for X_I and $dG(0)$ for Y_I) to the Crank-Nicolson method. But what exactly is the meaning of "corresponds"? For linear autonomous problems, the two methods are exactly equivalent. For all other

problems the time stepping method can be derived by numerical quadrature from the Galerkin method. However, this quadrature error is usually not of higher order, but of the same order as the Galerkin method's approximation order. Hence, we must distinguish between two separate methods.

One big problem of Galerkin time-discretizations is the higher effort. For setting up the system matrix, the term

$$\int_{I_m} A_I'(u_k)(w_k, \phi_k)\,\mathrm{d}t,$$

must be evaluated. For an accurate (higher order) approximation of the integral, Gauss quadrature rules must be considered. This quickly doubles the usual effort for assembling the matrix. Considering coupled problems like fluid-structure interactions, such an effort is impractical. If even higher order time-discretizations are used, e.g. a $dG(1)$-method, each time step couples two separate states. This increases the size of the system-matrix (and the effort) by a factor of 4. Nevertheless, Galerkin methods are often used, whenever the Galerkin structure is of importance, as it is in the context of gradient based optimization [47, 289, 317].

Finally, we shortly want to address the question of error control for efficient time stepping methods like the shifted Crank-Nicolson scheme or the Fractional-Step Theta method. These methods cannot be exactly written as Galerkin formulations. Instead, error estimation is based on the following principle

1. Solve the forward problem u_k by time stepping, e.g. with the Crank-Nicolson method
2. Split the error

$$|u - u_k| \leq |u - u_k^G| + |u_k^G - u_k|$$

in a Galerkin error $u - u_k^G$ and into a quadrature error $u_k^G - u_k$ that measures the difference between Galerkin scheme and time stepping scheme. The Galerkin solution u_k^G will not be numerically computed. It only serves as a tool of the error estimator.

We give details for the application to the Crank-Nicolson scheme.

Example 8.12 (DWR Method for the Crank-Nicolson Time Stepping Method) Let $t_0 < t_1 < \cdots < t_M = T$ be a subdivision of $I = [0, T]$ into M equidistant parts $I_m = (t_m - t_{m-1})$. By $u \in W(I)$ we define the variational solution of the heat equation given by

$$A(u)(\phi) = F(\phi) \quad \forall \phi \in W(I), \tag{8.29}$$

where

$$A(u,\phi) = \sum_{m=1}^{M} \int_{I_m} (u'(t),\phi(t))_\Omega + (\nabla u(t), \nabla\phi(t))_\Omega \mathrm{d}t + ([u]_{m-1}, \phi(t_{m-1})^+)_\Omega$$
$$F(\phi) = \sum_{m=1}^{M} \int_{I_m} (f(t),\phi(t))_\Omega \mathrm{d}t. \tag{8.30}$$

By $u_k = \{u_k^1, \ldots, u_k^M\} \in \mathcal{V}^M$ (with $\mathcal{V} = H_0^1(\Omega)$) we denote the Crank-Nicolson semidiscretization of the heat equation given by the bilinear form

$$A_k(u_k,\phi_k) = F_k(\phi_k) \quad \forall \phi_k \in \mathcal{X}^M, \tag{8.31}$$

where

$$A_k(u_k,\phi_k) = \sum_{m=1}^{M} k^{-1}(u_k^m - u_k^{m-1}, \phi_k^m)_\Omega + \frac{1}{2}(\nabla u_k^m + \nabla u_k^{m-1}, \nabla\phi_k^m)_\Omega$$
$$F_k(\phi_k) = \sum_{m=1}^{M} \frac{1}{2}(f(t_{m-1}) + f(t_m), \phi_k^m)_\Omega. \tag{8.32}$$

This is exactly the Crank-Nicolson time stepping scheme that is basis of an efficient numerical simulation. We will identify u_k with a piecewise linear function $\hat{u}_k$

$$\hat{u}_k(t)\Big|_{I_m} = \frac{t_m - t}{t_m - t_{m-1}} u_k^{m-1} + \frac{t - t_{m-1}}{t_m - t_{m-1}} u_k^m.$$

Further, let $\tilde{u}_k \in X_I$ be the Crank-Nicolson Galerkin approximation given by

$$A(\tilde{u}_k, \tilde{\phi}_k) = F(\tilde{\phi}_k) \quad \forall \tilde{\phi}_k \in Y_I,$$

where $X_I \subset W(I)$ is the space of piecewise linear (in time) and continuous functions and Y_I the space of piecewise constant (in time) globally discontinuous test functions. We will never compute $\tilde{u}_k$ but use it in the process of error estimation only. By $z \in W(I)$, $z_k \in \mathcal{V}^M$ and $\tilde{z}_k \in Y_I$ we define the adjoint solutions. We define to Lagrange functionals

$$L(u,z) = J(u) + F(z) - A(u,z), \quad L_k(u_k, z_k) = J(u_k) + F_k(z_k) - A_k(u_k, z_k), \tag{8.33}$$

where $J(\cdot)$ is supposed to be a linear error functional that measures the error at final time, e.g.

$$J(u) = j(u(T)).$$

For the functional error between continuous solution $u \in W(I)$ and Crank-Nicolson solution $u_k \in X_I$ it holds

$$\begin{aligned} J(u) - J(u_k) &= L(u,z) - J(u_k) \\ &= \underbrace{L(u,z) - L(\hat{u}_k, \hat{z}_k)}_{=\eta_I} + \underbrace{L(\hat{u}_k, \hat{z}_k) - J(u_k)}_{=\eta_{II}}. \end{aligned} \tag{8.34}$$

The first part η_I will be considered as the Galerkin error and it can be estimated with help of the DWR method. The second part indicates the difference between Galerkin scheme and Crank-Nicolson method. Using (8.33) it holds

$$\eta_{II} = L(\hat{u}_k, \hat{z}_k) - J(u_k) = \underbrace{J(\hat{u}_k) - J(u_k)}_{=0} + F(\hat{z}_k) - A(\hat{u}_k, \hat{z}_k) \tag{8.35}$$

Evaluation of this term requires knowledge of u_k and z_k (that can be computed) and the effort of one residual evaluation of the Galerkin scheme given in (8.29) and (8.30).

We continue with η_I in (8.34). The usual DWR theory of Theorem 8.10 cannot be directly applied, as we have no Galerkin orthogonality with respect to the Crank-Nicolson solution $\hat{u}_k$. We get an approximation

$$\eta_I \approx L'(\hat{u}_k, \hat{z}_k)(u - \hat{u}_k, z - \hat{z}_k)$$

up to a third order remainder. Instead of using Galerkin orthogonality we simply introduce the interpolations to achieve

$$\eta_I \approx \underbrace{L'(\hat{u}_k, \hat{z}_k)(u - i_k u, z - i_k^* z_k)}_{\eta_I^1} + \underbrace{L'(\hat{u}_k, \hat{z}_k)(i_k u - \hat{u}_k, i_k^* z - \hat{z}_k)}_{\eta_I^2}.$$

For the first part we obtain

$$\eta_I^1 = \frac{1}{2}\Big\{F(z - i_k^* z) - A(\hat{u}_k, z - i_k^* z)\Big\} + \frac{1}{2}\Big\{J(u - i_k u) - A(u - i_k u, \hat{z}_k)\Big\} \tag{8.36}$$

which we approximate with the usual reconstruction techniques for $u - i_k u$ and $z - i_k^* z$.

Using $i_k u - \hat{u}_k = i_k(u - \hat{u}_k)$ and $i_k^* z - \hat{z}_k = i_k^*(z - \hat{z}_k)$ we write the final part as

$$\eta_I^2 = \frac{1}{2}\Big\{F(i_k^*(z - \hat{z}_k)) - A(\hat{u}_k, i_k^*(z - \hat{z}_k))\Big\} + \frac{1}{2}\Big\{J(i_k(u - \hat{u}_k)) - A(i_k(u - \hat{u}_k), \hat{z}_k)\Big\}.$$

This term is a residual evaluation with a discrete projection of the approximation errors. It can be shown to be of higher order (it is actually of third order in the errors as the DWR remainder), see [239].

To conclude we summarize the necessary steps.

1. Given a temporal mesh $t_0 < t_1 < \cdots < t_M = T$ compute the Crank-Nicolson solution u_k and the adjoint Crank-Nicolson solution z_k by means of (8.29) and (8.30).
2. Estimate the error as

$$J(u) - J(u_k) \approx \eta_I^1 + \eta_{II},$$

   where η_I^1 is given by (8.36) and η_{II} by (8.34).
3. If necessary refine the mesh and iterate.

Details on how to extend this method to the shifted versions of the Crank-Nicolson scheme and to the fractional step theta method are found in [239, 240, 306].

8.2 Adaptivity

The approximation error $u - u_{k,h}$ is determined by the mesh size h and the time step size k. For $k \to 0$ and $h \to 0$ we expect that the discretization error will converge to zero. The efficiency of a discretization can be measured in error versus effort, where the effort depends on the discrete problem size. In the context of finite elements, we can measure the problem size in $N \cdot M$, where $N = \dim(V_h)$ is the dimension of the discrete function space and $M = T/k$ is the number of time steps. Given an optimal algorithm, where all parts have a linear run-time, the effort is proportional to $N \cdot M$.

Often it is not appropriate to use uniform meshes in space and time. Instead, different spatial and temporal regions may ask for a different resolution of the discretization. The general problem of adaptivity is to find the optimal distribution of spatial and temporal mesh points which gives the smallest error. We first consider spatial adaptivity only and formulate two optimization problems

$$\min |J(u) - J(u_h)| \text{ for all } u_h \in V_h \text{ with } \dim(V_h) = N_0,$$

i.e., to find the optimal discretization with N_0 unknowns, such that the resulting error is smallest. A second viewpoint is to optimize

$$\min |\dim(V_h)| \text{ such that } |J(u) - J(u_h)| < TOL,$$

i.e., to find the smallest mesh, such that the error is below a given bound. Both settings are important for application. The second optimization problem aims at satisfying a guaranteed error bound, while the first problem tries to get the best possible result for given resources, e.g. the available memory. See [57].

The construction of new meshes Ω_h and finite element spaces V_h can either be done by *refinement* of existing elements $K \in \Omega_h$ into smaller ones, by a complete *remeshing* of Ω_h to a new mesh Ω_h' or by *mesh grading* where the location of the

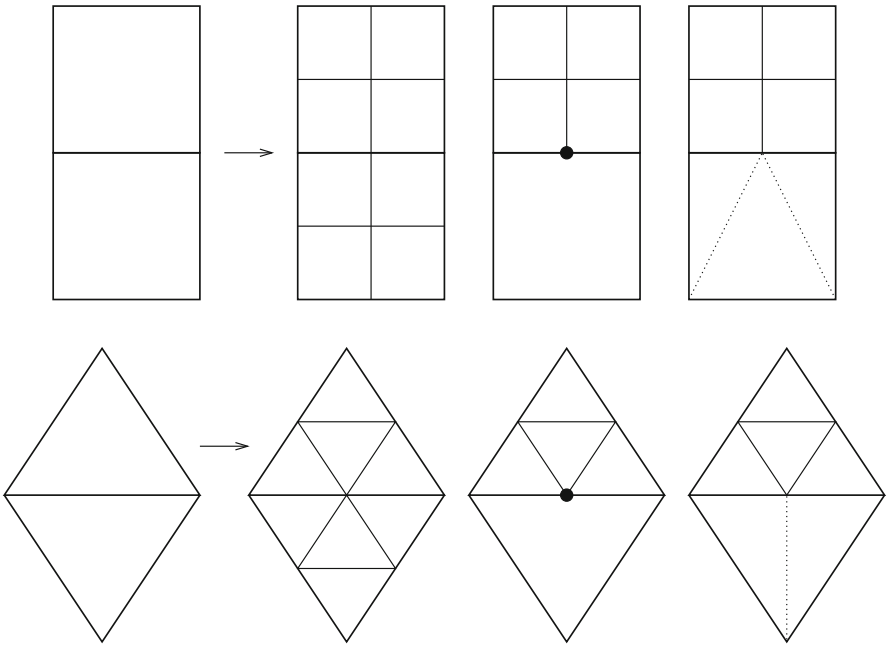

Fig. 8.4 Different refinement ways for splitting mesh-elements. *Both rows*: uniform refinement, local refinement with *hanging nodes* and local refinement using temporary elements for assuring structural regularity

unknowns are adapted, the mesh topology however is not changed. Remeshing gives greatest flexibility, as the mesh elements can be distributed arbitrarily in the domain, it however brings along the drawback of having no relationship between two finite element spaces V_h and V_h'. If the new mesh Ω_h' is constructed by mesh refinement, every mesh element $K \in \Omega_h'$ is either element of the preceding mesh $K \in \Omega_h$ or it results from refinement of a *father-element* $P \in \Omega_h$. In Fig. 8.4 we show typical refinements used for the splitting of elements. If only parts of the mesh are refined, it is necessary to assure the structural regularity of the mesh. This is needed to allow for conformity $V_h \subset H^1(\Omega)$. Basically, two different options exist. First, one can introduce temporary elements (the right sketches in Fig. 8.4). This are simply introduced to ensure structural regularity. Using such elements usually demands for meshes with mixed element types, i.e. mixing quadrilaterals with triangles. This additional effort can be circumvented by the concept of *hanging nodes*. These are nodes that belong to a refined element, but not to the adjacent coarse element. In these nodes, no real degrees of freedom exist. Instead, the values at such nodes are replaced by an interpolation between to neighboring nodes, see [25, 277].

Another advantage of refinement based adaptivity is the availability of a natural hierarchy of meshes and function spaces. Starting on a coarse mesh Ω_0

$$\Omega_0 \to \Omega_1 \to \cdots \to \Omega_l,$$

we construct a sequence of hierarchical finite element spaces

$$V_0 \subset V_1 \subset \cdots \subset V_l.$$

This sequence of spaces is a natural starting point for hierarchical multigrid solvers. The usually very difficult step of creating a coarse mesh hierarchy is easily established based on the already existing history, see [29, 36, 172].

For both refinement and remeshing, local error contributions must be available. The error estimators presented in the preceding section give global error measures

$$J(u) - J(u_h) \approx \eta_h(u_h, z_h).$$

To use such quantities for mesh refinement, we need a splitting into local contributions

$$\eta_h(u_h, z_h) = \sum_i \eta_i(u_h, z_h).$$

How to derive such localizations is topic of the following section.

8.2.1 Localization of A Posteriori Error Estimators

The decision whether to refine a mesh element $K \in \Omega_h$ or not will be based on local error indicators that measure the error contribution of a small area. In the following we will discuss different alternatives for localizing the dual weighted residual error

$$J(u) - J(u_h) \approx \sum_i \eta_i,$$

where the sum is usually a sum over the elements of the mesh (then, η_i is an element-wise error contribution) or a sum over the mesh nodes (then, η_i is a node-wise error contribution). Then, elements (or the elements at a node) a picked for refinement, if the local indicator $|\eta_i|$ is large compared to the other indicators. Techniques for picking elements for refinement are presented in the next section, Sect. 8.2.2.

In the following, we only discuss discretizations of the Laplace equation

$$A(u)(\phi) := (\nabla u, \nabla \phi) = F(\phi) := (f, \phi) \quad \forall \phi \in \mathcal{V} = H_0^1(\Omega).$$

For a reliable refinement based on the local indicators η_i, we will ask for robustness and effectivity of the indicators, e.g. for the existence of constants $c_1, c_2 > 0$

$$|J(u - u_h)| \leq c_1 \sum_i |\eta_i|, \quad \sum_i |\eta_i| \leq c_2 |J(u - u_h)|.$$

We have already discussed that the second inequality cannot hold for general functionals $J(\cdot)$, as the functional error can be very small or zero even for substantial discretization errors. Hence, we weaken the effectivity assumption to

$$\sum_i |\eta_i| \leq c_2 \|\nabla(u - u_h)\| \, \|\nabla(z - z_h)\|,$$

such that the error indicators are bound by the product of the energy errors that themselves are a bound for the functional error $|J(u - u_h)|$. For measuring the effectivity of error indicators, we define the *indicator index*

$$\mathrm{ind}_h(u_h, z_h) := \frac{\sum_i |\eta_i|}{|\eta_h|}$$

as the fraction of absolute indicator values by the error estimator. This definition is very similar to that of the effectivity index (8.14). In the following, we will describe and shortly analyze different localization techniques for the DWR error identities given in Theorems 8.3 and 8.5. For details on the analysis and further possibilities for localization we refer to [288].

8.2.1.1 Localization by Restriction to Elements

The most simple approach for a localization would be the restriction of the weak residual to the mesh elements

$$\eta_K = (f, z - i_h z)_K - (\nabla u_h, \nabla(z - i_h z))_K.$$

This simple approach fails with

$$\sum_{K \in \Omega_h} |\eta_K| \gg |\eta_h(u_h, z_h)|,$$

as the local restriction to K shows the wrong order

$$\eta_K = (f + \Delta u_h, z - i_h z)_K - \int_{\partial K} \partial_n u_h \cdot (z - i_h z) \, \mathrm{d}s.$$

While the volume term itself yields optimal order

$$|(f + \Delta u_h, z - i_h z)_K| \leq \|\Delta(u - u_h)\|_K \, \|z - i_h z\|_K,$$

the boundary term lacks the sufficient approximation order as can be seen using interpolation estimates and the trace inequality:

$$\left|\int_{\partial K} \partial_n u_h \cdot (z - i_h z)\,\mathrm{d}s\right| \leq c_{\mathrm{tr}} h_K^{-1} \left(\|\nabla u_h\|_K + h_K \|\nabla^2 u_h\|_K\right) \\ \left(\|z - i_h z\|_K + h_K \|\nabla(z - i_h z)\|_K\right).$$

While the adjoint solution enters the estimate with the proper local order, the boundary term does show convergence with respect to the primal residual. This result is well-known in literature, and the typical remedy is given by balancing boundary terms with adjacent finite elements, as shown in the following paragraph.

8.2.1.2 Localization Based on the Classical (Strong) Formulation

The typical localization procedure for residual based error estimators is based on the classical formulation of residual estimators [336]. For the functional error it holds (considering linear problems)

$$\begin{aligned} J(u - u_h) &= \sum_{K \in \Omega_h} \frac{1}{2}\Big\{(f, z - i_h z)_K - (\nabla u_h, \nabla(z - i_h z))_K\Big\} \\ &\quad + \sum_{K \in \Omega_h} \frac{1}{2}\Big\{(j, u - i_h u)_K - (\nabla(u - i_h u), \nabla z_h)_\Omega\Big\} \\ &= \sum_{K \in \Omega_h} \frac{1}{2}\Big\{(f + \Delta u_h, z - i_h z)_K - \langle \partial_n u_h, z - i_h z\rangle_{\partial K}\Big\} \\ &\quad + \sum_{K \in \Omega_h} \frac{1}{2}\Big\{(j + \Delta u_h)_K - \langle \partial_n z_h, u - i_h u\rangle_{\partial K}\Big\} \\ &= \sum_{K \in \Omega_h} \frac{1}{2}\Big\{(f + \Delta u_h, z - i_h z)_K - \frac{1}{2} - \langle [\partial_n u_h], z - i_h z\rangle_{\partial K}\Big\} \\ &\quad + \sum_{K \in \Omega_h} \frac{1}{2}\Big\{(j + \Delta u_h)_K - \frac{1}{2}\langle [\partial_n z_h], u - i_h u\rangle_{\partial K}\Big\}, \end{aligned} \tag{8.37}$$

where by $[\,\cdot\,]$ we denote the jump of the (discontinuous) normal derivative ∂u_h across the edge $e \subset \partial K$

$$[\partial_n u_h](x)\Big|_e := \lim_{h \downarrow 0} \partial_n u_h(x + h\mathbf{n}) - \lim_{h \downarrow 0} \partial_n u_h(x - h\mathbf{n}),$$

with a normal vector $\mathbf{n}$ facing outward of K. Now, (8.37) can be estimated to

$$|J(u-u_h)| \leq \sum_{K\in\Omega_h} \rho_K(u_h)\omega_K(z_h) + \rho_K^*(z_h)\omega_K^*(u_k), \tag{8.38}$$

with the residuals and weights

$$\begin{aligned}
\rho_K(u_h) &= \|f + \Delta u_h\|_K + \frac{1}{2}h_K^{-\frac{1}{2}}\|\partial_n u_h\|_{\partial K}\\
\rho_K^*(z_h) &= \|j + \Delta z_h\|_K + \frac{1}{2}h_K^{-\frac{1}{2}}\|\partial_n z_h\|_{\partial K}\\
\omega_K(z_h) &= \|z - i_h z\|_K + h_K^{\frac{1}{2}}\|z - i_h z\|_{\partial K}\\
\omega_K^*(u_h) &= \|u - i_h u\|_K + h_K^{\frac{1}{2}}\|u - i_h u\|_{\partial K}.
\end{aligned} \tag{8.39}$$

Half a power of h_K was introduced, such that edge and volume residuals and weights, respectively, have the same order. The benefit of this estimation is that positive local error quantities are directly available

$$\eta_h = \sum_{K\in\Omega_h} \eta_K, \quad \eta_K = \rho_K\omega_K + \rho_K^*\omega_K^*.$$

Based on η_K, refinement or remeshing can be pursued. By using Cauchy Schwarz estimate, possible orthogonality is lost. As this estimate is used locally, we still get good effectivity of the indicators.

Lemma 8.13 (Effectivity of the Localization Based on the Classical Residual) *Let $u, z \in V$ be the solution and adjoint solution to the Laplace equation with sufficient regularity. For the primal error estimator*

$$|J(u-u_h)| \leq \sum_{K} 2\rho_K(u_h)\omega_K(z_h),$$

where ρ_K and ω_K are defined in (8.39) it holds

$$\sum_{K\in\Omega_K} 2\rho_K\omega_K \leq |||u - i_h u|||_h |||z - i_h z|||_h,$$

where—given sufficient regularity—the norm $|||\cdot|||_h$ is equivalent to energy norm

$$|||u|||_h^2 = \|\nabla(u-u_h)\|^2 + \sum_{K\in\Omega_h} h_K^2\|\nabla^2(u-u_h)\|_K^2 + h_K^{-2}\|u-u_h\|_K^2. \tag{8.40}$$

Proof See [288]. □

This localization technique is often used and well documented in literature. It has two severe drawbacks: as it is based on Cauchy-Schwarz estimates in an early stage,

orthogonality effects are lost. Considering general differential operators $\mathcal{L}(u) = f$, the strong residuals $f - \mathcal{L}(u)$ and $j - \mathcal{L}'(u)(z)$ must be available. Such a computation can be very costly as we will discuss in Sect. 8.3 for fluid-structure interactions. Finally, the classical estimator requires the evaluation of jump-terms at the element edges, which is possibly costly. In an early application of the dual weighted residual method to the incompressible Navier-Stokes equations Becker [34] derived the goal oriented error estimator with three different residual terms and three different adjoint weights.

8.2.1.3 Localizations Based on the Variational Formulation

We can circumvent both problems, the strong residual as well as edge jump terms, if we base the localization on the variational formulation. Braack and Ern [60] introduced a localization of the DWR method based on a patch-wise filtering approach. Very good effectivities are obtained at the little cost of additional patch-structures in the mesh, see Fig. 8.3. Let V_h be the finite element space with $V_{2h} \subset V_h$ being the coarse space on the patches. By $\pi_{2h} : V_h \to V_{2h}$ we denote the embedding into this coarse space. By $i_{2h}^{(2)} : V_h \to V_{2h}^{(2)}$ we denote the higher order reconstruction introduced in Sect. 8.1.1, see Fig. 8.2. We can write for

$$z_h(x) = \sum_{i=1}^{N} \mathbf{z}_i \phi_h^{(i)}(x)$$

the interpolations into the same-degree coarse-space V_{2h} and the higher-degree space $V_{2h}^{(2)}$ by using the same nodal degrees:

$$i_{2h} z_h(x) = \sum_{i=1}^{N} \mathbf{z}_i i_{2h} \phi_h^{(i)}(x), \quad i_{2h}^{(2)} z_h(x) = \sum_{i=1}^{N} \mathbf{z}_i i_{2h}^{(2)} \phi_h^{(i)}(x),$$

and approximate the error identity as

$$\begin{aligned}
J(u - u_h) &= F(z - i_h z) - A(u_h)(z - i_h z) \\
&= F(z - i_h z - \pi_{2h}(z - i_h z)) - A(u_h)(z - i_h z - \pi_{2h}(z - i_h z)) \\
&\approx F\Big(i_{2h}^{(2)}(z_h - i_{2h} z_h) - (z_h - i_{2h} z_h)\Big) \\
&\qquad -A(u_h)\Big(i_{2h}^{(2)}(z_h - i_{2h} z_h) - (z_h - i_{2h} z_h)\Big) \\
&= \sum_{i=1}^{N} \Big(f(i_{2h}^{(2)} \phi_h^{(i)} - \phi_h^{(i)}) - A(u_h)(i_{2h}^{(2)} \phi_h^{(i)} - \phi_h^{(i)})\Big)\Big(\mathbf{z}_i - (i_{2h} z_h)_i\Big) \\
&=: \sum_{i=1}^{N} \eta_i.
\end{aligned}$$

By this localization, a node-wise indicator is derived. Due to the filtering $z_h - i_{2h}z_h$, the error indicators are zero on all coarse mesh-nodes causing a strong oscillation of the indicators, see [288]. For this local values, we can also show effectivity

$$\sum_{i=1}^{N} |\eta_i| \leq c|||u - u_h|||_h |||z - i_h z|||_h.$$

Finally, we introduce a new localization approach based on the variational formulation that combines the simplicity of the filtering approach—as it will be given in terms of variational residuals—with an easy interpretation possibility, as the local estimators η_i can be regarded as coefficient of a discrete error function. Let $\{\psi_i \in V,\ i = 1, \ldots, N\}$ be a partition of unity (POU) with $\sum_i \psi_1 \equiv 1$, where we usually consider $\psi_i := \phi_i$ the basis functions of the finite element space V_h. Then, it holds

$$\begin{aligned} J(u - u_h) &= F(z - i_h z) - A(u_h)(z - i_h z) \\ &= \sum_{i=1}^{N} F((z - i_h z)\psi_i) - A(u_h)((z - i_h z)\psi_i) \\ &\approx \sum_{i=1}^{N} F((i_{2h}^{(2)} z_h - z_h)\psi_i) - A(u_h)((i_{2h}^{(2)} z_h - z_h)\psi_i) =: \sum_{i=1}^{N} \eta_i. \end{aligned} \tag{8.41}$$

Again, we derived node-wise indicators for the local error. The partition of unity ψ_i is independent of the finite element space V_h. It is however reasonable to choose the standard space of piece-wise linear finite elements to define ψ_i.

Lemma 8.14 (Effectivity of the POU Localization) *Let $u \in \mathcal{V}$ be the solution to the Laplace equation, $z \in \mathcal{V}$ be the adjoint solution. $u_h, z_h \in V_h$ their discrete counter-part. Further, let $\sum \psi_i$ be a POU with $\|\nabla \psi_i\|_\infty = O(h^{-1})$. The error indicators given by (8.41) are effective, i.e.,*

$$\sum_{i=1}^{N} |\eta_i^P| \leq c\|\nabla(u - u_h)\| \, |||z - i_h z|||_h.$$

Proof See [288]. □

The advantage of variational localizations will be striking, if we consider the coupled FSI problem in Sect. 8.3. We simply do not know the classical residual of the adjoint problem including all edge terms. Furthermore, the evaluation of a strong residual for second order equations with many nonlinear coupling is computationally very demanding.

8.2.2 Techniques for Spatial Mesh Refinement

We assume that a reliable and effective localization of the error estimator is given

$$c_1 \sum_K |\eta_K| \leq |\eta_h| \leq c_2 \sum_K |\eta_K|.$$

For simplicity, we assume that this localization is element-wise. Node-wise values can easily be averaged to element-wise contributions. Our goal is to pick a subset of elements $\{K_1, \ldots, K_m\} \subset \Omega_h$ for refinement. Most strategies for DWR-type refinement are highly heuristically and based on assumptions that can only be proven under restrictive regularity assumptions, see e.g. [41, 57, 336]:

1. The most efficient discretizations have balanced error indicators

$$\eta_K \approx \eta_{K'} \quad \forall K, K' \in \Omega_h.$$

2. Once all error indicators are balanced, it is optimal to perform uniform steps of mesh-refinement.
3. It is always best to refine elements with largest indicator value.

The third assumption is the basic guideline for designing refinement strategies, and the most common used are:

1. *Fixed-number:* Refine the $p\%$ elements with the largest error

$$\text{refine } \{K_1, \ldots, K_{p \cdot \#\Omega_h}\}, \text{ for } \eta_{K_1} \geq \eta_{K_2} \cdots \geq \eta_{K_{\#\Omega_h}}$$

2. *Fixed-fraction:* Refine those elements with largest error, that sum up to $p\%$ of the overall error

$$\text{refine } \{K_1, \ldots, K_l\}, \text{ for } \min \arg_l \sum_{i=1}^{l} |\eta_{K_i}| \geq p \sum_{i=1}^{\#\Omega_h} |\eta_{K_i}|.$$

3. *Equilibration:* Refine all element with error indicator larger than α-times the average

$$\text{refine } K, \text{ if } |\eta_K| \geq \frac{\alpha}{\#\Omega_h} \sum_K |\eta_K|.$$

All three strategies require a parameter p, or α that control the amount of refinement done in every step. The two first techniques will never satisfy assumption 2., as even for completely balanced error indicators, only of subset of some $p\%$ elements will be refined. The equilibration strategy does satisfy all three assumptions, if $\alpha \leq 1$. Such a small value of α however can lead to very excessive over-refinement.

In practical applications, most refinement strategies will give similar results. Further, the parameters p and α must often be tuned to specific problem sets, and it is not possible to pick one optimal strategy. For more insight to refinement strategies and theoretical analysis of the three assumptions, see [57, 276].

8.3 Application to Fluid-structure Interactions in ALE Formulation

In Sects. 8.1 and 8.2 we have introduced a general framework for a posteriori error estimation and mesh adaptivity. Here, we apply this concept to fluid-structure interaction problems given in ALE coordinates. Again, we want to allow for error estimation with respect to general functionals depending on the solution of the coupled problem. Error estimator and adaptive mesh refinement are driven by the general nonlinear DWR formulation, see Sect. 8.1.1.2. We start with the fully stationary case and closely follow [280]. The variational formulation of the FSI system in ALE coordinates is given by

$$\begin{aligned} A(\mathbf{U})(\Phi) = &\left(J(\mathbf{F}^{-1}\mathbf{v}\cdot\nabla)\mathbf{v},\phi\right)_{\mathcal{F}} + \left(J\boldsymbol{\sigma}_f\mathbf{F}^{-T},\nabla\phi\right)_{\mathcal{F}} + \left(J\mathbf{F}^{-1}:\nabla\mathbf{v}^T,\xi\right)_{\mathcal{F}} \\ &+ (\mathbf{F}\boldsymbol{\Sigma}_s,\nabla\phi)_{\mathcal{S}} + (\nabla\mathbf{u},\nabla\psi_s)_{\mathcal{F}}, \end{aligned} \tag{8.42}$$

where (taking $\mathbf{v}|_{\mathcal{S}} = 0$ into account)

$$\mathbf{U} = \{\mathbf{v},\mathbf{u},p\} \in \mathcal{X} = H_0^1(\mathcal{F})^d \times H_0^1(\mathcal{F}\cup\mathcal{I}\cup\mathcal{S})^d \times L_0^2(\mathcal{F}).$$

We recapitulate the notation of the stresses $\boldsymbol{\sigma}_f$ and $\boldsymbol{\Sigma}_s$ of the St. Venant Kirchhoff material

$$\begin{aligned} &\boldsymbol{\Sigma}_s := 2\mu_s\mathbf{E}_s + \lambda\,\mathrm{tr}(\mathbf{E}_s), \quad \mathbf{F} := I + \nabla\mathbf{u}, \quad \mathbf{E}_s := \frac{1}{2}\left(\mathbf{F}^T\mathbf{F} - I\right), \\ &\boldsymbol{\sigma}_f = \rho_f\nu_f(\nabla\mathbf{v}\mathbf{F}^{-1} + \mathbf{F}^{-T}\nabla\mathbf{v}^T) - pI. \end{aligned} \tag{8.43}$$

The most important step for estimating goal oriented errors is the computation of an adjoint solution with respect to a given error functional $J(\cdot)$. In fluid-structure interactions, these sensitivities must properly include the correct adjoint coupling conditions between the fluid-problem and the solid problem. It is not sufficient to compute sensitivities for each fluid- and solid-problem and neglect the coupling. Such a strategy is only possible for problems with very weak coupling, see [49].

8.3.1 *Sensitivities for Stationary Fluid-structure Interactions in ALE Coordinates*

Given a differentiable error functional $J : \mathcal{X} \to \mathbb{R}$, the adjoint problem is defined as

$$\mathbf{Z} \in \mathcal{X} : \quad A'(\mathbf{U})(\Phi, \mathbf{Z}) = J'(\mathbf{U})(\Phi) \quad \forall \Phi \in \mathcal{X},$$

where $A'(\mathbf{U})(\Phi, \mathbf{Z})$ is the adjoint of the directional Gâteaux derivative, the Jacobian, which is defined by

$$A'(\mathbf{U})(\mathbf{W}, \Phi) := \frac{d}{ds} A(\mathbf{U} + s\mathbf{W})(\Phi)\Big|_{s=0}.$$

This Jacobian has already derived in Sect. 5.2.2 for the ALE formulation and in Sect. 6.4 for the Fully Eulerian model. Here, we only need to transpose the resulting matrix for obtaining the coupled system matrix of the adjoint problem.

For denoting solution $\mathbf{U} \in \mathcal{X}$, direction $\mathbf{W} \in \mathcal{X}$ and test function $\Phi \in \mathcal{X}$, we use

$$\mathbf{U} := \begin{pmatrix} \mathbf{v}_f \\ \mathbf{u} \\ p_f \end{pmatrix}, \quad \mathbf{W} := \begin{pmatrix} \mathbf{z}_f \\ \mathbf{w} \\ q_f \end{pmatrix}, \quad \Phi := \begin{pmatrix} \psi_f \\ \phi \\ \xi_f \end{pmatrix}$$

In Sect. 5.2.2 we have derived the Jacobian of the fluid-structure interaction problem in ALE coordinates (5.14). Here, we copy the stationary parts neglecting the time-derivatives $\partial_t \mathbf{v}_f$, $\partial_t \mathbf{v}_s$ and $\partial_t \mathbf{u}_f$. Furthermore we use $\mathbf{v}_s = 0$ in the fluid domain:

$$\begin{aligned}
A'(\mathbf{U})(\mathbf{W}, \Phi) = {} & \left(\rho_f J \left(\nabla \mathbf{z} \mathbf{F}^{-1} \mathbf{v} + \nabla \mathbf{v} \mathbf{F}^{-1} \mathbf{z}\right), \phi\right)_{\mathcal{F}} \\
& + \left(J \frac{d\boldsymbol{\sigma}_f}{d\mathbf{v}}(\mathbf{W}) \mathbf{F}^{-T}, \nabla\phi\right)_{\mathcal{F}} - \left(J\mathbf{F}^{-T} q_f, \nabla\phi\right)_{\mathcal{F}} \\
& + \left((J\mathbf{F}^{-1} : \nabla \mathbf{z}^T, \xi\right)_{\mathcal{F}} \\
& + \left(\rho_f J \operatorname{tr}(\mathbf{F}^{-1}\nabla\mathbf{w})\left(\nabla\mathbf{v}\mathbf{F}^{-1}\mathbf{v}\right), \phi\right)_{\mathcal{F}} - \left(\rho_f J \nabla\mathbf{v}\mathbf{F}^{-1}\nabla\mathbf{w}\mathbf{F}^{-1}\mathbf{v}, \phi\right)_{\mathcal{F}} \\
& + \left(J \operatorname{tr}(\mathbf{F}^{-1}\nabla\mathbf{w})\boldsymbol{\sigma}_f \mathbf{F}^{-T}, \nabla\phi\right)_{\mathcal{F}} - \left(J\boldsymbol{\sigma}_f \mathbf{F}^{-T} \nabla\mathbf{w}^T \mathbf{F}^{-T}, \nabla\phi\right)_{\mathcal{F}} \\
& + \left(J \frac{d\boldsymbol{\sigma}_f}{d\mathbf{u}}(\mathbf{W}) \mathbf{F}^{-T}, \nabla\phi\right)_{\mathcal{F}} \\
& + \left(J(\mathbf{F}^{-T} : \nabla\mathbf{w})(\mathbf{F}^{-1} : \nabla\mathbf{v}^T), \xi\right)_{\mathcal{F}} - \left(J\mathbf{F}^{-1}\nabla\mathbf{w}\mathbf{F}^{-1} : \nabla\mathbf{v}^T, \xi\right)_{\mathcal{F}} \\
& + \left(\nabla\mathbf{w}\boldsymbol{\Sigma}_s + \mathbf{F}\frac{d\boldsymbol{\Sigma}_s}{d\mathbf{u}}(\mathbf{W}), \nabla\phi\right)_{\mathcal{S}} \\
& + \left(\nabla\mathbf{w}, \nabla\psi_f\right)_{\mathcal{F}}
\end{aligned}$$

The adjoint system is given by the transposed of this bilinear form, which means that we have to switch the role of test function $\mathbf{W} \leftrightarrow \Phi$ and trial function $\Phi \Leftrightarrow \mathbf{Z}$.

Lemma 8.15 (Adjoint Problem for Fluid-structure Interactions) *Let* $\mathbf{U} \in \mathcal{X}$. *The linearized adjoint problem is given as to find* $\mathbf{Z} = \{\mathbf{z}_f, \mathbf{w}, q_f\} \in \mathcal{Y}$, *such that*

$$A'(\mathbf{U})(\Phi, \mathbf{Z}) = J'(\mathbf{U})(\Phi) \quad \forall \Phi = \{\psi, \phi, \xi\} \in \mathcal{X},$$

where

$$\begin{aligned}
A'(\mathbf{U})(\Phi, \mathbf{Z}) = &\left(\rho_f J \left(\nabla\psi \mathbf{F}^{-1}\mathbf{v} + \nabla\mathbf{v}\mathbf{F}^{-1}\psi\right), \mathbf{w}\right)_{\mathcal{F}} \\
&+ \left(J\frac{d\boldsymbol{\sigma}_f}{d\mathbf{v}}(\Phi)\mathbf{F}^{-T}, \nabla\mathbf{w}\right)_{\mathcal{F}} - \left(J\mathbf{F}^{-T}\xi_f, \nabla\mathbf{w}\right)_{\mathcal{F}} \\
&+ \left((J\mathbf{F}^{-1} : \nabla\psi^T, q_f\right)_{\mathcal{F}} \\
&+ \left(\rho_f J \operatorname{tr}(\mathbf{F}^{-1}\nabla\phi)\left(\nabla\mathbf{v}\mathbf{F}^{-1}\mathbf{v}\right), \mathbf{w}\right)_{\mathcal{F}} - \left(\rho_f J\nabla\mathbf{v}\mathbf{F}^{-1}\nabla\phi\mathbf{F}^{-1}\mathbf{v}, \mathbf{w}\right)_{\mathcal{F}} \\
&+ \left(J\operatorname{tr}(\mathbf{F}^{-1}\nabla\phi)\boldsymbol{\sigma}_f\mathbf{F}^{-T}, \nabla\mathbf{w}\right)_{\mathcal{F}} - \left(J\boldsymbol{\sigma}_f\mathbf{F}^{-T}\nabla\phi^T\mathbf{F}^{-T}, \nabla\mathbf{w}\right)_{\mathcal{F}} \\
&+ \left(J\frac{d\boldsymbol{\sigma}_f}{d\mathbf{u}}(\Phi)\mathbf{F}^{-T}, \nabla\mathbf{w}\right)_{\mathcal{F}} \\
&+ \left(J(\mathbf{F}^{-T} : \nabla\phi)(\mathbf{F}^{-1} : \nabla\mathbf{v}^T), q_f\right)_{\mathcal{F}} - \left(J\mathbf{F}^{-1}\nabla\phi\mathbf{F}^{-1} : \nabla\mathbf{v}^T, q_f\right)_{\mathcal{F}} \\
&+ \left(\nabla\phi\boldsymbol{\Sigma}_s + \mathbf{F}\frac{d\boldsymbol{\Sigma}_s}{d\mathbf{u}}(\Phi), \nabla\mathbf{w}\right)_{\mathcal{S}} \\
&+ \left(\nabla\phi, \nabla\mathbf{z}_f\right)_{\mathcal{F}},
\end{aligned} \tag{8.44}$$

This adjoint problem is linear in $\mathbf{Z} \in \mathcal{Y}$ and $\Phi \in \mathcal{X}$. The assembly of the adjoint system matrix is computationally intense. If the nonlinear fluid-structure interaction problem will be solved by a Newton's method, see Sect. 5.2.2 and the Jacobian is required in every step of the Newton iteration. Then, solving the adjoint problem simply corresponds to the effort required for transposing the matrix and performing one additional Newton-like step.

Remark 8.16 (Adjoint Problem) The variational formulation of the adjoint problem can be used to compute the sensitivities for the error estimator and it will also serve as adjoint solution in optimization problems, see Chap. 9. The variational formulation is not sufficient to understand the coupling character of the adjoint problem: what are the interface conditions of the adjoint solution $\mathbf{Z}$ at $\mathcal{I}$? It would be necessary to migrate to the classical formulation using integration by parts to free the test functions from all derivatives. Considering a term in (8.44) like

$$\left(\rho_f J \operatorname{tr}(\mathbf{F}^{-1}\nabla\phi)\nabla\mathbf{v}\mathbf{F}^{-1}, \mathbf{w}\right)_{\mathcal{F}},$$

reveals the complexity of this task. This example shows the value of localizations of error estimators that do not require knowledge of the classical residual and the edge jumps. see Sect. 8.2.1.3.

8.3.2 Numerical Examples: Error Estimation and Adaptivity

In this section, we study two problems and show the efficiency of the dual weighted residual method. First we consider the stationary fsi-1 benchmark as proposed by Hron et al. in [201]. In this two-dimensional problem, a laminar flow around a circular obstacle with an attached elastic beam is considered, see Fig. 8.5. Quantity of interest is the drag coefficient of the obstacle as well as the deformation of the tip of the beam.

Secondly, as a three-dimensional benchmark problem, the laminar flow over an elastic obstacle mounted on the wall is considered. As quantities of interest we again evaluate the deformation in a point within the elastic structure and the drag coefficient of the obstacle.

8.3.2.1 The fsi-1 Benchmark Problem

First, we consider the stationary benchmark problem fsi-1 [79, 80]. Here, the laminar flow around a cylinder, with an attached elastic beam is simulated. Figure 8.5 shows a sketch of the configuration.

Three benchmark problems have been proposed by Hron and Turek [201]. We limit the considerations to the stationary fsi-1 test case. The flow is laminar with Reynolds-number $Re = 20$ and driven by a parabolic inflow profile with average velocity $\bar{\mathbf{v}}_f = 0.2$. For the structural problem, the St. Venant-Kirchhoff material law is used in a slightly compressible setting with Poisson ratio $\nu_s = 0.4$

$$\rho_f = \rho_s = 1000, \quad \nu_f = 10^{-3}, \quad \mu_s = 5 \cdot 10^5, \quad \lambda_s = 2 \cdot 10^6, \quad \bar{v}_f = 0.2.$$

As quantities of interest, we measure the horizontal and vertical deflection of the structure in the point $A = (0.6, 0.2)$ on the tip of the beam, as well as the drag- and

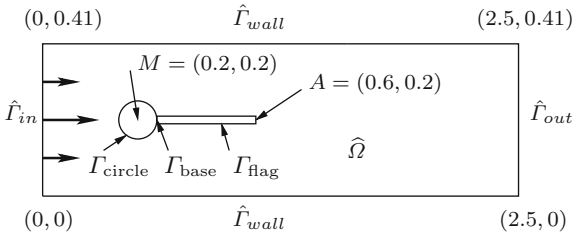

Fig. 8.5 Flow around cylinder with elastic beam with circle-center $M = (0.2, 0.2)$ and radius $r = 0.05$

lift- coefficient of the complete obstacle (including rigid circle and the elastic beam)

$$J_{\text{drag}}(\mathbf{U}) := \int_S (J\boldsymbol{\sigma}_f \mathbf{F}^{-T})\mathbf{n}_f \cdot e_1 \, \mathrm{d}s, \quad J_{\text{lift}}(\mathbf{U}) := \int_S (J\boldsymbol{\sigma}_f \mathbf{F}^{-T})\mathbf{n}_f \cdot e_2 \, \mathrm{d}s,$$
$$J_{\text{x}}(\mathbf{U}) := \mathbf{u}_1(A), \qquad J_{\text{y}}(\mathbf{U}) := \mathbf{u}_2(A),$$

where $e_i := (\delta_{i1}, \delta_{i2})$ are the Cartesian unit vectors and $S := \Gamma_{\text{flag}} \cup (\Gamma_{\text{circle}} \setminus \Gamma_{\text{base}})$.

Remark 8.17 (Evaluation of the Surface Integral) For easier evaluation, we modify the functional expression. Let Γ_{circle} be the boundary, $\Gamma_{\text{base}} \subset \Gamma_{\text{circle}}$ that part of the circle, where the solid domain $\mathcal{S}$ is attached. Then, by using the dynamic coupling condition on Γ_i it holds:

$$J_{\text{drag}}(\mathbf{U}) = \int_{\Gamma_{\text{circle}} \setminus \Gamma_{\text{base}}} (J\boldsymbol{\sigma}_f \mathbf{F}^{-T})\mathbf{n}_f \cdot e_1 \, \mathrm{d}s - \int_{\Gamma_i} (J\boldsymbol{\sigma}_s \mathbf{F}^{-T})\mathbf{n}_s \cdot e_1 \, \mathrm{d}s$$

Further, using $\operatorname{div}(J\boldsymbol{\sigma}_s \mathbf{F}^{-T}) = 0$ since no right hand side is given in this benchmark configuration, the surface integral can be transformed into an integral over the complete circle Γ_{circle}:

$$J_{\text{drag}}(\mathbf{U}) = \int_{\Gamma_{\text{circle}} \setminus \Gamma_{\text{base}}} (J\boldsymbol{\sigma}_f \mathbf{F}^{-T})\mathbf{n}_f \cdot e_1 \, \mathrm{d}s + \int_{\Gamma_{\text{base}}} (J\boldsymbol{\sigma}_s \mathbf{F}^{-T})\mathbf{n}_s \cdot e_1 \, \mathrm{d}s$$

An evaluation of this surface integral with higher accuracy is possible by expressing it in terms of residuals (the *Babuška-Miller-Trick*) [16–18, 63, 88] tested with a non-conforming test function $\hat{\mathbf{Z}}^{\text{drag}} \notin X$

$$J_{\text{drag}}(\mathbf{U}) = A(\mathbf{U})(\hat{\mathbf{Z}}^{\text{drag}}), \quad \hat{\mathbf{Z}}^{\text{drag}} := \{0, 0, \hat{\chi}^u\}, \tag{8.45}$$

where

$$\hat{\chi}^u_y := 0, \quad \hat{\chi}^u_x := \begin{cases} 1 : \ x \in \Gamma_{\text{circle}} \\ \text{extended to } 0 : \ x \notin \Gamma_{\text{circle}} \cup \Gamma_{\text{base}} \end{cases}.$$

Given sufficient regularity, the evaluation of the drag- and lift-coefficients using this technique yields a higher order of convergence [63], namely second order for linear finite elements. In the case of the lift-coefficients, the components $\hat{\chi}^u_y$ and $\hat{\chi}^u_x$ must be switched.

This benchmark problem is well analyzed in the collections [79, 80]. In Table 8.1 we collect reference values for all four functionals used in this work. These results are obtained by reviewing the cited references and extrapolating results using higher order finite elements on uniform meshes. The values are in very good agreement with those identified by Turek and coworkers [329].

Table 8.1 Reference values for the fsi-1 benchmark

Functional	Reference value	Accuracy
Drag	14.294	$\pm 5 \cdot 10^{-4}$
Lift	0.7648	$\pm 5 \cdot 10^{-5}$
x-deformation	$2.268 \cdot 10^{-5}$	$\pm 5 \cdot 10^{-9}$
y-deformation	$8.190 \cdot 10^{-4}$	$\pm 5 \cdot 10^{-7}$

Error Estimation and Results on Locally Refined Meshes

For error estimation with the dual weighted residual method we need to approximate the adjoint problems:

$$\mathbf{Z}_h \in X_h : \quad A_h'(\mathbf{U}_h)(\Phi_h, \mathbf{Z}_h) = J'(\mathbf{U}_h)(\Phi_h) \quad \forall \Phi_h \in X_h.$$

Details on the adjoint bilinear-form are given in the previous section. For the two deflection functionals J_x and J_y the right hand side of the adjoint problems is a Dirac and lacks the necessary regularity $J_x', J_y' \notin H^{-1}(\Omega)$. Hence, these functionals should be regularized with a small parameter $\varepsilon > 0$:

$$J_{x/y}(\mathbf{U}) = \frac{1}{|B_\varepsilon(A)|} \int_{B_\varepsilon(A)} u_{x/y} \, \mathrm{d}x, \quad B_\varepsilon(A) := \{x \in \Omega : \ |x - A| < \varepsilon\}. \tag{8.46}$$

In the case of the drag- and lift-coefficients, the right hand side of the adjoint problems is defined by using $\hat{\mathbf{Z}}^{\text{drag}}$ from (8.45)

$$J'_{\text{drag}}(\mathbf{U})(\Phi) = A'(\mathbf{U})(\Phi, \hat{\mathbf{Z}}^{\text{drag}}).$$

Since $\hat{\mathbf{Z}}^{\text{drag}}$ is a extension of (non-conforming) Dirichlet-values into the domain, this problem is related to solving a problem with homogenous right hand side and non-homogenous Dirichlet values on Γ_{circle}

$$\hat{\mathbf{Z}}_h \in \hat{\mathbf{Z}}^{\text{drag}} + X_h : \quad A_h'(\mathbf{U}_h)(\Phi_h, \hat{\mathbf{Z}}_h) = 0 \quad \forall \Phi_h \in X_h.$$

In Fig. 8.6, we compare the convergence history of all four error-functionals. In each sketch we compare the relative errors using uniform mesh refinement with those obtained on locally refined meshes using the dual weighted residual method. Further, on both sequences of meshes we plot the values of the error estimator. Finally, for comparison we give sketches of the error slopes corresponds to linear convergence $h \approx N^{-\frac{1}{2}}$ and quadratic convergence $h^2 \approx N^{-1}$. The apparent loss of convergency on fine meshes (in particular for the lift-coefficient and the

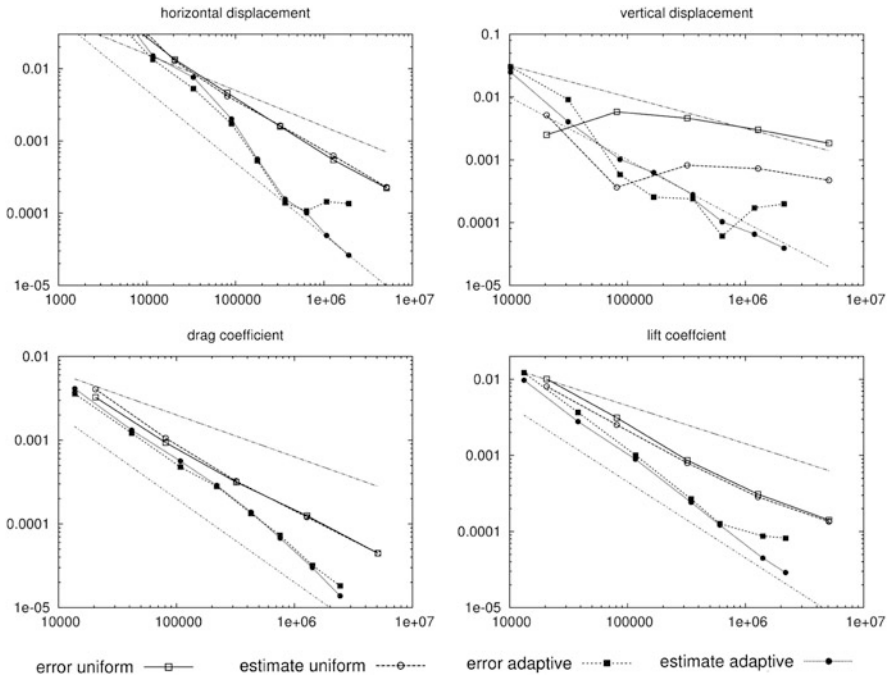

Fig. 8.6 Error and estimator for the different functionals on uniform meshes and locally refined meshes. *Top left to bottom right*: Error in horizontal and vertical deflection, drag- and lift-coefficient. For comparison: Slopes with linear and quadratic convergence

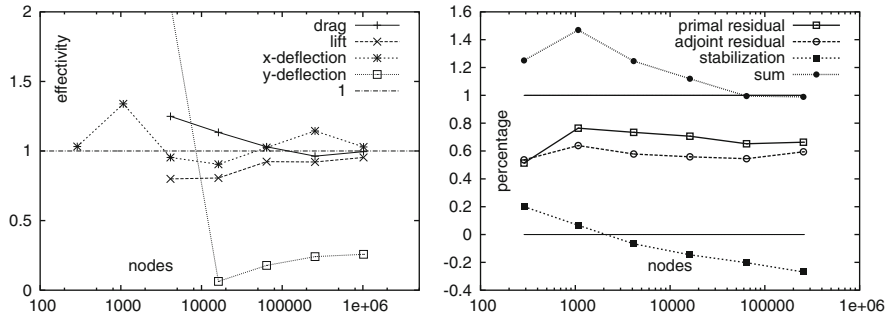

Fig. 8.7 Effectivity of the dual weighted residual method on uniform meshes. *Left*: effectivities for all four functional values on uniform meshes. *Right*: composition of the estimator into primal residual, adjoint residual and stabilization part for the drag coefficient w.r.t the exact error

displacement functionals) is due to an inexact knowledge of the reference values $J(\mathbf{U})$, see Table 8.1.

Next, in the left plot in Fig. 8.7 we show the effectivities of the error estimator

$$\mathrm{eff}_h := \frac{\eta_h(\mathbf{U}_h, \mathbf{Z}_h)}{J(\mathbf{U}) - J(\mathbf{U}_h)}$$

on a sequence of uniform meshes for all four error functionals. A value of one indicates error estimation with optimal accuracy. Apart from the vertical deflection $J_y(\mathbf{U})$ the effectivities of the estimator are very good and converging to one on fine meshes. The error in the vertical deflection is underestimated. This may be due to the limited regularity of the functional, as these computations have been done without a regularization of the right hand side as discussed in (8.46).

In the right plot of Fig. 8.7 we show the composition of the error estimator of the drag evaluation split into the primal residual, adjoint residual and stabilization part

$$\begin{aligned}
\eta^P(\mathbf{U}_h, \mathbf{Z}_h) &= F(\mathbf{Z} - i_h\mathbf{Z}) - A_h(\mathbf{U}_h)(\mathbf{Z} - i_h\mathbf{Z}),\\
\eta^A(\mathbf{U}_h, \mathbf{Z}_h) &= J'(\mathbf{U}_h)(\mathbf{U} - i_h\mathbf{U}) - A_h'(\mathbf{U}_h)(\mathbf{U} - i_h\mathbf{U}, \mathbf{Z}_h),\\
\eta^S(\mathbf{U}_h, \mathbf{Z}_h) &= S_h(\mathbf{U}_h)(\mathbf{Z}_h).
\end{aligned}$$

This splitting has been described in Theorem 8.7 of Sect. 8.1.1.2. The example shows that all parts are essential. Here, the stabilization part has a different sign, such that neglecting it would result in an overestimation of the error.

In Fig. 8.8 we show the adjoint solutions with regard to the drag-evaluation. In the top-row the two components of the adjoint variable $\mathbf{w}_f \in \mathcal{V}_f$ (which is only defined in the fluid domain $\mathcal{F}$) and in the bottom-row the two components of the variable $\mathbf{u} \in \mathcal{V}$ are shown. In the lower left plot, the x-component of the adjoint deformation one can identify the adjoint Dirichlet value $\mathbf{z} = 1$ on the obstacle used to evaluate the residual functional J_{drag} by means of the *Babuška-Miller-Trick*), compare Remark 8.17.

We start by discussing the results obtained on uniform meshes. Using piecewise linear finite elements, all four functionals should converge with second order (in the mesh size), given sufficient regularity of the solution. Figure 8.6 however depicts linear convergence only. This order reduction is due to limited regularity induced

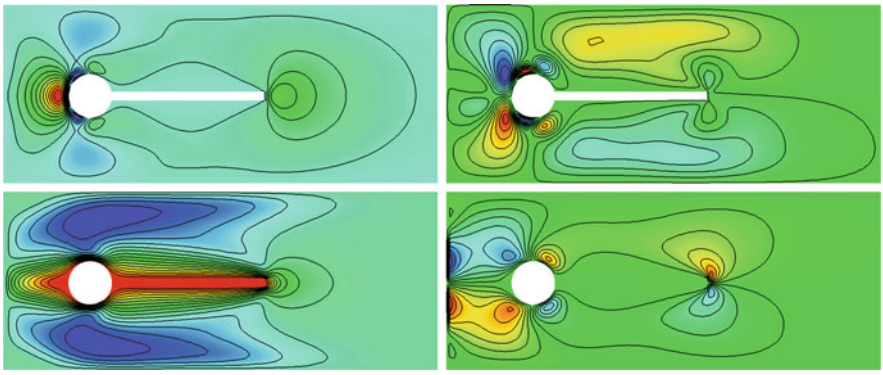

Fig. 8.8 Adjoint solution with regard to the drag-coefficient. *Top row*: Adjoint velocity $\mathbf{w}_f$ in x- and y-direction. *Bottom row*, Adjoint deformation $\mathbf{z}$ in x- and y-direction

by the reentrant edges at the interface Γ_i as seen from the fluid domain. Similar results are observed for pure fluid dynamics benchmark problems [63, 299]. When comparing the estimator value with the real error in Figs. 8.6 and 8.7, one observes very good effectivities

$$\mathrm{eff}_h(\mathbf{U}_h, \mathbf{Z}_h) \xrightarrow[h\to 0]{} 1$$

for the drag- and lift-coefficient (even if the regularity of the problem is not sufficient to guarantee higher order convergence of the remainders $\mathcal{R}^{(3)}(\mathbf{U} - \mathbf{U}_h, \mathbf{Z} - \mathbf{Z}_h)$). In the case of the two deflection functionals—and in particular for the vertical deflection functional J_y—the quality of the estimator is less. This is explained by additional regularity limitations due to the Dirac structure of the functionals J_x and J_y, as we do not work with a regularization as shown in (8.46).

The right sketch in Fig. 8.7 shows that all three parts of the error estimator are essential. It is well known [41] that for linear problems primal and adjoint parts in the error estimator coincide (in the limit $h \to 0$). For nonlinear problems all parts must be taken into account. Further, we see that the stabilization part cannot be neglected. In Fig. 8.9 we show two meshes with local mesh refinement obtained during the simulation with the drag functional.

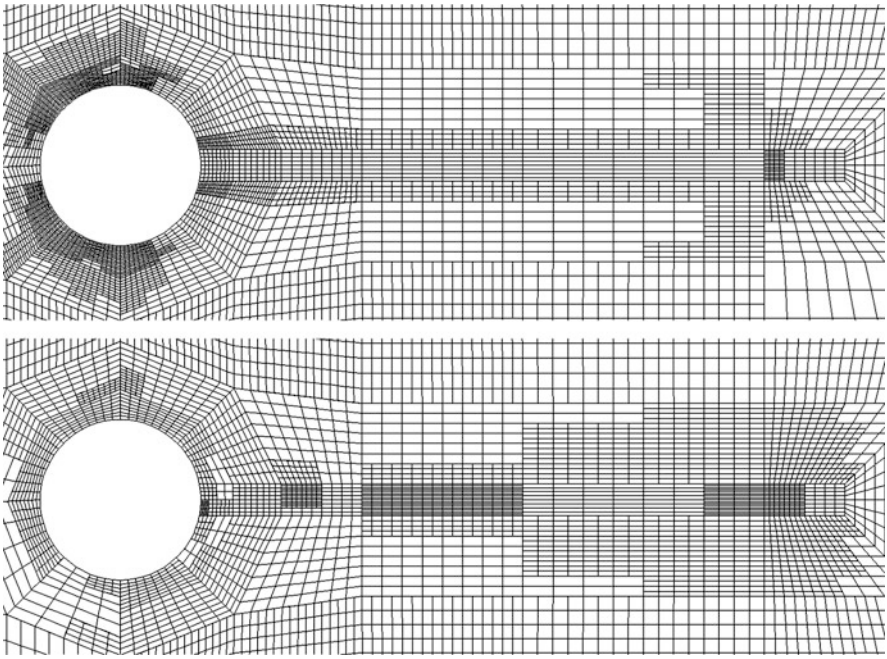

Fig. 8.9 Cut-out of locally refined meshes used to approximate the drag-coefficient (*top*) and the horizontal displacement functional (*bottom*)

8.3.2.2 3D Fluid-structure Interaction

Second, we present numerical simulations of a three dimensional test case that—in similar configuration—has already been used to test the performance of linear solvers in Sect. 7.5. In the domain $\Omega := (0, 1.5) \times (0, 0.4) \times (-0.4, 0.4)$ an elastic structure $\mathcal{S} := (0.4, 0.5) \times (0, 0.2) \times (-0.2, 0.2)$ is inscribed, see Fig. 8.10. The problem is considered to be symmetric in the x/y-plane. Hence, we run the simulation only in one half of the domain. On the inflow boundary $\Gamma_{\text{in}} = (0, 0.4) \times (-0.4, 0.4)$, a parabolic velocity profile is given as Dirichlet condition with peak velocity $\mathbf{v}_{\max} = 0.3\,\text{m} \cdot \text{s}^{-1}$. On the inner symmetry plane, we prescribe $\mathbf{v}_f \cdot \mathbf{n} = 0$ as Dirichlet condition, on the outflow boundary Γ_{out} the *do-nothing* condition for velocity and pressure. The no-slip condition is used on the remaining boundaries Γ_{wall}. The solid is fixed by a homogenous Dirichlet condition $\mathbf{u}_s = 0$ on the bottom Γ_{base}. Deformation in normal-direction is prohibited $\mathbf{u}_s \cdot \mathbf{n} = 0$ on the symmetry-plane Γ_{sym}. On the remaining boundaries Γ_{wall}, Γ_{out} and Γ_{in} the fluid's deformation is extended with homogenous Dirichlet values $\mathbf{u}_f = 0$.

The fluid is incompressible with $\rho_f = 10^3\,\text{kg} \cdot \text{m}^{-3}$ and $\nu_f = 10^{-3}\,\text{m}^2 \cdot \text{s}^{-1}$. The solid's density is $\rho_s = 10^3\,\text{kg} \cdot \text{m}^{-3}$, its Poisson ratio $\nu_s = 0.4$ with a shear modulus of $\mu_s = 5 \cdot 10^5\,\text{kg} \cdot \text{m}^{-1}\text{s}^{-2}$. With an average inflow velocity of $\bar{\mathbf{v}}_{\text{in}} \approx 0.15\,\text{m} \cdot \text{s}^{-1}$, and an obstacle of size 0.2 m, the Reynolds number is $Re \approx 25$ and the flow is in the laminar regime. For the LPS stabilization, we use the parameter $\delta_0 = 0.25$.

As quantities of interest, we measure the x-deflection of the obstacle at the coordinate $A = (0.45, 0.15, 0.15)$ close to the outer corner of the structure, as well

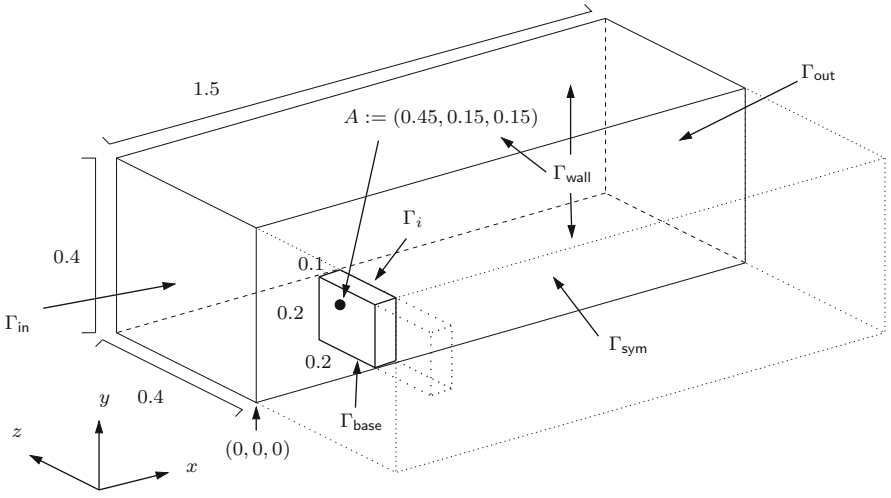

Fig. 8.10 Configuration of the three-dimensional test case. Domain and solution are symmetric in z-direction

as the force of the fluid on the structure in the dominant flow direction

$$J_{\mathrm{x}}(\mathbf{U}) := \mathbf{e}_1 \cdot \mathbf{u}(A), \quad J_{\mathrm{drag}}(\mathbf{U}) := \int_{\Gamma_i} (J\boldsymbol{\sigma}_f \mathbf{F}^{-T})\mathbf{n}_f \cdot \mathbf{e}_1 \, \mathrm{d}s.$$

Like in the two-dimensional case, the surface integral is first transformed using the structure equation and then expressed as a residual term $J_{\mathrm{drag}}(\mathbf{U}) = A(\mathbf{U})(\hat{\mathbf{Z}}^{\mathrm{drag}})$ using a function $\hat{\mathbf{Z}}^{\mathrm{drag}} \notin \mathcal{X}$ with non-conforming boundary values at Γ_{base}, compare (8.45).

For obtaining reference values we estimate the two error quantities on a sequence of meshes using uniform refinement. Table 8.2 we collect the results. By extrapolation, using the values on the finest three meshes, we define reference values in Table 8.3. We believe these values to be exact to a relative error of about 1%.

In Fig. 8.11 we plot the convergence history on uniform and locally refined meshes, both for the drag-coefficient and the horizontal displacement functional.

Table 8.2 Convergence history of the three dimensional fsi test case using piece-wise linear finite elements

dof's	$J_{\mathrm{drag}}(\mathbf{U}_h)$	Error (abs)	$J_{\mathrm{x}}(\mathbf{U}_h)$	Error (abs)
2975	1.5249	$1.98 \cdot 10^{-1}$	$4.9337 \cdot 10^{-5}$	$9.90 \cdot 10^{-6}$
18,711	1.4763	$1.49 \cdot 10^{-1}$	$5.5686 \cdot 10^{-5}$	$3.55 \cdot 10^{-6}$
131,495	1.4038	$7.68 \cdot 10^{-2}$	$5.8529 \cdot 10^{-5}$	$7.11 \cdot 10^{-7}$
983,367	1.3563	$2.93 \cdot 10^{-2}$	$\mathbf{5.9075 \cdot 10^{-5}}$	$\mathbf{1.65 \cdot 10^{-7}}$
7,600,775	**1.3380**	$\mathbf{1.10 \cdot 10^{-2}}$	$5.9202 \cdot 10^{-5}$	$3.80 \cdot 10^{-8}$

The bold values indicate that an error below 1% has been reached

Table 8.3 Reference values for the three dimensional benchmark problem

Functional	Reference value	Accuracy
Drag	1.33	1%
x-deflection	$5.95 \cdot 10^{-5}$	1%

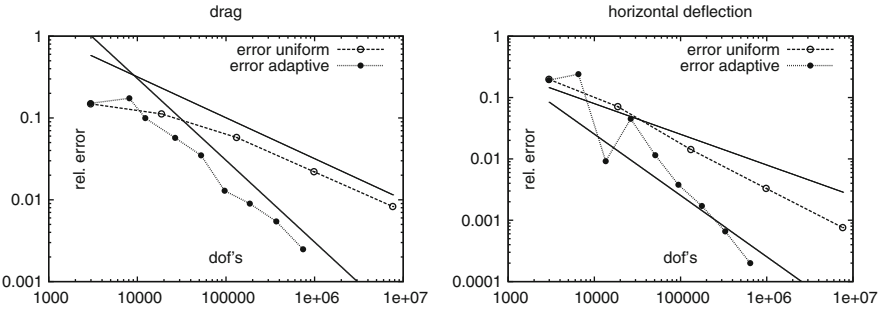

Fig. 8.11 Error history for the drag-coefficient (*left*) and horizontal displacement (*right*) on uniform and adaptively refined meshes. Linear and quadratic error slopes for comparison

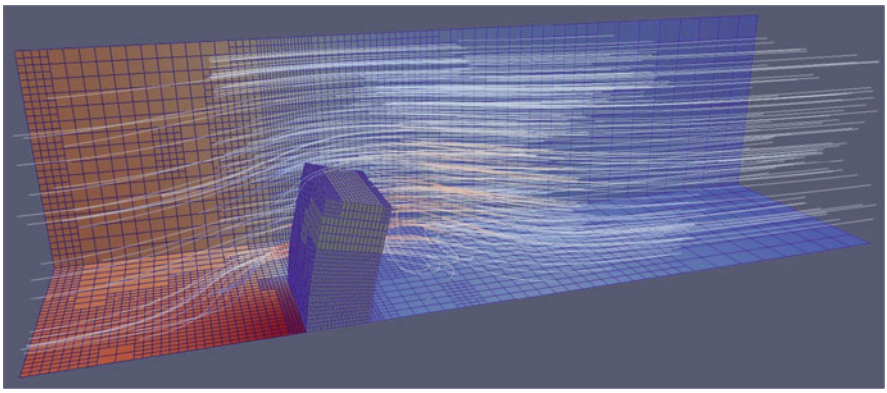

Fig. 8.12 Sketch of the numerical solution on locally refined meshes. The domain is cut at the symmetry plane Γ_{sym} in the front. For visualization, the deformation has been strengthened by the factor 100

This three dimensional test case has the same regularity limitations as the fsi-1 benchmark problem. The elastic obstacle induces corner singularities in the solution and the horizontal deflection functional J_{x} lacks regularity. In both cases, the computational effort necessary to reach a certain error tolerance is reduced significantly by using adaptive finite elements. Considering the complexity of three dimensional simulations these savings are substantial. In order to resolve the singularities caused by the reentrant corners of the embedded structure, it was essential to run the adaptation process very gently by choosing $\alpha = 8$ in the equilibration procedure described in Sect. 8.2.2.

Finally, Fig. 8.12 shows a visualization of a numerical solution. Here, adaptation is driven in order to optimize the functional value $J_{\text{x}}(\mathbf{U}_h)$. Deformation of the structure is scaled by 100 for better visualization.

8.4 Further Concepts of Adaptivity

Most fluid-structure interaction problems are non-stationary. Fully space-time adaptivity using dynamic meshes that change from time step to time step require the solution of adjoint solutions that run backward in time. The effort is substantial. To assemble the adjoint system, i.e. to assemble the linearized adjoint we must store the forward problem $\mathbf{U}_h(t_n)$ in all time steps. We have seen in Sect. 5.1.1 that very small time steps may be required. If this effort is considered, space-time adaptivity with the dual weighted residual method can be carried out as demonstrated by Meidner [238], Besier (né Schmich), Rannacher and Vexler [51, 302, 303]. In the context of fluid-structure interactions Failer [133] computed non-stationary adjoints for solving optimization problems. See also [134] for a linearized fluid-structure interaction system.

The computational effort (in terms of memory and time) for solving fluid-structure interactions is very large. Due to the very complex structure and as domains and functionals will often feature limited regularity, good efficiency can only be expected for simplified model problems. A promising alternative to fully resolved non-stationary error estimation is by means of averaging, where functionals of the type

$$J(\mathbf{U}) = \int_0^T j(\mathbf{U}(t))\mathrm{d}t$$

are considered. Braack, Burman and Taschenberger [65, 68] showed that the adjoint problem for such functionals can be approximated by a stationary system. This approach will not give temporally distributed error estimates that can be used to control dynamic meshes. It is however an efficient technique for designing optimal averaged meshes.

The efficiency of the adaptive finite element method can be further increased by considering anisotropic refinements, see Apel [7] for an introduction and overview. In terms of adaptive mesh refinement anisotropy offers the possibility to split elements only along single sides, see Fig. 8.13 for a sketch.

The use of anisotropic finite elements requires complex mesh structures. At least for quadrilateral and hexahedral meshes, the use of this concept is therefore rather rare. If the finite element framework will allow for such refinement types, the main difficulty is the identification of the dominant error directions. In addition to a localization of the error estimator we need the extract the anisotropic directions. The classical approach is based on a study of the solution's Hessian

$$\nabla^2 u = \begin{pmatrix} \partial_{xx}u & \partial_{xy}u \\ \partial_{xy}u & \partial_{yy}u \end{pmatrix} = \mathbf{X}^T \begin{pmatrix} \partial_{vv}u & 0 \\ 0 & \partial_{\eta\eta}u \end{pmatrix} \mathbf{X}$$

by means of a singular value decomposition. The eigenvectors constituting the matrix $\mathbf{X}$ will indicate the major directions, the eigenvalues $\partial_{vv}u$ and $\partial_{\eta\eta}u$ indicate the strength of anisotropy. This approach is well established and successfully used in many applications, see [28, 92, 111, 258, 361]. A combination with goal oriented error estimation using the DWR method is possible by using the DWR approach to choose the elements to be refined and use the Hessian to determine the refinement

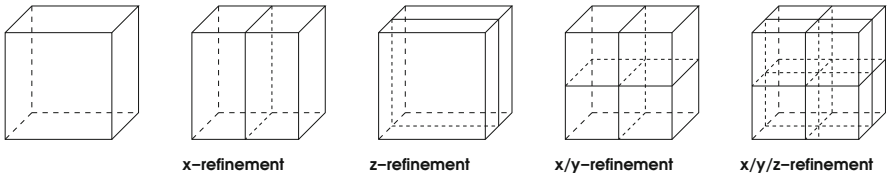

Fig. 8.13 Different possibilities for an anisotropic refinement of a hexahedra

direction, see [90, 145, 146, 224, 335]. Although very successful, these approaches have two shortcomings: which Hessian is to be used? The primal one $\nabla^2 u$ or the adjoint one $\nabla^2 z$. Anisotropic influences may origin from the solution itself or from the adjoint solution given by the functional. A proper balancing is not in all cases possible, as shown in [279]. Second, the Hessian is mostly relevant for linear finite element approaches. Using higher order finite elements, the Hessian does not carry any information on the error, as curvature is resolved exactly by second order approaches.

In [279] we have extended the DWR method, such that it is directly able to estimate directional errors. This allows the correct balancing of primal and adjoint residual information. In [281] we have applied this concept to the fsi-1 benchmark problem. In Fig. 8.14 we show a snapshot of an anisotropically refined adaptive mesh. Here, the maximum aspect ratio (shortest vs. longest edge in the elements) reaches $1:50$. By use of anisotropic adaptivity we can significantly reduce the error constant.

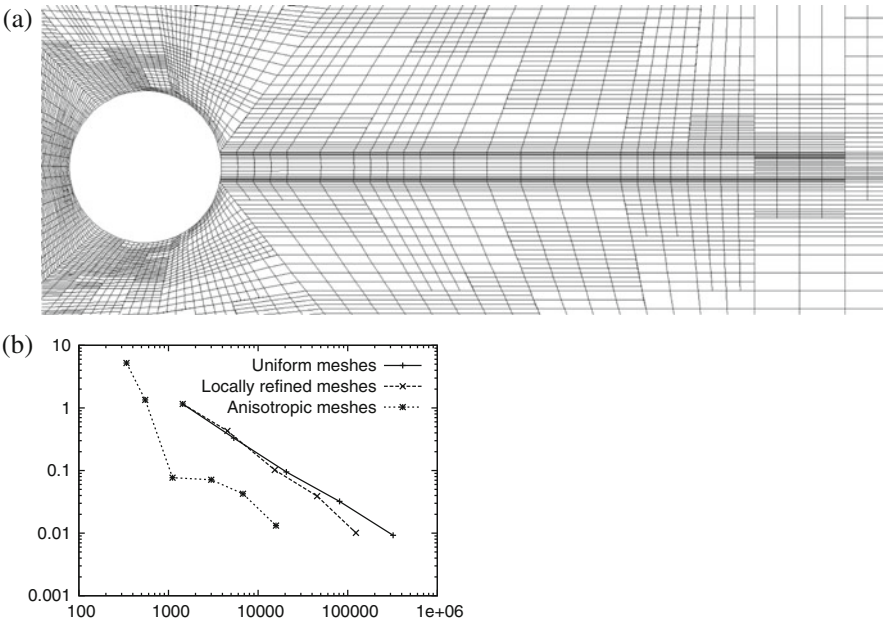

Fig. 8.14 Anisotropic simulation of the fsi-1 benchmark problem for identifying the drag coefficient. *Bottom*: Convergence history for the drag-coefficient on uniform meshes, isotropic adaptive meshes and anisotropic adaptive meshes. *Top*: Cut-out of the finite element mesh used for calculating the drag-coefficient. The maximum aspect ratio reaches $1:50$

Part III
Applications

In this last part, we will present different applications of fluid-structure interactions. Common to all these problems is the demand for a strong coupling, for monolithic formulations and implicit discretizations and solvers. Among the vast diversity of applications this presentation is only an very small subset with a focus on large deformation, laminar flows and a very strong coupling between the phases. We refer to the literature such as the monograph [32] with many advanced and challenging applications ranging from aeroelasticity, hemodynamics over wind turbines to parachute simulations.

Four different application problems will be discussed. In Chap. 9 we start with optimization and parameter identification problems that are subject to fluid-structure interactions as constraint. Typical applications for such problems are found in aeroelasticity: What is the optimal shape of a flying aircraft? This problem must be investigated as a dynamic fluid-structure interaction problem, as deformations are significant.

Next Chap. 10 deals with bio/chemical-fluid-structure interaction problems. We introduce systems of equations that describe the coupling of the mechanical fluid-structure problem with systems of reaction-diffusion problems, that can describe biological or chemical reactions. Such problems are typical in hemodynamics, where the walls of the blood vessels must be considered as active materials, with material parameters, size and volume depending on biological and chemical influences. Emphasis of this chapter is in the modeling of such active materials.

In Chap. 11 we investigate the vibration dynamics of coupled fluid-structure interaction problems. The question is easily described as follows: Elastic solids feature eigenfrequencies of oscillations that are intensified when stimulated. Fluid problems feature oscillations like the von Kármán vortex sheet with a frequency that depends on the Reynolds number. What will be the dominant frequency of the coupled problem?

Finally, Chap. 12 is a guest article by Stefan Frei [151]. He gives a modern and comprehensive analysis of fluid-structure interactions featuring the contact of

the solid with the boundary of the domain. Such problems cannot be modeled in standard monolithic ALE approaches. Frei presents an application of the *Fully Eulerian formulation* using efficient and accurate discretization techniques as described in Sects. 4.5 and 4.6.

Chapter 9
Optimization with Fluid-structure Interactions

Many applications involve inverse problems. A typical optimization problem could be the control of an inflow to reduce the vorticity or to stabilize the dynamics of a fluid-structure interaction problem. A related problem is the identification of parameters like Lamé coefficients by indirect measurements.

In this section, some basic principles for the optimization with partial differential equations and the application to simple, stationary fluid-structure interaction problems will be collected. For an intensive introduction to optimization and parameter identification with partial differential equations, we refer to the literature [191, 238, 325, 326]. On optimization with fluid-structure interactions, there is only little literature [79, 80, 134, 286]. From the large variety of different optimization techniques, we solely consider gradient based methods. The contents of this section have mainly been taken from [286], a collaboration with Thomas Wick.

A first thorough analysis of optimization problems with fluid-structure interactions is given by Failer [133, 134]. He also discusses the much more difficult and relevant case of non-stationary problems.

For gradient based optimization of coupled problems, it is necessary to assemble gradients of the fully coupled model. The adjoint solutions, based on these gradients, are sensitivities that indicate the impact of the control on the target functional. In partitioned methods, where the coupling is realized by an iterative algorithm only, this is a very difficult step. The sensitivities of fluid and solid problems alone are well studies. A proper inclusion of the coupling is a more difficult process. The correct transportation of adjoint information across the interface however will be essential.

T. Richter, *Fluid-structure Interactions*, Lecture Notes in Computational Science and Engineering 118, DOI 10.1007/978-3-319-63970-3_9

9.1 The Optimization Problem

We consider optimization problems, where the optimal solution is constraint to a stationary fluid-structure interaction problem. For simplicity, we will consider the ALE formulation from Chap. 5 only, such that $\mathbf{U} \in \mathbf{U}^D + \mathcal{X}$ is constraint to

$$\begin{aligned} A(\mathbf{U})(\Phi) = &\left(\rho_f J \left(\nabla \mathbf{v} \mathbf{F}^{-1} \mathbf{v}\right), \phi\right)_{\mathcal{F}} + \left(J \boldsymbol{\sigma}_f \mathbf{F}^{-T}, \nabla \phi\right)_{\mathcal{F}} - (J \rho_f \mathbf{f}, \phi)_{\mathcal{F}} \\ &+ \left(J \mathbf{F}^{-1} : \nabla \mathbf{v}^T, \xi\right)_{\mathcal{F}} + (\mathbf{F} \boldsymbol{\Sigma}_s, \nabla \phi)_{\mathcal{S}}, \end{aligned} \tag{9.1}$$

where $\mathbf{U}^D$ is an extension of the Dirichlet data and where $\mathbf{U} = \{\mathbf{v}, \mathbf{u}, p\}$ is found in

$$\mathcal{X} = H_0^1(\mathcal{F}; \Gamma_f^D)^d \times H_0^1(\mathcal{F} \cup \mathcal{I} \cup \mathcal{S}; \Gamma^D)^d \times L_0^2(\mathcal{F}).$$

We consider the following setting: by $K : \mathcal{X} \to \mathbb{R}$ we denote a given functional of interest. One example could be the outflow rate at a boundary part Γ_f^{out}

$$K_{\text{out}}(\mathbf{U}) = \int_{\Gamma_f^{\text{out}}} (\mathbf{v} \cdot \mathbf{n})^2 \, \mathrm{d}o, \tag{9.2}$$

or a functional of pointwise tracking type measuring the deflection of the solid

$$K_A(\mathbf{U}) = |\mathbf{u}(A) - \mathbf{u}^A|^2, \tag{9.3}$$

where $A \in \bar{\mathcal{S}}$ is a point within the solid, $\mathbf{u}^A \in \mathbb{R}^d$ a prescribed deflection. Regarding the discussion in Sect. 8.1.1.1, such a functional of point-type must be regularized to fit into the theoretical framework. In any case we assume that $K(\cdot)$ is two times Fréchet differentiable.

Furthermore, by $\mathbf{q} \in \mathbf{Q}_d$, we denote the control, coming from the control space $\mathbf{Q}_d$. Typical examples of controls could be the Lamé coefficients $\mathbf{q} = (\mu_s, \lambda_s)$, a two-dimensional control space $\mathbf{Q}_d \subset \mathbb{R}^2$, the inflow profile $\mathbf{q} = \mathbf{v}^{\text{in}}$, where $\mathbf{Q}_d = H^{1/2}(\Gamma_f^{\text{in}})$, a mean inflow pressure $\mathbf{q} = P^{\text{in}}$, where $\mathbf{Q}_d = \mathbb{R}$. Often, such controls are constrained, e.g. by allowing only for positive pressures up to a certain limit or by requiring the Lamé coefficients to satisfy some physical relations, i.e.

$$\mathbf{Q}_d = \{(\mu, \lambda) \in \mathbb{R}^2, \ \mu > 0\}.$$

In this study, we do not consider any control constraints.

The control $\mathbf{q}$ can enter the problem in various ways. We introduce the modified variational formulation

$$\mathbf{U} \in \mathbf{U}^D + \mathcal{X} : \quad A(\mathbf{q}, \mathbf{U})(\Phi) := A(\mathbf{U})(\Phi) + B(\mathbf{q}, \mathbf{U})(\Phi) = F(\Phi) \quad \forall \Phi \in \mathcal{X},$$

where by $B(\cdot,\cdot)(\cdot)$ we denote the *control form*. We specify this control form for two examples: First, we consider the case of controlling the average inflow pressure on the boundary Γ_f^{in}. We do not prescribe Dirichlet conditions for $\mathbf{v}$ on Γ_f^{IN} and use the trial space

$$\mathbf{v} \in \mathbf{v}^D + H_0^1(\mathcal{F}; \Gamma_f^D \setminus \Gamma_f^{\text{in}})^d,$$

such that natural Neumann conditions act. Together with

$$B(\mathbf{q},\mathbf{U})(\Phi) = -\langle \rho_f \nu_f J \nabla \mathbf{v}^T \mathbf{F}^{-T} \mathbf{F}^{-T} \mathbf{n}, \phi \rangle_{\Gamma_f^{\text{in}}} - \langle \mathbf{q} J \mathbf{F}^{-T} \mathbf{n}, \phi \rangle_{\Gamma_f^{\text{in}}}, \tag{9.4}$$

integration by parts reveals on Γ_f^{in} the condition

$$\rho_f \nu_f J \mathbf{F}^{-1} \nabla \mathbf{v} \mathbf{F}^{-T} \mathbf{n} - p J \mathbf{F}^{-T} \mathbf{n} = \mathbf{q} J \mathbf{F}^{-T} \mathbf{n},$$

which corresponds to an average inflow pressure of $\mathbf{q}$, see Sect. 2.4.2. Second, we consider the control of the parameter μ_s in the material law by introducing the control form

$$B(\mathbf{q},\mathbf{U})(\Phi) = (\mathbf{F}\boldsymbol{\Sigma}_s(\mathbf{q}) - \mathbf{F}\boldsymbol{\Sigma}_s(\mu_s^0), \nabla\phi)_{\mathcal{S}}, \tag{9.5}$$

where (for the St. Venant Kirchhoff material)

$$\boldsymbol{\Sigma}_s(\mathbf{q}) := 2\mathbf{q}\mathbf{E}_s + \lambda_s \operatorname{tr}(\mathbf{E}_s) I, \quad \mathbf{E}_s := \frac{1}{2}(\mathbf{F}^T\mathbf{F} - I). \tag{9.6}$$

By μ_s^0 we denote an initial guess. The goal of our optimization problem is to determine the optimal parameters $\mathbf{q} \in \mathbf{Q}_d$ such that the functional of interest $K(\cdot)$ gets minimal. This quantity of interest is completed by a regularization term of Tikhonov type, which involves a regularization parameter $\alpha > 0$

$$K(\mathbf{q},\mathbf{U}) := K(\mathbf{U}) + \frac{\alpha}{2} ||\mathbf{q} - \bar{\mathbf{q}}||_Q^2, \tag{9.7}$$

with a reference control $\bar{\mathbf{q}} \in \mathbf{Q}_d$ and a suitable norm $||\cdot||_Q$ in the control-space. With these preparations we can formulate the constrained optimization problem:

Problem 9.1 (Constrained Optimization Problem) *Find* $\mathbf{U} \in \mathbf{U}^D + \mathcal{X}$ *and* $\mathbf{q} \in \mathbf{Q}_d$, *such that*

$$K(\mathbf{q},\mathbf{U}) \to \min, \text{ where } A(\mathbf{q},\mathbf{U})(\Phi) = F(\Phi) \quad \forall \Phi \in \mathcal{X}.$$

Introducing the Lagrangian

$$L(\mathbf{q},\mathbf{U},\mathbf{Z}) = K(\mathbf{q},\mathbf{U}) + F(\mathbf{Z}) - \mathbf{A}(\mathbf{q},\mathbf{U})(\mathbf{Z}),$$

a minimum to Problem 9.1 must satisfy the first order optimality condition

$$L'(\mathbf{q},\mathbf{U},\mathbf{Z})(\delta\mathbf{q},\delta\mathbf{U},\delta\mathbf{Z}) = 0 \quad \forall\delta\mathbf{q}\in\mathbf{Q}_d,\ \forall\delta\mathbf{U}\in\mathcal{X},\ \forall\delta\mathbf{Z}\in\mathcal{X},$$

which corresponds to the following system of equations, the *Karush-Kuhn-Tucker conditions* (KKT):

$$\begin{aligned} A(\mathbf{q},\mathbf{U})(\Phi) &= F(\Phi) && \forall\Phi\in\mathcal{X},\\ A'_{\mathbf{U}}(\mathbf{q},\mathbf{U})(\Phi,\mathbf{Z}) &= K'_{\mathbf{U}}(\mathbf{q},\mathbf{U})(\Phi) && \forall\Phi\in\mathcal{X},\\ A'_{\mathbf{q}}(\mathbf{q},\mathbf{U})(\chi,\mathbf{Z}) &= K'_{\mathbf{q}}(\mathbf{q},\mathbf{U})(\chi) && \forall\chi\in\mathbf{Q}_d. \end{aligned} \tag{9.8}$$

The first equation is called the *state equation*, second the *adjoint equation* and the last one the *gradient equation*.

The adjoint equation is exactly the equation for the adjoint problem in the context of the *Dual Weighted Residual method* that has been introduced in Sect. 8.1.1 and which is detailed in (8.44). The specific form of the gradient equation strongly depends on the way that the control enters the problem. In the case of pressure control on the inflow boundary (9.4), this gradient equation reads

$$-\chi\langle J\mathbf{F}^{-T}\mathbf{n},\mathbf{z}\rangle_{\Gamma_f^{\text{in}}} = \chi\alpha(\mathbf{q}-\bar{\mathbf{q}}) \quad \forall\chi\in\mathbb{R}. \tag{9.9}$$

This allows to express the control $\mathbf{q}$ in terms of the other variables

$$\mathbf{q} = \bar{\mathbf{q}} - \frac{1}{\alpha}\langle J\mathbf{F}^{-T}\mathbf{n},\mathbf{z}\rangle_{\Gamma_f^{\text{in}}}, \tag{9.10}$$

which reduces the KKT system (9.8) to a coupled system of the state and the adjoint equation. Regarding the identification of the Lamé coefficient (9.5), the gradient equation gets

$$\chi\big(2\mathbf{F}\mathbf{E}_s,\nabla\mathbf{z}\big)_{\mathcal{S}} = \chi\alpha(\mathbf{q}-\bar{\mathbf{q}}) \quad \forall\chi\in\mathbb{R}, \tag{9.11}$$

where we directly computed the derivative of $\mathbf{\Sigma}_s(\mathbf{q})$ in direction of $\mathbf{q}$, compare (9.6). Again, we can explicitly compute the control $\mathbf{q}\in\mathbb{R}$ from this equation

$$\mathbf{q} = \bar{\mathbf{q}} + \frac{2}{\alpha}(2\mathbf{F}\mathbf{E}_s,\nabla\mathbf{z})_{\mathcal{S}}. \tag{9.12}$$

9.2 Reduced Formulation of the Optimization Problem

One possibility to solve the optimization problem is to approximate the KKT system (9.8). This however is a very large coupled system of equations involving prima problem, adjoint and control. Even if an explicit formula for the computation

of the control $\mathbf{q}$ can be used, a coupled problem in $\{\mathbf{U}, \mathbf{Z}\} \in \mathcal{X} \times \mathcal{X}$ remains to be solved. In terms of fluid-structure interaction, this refers to a coupled system of 10 (in 2d) and 14 (in 3d) equations. Instead, we first introduce a *reduced formulation* of the optimization, see problem [47, 191, 238, 325, 326] and [133, 134, 286] in the context of fsi.

Problem 9.2 (Unconstrained Optimization Problem) *Find* $\mathbf{q} \in \mathbf{Q}_d$, *such that*

$$k(\mathbf{q}) := K(\mathbf{q}, S(\mathbf{q})) \to \min, \tag{9.13}$$

where the solution operator $S : \mathbf{Q}_d \to \mathcal{X}$ *is defined as*

$$A(\mathbf{q}, S(\mathbf{q}))(\Phi) = F(\Phi) \quad \forall \Phi \in \mathcal{X}.$$

The solution of this unconstrained optimization problem is characterized by the first order necessary condition

$$k'(\mathbf{q})(\chi) = 0 \quad \forall \chi \in \mathbf{Q}_d, \tag{9.14}$$

a local minimum is guaranteed by the second-order optimality condition

$$k''(\mathbf{q})(\chi, \chi) \geq 0 \quad \forall \chi \in \mathbf{Q}_d.$$

To approximate the solutions of (9.14), we employ a Newton's method. Starting with $\mathbf{q}^0 \in \mathbf{Q}_d$ (one possibility is $\mathbf{q}^0 = \bar{\mathbf{q}}$) we iterate

$$k''(\mathbf{q}^l)(\delta\mathbf{q}^l, \chi) = -k'(\mathbf{q}^l)(\chi) \quad \forall \chi \in \mathbf{Q}_d, \quad \mathbf{q}^{l+1} = \mathbf{q}^l + \omega^l \delta\mathbf{q}^l,$$

where $\omega^l \in \mathbb{R}$ is a possible relaxation parameter. Every step of this Newton loop requires the evaluation of the residual and the solution of the Hessian. As the solution $\mathbf{U} = S(\mathbf{q})$ is implicitly given, this involves some effort.

Lemma 9.3 (Residual of the Newton Iteration) *Let* $\mathbf{q}^l \in \mathbf{Q}$ *be given. Then, the residual is given by*

$$-k'(\mathbf{q}^l)(\chi) := -\alpha(\mathbf{q}^l - \bar{\mathbf{q}}, \chi) + A'_{\mathbf{q}}(\mathbf{q}^l, \mathbf{U}^l)(\chi, \mathbf{Z}^l),$$

where the solution $\mathbf{U}^l \in \mathcal{X}$ *and the adjoint solution* $\mathbf{Z}^l \in \mathcal{X}$ *are given by*

$$\begin{aligned} &(1) \qquad A(\mathbf{q}^l, \mathbf{U}^l)(\Phi) = F(\Phi) && \forall \Phi \in \mathcal{X}, \\ &(2) \qquad A'_U(\mathbf{q}^l, \mathbf{U}^l)(\Phi, \mathbf{Z}^l) = K'_{\mathbf{U}}(\mathbf{q}^l, \mathbf{U}^l)(\Phi) && \forall \Phi \in \mathcal{X}. \end{aligned}$$

Proof Let $\mathbf{U}^l = S(\mathbf{q}^l)$ be the solution to (1) and $\mathbf{Z}^l \in \mathcal{X}$ be the solution to (2). Then, formal derivation of $k(\mathbf{q})$ yields

$$k'(\mathbf{q}^l)(\chi) = K'_{\mathbf{q}}(\mathbf{q}^l, S(\mathbf{q}^l)) + K'_{\mathbf{U}}(\mathbf{q}^l, S(\mathbf{q}^l))(S'(\mathbf{q}^l)\chi).$$

Deriving the state equation to $\mathbf{q}$ gives a relation for $S'(\mathbf{q}^l)\chi$

$$A'_q(\mathbf{q}^l, S(\mathbf{q}^l))(\Phi) = -A'_{\mathbf{U}}(\mathbf{q}^l, S(\mathbf{q}^l))(S'(\mathbf{q}^l)\chi, \Phi) \quad \forall \Phi \in \mathcal{X}. \tag{9.15}$$

Then, by using (9.7), the adjoint equation and this relation (9.15)

$$\begin{aligned} k'(\mathbf{q}^l)(\chi) &= \alpha(\mathbf{q} - \bar{\mathbf{q}}, \chi)_{\mathbf{Q}} + A'_{\mathbf{U}}(\mathbf{q}^l, S(\mathbf{q}^l))(S'(\mathbf{q}^l)\chi, \mathbf{Z}^l) \\ &= \alpha(\mathbf{q} - \bar{\mathbf{q}}, \chi)_{\mathbf{Q}} - A'_q(\mathbf{q}^l, S(\mathbf{q}^l))(\mathbf{Z}^l). \end{aligned}$$

□

For estimation of the residual, we must first solve the *state equation*, followed by a solution of the *adjoint equation*. These equations can be solved independently. Once the residual is given, the Hessian equation must be solved.

Lemma 9.4 (Hessian of the Newton Iteration) *Let $\mathbf{q}^l \in \mathbf{Q}$ be given, $\mathbf{U}^l$ and $\mathbf{Z}^l$ be the adjoint solutions defined in Lemma 9.3. Let $\{\chi_1, \ldots, \chi_{\#q}\}$ be a basis of $\mathbf{Q}$. Then, solve the $\#q$* tangent equations *and* adjoint for Hessian equations *for $\mathbf{U}^l_1, \ldots, \mathbf{U}^l_{\#q}$ and $\mathbf{Z}^l_1, \ldots, \mathbf{Z}^l_{\#q}$*

$$\begin{aligned} &i = 1, \ldots, \#q: \\ &A'_{\mathbf{U}}(\mathbf{q}^l, \mathbf{U}^l)(\mathbf{U}^l_i, \Phi) = -A'_{\mathbf{q}}(\mathbf{q}^l, \mathbf{U}^l)(\chi_i, \Phi) \qquad \forall \Phi \in \mathcal{X} \\ &A'_{\mathbf{U}}(\mathbf{q}^l, \mathbf{U}^l)(\Phi, \mathbf{Z}^l_i) = K''_{\mathbf{UU}}(\mathbf{q}^l, \mathbf{U}^l)(\mathbf{U}^l_i, \Phi) \\ &\qquad\qquad - A''_{\mathbf{qU}}(\mathbf{q}^l, \mathbf{U}^l)(\chi_i, \Phi, \mathbf{Z}^l) \\ &\qquad\qquad - A''_{\mathbf{UU}}(\mathbf{q}^l, \mathbf{U}^l)(\mathbf{U}^l_i, \Phi, \mathbf{Z}^l) \quad \forall \Phi \in \mathcal{X}. \end{aligned} \tag{9.16}$$

Then, the Hessian (in the Basis $\{\chi_i\}$) is given as

$$\begin{aligned} \mathbf{k}_{ij}(\mathbf{q}^l) := \alpha(\chi_i, \chi_j)_{\mathbf{Q}} &- A''_{\mathbf{qq}}(\mathbf{q}^l, \mathbf{U}^l)(\chi_i, \chi_j, \mathbf{Z}^l) \\ &- A''_{\mathbf{qU}}(\mathbf{q}^l, \mathbf{U}^l)(\chi_i, \mathbf{U}^l_j, \mathbf{Z}^l) - A'_{\mathbf{q}}(\mathbf{q}^l, \mathbf{U}^l)(\chi_i, \mathbf{Z}^l_j). \end{aligned}$$

Proof Derivation of the residual gives

$$\begin{aligned} k''(\mathbf{q}^l)(\chi, \tau) = \alpha(\chi, \tau)_{\mathbf{Q}} &- A''_{\mathbf{qq}}(\mathbf{q}^l, \mathbf{U}^l)(\chi, \tau, \mathbf{Z}^l) \\ &- A''_{\mathbf{qU}}(\mathbf{q}^l, \mathbf{U}^l)(\chi, S'(\mathbf{q}^l)\tau, \mathbf{Z}^l) - A'_{\mathbf{q}}(\mathbf{q}^l, \mathbf{U}^l)(\chi, Z'(\mathbf{q})\tau). \end{aligned} \tag{9.17}$$

The first two terms can be evaluated with the knowledge of $\mathbf{q}^l, \mathbf{U}^l$ and $\mathbf{Z}^l$. By derivation of the state equation we obtain the *tangent equation* which we solve for $\mathbf{U}^l_\tau := S'(\mathbf{q}^l)\tau$

$$A'_{\mathbf{U}}(\mathbf{q}^l, \mathbf{U}^l)(\mathbf{U}^l_\tau, \Phi) = -A'_{\mathbf{q}}(\mathbf{q}^l, \mathbf{U}^l)(\tau, \Phi) \quad \forall \Phi \in \mathcal{X}.$$

This allows to evaluate the third term $A''_{\mathbf{qu}}$ in (9.17). For evaluation of the last term we solve for $\mathbf{Z}^l_\tau = Z'(\mathbf{q}^l)\tau$ given by the derivative of the adjoint equation

$$\begin{aligned} A'_U(\mathbf{q}^l, \mathbf{U}^l)(\Phi, \mathbf{Z}^l_\tau) = K''_{\mathbf{UU}}(\mathbf{q}^l, \mathbf{U}^l)(\mathbf{U}^l_\tau, \Phi) \\ - A''_{\mathbf{qU}}(\mathbf{q}^l, \mathbf{U}^l)(\tau, \Phi, \mathbf{Z}^l) - A''_{\mathbf{UU}}(\mathbf{q}^l, \mathbf{U}^l)(\mathbf{U}^l_\tau, \Phi, \mathbf{Z}^l). \end{aligned}$$

□

Compared to the residual evaluation, the assembly of the Hessian calls for the additional effort of solving #*q tangent equations* and #*q adjoint for Hessian equations*. Each of these problems is linear and has the same dimension as the adjoint problem. The overall effort appears to be rather large, by using the reduced solution approach, one however circumvents the introduction of large systems, where state and adjoint solution are coupled. For the discussed examples with a one-dimensional control space $\mathbf{Q}_d$, one Newton iteration requires the solution of the nonlinear state equation, the solution of one linear adjoint, one *tangent* and one *adjoint for Hessian equation*.

9.3 Realization with Fluid-structure Interactions

The described Newton iteration for the optimization problem requires the evaluation of several further derivatives of the variational formulation. We have already derived the Jacobian in Sect. 5.2.2, which is the system matrix of the tangent equation (9.16). Its inverse is the system matrix of the adjoint equation and further the system matrix of the *adjoint for Hessian equation*, also shown in (9.16). All the remaining derivatives are required for different right hand sides of the problems. Their evaluation is partially simple, e.g. $A'_{\mathbf{q}}$, $K''_{\mathbf{UU}}$ or $A''_{\mathbf{qU}}$. Only the second derivative of $A(\cdot)(\cdot)$ with respect to the solution $\mathbf{U}$ will give rise to excessive terms due to the ALE mapping. Here, given $\mathbf{U}^l_i$ we propose the approximation by finite differences

$$A''_{\mathbf{UU}}(\mathbf{q}^l, \mathbf{U}^l)(\mathbf{U}^l_i, \Phi, \mathbf{Z}^l) \approx \frac{A'_{\mathbf{U}}(\mathbf{q}^l, \mathbf{U}^l + \varepsilon \mathbf{U}^l_i)(\Phi, \mathbf{Z}^l) - A'_{\mathbf{U}}(\mathbf{q}^l, \mathbf{U}^l)(\Phi, \mathbf{Z}^l)}{\varepsilon},$$

where $\varepsilon > 0$ is a parameter that has to be carefully chosen, compare the discussion in Sect. 5.2.3 and Fig. 5.8.

9.4 Parameter Identification Test

Based on the benchmark problem fsi-1 by Hron and Turek [199], see also Sect. 6.6, we formulate a parameter identification test case. According to [329, 330], the geometry has been changed by slightly widening the beam to $h = 0.04$ instead of $h = 0.02$ in the original problem, compare Fig. 9.1.

We initially "forget" the Lamé coefficient μ_s and try to reconstruct it based on a measurement of the deformation of the beam in the point $A = (0.6, 0.2)$. We introduce the regularized cost functional

$$K(\mathbf{q}, \mathbf{U}) = |\mathbf{u}_y(A) - \mathbf{u}_y^{\text{ref}}|^2 + \frac{\alpha}{2}|\mathbf{q} - \bar{\mu}|^2,$$

where $\bar{\mu} \in \mathbb{R}$ is an initial guess and $\alpha = 10^{-3}$ the Tikhonov parameter. The control $\mathbf{q} \in \mathbb{R}$ enters in form of a material parameter, such that the control form is given by (9.5).

The flow is driven by a parabolic inflow profile on Γ_{in} with maximum velocity $\bar{\mathbf{v}}^{\text{in}} = 1.5$ m/s and the remaining parameters used in this test case are given by

$$\rho_f = \rho_s = 10^3 \frac{kg}{m^3}, \quad \nu_f = 10^{-3} \frac{m^2}{s}, \quad \nu_s = 0.4.$$

On the outflow boundary Γ_f^{out} we prescribe the *do-nothing* outflow condition, see Sect. 2.4.2. All computations in this sections have been carried out by Thomas Wick [286, 347] using the software library deal.II [24].

In Table 9.1 we determine the deformation $\mathbf{u}_y(A)$ in the tip of the beam considering the Lamé coefficient $\mu^{\text{ref}} = 500{,}000$ on a sequence of two meshes in forward simulations. These values act as reference values $\mathbf{u}_y^{\text{ref}}$ for each optimization test case.

We start the actual optimization loop with the initial control $\mathbf{q}^0 = 5000$ far away from the optimal state $\mathbf{q}^{\text{opt}} = \mu^{\text{opt}} = 500{,}000$. In Table 9.2 we indicate the results of the optimization algorithm on two meshes, using the corresponding reference deformation $\mathbf{u}_y^{\text{ref}}(A)$ on each level. Here, it shows, that the presented

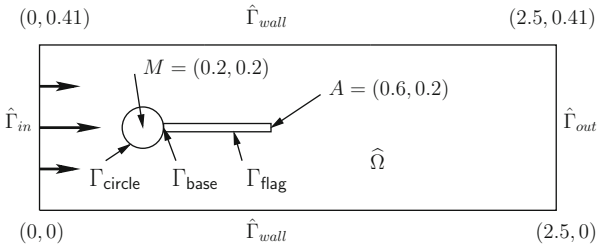

Fig. 9.1 Configuration of the parameter identification test case with the modified fsi-1 benchmark configuration. The thickness of the beam is increased to 0.04 (from 0.02 in the standard fsi benchmark problem)

Table 9.1 Forward computation for obtaining reference values $\mathbf{u}^{\text{ref}}(A)$ using the exact Lamé coefficient $\mu^{\text{opt}} = 500{,}000$ on two subsequent meshes

DoF	μ^{ref}	$\mathbf{u}_y^{\text{ref}}$
19,488	500,000	$8.2747 \cdot 10^{-4}$
76,672	500,000	$8.2289 \cdot 10^{-4}$

Table 9.2 *Modified fsi-1* parameter estimation problem

Step	μ	$\mathbf{u}_y(A)$	$\lvert\mathbf{u}_y(A) - \mathbf{u}_y^{\text{ref}}\rvert$	Residual
(a) Results on a mesh with 19,488 unknowns, $\mathbf{u}_y^{\text{ref}} = 0.00082747$				
1	5000	$2.0118 \cdot 10^{-3}$	$1.18 \cdot 10^{-3}$	$1.00 \cdot 10^{-0}$
2	188,133	$1.1992 \cdot 10^{-3}$	$3.72 \cdot 10^{-4}$	$5.90 \cdot 10^{-1}$
3	498,310	$8.2884 \cdot 10^{-4}$	$1.37 \cdot 10^{-6}$	$2.76 \cdot 10^{-3}$
4	499,767	$8.2770 \cdot 10^{-4}$	$2.30 \cdot 10^{-7}$	$4.01 \cdot 10^{-6}$
5	499,769	$8.2768 \cdot 10^{-4}$	$2.10 \cdot 10^{-7}$	$6.58 \cdot 10^{-9}$
(b) Results on a mesh with 76,672 unknowns, $\mathbf{u}_y^{\text{ref}} = 0.00082289$				
1	5000	$2.000 \cdot 10^{-3}$	$1.18 \cdot 10^{-3}$	$1.00 \cdot 10^{-0}$
2	118,309	$1.347 \cdot 10^{-3}$	$5.24 \cdot 10^{-4}$	$7.23 \cdot 10^{-1}$
3	493,626	$8.279 \cdot 10^{-4}$	$5.01 \cdot 10^{-6}$	$1.16 \cdot 10^{-2}$
4	499,756	$8.232 \cdot 10^{-4}$	$3.10 \cdot 10^{-7}$	$2.27 \cdot 10^{-5}$
5	499,768	$8.231 \cdot 10^{-4}$	$2.10 \cdot 10^{-7}$	$2.70 \cdot 10^{-8}$

Results of the optimization loop for two different meshes, using the reference values as collected in Table 9.1. Showing iteration, control $\mathbf{q}^l = \mu^l$, deformation $\mathbf{u}_y(A)$, absolute error in deformation and Newton residual

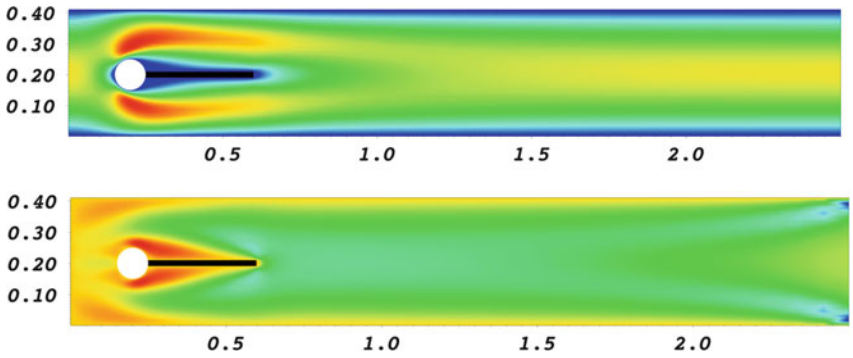

Fig. 9.2 *Modified fsi-1* parameter estimation: x-velocity profile $\mathbf{v}_x$ (*top*) and corresponding adjoint solution $\mathbf{z}_x$ (*bottom*)

Newton optimization scheme with the exactly derived adjoint problems for the monolithic variational formulation yields a very efficient (quadratic) convergence to the optimal state.

In Fig. 9.2, we show plots of *x*-velocity and the corresponding adjoint solution component for the solution of this optimization problem.

9.5 Optimal Control Test

As second problem we consider an optimal control test. Figure 9.3 shows the configuration. By controlling the inflow pressure on Γ_f^{in} by $p_f^{\text{in}} \in \mathbb{R} = \mathbf{q}_f \in \mathbb{R}$ we aim at maximizing the outflow at Γ_f^{out}. An elastic obstacle $\mathcal{S}$ is embedded in the flow domain. At increased velocities, this obstacle will be sucked to the top of the domain and closes the channel, such that the flow rate will decrease again.

The problem is constructed such that the optimal solution can be easily verified by forward simulations to offer an easy test case for the optimization routines and in particular for the derivation of the adjoint formulations. Control is realized by the pressure control form (9.4), the target function is given by

$$K_{\text{out}}(\mathbf{q}, \mathbf{U}) = -\int_{\Gamma_f^{\text{out}}} (\mathbf{n} \cdot \mathbf{v})^2 \, \mathrm{d}s + \frac{\alpha}{2} |\mathbf{q} - \bar{\mathbf{q}}|^2, \tag{9.18}$$

where $\alpha > 0$ is the regularization parameter. We changed the sign to obtain a minimization problem. The material parameters are chosen as

$$\rho_f = \rho_s = 10^3 \,\mathrm{kg} \cdot \mathrm{m}^{-3}, \quad \nu_f = 10^{-3} \,\mathrm{m}^2 \cdot \mathrm{s}^{-1}, \quad \nu_s = 0.4, \quad \mu_s = 500 \,\mathrm{kg} \cdot \mathrm{m}^{-1} \mathrm{s}^{-1}.$$

Velocity and deformation as set to zero on all outer boundaries Γ_{wall}.

Figure 9.4 shows results of forward simulation for different values of the control $\mathbf{q}$, i.e. the average inflow pressure on Γ_f^{in}. Considering higher pressures, the beam will narrow the channel and reduce the outflow rate; we refer the reader to Fig. 9.5 for snapshots of the solution for different inflow pressures $\mathbf{q} = p_{\text{in}}$. From the forward simulation we estimate $\mathbf{q}^{\text{opt}} \in [0.23, 0.24]$.

This test case is very challenging as control and target functional are both living within the fluid. Without the interaction to the solid, no effect would take place. This example asks for a careful analysis of the adjoint information transport from the fluid to the solid and back to the fluid. In [286] we study this problem with an

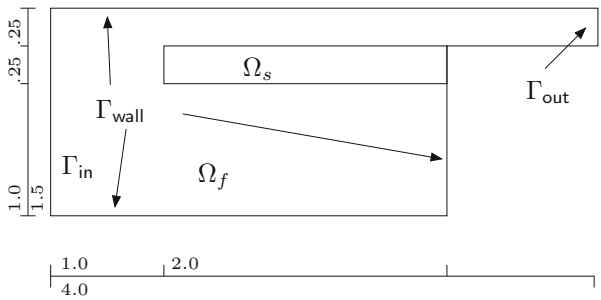

Fig. 9.3 Configuration of the optimal control test case. We control the inflow pressure on Γ_{in} with the goal to maximize the outflow rate on Γ_{out}

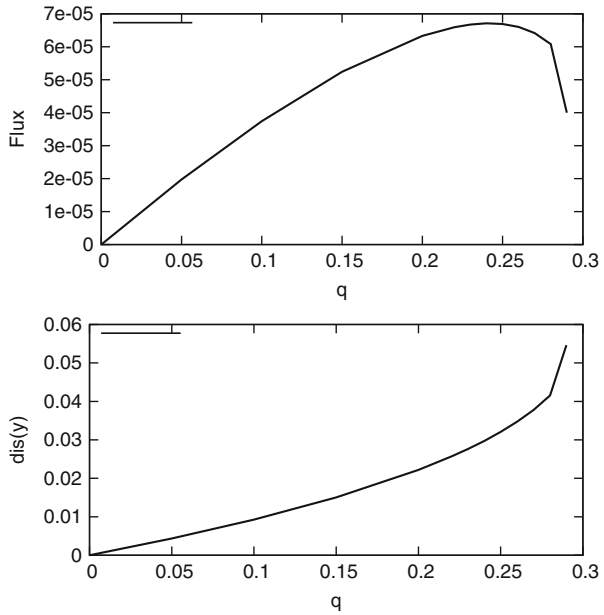

Fig. 9.4 Forward simulations for varying inflow pressures $\mathbf{q}$. In the *upper plot* we show the outflow rate $K_{\text{out}}(\mathbf{q}, \mathbf{U}(\mathbf{q}))$. In the *lower plot* we indicate the deformation of the tip of the beam $\mathbf{u}_y(A)$. The outflow rate decreases for $\mathbf{q} > 0.25$. We expect to find the optimal control close to this point

approximated adjoint that neglects the coupling conditions. It is shown that such an approximation does not carry sufficient information for efficiently solving the optimization problem.

To approximate this problem, we use an updated Tikhonov parameterization, where both the parameter α and the parameter $\bar{\mathbf{q}}$ in

$$K(\mathbf{q}, \mathbf{U}) = K_{\text{out}}(\mathbf{U}) + \frac{\alpha}{2}|\mathbf{q} - \bar{\mathbf{q}}|^2,$$

are updated. We start with $\bar{\mathbf{q}}^0 = \mathbf{q}^0 = 0.1$ and take the last available optimum in each step. Furthermore, the parameter α is reduced step by step. In Table 9.3, we show the convergence of this iterated Tikhonov scheme, together with the chosen values for α^i and the obtained controls p^i_{opt}. As expected by the forward computation, the maximal flux is reached for $p_{opt} \sim 0.23$–0.24. Indeed, it can be observed that the channel is narrowed in the maximized solution as illustrated in Fig. 9.5. Here, in the unloaded reference configuration, the gap has a width of 0.125. Using the initial control $\bar{p}^0_{\text{in}} = 0.1$, the gap is narrowed to 0.115 and in the optimum state, for $p_{\text{opt}} \approx 0.24$, the size of the gap is reduced to 0.095. This is an overall

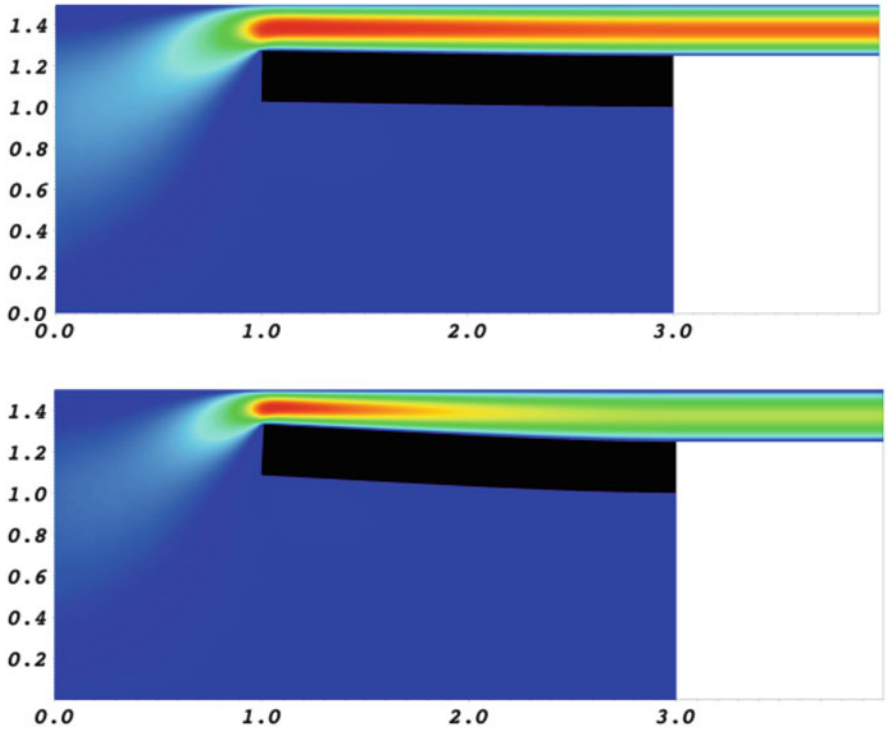

Fig. 9.5 Maximization of the outflow rate. At the *top* we show the velocity for the initial control $\mathbf{q}^0 = 0.1$ and in the *bottom* we show the solution close to the optimal control $\mathbf{q}^{\text{opt}} \approx 0.23$

Table 9.3 Maximizing the outflow rate $K_{\text{out}}(\mathbf{U})$ by controlling the inflow pressure $q = p_{\text{in}}$ on three globally refined meshes using an iterated Tikhonov regularization with Tikhonov parameter α and reference control $\bar{p}_{\text{in}}$

DoF	$\bar{p}_{\text{in}}$	α	$u_y(A)$	$K_{\text{out}}(U)$	p_{opt}
12,612	0.1000	$1.0 \cdot 10^{-5}$	$0.97 \cdot 10^{-2}$	$3.87 \cdot 10^{-5}$	0.1038
	0.1038	$7.5 \cdot 10^{-6}$	$1.02 \cdot 10^{-5}$	$4.04 \cdot 10^{-5}$	0.1090
	0.1090	$5.0 \cdot 10^{-6}$	$1.11 \cdot 10^{-5}$	$4.29 \cdot 10^{-5}$	0.1170
	0.1170	$2.5 \cdot 10^{-6}$	$1.30 \cdot 10^{-5}$	$4.78 \cdot 10^{-5}$	0.1335
	0.1335	$1.0 \cdot 10^{-6}$	$1.85 \cdot 10^{-5}$	$5.87 \cdot 10^{-5}$	0.1759
	0.1759	$7.5 \cdot 10^{-7}$	$2.43 \cdot 10^{-5}$	$6.53 \cdot 10^{-5}$	0.2254
	0.2254	$5.0 \cdot 10^{-7}$	$2.72 \cdot 10^{-5}$	$6.67 \cdot 10^{-5}$	0.2280
49,540	0.1759	$1.0 \cdot 10^{-6}$	$2.46 \cdot 10^{-5}$	$6.52 \cdot 10^{-5}$	0.2135
	0.2135	$7.5 \cdot 10^{-7}$	$2.84 \cdot 10^{-5}$	$6.70 \cdot 10^{-5}$	0.2330
196,356	0.1759	$1.0 \cdot 10^{-6}$	$2.42 \cdot 10^{-5}$	$6.50 \cdot 10^{-5}$	0.2111
	0.2111	$7.5 \cdot 10^{-7}$	$2.92 \cdot 10^{-5}$	$6.71 \cdot 10^{-5}$	0.2367

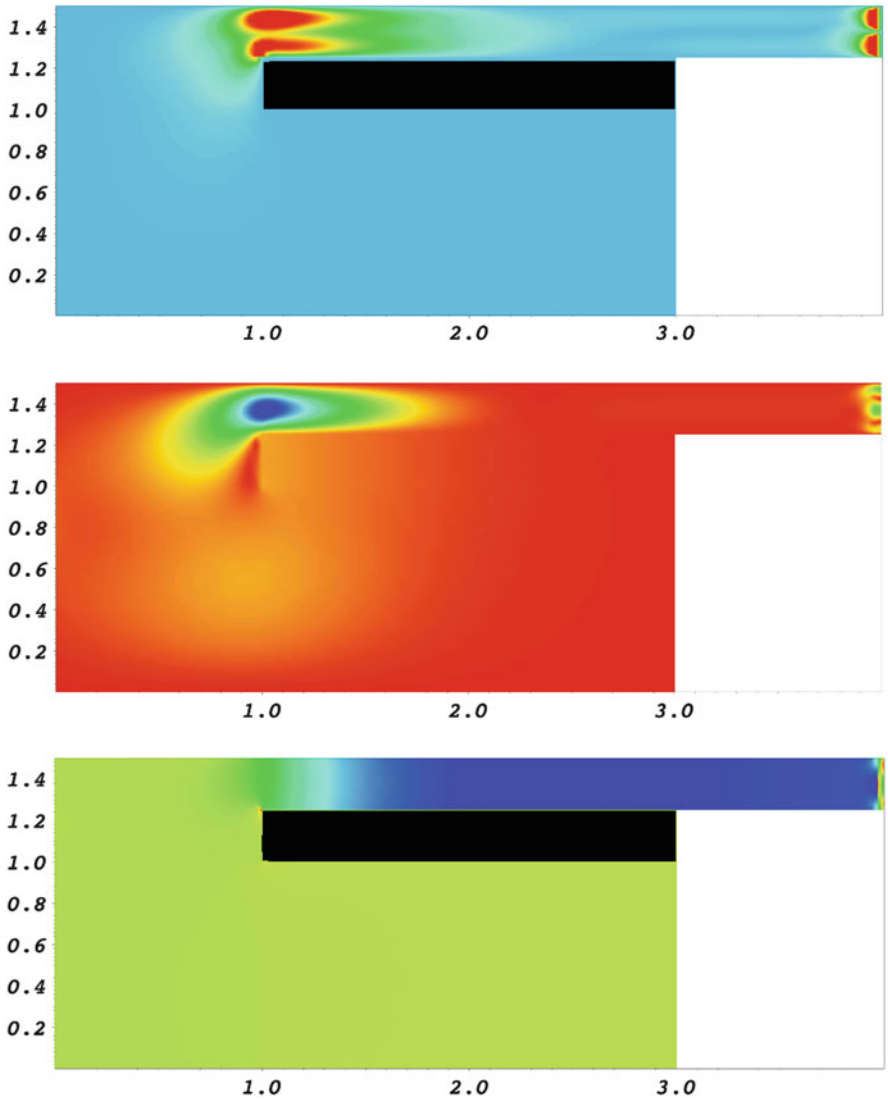

Fig. 9.6 Maximization of the outflow rate. Adjoint solution with respect to the velocity (*top*), displacement (*middle*) and pressure (*bottom*). All solutions are displaced in the undeformed reference configuration in ALE coordinates

reduction of about 25%. Finally, Fig. 9.6 illustrates the three components $\mathbf{z}_v, z_p, \mathbf{z}_n$ of the adjoint solution.

We finally note that we expect different results, if this problem would be treated with a fully non-stationary approach. At very high pressures one has to expect instabilities that will cause a flattering of the elastic obstacle and that might finally prevent the full closure of the channel.

Chapter 10
Mechano-Chemical Fluid-structure Interactions and Active Materials

Many aspects in solid dynamics cannot be explained by an elastic response of the material. In some applications, the material undergoes active changes, e.g. by growth, swelling or generation of material, by chemically induced contractions or bending. In other situations, the reference state is not stress-free. If a log of wood is cut in two pieces, these will afterwards deform and spread.

One model for the realization of active material modification is the introduction of an intermediate material configuration, the *grown configuration*, that is assumed to include the active growth or change of material, a configuration that is stress-free but non-physical, see Rodriguez et al. [291] and Jones and Chapman [209] for further examples. We call this configuration $\hat{\mathcal{S}}_a$, the active one and introduce a mapping that describes only this growth process

$$\hat{T}_a(t) : \hat{\mathcal{S}} \to \hat{\mathcal{S}}_a(t)$$

and that maps the Lagrangian reference state to the grown one. In Fig. 10.1 we show two possible models for active material growth, isotropic growth of control volumes and a volume-conserving constriction of control volumes. The grown state is understood to be stress-free but non-physical, as control volumes might overlap.

In a second step, the solid elastically reacts to this intermediate configuration. We denote by

$$\hat{T}_e(t) : \hat{\mathcal{S}}_a(t) \to \mathcal{S}(t)$$

the mapping of this elastic response. The overall material deformation is given by

$$\hat{T}(t) : \hat{\mathcal{S}} \to \mathcal{S}(t), \quad \hat{T}(t) = \hat{T}_e(t) \circ \hat{T}_a(t). \tag{10.1}$$

T. Richter, *Fluid-structure Interactions*, Lecture Notes in Computational Science and Engineering 118, DOI 10.1007/978-3-319-63970-3_10

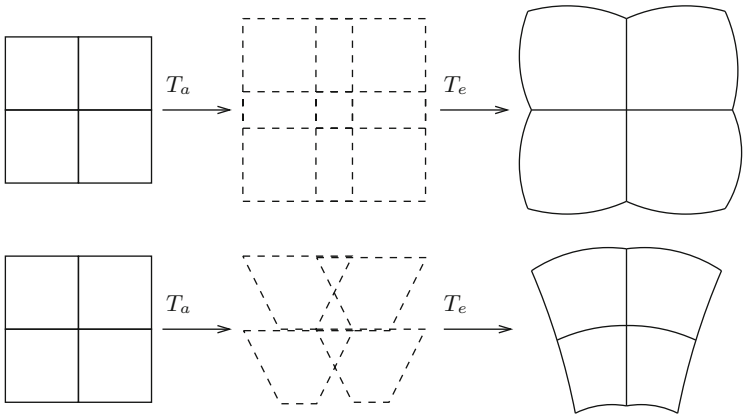

Fig. 10.1 Two different kinds of active material deformation. *Top row*: isotropic growth. *Bottom*: Constriction of volume elements. The intermediate configuration is grown and stress-free but not physical

The complete deformation $\hat{\mathcal{S}} \to \hat{\mathcal{S}}(t)$ is still described by $\hat{\mathbf{u}}$ including growth and elasticity, such that

$$\hat{T}(\hat{x}, t) = \hat{x} + \hat{\mathbf{u}}(\hat{x}, t).$$

As usual, we introduce the deformation gradient and its determinant

$$\hat{\mathbf{F}} := \hat{\nabla}\hat{T}, \quad \hat{J} := \det \hat{\mathbf{F}}. \tag{10.2}$$

The splitting into growth and elastic response is done on the level of the deformation gradient, see Fig. 10.2. We introduce

$$\hat{\mathbf{F}}_a := \hat{\nabla}\hat{T}_a, \quad \hat{J}_a := \det \hat{\mathbf{F}}_a, \tag{10.3}$$

and

$$\hat{\mathbf{F}}_e := \hat{\nabla}\hat{T}_e, \quad \hat{J}_e := \det \hat{\mathbf{F}}_e, \tag{10.4}$$

By means of (10.1) it holds

$$\hat{\mathbf{F}} = \hat{\mathbf{F}}_e\hat{\mathbf{F}}_a, \quad \hat{J} = \hat{J}_e\hat{J}_a.$$

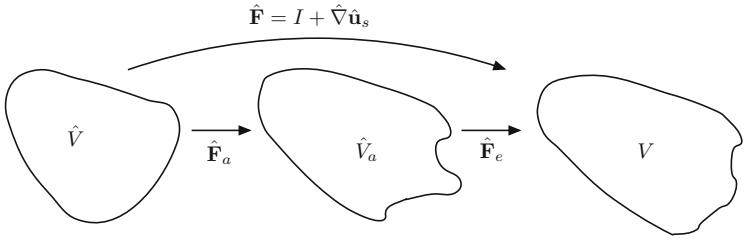

Fig. 10.2 Multiplicative decomposition of the deformation gradient into active part $\mathbf{F}_a$ and elastic response $\mathbf{F}_e$

If we assume that $\hat{T}_a$ is given by an external mechanism we can compute the elastic deformation gradient based on the deformation $\mathbf{u}$ and this growing part

$$\hat{\mathbf{F}}_e = \hat{\mathbf{F}}\hat{\mathbf{F}}_a^{-1} = (I + \hat{\nabla}\hat{\mathbf{u}})\hat{\mathbf{F}}_a^{-1}.$$

Now, stresses will depend solely on this elastic part. In terms of Definition 2.18, the first Piola Kirchhoff stress tensor of the St. Venant Kirchhoff material is given by

$$\hat{\mathbf{P}}_e = \hat{\mathbf{F}}_e\hat{\mathbf{\Sigma}}_e = 2\mu_s\hat{\mathbf{F}}_e\hat{\mathbf{E}}_e + \lambda_s \operatorname{tr}(\hat{\mathbf{E}}_e)\hat{\mathbf{F}}_e, \quad \hat{\mathbf{E}}_e := \frac{1}{2}(\hat{\mathbf{F}}_e^T\hat{\mathbf{F}}_e^T - I). \tag{10.5}$$

The tensor $\hat{\mathbf{P}}_e$ is formulated on the intermediate configuration $\hat{\mathcal{S}}_a(t)$. The equations of conservation are however given on the non-strained, non-grown reference configuration $\hat{\mathcal{S}}$. Therefore, in a last step we must pull back this tensor to $\hat{\mathcal{S}}$. We refer to [73]

$$\hat{\mathbf{\Sigma}} = \hat{J}_a\hat{\mathbf{F}}_a^{-1}\hat{\mathbf{\Sigma}}_e\hat{\mathbf{F}}_a^{-T}. \tag{10.6}$$

10.1 Growth Models

Growth can come in various forms. It is possible that new material is added. Then, material can simply swell while conserving its mass. *Growth* can also be the change of configuration without change of volume or mass, e.g. shearing or rotation.

We first consider the case, where the same type of material is locally added in an isotropic fashion. Let $\hat{V}$ be a control volume and $\hat{x}_0 \in \hat{V}$ be a reference point. We assume that this control volume isotropically growing

$$\hat{V} \to V_a(t), \quad V_a(t) := \{\hat{x}_0 + \alpha t(\hat{x} - \hat{x}_0),\ \hat{x} \in \hat{V}\},$$

where by $\alpha \in \mathbb{R}$ we denote the *growth rate*, see Fig. 10.1. By

$$\hat{T}_a(\hat{x}, t) = \hat{x} + \alpha t(\hat{x} - \hat{x}_0), \quad \hat{\mathbf{F}}_a = \hat{\nabla}\hat{T}_a = (1 + \alpha t)I, \quad \hat{J}_a = (1 + \alpha t)^d \tag{10.7}$$

we can express the active mapping and deformation gradient, where $d > 0$ is the spatial dimension. We assume that the new material has the same density $\hat{\rho}^0$, such that mass is added (or decreased for $\alpha < 0$)

$$m(V_a(t)) = \int_{V_a(t)} \rho^0 \, \mathrm{d}x = \int_{\hat{V}} \hat{J}_a \rho^0 \, \mathrm{d}\hat{x} =: \int_{\hat{V}} \hat{\rho}_a \, \mathrm{d}\hat{x}.$$

By

$$\hat{\rho}_a := \hat{J}_a \hat{\rho}^0 = (1 + \alpha t)^d \hat{\rho}^0, \tag{10.8}$$

we denote the grown density in the reference configuration.

Second, we consider the swelling of material, an isotropic growth without addition or removal of mass. The growth map is given as in (10.1), the mass however is conserved from $\hat{V}$ to $V_a(t)$

$$m(\hat{V}) = \int_{\hat{V}} \hat{\rho}^0 \, \mathrm{d}\hat{x} \overset{!}{=} \int_{V_a(t)} \rho_a \, \mathrm{d}x = \int_{\hat{V}} \hat{J}_a \hat{\rho}_a \, \mathrm{d}\hat{x} = \int_{\hat{V}} (1 + \alpha t)^d \hat{\rho}_a \, \mathrm{d}\hat{x},$$

such that

$$\hat{\rho}_a = (1 + \alpha t)^{-d} \hat{\rho}^0.$$

Third, we consider the case of a constriction, where both mass and volume of the control volumes stays the same, see the bottom row of Fig. 10.1. Let $\hat{V}$ be a reference volume and $\hat{x}^0 \in V$ be its center of mass. In two spatial dimensions, the active map is given by

$$\hat{T}_a(\hat{x}, t) = \begin{pmatrix} \hat{x}_1^0 + (\hat{x}_1 - \hat{x}_0^1)(1 + \alpha t(\hat{x}_2 - \hat{x}_2^0)) \\ \hat{x}_2 \end{pmatrix},$$

with deformation gradient and determinant

$$\hat{\mathbf{F}}_a(\hat{x}, t) = \begin{pmatrix} 1 + \alpha t(\hat{x}_2 - \hat{x}_2^0) & (\hat{x}_1 - \hat{x}_1^0)\alpha t \\ 0 & 1 \end{pmatrix}, \quad \hat{J}_a = 1 + \alpha t(\hat{x}_2 - \hat{x}_2^0).$$

10.2 Model Case: Formation and Growth of Atherosclerotic Plaques

We consider the coupled dynamics of an incompressible fluid with an elastic structure that undergoes active growth and deformation by bio/chemical processes. The mechanical fluid-structure interaction problem is coupled to the dynamics of chemical species that are transported that react and diffuse and that finally will cause solid growth. This model is a generalization of a detailed model for the dynamics of the formation and growth of plaques in blood vessels that has been discussed in [354–356].

We introduce a simplified model that describes the formation and growth of plaques in large blood vessels. For simplicity, we denote by $\Omega(t) \subset \mathbb{R}^2$ a two-dimensional domain, split into the vessel wall $\mathcal{S}(t) \subset \mathbb{R}^2$ and the fluid domain $\mathcal{F}(t) \subset \mathbb{R}^2$, which is occupied by blood. The interface between fluid and solid is denoted by $\mathcal{I}(t)$, see Fig. 10.3. We model blood as an incompressible Newtonian and homogenous fluid. The vessel wall is described by the St. Venant Kirchhoff material as stated above.

Our model for the fluid-solid interaction problem between blood and the vessel is overly simplified. The mechanical properties of vessels are complex with multi-layered anisotropic structures. We refer to the literature for advanced models and also for numerical approaches to deal with them [87, 147, 149, 195].

In short, the biological mechanism is evolving as follows (compare Fig. 10.3): First, monocytes (concentration called c_f) are transported by an advection-diffusion process within the blood flow. Second, they penetrate damaged parts of the vessel wall (in damaged areas) where they are transformed to macrophages (called c_s). The migration rate depends on the difference of monocyte and macrophage concentration $(c_f - c_s)$ on the interface, on the wall stress and the damage condition of the wall. Thirdly, within the vessel wall, the macrophages are again transported by an advection-diffusion process and transformed into foam cells (called c_s^*). Finally, accumulation of foam cells leads to plaque growth.

This problem is coupled to the dynamics of the fluid-structure interaction problem. Due to hemodynamical forces driven by the pulsating flow, the geometry deforms substantially. Furthermore, the formation of plaques significantly changes

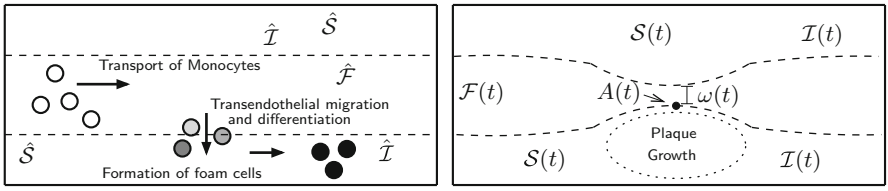

Fig. 10.3 Configuration of the domain and mechanism of plaque formation. *Left*: Domain in reference configuration split into fluid part $\hat{\mathcal{F}}$ and solid $\hat{\mathcal{S}}$ divided by the interface $\hat{\mathcal{I}}$. *Right*: Domain in the current (Eulerian) description with plaque formation and narrowing of vessel

the domains. Finally, the hemodynamical forces influence the penetration of monocytes into the vessel wall and therefore a two-way coupled problem must be considered. The complete set of equations is given by

$$\left.\begin{aligned} \rho_f(\partial_t \mathbf{v}_f + \mathbf{v}_f \cdot \nabla \mathbf{v}_f) - \operatorname{div} \boldsymbol{\sigma}_f &= 0 \\ \operatorname{div} \mathbf{v}_f &= 0 \\ \partial_t c_f + \mathbf{v}_f \cdot \nabla c_f - D_f \Delta c_f &= 0 \end{aligned}\right\} \text{ in } \mathcal{F}(t)$$

$$\left.\begin{aligned} \rho_s(\partial_t \mathbf{v}_s + \mathbf{v}_s \cdot \nabla \mathbf{v}_s) - \operatorname{div} \boldsymbol{\sigma}_s &= 0 \\ \partial_t c_s + \mathbf{v}_s \cdot \nabla c_s - D_s \Delta c_s &= -\beta c_s \\ \partial_t c_s^* + \mathbf{v}_s \cdot \nabla c_s^* &= \beta c_s \end{aligned}\right\} \text{ in } \mathcal{S}(t) \tag{10.9}$$

$$\left.\begin{aligned} \boldsymbol{\sigma}_f \mathbf{n}_f + \boldsymbol{\sigma}_s \mathbf{n}_s &= 0 \\ \mathbf{v}_f &= \mathbf{v}_s \\ D_f \nabla c_f \mathbf{n}_f + D_s \nabla c_s \mathbf{n}_s &= 0 \\ D_s \nabla c_s \mathbf{n}_s &= \zeta(c_f - c_s) \end{aligned}\right\} \text{ on } \mathcal{I}(t)$$

Here, $\mathbf{v}_f$ and $\mathbf{v}_s$ stand for the fluid and solid velocity. By ρ_f and ρ_s we denote the densities of blood and vessel wall and by $\mathbf{n}_f$ and $\mathbf{n}_s$ the outer normals of the fluid and solid domain, respectively. D_f and D_s are diffusion coefficients for monocytes and macrophages. In particular D_s depends on the concentration of foam cells c_s^* [355]. The coefficient ζ describes the migration of monocytes through the vessel wall. This parameter will depend on the hemodynamical stress $\zeta = \zeta(\boldsymbol{\sigma}_f \mathbf{n})$. The parameter β, usually depending on the concentration of foam cells, controls the transformation of macrophages to foam cells.

One of the major challenges in plaque modeling is the huge variety of temporal scales: While the heart beats once in about every 1 s, plaque growth takes place in a time span of months, i.e. $T \gg 1{,}000{,}000$ s. Although all scales have a significant influence on the coupled dynamics, a numerical simulation will not be able to resolve each detail while following the long-term process. Instead, we—as most approaches—consider an averaged flow problem and focus on the long-scale dynamics. Effective model parameters controlling the migration of monocytes through the vessel walls will be obtained by local (in time) small-scale simulations. The analysis of temporal multiscale problems with partial differential equations is still an open problem. Also we do not know efficient numerical multiscale methods for the approximation of such problems. We refer to the forthcoming dissertation of Sonner [315] for first steps in this direction.

Rather than developing a quantitative model, we concentrate in this paper on a robust numerical framework for the coupled long-term dynamics of fluid-structure interaction with active growth processes and large deformation. Hence, the approximation of the chemical dynamics plays a minor role. We therefore strongly simplify Model (10.9) and replace the complete chemical dynamics by a simple ode

modeling the total concentration of foam cells

$$\partial_t c_s^*(t) = \gamma(\boldsymbol{\sigma}_{WS}, t), \quad c_s^*(0) = 0, \tag{10.10}$$

where the function γ specifies the rate of foam cell accumulation. Here, this function depends on the wall stress in main stream direction $\boldsymbol{\sigma}_{WS}$

$$\gamma(\boldsymbol{\sigma}_{WS}, t) = \gamma_0 \left(1 + \frac{\boldsymbol{\sigma}_{WS}(t)}{\overline{\boldsymbol{\sigma}}}\right)^{-1}, \quad \overline{\boldsymbol{\sigma}} = 50 \, \frac{\mathrm{g}}{\mathrm{cm} \cdot \mathrm{s}^2}, \quad \gamma_0 = 5 \cdot 10^{-7}. \tag{10.11}$$

For details on models of the dependency of the monocyte migration rate on the wall stress we refer to [78]. The exact role and influence of the wall stress on the migration rate is not yet completely understood. For further discussion, we refer to [99]. The scalar concentration $c_s^* : [0, T] \to \mathbb{R}_+$ will directly determine the active growth. Growth will take part in the middle parts of the vessel walls, see Fig. 10.3.

Accurate handling of the different time-scales is an open problem. Most approaches use an averaging in time and focus on the long-scale dynamics only [94, 355]. A two-scale approach has been suggested in [158]. Here, we simply consider an averaged long-scale model. We neglect the pulsating flow and instead choose one constant inflow-rate. We fully acknowledge that this approach will result in enormous modeling errors and refer to [158] for a detailed discussion.

Problem 10.1 (Long-Scale Growth) *In $I = [0, T]$, find fluid-velocity $\mathbf{v}_f$, pressure p_f, solid deformation $\mathbf{u}_s$ and foam cell concentration c_s^*, given by*

$$\begin{aligned} \rho_f \mathbf{v}_f \cdot \nabla \mathbf{v}_f - \operatorname{div} \boldsymbol{\sigma}_f = 0, \quad \operatorname{div} \mathbf{v}_f = 0 \quad & \text{in } \mathcal{F}(t) \\ -\operatorname{div} \boldsymbol{\sigma}_s(c_s^*(t)) = 0 \quad & \text{in } \mathcal{S}(t) \\ \mathbf{v}_f = 0, \quad \boldsymbol{\sigma}_f \mathbf{n}_f + \boldsymbol{\sigma}_s(c_s^*(t)) \mathbf{n}_s = 0 \quad & \text{on } \mathcal{I}(t) \\ \partial_t c_s^*(t) = \gamma(\boldsymbol{\sigma}_{WS}), \quad c_s^*(0) = 0 \quad & \text{in } \mathcal{S}(t). \end{aligned} \tag{10.12}$$

The boundary data is described by

$$\begin{aligned} \mathbf{v}_f(t) = \bar{\mathbf{v}}^{in}(t) \quad & \text{on } \Gamma_f^{in}, \\ \rho_f \nu_f \mathbf{n} \cdot \nabla \mathbf{v}_f - p\mathbf{n} = 0 \quad & \text{on } \Gamma_f^{out}, \\ \mathbf{u}_s = 0 \quad & \text{on } \Gamma_s, \end{aligned} \tag{10.13}$$

where $\mathbf{n}$ is the outward facing normal vector and $\bar{\mathbf{v}}^{in}$ is an averaged inflow profile that depends on the width of the blood vessel.

10.3 Monolithic Schemes for the Coupled Problem

In this section, we derive monolithic variational formulations for Problem 10.1 in ALE and in *Fully Eulerian* coordinates. Growth can lead to substantial deformations of the solid up to a full closure of the vessel. Together with the stiff coupling between blood and tissue, this is a prototypical application for the Eulerian framework introduced in Chap. 6.

Problem 10.2 (Long-Scale Problem in ALE Formulation) *Find the fluid velocity* $\hat{\mathbf{v}}_f \in \bar{\mathbf{v}}^{in}(t) + \mathcal{V}_f$*, deformation* $\hat{\mathbf{u}} \in \mathcal{W}$ *and the pressure* $\hat{p}_f \in \mathcal{L}_f$*, such that*

$$\begin{aligned}\left(\hat{\rho}_f \hat{J}_f \hat{\mathbf{v}}_f \cdot \hat{\mathbf{F}}_f^{-1} \hat{\nabla} \hat{\mathbf{v}}_f, \hat{\phi}_f\right)_{\hat{\mathcal{F}}} + \left(\hat{J}_f \hat{\boldsymbol{\sigma}}_f \hat{\mathbf{F}}^{-T}, \hat{\nabla}\hat{\phi}\right)_{\hat{\mathcal{F}}} + \left(\hat{\mathbf{F}}\hat{\boldsymbol{\Sigma}}, \hat{\nabla}\hat{\phi}\right)_{\hat{\mathcal{S}}} = 0 \quad \forall \hat{\phi} \in \mathcal{W},\\ \left(\widehat{\operatorname{div}}\,(\hat{J}\hat{\mathbf{F}}^{-1}\hat{\mathbf{v}}_f), \hat{\xi}_f\right)_{\hat{\mathcal{F}}} = 0 \quad \forall \hat{\xi} \in \mathcal{L}_f,\end{aligned}$$

with $\boldsymbol{\Sigma}$ *as given in (10.6) and where the extension* $\hat{\mathbf{u}}_f$ *is defined as*

$$(\hat{\nabla}\hat{\mathbf{u}}_f, \hat{\nabla}\hat{\psi}_f)_{\hat{\mathcal{F}}} = 0 \quad \forall \hat{\psi}_f \in \mathcal{W}_f,$$

in the case of the harmonic extension. For the biharmonic extension we use

$$(\hat{\mathbf{w}}_f, \hat{\chi}_f)_{\hat{\mathcal{F}}} - (\hat{\nabla}\mathbf{u}_f, \hat{\nabla}\hat{\chi}_f)_{\hat{\mathcal{F}}} + (\hat{\nabla}\hat{\mathbf{w}}_f, \hat{\nabla}\hat{\psi}_f)_{\hat{\mathcal{F}}} = 0 \quad \forall \{\hat{\psi}_f, \hat{\chi}_f\} \in \tilde{\mathcal{W}}_f \times \mathcal{W}_f$$

The elastic deformation gradient is defined in (10.4) depending on the concentration of foam cells. The latter one is defined by the ode

$$\partial_t c_s^* = \gamma(\boldsymbol{\sigma}_{WS}, t), \quad c_s^*(0) = 0.$$

The function spaces are given by

$$\begin{aligned}\mathcal{V}_f &= [H_0^1(\hat{\mathcal{F}}; \hat{\mathcal{I}} \cup \hat{\Gamma}_f^{in})]^2, & \mathcal{L}_f &= L^2(\hat{\mathcal{F}}),\\ \mathcal{W} &= [H_0^1(\hat{\Omega}; \hat{\Gamma}_f^{in} \cup \hat{\Gamma}_s)]^2, & \mathcal{W}_f &= [H_0^1(\hat{\mathcal{F}})]^2, \quad \tilde{\mathcal{W}}_f = [H^1(\hat{\mathcal{F}})]^2.\end{aligned}$$

Remark 10.3 (Biharmonic Mesh Model) We have chosen a mixed formulation for the biharmonic extension, such that an efficient discretization with simple C^0-conforming finite elements is possible.

To express the coupled model including growth in *Fully Eulerian* coordinates, we must carry over the decomposition of the deformation gradients into the current system. We denote the inverse mappings of $\hat{T}_a$ and $\hat{T}_e$ by $T_a = \hat{T}_a^{-1}$ and $T_e = \hat{T}_e^{-1}$ and their gradients by $F_a = \nabla T_a$ and $F_e = \nabla T_e$ respectively. Using $\mathbf{F} = \hat{\mathbf{F}}^{-1}$, we have

$$\mathbf{F} = \hat{\mathbf{F}}^{-1} = \hat{\mathbf{F}}_a^{-1}\hat{\mathbf{F}}_e^{-1} =: \mathbf{F}_a\mathbf{F}_e. \tag{10.14}$$

Although a direct modeling in Eulerian coordinates is possible, we derive the Eulerian solid model by a mapping of the Lagrangian formulation to the Eulerian system

$$\begin{aligned} J_s\hat{\rho}_s^0(\partial_t \mathbf{v}_s + \mathbf{v}_s \cdot \nabla \mathbf{v}_s) - \operatorname{div}\left(J\boldsymbol{\Sigma}\mathbf{F}^{-T}\right) &= 0 \\ \partial_t \mathbf{u}_s + \mathbf{v}_s \cdot \nabla \mathbf{u}_s &= \mathbf{v}_s \end{aligned} \quad \text{in } \mathcal{S}(t), \tag{10.15}$$

where $\boldsymbol{\Sigma}$ is given in (10.6) with an Eulerian description

$$\begin{aligned} \boldsymbol{\Sigma} &= J_a^{-1}\mathbf{F}_a\boldsymbol{\Sigma}_e\mathbf{F}_a^T, \\ \boldsymbol{\Sigma}_e &= 2\mu\mathbf{E}_e + \lambda_s \operatorname{tr}(\mathbf{E}_e)I, \quad \mathbf{E}_e = \frac{1}{2}(\mathbf{F}_e^{-T}\mathbf{F}_e^{-1} - I). \end{aligned} \tag{10.16}$$

Frei [151] gives details on the transformation of the stresses of an active material to the Eulerian coordinate framework.

10.3.1 Solid Growth in Eulerian Coordinates

Next, we carry over the growth model to the Eulerian representation. We will use again the simple isotropic growth model

$$\hat{\mathbf{F}}_a = \hat{g}I \tag{10.17}$$

and define the Eulerian growth function g by setting $g(x,t) = \hat{g}(\hat{x},t)$. By the relation $\hat{\mathbf{F}}_a = \mathbf{F}_a^{-1}$, it holds that

$$\mathbf{F}_a = g^{-1}I. \tag{10.18}$$

By the decomposition (10.14) it follows that

$$\mathbf{F}_e = \mathbf{F}_a^{-1}\mathbf{F} = g\mathbf{F}, \quad J_e = g^2 J_s. \tag{10.19}$$

The complete Eulerian stresses are given by

$$J_a\boldsymbol{\sigma}_e\mathbf{F}_a^{-T} = J_s\mathbf{F}_e^{-1}\boldsymbol{\Sigma}_e\mathbf{F}^{-T} = g^{-1}J_s\mathbf{F}^{-1}(2\mu_s\mathbf{E}_e + \lambda_s \operatorname{tr}(\mathbf{E}_e)I)\mathbf{F}^{-T}, \tag{10.20}$$

with the Eulerian elastic strain tensor

$$\mathbf{E}_e = \frac{1}{2}(g^{-2}\mathbf{F}^{-T}\mathbf{F}^{-1} - I). \tag{10.21}$$

Finally, we derive the equation of mass conservation in Eulerian coordinates. We assume that homogenous material with the same parameters is added, such that the

density is constant $\hat{\rho}_a = \hat{\rho}_s$. Hence, if $m(\hat{V})$ is the mass of the reference state, $m(\hat{V}_a)$ is the mass of the grown material, which is conserved in the current configuration V

$$m(\hat{V}) = \int_{\hat{V}} \hat{\rho}_s^0 \, \mathrm{d}\hat{x}, \quad m(\hat{V}_a) = \int_{\hat{V}_a} \hat{\rho}_a \, \mathrm{d}\hat{x}^g = \hat{\rho}_s^0 \int_{\hat{V}} \hat{J}_a \, \mathrm{d}\hat{x} = \hat{\rho}_s^0 \int_V \hat{J}_a J_s \, \mathrm{d}x, \tag{10.22}$$

where $\hat{J}_a := \det(\hat{\mathbf{F}}_a) = \hat{g}^2$ is the determinant of the growth part, such that for the density ρ of the current configuration it holds

$$\rho = \hat{\rho} = g^2 \hat{\rho}_s^0 J_s. \tag{10.23}$$

Problem 10.4 (Long-Scale Problem in Fully Eulerian Coordinates) *Find velocity $\mathbf{v}_f(t) \in \bar{\mathbf{v}}^{in} + \mathcal{V}_f$, deformation $\mathbf{u} \in \mathcal{W}$ and pressure $p_f \in \mathcal{L}_f$, such that*

$$\begin{aligned} \left(\rho_f \mathbf{v}_f \cdot \nabla \mathbf{v}_f, \phi_f\right)_{\mathcal{F}(t)} + \left(\boldsymbol{\sigma}_f, \nabla \phi\right)_{\mathcal{F}(t)} + \left(J_a \boldsymbol{\sigma}_e \mathbf{F}_a^{-T}, \nabla \phi\right)_{\mathcal{S}(t)} &= 0 \quad \forall \phi \in \mathcal{W} \\ \left(\operatorname{div} \mathbf{v}_f, \xi_f\right)_{\mathcal{F}(t)} &= 0 \quad \forall \xi_f \in \mathcal{L}_f, \\ \left(\nabla \mathbf{u}_f, \nabla \psi_f\right)_{\mathcal{F}(t)} &= 0 \quad \forall \psi_f \in \mathcal{W}_f. \end{aligned}$$

The elastic deformation gradient is defined in (10.19). Accumulation of foam cells is described by the ode

$$\partial_t c_s^* = \gamma(\boldsymbol{\sigma}_{WS}, t).$$

The function spaces are defined as

$$\begin{aligned} \mathcal{V}_f &= H_0^1(\mathcal{F}(t); \mathcal{I}(t) \cup \Gamma_f^{in})^2, & \mathcal{L}_f &= L^2(\mathcal{F}(t)), \\ \mathcal{W} &= H_0^1(\Omega(t); \Gamma_f^{in} \cup \Gamma_s)^2, & \mathcal{W}_f &= H_0^1(\mathcal{F}(t))^2. \end{aligned}$$

10.4 Numerical Tests

Studying different test cases we compare the performance of two different formulations of the fluid-structure interaction problem, the *Arbitrary Lagrangian Eulerian* formulation from Chap. 5 and the *Fully Eulerian* formulation detailed in Chap. 6. We give further tests and an elaborate discussion in [158].

10.4.1 Problem Setting

As geometry we use a channel with length 10 cm and an initial width $\omega(0)$ (of the fluid part) of 2 cm as illustrated in Fig. 10.3. The solid parts on the top and

bottom have an initial thickness of 1 cm each. Fluid density and viscosity are given by $\rho_f = 1\,\mathrm{g}\cdot\mathrm{cm}^{-3}$ and $\nu_f = 0.3\,\mathrm{cm}^2\cdot\mathrm{s}^{-1}$. The solid parameters are given by $\rho_s = 1\,\mathrm{g}\cdot\mathrm{cm}^{-3}$ and the Lamé parameters $\nu_s = 10^4$ and $\lambda_s = 4\cdot 10^4\,\mathrm{dyn}\cdot\mathrm{cm}^{-2}$. We prescribe a pulsating velocity inflow profile on Γ_f^{in} given by

$$\begin{aligned}\mathbf{v}^{\mathrm{in}}(t,x,y) &= \frac{3}{2}\begin{pmatrix}\mathbf{v}^{\mathrm{in}}(t)(1-y^2)\\ 0\end{pmatrix},\\ \mathbf{v}^{\mathrm{in}}(t) &= \big(\varepsilon_\omega + 5\omega(t)\big)(1+\sin(2\pi t))\mathrm{cm}\cdot\mathrm{s}^{-1},\end{aligned} \tag{10.24}$$

depending on the width of the channel $\omega(t)$ (see Fig. 10.3). The parameter ε_ω is used to control the minimum flow rate and will be specified below. These parameters are similar to a real plaque growth configuration. The remaining boundary conditions are specified in (10.13). For the growth, we specify a function that depends on the concentration of the foam cells c_s^* that is defined by the ode (10.11). Growth is centered around the middle part of the vessel

$$\hat{g}(\hat{x},\hat{y},t) = 1 + c_s^*(t)\exp\left(-\hat{x}^2\right)(2-|\hat{y}|), \quad \hat{\mathbf{F}}_g(\hat{x},\hat{y},t) := \hat{g}(\hat{x},\hat{y},t)\,I. \tag{10.25}$$

Growth $\hat{g}$ and inflow rate $\mathbf{v}^{\mathrm{in}}(t)$ implicitly depend on the solution. As the configuration is symmetric in the vertical direction, we consider the lower half of the geometry for the simulation only.

The problem is driven by a parabolic inflow profile with an average inflow rate $\bar{\mathbf{v}}^{\mathrm{in}}(t)$. We use the averaged inflow profile of (10.24)

$$\bar{\mathbf{v}}^{\mathrm{in}}(t) = \big(\varepsilon_\omega + 5\omega(t)\big)\,\mathrm{cm}\cdot\mathrm{s}^{-1} \tag{10.26}$$

The dynamic configuration using the pulsating inflow field (10.24) is discussed in [158]. We discretize the coupled problem by a splitting in time and approximate by the following iteration.

Definition 10.5 (Mechano-Chemical Iteration) Initialize $\mathbf{v}^0 = 0, \mathbf{u}^0 = 0, g^0 = 0$ and the vessel-width $\omega^0 = 2$. Set time step $k_l = 0.1\,\mathrm{days} = 8\,640\,\mathrm{s}$. Iterate for $n = 1, 2, \ldots$.

1.	Solve (10.1)	$\{c_s^{*,n-1}, \omega^{n-1}\} \mapsto \{\mathbf{v}^n, \mathbf{u}^n, p^n\}$
2.	Compute wall stress	$\boldsymbol{\sigma}_{WS}^n = \int_{\mathcal{I}} \lvert\boldsymbol{\sigma}_f(\mathbf{v}^n, p^n)\mathbf{n}\cdot\mathbf{e}_1\rvert\,\mathrm{d}o$
3.	Update foam cells	$c_s^{*,n} = c_s^{*,n-1} + k_l\gamma_0\ \left(1+\boldsymbol{\sigma}_{WS}^n/\overline{\boldsymbol{\sigma}}\right)^{-1}$
4.	Compute vessel width	$\omega^n = 2 - 2\mathbf{u}_2^n(A(t_n), t_n)$

First, we choose a minimum inflow velocity of $\varepsilon_\omega = 0.1\,\mathrm{cm/s}$. In Fig. 10.4, the streamlines of the fluid and the deformed vessel walls at times $t = 10\,\mathrm{days}$ and $t = 50\,\mathrm{days}$ are shown.

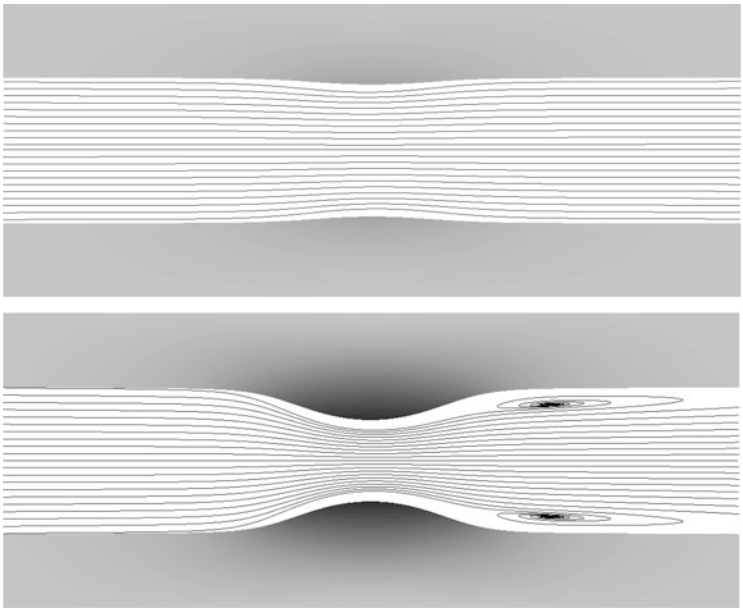

Fig. 10.4 Solution after 10 days (*top*) and 50 days (*bottom*). Streamlines of the fluid and the deformation of the vessel wall are shown

In Fig. 10.5 we show the course of different output functionals over time: the wall stress in main stream direction on the vessel wall $\mathcal{I}$ that is computed in step 2. of the iteration, the channel width $\omega(t) = 2 - 2\mathbf{u}_2(A(t_n))$ in the middle point $A(t_n)$ (see Fig. 10.3), the vorticity of the solution in the L^2-norm and the outflow at the right boundary defined by

$$J_{\text{vort}}(\mathbf{v}) = \int_{\mathcal{F}(t)} \left(\partial_y \mathbf{v}_1 - \partial_x \mathbf{v}_2\right)^2 dx, \quad J_{\text{out}}(\mathbf{v}) = \int_{\Gamma_{f,\text{out}}} \mathbf{v} \cdot \mathbf{n}. \tag{10.27}$$

The functional values for the *Arbitrary Lagrangian Eulerian* method (harmonic and biharmonic extension) and the *Fully Eulerian* approach show very good agreement. Using the harmonic extension, the ALE method broke down at $t = 63.2$ days due to degeneration of mesh cells, with the biharmonic extension, we were able to get results up to $t = 109.3$ days.

The fully Eulerian method, on the other hand, was able to yield reliable results until the channel was almost closed. As the inflow velocity is bounded from below by $\varepsilon_\omega = 0.1\,\text{cm} \cdot \text{s}^{-1}$ and as the fluid is incompressible, a passage must always remain. As higher wall stresses slow down plaque growth, see (10.11), the vertical displacement approaches a limit. However, increasing fluid-dynamical forces cause strong horizontal deflections that finally result in a breakdown of the simulation.

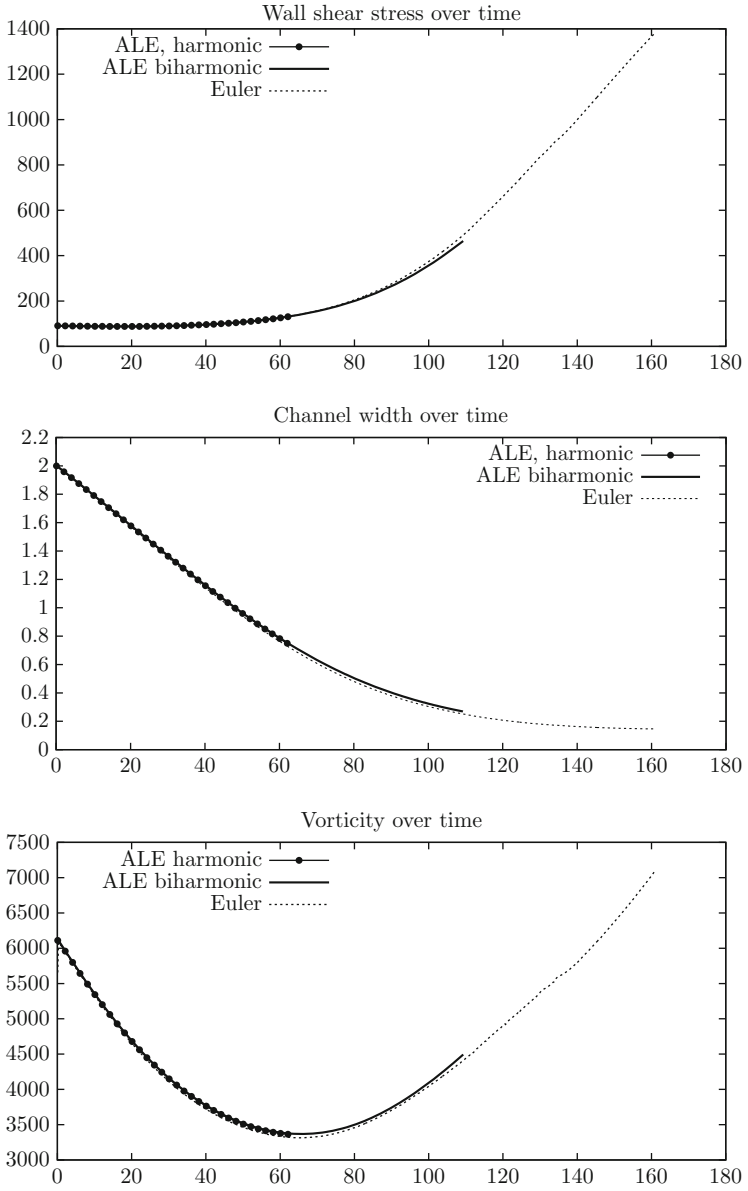

Fig. 10.5 Course of different output functionals over time during closing of channel. For small deformations, the three different modeling approaches give similar results. Once the deformation gets larger, the two ALE approaches with harmonic and biharmonic extensions will fail

As the results for the ALE method with harmonic and biharmonic extension are nearly identical until time $t = 63.1$ days, we will not show the harmonic variant anymore in the following tests.

In Fig. 10.6, we present the deformed meshes at time $t = 109.3$ days for the ALE approach with biharmonic mesh deformation and the fully Eulerian approach. In the case of the biharmonic ALE approach, this was the last mesh before the calculation broke down.

Next, we study the convergence with respect to the spatial grid size $h > 0$ for both the fully Eulerian and the ALE technique. The results are shown in Table 10.1. For the fully Eulerian approach, we use $Q^1 - Q^1$ equal-order elements and meshes with 256, 1024 and 4096 patch elements. For the ALE approach we use $Q^2 - P^{1,\mathrm{dc}}$ elements as introduced in Sect. 4.3.1. We choose slightly coarser meshes for a fair comparison.

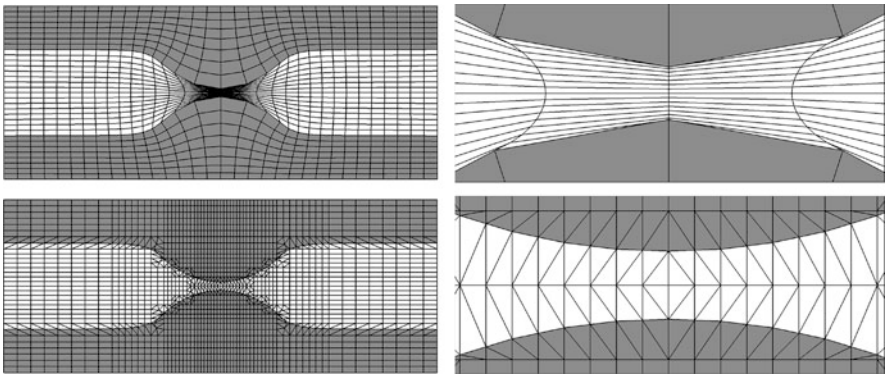

Fig. 10.6 *Top*: Biharmonic deformation close to breakdown at $t = 109.3$ days and zoom-in (*right*). *Bottom*: Corresponding results using the *Fully Eulerian* approach on fixed meshes

Table 10.1 Convergence of functional values at $t = 50$ days on three different grids for the fully Eulerian and the ALE approach

#patches	Wall stress	Width	Vorticity	Outflow
Euler 256	$1.033 \cdot 10^2$	1.092	$3.408 \cdot 10^3$	9.251
1024	$1.050 \cdot 10^2$	1.064	$3.457 \cdot 10^3$	9.547
4096	$1.060 \cdot 10^2$	1.052	$3.472 \cdot 10^3$	9.648
Extrapol.	$1.074 \cdot 10^2$	1.047	$3.479 \cdot 10^3$	9.700
Conv.	0.77	1.81	1.71	1.55
ALE 160	$1.087 \cdot 10^2$	1.033	$3.527 \cdot 10^3$	9.892
640	$1.076 \cdot 10^2$	1.037	$3.515 \cdot 10^3$	9.849
2560	$1.073 \cdot 10^2$	1.038	$3.510 \cdot 10^3$	9.834
Extrapol.	$1.072 \cdot 10^2$	1.039	$3.506 \cdot 10^3$	9.826
Conv.	1.87	1.49	1.26	1.52

We indicate estimated convergence rates and extrapolated limits

We evaluate the functionals at $t = 50$ days. The functional values for the ALE and the fully Eulerian approach converge roughly against the same values. Small differences are due to time discretization (the time step has been chosen as 0.1 days). Further, the implementation of the *Fully Eulerian* model is only semi-implicit, as the domain layout during the time step $t_n \to t_{n+1}$ is fixed to $\mathcal{F}^n$ and $\mathcal{S}^n$.

Furthermore, we estimated the convergence order for all functionals, see Table 10.1. Besides the wall stress, all estimated convergence orders lie between linear and quadratic convergence order and the ALE and the fully Eulerian approach converge similarly. The ALE approach, however, seems to yield better values already on very coarse grids. Furthermore, the ALE approach shows faster convergence in the wall stress functional. The reason for this better performance is the use of inf-sup stable Q^2 elements in the case of ALE, which is not yet possible with the parametric interface approximation scheme described in Sect. 4.5, where stabilized $Q^1 - Q^1$ elements are utilized.

An interesting aspect from a modeling point of view is the question if the channel closes completely or if there will remain a small layer of fluid between the vessel walls. As discussed before, a complete closure of the channel is not possible as long as the inflow rate ε_ω is positive.

To study closure, we decrease the minimal inflow velocity ε_ω from 0.1 to 0 and the velocity inflow by a factor of 10 to

$$\mathbf{v}_1^{\text{in}} = 0.15 \cdot (5\omega(t))(1 - y^2)\,\text{cm/s}. \tag{10.28}$$

This means that the flow through the narrow part of the channel will decrease considerably when the channel is almost closed. This has two important effects: First, the fluid forces acting against the growth of the solid are much smaller. Secondly, the wall stress becomes smaller which has a strengthening impact on the solid growth in our model. Altogether, this has the effect that in our simulation the channel closes completely at time $t = 55.8$ days. Of course full closure is only possible by using the *Fully Eulerian* formulation.

In Fig. 10.7, we show plots of the channel width and the vorticity over time. In contrast to the larger inflow velocity studied above, the fluid forces (e.g. the vorticity) decrease after $t \approx 40$ days which makes the closure of the channel possible. In Fig. 10.8, we show the last mesh obtained with the fully Eulerian approach ($t = 55.8$ days) where the channel is completely closed. The ALE calculation (with biharmonic extension) broke down at time $t = 40.6$ days.

These simplified simulations consider an averaged inflow velocity only. The main mechanical forcing however is due to the pulsating blood flow. In [158] a two-scale approach has been suggested, where effective parameters for the wall stress are computed from isolated short-scale simulations that resolve the pulsation. It is shown that substantial variations in plaque growth up to 20% exist.

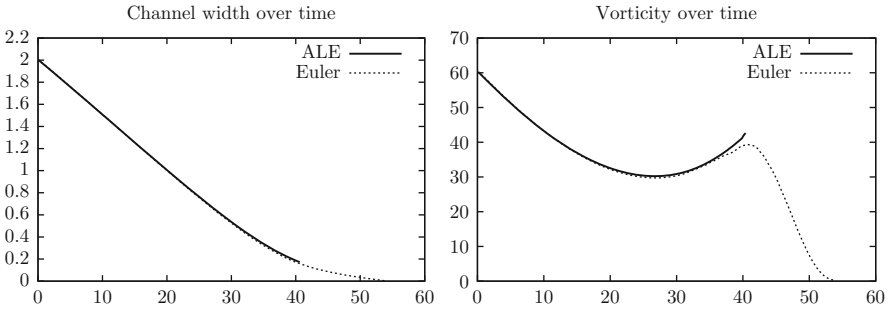

Fig. 10.7 Channel width and vorticity for a long-scale simulation with reduced inflow velocity. The inflow velocity goes to zero when the channel closes. This makes the complete closure of the channel possible

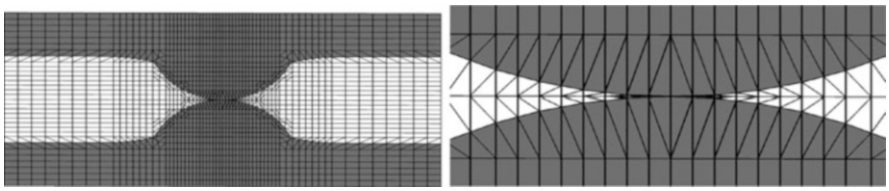

Fig. 10.8 Second test case. *Fully Eulerian* deformation at complete closure $t = 55.8$ days

Chapter 11
Non-stationary Dynamics and Coupled Oscillations

Inspired by a presentation of Sanjay Mittal [245, 250, 260] and a discussion with Paolo Galdi (private communication, 2016) we study the interaction of the *von Kármán vortex sheet* with the oscillation of an elastic obstacle. The flow around a blunt body develops self-excited oscillations. Elastic structures freely oscillate with Eigenfrequencies. We want to study the interplay between these two effects on a coupled elastic fluid-structure interaction problem.

Mittal and coworkers [260] studied the interaction of a freely oscillating rigid body in a laminar flow. They considered obstacles with circular and elliptical cross section that are freely suspended and attached to an (imaginary) spring. The solid problem alone—without interaction to a surrounding fluid—will show periodic oscillations of a fixed frequency and amplitude. The amplitude is related to the initial excitation, while the frequency of the oscillation is related to the spring constant and the mass of the obstacle. Second, the rigid obstacle is fixed and one studies the flow of an incompressible fluid around this obstacle. The resulting fluid pattern will strongly depend on key quantities like the Reynolds number

$$Re = \frac{\bar{\mathbf{v}} D}{\nu},$$

where by $\bar{\mathbf{v}}$ we denote the average velocity of the surrounding fluid, by D the diameter of the obstacle and by ν the viscosity of the fluid. Increasing the Reynolds number results in the following observations

- In the *subcritical regime* $Re < Re_{sub}$, the flow has stationary limit with $\partial_t \mathbf{v} = 0$.
- In the *laminar regime* $Re_{sub} < Re < Re_{lam}$, the flow develops an oscillatory pattern behind the obstacle, the so called *von Kármán vortex street*, see [333] or

T. Richter, *Fluid-structure Interactions*, Lecture Notes in Computational Science and Engineering 118, DOI 10.1007/978-3-319-63970-3_11

Fig. 11.3. The frequency f of the oscillation is connected to the *Strouhal number* St, that is like the *Reynolds number* an non-dimensional measure

$$St = \frac{fD}{\bar{\mathbf{v}}},$$

where f is the frequency, D the diameter of the object and $\bar{\mathbf{v}}$ the velocity of the surrounding fluid. For a large range of Reynolds numbers (in the laminar regime), it holds for the flow around circular objects

$$St \approx 0.2\left(1 - \frac{20}{Re}\right) \quad \Leftrightarrow \quad f = 0.2\left(\frac{\bar{\mathbf{v}}}{D} - \frac{20\nu}{D^2}\right), \tag{11.1}$$

showing that the frequency will linearly increase with the velocity.

- In the *transition regime* $Re_{lam} < Re < Re_{trans}$, the flow develops complex patterns. The dominant oscillation of the vortex street is overlayed with more and more overtones.
- Finally, the flow pattern completely changes in the *turbulent regime* for $Re \gg Re_{trans}$, where the motion appears chaotic.

In a series of papers, Mittal [244, 245, 260] analyzed the interaction of the non-stationary vortex street of laminar flows with an rigid, but freely supported obstacle: What is the resulting frequency and what is the resulting amplitude for the dynamically coupled problem? Two of the findings are the following: First, the coupled problem admits non-stationary periodic solutions at significantly reduced Reynolds numbers (as compared to the pure fluid problem). Second, and this effect is referred to as *synchronization* or *lock-in*, there is a region of Reynolds numbers, where the frequency of the coupled system is stable and usually equal or a multiple of the natural structure frequency [33, 297, 349].

Here, we aim at discussion this question for a fully coupled fluid-structure interaction problem with an elastic obstacle. We consider the benchmark problem that has already been introduced in many sections of this book. This situation is more complex than the configuration studied by Mittal. A rigid mass that is supported by an ideal spring and that is not subject to any damping shows only one single oscillation frequency. Here we study the interaction to a two dimensional elastic beam. This solid problem itself is more complex, the oscillation of the beam shows several modes in horizontal and vertical direction. Considering the coupling to a rigid body, the fluid forces act as averages on the center of mass and all possible motions of the solid can be described by a two dimensional vector. The elastic case asks for modeling of a distributed deformation vector in the two dimensional solid domain. Fluid's forces not necessarily cause a motion of the solid, they also give rise to bending and compression.

In the following section we first describe the coupled fluid-structure interaction test case. Then in Sect. 11.2, we discuss the solid problem without a surrounding fluid. In Sect. 11.3 we consider the fluid flow around a rigid obstacle and finally in Sect. 11.4 we analyze the coupling.

11.1 Configuration of the Test Case

The configuration of the benchmark problem is shown in Fig. 11.1a. The original *fsi-3* benchmark problem published by Hron and Turek [200] used the average inflow velocity $\bar{\mathbf{v}} = 2\,\mathrm{m}\cdot\mathrm{s}^{-1}$. This choice of parameters results in the Reynolds number

$$Re = \frac{\bar{\mathbf{v}}D}{\nu} = \frac{2\cdot 0.1}{0.001} = 200,$$

where $D = 0.1\,\mathrm{m}$ is the diameter of the circle, the rigid part of the obstacle. The attached elastic beam is not considered for computing the Reynolds number. In Fig. 11.1b we show the deflection in $A = (0.6, 0.2)$, a point in the tip of the beam, for these settings. The coupled dynamics results in a periodic oscillation with dominant frequency

$$f_{\bar{\mathbf{v}}=2} \approx \frac{1}{0.184} \approx 5.435. \tag{11.2}$$

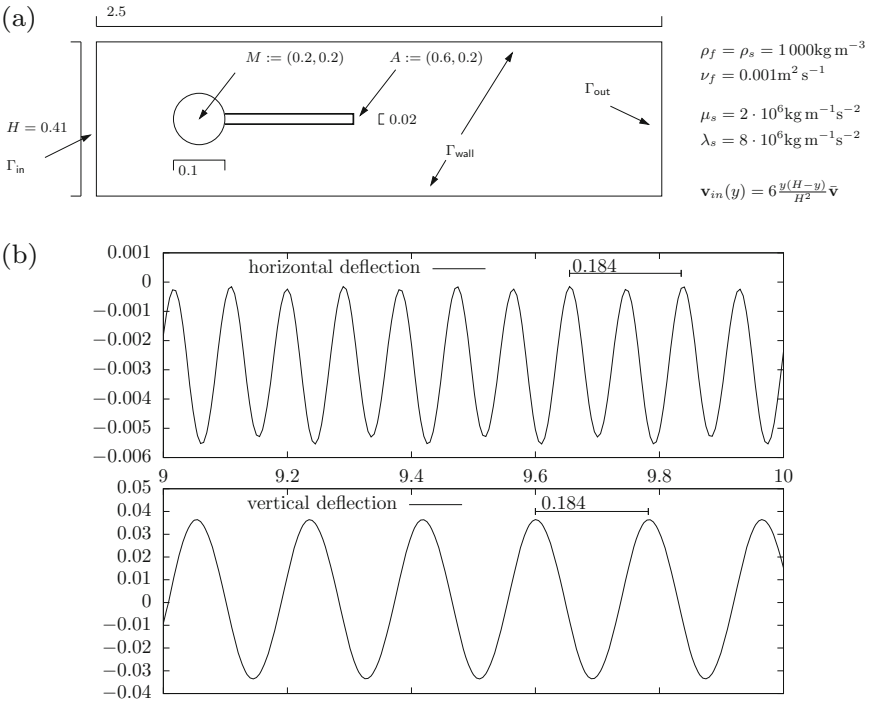

Fig. 11.1 We show the configuration of the benchmark problem as well as the dominant oscillation in the beam's tip. (**a**) Configuration of the fluid-structure interaction problem*fsi-3*. (**b**) Horizontal and vertical deflection $\mathbf{u}_x(A)$, $\mathbf{u}_y(A)$ in the tip of the beam $A = (0.6, 0.2)$

Considering the horizontal and vertical deflection of the tip of the beam, twice the amplitude of the oscillation is given by

$$2a^x_{\tilde{\mathbf{v}}=2} \approx 0.00538, \quad 2a^y_{\tilde{\mathbf{v}}=2} \approx 0.0701,$$

measures as the distance between maximal and minimal deflection. In Sect. 5.1.1 we have studied the discrete Fourier transform of the drag coefficient. Here we have found high frequent oscillations that superimpose the dominant frequency. While not visible at a first sight their numerical resolution is necessary to obtain the correct dynamics of the coupled system.

11.2 Dynamics of the Elastic Solid

To identify the dynamics of the isolated elastic structure we run preliminary tests without the fluid problem. These computations are comparable to the *csm-3* benchmark case published by Hron and Turek [200]. We initially expose the beam to a vertical force

$$\mathbf{f}_s(t) = \begin{pmatrix} 0 \\ -1 \end{pmatrix} \cdot \begin{cases} 10\rho_s & t \leq 0.05\,\mathrm{s} \\ 0 & t > 0.05\,\mathrm{s}. \end{cases}$$

The resulting oscillation of the beam's tip is shown in Fig. 11.2. The time interval $I = [8, 10]$ is chosen such that the dominant frequencies are visible. The beam is not oscillating with one single frequency but it shows a superposition of many different frequencies. We can however identify the dominant frequency (of the vertical deflection) as

$$f_s \approx \frac{1}{0.464} \approx 2.155,$$

which is about half of the *fsi-3* frequency $f_{\tilde{\mathbf{v}}=2}$ given in (11.2). Naturally, the horizontal deflection shows twice of the frequency, as the tip is deformed to the left two times in every cycle. The oscillations shown in Fig. 11.2a are far from a sine wave. Therefore we show in the lower part of Fig. 11.2b the discrete Fourier transformation of the periodic dynamics. First, one clearly identifies the dominant frequencies of the horizontal and vertical deflections, where the horizontal one is twice as large as the vertical one. In addition we observe oscillations at higher frequencies that explain the complex structure of the periodic solution.

In contrast to the test case studied by Mittal [245, 250, 260], the situation is less clear. If we want to show synchronization effects it is not obvious, if this will appear at the most dominant frequency or at an overtone.

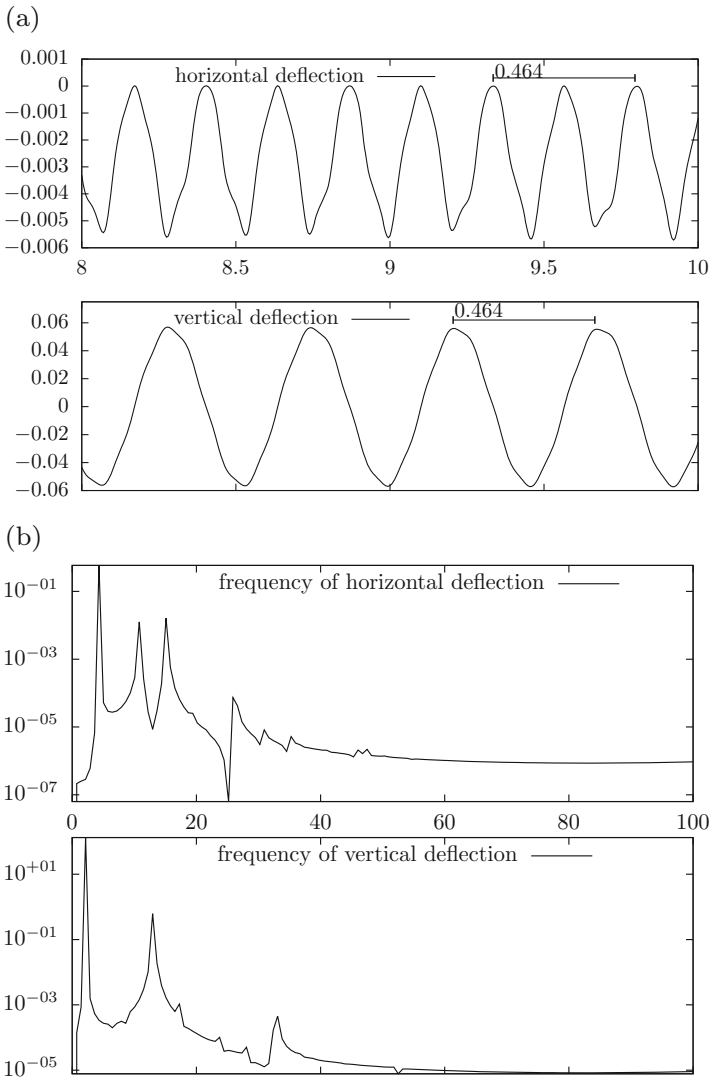

Fig. 11.2 Dynamics of the solid problem. The dominant Eigenfrequency for the horizontal deflection is $f \approx 4.3$ the vertical one is $f \approx 2.15$. (**a**) Deflection of the tip of the beam $A = (0.6, 0.2)$ in the temporal interval $I = [8, 10]$. (**b**) Discrete Fourier components of the beam's deflection. We indicate the strength of the signal for the different frequencies

11.3 Dynamics of the Flow Around a Fixed Obstacle

Next, we study the pure fluid-dynamics test case, where the obstacle is considered to be rigid. Of coarse, there will be no deflection. Instead we measure the *drag* and *lift coefficient* of the obstacles that should show a similar dynamic behavior.

For increasing average inflow velocity $\bar{\mathbf{v}}$ (which corresponds to increasing Reynolds numbers) we note the frequency of the vortex street. For easy measurement, we consider the forces of the fluid on the obstacle in cross-direction, measured as

$$F_y = -\int_{\mathcal{I}} \boldsymbol{\sigma}_f \mathbf{n} \cdot \mathbf{e}_y \mathrm{d}o,$$

where $\mathbf{e}_y = (0, 1)^T$. Up to a scaling, this function corresponds to the lift coefficient. We indicate frequency f_y and amplitude a_y for the functional in Table 11.1. The flow develops a periodic oscillation at $Re \approx 170$. We once more note that we did not include the beam into the definition of the Reynolds numbers. This is the reason for the rather high value of $Re \approx 170$ for the transition to the laminar periodic state in contrast to $Re \approx 50$ for the flow around a circular obstacle only. In Fig. 11.3 we show the pressure profile for the flow at different Reynolds numbers.

Table 11.1 Frequency and amplitude of the vertical force on the obstacle (ball & fixed beam) for increasing Reynolds numbers

$\bar{\mathbf{v}}$	1.4	1.5	1.6	1.7	1.8	1.9	2.0	2.1	2.2	2.3	2.4	2.5	2.6	2.7	2.8	2.9
Re	140	150	160	170	180	190	200	210	220	230	240	250	260	270	280	290
f_y	–	–	–	3.62	3.85	4.04	4.22	4.42	4.63	4.82	5.04	5.21	5.43	5.63	5.85	6.06
$2a_y$	–	–	–	<1	9.88	111	154	197	240	283	323	371	420	469	521	565

Fig. 11.3 Pressure profile for the flow around a fixed obstacle at different Reynolds numbers. *From top to bottom*: $Re = 100, 200, 300$

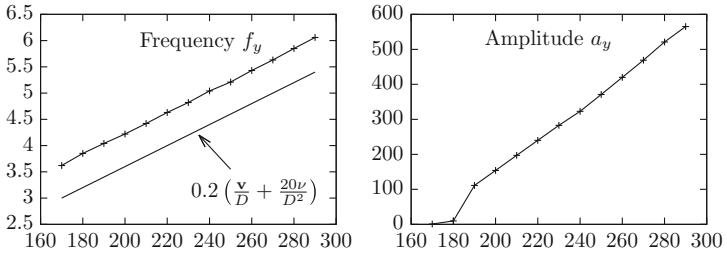

Fig. 11.4 Frequency and amplitude of the von Kármán vortex street for the flow around a fixed obstacle at different Reynolds numbers. The theoretical prediction for the frequency shows very good agreement (up to a constant shift)

Next, we compare the theoretical model for the oscillation frequency (11.1) with the numerical results. In Fig. 11.4, we show frequency and amplitude of the oscillation for different Reynolds numbers. Equation (11.1) predicts the slope of the frequency but gives a shifted curve. This is no contraction to theory, as our setting includes the fixed beam and is therefore more complex. We see that amplitude and frequency of the oscillation increase with the Reynolds number. For the frequency we derive the relation

$$f_y(Re) \approx 0.02Re + 0.24. \tag{11.3}$$

The amplitude also linearly depends on the Reynolds number and can be approximated as

$$2a_y(Re) \approx 4.5Re - 750. \tag{11.4}$$

Both relations are good approximations for $Re \in [180, 300]$.

11.4 Coupled Dynamics

Finally, we study the oscillation dynamics of the fully coupled fsi-3 fluid-structure interaction problem for different Reynolds numbers. Here we are interested in the interplay of von Kármán vortex sheet and structural oscillation. We start by showing snapshots of the solution for different Reynolds numbers starting in the stationary regime at $Re = 100$, see Fig. 11.5.

We also show the deformation of the beam. At low Reynolds numbers, the flow is stationary. Transition to a non-stationary oscillatory flow with large amplitudes is given for $Re \approx 135$ in contrast to $Re \approx 170$ for the pure fluid case. A closer look at the results even shows transition to non-stationary pattern (although at low amplitudes) for Reynolds numbers $Re \approx 115$.

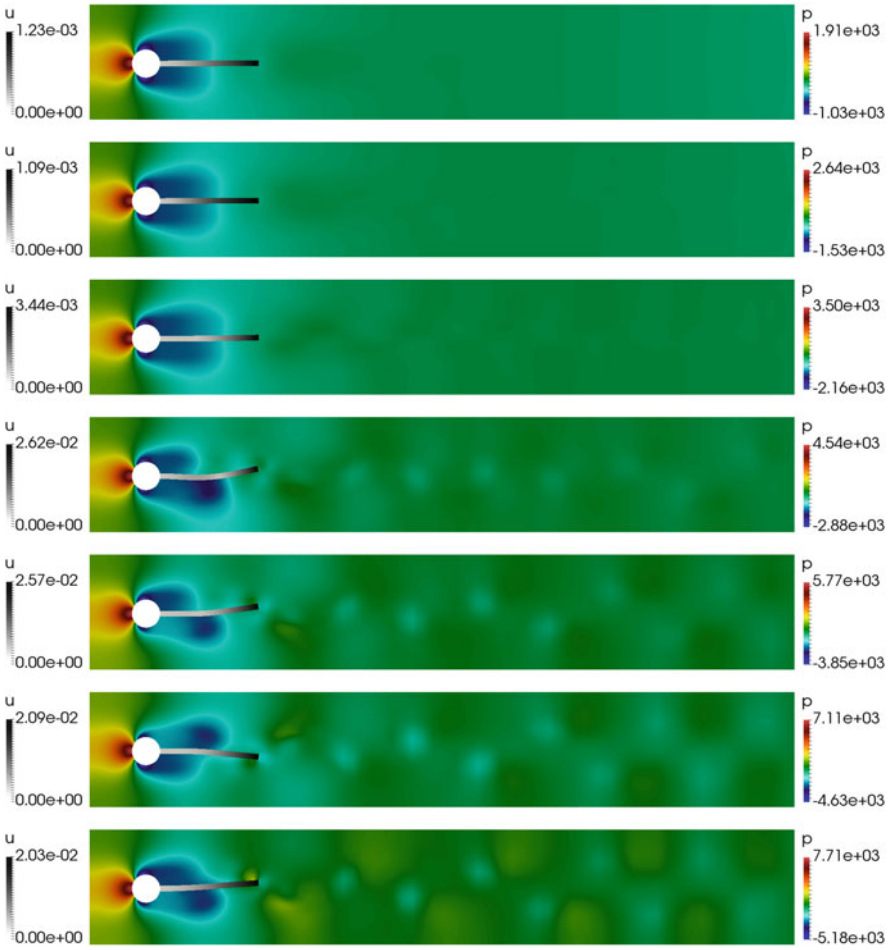

Fig. 11.5 Pressure profile for the flow and deformation $|\mathbf{u}_s|$ for the flow around an obstacle with elastic beam at different Reynolds numbers ranging from $Re = 100$ (*top*) to $Re = 200$ (every 20) and for $Re = 210$ (*bottom*)

In Table 11.2 we show the dominant frequency f_y and twice the amplitude $2a_y$ of the vertical deflection of the beam. Comparing to Table 11.1 we identify various differences. We also give a graphical representation of the findings in Fig. 11.6.

- A fully developed stable periodic solution is developed at $Re \approx 115$ compared to $Re \approx 170$ in the case with a fixed obstacle. For $115 \leq Re \leq 130$ there are however no significant forces on the obstacle. The deformation of the beam is very small such as the amplitude of the vertical force f_y.

Table 11.2 Frequency and amplitude of the vertical force for the coupled fluid-structure interaction problem at different Reynolds numbers

$\bar{\mathbf{v}}$	1.1	1.15	1.2	1.25	1.3	1.35	1.4	1.5	1.6	1.7	1.8	1.9	2.0	2.1	2.2	2.25	2.3
Re	110	115	120	125	130	135	140	150	160	170	180	190	200	210	220	225	230
f_y	4.82	4.97	5.10	5.19	5.40	5.52	4.09	4.34	4.57	4.79	5.00	5.26	5.48	5.71	5.95	14.8	14.9
$2a_y$	$\ll 1$	58	142	141	130	104	206	300	345	364	376	375	361	348	334	1020	1266

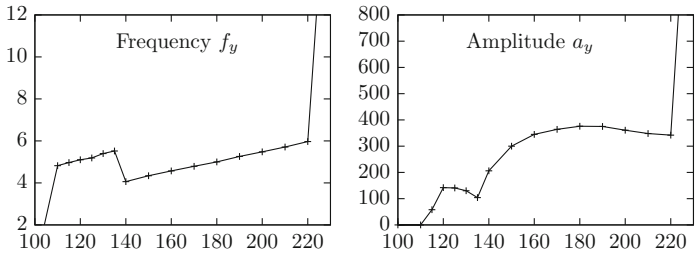

Fig. 11.6 Frequency and amplitude for the coupled fluid-structure interaction problem

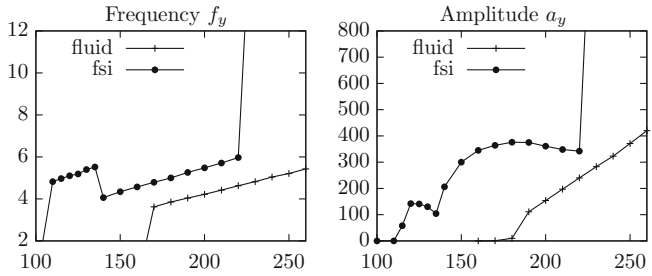

Fig. 11.7 Comparison of frequencies and amplitude for the fluid problem and the coupled fsi problem

- Starting with $Re \approx 135$ a stable periodic solution with significant amplitude and large deformations of the beam develops. This regime is stable up to $Re \approx 220$. For larger values of the Reynolds number the non-stationary dynamics are more complex with dominant overtones and rapidly increasing amplitude.
- The frequency of the oscillation increases with the Reynolds number. There is however a significant jump at $Re \approx 130{\sim}135$ where an oscillation with large amplitude appears. The slope of the frequency development $f_y(Re)$ is nearly the same as in the fluid case given in (11.3). We show a direct comparison of the two frequencies in Fig. 11.7.
- For the fluid problem the amplitude was linearly depending on the Reynolds number (11.4). The coupling to the solid has a stabilizing effect on the amplitude. For a large interval $Re \in (150, 220)$ the amplitude takes values of $2a_y \approx 375$. The direct comparison is given in Fig. 11.7.

From this numerical study, we cannot derive any analytical relation between the frequencies of the von Kármán vortex sheet, the Eigenfrequency of the solid and the frequency of the coupled dynamics. It is obvious that the elastic solid has a destabilizing effect. Relating to the discussion on the *added mass effect* given in Sect. 3.3 we have to expect this effect. Non-stationarities appear at lower Reynolds numbers.

As Mittal and coworkers [245] we could identify a sub-critical regime $Re \in (110, 170)$ where the pure fluid problem is stationary but a coupling to an elastic solid gives stable oscillatory solutions.

Mittal and coworkers [245, 260] found a synchronization regime for the frequency of the vortex shedding and the frequency of the solid's oscillation for a large range of Reynolds numbers. We could not identify such a synchronization for the elastic fluid-structure interaction problem in Fig. 11.6. No immediate relation between the frequencies of the coupled fluid-structure interaction problem and the structural frequency is observed. Instead, we get a linear dependency between frequency and Reynolds number with exception of a jump at the critical value $Re \approx 130 \sim 135$ where dynamics with a substantial amplitude developed.

However we see a strong stabilizing effect in the amplitude of the oscillation, compare Fig. 11.7. For the complete range of Reynolds numbers $Re \in (130, 210)$ we observe amplitudes $2a_y \approx 375$ that do not grow with increasing inflow velocities.

In Fig. 11.8 we show the oscillation of the vertical force plotted over time. We always show a time interval (each of them has the length 2 s where the flow reached a stable periodic state. We show the situation at $Re \approx 110 \sim 120$ where the transition to an periodic oscillation with an amplitude of $2a_y \approx 150$ is initiated. This regime is stable for $Re \in [120, 135]$. Here, larger Reynolds numbers will lead to higher frequencies but smaller amplitudes. Next, we show the transition at $Re \approx 135 \sim 140$, where we experience the jump to a lower frequency, but where the amplitude is increased to about $2a_y \approx 300$. This regime is stable for $Re \in [140, 220]$ showing an increase in frequency and more or less stable amplitudes for larger Reynolds numbers. Only in the transition zone for $Re \approx 140$ the functional pattern in Fig. 11.8b (right) shows a visible second mode. Finally we show the next transition at $Re \approx 220 \sim 225$ to a more complex flow pattern. Both the frequency and amplitude are strongly intensified. For even larger Reynolds numbers the computations will break down due to very large oscillations and instabilities of the ALE formulation.

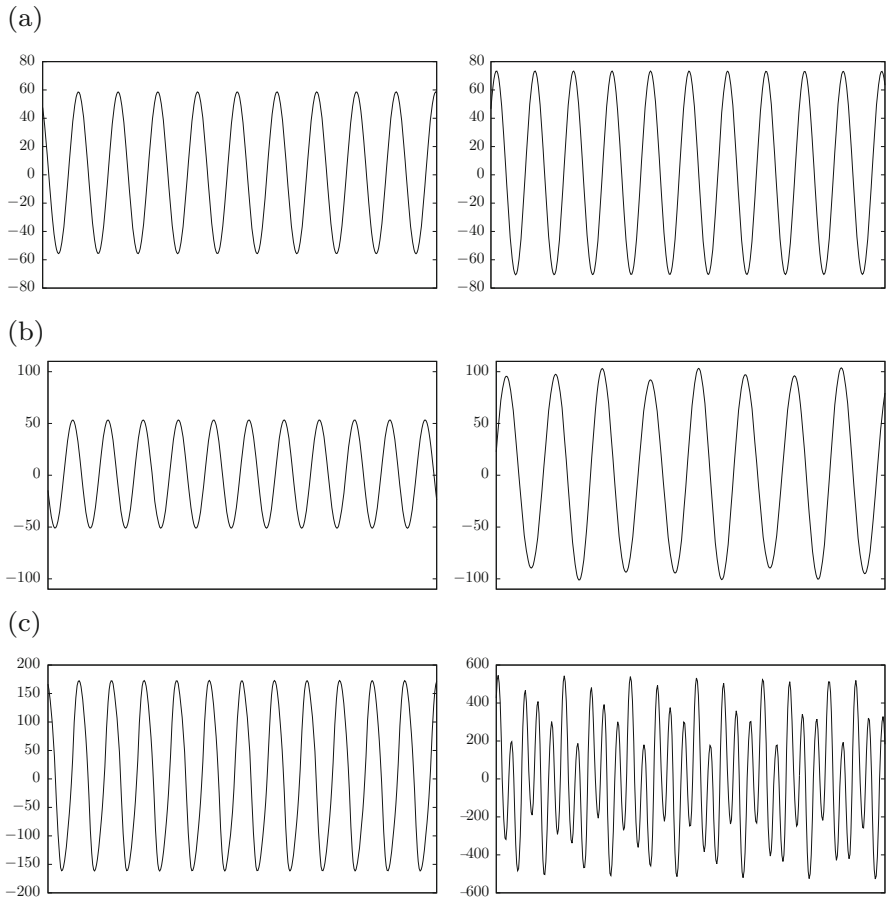

Fig. 11.8 Dynamics of the vertical force of the coupled fluid-structure interaction problem for different Reynolds numbers. We show the formation of the stable oscillation with large frequency and small amplitude at $Re \approx 115$ (**a**), the transition to a stable oscillation with smaller amplitude $Re \approx 135$ (**b**) and the transition to an unstable oscillation at $Re \approx 225$ (**c**). Note the different scaling on the vertical axis in the bottom row. On the horizontal axis we always show an interval of 2 s. (**a**) $Re = 115$ and $Re = 120$, (**b**) $Re = 135$ and $Re = 140$, (**c**) $Re = 220$ and $Re = 225$

Chapter 12
Fluid-structure Interaction with Contact

Guest Article by Stefan Frei
University College London
s.frei@ucl.ac.uk

Based on the dissertation
Eulerian finite element methods for interface problems and fluid-structure interactions.
Universität Heidelberg 2016 [151].

In this chapter, we revisit the problem of an elastic ball falling down towards the ground by gravity within a viscous fluid, that was already briefly discussed in Sect. 6.6.3. To deal with the topology change at contact time, we use a *Fully Eulerian approach* as introduced in Sect. 3.6 and detailed in Chap. 6.

An accurate study of the contact dynamics requires discretization techniques in space and time that take into account the interface movement. Here, we will use the *locally modified finite element* technique introduced in Sect. 4.5 for accurate space discretization and the modified Galerkin approach as described in Sect. 4.6 for time discretization.

We will be especially interested in the question of whether it comes to contact between ball and ground, or whether a thin fluid layer remains in between them. From the point of view of analysis, this is an open problem if the ball is considered elastic, cf. Remark 6.13. Physical experiments indicate that it comes to real contact in many situations, consider e.g. the fall of a steel ball towards the ground within air. In this case, some of the assumptions made in the derivation of the incompressible Navier-Stokes equations will not be valid anymore (e.g. the continuum assumption, a linear stress-strain-relationship and incompressibility). Due to the lack of a validated model for the fluid for the case of contact, however, we stick here to the incompressible Navier-Stokes equations, expecting that the small time slot around the contact interval, where they are not an appropriate model, does not influence the dynamics too much.

If it comes to contact, we have to deal with variational inequalities. Here, we use a simple contact algorithm based on a penalty formulation, motivated by a work of Sathe and Tezduyar [298].

T. Richter, *Fluid-structure Interactions*, Lecture Notes in Computational Science and Engineering 118, DOI 10.1007/978-3-319-63970-3_12

12.1 Problem Setting and Equations

We begin with a simple model problem, see Fig. 12.1, where an elastic ball falls down towards the planar ground $\Gamma_w = \{(x, y) \in \mathbb{R}^2 \,|\, y = -1\}$ by a gravity force. We consider a ball of radius $r = 0.4$ whose midpoint is initially located at the origin. As boundary condition, we impose a homogeneous velocity on Γ_w. In combination with the *kinematic condition* and the velocity—displacement relation $d_t \mathbf{u}_s = \mathbf{v}_s$ this ensures that the ball cannot pass "through the ground". We assume that the simulation domain $\Omega = (-1, 1) \times (-1, 0.5)$ is open on the lateral and upper boundaries and use the *do-nothing* outflow condition there.

The corresponding variational formulation in fully Eulerian coordinates reads (cf. Problem (6.6)):

Find the global velocity $\mathbf{v} \in \mathbf{v}^D + \mathcal{V}$, *the solid displacement* $\mathbf{u}_s \in \mathbf{u}_s^D + \mathcal{W}_s$, *and the fluid pressure* $p_f \in \mathcal{L}_f$ *such that*

$$\begin{aligned} &(\rho(\partial_t \mathbf{v} + \mathbf{v} \cdot \nabla \mathbf{v}), \phi)_\Omega \\ &\quad + (\boldsymbol{\sigma}, \nabla \phi)_\Omega - \langle \rho_f \nu_f \nabla \mathbf{v}^T \mathbf{n}_f, \phi \rangle_{\Gamma_f \setminus \Gamma_f^d} = (\rho \mathbf{f}, \phi)_\Omega \quad \forall \phi \in \mathcal{V}, \\ &\quad (\partial_t \mathbf{u}_s + \mathbf{v} \cdot \nabla \mathbf{u}_s - \mathbf{v}, \psi_s)_{\mathcal{S}(t)} = 0 \quad \forall \psi_s \in \mathcal{W}_s, \\ &\quad (\operatorname{div} \mathbf{v}, \xi_f)_{\mathcal{F}(t)} = 0 \quad \forall \xi_f \in \mathcal{L}_f. \end{aligned} \tag{12.1}$$

Here we have used the abbreviations $\rho|_{\mathcal{S}} = \rho_s = J\rho_s^0$ and $\rho|_{\mathcal{F}} = \rho_f$. Furthermore, we have defined $\boldsymbol{\sigma}|_{\mathcal{F}} = \boldsymbol{\sigma}_f$ and $\boldsymbol{\sigma}|_{\mathcal{S}} = \boldsymbol{\sigma}_s$ and analogously for the right-hand side $\mathbf{f}$. The function spaces are given by

$$\mathcal{V} = H_0^1(\Omega; \Gamma_f^d \cup \Gamma_s^d)^2, \quad \mathcal{W}_s := H_0^1(\mathcal{S}(t); \Gamma_s^d)^2, \quad \mathcal{L}_f := L^2(\mathcal{F}(t)).$$

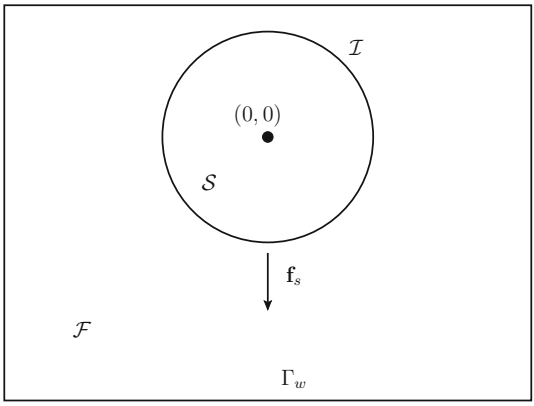

Fig. 12.1 Sketch of the configuration of the first test case

The fluid boundary term on the left-hand side stems from the fact that the full symmetric stress tensor

$$\boldsymbol{\sigma}_f = \rho_f \nu_f (\nabla \mathbf{v} + \nabla \mathbf{v}^T) - p_f I$$

enters the fluid equations, while the *do-nothing* condition on $\Gamma_f \setminus \Gamma_f^d$ includes the reduced stress tensor $\boldsymbol{\sigma}_f^{\text{red}} = \rho_f \nu_f \nabla \mathbf{v}_f - p_f I$. For the solid, we use a St.Venant Kirchhoff material law

$$\boldsymbol{\sigma}_s = J_s \mathbf{F}_s^{-1} \left(2\mu_s \mathbf{E}_s + \lambda_s \text{tr}(\mathbf{E}_s)\right) \mathbf{F}_s^{-T}. \tag{12.2}$$

with the Green-Lagrange strain $\mathbf{E}_s = \frac{1}{2}(\mathbf{F}_s^{-T}\mathbf{F}_s^{-1} - I)$.

To capture the moving interface, we use the initial point set method, as described in Sect. 6.2. The system is supplemented with the initial conditions

$$\mathbf{v}(x,0) = \mathbf{v}^0(x) \quad \text{in } \Omega, \qquad \mathbf{u}(x,0) = \mathbf{u}^0(x) \quad \text{in } \mathcal{S}(0).$$

12.2 Space Discretization and Pressure Stabilization

For spatial discretization, we use *equal-order* locally modified finite elements (cf. Sect. 4.5) for all the components of the solution. For ease of implementation, we use the global space $\mathcal{V}_h$ on the whole domain Ω for all the variables and use artificial extensions of the fluid pressure p_f and the solid displacement $\mathbf{u}_s$ to the complete domain Ω.

This choice for velocity and pressure violates the *inf-sup* condition in the fluid problem that is necessary to ensure the well-posedness of the discrete system of equations, cf. Sect. 4.3.2. To cope with this, we will add stabilization terms to the discrete variational formulation.

The challenge for pressure stabilization within the *locally modified finite element method* lies in the anisotropies that are present in the interface region including abrupt changes of anisotropy between neighboring cells, see Fig. 12.2 for an example. Typically, the stabilization methods used on anisotropic meshes require an assumption on the change of anisotropy between neighboring cells that can not be guaranteed here (see e.g. Braack and Richter [62]).

To deal with this, we will use a variant of the *Continuous Interior Penalty* (CIP) stabilization technique introduced by Burman and Hansbo [84–86]. We denote the set of cells of the fluid domain by Ω_h^f and the set of edges by $\mathcal{E}_h$. The original CIP technique is based on penalizing jumps of the gradient over element edges

$$S(p_h, \xi_h) := \gamma h^s \sum_{e \in \mathcal{E}_h} \int_e [\nabla p_h]_e \cdot [\nabla \xi_h]_e \, do,$$

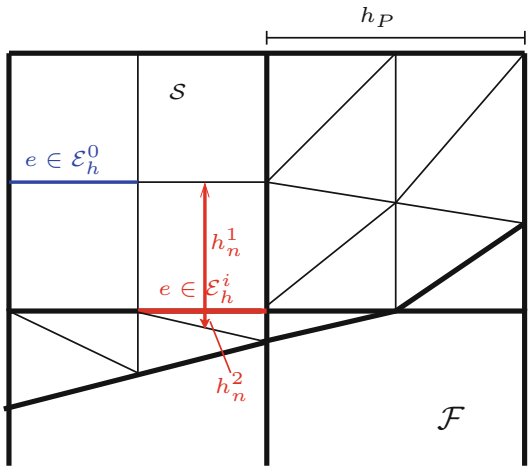

Fig. 12.2 Sketch of four patches in the interface region. The cell sizes in normal direction h_n^1 and h_n^2 for $e \in \mathcal{E}_h^i$ vary significantly

with $s = 2$ or $s = 3$. This does not guarantee stability in the case of abrupt changes of anisotropy, however, as the cell sizes of the two neighboring cells in direction normal to the edge can be very different. Hence, we have to modify this technique in the interface patches. Here, we will use a weighted average of the pressure gradient instead of the jump terms.

To define a variant suitable for anisotropic meshes, we split the set of edges into two parts: By $\mathcal{E}_h^0$, we denote all edges that lie between two quadrilateral cells $K_1, K_2 \subset \Omega_h^f$. By $\mathcal{E}_h^i$ we denote the edges that are edges of at least one triangular element $K \subset \Omega_h^f$, see Fig. 12.2. In other words, this means that $\mathcal{E}_h^i$ contains all edges that are part of patches cut by the interface.

We define the stabilization term by

$$S_{\text{aniso}}(p_h, \xi_h) := \gamma h_P^2 \sum_{e \in \mathcal{E}_h^i} \int_e \{h_n \nabla p_h \cdot \nabla \xi_h\}_e \, \mathrm{d}o + \gamma h_P^2 \sum_{e \in \mathcal{E}_h^0} \int_e h_n [\nabla p_h]_e \cdot [\nabla \xi_h]_e \, \mathrm{d}o,$$

where $\gamma > 0$ is a constant, h_P is the size of the patch, h_n is the cell size in the direction normal to e, $[\cdot]_e$ denotes the jump term across the edge e and

$$\{\mathbf{v}_h\}_e := \frac{1}{2} \left(\mathbf{v}_{h|K_1} + \mathbf{v}_{h|K_2} \right)$$

is the mean value of the two cells K_1, K_2 sharing the edge e. In the case that one of the cells K_1, K_2 does not lie in Ω_h^f, we set the respective contribution to zero. This term is then added to the divergence equation

$$(\text{div } \mathbf{v}_h, \xi_h)_{\mathcal{F}(t)} + S_{\text{aniso}}(p_h, \xi_h) = 0 \quad \forall \xi_h \in \mathcal{V}_h^f.$$

In contrast to the original CIP technique this stabilization is not consistent anymore, in the sense that the continuous solution fulfills the discrete, stabilized system. However, it can been shown [151] that the inconsistency is sufficiently small, such that the stabilized, discrete solution is of second-order, as is the discretization error of the *locally modified finite element* scheme of order one.

12.3 Time Discretization

For time discretization, we use the dG(0) variant of the modified time stepping scheme presented in Sect. 4.6. In this section, we will give practical details on how to compute a suitable mapping $T_m : \Omega_m \times I_m \to Q^m$ for a time interval $m = 1, \ldots, M$.

To simplify the implementation, we use the old deformation u^{m-1} to define the subdomains $\mathcal{F}^m$ and $\mathcal{S}^m$ and the interface $\mathcal{I}^m$ explicitly. Note that a fully implicit integration of the domain affiliation within a Newton-type algorithm would require the calculation of shape derivatives, compare Sect. 6.4.

Then, we use the new domain Ω^m as reference domain for the time interval $I_m = [t_{m-1}, t_m]$ and define a map $T_m : \Omega_m \times I_m \to Q^m$ which is linear in time. We define

$$T_m(x,t) = \frac{t_m - t}{t_m - t_{m-1}} T_m(x, t_{m-1}) + \frac{t - t_{m-1}}{t_m - t_{m-1}} x. \tag{12.3}$$

This implies in particular $T_m(x, t_m) = x$. It remains to specify the mapping T_m at time t_{m-1} in such a way that points x lying on the interface $\mathcal{I}(t_m)$ at time t_m are mapped to points on the interface $\mathcal{I}(t_{m-1})$ at time t_{m-1}. We have already seen in the numerical example in Sect. 4.6 that this requirement is fulfilled by the function

$$\tilde{T}_m(t_{m-1}) = (\Psi_{\text{IPS}}(t_{m-1}))^{-1} \circ \Psi_{\text{IPS}}(t_m)$$

where $\Psi_{\text{IPS}}(t_k)$ denotes the *Initial Point Set* function at time t_k that has been introduced in Sect. 6.2. In practice, we calculate $x^{m-1} := \tilde{T}_m(x^m, t_{m-1})$ in a point $x^m \in \Omega^m$ by applying Newton's method to

$$\Psi_{\text{IPS}}(t_{m-1})(x^{m-1}) = \Psi_{\text{IPS}}(t_m)(x^m),$$

i.e.

$$x^{m-1} - u^{m-2}(x^{m-1}) = x^m - u^{m-1}(x^m). \tag{12.4}$$

It is sufficient to use this mapping $\tilde{T}_m$ in the interface region. Far away from the interface, we define T_m as the identity. In between, we define a smooth transition by using a function g depending on the distance to the interface with $g = 1$ in a point $x \in \Omega^{m-1}$ with $\mathrm{dist}_{\mathcal{I}(t_{m-1})}(x) < \varepsilon$ and $g = 0$ if $\mathrm{dist}_{\mathcal{I}(t_{m-1})}(x) > \delta$ for $\delta > \varepsilon > 0$. We set

$$T_m(t,x) = g(x)\tilde{T}_m(t,x) + (1 - g(x))\,\mathrm{id}.$$

The modified $dG(0)$ time stepping scheme for the fluid-structure interaction problem (12.1) reads: *Find* $\mathbf{v} \in (\mathbf{v}^D + \mathcal{V}^m)$, $\mathbf{u}_s \in (\mathbf{u}_s^D + \mathcal{W}_s^m)$, *and* $p_f \in \mathcal{L}_f^m$ *such that*

$$\begin{aligned}
(\rho(\mathbf{v}^m - \mathbf{v}^{m-1}), \phi)_{\Omega^m} + k(\rho(\mathbf{v}^m - \partial_t T_m)\nabla\mathbf{v}^m, \phi)_{\Omega^m} + k(\boldsymbol{\sigma}, \nabla\phi)_{\Omega^m} \\
-k\langle \rho_f \nu_f \nabla^T \mathbf{v}_f^m \mathbf{n}, \phi\rangle_{\Gamma_f \setminus \Gamma_f^D} = k(\mathbf{f}^m, \phi)_{\Omega^m}, \\
(\mathbf{u}^m - \mathbf{u}^{m-1} - k\mathbf{v}^m, \psi_s)_{\mathcal{S}^m} + k((\mathbf{v}^m - \partial_t T_m)\nabla\mathbf{u}^m, \psi_s)_{\mathcal{S}^m} = 0, \\
(\mathrm{div}\ \mathbf{v}^m, \xi_f)_{\mathcal{F}(t)} + S(p^m, \xi_f) = 0
\end{aligned}$$

for all $\phi \in \mathcal{V}^m$, $\psi_s \in \mathcal{W}_s^m$ and for all $\xi_f \in \mathcal{L}_f^m$.

The only quantity related to the transformation to be calculated is $\partial_t T$. Therefore, we first compute the point $x^{m-1} = T_m(x^m, t_{m-1})$ by (12.4). Now, differentiating (12.3) yields

$$\partial_t T(x^m, t_m) = \frac{x^m - x^{m-1}}{t_m - t_{m-1}}.$$

With this time stepping scheme, we can get arbitrarily close to contact. Real contact is not possible, however, as this would destroy the local regularity of the mapping T_m. To cope with this, we modify the scheme in the contact region when the ball comes close to the ground by choosing $T_m = \mathrm{id}$ there.

12.4 Stabilization of the Solid Equations

The full fluid-structure interaction problem (12.1) contains a regularity problem at the interface $\mathcal{I}(t)$, as described in Sect. 3.1.4. The natural trial space for the solid velocity in the variational formulation is $L^2(\mathcal{S}(t))^2$, which means that a trace on the interface $\mathcal{I}(t)$ is not well-defined. The trace is however needed for the *kinematic* interface condition $\mathbf{v}_f = \partial_t \mathbf{u}_s$ on $\mathcal{I}(t)$. Furthermore, numerical tests show that the solid velocity is sensitive to stability problems caused by perturbations or discretization errors, especially in the interface region (see Chap. 4 in [151]).

To analyze this problem, we will first of all focus on the simplest form of a solid equation, a linear wave equation on a fixed domain $\mathcal{S}$, and study different techniques

to handle the aforementioned problems. In mixed variational formulation, the system of equations is given by: *Find* $\mathbf{u} \in \mathcal{W}, \mathbf{v} \in \mathcal{V}$ *such that*

$$\begin{aligned} (\partial_t \mathbf{v}, \phi)_{\mathcal{S}} + \lambda(\nabla \mathbf{u}, \nabla \phi)_{\mathcal{S}} = 0 \quad \forall \phi \in \mathcal{W}, \\ (\partial_t \mathbf{u}, \psi)_{\mathcal{S}} - (\mathbf{v}, \psi)_{\mathcal{S}} = 0 \quad \forall \psi \in \mathcal{V}, \end{aligned} \tag{12.5}$$

with a positive parameter $\lambda > 0$. Testing with $\phi = \partial_t \mathbf{u}$ and $\psi = \partial_t \mathbf{v}$ and integrating by parts in time, we see that the homogeneous wave equation is energy-conserving in the following sense for $t > 0$

$$\lambda \|\nabla \mathbf{u}(t)\|_{\mathcal{S}}^2 + \|\mathbf{v}(t)\|_{\mathcal{S}}^2 = \lambda \|\nabla \mathbf{u}(0)\|_{\mathcal{S}}^2 + \|\mathbf{v}(0)\|_{\mathcal{S}}^2. \tag{12.6}$$

Hence, any kind of perturbations will not be damped, but it is conserved and may accumulate over time. Furthermore, (12.6) gives neither control over derivatives of $\mathbf{v}$ nor over the trace of $\mathbf{v}$ on the boundary of $\mathcal{S}$.

To increase the stability, we use a simple, stabilization technique: *Find* $\mathbf{u}_h \in \mathcal{W}_h, \mathbf{v}_h \in \mathcal{V}_h$ *such that*

$$\begin{aligned} (\partial_t \mathbf{v}_h, \phi_h)_{\mathcal{S}} + \lambda(\nabla \mathbf{u}_h, \nabla \phi_h)_{\mathcal{S}} = 0 \quad \forall \phi_h \in \mathcal{W}_h, \\ (\partial_t \mathbf{u}_h, \psi_h)_{\mathcal{S}} - (\mathbf{v}_h, \psi_h)_{\mathcal{S}} - \alpha h^s (\nabla \mathbf{v}_h, \nabla \psi_h)_{\mathcal{S}} = 0 \quad \forall \psi_h \in \mathcal{V}_h. \end{aligned} \tag{12.7}$$

The exponent s is typically chosen in the interval $s \in [1, 2]$, see [151]. For this formulation, the energy conservation reads

$$\begin{aligned} \lambda \|\nabla \mathbf{u}_h(t)\|_{\mathcal{S}}^2 + \|\mathbf{v}_h(t)\|_{\mathcal{S}}^2 + \alpha h^s \|\nabla \mathbf{v}_h(t)\|_{\mathcal{S}}^2 \\ = \lambda \|\nabla \mathbf{u}_h(0)\|_{\mathcal{S}}^2 + \|\mathbf{v}_h(0)\|_{\mathcal{S}}^2 + \alpha h^s \|\nabla \mathbf{v}_h(0)\|_{\mathcal{S}}^2. \end{aligned} \tag{12.8}$$

We conclude that this formulation gives us control over the derivatives of $\mathbf{v}_h$ and thus (by the trace lemma) over the trace of the velocity on $\partial\mathcal{S}$.

To further motivate, why this formulation increases stability, we consider a standard time discretization with the backward Euler method and multiply the second equation by -1. Problem (12.7) reads in matrix form

$$\begin{pmatrix} \lambda A_h & \frac{1}{k} M_h \\ -\frac{1}{k} M_h & M_h + \alpha h^s A_h \end{pmatrix} \begin{pmatrix} \mathbf{u}_h^{m+1} \\ \mathbf{v}_h^{m+1} \end{pmatrix} = \begin{pmatrix} \frac{1}{k} \mathbf{v}_h^m \\ -\frac{1}{k} \mathbf{u}_h^m \end{pmatrix}, \tag{12.9}$$

where M_h is the discrete mass matrix and A_h the discrete Laplacian. We see that the stabilization term increases the diagonal part of the matrix significantly, especially for $s \leq 2$. It can be interpreted as adding artificial diffusion to the diagonal part of the system matrix. For the derivation of a priori error estimates depending on s for the stabilized, discrete formulation, we refer to [151, 152].

12.5 Treatment of Contact

In the cases where no fluid layer remains between the ball and the ground, we have to apply a contact algorithm to simulate the bounce-off of the ball. A simple contact algorithm has been used by Sathe and Tezduyar [298]. The idea is to add an artificial contact force g_c on the interface to the balance of momentum if the ball comes very close to the ground. The force depends on the distance to the ground and goes to infinity as the distance tends to zero. Hence, contact becomes in principle impossible. In this way, the modeling issues connected to the Navier-Stokes equations and contact that were mentioned at the beginning of this chapter are to a certain degree circumvented. We will see below, however, that numerical contact might still happen, at least unless the time step size is chosen sufficiently small.

The modified interface condition reads

$$(\boldsymbol{\sigma}_f - g_c I)\mathbf{n}_f = \boldsymbol{\sigma}_s \mathbf{n}_f,$$

where the contact force is defined by

$$g_c(x) = \begin{cases} 0 & \operatorname{dist}(x, \Gamma_w) \geq \operatorname{dist}_0, \\ \gamma_c \frac{\operatorname{dist}(x,\Gamma_w) - \operatorname{dist}_0}{\operatorname{dist}(x,\Gamma_w)} & \operatorname{dist}(x, \Gamma_w) < \operatorname{dist}_0, \end{cases}$$

on $\mathcal{I}$ with a contact parameter γ_c and a reference distance dist_0.

More involved contact strategies are based on variational inequalities (see e.g. Diniz dos Santos et al. [122], Mayer et al. [237], Pironneau [259]) imposing the constraint

$$\operatorname{dist}(x, \Gamma_w) \geq 0 \quad \text{on } \mathcal{I}.$$

To ensure the well-posedness of the system of equations, a Lagrange multiplier is added to the balance of momentum that acts similar to the contact force g_c when the constraint is active. Due to the additional computational complexity of numerical algorithms for variational inequalities, we stick here to the prior simple contact algorithm. For further studies we refer to the literature [155].

12.6 Numerical Examples

12.6.1 Example 1: Configuration Without Contact

For the first test, we use the Lamé parameters $\mu_s = 2 \cdot 10^5\,\mathrm{kg \cdot m^{-1} s^{-2}}$ and $\lambda_s = 8 \cdot 10^5\,\mathrm{kg \cdot m^{-1} s^{-2}}$ and the fluid viscosity $\nu_f = 10^{-3}\,\mathrm{m^2 \cdot s^{-1}}$. The fluid and solid density are $\rho_s = \rho_f = 10^3\,\mathrm{kg \cdot m^{-3}}$. In this example, we do not apply the

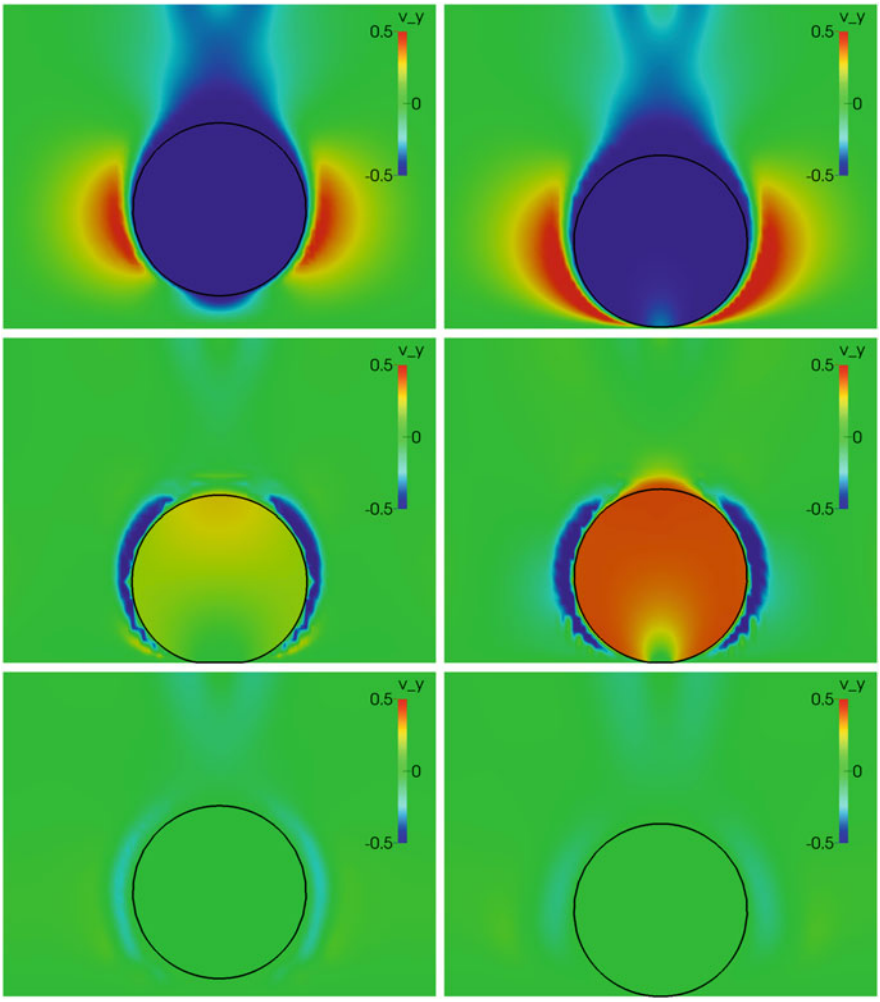

Fig. 12.3 Illustration of the free fall of an elastic ball, its contact with the ground and the subsequent rebound at six different times. The color illustrates the vertical velocity $\mathbf{v}_y$ and the *black contour line* is the discrete interface

contact force introduced in Sect. 12.5, as it turns out that for this specific choice of parameters, a small fluid layer remains between ball and bottom anyway.

In Fig. 12.3, we show the falling ball at six different instances of time. First, the ball is accelerated by gravity and falls down. At time $t \approx 1.6\,\mathrm{s}$, the bottom is almost reached and the ball slows down due to a high fluid pressure. It comes closest to the ground at time $t \approx 1.8\,\mathrm{s}$, where the minimal distance is $d \approx 1.2 \cdot 10^{-3}\,\mathrm{m}$. At this time the ball is significantly compressed at its bottom.

The discretization at this point is illustrated in Fig. 12.4 (top) for the coarsest mesh we used. The interface shows a domed shape due to a high fluid pressure in the middle (see Fig. 12.5) and the minimal distance is not attained in the center but left and right of it. In this configuration, there is no real contact but a small layer of fluid remains between ball and ground. Nevertheless, here and in the following we will call this period the "contact time" or "contact interval" for simplicity.

Then, due to the compression at the bottom the ball is accelerated upwards. The ball reaches its highest elevation at a maximum distance $d \approx 8.3 \cdot 10^{-2}$ m from the ground at time $t \approx 2.4$ s and falls down again. After a smaller second bounce with distance $d \approx 4.6 \cdot 10^{-3}$ m, it comes to rest, being in real contact with the ground at

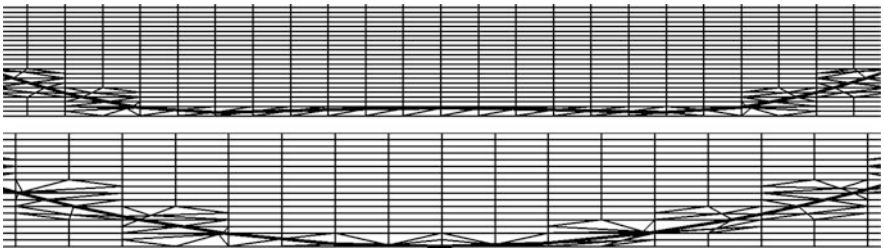

Fig. 12.4 Illustration of a coarse mesh during the first rebound (*top sketch*) and at the end time when the ball is at rest (*lower sketch*). During the first rebound, a small layer of fluid remains between ball and ground

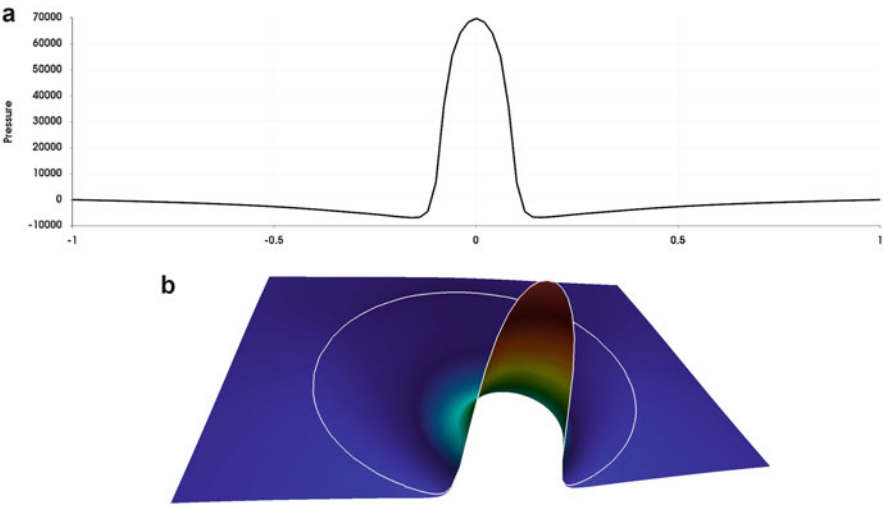

Fig. 12.5 Pressure peak during the contact between ball and ground. (**a**) Pressure value along the boundary line $\Gamma_w = \{(x, -1),\ 0 < x < 1\}$. (**b**) Pressure close to contact. Inside the ball we show the harmonic extension of the pressure (without a physical connotation). The *white contour line* shows the boundary of the elastic ball

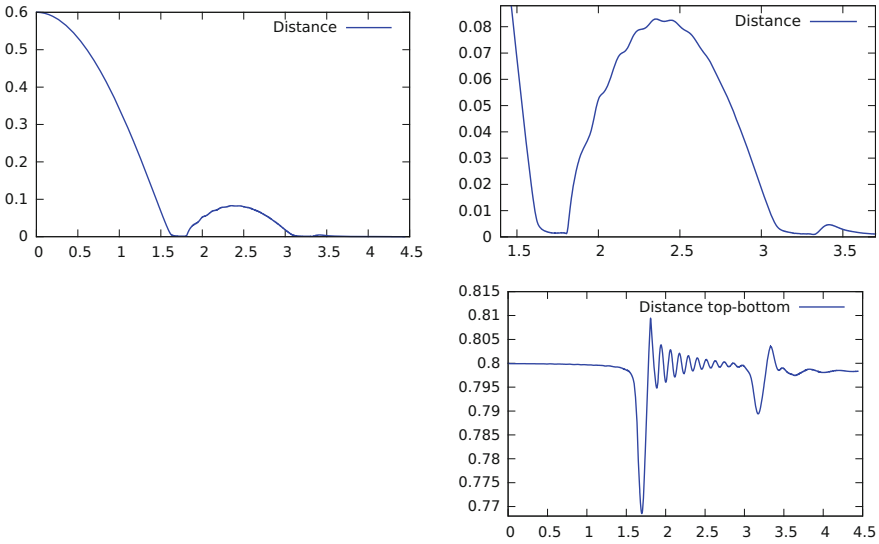

Fig. 12.6 Distance of the ball from the bottom and width of the ball. *Top:* Minimal distance between ball and ground over time and a zoom-in at the interval of contact and rebound. *Right:* Size of the ball (distance between *top and bottom*)

time $t \approx 4.4\,\mathrm{s}$, see Fig. 12.4 (bottom) for an illustration of the mesh at the time of real contact.

In Fig. 12.6, we plot the minimal distance between the ball and the ground including a zoom-in of the contact and rebound interval in the upper row. Furthermore, we show the distance between the top and the bottom of the ball and an averaged vertical velocity of the solid in the lower row.

In the lower left plot, we observe that the distance between the top and the bottom of the ball attains minima at the two contact times due to the compression. After the rebounds, we observe oscillations that get smaller over time. These oscillations are physical: First, the ball is maximally compressed at the bottom at the contact time. Once the ball bounces off again, the deformation is relaxed. The ball is even overstretched at some point and starts to oscillate between an expanded and a compressed state periodically.

12.6.2 Convergence Studies

We study the test configuration on different grids and for different time step sizes. The finite element meshes, we use are highly refined in the contact region. The coarsest mesh consists of patches of size of size $2.5 \cdot 10^{-2}\,\mathrm{m} \times 3.1 \cdot 10^{-3}\,\mathrm{m}$ in the contact region and $0.1\,\mathrm{m} \times 0.15\,\mathrm{m}$ in the upper right and upper left part. Furthermore,

Table 12.1 *Top:* Minimal distance between ball and ground during the first contact interval and maximal distance after the first rebound

	First contact: minimum distance			First bounce: maximum distance		
#nodes \ k	$2 \cdot 10^{-3}$	$1 \cdot 10^{-3}$	$5 \cdot 10^{-4}$	$2 \cdot 10^{-3}$	$1 \cdot 10^{-3}$	$5 \cdot 10^{-4}$
4225	$6.38 \cdot 10^{-4}$	$6.49 \cdot 10^{-4}$	$6.26 \cdot 10^{-4}$	$4.71 \cdot 10^{-2}$	$5.19 \cdot 10^{-2}$	$5.20 \cdot 10^{-2}$
16641	$1.22 \cdot 10^{-3}$	$1.24 \cdot 10^{-3}$	$1.24 \cdot 10^{-3}$	$7.41 \cdot 10^{-2}$	$8.29 \cdot 10^{-2}$	$8.49 \cdot 10^{-2}$
66049	–	$1.27 \cdot 10^{-3}$	$1.27 \cdot 10^{-3}$	–	$8.71 \cdot 10^{-2}$	$8.96 \cdot 10^{-2}$

	Relative mass conservation error		
#nodes \ k	$2 \cdot 10^{-3}$	$1 \cdot 10^{-3}$	$5 \cdot 10^{-4}$
4225	$8.96 \cdot 10^{-3}$	$8.94 \cdot 10^{-3}$	$8.94 \cdot 10^{-3}$
16641	$2.54 \cdot 10^{-3}$	$2.36 \cdot 10^{-3}$	$2.31 \cdot 10^{-3}$
66049	–	$5.07 \cdot 10^{-4}$	$5.05 \cdot 10^{-4}$

Bottom: Relative error in mass conservation at time $t = 3$ s. The three functionals are calculated for three different time step sizes and on three different meshes

we show the results on two finer meshes that are obtained from this coarse mesh by global refinement.

In the upper part of Table 12.1, we show the minimal distance during the first contact and the maximum elevation after the first rebound and the error in mass conservation on these meshes for three different time step sizes. We observe that both the minimal distance during the contact and the maximal distance after the rebound are significantly smaller on the coarsest mesh. On the other hand, the results on the finer meshes show good agreement. While on the finest mesh, the minimum distance, i.e. the minimum height of the fluid layer, is a little less then two patches, on the coarsest patch only about a quarter of a patch remains on the fluid side at the narrowest point. We conclude that the resolution of the contact region on the coarse mesh was not fine enough to resolve the contact dynamics appropriately.

In the lower part of Table 12.1, we show the relative error in mass conservation is defined by

$$j_{\text{mass}} = \left| \frac{\pi r^2 \rho_s^0 - \int_S J \rho_s^0 \, \mathrm{dx}}{\pi r^2 \rho_s^0} \right|$$

for different spatial and temporal discretization parameters. We observe a good convergence behavior in both space and time, even on the coarsest mesh. The spatial discretization error is dominating and decreases with order $\mathcal{O}(h_P^2)$. This convergence behavior was expected, as it is the approximation error of the interface, see Sect. 4.5. Furthermore, this result indicates that the Eulerian approach in combination with the described discretization techniques, shows very good mass conservation properties.

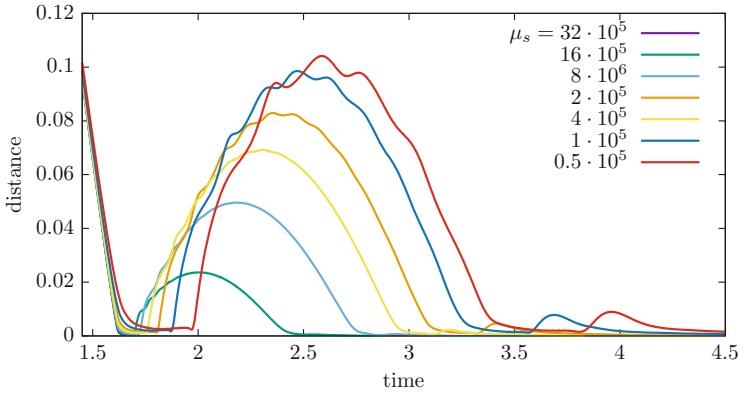

Fig. 12.7 Distance between ball and ground over time for different solid parameters μ_s during the contact and rebound interval. The first Lamé parameter is chosen as $\lambda_s = 4\mu_s$. The rebound height is higher for softer solids

12.6.3 Influence of Material Parameters

Next, we want to address the question of whether a small layer of fluid is maintained between ball also for different parameters. Therefore, we increase and decrease the solid Lamé parameters, keeping the ratio between the Lamé parameters μ_s and λ_s constant, $\lambda_s = 4\mu_s$ (which corresponds to a Poisson ration of $\nu_s = 0.4$).

For a set of parameters ranging from $\mu_s = 5 \cdot 10^4\,\mathrm{kg \cdot m^{-1}s^{-2}}$ to $3.2 \cdot 10^6\,\mathrm{kg \cdot m^{-1}s^{-2}}$, we plot the distances between ball and ground over time in Fig. 12.7. For the stiffest material ($\mu_s = 3.2 \cdot 10^6\,\mathrm{kg \cdot m^{-1}s^{-2}}$) no fluid layer remains during the first contact interval. Ball and ground are in real contact. Once the ball is in contact with the ground, the *no-slip* condition on Γ_w used here, prevents it from bouncing. The same happens for the second stiffest material ($\mu_s = 1.6 \cdot 10^6\,\mathrm{kg \cdot m^{-1}s^{-2}}$) at the second contact time. It is, however, questionable, whether this corresponds to the physical situation. Instead, the contact might be caused by numerical errors due to a too large time step or an insufficient grid resolution in the contact region. We will use the configuration with the largest Lamé parameters below to study the proposed contact algorithm.

For the remaining parameters, the solid bounces twice. Due to a higher compression during the contact, the first and the second rebound heights are bigger, the softer the solid is.

12.6.4 Contact Algorithm

As the simple contact algorithm used is not physically motivated, but is based on an artificial force g_d, we have to analyze its effect on the contact dynamics. Therefore,

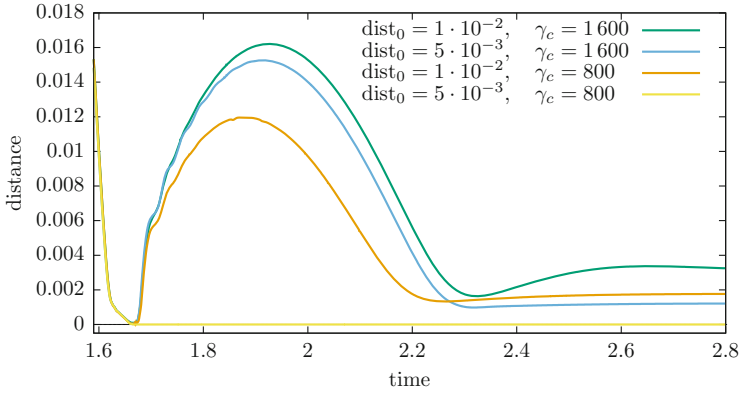

Fig. 12.8 Influence of different contact parameters γ_c and dist_0 for the Lamé parameters $\mu_s = 3.2 \cdot 10^6\,\text{kg} \cdot \text{m}^{-1}\text{s}^{-2}$, $\lambda_s = 1.28 \cdot 10^7\,\text{kg} \cdot \text{m}^{-1}\text{s}^{-2}$. The contact force with parameters $\gamma_c = 800$ and $\text{dist}_0 = 5 \cdot 10^{-3}$ m as well as for $\gamma_c \leq 400$ or $\text{dist}_0 \leq 10^{-3}$ m was not large enough to prevent the contact

we consider the situation from above with the stiffest material parameters $\mu_s = 3.2 \cdot 10^6\,\text{kg} \cdot \text{m}^{-1}\text{s}^{-2}$ and $\lambda_s = 1.28 \cdot 10^7\,\text{kg} \cdot \text{m}^{-1}\text{s}^{-2}$ where a contact algorithm is necessary. We use $\text{dist}_0 = 10^{-3}$ m, $5 \cdot 10^{-3}$ m and 10^{-2} m and the contact parameters $\gamma_c = 800$ and 1600.

For the smallest contact distance $\text{dist}_0 = 10^{-3}$ m, contact could not be prevented with the chosen time step and grid size. The same occurred for $\text{dist}_0 = 5 \cdot 10^{-3}$ m and the smaller parameter $\gamma_c = 800$. We plot the distances to the ground over time in Fig. 12.8 for the calculations with $\text{dist}_0 \geq 5 \cdot 10^{-3}$ m. The plot shows significant differences. For example, for the largest parameters $\text{dist}_0 = 10^{-2}$ m and $\gamma_c = 1600$, the rebound height is 35% bigger than for the same reference distance with $\gamma_c = 800$.

Furthermore, the ball stays at rest at a distance of $3.18 \cdot 10^{-3}$ m from the ground which is rather large compared to $\text{d}_{\text{rest}} \approx 1.77 \cdot 10^{-3}$ m for $\gamma_c = 800$ and $\text{d}_{\text{rest}} \approx 1.21 \cdot 10^{-3}$ m for $\text{dist}_0 = 5 \cdot 10^{-3}$ m. Here it is obvious that this distance depends more on the artificial contact force than on physical effects.

We conclude that the contact parameters have to be chosen carefully and their influence must be taken into account when interpreting the results. The investigation of more sophisticated contact algorithms is subject to ongoing research.

12.6.5 Example 2: Bouncing Down the Stairs

Finally, we will study a more complex numerical example, i.e. an elastic ball bouncing down some stairs. We give a sketch of the geometry under consideration in Fig. 12.9. In order to get the desired direction, we let the ball bounce on an inclined

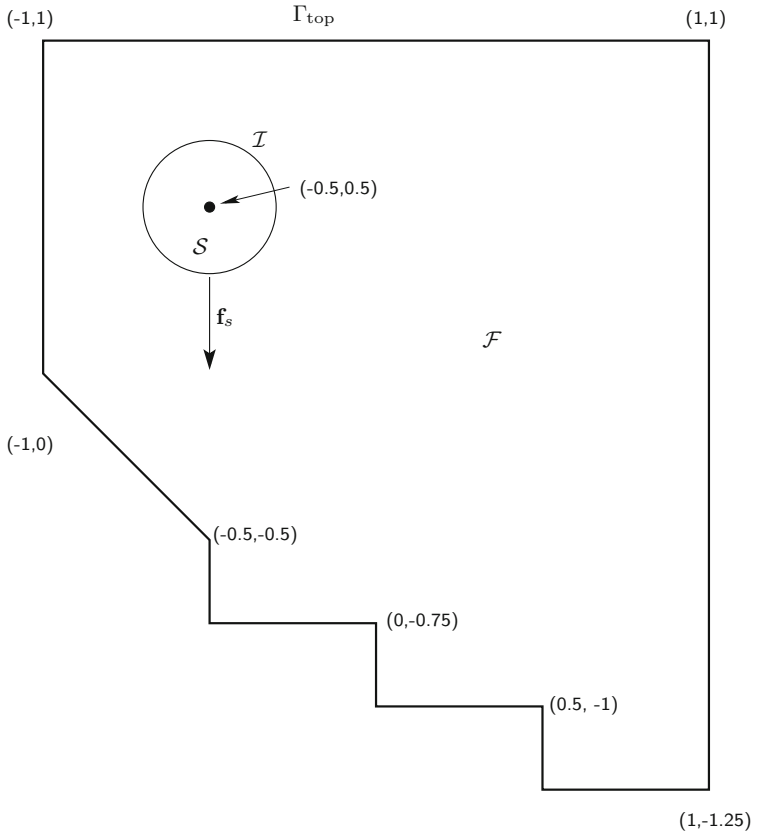

Fig. 12.9 Sketch of the configuration of the second example and the initial mesh. To simulate the contact dynamics accurately, fine mesh cells are used in the contact regions

plane first. Afterwards, it bounces down three stairs. Depending on the material parameters it can bounce once or several times on a stair or just roll over it. We consider the lower, left and right walls as rigid and impose a homogeneous Dirichlet condition for the velocity there. On the top Γ_{top}, we use again a *do-nothing* boundary condition. We use the same material parameters as in Sect. 12.6.1 and vary only the fluid density to $\rho_f = 100\,\text{kg}\cdot\text{m}^{-3}$, $150\,\text{kg}\cdot\text{m}^{-3}$, $300\,\text{kg}\cdot\text{m}^{-3}$ and $1000\,\text{kg}\cdot\text{m}^{-3}$.

We show snapshots of the horizontal velocity at twelve different times in Fig. 12.10 for $\rho_f = 300\,\text{kg}\cdot\text{m}^{-3}$. The ball drops onto the inclined plane and bounces to the right. The next contact is on the right part of the first stair. Afterwards, we observe three bounces on the second stair and two on the third one, before the ball comes to rest.

In Fig. 12.11, we show contours of the ball for calculations with $\rho_f = 100\,\text{kg}\cdot\text{m}^{-3}$, $150\,\text{kg}\cdot\text{m}^{-3}$, $300\,\text{kg}\cdot\text{m}^{-3}$ and $1000\,\text{kg}\cdot\text{m}^{-3}$. For the two larger density values, we use a contact force with parameters $\gamma_c = 5\cdot 10^3$ and

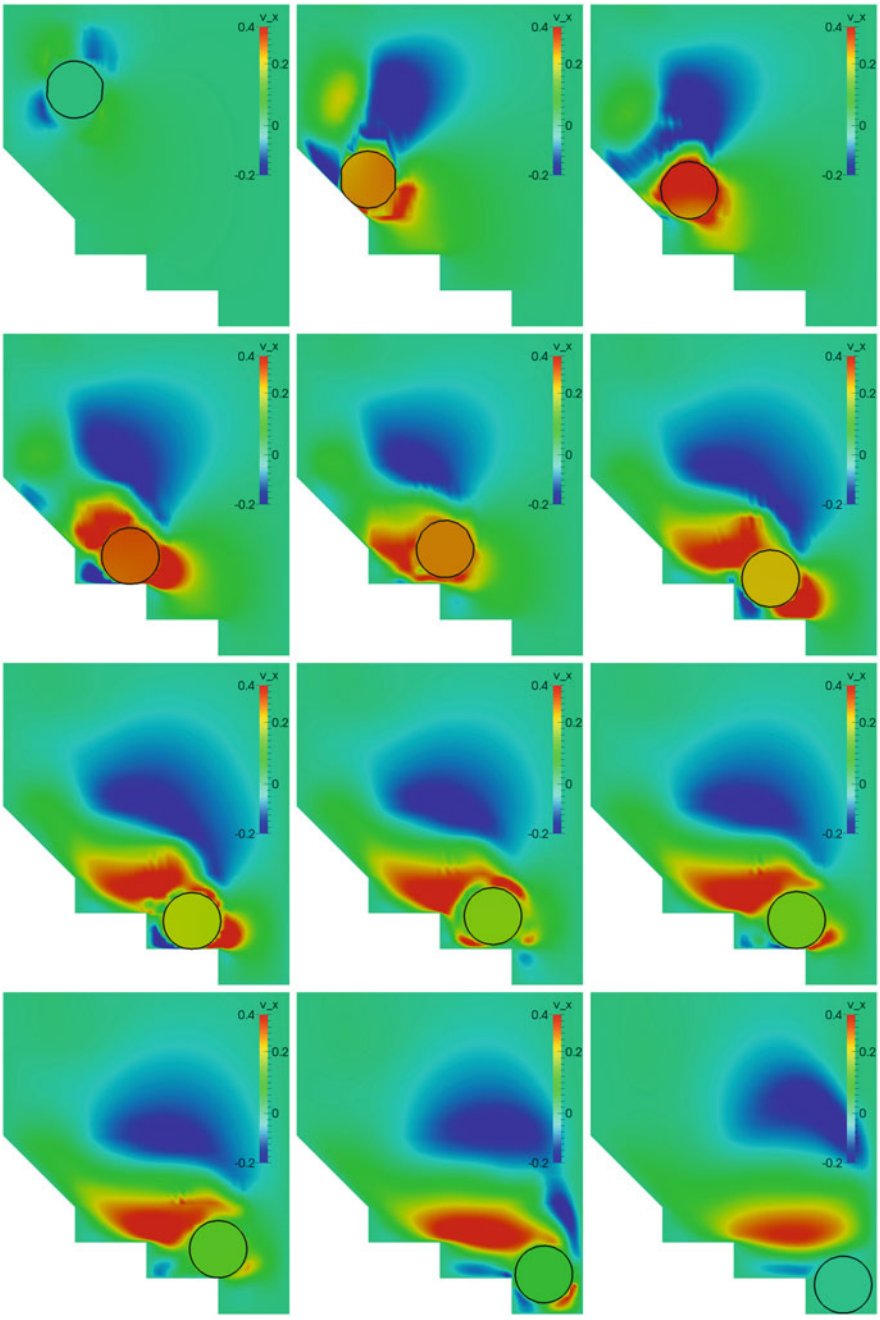

Fig. 12.10 Ball bouncing down three stairs for $\rho_f = 300\,\mathrm{kg}\cdot\mathrm{m}^{-3}$ at twelve different times. The *color* illustrates the horizontal velocity $\mathbf{v}_x$, the *black contour line* is the discrete interface. *First row:* Free fall, contact with the inclined plane and rebound. *Second row:* Contact with the first stair and rebound. *Third row:* First contact with the second stair, small bounce and second contact. *Last row:* Third contact with the second stair, fall and position at rest

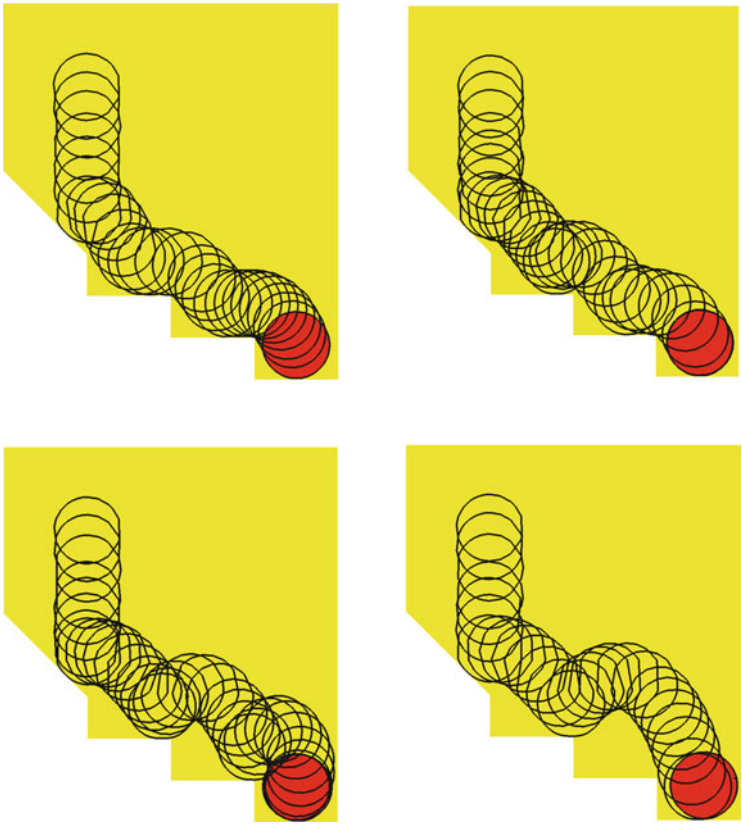

Fig. 12.11 Contour plots of the interface at several times. *Top left:* $\rho_f = 1000\,\mathrm{kg}\cdot\mathrm{m}^{-3}$, *top right:* $\rho_f = 300\,\mathrm{kg}\cdot\mathrm{m}^{-3}$, *bottom left:* $\rho_f = 150\,\mathrm{kg}\cdot\mathrm{m}^{-3}$, *bottom right:* $\rho_f = 100$. While for $\rho_f = 1000\,\mathrm{kg}\cdot\mathrm{m}^{-3}$ the ball rolls over the stairs, the ball bounces exactly once on each stair for $\rho_f = 150\,\mathrm{kg}\cdot\mathrm{m}^{-3}$. For $\rho_f = 100\,\mathrm{kg}\cdot\mathrm{m}^{-3}$, the ball jumps and skips the second stair

$\mathrm{dist}_0 = 10^{-2}\,\mathrm{m}$. For $\rho_f \leq 150\,\mathrm{kg}\cdot\mathrm{m}^{-3}$ this force was not large enough to prevent the contact (see the contact parameter studies below). Here, we use $\gamma_c = 10^4$.

The rebounds are higher, the smaller the fluid density is. For $\rho_f = 100\,\mathrm{kg}\cdot\mathrm{m}^{-3}$ the rebound at the first stair is so high that the ball jumps over the second stair and has its next contact on the third one. On the third stair we obtain six small bounces before the ball comes to rest.

For $\rho_f = 150\,\mathrm{kg}\cdot\mathrm{m}^{-3}$, the ball bounces exactly once on the first and second stair. Before dropping onto the last stair, the ball gets quite close to the right wall with a minimal distance of approximately $2\cdot 10^{-2}\,\mathrm{m}$. However, it is slowed down by fluid forces before the contact force corresponding to the right wall would get active. For $\rho_f = 300\,\mathrm{kg}\cdot\mathrm{m}^{-3}$, the rebounds are already significantly smaller and for $\rho_f = 1000\,\mathrm{kg}\cdot\mathrm{m}^{-3}$, the ball bounces once on each stair and continues rolling to the right.

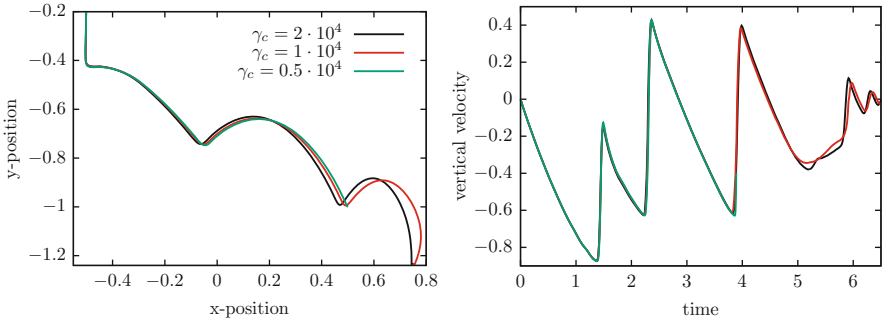

Fig. 12.12 *Left:* Position of the bottom of the ball. *Right:* Averaged vertical velocity over time for $\rho_f = 150\,\mathrm{kg} \cdot \mathrm{m}^{-3}$ and different values of the contact force. For $\gamma_c = 5 \cdot 10^3$ the contact could not be prevented at the contact time with the second stair

Finally, we study the influence of the contact force. In Fig. 12.12 (left sketch), we plot the trajectories of the lower bottom of the ball for $\rho_f = 150\,\mathrm{kg} \cdot \mathrm{m}^{-3}$ and three different contact force parameters γ_c. On the right, we plot an averaged vertical velocity $\overline{\mathbf{v}}_y$ over time.

The contact force with parameter $\gamma_c = 5 \cdot 10^3$ prevents the contact on the inclined plane and on the first stair, but it fails on the second one. Moreover, we observe that for larger contact parameters the velocity of the ball is slightly higher, and the ball bounces earlier on each stair. As a consequence, the ball almost touches the right wall for $\gamma_c = 10^4$ when it falls down towards the third stair, while it remains at a significantly larger distance of around $6 \cdot 10^{-2}\,\mathrm{m}$ for $\gamma_c = 2 \cdot 10^4$. The averaged velocities show good agreement before the bounce on the second stair and differ slightly afterwards due to the different trajectories.

We conclude that in this final example the influence of the contact force was relatively small. However, some quantities of interest, e.g. the contact distance (if there is any) or the distance at rest, cannot be determined with this approach and require more sophisticated contact algorithms.

References

1. M. Ainsworth, J.T. Oden, A unified approach to a posteriori error estimation using element residual methods. Numer. Math. **65**(1), 23–50 (1993)
2. M. Ainsworth, J.T. Oden, A posteriori error estimation in finite element analysis. Comput. Methods Appl. Mech. Eng. **142**(1–2), 1–88 (1997)
3. F. Alauzet, W. Hassan, M. Picasso, Goal oriented, anisotropic, a posteriori error estimates for the laplace equation, in *Proceedings of ENUMATH 2009, the 8th European Conference on Numerical Mathematics and Advanced Applications, Uppsala*, July 2009, ed. by G. Kreiss, P. Lötstedt, M. Neytcheva, A. Målqvist (Springer, Berlin, 2010), pp. 47–58
4. P.R. Amestoy, I.S. Duff, J.-Y. L'Excellent, Multifrontal parallel distributed symmetric and unsymmetric solvers. Comput. Methods Appl. Mech. Eng. **184**(2–4), 501–520 (2000). doi: 10.1016/S0045-7825(99)00242-X.
5. P.R. Amestoy, I.S. Duff, J. Koster, J.-Y. L'Excellent, A fully asynchronous multifrontal solver using distributed dynamic scheduling. SIAM J. Appl. Matrix Anal. **23**(1), 15–41 (2001)
6. P.R. Amestoy, A. Guermouche, J.-Y. L'Excellent, S. Pralet, Hybrid scheduling for the parallel solution of linear systems. Parallel Comput. **32**(2), 136–156 (2006)
7. T. Apel, *Anisotropic Finite Elements: Local Estimates and Applications*. Advances in Numerical Mathematics (Teubner, Stuttgart, 1999)
8. T. Apel, S. Nicaise, The finite element method with anisotropic mesh grading for elliptic problems in domains with corners and edges. Math. Methods Appl. Sci. **21**, 519–549 (1998)
9. E. Aulisa, S. Bna, G. Bornia, A monolithic ALE Newton-Krylov solver with multigrid-Richardson-Schwarz preconditioning for incompressible fluid structure interaction. SIAM J. Sci. Comput. (2017, accepted)
10. G. Avalos, R. Triggiani, The coupled PDE system arising in fluid/structure interaction. i. explicit semigroup generator and its spectral properties, in *Fluids and Waves*. Contemporary Mathematics, vol. 440 (American Mathematical Society, Providence, RI, 2007), pp. 15–54
11. G. Avalos, R. Triggiani, Semigroup well-posedness in the energy space of a parabolic-hyperbolic coupled Stokes-Lamé PDE system of fluid-structure interaction. Discrete Contin. Dyn. Syst. Ser. S **2**, 417–447 (2009)
12. G. Avalos, R. Triggiani, Fluid-structure interaction with and without internal dissipation of the structure: a contrast study in stability. Evol. Equ. Control Theory **2**, 563–598 (2013)
13. G. Avalos, I. Lasiecka, R. Triggiani, Higher regularity of a coupled parabolic hyperbolic fluid-structure interactive system. Georgian Math. J. **15**, 402–437 (2008)
14. I. Babuška, The finite element method for elliptic equations with discontinuous coefficients. Computing **5**, 207–213 (1970)

T. Richter, *Fluid-structure Interactions*, Lecture Notes in Computational Science and Engineering 118, DOI 10.1007/978-3-319-63970-3

15. I. Babuška, Feedback, adaptivity and a posteriori estimates in finite elements, aims, theory, and experience, in *Accuracy Estimates and Adaptive Refinements in Finite Element Computations*, ed. by I. Babuška et al. (Wiley, New York, 1986), pp. 3–23
16. I. Babuška, A.D. Miller, The post-processing approach in the finite element method. I. calculations of displacements, stresses and other higher derivatives of the displacements. Int. J. Numer. Methods Eng. **20**, 1085–1109 (1984)
17. I. Babuška, A.D. Miller, The post-processing approach in the finite element method. II. the calculation of stress intensity factors. Int. J. Numer. Methods Eng. **20**, 1111–1129 (1984)
18. I. Babuška, A.D. Miller, The post-processing approach in the finite element method. III. a posteriori error estimation and adaptive mesh selection. Int. J. Numer. Methods Eng. **20**, 2311–2324 (1984)
19. I. Babuška, W.C. Rheinboldt, Error estimates for adaptive finite element computations. SIAM J. Numer. Anal. **15**, 736–754 (1978)
20. I. Babuška, U. Banarjee, J.E. Osborn, Generalized finite element methods: main ideas, results, and perspective. Int. J. Comput. Methods **1**, 67–103 (2004)
21. S. Badia, A. Quaini, A. Quarteroni, Splitting methods based on algebraic factorization for fluid-structure interaction. SIAM J. Sci. Comput. **30**(4), 1778–1805 (2008)
22. S. Badia, F. Nobile, C. Vergar, Robin-robin preconditioned Krylov methods for fluid-structure interaction problems. Comput. Methods Appl. Mech. Eng. **198**, 1768–2784 (2009)
23. W. Bangerth, M. Geiger, R. Rannacher, Adaptive Galerkin finite element methods for the wave equation. Comput. Methods Appl. Math. **10**, 3–48 (2010)
24. W. Bangerth, T. Heister, L. Heltai, G. Kanschat, M. Kronbichler, M. Maier, B. Turcksin, The `deal.II` library, version 8.3 (2015, preprint)
25. R.E. Bank, A.H. Sherman, A. Weiser, Some refinement algorithms and data structures for regular local mesh refinement, in *Scientific Computing. Applications of Mathematics and Computing to the Physical Sciences*, ed. by Stepleman et al. Transactions on Scientific Computing, vol. 1 (North-Holland, Amsterdam, 1983), pp. 3–17
26. E. Bänsch, S Weller, Fully implicit time discretization for a free surface flow problem. PAMM **11**(1), 619–620 (2011)
27. A. Barker, X.-C. Cai, Scalable parallel methods for monolithic coupling in fluid-structure interaction with application to blood flow modeling. J. Comput. Phys. **229**(3), 642–659 (2010)
28. R.E. Barnhill, J.A. Gregory Interpolation remainder theory from Taylor expansions on triangle. Numer. Math. **25**, 401–408 (1976)
29. P. Bastian, Parallel adaptive multigrid methods. Technical Report 93–60, Interdisziplinäres Zentrum für Wissenschaftliches Rechnen, 1993
30. S. Basting, A. Quaini, S. Čanić, R. Glowinski, Extended ALE Method for fluid-structure interaction problems with large structural displacements. J. Comput. Phys. **331**, 312–336 (2017)
31. Y. Bazilevs, V.M. Calo, T.J.R Hughes, Y. Zhang, Isogeometric fluid-structure interaction: theory, algorithms, and computations. Comput. Mech. **43**, 3–37 (2008)
32. Y. Bazilevs, K. Takizawa, T.E. Tezduyar, *Computational Fluid-Structure Interaction: Methods and Applications* (Wiley, New York, 2013)
33. P.W. Bearman, Vortex shedding from oscillating bluff bodies. Ann. Rev. Fluid Mech. **16**, 195–222 (1984)
34. R. Becker, Weighted error estimators for finite element approximations of the incompressible Navier-Stokes equations. Rapport de Recherche RR-3458, INRIA Sophia-Antipolis, 1998
35. R. Becker, M. Braack, Multigrid techniques for finite elements on locally refined meshes. Numer. Linear Algebra Appl. **7**, 363–379 (2000). Special Issue
36. R. Becker, M. Braack, Solution of a benchmark problem for natural convection at low mach number natural convection at low mach number. SFB Preprint, 30, 2000
37. R. Becker, M. Braack, A finite element pressure gradient stabilization for the Stokes equations based on local projections. Calcolo **38**(4), 173–199 (2001)
38. R. Becker, M. Braack, Solution of a stationary benchmark problem for natural convection with high temperature difference. Int. J. Therm. Sci. **41**, 428–439 (2002)

39. R. Becker, M. Braack, A two-level stabilization scheme for the Navier-Stokes equations, in *Numerical Mathematics and Advanced Applications, ENUMATH 2003*, ed. by M. Feistauer et al. (Springer, New York, 2004), pp. 123–130
40. R. Becker, R. Rannacher, Weighted a posteriori error control in FE methods, in *ENUMATH'97*, ed. by H.G. Bock et al. (World Science Publisher, Singapore, 1995)
41. R. Becker, R. Rannacher, An optimal control approach to a posteriori error estimation in finite element methods, in *Acta Numerica 2001*, vol. 37, ed. by A. Iserles (Cambridge University Press, Cambridge, 2001), pp. 1–225
42. R. Becker, B. Vexler, A posteriori error estimation for finite element discretization of parameter identification problems. Numer. Math. **96**(3), 435–459 (2004)
43. R. Becker, M. Braack, D. Meidner, T. Richter, B. Vexler, The finite element toolkit GASCOIGNE. http://www.gascoigne.uni-hd.de
44. R. Becker, M. Braack, R. Rannacher, On error control for reactive flow problems, in *Computational Fluid Dynamics, Reaction Engineering, and Molecular Properties*. Scientific Computing in Chemical Engineering II, vol. 1 (Springer, Berlin, 1999), pp. 320–327
45. R. Becker, M. Braack, R. Rannacher, C. Waguet Fast and reliable solution of the Navier-Stokes equations including chemistry. Comput. Visual. Sci. **2**(2–3), 107–122 (1999)
46. R. Becker, M. Braack, T. Richter, Parallel multigrid on locally refined meshes, in *Reactive Flows, Diffusion and Transport*, ed. by R. Rannacher et al. (Springer, Berlin, 2006)
47. R. Becker, D. Meidner, B. Vexler, Efficient numerical solution of parabolic optimization problems by finite element methods. Optim. Methods Softw. **22**(5), 813–833 (2007)
48. T. Belytschko, Fluid-structure interaction. Comput. Struct. **12**, 459–469 (1980)
49. F. Bengzon, M.G. Larson, Adaptive finite element approximation of multiphysics problems: a fluid-structure interaction model problem. Int. J. Numer. Methods Eng. **84**, 1451–1465 (2010)
50. F. Bertrand, S. Münzenmaier, G. Starke, First-order system least squares on curved boundaries: lowest-order Raviart–Thomas elements. SIAM J. Numer. Anal. **52**(2), 880–894 (2014)
51. M. Besier, R. Rannacher, Goal-oriented space-time adaptivity in the finite element Galerkin method for the computation of nonstationary incompressible flow. Int. J. Numer. Math. Fluids. **70**(9), 1139–1166 (2012)
52. H. Blum, Asymptotic error expansion and defect correction in the finite element method. Habilitationsschrift, Institut für Angewandte Mathematik, Universität Heidelberg, 1991. SFB-123 Preprint 640
53. H. Blum, R. Rannacher, On the boundary value problem for the biharmonic operator on domains with angular corners. Math. Methods Appl. Sci. **2**, 556–581 (1980)
54. H. Blum, Q. Lin, R. Rannacher, Asymptotic error expansion and Richardson extrapolation for linear finite elements. Numer. Math. **49**, 11–37 (1986)
55. O. Boiarkine, D. Kuzmin, S. Čanić, G. Guidoboni, A. Mikelic, A positivity-preserving ALE finite element scheme for convection-diffusion equations in moving domains. J. Comput. Phys. **230**, 2896–2914 (2011)
56. C. Börgers, A triangulation algorithm for fast elliptic solvers based on domain imbedding. SIAM J. Numer. Anal. **27**, 1187–1196 (1990)
57. M. Braack, An adaptive finite element method for reactive flow problems, Ph.D. thesis, Universität Heidelberg, 1998
58. M. Braack, A stabilized finite element scheme for the Navier Stokes equations on anisotropic meshes. M2AN **42**(6), 903–924 (2008)
59. M. Braack, A. Ern, A posteriori control of modeling errors and discretization errors. Multiscale Model. Simul. **1**(2), 221–238 (2003)
60. M. Braack, A. Ern, Adaptive computation of reactive flows with local mesh refinement and model adaptation, in *Numerical Mathematics and Advanced Applications, ENUMATH 2003*, ed. by M. Feistauer et al. (Springer, Berlin, 2004), pp. 159–168
61. M. Braack, P.B. Mucha, Directional do-nothing condition for the Navier-Stokes equations. J. Comput. Math. **32**(5), 507–521 (2014)

62. M. Braack, T. Richter, Local projection stabilization for the stokes system on anisotropic quadrilateral meshes, in *Enumath*, ed. by Bermudez de Castro et al. (Springer, Berlin, 2005), pp. 770–778
63. M. Braack, T. Richter, Solutions of 3D Navier-Stokes benchmark problems with adaptive finite elements. Comput. Fluids **35**(4), 372–392 (2006)
64. M. Braack, T. Richter, Stabilized finite elements for 3-d reactive flows. Int. J. Numer. Math. Fluids **51**, 981–999 (2006)
65. M. Braack, N. Taschenberger, A posteriori control of modeling and discretization errors for quasi periodic solutions. J. Numer. Math. **22**(2), 87–108 (2014)
66. M. Braack, R. Becker, R. Rannacher, Adaptive finite elements for reactive flows, in *ENUMATH-97, Second European Conference on Numerical Mathematics and Advanced Applications*, Enumath (World Scientific Publisher, Singapore, 1998), pp. 206–213
67. M. Braack, E. Burman, V. John, G. Lube, Stabilized finite element methods for the generalized Oseen problem. Comput. Methods Appl. Mech. Eng. **196**, 853–866 (2007)
68. M. Braack, E. Burman, N. Taschenberger, Duality based a posteriori error estimation for quasi-periodic solutions using time averages. SIAM J. Sci. Comput. **33**, 2199–2216 (2011)
69. D. Braess, *Finite Elemente* (Springer, Berlin, 1997)
70. J.H. Bramble, J.T. King, A finite element method for interface problems in domains with smooth boundaries and interfaces. Adv. Comput. Math. **6**, 109–138 (1996)
71. F. Brezzi, M. Fortin, *Mixed and Hybrid Finite Element Methods* (Springer, Berlin, 1991)
72. F. Brezzi, M. Fortin, A minimal stabilisation procedure for mixed finite element methods. Numer. Math. **89**, 457–491 (2000)
73. F. Brinkmann, Mathematical models and numerical simulation of mechanochemical pattern formation in biological tissues, Ph.D. thesis, University of Heidelberg, 2017
74. M.O. Bristeau, R. Glowinski, J. Periaux, Numerical methods for the Navier-Stokes equations. Comput. Phys. Rep. **6**, 73–187 (1987)
75. A.N. Brooks, T.J.R. Hughes, Streamline upwind Petrov-Galerkin formulation for convection dominated flows with particular emphasis on the incompressible Navier-Stokes equations. Comput. Methods Appl. Mech. Eng. **32**, 199–259 (1982)
76. E.H. van Brummelen, K.G. van der Zee, R. de Borst, Space/time multigrid for a fluid-structure-interaction problem. Appl. Numer. Math. **58**(12), 1951–1971 (2008)
77. M. Bukač, S. Čanić, R. Glowinski, B. Muha, A. Quaini, A modular, operator-splitting scheme for fluid-structure interaction problems with thick structures. Int. J. Numer. Math. Fluids **74**, 577–604 (2014)
78. M.A.K. Bulelzai, J.L.A. Dubbeldam, Long time evolution of atherosclerotic plaques. J. Theor. Biol. **297**, 1–10 (2012)
79. H.-J. Bungartz, M. Schäfer (eds.), *Fluid-Structure Interaction. Modelling, Simulation, Optimisation*. Lecture Notes in Computational Science and Engineering, vol. 53 (Springer, Berlin, 2006). ISBN-10: 3-540-34595-7
80. H.-J. Bungartz, M. Schäfer (eds.), *Fluid-Structure Interaction II. Modelling, Simulation, Optimisation*. Lecture Notes in Computational Science and Engineering (Springer, Berlin, 2010)
81. E. Burman, Consistent SUPG-method for transient transport problems: stability and convergence. Comput. Methods Appl. Mech. Eng. **199**, 1114–1123 (2010)
82. E. Burman, M. Fernández, Stabilization of explicit coupling in fluid-structure interaction involving fluid incompressibility. Comput. Methods Appl. Mech. Eng. **198**, 766–784 (2009)
83. E. Burman, M. Fernández, Explicit strategies for incompressible fluid-structure interaction problems: Nitsche type mortaring versus Robin-Robin coupling. Int. J. Numer. Methods Eng. **97**, 739–758 (2014)
84. E. Burman, P. Hansbo, Edge stabilization for Galerkin approximations of convection–diffusion–reaction problems. Comput. Methods Appl. Mech. Eng. **193**(15), 1437–1453 (2004)
85. E. Burman, P. Hansbo, Edge stabilization for the generalized Stokes problem: a continuous interior penalty method. Comput. Methods Appl. Mech. Eng. **195**(19), 2393–2410 (2006)

86. E. Burman, M. Fernández, P. Hansbo, Edge stabilization for the Navier-Stokes equations: a conforming interior penalty finite element method. Technical report, INRIA, 2004. Research Report RR-5439, inria-00070653
87. S. Čanić, E.H. Kim, Mathematical analysis of the quasilinear effects in a hyperbolic model of blood flow through compliant axisymmetric vessels. Math. Methods Appl. Sci. **26**(14), 1161–1186 (2003)
88. G.F. Carey, S.S. Chow, M.K. Seager, Approximate boundary-flux calculations. Comput. Methods Appl. Mech. Eng. **50**, 107–120 (1985)
89. J. Carlson, A. Jaffe, A. Wiles (eds.), *Millennium Prize Problems* (CMI/American Mathematical Society, Cambridge, 2006). ISBN-13: 978-0-8218-3679-8
90. J. Carpio, J.L. Prieto, R. Bermejo, Anisotropic "goal-oriented" mesh adaptivity for elliptic problems. SIAM J. Sci. Comput. **35**(2), A861–A885 (2013)
91. C. Carstensen, Convergence of adaptive finite element methods in computational mechanics. Appl. Numer. Math. **59**, 2119–2130 (2009)
92. M.J. Castro-Diaz, F. Hecht, B. Mohammadi, O. Pironneau, Anisotropic unstructured mesh adaptation for flow simulations. Int. J. Numer. Math. Fluids **25**, 475–491 (1997)
93. P. Causin, J.F. Gereau, F. Nobile, Added-mass effect in the design of partitioned algorithms for fluid-structure problems. Comput. Methods Appl. Mech. Eng. **194**, 4506–4527 (2005)
94. C.X. Chen, Y. Ding, J.A. Gear, Numerical simulation of atherosclerotic plaque growth using two-way fluid-structural interaction. ANZIAM J. **53**, 278–291 (2012)
95. J. Chessa, P. Smolinski, T. Belytschko, The extended finite element method (XFEM) for solidication problems. Int. J. Numer. Methods Eng. **53**, 1959–1977 (2002)
96. P.G. Ciarlet, *Finite Element Methods for Elliptic Problems* (North-Holland, Amsterdam, 1978)
97. P.G. Ciarlet, *Mathematical Elasticity*. Three-Dimensional Elasticity, vol. I (North-Holland, Amsterdam, 1991)
98. P.G. Ciarlet, On Korn's Inequality. Chin. Ann. Math. **31**, 607–618 (2010)
99. M. Cilla, E. Peña, M.A. Martínez, Mathematical modelling of atheroma plaque formation and development in coronary arteries. J. R. Soc. Interface **11**(90) (2013). http://dx.doi.org/10.1098/rsif.2013.0866
100. P. Clément, Approximation by finite element functions using local regularization. R.A.I.R.O. Anal. Numer. **9**, 77–84 (1975)
101. B. Cockburn, G.E. Karniadakis, C.-W. Shu (eds.), *Discontinuous Galerkin Methods. Theory, Computation and Applications*. Lecture Notes in Computational Science and Engineering, vol. 11 (Springer, Berlin, 2000)
102. R. Codina, Stabilization of incompressibility and convection through orthogonal subscales in finite element methods. Comput. Methods Appl. Mech. Eng. **190**(13/14), 1579–1599 (2000)
103. G.-H. Cottet, E. Maitre, A level set method for fluid-structure interactions with immersed surfaces. Math. Models Methods Appl. Sci. **16**(3), 415–438 (2006)
104. G.-H. Cottet, E. Maitre, T. Milcent, An Eulerian method for fluid-structure coupling with biophysical applications, in *Proceedings of the European Conference on Computational Fluid Dynamics*, Delft University of Technology, Sept 5–8, 2006
105. G.-H. Cottet, E. Maitre, T. Milcent, Eulerian formulation and level set models for incompressible fluid-structure interaction. ESAIM: M2AN **42**(3), 471–492 (2008)
106. D. Coutand, S. Shkoller, Motion of an elastic solid inside an incompressible viscous fluid. Arch. Ration. Mech. Anal. **176**, 25–102 (2005)
107. D. Coutand, S. Shkoller, The interaction between quasilinear elastodynamics and the Navier-Stokes equations. Arch. Ration. Mech. Anal. **179**, 303–352 (2007)
108. P. Crosetto, S. Deparis, G. Fourestey, A. Quarteroni, Parallel algorithms for fluid-structure interaction problems in haemodynamics. SIAM J. Sci. Comput. **33**(4), 1598–1622 (2011)
109. R. Dautray, J.-L. Lions, *Evolution Problems I*. Mathematical Analysis and Numerical Methods for Science and Technology, vol. 5 (Springer, New York, 1992)
110. T.A. Davis, Umfpack, an unsymmetric-pattern multifrontal method. ACM Trans. Math. Softw. **30**(2), 196–199 (2014)

111. E.F. D'Azevedo, R.B. Simpson, On optimal interpolation triangle incidences. SIAM J. Sci. Stat. Comput. **10**(6), 1063–1075 (1989)
112. G. de Rham, *Variétés Différentiables* (Hermann, Paris, 1960)
113. J. Degroote, S. Annerel, J. Vierendeels, A multi-solver quasi-Newton method for the partitioned simulation of fluid-structure interaction. IOP Conf. Ser. Mater. Sci. Eng. **10** (2010). 10.1088/1757-899X/10/1/012020
114. M.C. Delfour, J.-P. Zolésio, *Shapes and Geometries: Metrics, Analysis, Differential Calculus and Optimization*. Advances in Design and Control, 2nd edn. (SIAM, Philadelphia, 2011)
115. B. Desjardins, M.J. Esteban, Existence of weak solutions for the motion of rigid bodies in a viscous fluid. Arch. Ration. Mech. Anal. **146**, 59–71 (1999)
116. P. Deuflhard, *Newton Methods for Nonlinear Problems* (Springer, Berlin, 2005). ISBN-13: 978-3540210993
117. P. Deuflhard, *Newton Methods for Nonlinear Problems. Affine Invariance and Adaptive Algorithms*. Computational Mathematics, vol. 35 (Springer, Berlin, 2011)
118. P. Deuflhard, F. Bornemann, *Numerische Mathematik II* (Walter de Gruyter, Berlin, 1994)
119. M. Dobrowolski, On the LBB constant on stretched domains. Math. Nachr. **254/255**, 64–67 (2003)
120. J. Donea, An arbitrary Lagrangian-Eulerian finite element method for transient dynamic fluid-structure interactions. Comput. Methods Appl. Mech. Eng. **33**, 689–723 (1982)
121. W. Dörfler, A convergent adaptive algorithm for Poisson's equation. SIAM J. Numer. Anal. **33**(3), 1106–1124 (1996)
122. N.D. dos Santos, J.-F. Gerbeau, J.-F. Bourgat, A partitioned fluid–structure algorithm for elastic thin valves with contact. Comput. Methods Appl. Mech. Eng. **197**(19), 1750–1761 (2008)
123. J.J. Droux, T.J.R. Hughes, A boundary integral modification of the Galerkin least squares formulation for the Stokes problem. Comput. Methods Appl. Mech. Eng. **113**(173–182) (1994)
124. Q. Du, M. Gunzburger, L. Hou, J. Lee, Analysis of a linear fluid-structure interaction problem. Discrete Contin. Dyn. Syst. Ser. A **9**(3), 633–650 (2003)
125. Q. Du, M. Gunzburger, L. Hou, J. Lee, Semidiscrete finite element approximations of a linear fluid-structure interaction problem. SIAM J. Numer. Anal. **42**, 1–29 (2004)
126. T. Dunne, An Eulerian approach to fluid-structure interaction and goal-oriented mesh refinement. Int. J. Numer. Math. Fluids **51**, 1017–1039 (2006)
127. T. Dunne, Adaptive finite element approximation of fluid-structure interaction based on Eulerian and arbitrary Lagrangian-Eulerian variational formulations, Ph.D. thesis, University of Heidelberg, 2007. http://urn:nbn:de:bsz:16-opus-79448
128. T. Dunne, R. Rannacher, T. Richter, Numerical simulation of fluid-structure interaction based on monolithic variational formulations, in *Contemporary Challenges in Mathematical Fluid Mechanics*, ed. by G.P. Galdi, R. Rannacher (World Scientific, Singapore, 2010)
129. R. Dziri, J.-P. Zolésio, Eulerian derivative for non-cylindrical functionals, in *Shape Optimization and Optimal Design*, vol. 216, ed. by J. Cagnol, M.P. Polis, J.-P. Zolésio (Dekker, New York, 2001), pp. 87–108
130. K. Eriksson, D. Estep, P. Hansbo, C. Johnson, Introduction to adaptive methods for differential equations, in *Acta Numerica 1995*, ed. by A. Iserles (Cambridge University Press, Cambridge, 1995), pp. 105–158
131. K. Eriksson, D. Estep, P. Hansbo, C. Johnson, *Computational Differential Equations* (Cambridge University Press, Cambridge, 1996)
132. D. Estep, A posteriori error bounds and global error control for approximation of ordinary differential equations. SIAM J. Numer. Anal. **32**(1), 1–48 (1995)
133. L. Failer, Optimal control for time dependent nonlinear fluid-structure interaction, Ph.D. thesis, Technische Universität München, 2017
134. L. Failer, D. Meidner, B. Vexler, Optimal control of a linear unsteady fluid-structure interaction problem. J. Optim. Theory Appl. **170**(1), 1–27 (2016)
135. X. Fang, An isoparametric finite element method for elliptic interface problems with nonhomogeneous jump conditions. WSEAS Trans. Math. **12** (2013)

136. E. Feireisl, On the motion of rigid bodies in a viscous incompressible fluid. J. Evol. Equ. **3**(3), 419–441 (2003)
137. M. Feistauer, V. Sobotíková, Finite element approximation of nonlinear problems with discontinuous coefficients. Modèl. Math. Anal. Numér. **24**, 457–500 (1990)
138. M. Feistauer, J. Hasnedlová-Prokopová, J. Horáček, A. Kosík, V. Kučera, DGFEM for dynamical systems describing interaction of compressible fluid and structures. J. Comput. Appl. Math. **254**, 17–30 (2013)
139. M.A. Fernández, Coupling schemes for incompressible fluid-structure interaction: implicit, semi-implicit and explicit. SeMA J. **55**(1), 59–108 (2013)
140. M.A. Fernández, J.-F. Gerbeau, Algorithms for fluid-structure interaction problems, in *Cardiovascular Mathematics: Modeling and Simulation of the Circulatory System*. MS & A, vol. 1, ed. by L. Formaggia, A. Quarteroni, A. Veneziani (Springer, Berlin, 2009), pp. 307–346
141. M.A. Fernández, M. Moubachir, A Newton method using exact Jacobians for solving fluid-structure coupling. Comput. Struct. **83**, 127–142 (2005)
142. M.A. Fernández, J.-F. Gerbeau, C. Grandmont, A projection semi-implicit scheme for the coupling of an elastic structure with an incompressible fluid. Int. J. Numer. Methods Eng. **69**(4), 794–821 (2007)
143. L. Formaggia, F. Nobile, A stability analysis for the Arbitrary Lagrangian Eulerian formulation with finite elements. East-West J. Numer. Math **7**, 105–132 (1999)
144. L. Formaggia, F. Nobile, Stability analysis of second-order time accurate schemes for ALE-FEM. Comput. Methods Appl. Mech. Eng. **193**(39–41), 4097–4116 (2004)
145. L. Formaggia, S. Perotto, P. Zunino, An anisotropic a-posteriori error estimate for a convection-diffusion problem. Comput. Visual. Sci. **4**, 99–2001 (2001)
146. L. Formaggia, S. Micheletti, S. Perotto, Anisotropic mesh adaptation in computational fluid dynamics: application to the advection-diffusion-reaction and the stokes problems. Appl. Numer. Math. **51**(4), 511–533 (2004)
147. L. Formaggia, A. Quarteroni, A. Veneziani, *Cardiovascular Mathematics: Modeling and Simulation of the Circulatory System* (Springer, Milan, 2009)
148. C. Förster, W. Wall, E. Ramm, Artificial mass instabilities in sequential staggered coupling of nonlinear structures and incompressible viscous flows. Comput. Methods Appl. Mech. Eng. **196**, 1278–1293 (2007)
149. D. Forti, A. Quaini, M. Bukač, S. Čanić, S. Deparis, A monolithic approach to fluid-composite structure interaction. J. Sci. Comput. **71**(1), 396–421 (2017)
150. R.L. Fosdick, E.G. Virga, A variational proof of the stress theorem of Cauchy. Arch. Ration. Mech. Anal. **105**(2), 95–103 (1989)
151. S. Frei, Eulerian finite element methods for interface problems and fluid-structure interactions, Ph.D. thesis, Universität Heidelberg, Aug 2016. doi:10.11588/heidok.00021590
152. S. Frei, An edge-based pressure stabilisation technique for anisotropic finite element grids (2017, submitted)
153. S. Frei, T. Richter, A locally modified parametric finite element method for interface problems. SIAM J. Numer. Anal. **52**(5), 2315–2334 (2014)
154. S. Frei, T. Richter, An accurate Eulerian approach for fluid-structure interactions, in *Fluid-Structure Interactions. Modeling, Adaptive Discretization and Solvers*. Radon Series on Computational and Applied Mathematics, vol. 20 (de Gruyter, Berlin, 2017)
155. S. Frei, T. Richter, Contact strategies for fluid-structure interactions using a fully Eulerian approach (2018, submitted)
156. S. Frei, T. Richter, T. Wick, Eulerian techniques for fluid-structure interactions: part i - modeling and simulation, in *Numerical Mathematics and Advanced Applications-ENUMATH 2013* (Springer, Berlin, 2013), pp. 745–753
157. S. Frei, T. Richter, T. Wick, Eulerian techniques for fluid-structure interactions: part ii – applications, in *Numerical Mathematics and Advanced Applications-ENUMATH 2013* (Springer, Berlin, 2013), pp. 755–762

158. S. Frei, T. Richter, T. Wick, Long-term simulation of large deformation, mechano-chemical fluid-structure interactions in ALE and fully Eulerian coordinates. J. Comput. Phys. **321**, 874–891 (2015)
159. T.-P. Fries, A. Zilian, On time integration in the XFEM. Int. J. Numer. Methods Eng. **79**(1), 69–93 (2009)
160. G.P. Galdi, *An Introduction to the Mathematical Theory of the Navier-Stokes Equations, Vol. I, Steady-State Problems* (Springer, New York, 2011)
161. P. Gangl, U. Langer, A local mesh modification strategy for interface problems with application to shape and topology optimization problems. Technical report, RICAM, 2016. https://arxiv.org/abs/1609.06236
162. F. Gazzola, M. Squassina, Global solutions and finite time blow up for damped semilinear wave equations. Ann. I.H. Poincaré **23**, 185–207 (2006)
163. M.W. Gee, U. Küttler, W.A. Wall, Truly monolithic algebraic multigrid for fluid-structure interaction. Int. J. Numer. Methods Eng. **85**, 987–1016 (2010)
164. M.B. Giles, E. Süli, Adjoint methods for PDEs: a posteriori error analysis and postprocessing by duality, in *Acta Numerica 2002*, ed. by A. Iserles (Cambridge University Press, Cambridge, 2002), pp. 145–236
165. V. Girault, P.-A. Raviart, *Finite Elements for the Navier Stokes Equations* (Springer, Berlin, 1986)
166. R. Glowinski, Finite element methods for the numerical simulation of incompressible viscous flow. introduction to the control of the Navier-Stokes equations. Lect. Appl. Math. **28**, 219–301 (1991)
167. C. Grandmont, Existence for the three-dimensional steady state fluid-structure interaction problem. J. Math. Fluid Mech. **4**, 1–94 (2002)
168. C. Grandmont, Existence of weak solutions for the unsteady interaction of a viscous fluid with an elastic plate. SIAM J. Math. Anal. **40**, 716–737 (2008)
169. C. Grandmont, M. Hillairet, Existence of global strong solutions to a beam-fluid interaction system. Arch. Ration. Mech. Anal. **220**, 1283–1333 (2016)
170. T. Grätsch, K.J. Bathe, Goal-oriented error estimation in the analysis of fluid flows with structural interactions. Comput. Methods Appl. Mech. Eng. **195**, 5673–5684 (2006)
171. A. Griewank, On automatic differentiation, in *Mathematical Programming: Recent Developments and Applications*, ed. by M. Iri, K. Tanabe (Kluwer Academic Publishers, Boston, 1989), pp. 83–108
172. W. Hackbusch, *Multi-Grid Methods and Applications* (Springer, Berlin, 1985)
173. E. Hairer, G. Wanner, *Solving Ordinary Differential Equations II. Stiff and Differential-Algebraic Problems*. Computational Mathematics, vol. 14 (Springer, Berlin, 1996)
174. A. Hansbo, P. Hansbo, An unfitted finite element method, based on Nitsche's method, for elliptic interface problems. Comput. Methods Appl. Mech. Eng. **191**(47–48), 5537–5552 (2002)
175. A. Hansbo, P. Hansbo, A finite element method for the simulation of strong and weak discontinuities in solid mechanics. Comput. Methods Appl. Mech. Eng. **193**, 3523–3540 (2004)
176. R. Hartmann, Adaptive FE-methods for conservation equations, in *Eighth International Conference on Hyperbolic Problems. Theory, Numerics, Applications (HYP2000)*, ed. by G. Warnecke (Birkhauser, Basel, 2000)
177. R. Hartmann, Multitarget error estimation and adaptivity in aerodynamic flow simulations. SIAM J. Sci. Comput. **31**(1), 708–731 (2008)
178. W. Hassan, Algorithmes d'adaptation de maillages anisotropes et application á l'aérodynamique, Ph.D. thesis, École Polytechnique Fédérale de Lausanne, 2012. doi:10.5075/epfl-thesis-5304
179. P. He, R. Qiao, A full-Eulerian solid level set method for simulation of fluid-structure interactions. Microfluid. Nanofluid. **11**, 557–567 (2011)
180. M. Heil, An efficient solver for the fully coupled solution of large-displacement fluid-structure interaction problems. Comput. Methods Appl. Mech. Eng. **193**, 1–23 (2004)

181. M. Heil, A.L. Hazel, J. Boyle, Solvers for large-displacement fluid-structure interaction problems: Segregated vs. monolithic approaches. Comput. Mech. **43**, 91–101 (2008)
182. B.T. Helenbrook, Mesh deformation using the biharmonic operator. Int. J. Numer. Methods Eng. **56**(7), 1–30 (2001)
183. W. Henshaw, J. Banks, D. Schwendeman, An analysis of a new stable partitioned algorithm for FSI problems. Part i: Incompressible flow and elastic solids. J. Comput. Phys. **269**, 108–137 (2014)
184. W. Henshaw, J. Banks, D. Schwendeman, An analysis of a new stable partitioned algorithm for FSI problems. Part ii: Incompressible flow and structural shells. J. Comput. Phys. **269**, 399–416 (2014)
185. V. Heuveline, R. Rannacher, Duality-based adaptivity in the hp-finite element method. J. Numer. Math. **11**(2), 95–113 (2003)
186. J. Heywood, R. Rannacher, Finite element approximation of the nonstationary Navier-Stokes problem. iii. smoothing property and higher order error estimates for spatial discretization. SIAM J. Numer. Anal. **25**(3), 489–512 (1988)
187. J. Heywood, R. Rannacher, Finite element approximation of the nonstationary Navier-Stokes problem. iv. error analysis for second-order time discretization. SIAM J. Numer. Anal. **27**(3), 353–384 (1990)
188. J.G. Heywood, R. Rannacher, S. Turek, Artificial boundaries and flux and pressure conditions for the incompressible Navier-Stokes equations. Int. J. Numer. Math. Fluids **22**, 325–352 (1992)
189. M. Hillairet, Lack of collision between solid bodies in a 2d incompressible viscous flow. Commun. Partial Differ. Equ. **32**, 1345–1371 (2007)
190. M. Hillairet, T. Takahashi, Collisions in 3d fluid structure interactions problems. SIAM J. Math. Anal. **40**(6), 2341–2377 (2009)
191. M. Hinze, R. Pinnau, M. Ulbrich, S. Ulbrich (eds.), *Optimization with PDE Constraints*. Mathematical Modelling: Theory and Applications, vol. 23 (Springer, Dordrecht, 2009)
192. C.W. Hirt, A.A. Amsden, J.L. Cook, An arbitrary Lagrangian-Eulerian computing method for all flow speeds. J. Comput. Phys. **14**, 227–469 (1974)
193. J. Hoffman, B. Holm, T. Richter, The locally adapted patch finite element method for interface problems on triangular meshes, in *Fluid-Structure Interaction. Modeling, Adaptive Discretisations and Solvers*. Radon Series on Computational and Applied Mathematics, vol. 20 (de Gruyter, Berlin, 2017)
194. M. Holst, S. Pollock, Convergence of goal-oriented adaptive finite element methods for nonsymmetric problems. Numer. Methods Partial Differ. Equ. **32**(2), 479–509 (2015, online)
195. G.A. Holzapfel, *Nonlinear Solid Mechanics: A Continuum Approach for Engineering* (Wiley-Blackwell, Chichester, 2000)
196. C.O. Horgan, Korn's inequalities and their applications in continuum mechanics. SIAM Rev. **37**, 491–511 (1995)
197. G. Hou, J. Wang, A. Layton, Numerical methods for fluid-structure interactions - a review. Commun. Comput. Phys. **12**(2), 337–377 (2012)
198. J. Hron, S. Turek, A monolithic FEM solver for an ALE formulation of fluid-structure interaction with configuration for numerical benchmarking, in *European Conference on Computational Fluid Dynamics ECCOMAS CDF 2006*, ed. by P. Wesseling, E. Onate, J. Périaux (TU Delft, 2006), pp. 1–21
199. J. Hron, S. Turek, A monolithic FEM/Multigrid solver for an ALE formulation of fluid-structure interaction with applications in biomechanics, in *Fluid-Structure Interaction: Modeling, Simulation, Optimization*, ed. by H.-J. Bungartz, M. Schäfer. Lecture Notes in Computational Science and Engineering (Springer, Berlin, 2006), pp. 146–170
200. J. Hron, S. Turek, Proposal for numerical benchmarking of fluid-structure interaction between an elastic object and laminar incompressible flow, in *Fluid-Structure Interaction: Modeling, Simulation, Optimization*, ed. by H.-J. Bungartz, M. Schäfer. Lecture Notes in Computational Science and Engineering (Springer, Berlin, 2006), pp. 371–385

201. J. Hron, S. Turek, M. Madlik, M. Razzaq, H. Wobker, J.F. Acker, Numerical simulation and benchmarking of a monolithic multigrid solver for fluid-structure interaction problems with application to hemodynamics, in *Fluid-Structure Interaction II: Modeling, Simulation, Optimization*, ed. by H.-J. Bungartz, M. Schäfer. Lecture Notes in Computational Science and Engineering (Springer, Berlin, 2010), pp. 197–220
202. T.J.R. Hughes, W.K. Liu, T.K. Zimmermann, Lagrangian-Eulerian finite element formulations for incompressible viscous flows. Comput. Methods Appl. Mech. Eng. **29**, 329–349 (1981)
203. T.J.R. Hughes, L.P. Franca, M. Balestra, A new finite element formulation for computational fluid dynamics: V. circumvent the Babuska-Brezzi condition: A stable Petrov-Galerkin formulation for the Stokes problem accommodating equal order interpolation. Comput. Methods Appl. Mech. Eng. **59**, 89–99 (1986)
204. T.J.R. Hughes, J.A. Cottrell, Y. Bazilevs, Isogeometric analysis: Cad, finite elements, nurbs, exact geometry and mesh refinement. Comput. Methods Appl. Mech. Eng. **194**(39–41), 4135–4195 (2005)
205. M. Ignatova, I. Kukavica, I. Lasiecka, A. Tuffaha, On well-posedness for a free boundary fluid-structure model. J. Math. Phys. **53**(115624), 2012. doi:10.1063/1.4766724
206. B. Irons, R.C. Tuck, A version of the Aitken accelerator for computer implementation. Int. J. Numer. Methods Eng. **1**, 275–277 (1969)
207. C. Johnson, *Numerical Solution of Partial Differential Equations by the Finite Element Method* (Dover Publications, New York, 2009). ISBN-13: 978-0-486-46900-3
208. C. Johnson, A. Szepessy, Adaptive finite element methods for conservation laws based on a posteriori error estimates. Commun. Pure Appl. Math. **48**(3), 199–234 (1995)
209. G.W. Jones, S.J. Chapman, Modeling growth in biological materials. SIAM Rev. **54**(1), 52–118 (2012)
210. G. Karypis, V. Kumar, MeTis: Unstructured Graph Partitioning and Sparse Matrix Ordering System, Version 4.0 (2009), http://www.cs.umn.edu/~metis
211. M. Kimmritz, T. Richter, Parallel multigrid method for finite element simulations of complex flow problems on locally refined meshes. Numer. Linear Algebra Appl. **18**(4), 615–636 (2010)
212. S. Knauf, S. Frei, T. Richter, R. Rannacher, Towards a complete numerical description of lubricant film dynamics in ball bearings. Comput. Mech. **53**, 239–255 (2014)
213. U. Kuettler, W.A. Wall, Fixed-point fluid-structure interaction solvers with dynamic relaxation. Comput. Mech. **43**(1), 61–72 (2008)
214. I. Kukavica, A. Tuffaha, Solutions to a fluid-structure interaction free boundary problem. Discrete Contin. Dyn. Syst. **32**, 1355–1389 (2012)
215. U. Küttler, M.W. Gee, Ch. Förster, A. Comerford, W.A. Wall, Coupling strategies for biomedical fluid-structure interaction problems. Int. J. Numer. Methods Biomed. Eng. **26**(3–4), 305–321 (2010)
216. D. Kuzmin, On the design of general-purpose flux limiters for implicit FEM with a consistent mass matrix. I. Scalar convection. J. Comput. Phys. **219**, 513–531 (2006)
217. D. Kuzmin, J. H"amäläinen, *Finite Element Methods for Computational Fluid Dynamics* (SIAM, Philadelphia, 2015)
218. D. Kuzmin, R. Löhner, S. Turek (eds.), *Flux-Corrected Transport: Principles, Algorithms and Applications*. Scientific Computation (Springer, Berlin, 2005)
219. A. Kuzmin, M. Luisier, O. Schenk, Fast methods for computing selected elements of the greens function in massively parallel nanoelectronic device simulations, in *Euro-Par 2013 Parallel Processing*, ed. by F. Wolf, B. Mohr, D. Mey. Lecture Notes in Computer Science, vol. 8097 (Springer, Berlin/Heidelberg, 2013), pp. 533–544
220. U. Langer, H. Yang, Recent development of robust monolithic fluid-structure interaction solvers, in *Fluid-Structure Interactions. Modeling, Adaptive Discretization and Solvers*. Radon Series on Computational and Applied Mathematics, vol. 20 (de Gruyter, Berlin, 2017)
221. P. Le Tallec, J. Mouro, Fluid structure interaction with large structural displacement. Comput. Methods Appl. Mech. Eng. **190**, 3039–3067 (2001)

222. A. Legay, J. Chessa, T. Belytschko, An Eulerian-Lagrangian method for fluid-structure interaction based on level sets. Comput. Methods Appl. Mech. Eng. **195**, 2070–2087 (2006)
223. C. Lehrenfeld, A. Reusken, Analysis of a Nitsche XFEM-DG discretization for a class of two-phase mass transport problems. SIAM J. Numer. Anal. **51**(2), 958–983 (2013)
224. T. Leicht, R. Hartmann, Anisotropic mesh refinement for discontinuous Galerkin methods in two-dimensional aerodynamic flow simulations. Int. J. Numer. Math. Fluids **56**, 2111–2138 (2007)
225. M. Lenoir, Optimal isoparametric finite elements and error estimates for domains involving curved boundaries. SIAM J. Numer. Anal. **23**(3), 562–580 (1986)
226. X.S. Li, An overview of SuperLU: Algorithms, implementation, and user interface. ACM Trans. Math. Softw. **31**(3), 302–325 (2005)
227. A. Linke, G. Matthies, L. Tobiska, Robust arbitrary order mixed finite element methods for the incompressible stokes equations with pressure independent velocity errors. ESAIM: Math. Model. Num. Anal. **50**(1), 289–309 (2015, in press)
228. A. Linke, C. Merdon, W. Wollner, Optimal L^2 velocity error estimate for a modified pressure-robust Crouzeix-Raviart Stokes element. IMA J. Numer. Anal. **37**(1), 354–374 (2017)
229. M. Lukáčová-Medvidóvá, G. Rusnáková, A. Hundertmark-Zaušková, Kinematic splitting algorithm for fluid-structure interaction in hemodynamics. Comput. Methods Appl. Mech. Eng. **265**, 83–106 (2013)
230. M. Luskin, R. Rannacher, On the smoothing property of the Crank-Nicholson scheme. Appl. Anal. **14**, 117–135 (1982)
231. L. Machiels, A.T. Patera, J. Peraire, Output bound approximation for partial differential equations; application to the incompressible Navier-Stokes equations, in *Industrial and Environmental Applications of Direct and Large Eddy Numerical Simulation*, ed. by S. Biringen (Springer, Berlin/Heidelberg/New York, 1998)
232. R.J. MacKinnon, G.F. Carey, Treatment of material discontinuities in finite element computations. Int. J. Numer. Methods Eng. **24**, 393–417 (1987)
233. K.-A. Mardal, J. Schöberl, R. Winther, A uniformly stable Fortin operator for the Taylor-Hood element. Numer. Math. **123**(3), 537–551 (2012)
234. Matlab and Statistics Toolbox Release 2012b, The MathWorks Inc., Natick, MA
235. H.G. Matthies, J. Steindorf, Partitioned but strongly coupled iteration schemes for nonlinear fluid-structure interactions. Comput. Struct. **80**, 1991–1999 (2002)
236. H.G. Matthies, J. Steindorf, Partitioned strong coupling algorithms for fluid-structure interaction. Comput. Struct. **81**, 805–812 (2003)
237. U. Mayer, A. Popp, A. Gerstenberger, W.A. Wall, 3d fluid–structure-contact interaction based on a combined XFEM FSI and dual mortar contact approach. Comput. Mech. **46**(1), 53–67 (2010)
238. D. Meidner, Adaptive space-time finite element methods for optimization problems governed by nonlinear parabolic systems, Ph.D. thesis, University of Heidelberg, 2008
239. D. Meidner, T. Richter, Goal-oriented error estimation for the fractional step theta scheme. Comput. Methods Appl. Math. **14**, 203–230 (2014)
240. D. Meidner, T. Richter, A posteriori error estimation for the fractional step theta discretization of the incompressible Navier-Stokes equations. Comput. Methods Appl. Mech. Eng. **288**, 45–59 (2015)
241. E. Michel, On the motion of rigid bodies submerged in incompressible fluids, Ph.D. thesis, University of Heidelberg, 2008. URN:nbn:de:bsz:16-opus-85761
242. T. Milcent, E. Maitre, Eulerian model of immersed elastic surfaces with full membrane elasticity. Commun. Math. Sci. **14**(3), 857–881 (2016)
243. M. Mitrea, S. Monniaux, Maximal regularity for the Lamé system in certain classes of non-smooth domains. J. Evol. Equ. **10**(4), 811–833 (2010)
244. S. Mittal, V. Kumar, Flow-induced vibrations of a light circular cylinder at Reynolds numbers 10^3 to 10^4. J. Sound Vib. **245**(5), 923–946 (2001)
245. S. Mittal, S. Singh, Vortex-induced vibrations at subcritical *re*. J. Fluid Mech. **534**, 185–194 (2005)

246. N. Moës, J. Dolbow, T. Belytschko, A finite element method for crack growth without remeshing. Int. J. Numer. Methods Eng. **46**, 131–150 (1999)
247. M. Molnar, Stabilisierte Finite Elemente für Strömungsprobleme auf bewegten Gebieten, Master's thesis, Universität Heidelberg, 2015
248. P. Morin, R.H. Nochetto, K.G. Siebert, Convergence of adaptive finite element methods. SIAM Rev. **44**(4), 631–658 (2002)
249. R.L. Muddle, M. Mihajlović, An efficient preconditioner for monolithically-coupled large-displacement fluid-structure interaction problems with pseudo-solid mesh updates. J. Comput. Phys. **231**, 7315–7334 (2012)
250. Y. Navrose, S. Sen, S. Mittal, Free vibrations of an elliptic cylinder at low Reynolds numbers. J. Fluids Struct. **51**, 55–67 (2014)
251. J. Nečas, *Equations aux Derivees Partielles* (Presses de Université de Montréal, Montréal, 1965)
252. R.H. Nochetto, A. Veeser, M. Verani, A safeguarded dual weighted residual method. IMA J. Numer. Anal. **29**(1), 126–140 (2009)
253. S. Norburn, D. Silvester, Stabilised vs stable mixed methods for incompressible flow. Comput. Methods Appl. Mech. Eng. **33**(1), 107–127 (1996)
254. C. Nystedt, A priori and a posteriori error estimates and adaptive finite element methods for a model eigenvalue problem. Technical Report Preprint NO 1995-05, Department of Mathematics, Chalmers University of Technology, 1995
255. J.T. Oden, K. Vemaganti, Estimation of local modeling error and goal-oriented modeling of heterogeneous materials; part II: a computational environment for adaptive modeling of heterogeneous elastic solids. Comput. Methods Appl. Mech. Eng. **190**, 6089–6124 (2001)
256. M.O. Olshanskii T. Gelhard, G. Lube, J.H. Starcke, Stabilized finite element schemes with LBB-stable elements for incompressible flows. J. Comput. Appl. Math. **177**, 243–267 (2005)
257. S. Osher, R. Fedkiw, *Level Set Methods and Dynamic Implicit Surfaces*. Applied Mathematical Sciences (Springer, New York, 2003)
258. J. Peraire, M. Vahdati, K. Morgan, O.C. Zienkiewicz, Adaptive remeshing for compressible flow computations. J. Comput. Phys. **72**, 449–466 (1987)
259. O. Pironneau, An energy stable monolithic Eulerian fluid-structure numerical scheme with compressible materials. To appear in P.G. Ciarlet 80th Birthday Volume (2018). arXiv:1607.08083
260. T.K. Prasanth, S. Mittal, Vortex-induced vibrations of a circular cylinder at low Reynolds numbers. J. Fluid Mech. **594**, 463–491 (2008)
261. T.K. Prasanth, S. Mittal, Vortex-induced vibration of two circular cylinders at low Reynolds number. J. Fluids Struct. **25**, 731–741 (2009)
262. A. Prohl, *Projection and Quasi-Compressibility Methods for Solving the Incompressible Navier-Stokes Equations*. Advances in Numerical Mathematics (Springer, Berlin, 1997)
263. A. Quaini, A. Quarteroni, A semi-implicit approach for fluid-structure interaction based on an algebraic fractional step method. Math. Models Methods Appl. Sci. **17**, 957–983 (2007)
264. L.B. Rall, *Automatic Differentiation - Techniques and Applications*. Lecture Notes in Computer Science, vol. 20 (Springer, Berlin, 1981)
265. R. Rannacher, On finite element approximation of general boundary value problems in nonlinear elasticity. Calcolo **17**(2), 175–193 (1980)
266. R. Rannacher, Finite element solution of diffusion problems with irregular data. Numer. Math. **43**, 309–327 (1984)
267. R. Rannacher, On the convergence of the Newton-Raphson method for strongly nonlinear problems, in *Nonlinear Computational Mechanics, State of the Art*, ed. by P. Wriggers, W. Wagner (Springer, Berlin, 1991), pp. 11–30
268. R. Rannacher, *Numerik Partieller Differentialgleichungen*. Universität Heidelberg, 2008, http://numerik.iwr.uni-heidelberg.de/~lehre/notes/. Vorlesungsskriptum
269. R. Rannacher, *Special Topics in Numerics I (FEM for Nonlinear Problems)*. Universität Heidelberg, 2016, http://numerik.iwr.uni-heidelberg.de/~lehre/notes/. Vorlesungsskriptum

270. R. Rannacher, T. Richter, An adaptive finite element method for fluid-structure interaction problems based on a fully Eulerian formulation, in *Fluid-Structure Interaction II, Modelling, Simulation, Optimization*, ed. by H.J. Bungartz, M. Mehl, M. Schäfer. Lecture Notes in Computational Science and Engineering, vol. 73 (Springer, Berlin, 2010), pp. 159–192
271. R. Rannacher, T. Richter, A priori estimates for the stokes equations with slip boundary conditions on curved domains (2017, submitted)
272. R. Rannacher, L.R. Scott, Some optimal error estimates for piecewise linear finite element approximations. Math. Comput. **38**, 437–445 (1982)
273. R. Rannacher, F.-T. Suttmeier, A posteriori error control in finite element methods via duality techniques: Application to perfect plasticity. Comput. Mech. **21**, 123–133 (1998)
274. R. Rannacher, F.-T. Suttmeier, A posteriori error estimation and mesh adaptation for finite element models in elasto-plasticity. Comput. Methods Appl. Mech. Eng. **176**, 333–361 (1999)
275. M. Razzaq, H. Damanik, J. Hron, A. Ouazzi, S. Turek, FEM multigrid techniques for fluid-structure interaction with application to hemodynamics. Appl. Numer. Math. **62**(9), 1156–1170 (2012)
276. T. Richter, Funktionalorientierte Gitteroptimierung bei der Finite-Elemente Approximation elliptischer Differentialgleichungen. Diplomarbeit, Universität Heidelberg, June 2001
277. T. Richter, Parallel multigrid for adaptive finite elements and its application to 3D flow problem, Ph.D. thesis, Universität Heidelberg, 2005. URN:nbn:de:bsz:16-opus-57433
278. T. Richter, A fully Eulerian formulation for fluid-structure-interaction problems with large deformations and free structure movement, in *V. European Conference on Computational Fluid Dynamics ECCOMAS CFD*, Lisbon, Portugal, ed. by J.C.F. Pereira, A. Sequira (2010)
279. T. Richter, A posteriori error estimation and anisotropy detection with the dual weighted residual method. Int. J. Numer. Math. Fluids **62**(1), 90–118 (2010)
280. T. Richter, Goal oriented error estimation for fluid-structure interaction problems. Comput. Methods Appl. Mech. Eng. **223/224**, 28–42 (2012)
281. T. Richter, Anisotropic finite elements for fluid-structure interactions, in *Numerical Mathematics and Advanced Applications-ENUMATH 2011* (Springer, Berlin, 2013), pp. 73–70
282. T. Richter, A fully Eulerian formulation for fluid-structure interactions. J. Comput. Phys. **223**, 227–240 (2013)
283. T. Richter, A monolithic geometric multigrid solver for fluid-structure interactions in ALE formulation. Int. J. Numer. Methods Eng. **104**(5), 372–390 (2015)
284. T. Richter, S. Frei, Second order time-stepping for parabolic interface problems with moving interfaces. Modèl. Math. Anal. Numér. (2017) . https://doi.org/10.1051/m2an/2016072
285. T. Richter, T. Wick, Finite elements for fluid-structure interaction in ALE and fully Eulerian coordinates. Comput. Methods Appl. Mech. Eng. **199**(41–44), 2633–2642 (2010)
286. T. Richter, T. Wick, Optimal control and parameter estimation for stationary fluid-structure interaction problems. SIAM J. Sci. Comput. **35**(5), B1085–B1104 (2013)
287. T. Richter, T. Wick, On time discretizations of fluid-structure interactions, in *Multiple Shooting and Time Domain Decomposition Methods*, ed. by T. Carraro, M. Geiger, S. Körkel, R. Rannacher. Contributions in Mathematical and Computational Science, vol. 9 (Springer, Cham, 2015), pp. 377–400
288. T. Richter, T. Wick, Variational localizations of the dual weighted residual method. J. Comput. Appl. Math. **279**, 192–208 (2015)
289. T. Richter, A. Springer, B. Vexler, Efficient numerical realization of discontinuous Galerkin methods for temporal discretization of parabolic problems. Numer. Math. **124**(1), 151–182 (2013)
290. R.S. Rivlin, J.L. Ericksen, Stress-deformation relations for isotropic materials. J. Ration. Mech. Anal., **4**, 323–425 (1955). Reprinted in Rational Mechanics of Materials. International Science Review Series, (Gordon & Breach, New York, 1965)
291. E.K. Rodriguez, A. Hoger, A.D. McCulloch, Stress-dependent finite growth in soft elastic tissues. J. Biomech. **4**, 455–467 (1994)
292. A. Rössle, Corner singularities and regularity of weak solutions for the two-dimensional Lamé equations on domains with angular corners. J. Elast. **60**, 57–75 (2000)

293. W. Rudin, *Functional Analysis*. International Series in Pure and Applied Mathematics (McGraw-Hill, New York, 1991)
294. M. Rumpf, A variational approach to optimal meshes. Numer. Math. **72**, 523–540 (1996)
295. Y. Saad, *Iterative Methods for Sparse Linear Systems* (PWS Publishing Company, Boston, 1996)
296. P. Sackinger, P. Schunk, R. Rao, A Newton-Raphson pseudo-solid domain mapping technique for free and moving boundary problems: a finite element implementation. J. Comput. Phys. **125**(1), 83–103 (1996)
297. T. Sarpkaya, A critical review of the intrinsic nature of vortex-induced vibrations. J. Fluids Struct. **19**, 389–447 (2004)
298. S. Sathe, T.E. Tezduyar, Modeling of fluid-structure interactions with the space-time finite elements: contact problems. Comput. Mech. **43**(1), 51–60 (2008)
299. M. Schäfer, S. Turek, Benchmark computations of laminar flow around a cylinder. (With support by F. Durst, E. Krause and R. Rannacher), in *Flow Simulation with High-Performance Computers II. DFG Priority Research Program Results 1993–1995*, ed. by E.H. Hirschel. Notes on Numerical Fluid Mechanics, vol. 52 (Vieweg, Wiesbaden, 1996), pp. 547–566
300. M. Schäfer, D.C. Sternel, G. Becker, P. Pironkov, Efficient numerical simulation and optimization of fluid-structure interaction, in *Fluid-Structure Interaction II: Modeling, Simulation, Optimization*, ed. by H.-J. Bungartz, M. Schäfer. Lecture Notes in Computational Science and Engineering (Springer, Berlin, 2010), pp. 131–158
301. A.H. Schatz, L.B. Wahlbin, On the quasi-optimality in L^∞ of the H^1-projection into finite element spaces. Math. Comput. **38**, 1–22 (1982)
302. M. Schmich, Adaptive finite element methods for computing nonstationary incompressible flows, Ph.D. thesis, Universität Heidelberg, 2009. URN:nbn:de:bsz:16-opus-102001
303. M. Schmich, B. Vexler, Adaptivity with dynamic meshes for space-time finite element discretizations of parabolic equations. SIAM J. Sci. Comput. **30**(1), 369–393 (2008)
304. B. Schweizer, *Partielle Differentialgleichungen. Eine anwendungsorientierte Einführung* (Springer, Berlin, 2013)
305. L.R. Scott, S. Zhang, Finite element interpolation of nonsmooth functions satisfying boundary conditions. Math. Comput. **54**(190), 483–493 (1990)
306. A. Seitz, Vergleich von Teilschritt-Theta-Verfahren, Master's thesis, Universität Heidelberg, 2013. Diploma's thesis, Universität Heidelberg
307. J.A. Sethian, *Level Set Methods and Fast Marching Methods Evolving Interfaces in Computational Geometry*. Fluid mechanics, Computer Vision and Material Science. (Cambridge University Press, Cambridge, 1999)
308. P. Shi, S. Wright, $W^{2,p}$-regularity of the displacement problem for the lamé system on $W^{2,s}$ domains. J. Math. Anal. Appl. **239**(2), 291–305 (1999)
309. G.R. Shubin, J.B. Bell, An analysis of grid orientation effect in numerical simulation of miscible displacement. Comput. Math. Appl. Mech. Eng. **47**, 47–71 (1984)
310. T. Siekmann, Parallelisierte Vanka-Glätter für komplexe Strömungsprobleme, Master's thesis, Universität Heidelberg, 2015
311. J. Simon, Differentiation with respect to the domain in boundary value problems. Numer. Funct. Anal. Optim. **2**(7–8), 649–687 (1980)
312. H. Sohr, *The Navier-Stokes Equations. An Elementary Functional Analytic Approach*. Birkhäuser Advanced Texts (Birkhäuser, Basel, 2001)
313. J. Sokołowski, J.-P. Zolésio, *Introduction to Shape Optimization*. Computational Mathematics, vol. 16 (Springer, Berlin, 1992)
314. F. Sonner, Monolithische Löser für ein lineares Fluid-Struktur-Interaktionsproblem, Master's thesis, Universität Heidelberg, 2015
315. F. Sonner, Analysis of temporal multiscales with partial differential equations, Ph.D. thesis, University of Erlangen-Nuremberg, 2018 (in preparation)
316. F. Sonner, T. Richter, Optimal pressure estimates for the Crank-Nicolson discretization of the incompressible Navier-Stokes Equations (2017, submitted)

317. A. Springer, Efficient higher order discontinuous Galerkin time discretizations for parabolic optimal control problems, Ph.D. thesis, Technische Universität München, 2015. URN:nbn:de:bvb:91-diss-20150519-1237294-1-6
318. K. Stein, T.E. Tezduyar, R. Benney, Mesh moving techniques for fluid-structure interactions with large displacements. J. Appl. Math. **70**, 58–63 (2003)
319. R. Stevenson, An optimal adaptive finite element method. SIAM J. Numer. Anal. **42**(5), 2188–2217 (2005)
320. K. Stüben, A review of algebraic multigrid. J. Comput. Appl. Math. **128**(1–2), 281–309 (2001)
321. R. Temam, *Navier-Stokes Equations: Theory and Numerical Analysis* (American Mathematical Society, Providence, 2000)
322. T.E. Tezduyar, Stabilized finite element formulations for incompressible flow computations. Adv. Appl. Mech. **28**, 1–44 (1992)
323. V. Thomée, *Galerkin Finite Element Methods for Parabolic Problems*. Springer Series in Computational Mathematics, vol. 25 (Springer, Berlin, 1997)
324. A.N. Tikhonov, A.A. Samarskii, Homogeneous difference schemes. USSR Comput. Math. Math. Phys. **1**, 5–67 (1962)
325. F. Tröltzsch, *Optimale Steuerung partieller Differentialgleichungen - Theorie, Verfahren und Anwendungen* (Vieweg, Wiesbaden, 2005)
326. F. Tröltzsch, *Optimal Control of Partial Differential Equations - Theory, Methods and Applications*. Graduate Studies in Mathematics, vol. 112 (American Mathematical Society, Providence, 2010). Translation of the second German edition by J. Sprekels
327. C. Truesdell, W. Noll, *The Non-Linear Field Theories of Mechanics* (Springer, Berlin, 2004)
328. S. Turek, L. Rivkind, J. Hron, R. Glowinski, Numerical study of a modified time-stepping theta-scheme for incompressible flow simulations. J. Sci. Comput. **28**(2–3), 533–547 (2006)
329. S. Turek, J. Hron, M. Madlik, M. Razzaq, H. Wobker, J. Acker, Numerical simulation and benchmarking of a monolithic multigrid solver for fluid-structure interaction problems with application to hemodynamics. Technical report, Fakultät für Mathematik, TU Dortmund, Feb 2010. Ergebnisberichte des Instituts für Angewandte Mathematik, Nummer 403
330. S. Turek, J. Hron, M. Razzaq, H. Wobker, M. Schäfer. Numerical benchmarking of fluid-structure interaction: A comparison of different discretization and solution approaches, in *Fluid Structure Interaction II: Modeling, Simulation and Optimization*, ed. by H.J. Bungartz, M. Mehl, M. Schäfer (Springer, Berlin, 2010)
331. E. van Brummelen, Added mass effects of compressible and incompressible flows in fluid-structure interaction. J. Appl. Mech. **76**, 021206 (2009)
332. E. van Brummelen, Partitioned iterative solution methods for fluid-structure interaction. Int. J. Numer. Math. Fluids. **65**, 3–27 (2011)
333. M. Van Dyke, *An Album of Fluid Motion* (Parabolic Press, Stanford, 1982)
334. S.P. Vanka, Block-implicit multigrid solution of Navier-Stokes equations in primitive variables. J. Comput. Phys. **65**, 138–158 (1985)
335. D.A. Venditti, D.L. Darmofal, Anisotropic grid adaptation for functional outputs: application to two-dimensional viscous flows. J. Comput. Phys. **187**, 22–46 (2003)
336. R. Verfürth, *A Review of A Posteriori Error Estimation and Adaptive Mesh-Refinement Techniques* (Wiley/Teubner, New York/Stuttgart, 1996)
337. B. Vexler, W. Wollner, Adaptive finite elements for elliptic optimization problems with control constrains. SIAM J. Contin. Opt. **47**, 509–534 (2008)
338. M. von Laer, Finite element simulation of non-newtonian flows, Master's thesis, Universität Heidelberg, 2013
339. W.A. Wall, Fluid-structure interaction with stabilized finite elements, Ph.D. thesis, University of Stuttgart, 1999. URN:nbn:de:bsz:93-opus-6234
340. T. Washio, T. Hisada, H. Watanabe, T.E. Tezduyar, A robust preconditioner for fluid-structure interaction problems. Comput. Methods Appl. Mech. Eng. **194**(39–41), 4027–4047 (2005)
341. P. Wesseling, *An Introduction to Multigrid Methods* (Wiley, Chichester, 1991)

342. T. Wick, Fluid-structure interactions using different mesh motion techniques. Comput. Struct. **89**, 1456–1467 (2011)
343. T. Wick, Adaptive finite element simulation of fluid-structure interaction with application to heart-valve dynamics. Ph.D. thesis, Universität Heidelberg, 2012. URN:nbn:de:bsz:16-opus-129926
344. T. Wick, Benchmark results for fluid-structure interaction problems in ALE coordinates using different mesh motion techniques, Technical report, University of Heidelberg, 2012
345. T. Wick, Fully Eulerian fluid-structure interaction for time-dependent problems. Comput. Methods Appl. Mech. Eng. **255**(0), 14–26 (2012)
346. T. Wick, Coupling of fully Eulerian and arbitrary Lagrangian-Eulerian methods for fluid-structure interaction computations. Comput. Mech. **52**(5), 1113–1124 (2013)
347. T. Wick, Solving monolithic fluid-structure interaction problems in arbitrary Lagrangian Eulerian coordinates with the deal.ii library. Arch. Numer. Softw. **1**, 1–19 (2013)
348. T. Wick, Stability estimates and numerical comparison of second order time-stepping schemes for fluid-structure interactions, in *Numerical Mathematics and Advanced Applications 2011:, Proceedings of ENUMATH 2011*, Leicester, Sept 2011, A. Cangiani, R.L. Davidchack, E. Georgoulis, A.N. Gorban, J. Levesley, M.V. Tretyakov (2013), pp. 625–632
349. C.H.K. Williamson, R. Govardhan, Vortex induced vibration. Ann. Rev. Fluid Mech. **36**, 413–455 (2004)
350. J. Wloka, *Partielle Differentialgleichungen* (Teubner, Stuttgart, 1982)
351. J. Wloka, *Partial Differential Equations* (Cambridge University Press, Cambridge, 1987)
352. H. Xie, K. Ito, Z.-L. Li, J. Toivanen, A finite element method for interface problems with locally modified triangulation. Contemp. Math. **466**, 179–190 (2008)
353. H. Yang, W. Zulehner, Numerical simulation of fluid-structure interaction problems on hybrid meshes with algebraic multigrid methods. J. Comput. Appl. Math. **235**(18), 5367–5379 (2011)
354. Y. Yang, Mathematical modeling and simulation of the evolution of plaques in blood vessels, Ph.D. thesis, Universität Heidelberg, 2014. doi:10.11588/heidok.00016425
355. Y. Yang, W. Jäger, M. Neuss-Radu, T. Richter, Mathematical modeling and simulation of the evolution of plaques in blood vessels. J. Math. Biol. **72**(4), 973–996 (2016)
356. Y. Yang, T. Richter, W. Jaeger, M. Neuss-Radu, An ALE approach to mechano-chemical processes in fluid-structure interactions. Int. J. Numer. Math. Fluids **84**(4), 199–220 (2017)
357. S. Yirgit, M. Schäfer, M. Heck, Grid movement techniques and their influence on laminar fluid-structure interaction problems. J. Fluids Struct. **24**(6), 819–832 (2008)
358. K.G. van der Zee, E.H. van Brummelen, R. de Borst, Goal-oriented error estimation and adaptivity for free-boundary problems: the domain-map linearization approach. SIAM J. Sci. Comput. **32**(2), 1074–1092 (2010)
359. K.G. van der Zee, E.H. van Brummelen, R. de Borst, Goal-oriented error estimation and adaptivity for free-boundary problems: the shape-linearization approach. SIAM J. Sci. Comput. **32**(2), 1093–1118 (2010)
360. A. Ženíšek, The finite element method for nonlinear elliptic equations with discontinuous coefficients. Numer. Math. **58**, 51–77 (1990)
361. O.C. Zienkiewicz, J. Wu, Automatic directional refinement in adaptive analysis of compressible flows. Int. J. Numer. Methods Eng. **37**, 2189–2210 (1994)
362. J.-P. Zolesio, M.C. Delfour, *Shapes and Geometries: Analysis, Differential Calculus and Optimization* (SIAM, Philadelphia, 2001)
363. P. Zunino, Analysis of backward Euler/extended finite element discretization of parabolic problems with moving interfaces. Comput. Methods Appl. Mech. Eng. **258**, 152–165 (2013)

Index

T. Richter, *Fluid-structure Interactions*, Lecture Notes in Computational Science and Engineering 118, DOI 10.1007/978-3-319-63970-3

Editorial Policy

1. Volumes in the following three categories will be published in LNCSE:

i) Research monographs
ii) Tutorials
iii) Conference proceedings

Those considering a book which might be suitable for the series are strongly advised to contact the publisher or the series editors at an early stage.

2. Categories i) and ii). Tutorials are lecture notes typically arising via summer schools or similar events, which are used to teach graduate students. These categories will be emphasized by Lecture Notes in Computational Science and Engineering. **Submissions by interdisciplinary teams of authors are encouraged.** The goal is to report new developments – quickly, informally, and in a way that will make them accessible to non-specialists. In the evaluation of submissions timeliness of the work is an important criterion. Texts should be well-rounded, well-written and reasonably self-contained. In most cases the work will contain results of others as well as those of the author(s). In each case the author(s) should provide sufficient motivation, examples, and applications. In this respect, Ph.D. theses will usually be deemed unsuitable for the Lecture Notes series. Proposals for volumes in these categories should be submitted either to one of the series editors or to Springer-Verlag, Heidelberg, and will be refereed. A provisional judgement on the acceptability of a project can be based on partial information about the work: a detailed outline describing the contents of each chapter, the estimated length, a bibliography, and one or two sample chapters – or a first draft. A final decision whether to accept will rest on an evaluation of the completed work which should include

– at least 100 pages of text;
– a table of contents;
– an informative introduction perhaps with some historical remarks which should be accessible to readers unfamiliar with the topic treated;
– a subject index.

3. Category iii). Conference proceedings will be considered for publication provided that they are both of exceptional interest and devoted to a single topic. One (or more) expert participants will act as the scientific editor(s) of the volume. They select the papers which are suitable for inclusion and have them individually refereed as for a journal. Papers not closely related to the central topic are to be excluded. Organizers should contact the Editor for CSE at Springer at the planning stage, see *Addresses* below.

In exceptional cases some other multi-author-volumes may be considered in this category.

4. Only works in English will be considered. For evaluation purposes, manuscripts may be submitted in print or electronic form, in the latter case, preferably as pdf- or zipped ps-files. Authors are requested to use the LaTeX style files available from Springer at http://www.springer.com/gp/authors-editors/book-authors-editors/manuscript-preparation/5636 (Click on LaTeX Template → monographs or contributed books).

For categories ii) and iii) we strongly recommend that all contributions in a volume be written in the same LaTeX version, preferably LaTeX2e. Electronic material can be included if appropriate. Please contact the publisher.

Careful preparation of the manuscripts will help keep production time short besides ensuring satisfactory appearance of the finished book in print and online.

5. The following terms and conditions hold. Categories i), ii) and iii):

Authors receive 50 free copies of their book. No royalty is paid.
Volume editors receive a total of 50 free copies of their volume to be shared with authors, but no royalties.

Authors and volume editors are entitled to a discount of 33.3 % on the price of Springer books purchased for their personal use, if ordering directly from Springer.

6. Springer secures the copyright for each volume.

Addresses:

Timothy J. Barth
NASA Ames Research Center
NAS Division
Moffett Field, CA 94035, USA
barth@nas.nasa.gov

Michael Griebel
Institut für Numerische Simulation
der Universität Bonn
Wegelerstr. 6
53115 Bonn, Germany
griebel@ins.uni-bonn.de

David E. Keyes
Mathematical and Computer Sciences
and Engineering
King Abdullah University of Science
and Technology
P.O. Box 55455
Jeddah 21534, Saudi Arabia
david.keyes@kaust.edu.sa

and

Department of Applied Physics
and Applied Mathematics
Columbia University
500 W. 120 th Street
New York, NY 10027, USA
kd2112@columbia.edu

Risto M. Nieminen
Department of Applied Physics
Aalto University School of Science
and Technology
00076 Aalto, Finland
risto.nieminen@aalto.fi

Dirk Roose
Department of Computer Science
Katholieke Universiteit Leuven
Celestijnenlaan 200A
3001 Leuven-Heverlee, Belgium
dirk.roose@cs.kuleuven.be

Tamar Schlick
Department of Chemistry
and Courant Institute
of Mathematical Sciences
New York University
251 Mercer Street
New York, NY 10012, USA
schlick@nyu.edu

Editor for Computational Science
and Engineering at Springer:
Martin Peters
Springer-Verlag
Mathematics Editorial IV
Tiergartenstrasse 17
69121 Heidelberg, Germany
martin.peters@springer.com

Lecture Notes in Computational Science and Engineering

1. D. Funaro, *Spectral Elements for Transport-Dominated Equations.*
2. H.P. Langtangen, *Computational Partial Differential Equations.* Numerical Methods and Diffpack Programming.
3. W. Hackbusch, G. Wittum (eds.), *Multigrid Methods V.*
4. P. Deuflhard, J. Hermans, B. Leimkuhler, A.E. Mark, S. Reich, R.D. Skeel (eds.), *Computational Molecular Dynamics: Challenges, Methods, Ideas.*
5. D. Kröner, M. Ohlberger, C. Rohde (eds.), *An Introduction to Recent Developments in Theory and Numerics for Conservation Laws.*
6. S. Turek, *Efficient Solvers for Incompressible Flow Problems.* An Algorithmic and Computational Approach.
7. R. von Schwerin, ***M**ulti **B**ody **S**ystem **SIM**ulation.* Numerical Methods, Algorithms, and Software.
8. H.-J. Bungartz, F. Durst, C. Zenger (eds.), *High Performance Scientific and Engineering Computing.*
9. T.J. Barth, H. Deconinck (eds.), *High-Order Methods for Computational Physics.*
10. H.P. Langtangen, A.M. Bruaset, E. Quak (eds.), *Advances in Software Tools for Scientific Computing*.
11. B. Cockburn, G.E. Karniadakis, C.-W. Shu (eds.), *Discontinuous Galerkin Methods.* Theory, Computation and Applications.
12. U. van Rienen, *Numerical Methods in Computational Electrodynamics.* Linear Systems in Practical Applications.
13. B. Engquist, L. Johnsson, M. Hammill, F. Short (eds.), *Simulation and Visualization on the Grid.*
14. E. Dick, K. Riemslagh, J. Vierendeels (eds.), *Multigrid Methods VI.*
15. A. Frommer, T. Lippert, B. Medeke, K. Schilling (eds.), *Numerical Challenges in Lattice Quantum Chromodynamics.*
16. J. Lang, *Adaptive Multilevel Solution of Nonlinear Parabolic PDE Systems.* Theory, Algorithm, and Applications.
17. B.I. Wohlmuth, *Discretization Methods and Iterative Solvers Based on Domain Decomposition.*
18. U. van Rienen, M. Günther, D. Hecht (eds.), *Scientific Computing in Electrical Engineering.*
19. I. Babuška, P.G. Ciarlet, T. Miyoshi (eds.), *Mathematical Modeling and Numerical Simulation in Continuum Mechanics.*
20. T.J. Barth, T. Chan, R. Haimes (eds.), *Multiscale and Multiresolution Methods.* Theory and Applications.
21. M. Breuer, F. Durst, C. Zenger (eds.), *High Performance Scientific and Engineering Computing.*
22. K. Urban, *Wavelets in Numerical Simulation.* Problem Adapted Construction and Applications.
23. L.F. Pavarino, A. Toselli (eds.), *Recent Developments in Domain Decomposition Methods.*

24. T. Schlick, H.H. Gan (eds.), *Computational Methods for Macromolecules: Challenges and Applications.*

25. T.J. Barth, H. Deconinck (eds.), *Error Estimation and Adaptive Discretization Methods in Computational Fluid Dynamics*.

26. M. Griebel, M.A. Schweitzer (eds.), *Meshfree Methods for Partial Differential Equations*.

27. S. Müller, *Adaptive Multiscale Schemes for Conservation Laws*.

28. C. Carstensen, S. Funken, W. Hackbusch, R.H.W. Hoppe, P. Monk (eds.), *Computational Electromagnetics*.

29. M.A. Schweitzer, *A Parallel Multilevel Partition of Unity Method for Elliptic Partial Differential Equations*.

30. T. Biegler, O. Ghattas, M. Heinkenschloss, B. van Bloemen Waanders (eds.), *Large-Scale PDE-Constrained Optimization*.

31. M. Ainsworth, P. Davies, D. Duncan, P. Martin, B. Rynne (eds.), *Topics in Computational Wave Propagation*. Direct and Inverse Problems.

32. H. Emmerich, B. Nestler, M. Schreckenberg (eds.), *Interface and Transport Dynamics.* Computational Modelling.

33. H.P. Langtangen, A. Tveito (eds.), *Advanced Topics in Computational Partial Differential Equations.* Numerical Methods and Diffpack Programming.

34. V. John, *Large Eddy Simulation of Turbulent Incompressible Flows.* Analytical and Numerical Results for a Class of LES Models.

35. E. Bänsch (ed.), *Challenges in Scientific Computing - CISC 2002.*

36. B.N. Khoromskij, G. Wittum, *Numerical Solution of Elliptic Differential Equations by Reduction to the Interface.*

37. A. Iske, *Multiresolution Methods in Scattered Data Modelling.*

38. S.-I. Niculescu, K. Gu (eds.), *Advances in Time-Delay Systems.*

39. S. Attinger, P. Koumoutsakos (eds.), *Multiscale Modelling and Simulation.*

40. R. Kornhuber, R. Hoppe, J. Périaux, O. Pironneau, O. Wildlund, J. Xu (eds.), *Domain Decomposition Methods in Science and Engineering.*

41. T. Plewa, T. Linde, V.G. Weirs (eds.), *Adaptive Mesh Refinement – Theory and Applications.*

42. A. Schmidt, K.G. Siebert, *Design of Adaptive Finite Element Software.* The Finite Element Toolbox ALBERTA.

43. M. Griebel, M.A. Schweitzer (eds.), *Meshfree Methods for Partial Differential Equations II.*

44. B. Engquist, P. Lötstedt, O. Runborg (eds.), *Multiscale Methods in Science and Engineering.*

45. P. Benner, V. Mehrmann, D.C. Sorensen (eds.), *Dimension Reduction of Large-Scale Systems.*

46. D. Kressner, *Numerical Methods for General and Structured Eigenvalue Problems.*

47. A. Boriçi, A. Frommer, B. Joó, A. Kennedy, B. Pendleton (eds.), *QCD and Numerical Analysis III*.

48. F. Graziani (ed.), *Computational Methods in Transport.*

49. B. Leimkuhler, C. Chipot, R. Elber, A. Laaksonen, A. Mark, T. Schlick, C. Schütte, R. Skeel (eds.), *New Algorithms for Macromolecular Simulation.*

50. M. Bücker, G. Corliss, P. Hovland, U. Naumann, B. Norris (eds.), *Automatic Differentiation: Applications, Theory, and Implementations.*

51. A.M. Bruaset, A. Tveito (eds.), *Numerical Solution of Partial Differential Equations on Parallel Computers.*

52. K.H. Hoffmann, A. Meyer (eds.), *Parallel Algorithms and Cluster Computing.*

53. H.-J. Bungartz, M. Schäfer (eds.), *Fluid-Structure Interaction.*

54. J. Behrens, *Adaptive Atmospheric Modeling.*

55. O. Widlund, D. Keyes (eds.), *Domain Decomposition Methods in Science and Engineering XVI.*

56. S. Kassinos, C. Langer, G. Iaccarino, P. Moin (eds.), *Complex Effects in Large Eddy Simulations.*

57. M. Griebel, M.A Schweitzer (eds.), *Meshfree Methods for Partial Differential Equations III.*

58. A.N. Gorban, B. Kégl, D.C. Wunsch, A. Zinovyev (eds.), *Principal Manifolds for Data Visualization and Dimension Reduction.*

59. H. Ammari (ed.), *Modeling and Computations in Electromagnetics: A Volume Dedicated to Jean-Claude Nédélec.*

60. U. Langer, M. Discacciati, D. Keyes, O. Widlund, W. Zulehner (eds.), *Domain Decomposition Methods in Science and Engineering XVII.*

61. T. Mathew, *Domain Decomposition Methods for the Numerical Solution of Partial Differential Equations.*

62. F. Graziani (ed.), *Computational Methods in Transport: Verification and Validation.*

63. M. Bebendorf, *Hierarchical Matrices.* A Means to Efficiently Solve Elliptic Boundary Value Problems.

64. C.H. Bischof, H.M. Bücker, P. Hovland, U. Naumann, J. Utke (eds.), *Advances in Automatic Differentiation.*

65. M. Griebel, M.A. Schweitzer (eds.), *Meshfree Methods for Partial Differential Equations IV*.

66. B. Engquist, P. Lötstedt, O. Runborg (eds.), *Multiscale Modeling and Simulation in Science.*

67. I.H. Tuncer, Ü. Gülcat, D.R. Emerson, K. Matsuno (eds.), *Parallel Computational Fluid Dynamics 2007.*

68. S. Yip, T. Diaz de la Rubia (eds.), *Scientific Modeling and Simulations*.

69. A. Hegarty, N. Kopteva, E. O'Riordan, M. Stynes (eds.), *BAIL* 2008 – *Boundary and Interior Layers.*

70. M. Bercovier, M.J. Gander, R. Kornhuber, O. Widlund (eds.), *Domain Decomposition Methods in Science and Engineering XVIII.*

71. B. Koren, C. Vuik (eds.), *Advanced Computational Methods in Science and Engineering.*

72. M. Peters (ed.), *Computational Fluid Dynamics for Sport Simulation.*

73. H.-J. Bungartz, M. Mehl, M. Schäfer (eds.), *Fluid Structure Interaction II - Modelling, Simulation, Optimization.*

74. D. Tromeur-Dervout, G. Brenner, D.R. Emerson, J. Erhel (eds.), *Parallel Computational Fluid Dynamics 2008.*

75. A.N. Gorban, D. Roose (eds.), *Coping with Complexity: Model Reduction and Data Analysis.*

76. J.S. Hesthaven, E.M. Rønquist (eds.), *Spectral and High Order Methods for Partial Differential Equations.*

77. M. Holtz, *Sparse Grid Quadrature in High Dimensions with Applications in Finance and Insurance*.

78. Y. Huang, R. Kornhuber, O.Widlund, J. Xu (eds.), *Domain Decomposition Methods in Science and Engineering XIX*.

79. M. Griebel, M.A. Schweitzer (eds.), *Meshfree Methods for Partial Differential Equations V*.

80. P.H. Lauritzen, C. Jablonowski, M.A. Taylor, R.D. Nair (eds.), *Numerical Techniques for Global Atmospheric Models*.

81. C. Clavero, J.L. Gracia, F.J. Lisbona (eds.), *BAIL 2010 – Boundary and Interior Layers, Computational and Asymptotic Methods*.

82. B. Engquist, O. Runborg, Y.R. Tsai (eds.), *Numerical Analysis and Multiscale Computations*.

83. I.G. Graham, T.Y. Hou, O. Lakkis, R. Scheichl (eds.), *Numerical Analysis of Multiscale Problems*.

84. A. Logg, K.-A. Mardal, G. Wells (eds.), *Automated Solution of Differential Equations by the Finite Element Method*.

85. J. Blowey, M. Jensen (eds.), *Frontiers in Numerical Analysis - Durham 2010*.

86. O. Kolditz, U.-J. Gorke, H. Shao, W. Wang (eds.), *Thermo-Hydro-Mechanical-Chemical Processes in Fractured Porous Media - Benchmarks and Examples*.

87. S. Forth, P. Hovland, E. Phipps, J. Utke, A. Walther (eds.), *Recent Advances in Algorithmic Differentiation*.

88. J. Garcke, M. Griebel (eds.), *Sparse Grids and Applications*.

89. M. Griebel, M.A. Schweitzer (eds.), *Meshfree Methods for Partial Differential Equations VI*.

90. C. Pechstein, *Finite and Boundary Element Tearing and Interconnecting Solvers for Multiscale Problems*.

91. R. Bank, M. Holst, O. Widlund, J. Xu (eds.), *Domain Decomposition Methods in Science and Engineering XX*.

92. H. Bijl, D. Lucor, S. Mishra, C. Schwab (eds.), *Uncertainty Quantification in Computational Fluid Dynamics*.

93. M. Bader, H.-J. Bungartz, T. Weinzierl (eds.), *Advanced Computing*.

94. M. Ehrhardt, T. Koprucki (eds.), *Advanced Mathematical Models and Numerical Techniques for Multi-Band Effective Mass Approximations*.

95. M. Azaïez, H. El Fekih, J.S. Hesthaven (eds.), *Spectral and High Order Methods for Partial Differential Equations ICOSAHOM 2012*.

96. F. Graziani, M.P. Desjarlais, R. Redmer, S.B. Trickey (eds.), *Frontiers and Challenges in Warm Dense Matter*.

97. J. Garcke, D. Pflüger (eds.), *Sparse Grids and Applications – Munich 2012*.

98. J. Erhel, M. Gander, L. Halpern, G. Pichot, T. Sassi, O. Widlund (eds.), *Domain Decomposition Methods in Science and Engineering XXI*.

99. R. Abgrall, H. Beaugendre, P.M. Congedo, C. Dobrzynski, V. Perrier, M. Ricchiuto (eds.), *High Order Nonlinear Numerical Methods for Evolutionary PDEs - HONOM 2013*.

100. M. Griebel, M.A. Schweitzer (eds.), *Meshfree Methods for Partial Differential Equations VII*.

101. R. Hoppe (ed.), *Optimization with PDE Constraints - OPTPDE 2014*.

102. S. Dahlke, W. Dahmen, M. Griebel, W. Hackbusch, K. Ritter, R. Schneider, C. Schwab, H. Yserentant (eds.), *Extraction of Quantifiable Information from Complex Systems*.

103. A. Abdulle, S. Deparis, D. Kressner, F. Nobile, M. Picasso (eds.), *Numerical Mathematics and Advanced Applications - ENUMATH 2013*.

104. T. Dickopf, M.J. Gander, L. Halpern, R. Krause, L.F. Pavarino (eds.), *Domain Decomposition Methods in Science and Engineering XXII*.

105. M. Mehl, M. Bischoff, M. Schäfer (eds.), *Recent Trends in Computational Engineering - CE2014*. Optimization, Uncertainty, Parallel Algorithms, Coupled and Complex Problems.

106. R.M. Kirby, M. Berzins, J.S. Hesthaven (eds.), *Spectral and High Order Methods for Partial Differential Equations - ICOSAHOM'14*.

107. B. Jüttler, B. Simeon (eds.), *Isogeometric Analysis and Applications 2014*.

108. P. Knobloch (ed.), *Boundary and Interior Layers, Computational and Asymptotic Methods – BAIL 2014*.

109. J. Garcke, D. Pflüger (eds.), *Sparse Grids and Applications – Stuttgart 2014*.

110. H. P. Langtangen, *Finite Difference Computing with Exponential Decay Models*.

111. A. Tveito, G.T. Lines, *Computing Characterizations of Drugs for Ion Channels and Receptors Using Markov Models*.

112. B. Karazösen, M. Manguoğlu, M. Tezer-Sezgin, S. Göktepe, Ö. Uğur (eds.), *Numerical Mathematics and Advanced Applications - ENUMATH 2015*.

113. H.-J. Bungartz, P. Neumann, W.E. Nagel (eds.), *Software for Exascale Computing - SPPEXA 2013-2015*.

114. G.R. Barrenechea, F. Brezzi, A. Cangiani, E.H. Georgoulis (eds.), *Building Bridges: Connections and Challenges in Modern Approaches to Numerical Partial Differential Equations*.

115. M. Griebel, M.A. Schweitzer (eds.), *Meshfree Methods for Partial Differential Equations VIII*.

116. C.-O. Lee, X.-C. Cai, D.E. Keyes, H.H. Kim, A. Klawonn, E.-J. Park, O.B. Widlund (eds.), *Domain Decomposition Methods in Science and Engineering XXIII*.

117. T. Sakurai, S. Zhang, T. Imamura, Y. Yusaku, K. Yoshinobu, H. Takeo (eds.), *Eigenvalue Problems: Algorithms, Software and Applications, in Petascale Computing*. EPASA 2015, Tsukuba, Japan, September 2015.

118. T. Richter (ed.), *Fluid-structure Interactions*. Models, Analysis and Finite Elements.

For further information on these books please have a look at our mathematics catalogue at the following URL: www.springer.com/series/3527

Monographs in Computational Science and Engineering

1. J. Sundnes, G.T. Lines, X. Cai, B.F. Nielsen, K.-A. Mardal, A. Tveito, *Computing the Electrical Activity in the Heart.*

For further information on this book, please have a look at our mathematics catalogue at the following URL: www.springer.com/series/7417

Texts in Computational Science and Engineering

1. H. P. Langtangen, *Computational Partial Differential Equations.* Numerical Methods and Diffpack Programming. 2nd Edition
2. A. Quarteroni, F. Saleri, P. Gervasio, *Scientific Computing with MATLAB and Octave.* 4th Edition
3. H. P. Langtangen, *Python Scripting for Computational Science*. 3rd Edition
4. H. Gardner, G. Manduchi, *Design Patterns for e-Science*.
5. M. Griebel, S. Knapek, G. Zumbusch, *Numerical Simulation in Molecular Dynamics*.
6. H. P. Langtangen, *A Primer on Scientific Programming with Python.* 5th Edition
7. A. Tveito, H. P. Langtangen, B. F. Nielsen, X. Cai, *Elements of Scientific Computing.*
8. B. Gustafsson, *Fundamentals of Scientific Computing.*
9. M. Bader, *Space-Filling Curves.*
10. M. Larson, F. Bengzon, *The Finite Element Method: Theory, Implementation and Applications.*
11. W. Gander, M. Gander, F. Kwok, *Scientific Computing: An Introduction using Maple and MATLAB.*
12. P. Deuflhard, S. Röblitz, *A Guide to Numerical Modelling in Systems Biology*.
13. M. H. Holmes, *Introduction to Scientific Computing and Data Analysis*.
14. S. Linge, H. P. Langtangen, *Programming for Computations* - A Gentle Introduction to Numerical Simulations with MATLAB/Octave.
15. S. Linge, H. P. Langtangen, *Programming for Computations* - A Gentle Introduction to Numerical Simulations with Python.
16. H.P. Langtangen, S. Linge, *Finite Difference Computing with PDEs* - A Modern Software Approach.

For further information on these books please have a look at our mathematics catalogue at the following URL: www.springer.com/series/5151